AN INVESTIGATION OF INTERFACIAL INSTABILITY DURING AIR ENTRAINMENT

A thesis submitted by

Peter John Veverka

B.ChE. 1988, University of Delaware
Newark, Delaware

M.S. 1991, Institute of Paper Science and Technology
Atlanta, Georgia

in partial fulfillment of the requirements
for the degree of Doctor of Philosophy from
the Institute of Paper Science and Technology
Atlanta, Georgia

December 1995

TABLE OF CONTENTS

LIST OF FIGURES

LIST OF TABLES

NOMENCLATURE

Dimensions

A-Ampere
L-Length
M-Mass
t-time
V-Volt

SYMBOLS

Roman Alphabet

a_c cavity aspect ratio, $a_c = d_c/H_L$
a_s acceleration rate of substrate during ramping type experiments, $[L/t^2]$
A_e area of substrate over which electrostatic charge is measured, $[L^2]$
A_1 fitted constant in Eq. [6.4] along with B_1, C_1, D_1, and E_1.
C capacitance of a small area of the substrate, [farads] = [A t/V]
d characteristic length scale used in dimensionless groups, [L]
d_c depth of coating cavity, [L]
d_t distance from tip of air pocket to first fringe, [L]
e coefficient in correlation $Ca_{ae} = eN_{pp}^{f}$
f coefficient in correlation for $Ca_{ae} = eN_{pp}^{f}$
f_N Nyquist sampling frequency, $[t^{-1}]$
f_s sampling frequency, $[t^{-1}]$
$F(x^*,\lambda)$ function used in predicting the stream function
g standard gravitational constant, 980.7 cm/s^2, $[L/t^2]$
G correction angle between the solid substrate and the optical axis, [°]
h height or thickness of an individual air pocket at any location measured normal to the solid/gas interface to gas/liquid interface, [L]
h_c height of wall in coating cavity, [L]
h_{cc} gap between lip and substrate in curtain coater Yasui and Tanaka (1990), [L]
h_i discretized height or thickness of an individual air pocket at any location measured normal from the solid/gas interface to the gas/liquid interface, [L]
h_s slot coater gap defined by Levi(1966), [L]
H_L height of liquid in cavity, [L]
k Boltzmann's constant, 1.3805×10^{-16} erg/molecule-°K, [L M/molecule-T]

k wavenumber equal to amplitude divided by wavelength,

$\vec{k}$ normal to solid substrate surface

K_c PID controller proportional gain constant

l_e electrostatic gap between substrate and grounded object, [L]

L_1 length of entire triangular air film from base to vertex, [L]

L_2 length of triangular air film in "air film" region from base to angular inflection point when $\varnothing_1/2 \neq (90\text{-}\varnothing_2)$, [°] or [radians]

L_3 length of triangular air film in "capillary tip" region from vertex to angular inflection point when $\varnothing_1/2 \neq (90\text{-}\varnothing_2)$, [°] or [radians]

L_c Capillary characteristic length, [L]

L_d Deryagin characteristic length, [L]

N Avogadro's number, 6.023×10^{23} molecules/mole

N_v number of triangular air tongue per unit length, [L^{-1}]

n number of adsorption/desorption sites per unit area at solid/fluid interface [L^{-2}]

$\vec{n}$ normal to a translationally symmetric gas liquid interface of a triangular air pocket

$\vec{o}$ normal to the optical axis of the stereo zoom microscope

P vacuum pressure in a slot coater with Levi and Akulov (1964), [M/Lt^2]

P_f Ronchi ruling fringe pitch, [cycles/L]

P_g gas pressure above atmospheric, [$M\,T^2/L$]

P_g^* dimensionless gas pressure above atmospheric

P_l liquid pressure above atmospheric, [$M\,T^2/L$]

P_l^* dimensionless liquid pressure above atmospheric

q flowrate of curtain coater, [L^3/t]

Q magnitude of electrostatic charge between two bodies, [coulombs] =[A t]

r radial position measured from the DCL, [L]

R radius of curvature near DCL, [L]

R^* dimensionless radius of curvature near DCL

R_a arithmetic mean roughness, [L]

R_q root mean square roughness, [L]

R_{eq} equivalent radius of curvature of the triangular air film measured parallel to the DCL, [L]

t_{ae} time of triangular air film onset of air entrainment, [t]

t_c coating thickness used in estimating G, [L]

t_i thickness of layer i that a light ray passes through, [L]

t_{pp} time constant based on physical properties of fluid, [t]
t_v time of contact line instability and onset of the "V" structures, [t]
T_i temperature of phase i, [°]
T sampling period used in PID control algorithm, [t]
u x-component of velocity, [L/t]
u* dimensionless x-component of velocity
U substrate velocity, [L/t]
U_{ae} critical substrate speed for onset of air entrainment, [L/t]
U_v critical substrate speed for contact line instability and onset of the "V" structures, [L/t]
v wetting velocity at dynamic contact line, [L/t]
$v_{180°}$ wetting velocity when the dynamic contact angle is 180°, [L/t]
V curtain coater liquid impingement velocity, [L/t]
V_e electrostatic voltage, [V]
V_i molecular flow volume of phase i, [L^3]
w irreversible shear stress per unit displacement of unit length of the dynamic contact line, [M L/t]
W_1 width of triangular air tongue measured from intersection of $Ø_2$ with the base of the air tongue, [L]
w_s width of coated substrate, [L]
w_c width of coating cavity used in this thesis experiment, [L]
x_d interfacial displacement depth used by Burley and Kennedy (1977), [L]
x* dimensionless x-coordinate used in scaling a free surface side driven cavity
y* dimensionless x-coordinate used in scaling a free surface side driven cavity
Y distance of the DCL below the surface, [L]

Greek Alphabet

α angle between normal to the liquid surface, $\bar{n}$, and normal to the solid support, $\bar{k}$, [°] or [radians]
α_s angle of entry between substrate and plane of fluid, [°] or [radians]
α_i^* numerical coefficient in Blake's (1988,1993) hydrodynamic theory
β_{ij} angle through which a light ray is bent by refraction at the interface ij, [°] or [radians]
β_i, β_t incident and transmitted angles in Snell's law, [°] or [radians]
δx_i displacement of ronchi ruling image in x-direction due to refraction at interface with slope dh/dx, [L]

δy_i displacement of ronchi ruling image in y-direction due to refraction at interface with slope dh/dy, [L]

ε perturbation parameter

ε_o permittivity of free space

ΔG_w^* molar activation free energy of wetting , [L M/mole]

$\Delta G_{vis,i}^*$ molar activation free energy of bulk flow for phase i, [L M/mole]

ΔG_S^* molar activation component of ΔG_w^* due to interaction between solid and liquid, [L M/mole]

ΔU speed window between U_v and U_{ae}, [L/t]

γ liquid surface tension, [M L/t]

γ_{12} interfacial surface tension between fluid 1 and 2, [M L/t]

γ_l^d dispersive component of the liquid surface energy, [M L/t]

γ_l^n nondispersive or polar component of the liquid surface energy, [M L/t]

γ_s^d dispersive component of the solid surface energy, [M L/t]

γ_s^n nondispersive or polar component of the solid surface energy, [M L/t]

κ_+ frequency of molecular displacement in positive direction from phase 1 to phase 2 at three phase line, [t^{-1}]

κ_- frequency of molecular displacement in negative direction from phase 2 to phase 1 at the three phase line, [t^{-1}]

κ_s° frequency of molecular displacements at equilibrium due only to surface forces, [t^{-1}]

κ_w net frequency of molecular displacements at the wetting line, [t^{-1}]

κ_w° frequency of molecular displacements at equilibrium, [t^{-1}]

λ i) average length of an individual molecular displacement at the three phase wetting zone used in Blake's model (Appendix I), [L], or
ii) integration parameter used to estimate the stream function in Chapter V

λ_μ viscosity ratio of displaced phase (e.g. air) over displacing phase (e.g. coating liquid)

μ viscosity of liquid phase, [M/L t]

μ_i viscosity of phase i, [M/L t]

ρ density of liquid phase, [M/L^3]

ρ_i density of phase i, [M/L^3]

π^* dimensionless gas normal stress

σ sample standard deviation of any parameter $\bar{x} \pm \sigma$

τ dimensionless time, $\tau = t/t_{pp}$

τ_d derivative time constant in PID control algorithm, [t]
τ_i integral time constant in PID control algorithm, [t]
τ^*_{xx} dimensionless normal stress acting in the x-direction
τ_{xx} normal stress acting in the x-direction, [M/L t]
Φ angular digitization correction factor for fringes out of alignment with horizontal when converting film to digital images, [°] or [radians]
η_i refractive index, phase i, measured with respect to air at sodium d line (647 nm).
$\eta_{i,j}$ relative refractive index between phase i and phase j
θ_d dynamic contact angle, [°] or [radians]
θ_d' experimentally observed dynamic contact angle, [°] or [radians]
θ_d^{tip} "dynamic contact angle" of the vertical tip = $(180-\emptyset_3)$, [°] or [radians]
θ_{eq} equilibrium contact angle, [°] or [radians]
θ_m macroscopic contact angle for Cox's (1986) model, [°] or [radians]
$\emptyset$ angle of triangular air tongue edge from horizontal, [°] or [radians]
$\emptyset_1$ tip or vertex angle of triangular air tongue, [°] or [radians]
$\emptyset_2$ angle of inclination from base of triangular air tongue, $\emptyset_2 = (90°-\emptyset)$, [°] or [radians]
$\emptyset_3$ tip vertical angle of triangular air tongue, [°] or [radians]
ψ dimensionless length of the air tongue = $L_1/(20L_c/Ca)$
ψ_{max} maximum dimensionless length measured during a case
ψ_{sf} stream function for the liquid phase used in Chapter V
Ψ_s angle between the substrate velocity vector and the liquid surface measured in the plane of the substrate as defined by Blake and Ruschak (1979), [°] or [radians]
χ dimensionless half width of the air film = $W_1/(40L_c/Ca)$
χ_s dimensionless width of the air sheet that forms with precursor structures
χ_{max} maximum dimensionless half width of the air film during a case
ζ dimensionless thickness of air tongue = h/L_c
ζ_b dimensionless thickness based on the entrained bubble diameter
ζ_{amp} amplitude term for thickness near tail based on Eq. [6.4]
ζ_{max} maximum dimensionless thickness measured from the profiles during a case

Phases

1 or l Liquid
2 or g Gas
3 or s Solid

ABSTRACT

Results from visualization of dynamic contact line (DCL) instability and macroscopic air entrainment in coating systems are presented along with quantitative measurement of interfacial motion of entrained triangular air films. The measurements employ a deflectometry technique based on a refractive index change at curved interfaces using a ronchi ruling as applied to a side driven free surface cavity. The accuracy of the deflectometry results were validated with two independent methods.

Events occurring immediately after formation of distinct serrated wetting and air entrainment are documented using high-speed cinematography and videography. The first critical substrate velocity, U_v, is when the DCL forms multiple triangular air films that comprise the serrated wetting line, while U_{ae} is the second critical substrate velocity when a triangular air film becomes unstable resulting in a air bubble entering the coating. Experimental evidence is shown that the triangular air film can form and exist for a finite period prior to air entrainment when the ratio of gas to liquid viscosity, λ_μ, is greater than 2×10^{-4} and the capillary number, Ca, less than unity.

These experiments used a quasi-steady state approach by gradually varying the speed to locate the first, U_v, and second, U_{ae}, critical speeds of air entrainment. It is shown statistically that $\Delta U = U_{ae} - U_v \neq 0$ when $\lambda_\mu > 2 \times 10^{-4}$ and $Ca < 1$. Significant differences in U_{ae}, independent of substrate properties, are found for a side driven free surface cavity of aspect ratio, $a_c = 1/3$ versus the extensive plunging tape data

found in the literature. The differences are attributed to the liquid normal stress acting on the gas liquid interface near the DCL prior to air entrainment. A qualitative analysis based on a force balance at the gas liquid interface is used to explain these results.

The spatio-temporal gas/liquid interface profile for an axisymetric triangular air film is measured at steady Ca for the range $0.34 \leq Ca \leq 2.82$. The triangular air film thickness and length are found to be inversely proportional to liquid viscosity. The maximum thickness measured is 600 μm and the minimum 10 μm. Fluctuations in thickness, ζ, are seen to precede the air entrainment phenomena. Previously undocumented precursor structures leading to triangular air tongue formation are presented for $Ca < 1$ and $\lambda_\mu > 2 \times 10^{-4}$ that support evidence for destabilization of the dynamic contact line due to the gas flow in the converging gap near the DCL.

Practical implications for the paper industry and a modification to current coater design are discussed.

CHAPTER I

INTRODUCTION

The motivation for this thesis is to answer a number of significant questions that have arisen from previous work on air entrainment and dynamic contact line (DCL) instability. Previous studies have not seriously studied the transition region from U_v to U_{ae}, with a majority of researchers only determining the second critical speed of air entrainment, U_{ae}. Some of the questions about this transition region include whether triangular air films exist prior to entrainment and whether measurable waves exist at the gas liquid interface of the film. These waves with amplitude much less than the wavelength, lead to the nucleation, isolation and bubble formation mechanism of air entrainment first reported by Veverka (1991). Additionally, no concrete experimental or theoretical explanation has been presented documenting the rationale for the shape of the triangular air tongue. Is this distinct shape due to microscopic events not easily accessible by direct experimentation or is it dictated by the gas and liquid flow fields of which it is a part? These questions must be answered in order to compliment and guide theoretical as well as computational predictions of DCL destabilization.

The specific applications of this work are relevant to any industry where forced wetting is used to coat a substrate and where a DCL exists. Examples abound in the paper and film coating industries as well as in the wire coating industry. Correlations of the second critical speed of air entrainment, are dependent on the coating method employed and are not the direct goal of this thesis. Rather, the

desired result is to obtain experimental evidence that under the proper conditions a triangular air film can form and retract for a finite period without entrainment. With this evidence, using a non-intrusive technique we can obtain three dimensional information about the gas liquid interface behavior as a function of time.

The relevant literature concerning medium and high speed wetting and air entrainment are covered in the Chapter II. The goal is to introduce the reader to the relevant previous studies emphasizing the fact that the approach used in this thesis is novel and provides definitive answers in our system as to when an air tongue is stable, i.e. no entrainment via nucleation, isolation and bubble formation. The interfacial long wave instability, which is necessary for the nucleation to occur, is also reviewed with emphasis that this interface motion has never been quantitatively documented. Other related systems are also covered.

Chapter III outlines the difficulty in studying DCL stability and how to verify that a triangular air film is stable between the first, U_v and second, U_{ae}, critical speeds. The rationale for the experimental setup in Chapter IV is therefore contrived.

Chapter IV is broken into three subsections (4.1, 4.2, and 4.3) which discuss the experimental apparatus, optical deflectometry technique and the model substrate and fluid properties. The apparatus design covered in Section 4.1 is unique and provides adequate access to the DCL unlike previous studies or industrial configurations. In Section 4.2 the theory behind the deflectometry technique, refraction, and its direct application to obtaining information about the gas liquid

interface motion along the triangular air film centerline is discussed. Section 4.3, briefly discusses the results characterizing the liquid and solid materials chosen as the experimental model system. The test fluids were 10 - 1000 cs silicone oils and glycerol-water mixtures. The main test substrate was a coated PET poly(ethyleneterephthlate) film base.

The propositions discussed in Chapters II and III regarding a finite speed interval between U_v and U_{ae} are experimentally verified using a quasi steady state approach in Chapter V. This verification provides the necessary groundwork for the deflectometry technique used in Chapter VI to study the triangular air film. The interval for a parameter dependent on the Reynolds and Bond numbers, $\Delta(Re/\sqrt{Bo})$, is found to be a good predictor of when a triangular air film can exist prior to entrainment with low viscosity fluids, $\lambda_\mu > 2 \times 10^{-4}$. The differences with highly viscous fluids, i.e. low gas to liquid viscosity ratios, $\lambda_\mu < 2 \times 10^{-4}$, between previous plunging tape studies and our system are not attributed to the substrate properties. Rather the liquid normal stresses are believed to delay air entrainment in our system for $Ca > 1$ and $\lambda_\mu < 2 \times 10^{-4}$. The cutoff between these two regions, $\lambda_\mu \approx 2 \times 10^{-4}$, requires additional work to determine the exact transition value for λ_μ.

Chapter VI presents the results of the deflectometry experiments and the non-dimensional length scales of the triangular air film. A summary of the observations that are repetitive throughout the cases is also discussed. A synopsis of the forces that may determine the triangular air film shape is also presented. How these results support the interfacial long wave instability is discussed.

Since no complete theory for the formation of the triangular air tongue has been previously proposed, the discovery of triangular shaped precursor structures recorded in Chapter VI provides a future direction for research on air entrainment.

The objective of this thesis is to determine the measurable bounds of the destabilization at the liquid-air interface for the solid substrate speed range $U_v < U < U_{ae}$. The effects of fluid properties on the instability and the hypothesized gas velocity profile are investigated and explained.

Chapter VII summarizes the results of the experimental and qualitative modeling analysis regarding the delay of air entrainment in our system and the triangular air film profiles. Some implications for the paper industry and suggestions for future work are discussed in Chapter VIII.

The following hypothesis are tested:

1) A finite speed window exists where stable air pockets can grow and retract on a time scale longer than that required for air entrainment.

2) Surface waves at the liquid-air interface are due to a interfacial instability along the edge of a triangular air film.

3) An increase in the coating surface tension will decrease the amplitude of surface waves at the liquid-air interface and the dampening effect will become greater as the viscosity increases.

This thesis addresses two new and important contributions regarding triangular air film formation and nucleation at the DCL when the substrate velocity is in the range of U_v, i.e. $U \approx U_v$. At high liquid viscosity and low surface tension air entrainment is delayed in our system. The mechanism of air entrainment is further

investigated in terms of the interfacial profile of the triangular air film and how the variations in thickness based on coating properties change the sequence. The effects of electrostatic surface charge, surfactants, liquid volatility, and non-Newtonian rheology are excluded. Understanding the air entrainment phenomena should provide qualitative and quantitative insight into the physics of air entrainment.

CHAPTER II

LITERATURE REVIEW

2.1 The Basics of Coating and the Dynamic Contact Line

The goal of coating a solid surface is to uniformly displace one fluid, usually air, evenly with another, usually liquid, while the liquid front or substrate is externally driven at a constant speed, U, normal to the wetting line. This forced action is known as dynamic wetting and occurs at the so-called dynamic contact line (DCL). The qualifiers "externally" and "forced" are used to distinguish dynamic wetting from spontaneous wetting such as a drop spreading on a surface or capillary rise in a tube. Many industries utilize coating processes that are meant to protect, enhance functionality, or alter the surface characteristics of the substrate upon which the coating is applied. The word "coating" applies to both the material and the process. The substrate or base may be paper (an anisotropic network structure consisting of cellulose fiber from plant material), plastic film such as poly(ethylene terephthalate) (PET), magnetic disks from aluminum and PET film, optical fibers, conductive wires or other ubiquitous examples. It is estimated that the value of coated products produced in 1990 in the United States is $24,796,700,000 in 1990 dollars (Cohen and Gutoff 1992). The total contribution by printing and publishing is 68%, mainly because of the huge production volume associated with the paper industry.

The number of layers may be as many as 12 (for example, in photographic films) or as few as one when dealing with coated-one-side (C1S) production papers.

Thickness ranges from the order of millimeters to an order of single layers of molecules. The coating fluid may exhibit non-Newtonian rheological behavior, and the list of ingredients used in the coating formulation is almost endless. The application methods vary widely according to each industry's requirements for precision, speed, and functionality. The postapplication drying and consolidation processes are sometimes essential in the final product performance (Scriven 1991). The above-mentioned difficulties present a formidable task in summarizing this important unit operation. Some examples of this unit operation will be examined in the next section.

2.2 Types of Coaters

From the first brush coaters used by the paper industry in the 1850's that applied a clay coating to paper (Booth 1970, 54) to today's precision film coaters, there are basically four unit functions of a coater. These functions are:

- Feeding and distribution of coating liquid across the width of the coater,
- Metering the flow or coating to the desired thickness,
- Application of coating to substrate or web, and
- Solidification and annealing of coating (Scriven 1991).

Figure 2.1 shows some of the coating flows that are most frequently encountered in a wide variety of industries. Most noteworthy is that six out of the eight coaters depicted have a DCL where microscopic and catastrophic macroscopic air entrainment can occur. The two exceptions occur with dip coating and the metering action of the wire round rod which depends on a previous premetering application

step where air entrainment can occur. A common defect associated with the paper industry's puddle coater (shown in Figure 2.2), is air entrainment at the DCL which is similar to the blade coater of Figure 2.1. The features of the puddle coater head are similar to the experimental system used in this thesis. It is air entrainment that leads to foaming problems in the coating recirculation tank and coating defects such as "skips" and "streaking" beyond some critical speed (Ducey 1984; Sommers 1988; Li and Burns 1992a,b; Aidun 1991, 1993; Aidun and Triantafillopoulos 1994; Teirfolk 1995).

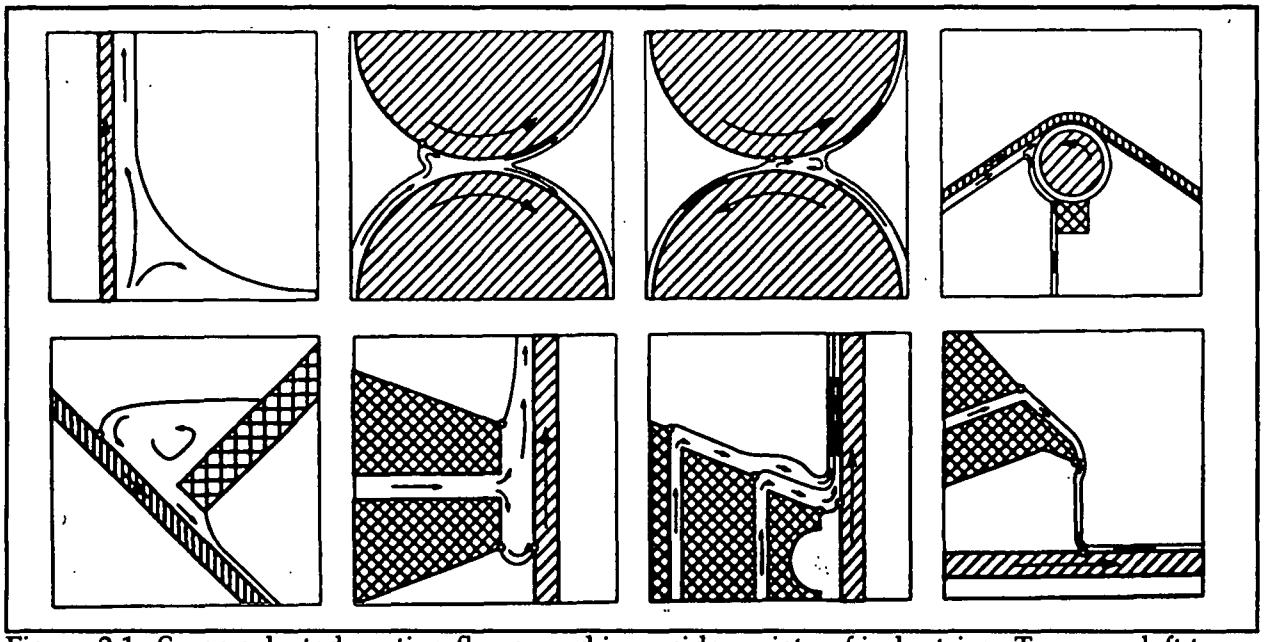

Figure 2.1. Some selected coating flows used in a wide variety of industries. Top row, left to right: dip, forward roll, reverse roll, wire round rod. Bottom row, left to right: blade, slot, slide, and curtain coating. (Reprinted from Scriven [1990] with permission of the American Institute of Chemical Engineers and Prof. L.E. Scriven.)

There also has been significant industrial as well as academic interest in correcting some of the problems associated with the short dwell coater shown in Figure 2.3. These include incorporating innovations that lead to the elimination of the central vortex (Aidun 1994a,b; Aidun and Kovacs 1995; Moran 1995) or insertion of a

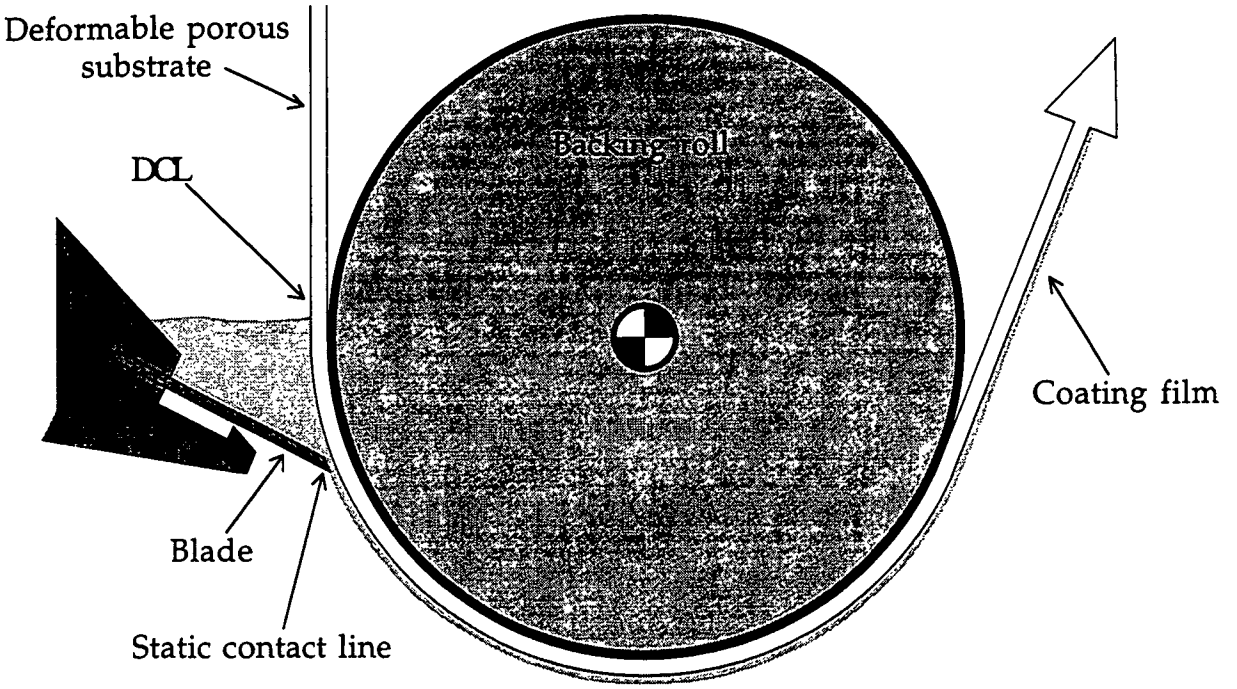

Figure 2.2. A schematic of a puddle coater used in the paper industry. The general configuration of the coater head is similar to that used in this thesis.

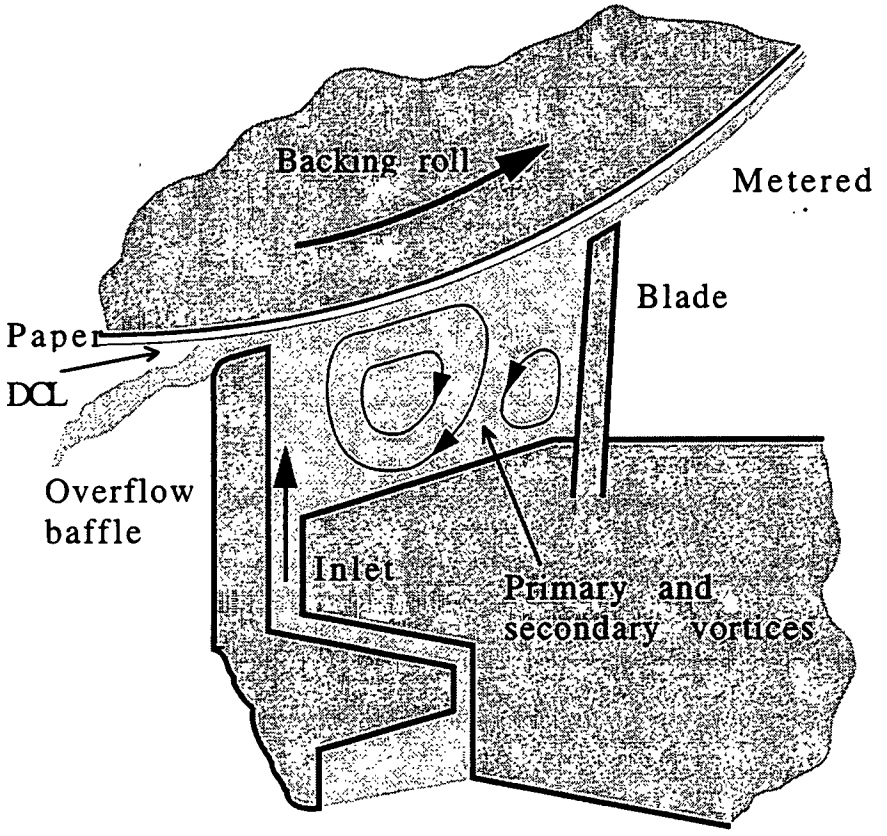

Figure 2.3 Side view of the primary recirculation flows in the short dwell coater showing the dynamic contact line to the left of the overflow baffle.

suction tube to remove air in the low pressure region of the central vortex (Li and Burns 1992a,b). The work of Li and Burns (1992a,b) represents the first published study in paper industry coaters recognizing the deleterious effect of air entrainment in maintaining a good cross machine direction coat weight profile. Equipment suppliers have even developed systems to remove entrained air prior to distribution at the coating head (Taylor 1993). Perhaps some of the greatest requirements of all future coaters, regardless of the industry, is best summarized by Philip Norrdahl's quotation (O'Brien 1992):

> Requirements for the next generation of coating heads have been set by the industry's needs for faster machines and higher quality. We've reached the upper speed limits with existing coating technology. Further productivity gains will require new breakthroughs in technology to increase the speed of the coater.

There are a number of books related to coating flows in the paper industry, such as Booth (1970), Walter (1992), Satas (1984), and Weiss (1977), that usually take a technological and descriptive approach. A review by Ruchak (1985) and a recent book edited by Berg (1993) cover the important physics as related to coating flows and wettability, respectively. A more recent multi-authored book on the topic edited by Kistler and Schweizer is scheduled for publication in 1996 by Chapman and Hall.

The next section will concentrate on the material properties and dimensionless groups that are commonly used in air entrainment coating studies.

2.3 Relevant Parameters

Considering the gravitational, viscous, inertial, and surface tension forces (all of the forces excluding the electrostatic and disjoining forces that cannot be modeled with bulk properties), some of the relevant parameters for comparing results and scaling dimensions with different liquids under dynamic conditions are listed in Table 2.1. Any material property without a subscript represents the liquid phase while subscripts g and s represent gas and solid phases respectively. The liquid viscosity, μ, surface tension, γ and the density, ρ, are the common material properties used to describe the system. The substrate velocity, U, length scale, d, and gravity, g, are often needed to calculate a dimensionless parameter. The disjoining pressure introduced by Deryagin (1940) is defined in terms of thermodynamics of thin films and reflects the difference in behavior between a film and a bulk liquid phase (Miller and Ruckenstein 1974). Sometimes the physical property number, N_{pp}, is written as the reciprocal, sometimes as the third or fourth root (Cohen and Gutoff 1992, 137), and sometimes is called the capillarity-buoyancy number. It was originally derived from dimensional analysis by Kapitsa and Kapitsa (1949) to describe wave motion in thin liquid films. The most significant groups in Table 2.1 related to air entrainment are the capillary number, Ca, physical property number, N_{pp}, (Cohen and Gutoff 1992), and the viscosity ratio, λ_μ, (Kistler 1993, 342).

Table 2.1. Relevant parameters for coating flows.

Symbol	Definition	Parameters	Ratio of forces
Bo	Bond or Eötuos #	$\frac{\rho g d^2}{\gamma}$	Buoyancy/Surface Tension
Ca	Liquid Capillary #	$\frac{U\mu}{\gamma}$	Viscous/Surface Tension
Ca_g	Gas Capillary #	$\frac{U\mu_g}{\gamma}$	Viscous/Surface Tension
Re	Reynolds #	$\frac{\rho U d}{\mu}$	Inertial/Viscous
We	Weber #	$\frac{d\rho U^2}{\gamma}$	Inertial/Surface Tension
λ_μ	Viscosity ratio	$\frac{\mu_g}{\mu}$	N/A
λ_ρ	Density ratio	$\frac{\rho}{\rho_g}$	N/A
N_{pp}	Physical Property # or Capillarity-Buoyancy #	$\frac{g\mu^4}{\rho\gamma^3}$	N/A
t_{pp}	Liquid Time Scale	$\frac{\gamma}{\mu g} = \frac{\rho L_c^2}{\mu}$	Dimensional Time Scale
L_c	Capillary Length	$\sqrt{\frac{\gamma}{\rho g}}$	Dimensional Surface Tension/Buoyancy
L_d	Deryagin Length	$\sqrt{\frac{\mu U}{\rho g}}$	Dimensional Viscous/Buoyancy

2.4 Macroscopic Air Entrainment Mechanisms and the Dynamic Contact Angle

The pioneering work of Deryagin and Levi (1959) reveals an important event and limitation in the wetting of solids by a liquid. In Fig. 2.4 we can see how the DCL, originally straight, breaks into a single "sawtooth" pattern at a critical speed when the apparent dynamic contact angle, θ_d, approaches 180°. This sawtooth flow

behavior at the wetting line appears to be universal for smooth surfaces regardless of the substrate material and liquid properties. The sawtooth shape, i.e. the length and width, although is affected by the liquid properties. In the ideal situation, where the DCL is infinitely long, this behavior can be viewed as a transition from a two-dimensional flow to a three-dimensional state. The macroscopic or catastrophic air entrainment mechanism results in bubbles forming from the breakdown of the triangular air film. This breakdown, or nucleation, is discussed later.

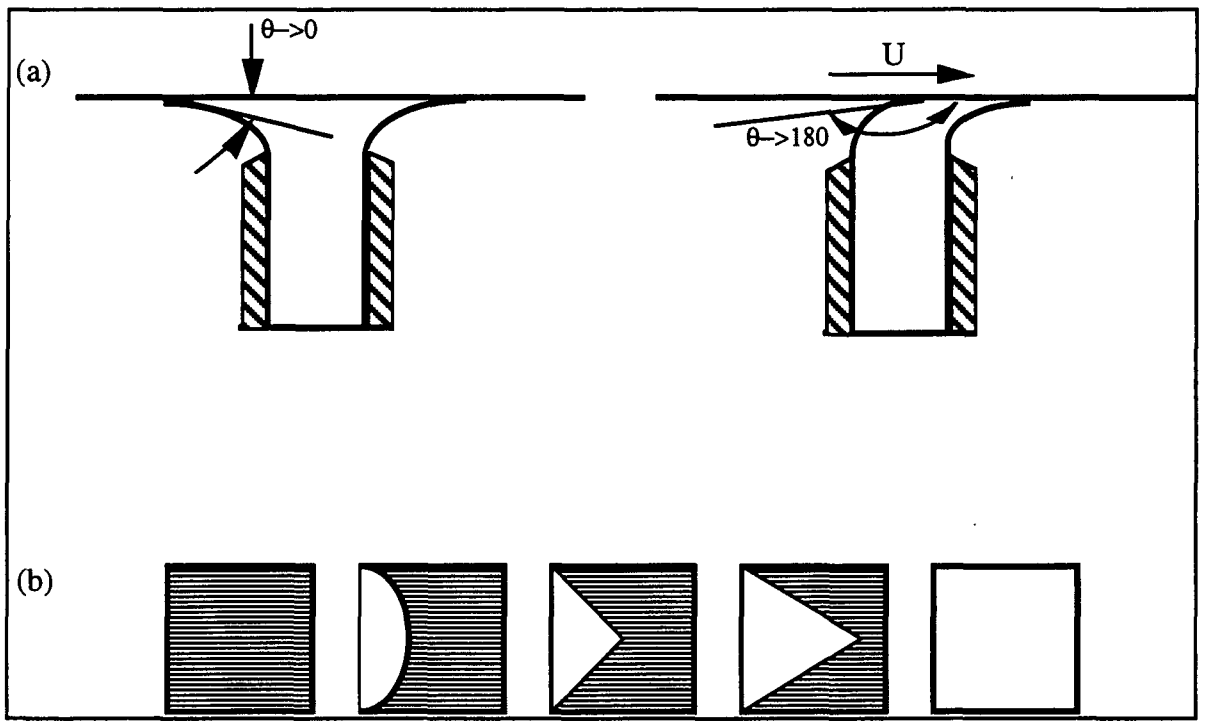

Figure 2.4. (a) Side view of displacement of the wetting boundary in a slide hopper coater. (b) Top view of kinetic hysteresis of boundary angle of wetting during coating. Adapted from Deryagin and Levi (1959).

The criterion that θ_d approach 180° for catastrophic air entrainment presents a number of major difficulties. First, the dynamic contact angle is termed "apparent" because it depends on the length scale at which the meniscus is examined. In Fig. 2.5, the DCL meniscus curvature and θ_d are shown from a macroscopic to molecular

level. The dynamic contact angle must be considered apparent when measured with conventional optical means if resolved to within 20 μm (Kistler 1993, 314). The intricate coupling between the molecular and continuum flow fields represents a significant challenge to interpreting both experimental results and modeling

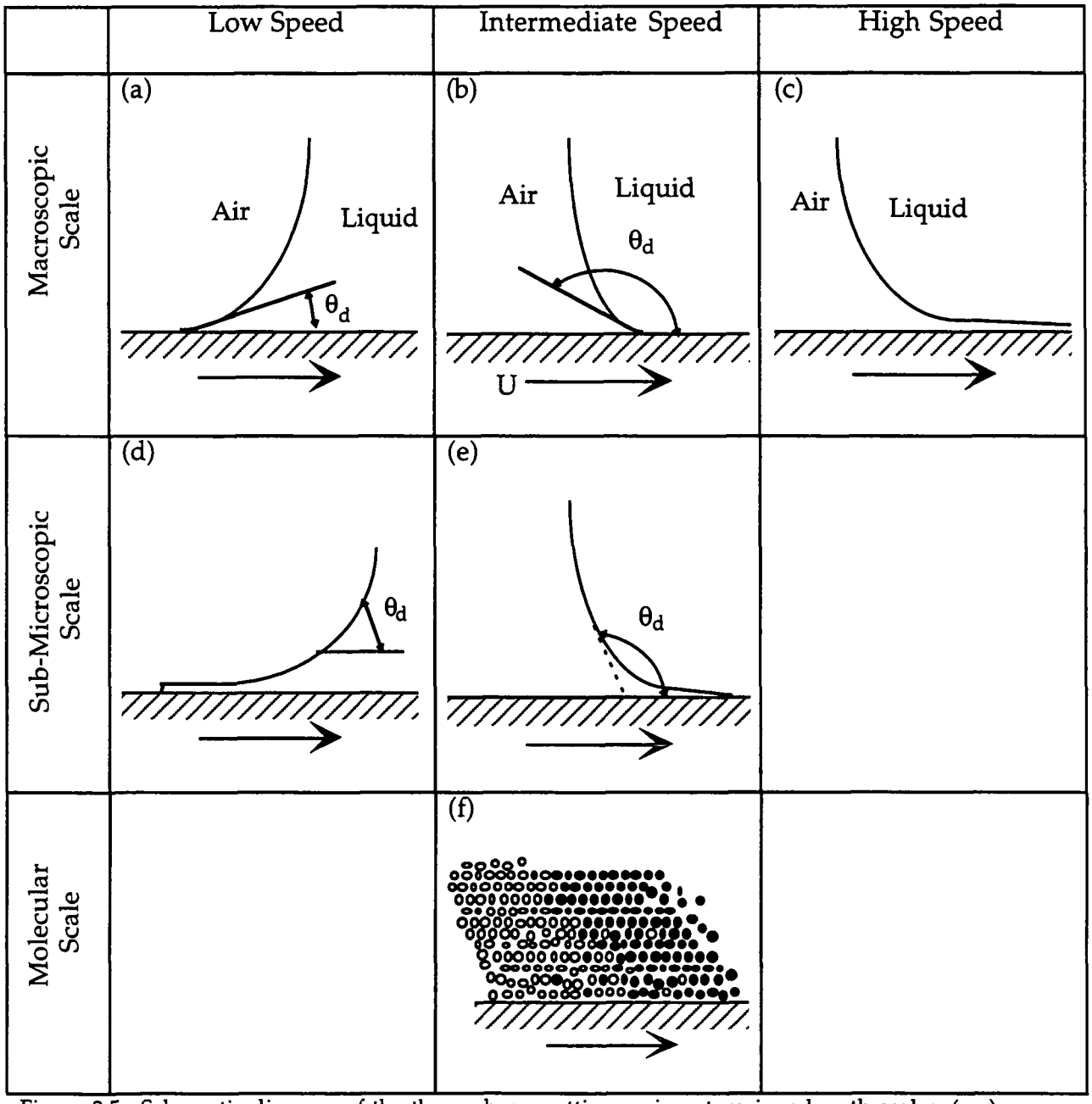

Figure 2.5. Schematic diagram of the three-phase wetting region at various length scales: (a-c) macroscopic length scale of at least several tens of microns; (d) and (e) submicroscopic length scale between 30 and 1000Å; (f) molecular scale with the gas and liquid molecules not to scale. Adapted from Kistler (1993).

three-phase forced wetting. Another difficulty in measuring θ_d is that its value not only depends on the properties of the liquid, solid, and gas, as well as the wetting speed, but also on the detailed flow field of which it is a part (Ruchak 1985, 84-85). Therefore, measurement of θ_d in a particular geometry will not be a suitable boundary condition in another hydrodynamic system. Another major problem in modeling the DCL is that the classical no-slip boundary condition predicts an infinite force by the fluid on the solid, as first documented by Huh and Scriven (1971). Some of the methods to eliminate this mathematical singularity are discussed by Dussan (1979).

New approaches such as the microstructural Lattice-Boltzman method (Lu and Aidun, 1995) or molecular dynamic simulations (Koplik, J, Ganavar, J.R. and Willemsen, J.F., 1989; Kistler 1993, 412-413) may be at the point in the near future where computational limitations are nullified thus enabling realistic predictions of DCL motion. Blake (1993) discusses how the statistical kinetics of molecular events might influence wetting dynamics through θ_d with a slight emphasis on hydrodynamic effects. Blake's work (1966, 1988, 1993) is further detailed in Appendix I and the adsorption/desorption models for predicting θ_d as a function of U discussed. It has not been indisputably established experimentally that the speed at which visible bubbles are entrained, U_{ae}, is the same as the speed where the triangular air film forms, U_v (Kistler 1993, 340).

The visible macroscopic mechanisms of air entrainment were first documented by Veverka (1991) and Veverka and Aidun (1992a,b) using a glycerol-water system on a partially wetted Plexiglas roll. They documented the basic fundamental mechanism where nucleation of wetting for $U > U_{ae}$ occurred near the base of the air film as shown in Fig. 2.6. This mechanistic sequence is also repeated in still photos (Veverka 1991; Veverka and Aidun 1992a,b) taken from the 16-mm film for a number of different speeds and liquid viscosities. The term "base" is used to describe the area nearest the unperturbed straight DCL while the "tip" is the vertex of a triangular air film. This nucleation event led to the isolation of an air film at the tip and consequently the development of an air bubble. The sequence of

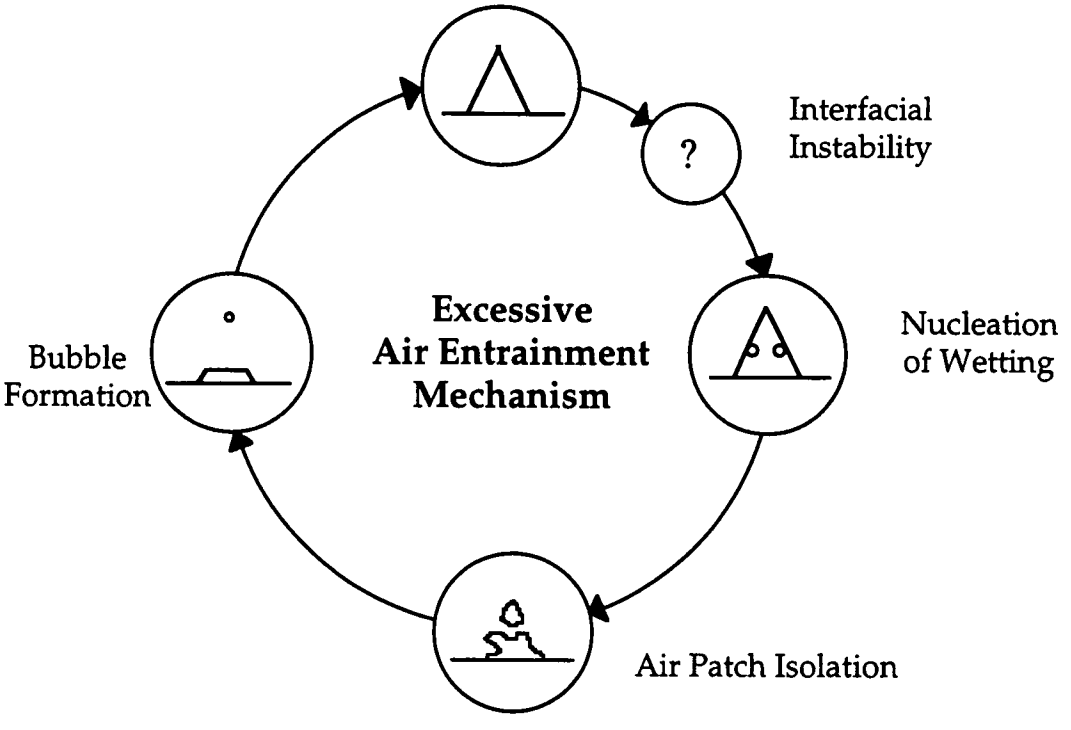

Figure 2.6. The cyclical nature of the excessive air entrainment mechanism.

events required only tens of milliseconds from initiation to bubble formation, thus illustrating the difficulty in studying this transient event.

Aidun, Veverka, and Scriven (1992, 1993) advanced the theory that there exists a speed prior to U_{ae}, and after U_v, where an air film can remain stable without nucleation near the base. They hypothesized that the nucleation was due to waves from an unstable interfacial mode and verified this theory with a long-wave stability analysis (Aidun and Chen 1994; Severtson and Aidun 1995).

2.5 Quantitative Studies of Air Entrainment Parameters

The purpose of this section is to briefly overview the available work on air entrainment with latter sections focusing on details of studies with the plunging tape, wetted roll, curtain, and slot coaters. The plunging tape and wetted roll systems have been the mainstay of air entrainment studies because of their ease of use and inexpensive setup as seen in Fig. 2.7. Table 2.2 chronologically summarizes the

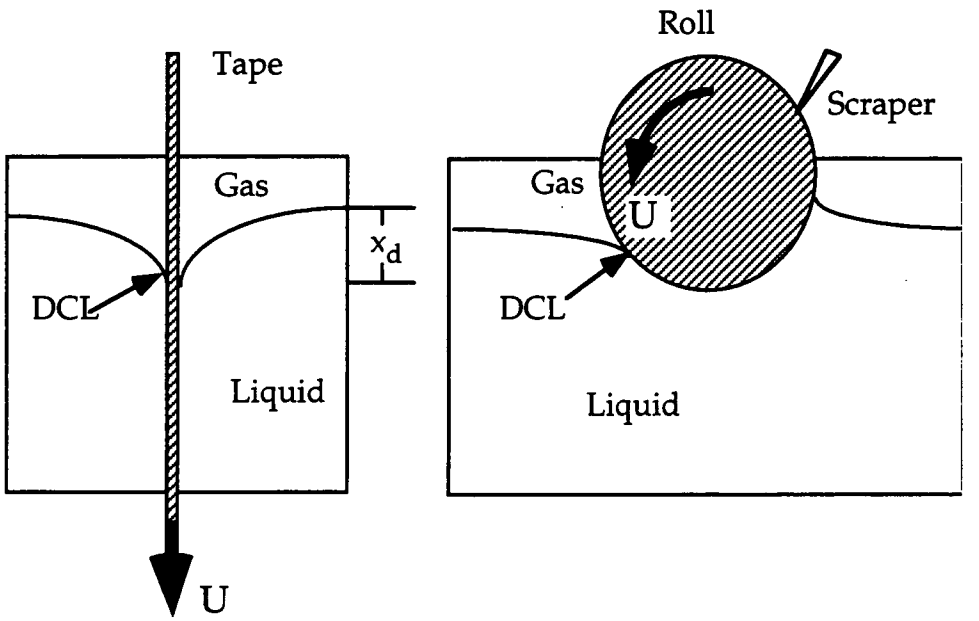

Figure 2.7. Simplified side views of the plunging tape (left) and wetted roll (right) systems used in previous air entrainment studies.

experimental studies with all systems. Any additional variables not previously presented are defined in the Nomenclature section.

Table 2.2. Air entrainment studies and experimental variables.

Researchers	Year	Geometry	Variables studied	Viscosity (cp)
Ablett	1926	WR	θ_d, $U<U_v$,x_d	1
Deryagin & Levi	1959	Film slot coater	U_{ae}	N/A
Brown	1961	Prewetted curtain coater roll	U	120 - 990
Levi & Akulov	1964	Film slot coater	U_{ae},P	N/A. 2% photographic gelatin solution
Levi	1966	Film slot coater	U_{ae},h_s	N/A. 2% photographic gelatin solution
Perry	1967	PT/25 mm, Liquid jets, Fiber strand	U_{ae}	1 - 300
Inverarity	1969	Fiber strand	U_{ae}, x_d, θ_d	100-1060
Burley	1971	Fiber strand	Descriptive	N/A
Burley & Brady	1973	Fiber web	U_{ae}, x_d	N/A
Wilkinson	1975	WR	U_{ae}, x_d, α_s	29-288
Kennedy	1975	PT/25 mm	U_{ae}, x_d, θ_d	0.6-461
Burley & Kennedy	1976a,b	PT/25 mm	U_{ae}, x_d, θ_d	0.6-461
Kennedy & Burley	1977	PT/25 mm	U_{ae}, x_d	10-118
Blake & Ruschak	1979	PT/50 mm	U_{ae}, x_d, θ_d	23-100
Bolton & Middleman	1980	WR, undoctored	U_{ae}	1-1080
Ishizaki et al.	1982	Slide hopper coater	U_{ae}, γ_s^d , γ_s^n	N/A. Eight photographic gelatin solutions
Gutoff & Kendrick	1982	PT/16 mm.	U_{ae}, θ_e, θ_d	1-993
Researchers	Year	Geometry	Dependent var.	Viscosity (cp)
Burley & Jolly	1984	PT/ up to 25 cm.	U_{ae}, x_d, α_s, w_s	22-330
Kistler	1984	Prewetted curtain coater roll	U_{ae}	110-?
Kistler et al.	1984	Curtain coater	U_{ae}	110-?
Petrov & Sedev	1985	Glass rod/2.75 cm dia. 6.4 x 9.0 x 0.1 cm glass plates	U_{ae}	23,325
Buonopane et al.	1986	PT/16 mm.	U_{ae}, R_q	50-2830
Blake	1988	PT/35 mm	U_{ae}, θ_e, θ_d	1.5-104.3
Gutoff & Kendrick	1987	Slide coater	U, U_{ae}	0.98-1110

Table 2.2. (continued)

Canedo & Denson	1989	Driven cavity with free surface	U	50-650,000
Sedev & Petrov	1988/89	Glass rods 0.25 to 4.5 mm dia.	U_{ae}	171 (Single fluid)
O'Connell	1989	PT/25 mm	?	4-1930
Bracke, De Voeght & Joos	1989	PT/(N/A)	U_{ae}, θ_d	10.4-121.4
Esmail & Ghannam	1990	WR doctored	U_{ae}, x_d, θ_d	197-748
Yasui & Tanaka	1990	Curtain coater	U_{ae}, R_q, h_{cc}	10,000 Non-Newtonian solution
Miyamoto	1991	Curtain coater	$U < U_{ae}$, d	N/A.
Ghannam & Esmail	1990	WR doctored	U_{ae}, x_d, θ_e, θ_d, α_s	71-748
Veverka	1991	WR doctored	U_v, U_{ae}	138 - 770
Ghannam & Esmail	1992	WR, doctored and undoctored	U_{ae}, x_d, θ_d, α_s	104-748
Esmail & Ghannam	1993	Fiber strand	U_{ae}, x_d, θ_d	75.2-910.7
Blake et. al.	1994	Curtain coater/35 mm	U_{ae}, x_d, q	21-600

PT - Acronym for plunging tape
WR - Acronym for wetted roll
N/A - Author did not indicate in reference
? - Thesis or paper not available

Ablett's (1926) study was conducted at speeds well below U_v but is included because of the relevance of dynamic contact angle measurements. Detailed surveys of previous work in these areas are also presented by Dussan (1979), Burley and Kennedy (1976), Gutoff and Kendrick (1982), Esmail and Ghannam (1990), Burley (1992a,b), Cohen and Gutoff (1992), and Kistler (1993). These papers supplement this review.

The most relevant information gathered from these studies includes the following:

• Air entrainment generally occurs before the liquid capillary number exceeds unity in plunging tape systems (Blake, Clarke, and Ruschak 1994). The critical capillary number, C_{ae}, is slightly higher for wetted roll systems compared to the plunging tape

(Esmail and Ghannam 1990; Wilkinson 1975). When a thick layer is left on the wetted roll, i.e. no doctoring, the critical capillary number can be an order of magnitude higher than plunging tape or wetted roll systems (Bolton and Middleman 1980).

• The critical air entrainment velocity, U_{ae}, varies inversely with fluid viscosity raised to the 0.67-0.78 power in plunging tape systems (Perry 1967; Burley and Kennedy 1976a, Kennedy and Burley 1977; Gutoff and Kendrick 1982; Burley and Jolly 1984) to the 0.56-0.71 power in wetted roll systems (Veverka 1991; Esmail and Ghannam 1990; Ghannam and Esmail 1992) and to the 0.804 power in plunging fiber experiments (Ghannam and Esmail, 1993). A good general rule of thumb is that the air entrainment velocity is proportional to γ/μ raised to the 2/3 power (Gutoff 1992).

• The substrate entry angle, α_s, is defined as the angle between the plane of the substrate and the plane of the fluid. It, α_s, has been found both to significantly affect U_{ae} (Ghannam and Esmail 1990; Ghannam and Esmail 1992; Wilkinson[1] 1975) and not to significantly affect U_{ae} (Burley and Jolly 1984). In plunging fiber experiments Ghannam and Esmail (1993) found a slight increase in U_{ae} for only the case when α_s was equal to 90°. The substrate entry angle, α_s, is different than the angle Ψ_s discussed by Blake and Ruchak (1979) and elaborated on in a later section.

• The critical air entrainment velocity has been claimed to be both independent (Inverarity 1969; Burley and Kennedy 1976a,b; Burley and Jolly 1984; Bracke, de Voeght, and Joos 1989) and dependent (Perry 1967; Buonopane, Gutoff, and Rimore

---

[1] Wilkinson (1975, 1230) originally claimed that Ca_{ae} was not "greatly affected" by changing a_s but

1986) on the tape surface properties. The second study (Buonopane, Gutoff, and Rimore 1986) has a greater range of surface roughness and tape surface energies giving greater credence to the observation that U_{ae} is dependent on the tape surface properties. One major difficulty with these studies is that the surface properties have not been systematically studied thus confounding the interpretation of roughness vs. chemical surface effects. For curtain coating experiments with two substrates Blake, Clark, and Ruschak (1994) did not see a difference in air entrainment. For a slide hopper coater Ishizaki, Chino, and Fuchigami (1982) saw a slight effect of U_{ae} with the dispersion component of the solid surface tension, γ_s^d.

• The apparent dynamic contact angle on a macroscopic scale approaches 180° as the substrate velocity approaches U_v.

These studies do not offer a simple explanation for the mechanisms of air entrainment, but they do present the bounds which have been explored. All of the correlations offered by these studies are affected by the geometry and dimensions of the experimental apparatus. In fact, no definitive quantitative criteria for air entrainment onset is specified in any of these studies. The appearance of visible bubbles is often the criterion for air entrainment onset. The lack of a universal criterion for analyzing air entrainment has to a certain extent prevented further progress. The two-dimensional criteria that θ_d approach 180° is unsatisfactory because of the inherent three-dimensional structure that forms and the three-dimensional nature of the initial destabilization prior to U_v. The fact that the DCL breaks into the sawtooth, vee-shape, or triangular air film configuration at speeds

---

reexamination or his data by Burley (1992a,b) refuted this claim.

above U_{ae} is undisputed for the range of fluid properties studied. The transition between U_v and U_{ae} has not been extensively studied except for limited research by Veverka (1991) where the velocity difference $\Delta U = U_{ae} - U_v$ ($U_{ae} > U_v$) appeared to decrease at higher viscosity. The low magnification used by Veverka (1991) still leaves doubt that ΔU is finite. Kistler (1993, 340) states, "The data available, however, do not indisputably establish that the speed at which visible air bubbles are first entrained, U_{ae}, is the same as U_v." The transition region needs additional attention because of the need for boundary conditions within a single triangular air film. Verification of instability analysis is also needed.

2.5.1 Plunging Tape Studies

Perry (1967) in his Ph.D. thesis was the first to confirm that the critical air entrainment velocity, U_{ae}, was dependent not only on the physical properties of the liquid but also on the nature of the surface and the geometry used. Kennedy (1975) confirmed Perry's observations.

Studies with a 2.5-cm plunging tape were done by Burley and Kennedy (1977; 1976a,b). In the experimental work (1976a,b) they found that for viscosities greater than 4.62 poise, all liquids were found to entrain air at solid surface velocities around 0.1 m/sec. They also proposed dimensional correlations between the air entrainment velocity. At higher tape speeds, as θ_d approached 180°, they developed a dimensionless correlation from a force balance in the DCL region between the Weber and Bond numbers. A problem encountered in this analysis (Kennedy and Burley 1977) was in the length scale, x_d ,which was defined as the interfacial

displacement from the fluid plane. The authors go on to say that "x_d is however unsuitable on several grounds, not the least of which is that it is a dimension in contact with the fluid velocity" (Kennedy and Burley 1977).

Papers by Dussan (1976), deGennes, Hua and Levinson (1990) and Dussan, Rame, and Garoff (1991) attempt to address the questions regarding length scale at speeds well below U_{ae}. In the limit Ca<<1 these authors divide the contact line into inner, intermediate and outer regions. In the inner region a slip lengthscale or a dimension of molecular size are appropriate. The lengthscale of the outer region is the capillary length, L_c. Matching of solutions between the inner and outer regions is used to obtain a solution in the intermediate region.

Blake and Ruchak (1979) have considered the wetting behavior of a vertically plunging tape in terms of the component of the tape velocity normal to the contact line. By graphing the angle of inclination with respect to the horizontal base of an individual sawtooth, $\varnothing_2$, vs. the solid surface speed, $U > U_v$, they were able to predict the maximum speed of wetting within 25%. The authors also gave an explanation why the DCL takes a sawtooth or vee-shape configuration at speeds above U_v. For some solid surface velocity U, greater than U_v, the DCL slants away from the horizontal base at an angle, $\varnothing_2$; this ensures that the component of the tape velocity normal to the DCL never exceeds U_v. This is expressed analytically in Eq.[2.1] and depicted in Figure 2.8. Blake and Ruchak (1979) also advanced the hypothesis that breakup of the contact line can be postponed when the tape does not enter the liquid vertically; that is, the angle Ψ_s, corresponds to the angle between the substrate velocity vector and the liquid surface measured in the plane of the substrate.

Considerable confusion still exists about the interpretation of Ψ_s (Blake 1995) originally proposed by Blake and Ruchak (1979). In misconstrued efforts to verify that U_v changes with Ψ_s, some authors (Burley and Jolly 1984; Ghannam and Esmail 1990; Ghannam and Esmail 1992) have changed α_s, i.e. the substrate entry angle, with little or no change in U_{ae}.

$$\cos\varnothing_2 = \frac{U_v}{U} \qquad [2.1]$$

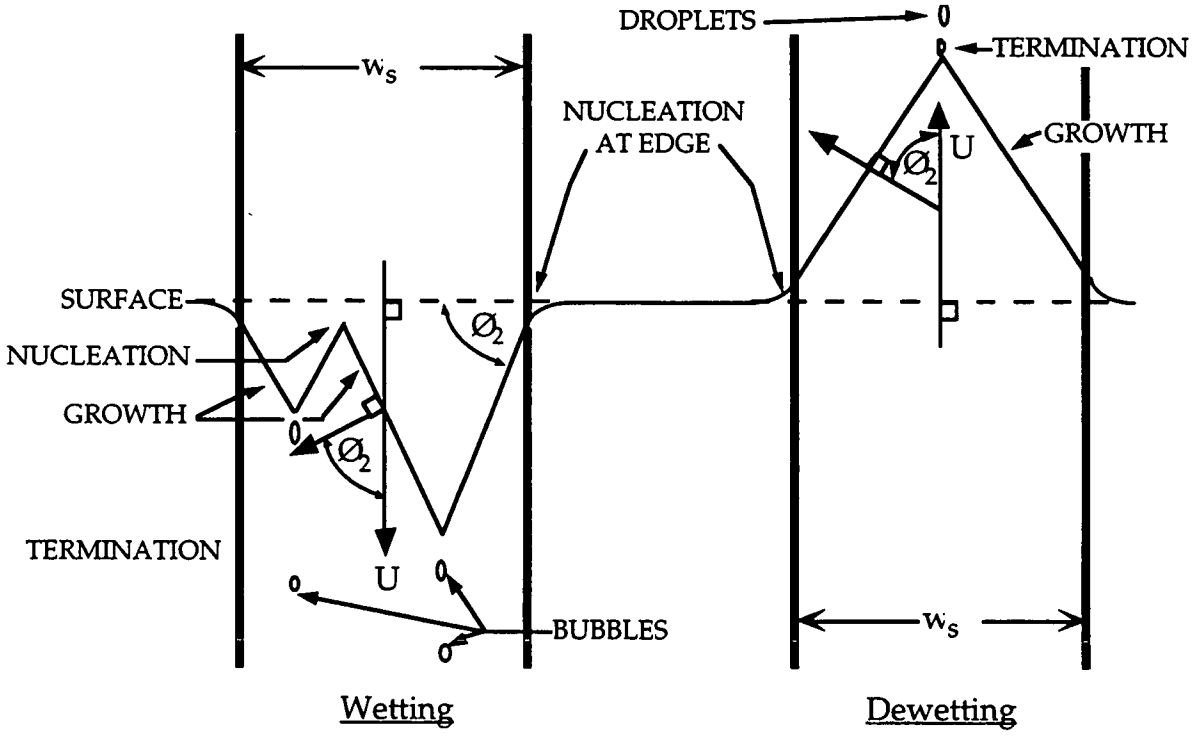

Figure 2.8. The sawtooth configuration of wetting and dewetting that occur during entrainment of a plunging tape system as it enters and exits a liquid pool. This is a front view of the tape compared to Figure 2.7 with the cavity boundaries not shown. Adapted from Blake (1988).

Gutoff and Kendrick (1982) used 16-mm tapes and investigated the effect of a wide range of liquid properties on dynamic air entrainment and the dynamic contact angle. The effect of the upper fluid was studied by replacing the air normally present with immiscible oils. Ishimi, Hikita, and Esmail (1986) applied others' data

(Kennedy and Burley 1977; Gutoff and Kendrick 1982) to compare solutions for an analytical model of the dynamic meniscus height at speeds below U_v. These authors hypothesized that a monomolecular film of the displacing phase preceded the apparent contact line to alleviate the no-slip mathematical singularity at the DCL. The model is two-dimensional and does not predict the sawtooth pattern observed during air entrainment.

Burley and Jolly (1984) used plunging tapes up to 25-cm wide. The air entrainment velocities were claimed to be independent of the angle of entry, α_s, and the width of the tape, w_s.

Another plunging tape study by Buonopane, Gutoff, and Rimore (1986) comes from a suggestion by Scriven (1982) regarding air entrainment and tape surface properties. They had shown very clearly by the data in Table 2.3 that the air entrainment velocity seems to increase with root mean square roughness. The data was normalized to the polystyrene tape. Their data also indicate that the wettability

Table 2.3. Air entrainment velocities for plunging tapes normalized to polystyrene. Adapted from Buonopane, Burley and Rimore (1986).

Tape Surface	rms Roughness (μm)	Mean	Low	High
Polystyrene	0.2	1.00	1.00	1.00
Polyester	0.3	0.92	0.46	1.41
Polypropylene	0.4	1.21	0.88	2.32
Polypropylene	1.0	1.05	0.78	1.22
Polypropylene	1.0	1.20	0.82	1.98
Baryta	1.0	1.08	0.25	1.39
Polyethylene	1.8	5.0	3.5	11.2
Polyethylene	2.4	5.8	3.5	11.2
Paper	5.0	4.7	1.5	12.2
Paper	5.0	1.6	0.34	2.92

of the tape surface has little or no effect on the air entrainment velocities, when comparing the wettable polystyrene and baryta to the polyester and nonwettable polypropylene. In order to verify his simple molecular event model at the DCL, Blake (1988) presented additional data for θ_d as a function of the fluid properties using 35-mm poly(ethyleneterepthalate) plunging tape system. The molecular event model is discussed in detail in Appendix I. By using Blake's data for $\theta_d \approx 180°$, additional plunging tape data is obtained and used by Kistler (1993) for comparing all plunging tape studies.

In an effort to distill the results of plunging tape studies, Kistler (1993) presented master curves of U_{ae} vs. μ and Ca_{ae} vs. the viscosity ratio, λ_∞, which are given in Figures 2.9 a and b. A simple power law in viscosity correlates U_{ae} well over almost three decades in μ and is given in Eq.[2.2]. He also states that the viscosity ratio, λ_μ, is a key parameter in correlating the onset of visible air entrainment, second only in importance to Ca_{ae} (Kistler 1993, 342). This correlation is given in Eq.[2.3]. If the receding phase density is also included, a correlation given in Eq.[2.4] also incorporates the density ratio, λ_ρ.

$$U_{ae}(m/s) = 0.048[\eta_l(Pa \cdot s)]^{-0.74} \qquad [2.2]$$

$$Ca_{ae} = 0.034\lambda_\mu^{-0.30} \qquad [2.3]$$

$$Ca_{ae} = 0.00019\lambda_\mu^{-0.33}\lambda_\rho^{-0.74} \qquad [2.4]$$

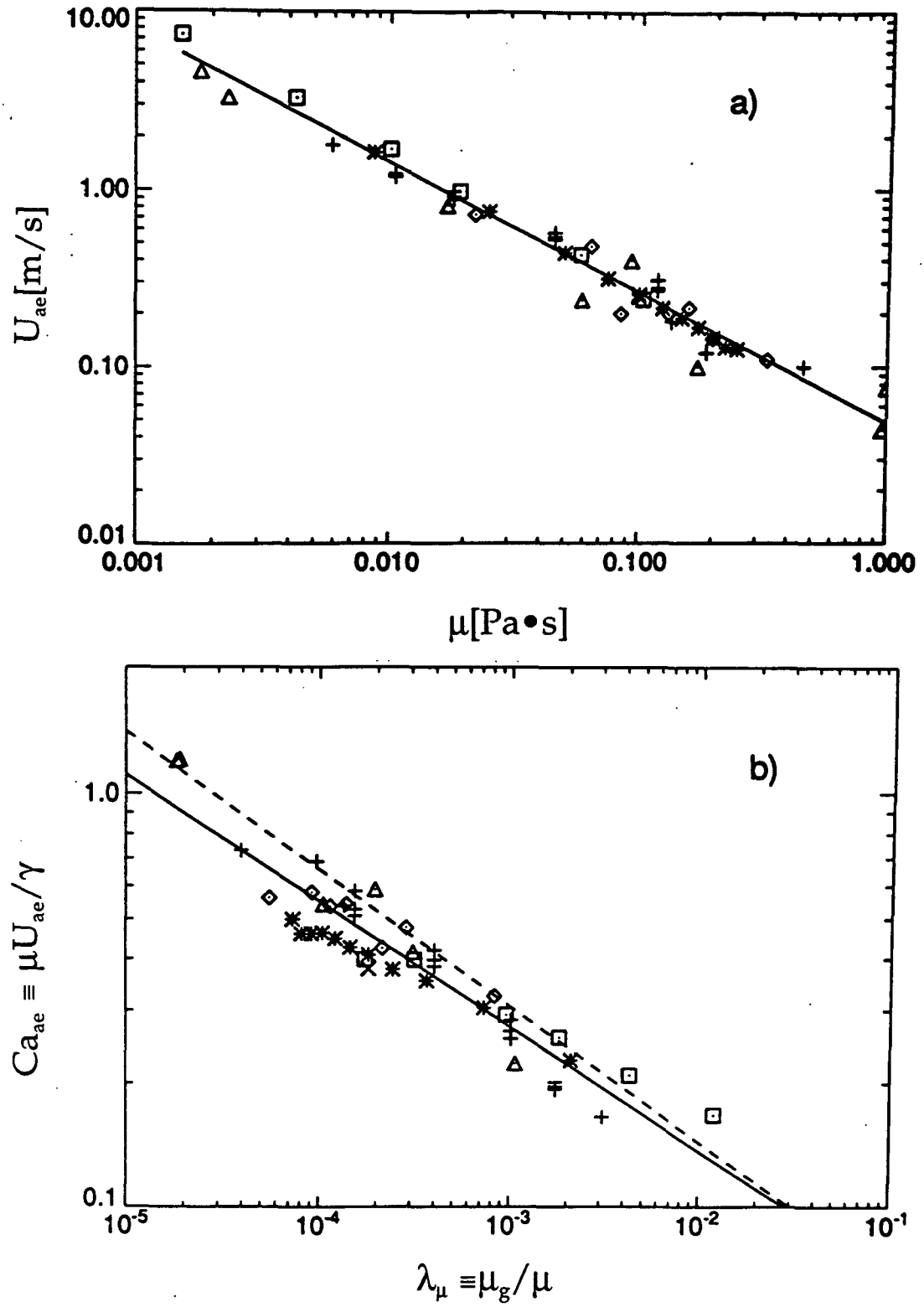

Figure 2.9. Onset of visible air entrainment in plunging tape experiments: a) air entrainment velocity U_{ae} vs. liquid viscosity μ. (straight line ——— Eq. [2.2]; + Burley and Kennedy (1976a); × Blake and Ruchak (1979); Δ Gutoff and Kendrick (1982); ◊ Burley and Jolly (1984); □Blake (1988); . Bracke, de Voeght, and Joos (1989); b) Critical capillary number as a function of viscosity ratio, where μ_g=1.83 x 10^{-5} Pa•s; —— Eq.[2.3]; ---- Eq.[2.4]. From Kistler (1993, 341). Used with permission of Marcel Dekker

2.5.2 Wetted Roll Studies

Ablett's study (1926) was conducted to determine the advancing and receding dynamic contact angles and found that maximum values existed for the low speed range studied. His study is often referenced because it represents the first wetted roll study. Wilkinson (1979) studied the air entrainment phenomenon with a doctored wetted roll rotating in a bath using Newtonian fluids. The study concluded that air entrainment took place at a critical capillary number of 1.2. It has often been cited by other authors (Kennedy and Burley 1977; Gutoff and Kendrick 1982; Burley and Jolly 1984; Bolton and Middleman 1980) for reaching the incorrect conclusion about the critical capillary number. Burley (1992a,b) reexamined Wilkinson's data with a log-log plot of Ca_{ae} vs. N_{pp} for only the glycerol/water solutions at $\alpha_s = 90°$ and the correlation is given by

$$Ca_{ae} = 1.23N_{pp}^{0.038} \qquad [2.5]$$

which corresponds well to similar studies.

Bolton and Middleman (1980) also conducted a comparable study with an undoctored wetted roll system but used a model based on simple force balances to correlate the critical capillary number. At 1000-cp fluid viscosity, the air entrainment speed was about five times greater compared to plunging tape data (Burley 1992a,b).

Two recent studies use glycerol solutions in a wetted roll setup that is similar to Veverka (1991). The first study by Esmail and Ghannam (1990) provides a dimensional analysis to base the later study on. Their correlation at $\alpha_s = 90°$ for the critical capillary number and physical property number is given by

$$Ca_{ae} = 1.17N_{pp}^{0.083} \qquad [2.6]$$

The second study (Ghannam and Esmail 1990) reported that the angle of entry influences U_{ae} and the interface displacement for doctored wetted roll systems. Table 2.4 gives correlations at different angles. In general, the dependence of Ca_{ae} on N_{pp} increases as α_s approaches 90°; i.e., both coefficients e and f contained in Table 2.4 increase as α_s approaches 90°.

Table 2.4. Regression analysis for e and f, $Ca_{ae} = eN_{pp}^{f}$ (Ghannam and Esmail 1990).

α_s	e	f	r
40	0.96	0.02	0.92
50	1.10	0.05	0.90
60	1.23	0.06	0.93
70	1.26	0.06	0.93
80	1.41	0.07	0.88

Veverka (1991) used more detailed high-speed flow visualization of the DCL instability and also collected data on U_v and U_{ae}. This work was the first published (Veverka and Aidun 1991a,b) documentation of the events depicted earlier in Figure 2.6. Veverka's wetted roll system had a thin layer of fluid on the roll entering at the DCL because of imperfect doctoring. The first critical velocity, U_v, represents the

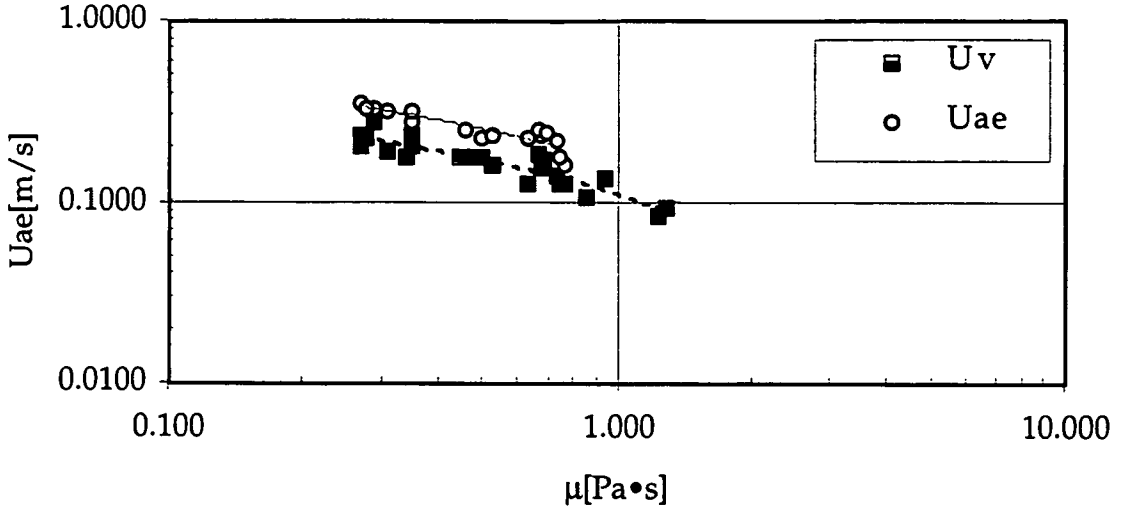

Figure 2.10. The variation in the first and second critical air entrainment velocities as a function of viscosity. From the data of Veverka (1991). Correlation of the same type as Eq.[2.2] are U_v [m/s]= 0.57 μ[Pa•s]$^{-0.951}$ (R^2=0.83) = and U_{ae}[m/s]= 0.59 μ[Pa•s]$^{-0.765}$ (R^2=0.82).

transition of the DCL from the straight configuration to an intermediate configuration which does have the sawtooth pattern. The magnification used by Veverka (1991) was only 1.5X, and therefore the estimates of U_v based on these observations are thus still approximate but intriguing nevertheless for ΔU. Figure 2.10 shows a graph with both U_v and U_{ae}. Correlations of the critical capillary number as a function of the physical property number for Veverka's data (1991) is given by

$$Ca_{ae} = 1.82N_{pp}^{0.11} \qquad [2.7]$$

is close to Esmail and Ghannam (1990) result's at α_s = 90°.

The apparent discrepancy that the angle of entry influences the air entrainment speed when comparing wetted roll and plunging tape studies is most likely a function of the surface not being completely dry and the realization of a greater slip length.

2.5.3 Curtain Coating and Film Slot Coater Studies

Brown (1961) was the first to discuss the curtain coater operation window by varying the liquid curtain impingement velocity, V. He was also the first to publish photos of the triangular air film in open literature, notwithstanding Deryagin and Levi's (1959) pictorial depiction of the triangular air film. He found that altering the boundary layer by applying a scraper close to the DCL affects the shape of the triangular air film and air entrainment speed.

Kistler, Hanauska, and Scriven (1984) have reported that much higher speeds are attainable with curtain coating prior to excessive air entrainment with plunging tape systems. Curtain coating presents other difficulties because the impingement speed, V, of the vertically falling curtain represents another independent variable to be controlled. The inertia gained by the curtain during the free fall seemingly causes significant stagnation pressure at the impact point and prevents air from becoming entrained between the liquid and substrate (Kistler 1984).

Experiments by Miyamoto (1986, 1991, 1992) confirms the hypothesis (Miyamoto and Scriven 1982) that air entrainment always occurs but that the entrained air bubbles are sufficiently small that they are not visible to the naked eye. By using a differential interference microscope on a curtain coater he was able to view entrained bubbles of diameter 5 to 20 μm at speeds one-third of U_{ae}. We term this type of air entrainment as "microscopic," which does not produce deleterious effects except in critical applications.

Two patents using a higher solubility gas (Miyamoto 1989) and employing ultrasonic waves (Nakajima and Miyamoto 1993) expanded on Miyamoto's idea (1991) about the microscopic air entrainment phenomena. By using CO_2 as a gas phase (Miyamoto 1989), any bubbles that are produced have a dissolution time 375 times faster than air and are therefore not visible. The ultrasonic waves (Nakajima and Miyamoto 1993) were directed at the DCL in the frequency range of 10 - 120 kHz so that air layer is vibrated producing smaller bubbles that are dissolved more rapidly. Hartman (1989) was issued a patent for curtain coaters with data supporting that an electrostatic polar charge provides an attraction between the falling curtain and the support which is sufficiently strong to provide a uniform and defect-free coating with higher speeds for U_{ae} (Hartman 1989, 4).

Just as altering the flow field in a curtain coater gives greater U_{ae}, similar ideas have been applied with slot coaters to increase U_{ae}. Levi and Akulov (1964) applied vacuum in a film slot coater to increase U_{ae} while in another study by decreasing the gap (Levi 1966) an increase in U_{ae} was achieved.

2.6 Qualitative Observation of Air Entrainment and Dimensions

Deryagin and Levi (1959, 141, Fig. 49) were the first to depict that the triangular air film base angle, $\varnothing_2$, increases, with increasing speed as previously shown in Figure 2.4.

Wilkinson (1979) reported on the results of 25-cm wetted roll trials with clear fluids. Wilkinson states, "...air was being entrained initially in the form of small bubbles originating from the top of the peaks."

Burley and Kennedy (1976a,b) found that the characteristic behavior of air entrainment onset varied markedly with fluid viscosity. They showed four modes of air entrainment as a function of fluid viscosity (Burley and Kennedy 1976a, Fig. 3) and schematically depicted that the number of vee shapes per unit length, N_v, increased as the liquid viscosity increases. Kennedy and Burley (1977, 50) also note that in general smaller bubbles are entrained as the viscosity increases. Burley (1992a, 102, 1992b, 199) reiterated this observation. Their explanation (1976a) for the vee-shape was due to the "effect of the hydrostatic pressure displacing the vertical fluid/air interface at the side of the moving surface, forming a symmetrical triangular shaped intrusion into the fluid." They also depicted that the base angle, $\varnothing_2$, increases with U_{ae} (1976a, Fig. 4) for the case of low viscosity, 47 cp glycerol-water, and narrow width, 25-mm tape. O'Connell's (1989) results, also reported by Burley (1992b, 193, Fig. 2) showed that $\varnothing_2$ increases with U_{ae}. Veverka's (1991) 50-cm-wide wetted roll system did not show a substantial increases in N_v using glycerol in the 150-650- cp range, although this observation is still qualitative. In studying 2.5 to 25-cm plunging tapes, Burley and Jolly (1984, 1362) reported that using low viscosity liquids and narrow tapes, e.g., 2.5 cm, formed only one or two vee shapes. In comparison, wider tapes, above 5.0 cm, more than two peaks, could be observed that would combine into a larger single vee at higher speeds. This gives clear evidence that edge effects interfere with the natural width that a triangular air film would obtain in an ideal system, i.e., infinite width and tank dimensions.

Ghannam and Esmail's (1990a,b) note similar observations of air entrainment which are consistent with previous studies.

Scriven (1982) proposed mechanisms for air entrainment with both smooth and rough, porous substrates. He also reported that the gas capillary number is a critical parameter. For a smooth surface below U_{ae} the sawtooth pattern emerges as shown in Figure 2.11. At speeds much higher than U_{ae}, the supercritical region, the tip of the air film is hypothesized to be unstable and to entrain large quantities of air.

Although Mues, Hens, and Boiy (1989) were not directly studying air entrainment, their results with laser doppler velocimetry on a slide coater, near the apparent contact line, assert confirmation of the thin air film hypothesis put forth by Scriven and coworkers (Miyamoto and Scriven 1982; Miyamoto 1991; Scriven 1982).

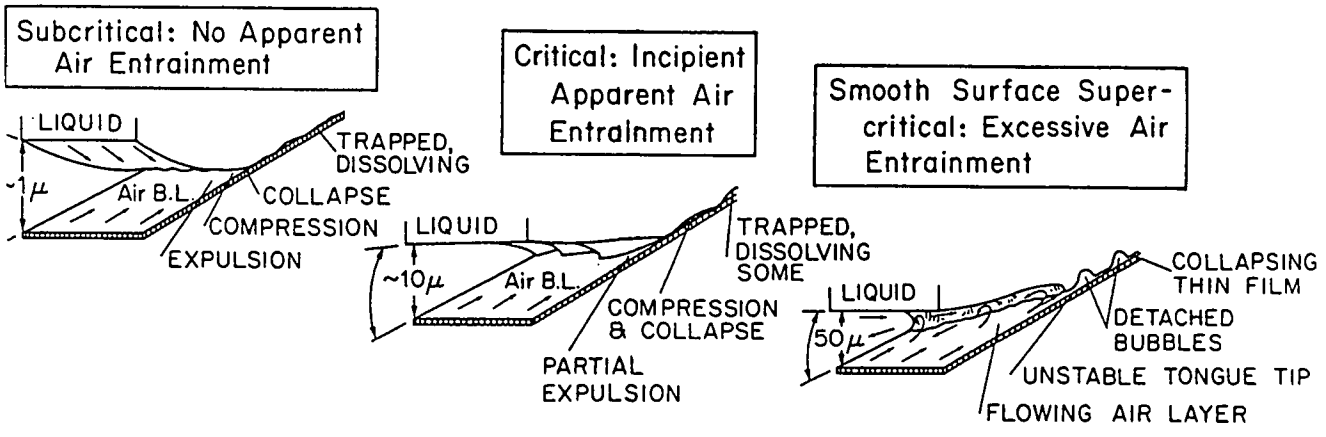

Figure 2.11. The breakdown of air film entrained by liquid coated on web as envisioned by Scriven (1982) for the subcritical, critical and supercritical speeds. This figure is a copy of that originally presented by Miyamoto and Scriven (1982).

Mues et al. deduce that the real contact line is 50 to 105 μm downstream from the apparent contact line and implied that a thin invisible air film may be entrained between the liquid and the web. At the apparent contact line the liquid velocity, measured using the electronically filtered laser doppler velocimetry signal, is 40 to

60% of the substrate velocity. Using these mean acceleration from the apparent to real contact line is around 428g. Kistler (1993, 347) discusses some considerable deficiencies in using laser doppler velocimetry near the DCL as applied to the results of Mues, Hens, and Boiy (1989).

In summary, despite all of the previous studies relating to air entrainment no quantitative measurements are available for the out of plane thickness of a triangular air film. To provide additional evidence for the interfacial long wave instability mode of air entrainment this information is required. The first presentation hypothesizing why this unstable mode is dominant is reviewed in the following section.

2.7 A Review of "The Mechanism for Excessive Air Entrainment in Coating Systems" (Aidun, Veverka and Scriven 1993)

In this paper a theoretical basis was derived to explain why the triangular air film initially nucleated near the edge of the triangular air film base. For convenience this paper is provided in Appendix XV. The flow visualization results of Veverka (1991) and Aidun ,Veverka and Scriven (1992) suggests that air flows into the triangular air film with the solid surface at the mid part of the triangular base, changes direction near the tip and moves outward at the sides. Because the thickness of the air layer is an order of magnitude smaller than the other dimensions we can assume two-dimensional velocity profiles in the central section A and edge section B (see Figure 2.12) and also that the lubrication approximations

apply. A standard linear stability analysis was used with the disturbance function expanded in normal modes for the liquid and gas velocity vectors, the liquid and gas pressure profiles, and the interface position. The assumed velocity profile resulted in a velocity gradient that was positive(negative) in section A(B) as we approach the interface as seen in Figure 2.12. Using this result, the authors show why the real part of the first order correction for the temporal growth rate, s, is unstable for a

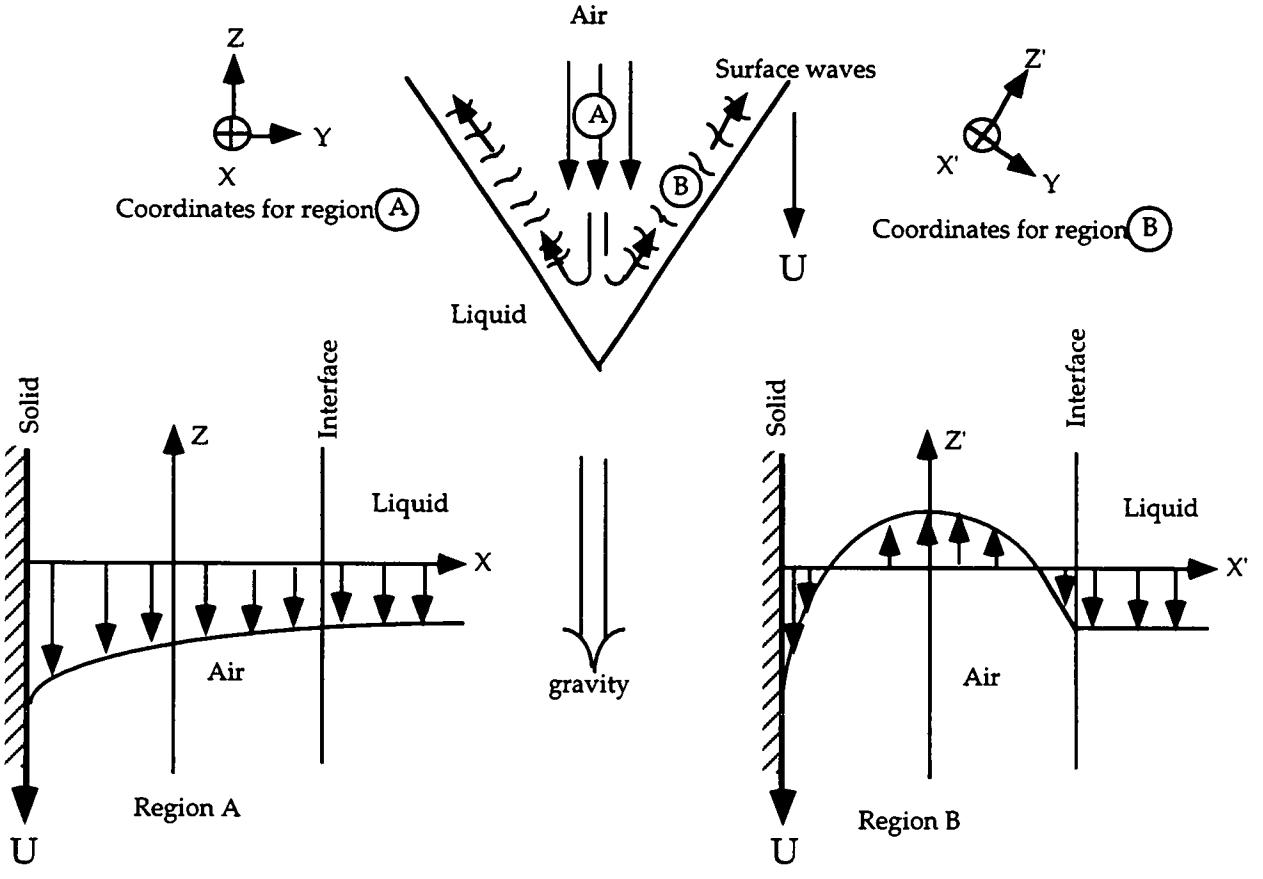

Figure 2.12. The hypothesized air and liquid velocity profiles at the center and edge of an individual triangular air film for a substrate velocity, U, where $U_v < U < U_{ae}$.

negative velocity gradient and positive values of the parameter[2] $\alpha > 1/4$. In other words, the velocity profile in section B, under the proper conditions can produce an interfacial wave of growing amplitude that will touch the solid surface thus leading to nucleation of wetting. The phase speed is also shown to be consistent with experiments where interfacial waves propagate in the direction opposite the solid.

Expanding this work in much more detail, Severtson and Aidun (1995) analyzed the stability of general stratified two-layer Poiseulle-Couette flow with specific application to the air entrainment problem in coating systems. Their analysis revealed an additional "inviscid" mode as well as the interfacial and shear modes. The interfacial mode is shown to be the only mode of instability with realistic parameters because of the large density variation between the gas and liquid layers. This agrees with the work of Aidun, Veverka and Scriven (1993).

[2] The parameter α is a function of the air density and viscosity, the pressure gradient, the length scale, and the substrate velocity.

CHAPTER III

PROBLEM ANALYSIS

The productivity of any blade coater is ultimately limited by the onset of air entrainment beyond the second critical speed, U_{ae}. Many of the previous studies presented earlier in Table 2.2, have resulted in correlations based on fluid properties for U_{ae}. This information is pertinent for setting ultimate speed limits but prediction of the first and second critical speeds from first principles is still not possible. A few major pieces of information still need to be obtained in order to guide construction of analytical and computational solutions of the coupled equations of motion for the liquid and gas flow fields as well as the interfacial profile.

Experimentally studying air entrainment in a conventional short-dwell blade coater with a paper substrate is complicated by a number of factors (Li and Burns 1992a,b). First, the coating fluid itself has high concentrations of solid particles and is difficult to model with rheological constitutive equations. The coating opacity currently precludes most flow visualization experiments except for flash x-ray (Triantafillopoulus and Farrington 1988) and NMR (nuclear magnetic resonance) imaging (Powell et. al. 1995) experiments. Second, most conventional coater head geometry's prevent visualization of the DCL and the events occurring within the coater head during air entrainment. Third, the surface roughness of the substrate and coating speeds (approaching 2000 m/min, Tierfolk and Laaja 1995) make it very difficult to study rapid transient events because of the short time scale. The use of

wetted roll and plunging tape experimental apparatus are examples of why conventional coater heads are not used for flow visualization research on air entrainment.

The first obstacle can be overcome by using a model fluid. The model fluid should be clear, Newtonian, and have physical properties which remain constant with time. The properties of the fluid should be easily varied over the range of values needed for this study and the fluid must be safe to handle. Silicone oil is ideally suited because its low surface tension minimizes the tendency of the fluid interface to attract contaminants. Silicone oil is not hygroscopic thus eliminating viscosity variations due to humidity changes.

The second obstacle can be overcome by using a unique experimental system unlike the plunging tape and wetted apparatus previously described in Chapter II. The proposed design should use an optically clear tape and a planar viewing area with close access to the DCL through a transparent coating head.

The most critical assumptions made from the previous work of Veverka (1991) is that a triangular air film can be successfully studied in the speed range between U_v and U_{ae}. The time scale that a stable triangular air film can exist must therefore be longer than that of air entrainment.

Flow characteristics at the liquid-air interface and triangular air film interior in the region $U_v < U < U_{ae}$ have not been previously investigated and are critical in understanding the physics of the process. The triangular air pocket can be externally perturbed (e.g. dust particle, vibration) thus leading to air entrainment. A very precise, vibration free, and clean experimental setup is thus required in order to

study the physics. Additionally, the experimental coating head should have some analogous industrial counterpart which in the case of our setup is the puddle coater previously discussed in Chapter II.

A significant advance will be made if the region when $\Delta U \neq 0$ is studied with non-intrusive methods capable of measuring the interface height from the solid surface, h(t), where $\Delta h(t) \geq 1$ μm. The results of these types of experiments will give additional quantitative evidence for the theory that the interfacial mode obtained in the long-wave asymptotic limit (Severtson and Aidun 1995) produces nucleation of the triangular air film near the base region.

CHAPTER IV

EXPERIMENTAL

Chapter IV has three subsections. The first, Section 4.1, is where the apparatus is presented and described. The second, Section 4.2, discusses the physical basis and application of the deflectometry technique. Finally, in Section 4.3, the relevant physical properties of the coating liquid and substrate are presented.

4.1 Introduction to the Experimental Setup

The apparatus designed for the air entrainment experiments is comprised of four components — the unwind/rewind system, the coating application system, the process control and data acquisition system, and the optical system. Each component is identified in Figures 4.1 and 4.2. A schematic diagram of the experimental system is seen in Figure 4.3. The blueprints for the apparatus are presented in Appendix II with details of the fabricated and purchased components of the apparatus listed in Appendix III. Additional details regarding the four components and operating protocol are contained in Appendix XVI.

4.1.1 Overview of Main Components

The experimental paper/film coater was designed with the following requirements: (i) the substrate must be clear and free from defects, (ii) substrate speed and vibration must be precisely controlled, (iii) the DCL must be highly accessible, and (iv) the system must be adaptable to test other configurations.

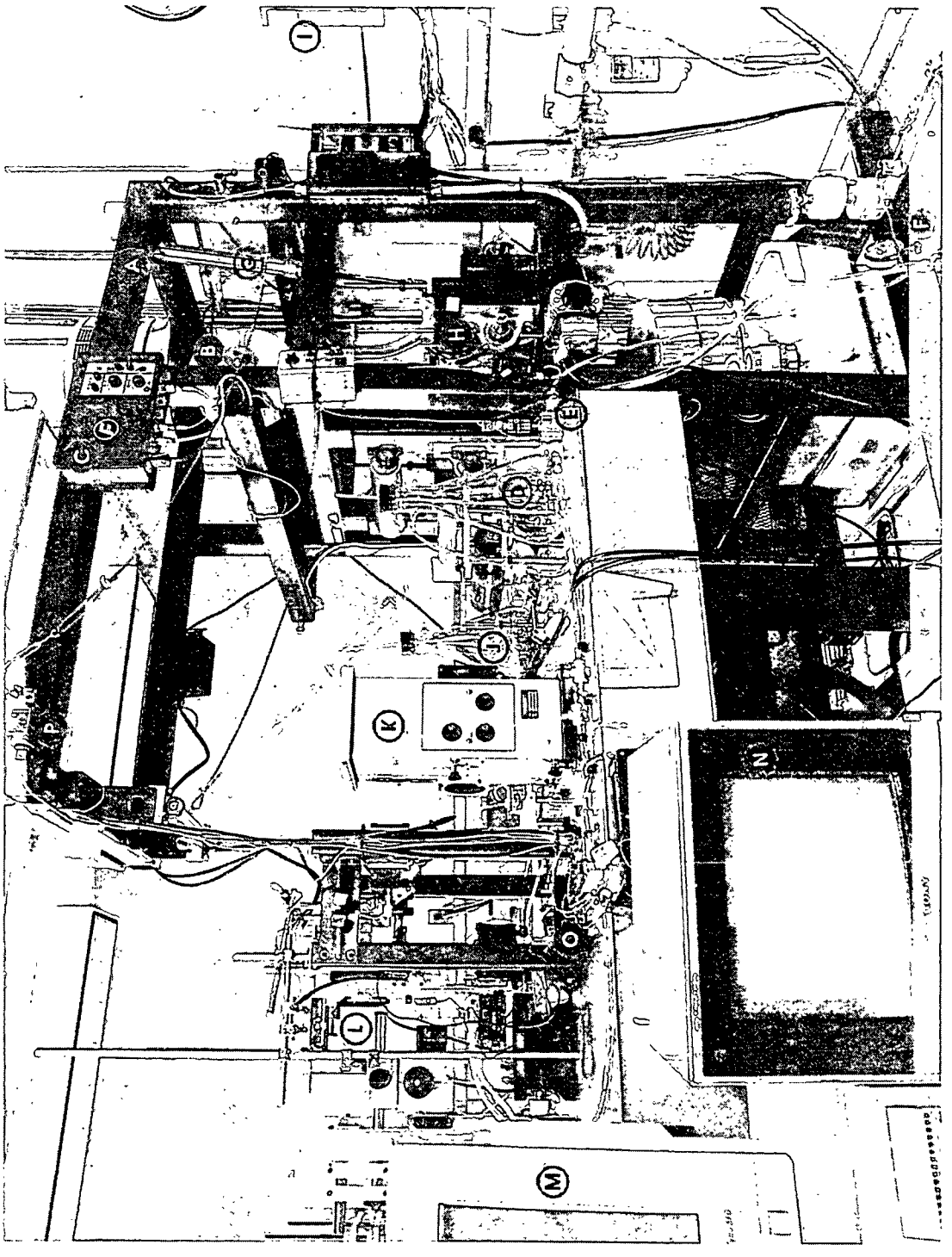

Figure 4.1. A photograph of the experimental paper/film coater. A - unwind/rewind stand; B - supply roll; C - web guide controller; D - pump supply flask; E - gear flowmeter; F - moyno pump, drive, reducer; G - air cylinder lift; H - surface rewind; I - tension controller; J - coating recovery flask; K - Oriel 1000W illuminator; L - optics, coater head and shoe; M - data acquisition and control computer; N - frame grabber monitor; O - thermocouple amplifier; P - emergency stop line.

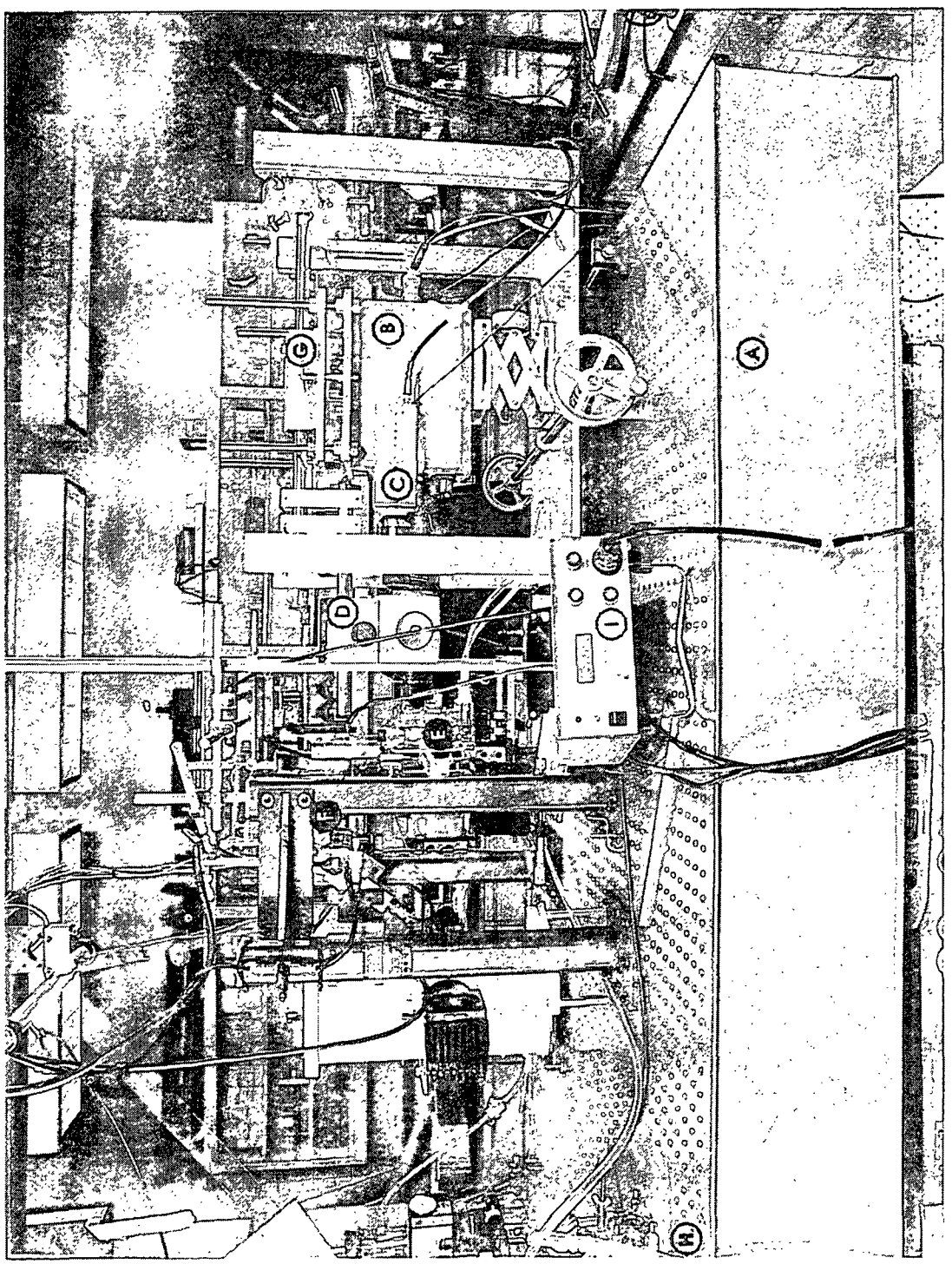

Figure 4.2. A photograph of the optics section of the experimental paper/film coater. A - optical bench; B - LOCAM II 16-mm high-speed camera; C - CCD camera; D - stereo zoom microscope; E - coater head; F - ionizing air knife; G - camera/microscope translator and level; H - coating recovery pump.

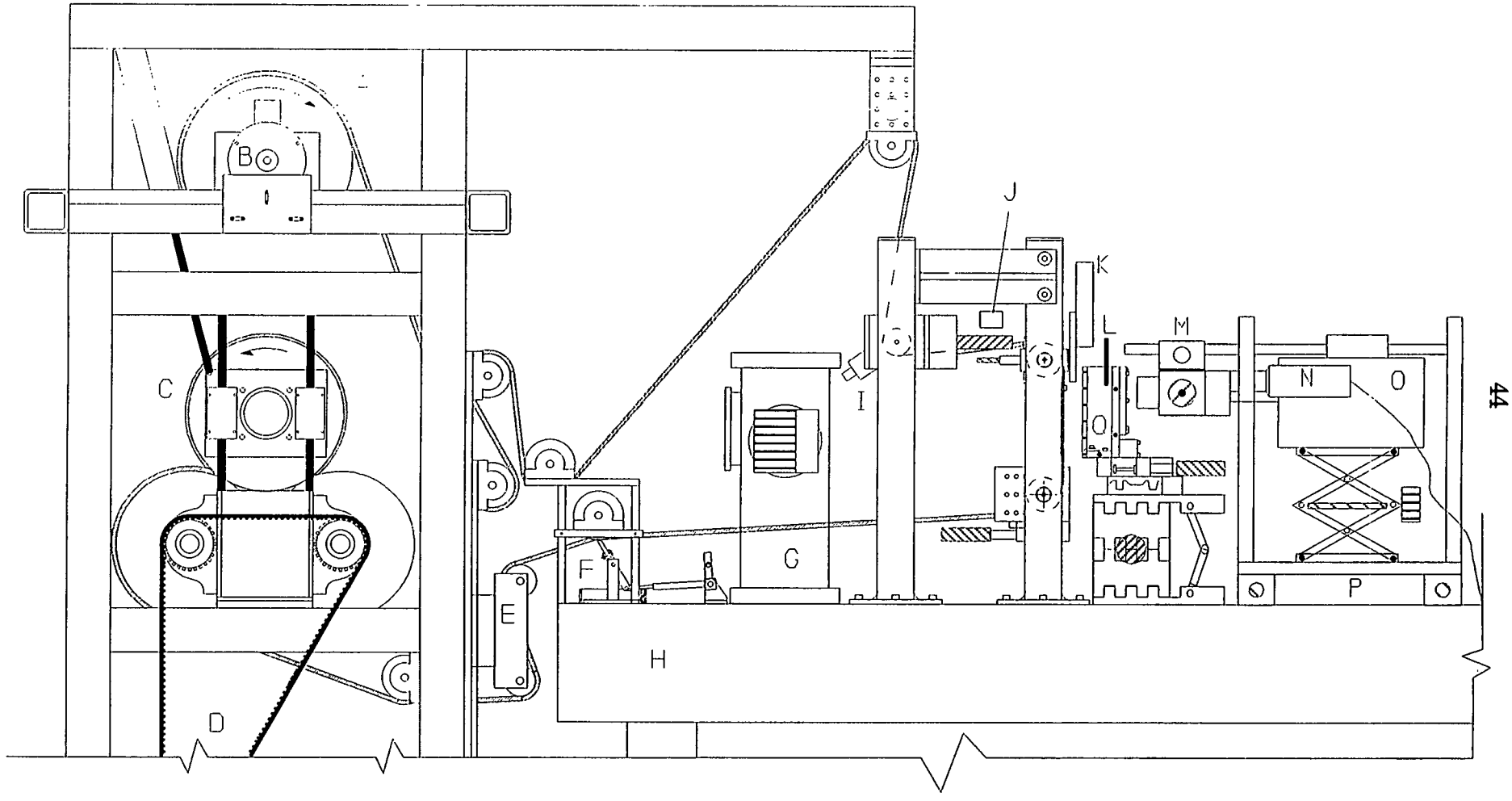

Figure 4.3. A schematic diagram of the experimental paper/film coater. A - unwind reel; B - magnetic particle brake; C - rewind reel; D - drive belt and gears to motor; E - web guidance system; F - second doctoring blade; G - Oriel 1000 W illuminator; H - vibration isolation optical bench; I - tension transducer; J - ionizing air knife; K - Monroe static probe with holder; L - fiber optic displacement sensor; M - stereo zoom microscope; N - CCD video camera on port A; O - 16-mm high speed camera; P - traversing assembly; Q - "puddle coater" head with x, y, z, positioners.

The unwind/rewind system provides motive power, guidance, tension control, and postapplication doctoring of the substrate. A surface wind system was selected to eliminate the need for speed compensation as the rewind reel diameter increases. By varying the belt and gear dimensions a wide range of speeds can be tested. The main motor is supervised by a closed loop digital controller with a gear ring proximity feedback sensor on the main motor shaft.

The cantilevered unwind reel is attached to the controlled magnetic particle brake. The tension was generally set at 1.7 to 2.2 kg/cm with the primary substrate poly(ethyleneteraphthlate) Melinex™ 454. This substrate is designated coated PET throughout this work. The system is designed to accommodate a usable roll diameter of 40.6 cm, and total running time is a function of substrate gage and velocity.

The use of precision bearings and rolls and placement of the coating head assembly on a vibration isolation system are intended to minimize external disturbances.

The head is loaded onto the shoe by an x-y linear translator. Its dimensions are 3.51 x 11.73 x 9.73 cm (depth, d_c, x height, h_c, x width, w_c) with a schematic layout of the optics and coater head shown in Figure 4.4. The aspect ratio of the cavity, a_c, is defined as the cavity depth, d_c, divided by the liquid height, H_L, ($a_c=d_c/H_L$). The blueprints for the coating head are contained in Appendix II. The coating shoe, provides a surface to seal the cavity edges, and a surface to load the cavity metering blade into the sliding substrate. In the center of the shoe a ronchi ruling window is

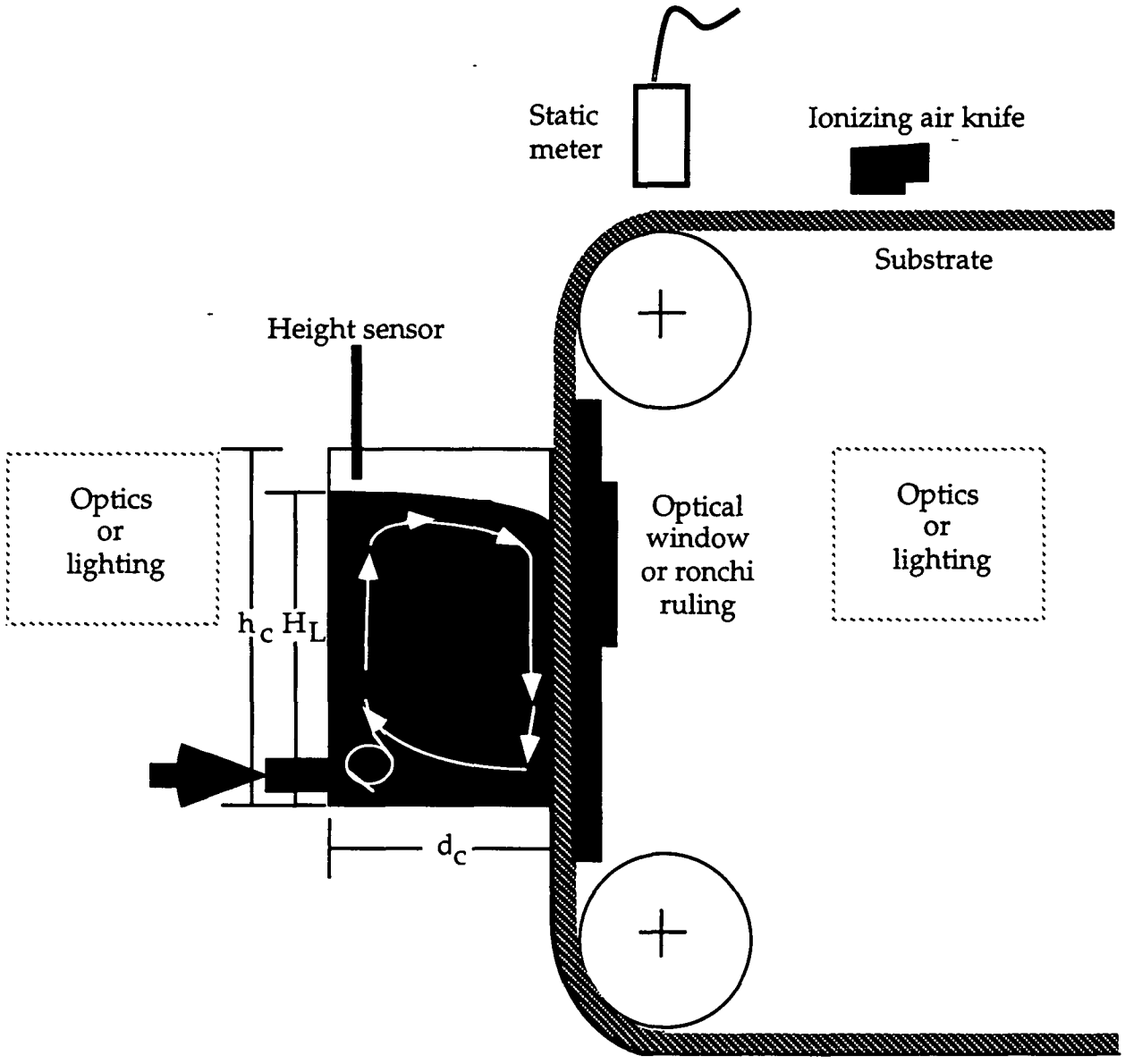

Figure 4.4. The experimental coater head similar to a puddle coater. The optics section can be on either side of the coater head because of the adaptable configuration.

mounted. A ronchi ruling, which is a glass transmission grating with variable number of lines/cm, is used to generate a reference pattern. Mechanical yielding of the shoe due to the metering blade loading creates misalignment between the optical axis and the axis normal to the ronchi ruling surface. This misalignment correction angle, G, was measured as a function of the coating weight thickness, t_c, in Figure 4.5 This design is primarily for DCL visualization and not precision coating.

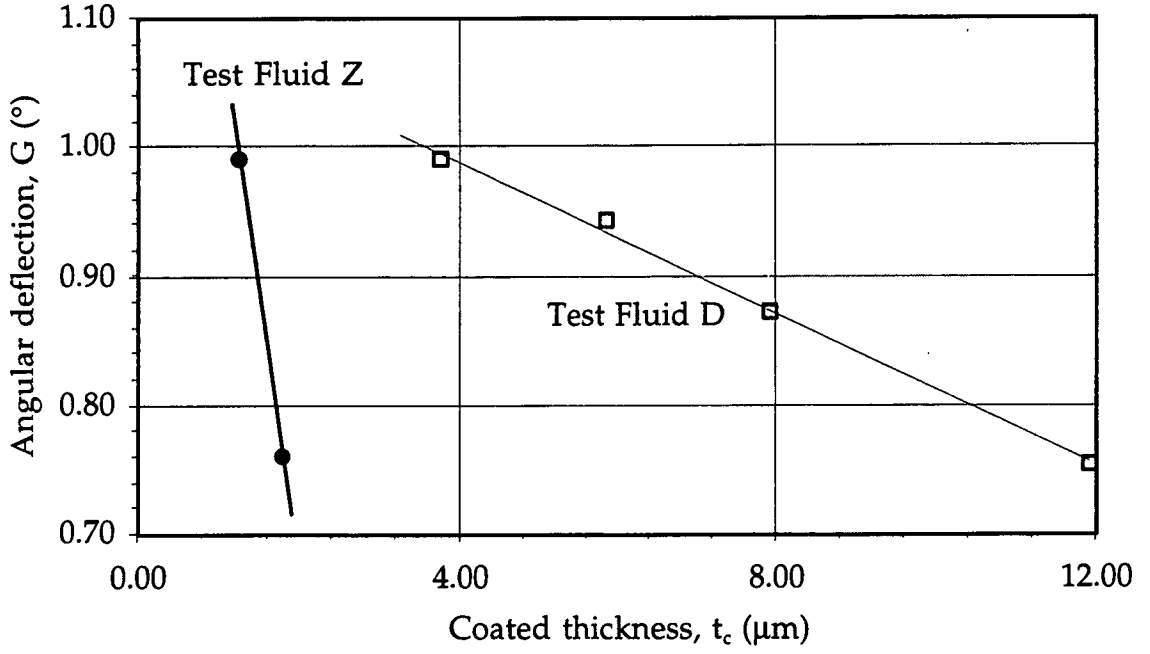

Figure 4.5. Variations in the angular deflection of the window shoe, G. The two fluids are Fluid D - 500 cs DC200 silicone oil, Fluid Z - 20 cs DC200 silicone oil. The correlation for G based on the average coated thickness and fluid viscosity is $G(°) = 0.00007\mu_l(cp) + 0.892°$.

The coating head inlet tubing was supplied by a 1034 kPa progressive cavity pump and distributed from the inlet line by a slot on the cavity back wall. The rear wall of the cavity is a precision optical glass window for visualization through the main recirculating vortex with transparent fluids. A positive displacement gear flow transmitter measured the cavity inlet flow rate. The control signal for the supply pump motor came from an IR fiber optic displacement sensor. The sensor was mounted normal to the free surface on top of the coating cavity, allowing for automatic cavity liquid height control, $H_L = 10 \pm 0.002$ cm, using a proportional integral control algorithm and data acquisition and control software. Seven analog input signals and one analog output signal were acquired by a 12-bit A/D board on a

486DX2 host computer. A graphical interface was used to update substrate velocity, U, liquid temperature, T_l, liquid Capillary number, Ca, and liquid Reynolds number, Re.

The remaining substrate coating is metered by a second pressure-loaded blade system. It is necessary to remove all residual fluid from the tape to prevent lubrication slippage and telescoping of the reels. A narrow web guidance system keeps the substrate in the same path. In addition quick disconnect safety chucks and air shafts were used with standard 10.16-cm diameter cores for substrate handling.

4.1.2 Reducing Substrate Charge Prior to Coating Head

In the design of previous plunging tape and wetted apparatus, attention to eliminating static has been made by using grounded rolls (Burley and Jolly 1984; Buonopane, Gutoff, and Rimore 1986). The types of electrostatic charges found on dielectric webs are free and bound charges with the bound charge due to internal polarization (Kisler 1991). In the system designed for this work, frictional charging and charging due to separation of surfaces at the unwind reel, as well as subsequent roll contact/separation may lead to dielectric web charging. Vosteen (1986) gives a concise discussion about the general principles of electrostatic measurement (which is briefly summarized below) to demonstrate the rationale for the design used in this thesis.

For a web that is uniformly "charged," the capacitance, C, of any small area of the web is proportional to its area, A_e, divided by the distance, l_e, between the web and any grounded object (Vosteen 1986). This is expressed in Eq. [4.1] with ε_o the

permittivity of free space (8.855×10^{-12} farad/meter). When the web is in free space, l_e is at a maximum and, thus C goes to almost zero. When the web is in close contact with a roller, or the window shoe in our case, l_e is at a minimum and, therefore, C is at a maximum. The web changes in potential or voltage, V_e, proportionally to the capacitance of the web as shown in Eq. [4.2] where Q represents the magnitude of the charge between the two bodies.

$$C = \varepsilon_o \frac{A_e}{l_e} \qquad [4.1]$$

$$V_e = \frac{Q}{C} = \frac{Ql_e}{\varepsilon_o A_e} \qquad [4.2]$$

Since both glass and the PET substrates are dielectric materials with volume resistivities of 2×10^{13} and 1×10^{14} Ω-cm, respectively, conductive aluminum foil with volume resistivity of 2.82×10^{-6} Ω-cm, was placed between the tape and the shoe for the first 7.6 cm of the shoe length from the top precision roll. This reduces the distance, l_e, between the tape and a grounded surface, and minimizes the frictional electrostatic charging that would have occurred between the dielectric materials. Additionally, an ionizing air knife-type active static eliminator was placed immediately prior to the first precision roll of the shoe to neutralize the free charge on the web and blow any surface contamination (Moore 1973, Kisler 1991).

It is also a known that the surface resistivity of a dielectric material is a strong function of humidity decreasing as much as 10^{15} Ω/square at 10% RH to 10^{10} Ω/square at 50% RH (Kisler 1991). The experimental paper/film coater is located in

a climate-controlled room at 50% RH and 23.9°C additionally minimizing static charging effects.

Taylor and McEwan (1964) first studied the neutral equilibrium equation for a horizontal fluid interface in a vertical electric field and the vertical displacement. For the condition of no free interfacial charge, they solved for the limiting gradient at which it becomes unstable. In our system, we have a vertical fluid interface in a horizontal electric field with dynamic pressures, surface tension, viscous and hydrodynamic forces acting on the wetting region. Our goal will be to minimize the substrate electric charge and thus minimize electrostatic attraction.

Two types of electrostatic charge detectors were used - a hand-held field-type meter and a precision localized type - to verify that the substrate surface was fairly close to neutral electrostatic charge. A 3M 709 hand-held static sensor was mounted with a 2.5-cm gap over the web as it passed the first precision roll and approximately 5-cm before the DCL. This type of device measures the electrostatic field of the web, i.e., the average charge over a large area. A MONROE Isoprobe® electrostatic voltmeter using a model 1017S probe with a miniature 1.75-mm sensing aperture permitted measurements of a small charged area in the same region as the optical observation region. The 10 to 90% response speed for a 1 kV input step is less than 2.5 milliseconds. Mounting of both detectors at a uniform gap is fundamental to ensure accurate measurements and comparison between experiments (Blitshteyn 1984).

4.1.3 Imaging Components

The core of the imaging system is a common objective Wild-Heerbrugg M8 stereo zoom microscope. This type of microscope was chosen for the following reasons: (i) its long working distance, (ii) the availability of a wide variety of objectives, (iii) its ability to interface with multiple cameras, and (iv) the intermediate image planes are parallel to the object plane and there is no tilt between them. The lens elements are apochromatic and corrected for flatness.

Two different optical recording devices were used with the stereo zoom microscope. A monochrome charged coupled device (CCD) video camera was interfaced with port A on the stereo zoom microscope and recorded on a super-VHS video deck connected in series to a time code generator. The CCD video camera was operated at 1/10,000'th of a second shutter speed with auto gain in field mode during all experiments. Port B on the stereo zoom microscope was interfaced with a 16-mm pin register camera that is capable of up to 500 full frames/second. The camera is outfitted with the alpha numeric data system (A.N.D.S.) which is a microcomputer controlled optical time and data annotation unit. Black and white reversal film with a 200 ASA rating was used in 100- and 400-ft rolls for high-speed filming trials.

Rear lighting of the experimental area was used with an opal glass diffuser lens over the Oriel 1000 W tungsten halogen lamp aperture. This lamp is equipped with an IR absorbing mirror which reduces radiative heating of the test section. The lamp and opal glass worked best with the CCD and the ramping experiments discussed later in Chapter V. The ramping experiment setup and methodology to find U_v and U_{ae} are discussed at great length in Appendix Section XVI.6.

During 16-mm deflectometry experiments, the lamp was tilted approximately 10° off the stereo zoom microscope primary objective axis and the opal glass diffuser was removed. High light fluxes were needed to expose the 16-mm film at 500 frames/sec and a 1/9700'th of a second exposure time. Correct exposure was determined directly through port B using a camera light meter.

To facilitate positioning of the entire array uniformly, and maintain optical axis perpendicularity to the unloaded shoe window, a traversing alignment system was used. The 16-mm camera and stereo zoom microscope were both mounted on a dual offset shaft that kept correct adapter-to-phototube distances and allowed for angular adjustment of the optical axis.

The shoe window was 10.16 x 10.16-cm custom ronchi ruling with 4 different quadrants (shown in Figure 4.6). The advantages of this ruling include the ability

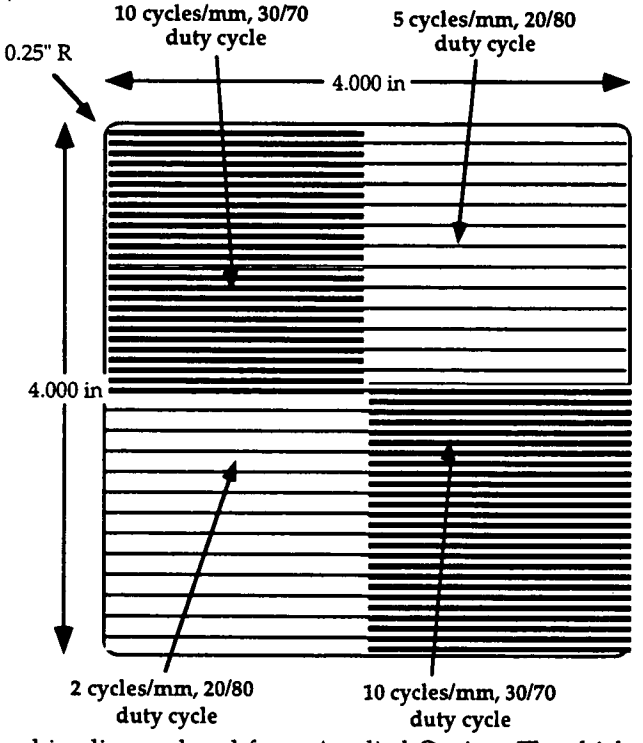

Figure 4.6. Specialized ronchi ruling ordered from Applied Optics. The thickness of the soda-lime-silica-type glass plate was 1588±4 μm, and it has a sodium D-line refractive index of 1.515±0.005 at 632.8 nm. The duty cycle is the percentage black area/percentage white area.

to vary the ruling spacing simply by translating the optics assembly to a new region of interest.

An 8-bit monochrome frame grabber board, was used with image analysis software to manipulate the image and quantitatively measure ruling line deflection. An individual frame of 16-mm film was digitized by using the frame grabber with another stereo zoom microscope (Wild-Zeiss M3) to manually select a particular region of interest where an air pocket had formed. The triangular air film may occupy 25% or less of the frame and thus zooming in on a particular region allowed the digital image to contain the maximum number of pixels per ruling line. Since silver halide film has a very high information density it was possible to discern very small features that gave clues about air entrainment.

Four common features were used to measure fringe deflection, δy_i or δx_i, using image analysis namely: thresholding, binarization, skeletonization, and marker line identification. The threshold function allows you to create a range of luminance values that are the window for discrimination in a selection routine, i.e., background vs. foreground. For example, if the ruling lines had grayscale luminance values of 0-40 (very dark foreground) while the lighter bands in between were 160-200 (medium background) this would provide an adequate window for setting thresholds to select one feature over another. Once a threshold is set, the image can be made binary with white (255) and black (0) grayscale values used to represent the image. Image skeletonization is executed through erosion of the foreground pixels in the binary image with a variation of the Zhang and Suen (1984)

skeletonization algorithm. The midpoint of the deflected ruling line can be identified using this repeatable technique. An automatic method was used for detecting changes in grayscale luminance values along a line. The line was broken into 4096 sample intervals and the gradient where the grayscale changed white to dark was used to detect the ruling line position. The previously mentioned capabilities permit many images to be measured fairly rapidly and to determine δy_i or δx_i with good accuracy. Additional details concerning the accuracy are contained in Appendix Section XVI.7.

The proceeding section has discussed the salient features of the experimental paper film coater. Emphasis is placed on the precision and uniqueness for obtaining access to the DCL using non-contact optical deflectometry. This will be proven viable in Section 4.2 and experimentally applied in Chapter VI. Before the deflectometry technique can be used, a parameter space will be identified in Chapter V when a triangular air film is stable.

4.2 Experimental Application of the Laws of Geometrical Optics

This Section outlines the optical laws for the deflectometry technique applied in Chapter VI after the necessary foundation of Chapter V. In Section 4.2.2, the three interface system relationship is derived for the continuous case. The error between the exact and linearized equation is less than 0.6% for $dh/dy < 0.1$. Section 4.2.3 presents the discretized quadratic equation, Eq. [4.22], for interface height, h_i. The uncertainty error and the analysis applied to a representative image are discussed in Section 4.2.4.

4.2.1 Introduction to Geometrical Optics

Geometrical optics utilizes the laws of reflection and refraction to study the action of optical components on light and is able to adequately represent the physical action of these components on rays of light (Born and Wolf 1980; Higgins 1994; Durst 1981). The actual paths of light rays are computed by taking reflection and refraction into account and by considering the angle relationships given in Fig. 4.7. For the case

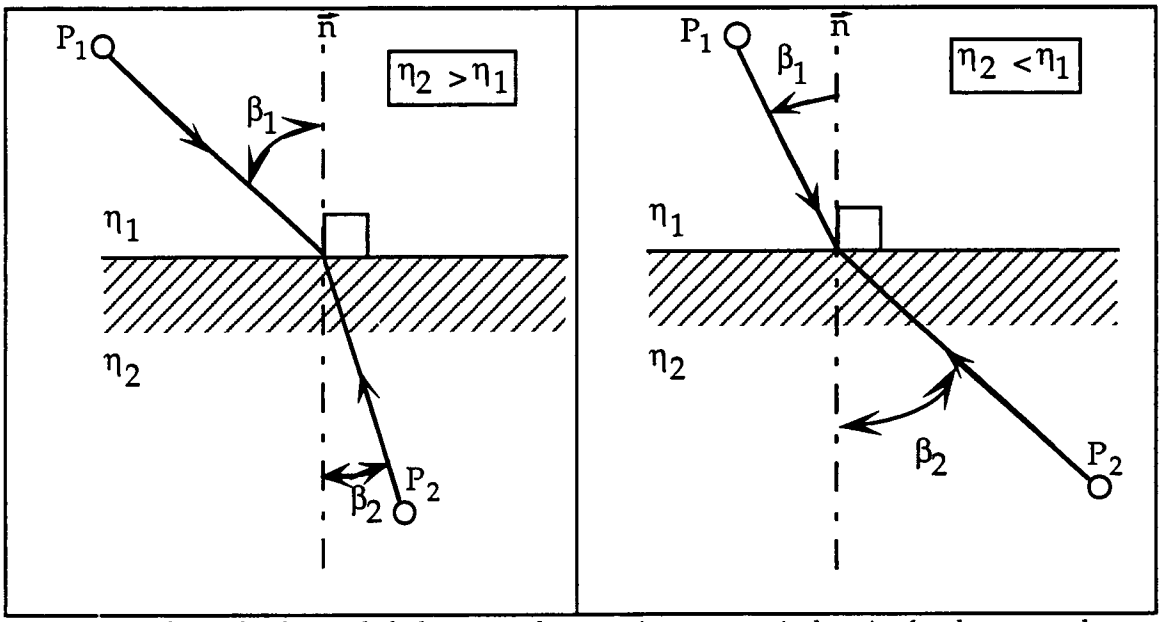

Figure 4.7. The path of a single light ray as shown using geometrical optics for the cases where $\eta_{2,1} < 1$ and $\eta_{2,1} > 1$.

when a light ray enters an optically denser medium, the beam is refracted toward the normal, $\vec{n}$, of the surface element through which the ray passes because the relative refractive index of the media, $\eta_{2,1} = \eta_2/\eta_1$, is larger than 1.0. The opposite occurs if the light passes the interface from the optically denser medium, e.g., from water or glass into air. Snell's law (Born and Wolf 1980) or Fermat's principle for refraction (Durst 1981) is the relationship that governs the transmitted angle ,$\beta_t = \beta_2$, as given by the equation:

$$\eta_1 \sin\beta_1 = \eta_2 \sin\beta_2 \qquad [4.3]$$

By applying the law of refraction, in conjunction with geometrical relationships, an analytical expression for the displacement of a light ray can be made for the simple three-interface system that is encountered in this work. The deflectometry method is a modification of the moiré topography technique developed by Kheshgi and Scriven (1983) to study coating flows. By using a single main objective type stereo zoom microscope the deflectometry optics in Fig. 4.8 are simplified and confined to a narrow depth of field. This is ideal for studying triangular air film formation and entrainment.

4.2.2 Calculation of Fringe Deflection

The experimental setup side view is shown in Fig. 4.9 for the case when the ruling fringe lines are parallel to the x-axis. Fringe deflection, δy_i, depends on the slope of the air/liquid interface, i.e., dh/dy, solely in the direction perpendicular to the

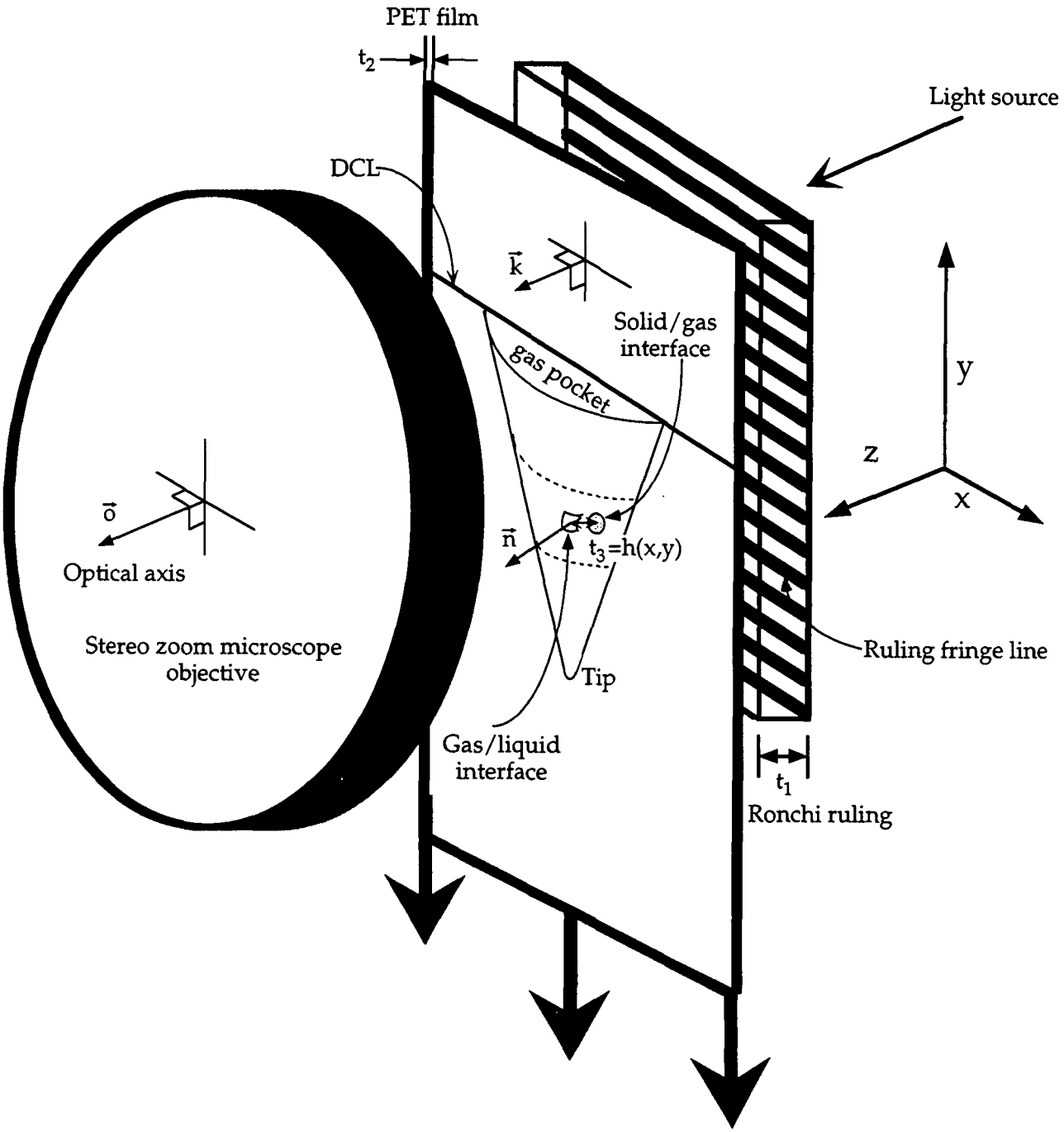

Figure 4.8. Schematic diagram of apparatus optical setup for measuring the gas/liquid interface shape for a triangular air pocket. Note that the dimensions are not to scale.

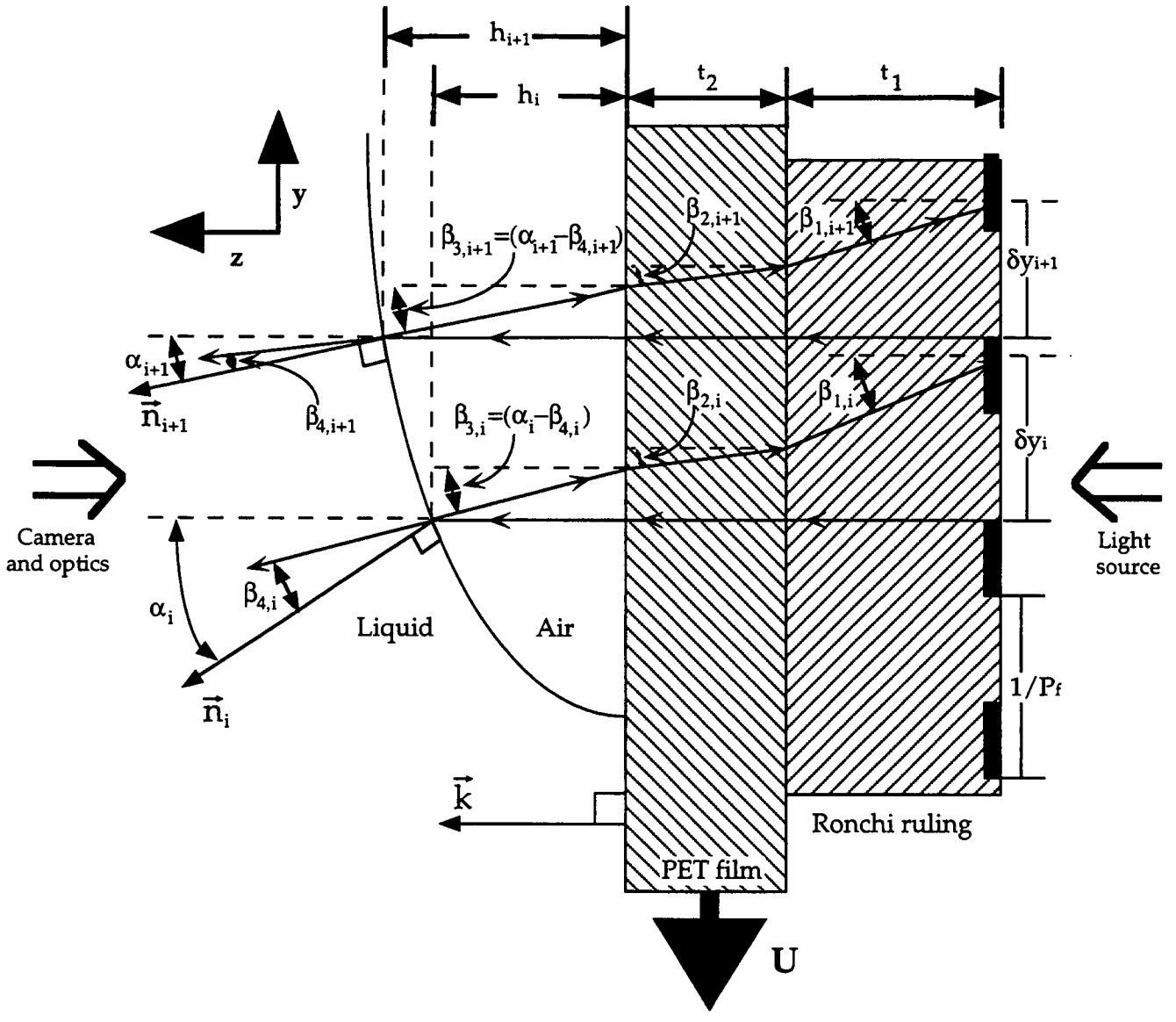

Figure 4.9. Side view of the basic optical components that influence the measurement of fringe deflection due to changes in the surface slope.

rulings of the grating. This is true when the layers are plane and parallel as indicated in Fig. 4.9, and when the normal to the optical axis, $\vec{o}$, and the normal to the solid surface, $\vec{k}$, are parallel. The correction for angular misalignment, G, between $\vec{o}$ and $\vec{k}$ is given in Eq. [4.4] and is necessary under all physical loading of the window shoe leading to the condition that $\vec{o} \bullet \vec{k} \neq 1$. Numerical values for G were presented earlier in Section 4.1.1 and range from 0.90° to 0.93° for the corrections applied in Chapter VI.

$$G = \cos^{-1}\left(\vec{o}\cdot\vec{k}\right) \qquad [4.4]$$

Since h = h(x,y), if the fringe deflection is measured at the centerline of an air pocket, a translationally symmetric interface results. Thus, h ≈ h(y) very close to the centerline. As seen in Fig. 4.9, the angle, α, between the normal to the liquid/gas interface, $\vec{n}$, and the normal to the PET film, $\vec{k}$, is a function of the surface slope, dh/dy:

$$\alpha = \cos^{-1}\left(\vec{n}\cdot\vec{k}\right) = \tan^{-1}\left(\frac{dh}{dy}\right) \qquad [4.5]$$

For dh/dy « 1, we can approximate α = dh/dy. This can be seen from the negligible contribution of the higher order terms in the Taylor series expansion for $\tan^{-1}$:

$$\tan^{-1}\left(\frac{dh}{dy}\right) = \frac{dh}{dy} + \frac{\left(\frac{dh}{dy}\right)^3}{3} + \frac{2\left(\frac{dh}{dy}\right)^5}{5} + \frac{17\left(\frac{dh}{dy}\right)^7}{315} + \ldots \qquad [4.6]$$

By applying Snell's law at the gas/liquid interface, we can calculate the transmitted angle, β_4, from the incident angle, α, as a function of dh/dy:

$$\eta_3 \sin\alpha = \eta_4 \sin\beta_4 \qquad [4.7]$$

$$\eta_3 \sin\left(\frac{dh}{dy}\right) = \eta_4 \sin\beta_4 \qquad [4.8]$$

$$\beta_4 = \sin^{-1}\left[\frac{\eta_3}{\eta_4}\sin\left(\frac{dh}{dy}\right)\right] \qquad [4.9]$$

For small values of dh/dy, we can linearize Eq. [4.9] to Eq. [4.10] because of the negligible contribution from the higher order terms in the Taylor series expansion for inverse sine and sine:

$$\beta_4 \approx \frac{\eta_3}{\eta_4}\left(\frac{dh}{dy}\right) \qquad [4.10]$$

$$sin^{-1}\left(\frac{dh}{dy}\right) = \frac{dh}{dy} + \left(\frac{1}{2}\right)\frac{\left(\frac{dh}{dy}\right)^3}{3} + \left(\frac{1}{2}\right)\left(\frac{3}{5}\right)\frac{\left(\frac{dh}{dy}\right)^5}{5} + \ldots \qquad [4.11]$$

$$sin\left(\frac{dh}{dy}\right) = \frac{dh}{dy} - \frac{\left(\frac{dh}{dy}\right)^2}{2!} + \frac{\left(\frac{dh}{dy}\right)^4}{4!} - \frac{\left(\frac{dh}{dy}\right)^6}{6!} + \ldots \qquad [4.12]$$

The expressions for β_4 and α are relative to the normal, $\vec{n}$, at any position on the gas/liquid interface and thus must be translated normal to the coated substrate support. The equation that translates this back is (see also Kheshgi and Scriven, 1983):

$$(\alpha - \beta_4) \approx \left(1 - \frac{\eta_3}{\eta_4}\right)\frac{dh}{dy} \qquad [4.13]$$

Applying Snell's law at the coating substrate/gas interface and linearizing for small values of dh/dy by neglecting higher order terms in the Taylor expansions, gives the following expression for β_2 as a function of dh/dy:

$$\eta_3 \, sin(\alpha - \beta_4) = \eta_2 \, sin\beta_2 \qquad [4.14]$$

$$\beta_2 \approx \left(\frac{\eta_3}{\eta_2}\right)\left(1-\frac{\eta_3}{\eta_4}\right)\frac{dh}{dy} \qquad [4.15]$$

Once again utilizing Snell's law at the ronchi ruling/coating substrate interface, linearizing for small values of dh/dy, and substituting previous equations gives an expression for β_1 as a function of dh/dy:

$$\eta_1 sin\beta_1 = \eta_2 sin\beta_2 \qquad [4.16]$$

$$\beta_1 \approx \left(\frac{\eta_3}{\eta_1}\right)\left(1-\frac{\eta_3}{\eta_4}\right)\frac{dh}{dy} \qquad [4.17]$$

The displacement of a fringe, δy_i , is not only a function of the optical properties of the layers, but also geometrically dependent on their thickness according to:

$$\delta y_i = h(x,y)tan(\alpha-\beta_4) + t_2 tan\beta_2 + t_1 tan\beta_1 \qquad [4.18]$$

Applying the same linearization for the tangent of β_1, β_2 and $\beta_3 = (\alpha-\beta_4)$, i.e., dh/dy « 1, and simplifying, results in a tractable first order ordinary differential equation (o.d.e.) given by

$$\delta y_i = h(x,y)\left(1-\frac{\eta_3}{\eta_4}\right)\frac{dh}{dy} + t_2\left(\frac{\eta_3}{\eta_2}\right)\left(1-\frac{\eta_3}{\eta_4}\right)\frac{dh}{dy} + t_1\left(\frac{\eta_3}{\eta_1}\right)\left(1-\frac{\eta_3}{\eta_4}\right)\frac{dh}{dy} \qquad [4.19]$$

$$\delta y_i = \frac{dh}{dy}\left[h(x,y) + t_2\left(\frac{\eta_3}{\eta_2}\right) + t_1\left(\frac{\eta_3}{\eta_1}\right)\right]\left(1-\frac{\eta_3}{\eta_4}\right) \qquad [4.20]$$

Since the refractive index for air in the gas phase is 1.003, the equation can be simplified further to:

$$\delta y_i = \frac{dh}{dy}\left[h(x,y) + \left(\frac{t_2}{\eta_2}\right) + \left(\frac{t_1}{\eta_1}\right)\right]\left(\frac{\eta_4 - 1}{\eta_4}\right) \qquad [4.21]$$

The differences between the linearized value for a ray deflection, δy_i, and the exact ray deflection, δy_e, using the exact trigonometric functions are given in Fig. 4.10. For $(dh/dy) < 0.1$, the absolute error is less than 0.6% and is therefore negligible for most of the cases studied. The calculated slope, dh/dy, for an entire air film centerline profile is given in Appendix VII for a consecutive series of images.

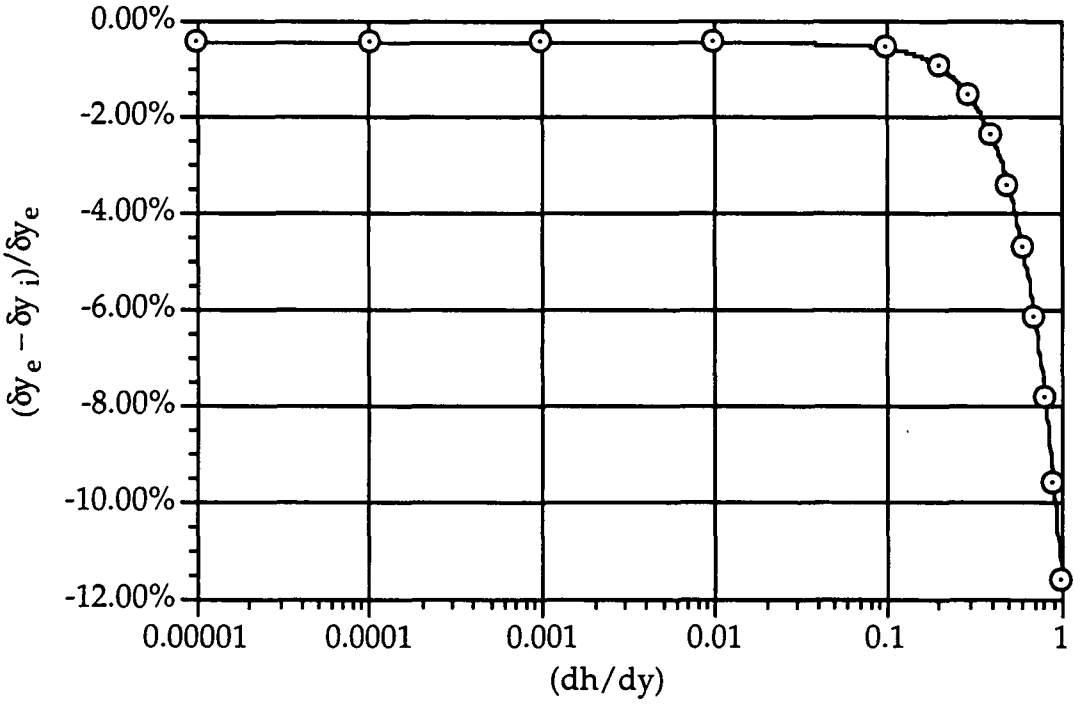

Figure 4.10. Linearization error in trigonometric functions for (dh/dy).

4.2.3 Discretization of the Fringe Deflection

When using a ronchi ruling to examine the slope of the gas/liquid interface by measuring the fringe deflection, δy_i, a continuous function for the surface slope is not known and thus the set of equations can be discretized. The spacing between fringes, $(1/P_f)$, creates a natural spacing between linear "nodes" in the y-direction for the case being analyzed. If we used a grating with perpendicular lines in the x- and y-directions, information for the slope in each direction can be obtained. When using the finite element method to solve sets of o.d.e.'s in heat and mass transfer problems, a domain mesh is created with the nodes being a repetitive location on each cell in the mesh. Once enough boundary conditions are specified, the o.d.e.'s can be iteratively solved to a certain tolerance in each of nodes. The same type of approach can be used to explicitly solve for the gas/liquid interface contour, $h(y)=h_i(y)$, at the air pocket centerline. A suitable initial boundary condition is that the tip of the air pocket is contacting the solid substrate surface. This creates a zero reference height, h_o, from which the interface height at any location is compared. The resulting discretized equation is quadratic in h_i, and can easily be solved for the positive real root in the equation given by

$$\delta y_i = \frac{h_i - h_{i-1}}{y_i - y_{i-1}}\left[h_i(x,y) + \left(\frac{t_2}{\eta_2}\right) + \left(\frac{t_1}{\eta_1}\right)\right]\left(\frac{\eta_4 - 1}{\eta_4}\right) \qquad [4.22]$$

which leads to

$$0 = h_i^2 + \left[\left(\frac{t_1\eta_2 + t_2\eta_1}{\eta_1\eta_2}\right) - h_{i-1}\right]h_i - \left[h_{i-1}\left(\frac{t_1\eta_2 + t_2\eta_1}{\eta_1\eta_2}\right) + \left(\frac{\delta y_i \eta_4 (y_i - y_{i-1})}{(\eta_4 - 1)}\right)\right] \qquad [4.23]$$

This quadratic equation, Eq. [4.23] in h_i can be rewritten as

$$0 = ah_i^2 + bh_i + c \qquad [4.24]$$

with the coefficients a, b, and c defined as:

$$a=1 \qquad [4.25]$$

$$b = b^* - h_{i-1} \because b^* = \left(\frac{t_1\eta_2 + t_2\eta_1}{\eta_1\eta_2} \right) \qquad [4.26]$$

$$c = -\left(h_{i-1}b^* + \delta y_i c^*\right) \because c^* = \frac{\eta_4\left(y_i - y_{i-1}\right)}{\left(\eta_4 - 1\right)} \qquad [4.27]$$

It should be noted that a, b^*, and c^* are constants for all $i > 1$, except for $(y_1\text{-}y_0)=d_t$, with d_t being the distance from the tip to the first fringe. The spacing between the remaining lines is constant, being the inverse of P_f, for example:

$$y_i - y_{i-1} = d_t; \quad i = 1 \qquad [4.28]$$

$$y_i - y_{i-1} = \frac{1}{P_f}; \quad i = 2, 3, 4... \qquad [4.29]$$

4.2.4 Error in Calculation of the Interface Height, h_i, along the Profile

The uncertainty in the positive real root of the quadratic in Equation [4.23] is a function of its precision index, S_{h_i}, which requires propagation of the errors in measurements of the parameters, S_b, S_c, $S_{\delta y_i}$, $S_{P_f^{-1}}$, S_{t_1}, S_{t_2}, S_{η_1}, S_{η_2}, S_{η_4}, and $S_{h_{i-1}}$. Using the ASME root sum square method for error propagation through a calculation (Abernathy, Benedict and Dowdell, 1985), the results are given in Eqs. [4.30-4.32].

$$S_{h_i} = \sqrt{\left[\left(\frac{b - \sqrt{b^2 - 4c}}{2\sqrt{b^2 - 4c}}\right)S_b\right]^2 + \left[\left(\frac{-1}{\sqrt{b^2 - 4c}}\right)S_c\right]^2} \qquad [4.30]$$

$$S_b = \sqrt{\left(\frac{S_{t_1}}{\eta_1\eta_2}\right)^2 + \left(\frac{S_{t_2}}{\eta_1\eta_2}\right)^2 + \left(\frac{-t_1 S_{\eta_1}}{\eta_1^2}\right)^2 + \left(\frac{-t_2 S_{\eta_2}}{\eta_2^2}\right)^2 + \left(-S_{h_{i-1}}\right)^2} \qquad [4.31]$$

$S_c =$ [4.32]

$$\sqrt{\left(\frac{h_{i-1}t_1 S_{\eta_1}}{\eta_1^2}\right)^2 + \left(\frac{h_{i-1}t_2 S_{\eta_2}}{\eta_2^2}\right)^2 + \left(\frac{-h_{i-1}S_{t_1}}{\eta_1}\right)^2 + \left(\frac{-h_{i-1}S_{t_2}}{\eta_2}\right)^2 + \left(-b^* S_{h_{i-1}}\right)^2 + \left(c^* S_{\delta y_i}\right)^2 + \left(\delta_{y_i} c^* S_{P_f^{-1}}\right)^2 + \left(\frac{-\delta_{y_i} c^* S_{\eta_4}}{\eta_4 - 1}\right)^2}$$

The values of the precision indices are given in Table 4.1 with the precision indices for the previous height, $S_{h_{i-1}}$, calculated during the determination of the profile shape. The measurement of fringe deflection is the key parameter in solving Eq. [4.23]. Therefore, the precision indices for $S_{\delta y_i}$ and $S_{P_f^{-1}}$ are at the 99% confidence level using the automatic line detection methods extensively tested in Appendix Section XVI.7

Table 4.1. Precision indices of optical and measured parameters

S_{η_1}	S_{η_2}	S_{η_4}	S_{t_1}	S_{t_2}	$S_{\delta y_i}$	$S_{P_f^{-1}}$
±0.005	±0.005	±0.005	±4.4 μm	±1.6 μm	±7 μm	±7 μm
Kodak data sheet photographic glass	ICI data sheet Melinex™ 454	Dow Corning data sheet DC200 oils	Measured with electronic microgage	Measured with electronic microgage	Estimated using image analysis	Estimated using image analysis

Using the original image and skeletonized image in Figure 4.11a,b, the deflections were calculated for the exact and linear cases. This result, applying

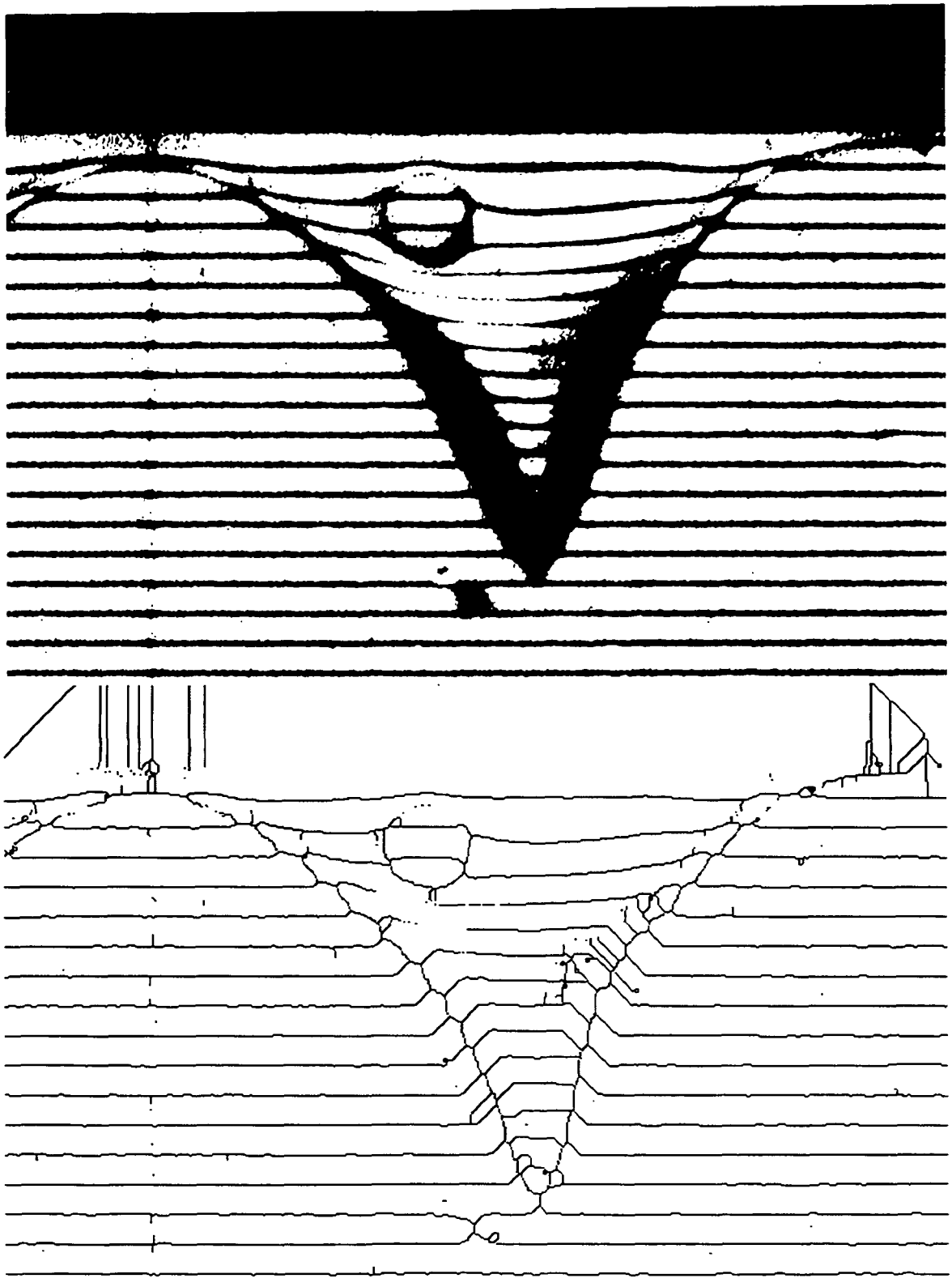

Figure 4.11. a) (Top) Original image digitized directly from film for the image U15CA488.TIF. The distance between the rulings lines is 100 μm, P_f = 10 cycles/mm, 70/30 duty cycle. b) (Bottom) Binarized and skeletonized version of the top image. The ruling lines not visible in the top image were detected by enlarging the tip region with both a stereo zoom microscope and digital zoom.

Eq. [4.22] vs. the exact trigonometric functions for the angular misalignment correction, G = 0° and G = 0.91°, is shown in Fig. 4.12. All three curves have the same shape with the curve for G = 0° pivoted counterclockwise about h_o. Therefore the correction for angular misalignment, G, removes the unrealistic negative thicknesses predicted near the base of the triangular air film for L = 0 μm. The uncertainty in the results show that the differences between the linearized equations and exact equations are negligible even considering that the initial slope is 0.345 calculated using Eq. [4.22] and 0.352 for the exact trigonometric functions.

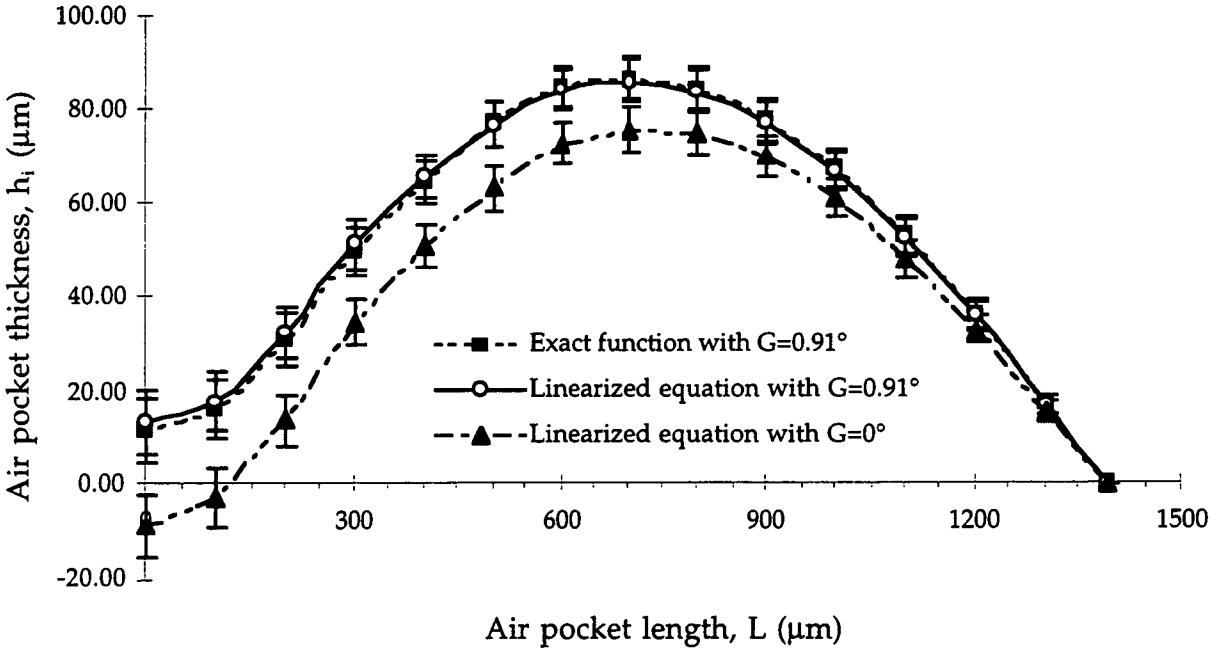

Figure 4.12. The dimensional interface centerline profile for image U15CA488.TIF from run U15ACA4 with Fluid A - DC200-100cs silicone oil and substrate velocity 12.8 cm/sec, Ca=0.657. The error bars represent the 99% confidence level for the data based on Eq. [4.30].

4.3 Introduction to Physical Properties

The purpose of Section 4.3 is to briefly discuss the relevant liquid and solid properties that were measured. Accurate measurement of the liquid properties is a prerequisite for obtaining useful air entrainment results in (Chapters V and VI). The surface properties of the substrates are summarized in Table 5.3 (Section 5.6). They are used to determine any substrate affect on the air entrainment speed, U_{ae}, for the high viscosity silicone oil. Additional details concerning the substrate and physical property data are contained in the appropriate Appendices.

The four substrates used in the experiments are: 1) uncoated PET [poly(ethleneterephthlate)], 2) coated PET, 3) cellulose acetate, and 4) an uncoated base sheet paper. A majority of the experiments used the uncoated PET. The four substrates were characterized using the following surface chemistry and analytical techniques:

- equilibrium contact angles, θ_{eq}, and the solid dispersion, γ_s^d, and polar, γ_s^n, components of surface tension.
- surface roughness measurements, R_a and R_q, using three separate instruments.
- electron spectroscopy for chemical analysis (ESCA).
- surface and bulk electrical resistivity of the substrates.
- scanning electron microscopy (SEM).

4.3.1 Fluid Property Measurement

The liquid transport properties of the test liquids, namely density, ρ, surface tension, γ, and viscosity, μ, were measured in the 18 - 30°C range. A linear correlation of the desired property as a function of temperature is used for property

prediction at the fluid temperature corresponding to U_v and U_{ae}. The uncertainty in temperature measurement was ±0.5°C. The regression coefficients are found in Appendix XVII for the silicone oil and glycerol-water test fluids.

Density, surface tension, and viscosity all exhibited a negative slope for their temperature dependence. This behavior is expected over the 18 - 30°C temperature interval. The correlation coefficient, R^2, has lows of 0.89, 0.72, and 0.87 for γ, ρ, and μ, respectively. This data is also contained in Appendix XVII.

4.3.2 Components of the Liquid Surface Tension

The measurements of the equilibrium contact angle, θ_{eq}, which is also called the static contact angle, are contained in Appendix Section IX.4. The value, θ_{eq}, is frequently reported in wetting literature for a given solid and provides a boundary condition for computational modeling. Blake's wetting model, presented in Appendix I, also requires θ_{eq} to predict the behavior of the dynamic contact angle with substrate speed.

For the coated PET substrate ,θ_{eq}, increased from 9.6° to 32.3° as the silicone oil kinematic viscosity changed from 20 to 1000 cs, respectively. Glycerol has a higher value of θ_{eq} at 72.6° on the uncoated PET.

4.3.3 Components of the Solid Surface Tension

The dispersion, γ_s^d, and polar, γ_s^n, components of the solid surface tension are also reported in Appendix Section IX.3 for the four substrates. These compared

favorably to literature data of similar materials. In the past, attempts have been made to correlate U_{ae} with these parameters, as discussed in the literature review (Section 2.5, Table 2.2), without much success.

4.3.4 ESCA - Electron Spectroscopy for Chemical Analysis

Electron spectroscopy for chemical analysis (ESCA), also known as X-ray photoelectron spectroscopy (XPS), uses a soft source of x-rays (usually the K lines of magnesium or aluminum) to irradiate the sample surface and produce photoelectrons (Schreiber 1979). It was used to verify the chemical composition of the uncoated and coated base substrates as poly(ethyleneterephthlate). The cellulose acetate had atomic percentage ratios close to pure α-cellulose. Some indications of the proprietary coating compound on the coated PET are also discussed in Appendix X. No firm identification was made of this adhesion pretreatment coating.

The main results included the surface oxygen to carbon ratios as well as their atomic percentages which are used later (Chapter V) to determine if they affect the air entrainment velocity. A detailed description of the technique and the survey spectra (full and high resolution) are contained in Appendix X.

4.3.5 Surface and Bulk Electrical Properties

The volume and surface resistivity are measured for the four different substrates. The results are summarized in Section 5.7. This parameter is important if an electrostatic assist coating method is employed. The polymeric and paper

substrates were tested at 23.9°C and 50% RH, which is the same as the experimental lab conditions.

The atomic percent oxygen was also a good indicator of the surface resistivity (see Appendix X, Figure X.1).

4.3.6 Scanning Electron Microscope Results

The scanning electron microscope provides qualitative information about the surface morphology at high magnification and compliments chemical surface analysis techniques.

A JEOL JSM 6400 scanning electron microscope available at IPST was operated at 5 kV accelerating potential with the secondary electron (SE) detector. The samples of coated PET, uncoated PET, and cellulose acetate were observed at X10, 100, 1000, 5000, and 10,000 magnification. The coated PET sample was tested on both sides (inside and outside) to determine if the adhesion pretreatment coating exhibited a different microstructure between each side. This was important since either side might be coated during the experiments, i.e., the side to be coated was a function of the loading orientation on the unwind shaft.

The SEM's showed that at 5000X magnification the *inside* surface of the coated PET (Appendix Fig. XI.3) has a grainy appearance, while the *outside* surface has oriented ridges approximately 0.3 μm apart (Appendix Fig. XI.6). It is uncertain if this difference between sides is due to the coating layer structure or solvent evaporation during drying. This side-to-side variation with coated PET is not believed to affect the air entrainment speed because the length scale is small.

A full description of the operating procedure and conditions as well as images at X1000, 5000, and 10,000 are contained in Appendix XI.

4.3.7 Surface Roughness Measurement

Increases in the root mean square surface roughness has been previously documented in Section 2.5.1 and Section 2.6 as correlating with an increase in the air entrainment speed. It is, therefore, an important parameter that may dictate the mechanism of air entrainment.

In order to characterize the surface of the substrate, three different profilometer systems were used, namely (1) ECC International's TALYSTEP stylus profilometer system, (2) Champion International's SURFANALYZER stylus profilometer unit, and (3) the noncontact optical WYKO RST Plus Rough Surface/Step Tester. The RST and TALYSTEP gave quantitative surface roughness statistics for R_a, the arithmetic average roughness, and the r.m.s. deviation, R_q, of the profile. These parameters as defined by the International Organization for Standardization (ISO Standard 1984) and discussed in detail in Appendix XII. The statistics were corrected so that any tilt, as shown in Fig. 4.13, is removed by fitting the profile to a linear fit and adjusting the profile as seen in Fig. 4.14. The tilt correction is discussed in Appendix XII. This approach is valid if the slope is increasing or decreasing uniformly. It is clear from Figures 4.13 and 4.14 that the corrected profile "levels" the system tilt over the 25-mm scan length. The 3-μm difference for the uncorrected profile over 25-mm is very conceivable within the

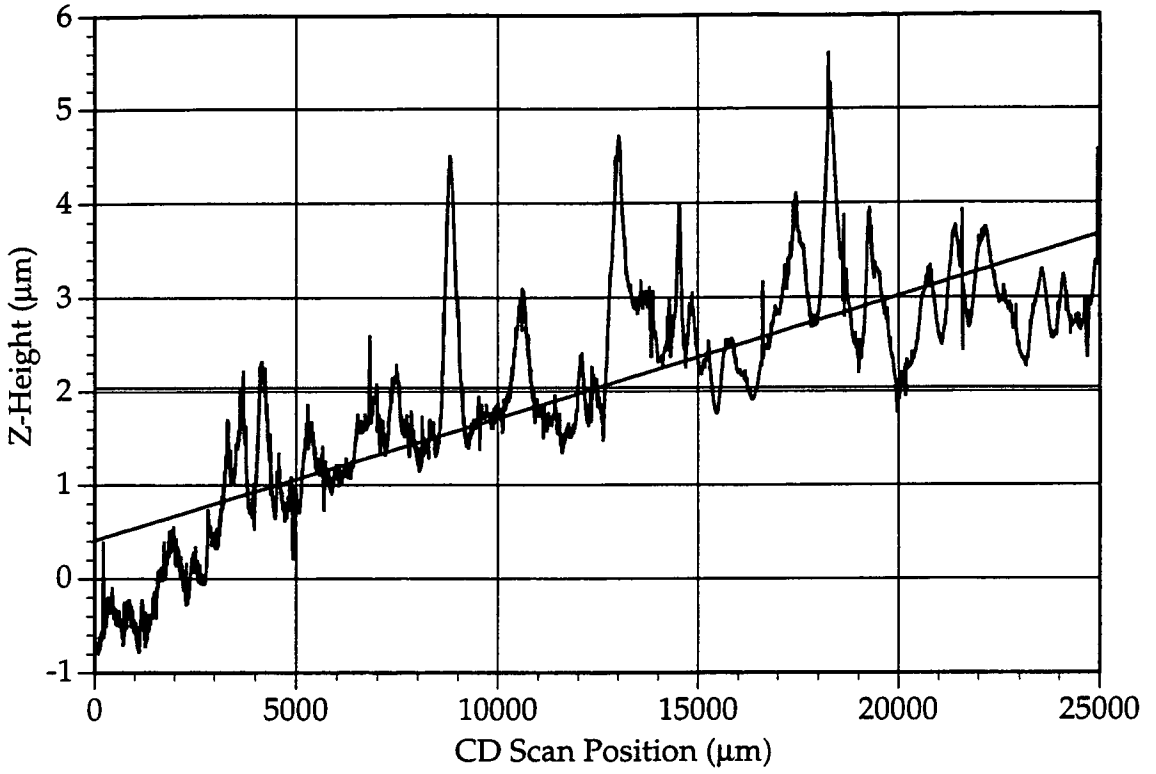

Figure 4.13. Uncorrected roughness profile for cellulose acetate sample taken with the TALYSTEP unit. The average height from the reference plane is around 2 µm.

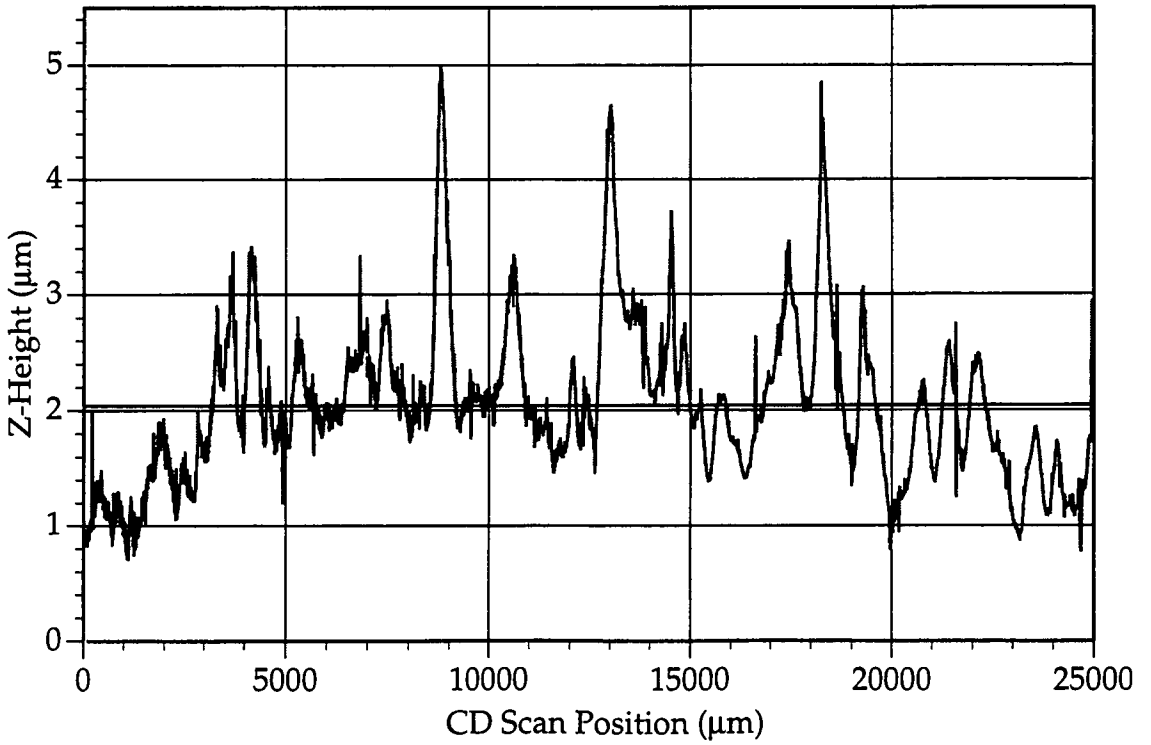

Figure 4.14. Corrected roughness profile for cellulose acetate sample taken with the TALYSTEP unit. The average height from the reference plane is around 2 µm.

tolerances of the linear bearing system and the machining tolerances for the sample holder.

As expected, the paper substrate has the highest roughness with the decreasing order for R_a as paper > uncoated PET > coated PET > cellulose acetate as shown in Table 4.2.

Table 4.2. TALYSTEP surface roughness statistics for experimental substrates

	coated PET	uncoated PET	cellulose acetate	paper
R_a	1.09±0.30	1.45±0.48	0.57±0.07	5.53±0.90
R_q	1.40±0.40	1.85±0.60	0.77±0.60	6.97±1.17

Comparing the SEM micrographs in Appendix XI to the roughness statistics, uncoated PET had a greater measured profilometer roughness even though the SEM image "appears" to be rougher for coated PET. With a 13-μm stylus tip radius on the TALYSTEP, the striated orientation (see Figures XI.3, XI.6 vs. XI.9) was not detected by the profilometer because the average difference between ridges is 0.3 μm as discussed previously in Section 4.3.6. Thus, the stylus cannot contour the small-scale roughness.

To verify the profilometer tests with the coated PET, the substrate was retested using the noncontact optical RST unit. This unit, with the sample tilt removed, gave an R_a= 1.09 μm and R_q= 1.44 μm, which is equal to the contact profilometer results. The surface roughness differences between samples are reconfirmed with the roughest being paper, and uncoated PET the smoothest in the order specified earlier.

4.3.8 Multiple Cross Directional Profile Scans to Evaluate Uniformity

The SURFANALYZER system was used to qualitatively evaluate how frequently a profile is repeated as you move along the web length. This test was conducted to determine if the distance between triangular air films at U_{ae}, correlated with the distance between peaks on the substrate. No definitive correlation was found. This comparison will be further discussed in Chapter VI.

The methodology is discussed in Appendix XII. Only the coated PET and uncoated PET samples were tested mainly to determine if the surface coating affected the profile uniformity. The SEM work had hinted that this might be true. In Fig. 4.15, an example of multiple profiles repeated at various distances from the starting position is reconstructed so all edges are aligned. The profiles were taken from the SURFANALYZER's tape printout and digitized using a scanner and graphics program. Peak #6, which is fairly close to the right edge in Fig. 4.15, has a definitive repeating ridge throughout the machine direction. This could be a small nick in the extrusion die lip or a localized debris clog in the lip. Both of these are conceivable considering the thin gage tolerances being sought. The remainder of the scans are contained in Appendix XII.

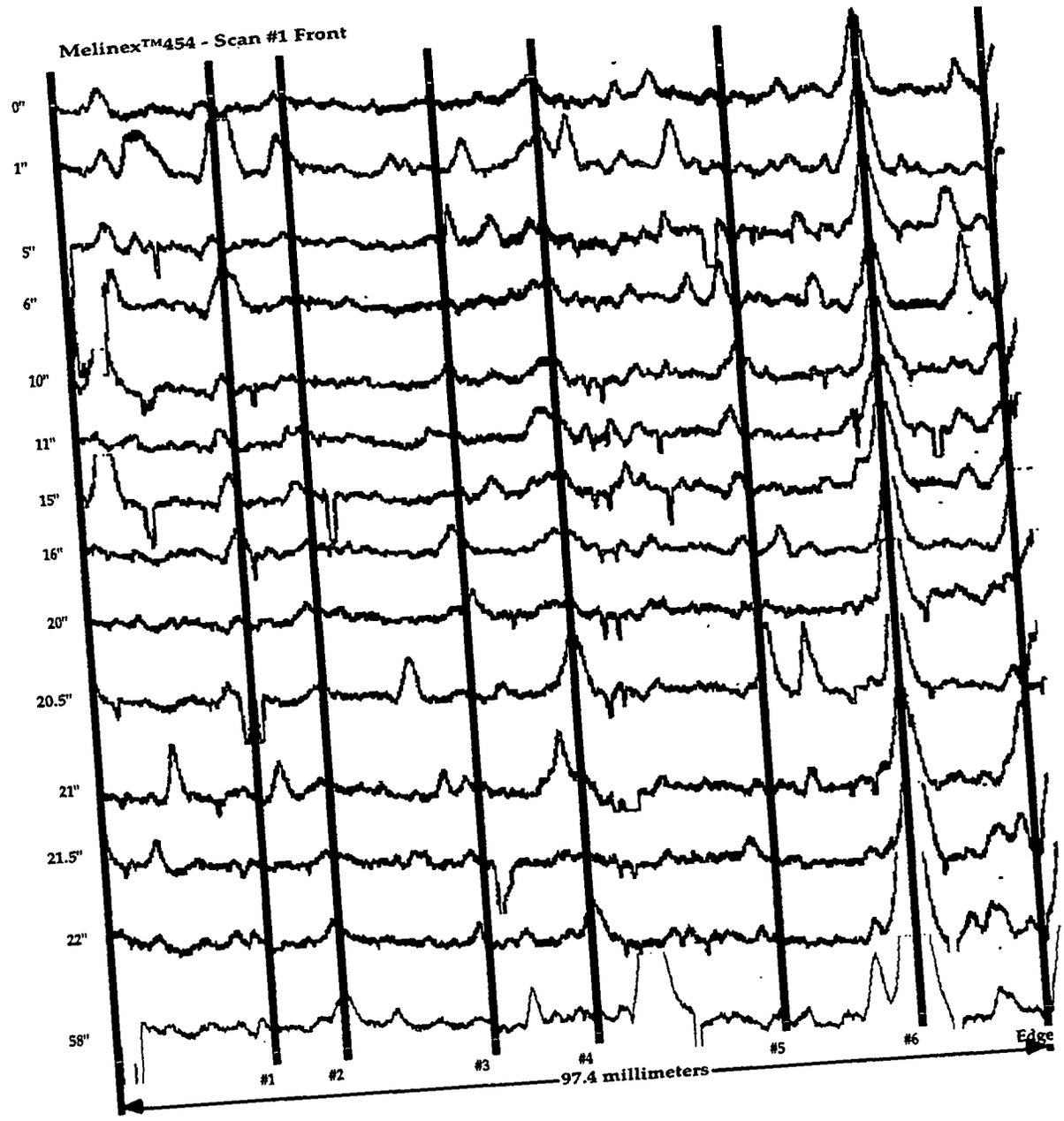

Figure 4.15. Overlapped scan profiles of the coated PET using Surfanalyzer system. The maximum valley to peak distance is 10 μm. The repetitive patterns are evident by following a line as it progresses from 0" to 58" along the starting position.

4.3.9 Fast Fourier Transfer Analysis of TALYSTEP Data

A forward fast Fourier transfer (FFT) routine using PS-PLOT[1] was performed on all valid profiles using the digital TALYSTEP data since the data from the SURFANALYZER is only a tape printout. The main reason for doing this analysis was to compare the average distance between entraining triangular air films for $U > U_{ae}$ to see if any correlation exists between the scales. These results will be discussed in detail later in Chapter VI. The primary result is that this distance is not suitable for predicting the average interval between triangular air films.

The first fundamental wavelength for all the samples is given in Table 4.3. This first wavelength is the result of the FFT and represents the equivalent periodic waveform frequency of the profile data. The first through third fundamental wavelengths were recorded and are given in Appendix XII Table XII.5.

Table 4.3. First fundamental wavelength from forward FFT of TALYSTEP data.

	Coated PET	Uncoated PET	Cellulose acetate	Paper
Wavelength(mm)	8.9	11.0	10.8	5.4

The summarized results of Section 4.3 will be used in Section 5.6 to see if any of the substrate properties affect the air entrainment speed. Additionally, in Chapter VI, a comparison will be made as to whether the distance between triangular air films is related to the average distance between peaks on the substrate profile. In Chapter V we will attempt to identify when an air film can remain stable using the apparatus, fluids, and techniques presented in Chapter IV.

---

[1] Poly Software International, v1.12, Salt Lake City, UT.

CHAPTER V

RESULTS FOR CRITICAL SPEED OF AIR ENTRAINMENT

5.1 Introduction to Results

Two main results are established in Chapter V. First, at low liquid viscosity, a state can be distinguished when an air film can form, remain stable for a period of time and retract *without* air bubble formation and entrainment using a new criteria discussed in Section 5.2. This stable period is more clearly observed at higher gas to liquid viscosity ratio, λ_μ, as shown in Section 5.3 for a parameter based on the Reynolds and Bond numbers, $\Delta(\mathrm{Re}/\sqrt{\mathrm{Bo}})$. This result is tested in Section 5.4 using standard statistical methods.

Second, in Section 5.5 we show that for our work with high viscosity liquids, there are major differences in the critical air entrainment speed between low surface silicone oils ($\gamma \approx 20$ dynes/cm) and the moderate surface tension glycerol-water mixtures ($\gamma \approx 50$ - 60 dynes/cm). This result is considerably different from the previous plunging tape data. The differences are explored in terms of the substrate properties (Section 5.6), a qualitative interface stress balance (Section 5.7), the 3D nature of the plunging tape system data (Section 5.8), and application of an analytical solution to estimate the difference in liquid normal stresses between the free surface side driven cavity and the plunging tape (Section 5.9).

Chapter V also discusses the preparatory results required to verify that the triangular air film can be studied with the deflectometry technique in Chapter VI.

5.2 Rationale and Methodology

As mentioned earlier, measurement of the first and second critical speeds of air entrainment is a desired goal. A quasi-steady state method for verifying that ΔU exists was developed based on acceleration of the substrate from a speed below U_v to a speed much greater than U_{ae}. This is the ramping type of experiment discussed briefly in experimental Section 4.1.3 and in more depth in Appendix XVI.6.

The stereo zoom microscope was focused through the coating cavity normal to the substrate and the dynamic contact line. The acceleration rate of the motor controller was variable, based on the setpoint time to reach the maximum motor speed. Drive gearing and controller stepping limitations prohibit the use of the same acceleration rate for all experiments. The sensitivity to different substrate acceleration rates was also measured during experiments with silicone oils D (500 cs) and Y (10 cs). There were no significant difference as displayed in Fig. 5.1.

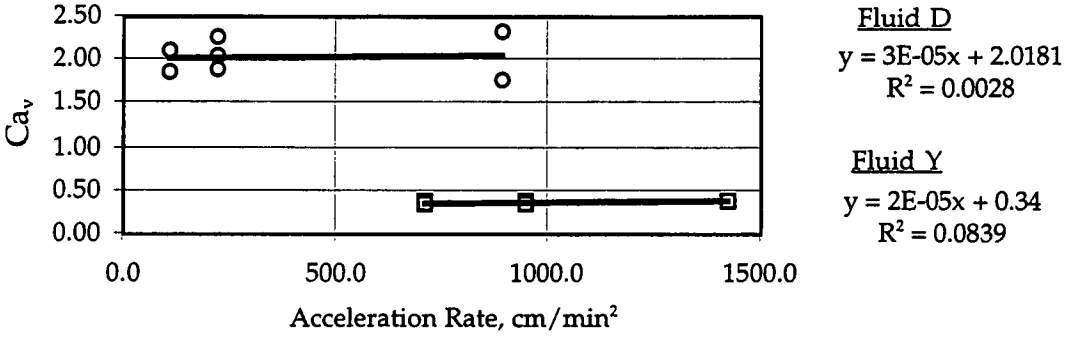

Figure 5.1. Variation of Ca_v to different acceleration rates for two silicone oils. The small slope and low R^2 show that the dependence of Ca_v in the varied acceleration rate range is negligible. Fluid Y is 10 cs silicone oil and Fluid D is 500 cs silicone oil.

Ramping was achieved by synchronizing the video time code generator with substrate acceleration. Since acceleration rates and starting conditions are known, the video time code provides a convenient method for calculating the speed.

Multiple experiments were run consecutively, with the same test fluid emptied and refilled in the cavity, to ascertain $\Delta U=U_v-U_{ae}$. The criteria for determining when U_v and U_{ae} occur are discussed below.

The times of triangular air film initiation and entrainment, t_v and t_{ae}, respectively, are the time elapsed from initial velocity to the corresponding substrate velocities U_v and U_{ae}. These times, t_v and t_{ae}, are determined by viewing the video tape of each experiment replicate. The locations of triangular air film initiation and entrainment are not always the same. Operator bias was assessed by repeating video measurements nonsubjectively. Similar results are obtained for U_v and U_{ae} during each repeat. Examples of the events when the contact line initially became serrated for $U=U_v$ and when air entrainment initiated, $U=U_{ae}$, are shown in Fig. 5.2. The first example from the original image and schematic in Figure 5.2a is for a triangular air film when $U_v < U < U_{ae}$. Figure 5.2b displays the DCL prior to U_v. The liquid protrusion at the right hand edge is not considered $U \geq U_v$. The final image and schematic in Fig. 5.2c show a triangular air film when $U > U_{ae}$. The evolution of visible bubbles was also considered a criteria for $U > U_{ae}$. The visible bubble must have originated from the same location across the DCL where an air film previously existed in immediately prior video frames.

Some observations and limitations of this ramping technique to determine U_v and U_{ae} include: (i) the microscope field of view must be the same order as the length scale of the initial disturbance, e.g. for an initial air film that extends over 100 μm past the mean dynamic contact line position, the field of view should be around 1 x 1 mm; (ii) the time between video fields is 16.67 milliseconds, therefore, the

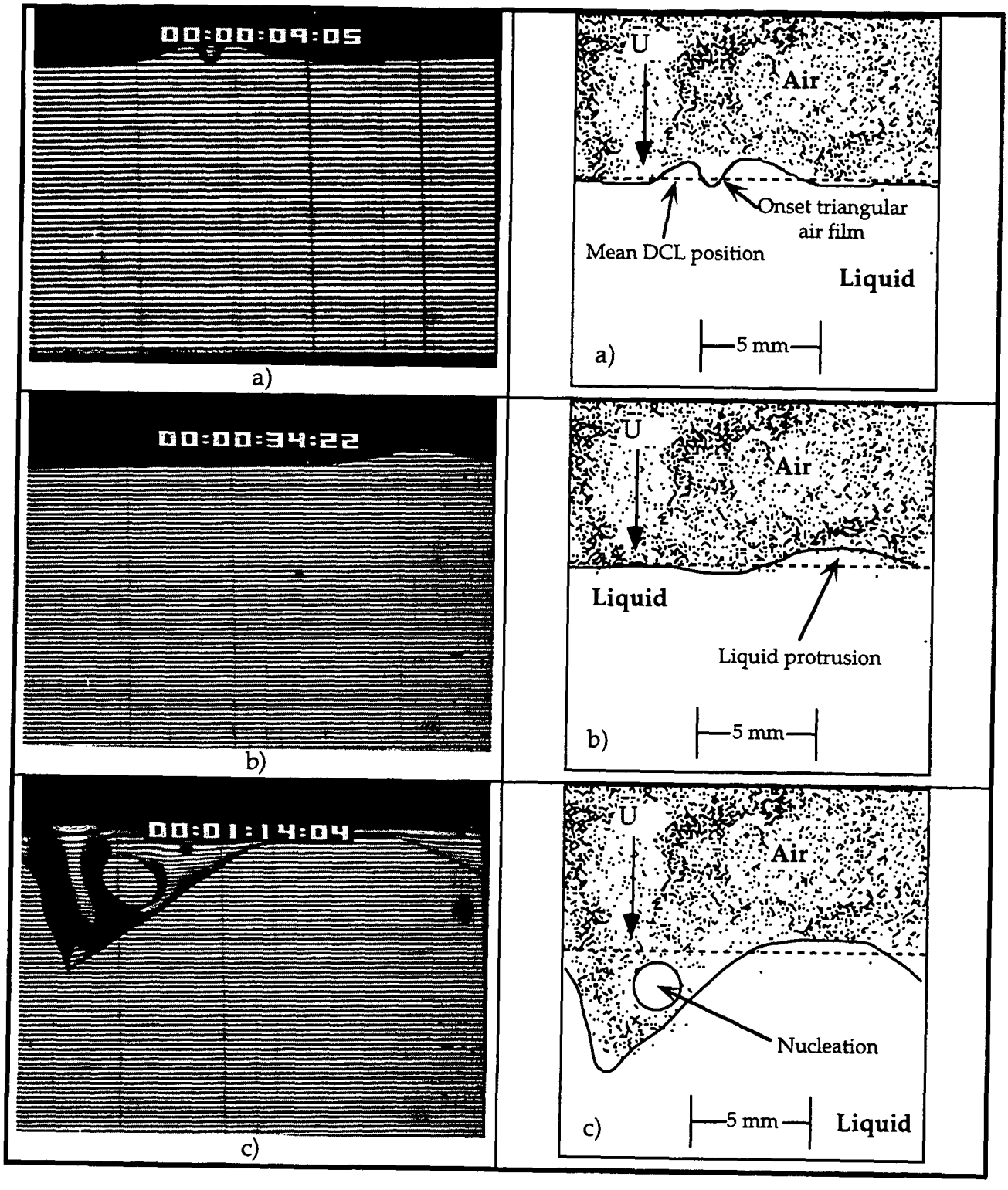

Figure 5.2. Examples of the criteria for air film formation and nucleation. a) $U = U_v$, the initial triangular air film is below the mean DCL position but does not entrain bubbles into the liquid. b) $U < U_v$, the liquid protrudes above the mean contact line position and is not considered the initial destabilization of the DCL. c) $U = U_{ae}$, the onset of air entrainment when an air bubble is formed by nucleation at a wetting site.

events with a shorter timescale may not be captured on a video frame; (iii) there is a tradeoff between resolution and the field of view. A magnification was then chosen that was one order greater than that of the smallest triangular air film. Air entrainment always occurred at a much lower substrate velocity near the outer walls of the coating cavity due to the decreased normal stress, i.e. normal forces acting on the gas liquid interface, that are unable to counteract the pressure building in the converging air layer near the dynamic contact line. This is addressed in Section 5.7. Air entrainment at the central region across the DCL width was chosen as the criterion to determine the critical speed, U_{ae}. Blake, Clarke and Ruschak (1994, p.236) also found that edge effects led to a significantly lower air entrainment speed adjacent to their viewing windows.

Thus, using this more precise criteria rather than the observation of visible bubbles in the pond, multiple experiments were conducted over two decades variation in fluid viscosity. The result of these experiments with acceleration of the substrate from well below U_v to past U_{ae} are presented in the next Section.

5.3 Parameter Range When a Triangular Air Film is Stable

The seven fluids used in the experiments are glycerol-water mixtures and varying viscosity silicone oils (polydimethylsiloxane). The silicone oils all have a surface tension around 20 dynes/cm while the glycerol-water mixtures are between 50 - 60 dynes/cm. The relevant physical property measurements for these fluids are discussed in Section 4.3 and Appendix XVII. The liquid density, ρ, surface tension, γ, and viscosity, μ, are corrected for the cavity temperature at $U=U_v$ and $U=U_{ae}$. Slight

temperature dependent variations in gas phase viscosity, μ_g, are corrected using Mason and Monchick's (1963) correlation for humid air. The laboratory conditions were maintained at 24±3°C and 50±5% relative humidity. Table 5.1 contains the relevant average results for each fluid. The number of replicate experiments is also specified for each fluid. Parameters based on the fluid properties, λ_μ, N_{pp}, and L_c are included. Also, the important dimensionless parameters for formation and entrainment of a triangular air film are shown. The entire raw data sets are contained in Appendix VI.

The characteristic length used in the calculation of the Reynolds and the Weber numbers, Re and We, in Table 5.1 is the capillary length, $L_c = \sqrt{\gamma/\rho g}$. The Reynolds number based on L_c can also be presented as

$$\frac{\rho U L_c}{\mu} = \frac{U\sqrt{\gamma\rho}}{\mu\sqrt{g}} = \mathrm{Re}/\sqrt{\mathrm{Bo}} \qquad [5.1]$$

which is only a function of the fluid properties, gravity, and substrate velocity. The dimensionless parameter, Bo, is the Bond number. By defining the interval between the first and second critical speeds as

$$\Delta(\mathrm{Re}/\sqrt{\mathrm{Bo}}) = (\mathrm{Re}/\sqrt{\mathrm{Bo}})_{ae} - (\mathrm{Re}/\sqrt{\mathrm{Bo}})_{v} \qquad [5.2]$$

and plotting this in log-log format as a function of the viscosity ratio, λ_μ, a detectable interval is seen in Fig. 5.3 when $\Delta(\mathrm{Re}/\sqrt{\mathrm{Bo}})>0.01$ for fluids A, G, Y, and Z. Correspondingly for this region, when $\lambda_\mu > 2 \times 10^{-4}$, a triangular air film can exist in our experimental system based on the limitations of the experiments. In other

TABLE 5.1. - Experimental conditions for air film formation and air entrainment initiation.

	TEST FLUIDS								
	A	B	C	D	E	F	G	Y	Z
Type	Silicone oil 100 cs	Silicone oil 200 cs	Silicone oil 350 cs	Silicone oil 500 cs	Silicone oil 1000 cs	Glycerin 710 cs	Glycerin-water 90 cs	Silicone oil 10 cs	Silicone oil 20 cs
# Replicates †	16 = (3,5,8)	5	12 = (6,6)	7 = (3,4)	11 = (5,3,3)	4	4	6	7 = (3,4)
$\lambda_\mu \times 10^4$	2.57±0.04	1.364±0.005	0.85±0.04	0.575±0.009	0.26±0.01	0.316±0.005	2.46±0.01	23±1	13.6±0.9
$N_{pp} \times 10^4$	1,490±8	20,800±300	143,000±13,000	521,000±7,100	11,240,000±1,640,000	406,000±28,000	105±2	0.32±0.05	2.3±0.6
L_c (μm)	1503±1	1499±1	1515±5	1541±5	1534±3	2002±1	2040±1	1485±2	1470±3
U_v (cm/s)	12.8±0.1	11.9±0.1	10.9±0.7	9.3±0.8	13.7±0.6	4.0±0.3	15.4±0.4	57.4±2.1	32.3±1.1
U_{ae} (cm/s)	13.1±0.2	11.9±0.1	11.0±0.7	9.4±1.0	13.8±0.6	4.1±0.4	15.7±0.5	61.0±1.0	33.3±0.8
Ca_v	0.66±0.01	1.18±0.01	1.74±0.13	2.03±0.21	6.47±0.51	0.72±0.06	0.35±0.01	0.36±0.02	0.33±0.03
Ca_{ae}	0.67±0.01	1.18±0.01	1.75±0.14	2.05±0.22	6.50±0.53	0.74±0.08	0.36±0.01	0.38±0.02	0.34±0.03
*Re_v	1.70±0.03	0.82±0.01	0.46±0.03	0.28±0.03	0.19±0.01	0.11±0.01	3.39±0.08	63.4±3.8	21.9±0.7
*Re_{ae}	1.73±0.04	0.82±0.01	0.46±0.03	0.29±0.03	0.20±0.01	0.12±0.01	3.46±0.10	67.5±3.5	22.6±1.1
We_v	1.12±0.03	0.97±0.01	0.80±0.08	0.57±0.08	1.23±0.11	0.08±0.01	1.19±0.04	22.8±1.9	7.23±0.69
We_{ae}	1.16±0.03	0.97±0.01	0.80±0.08	0.59±0.08	1.30±0.12	0.09±0.01	1.25±0.05	25.7±1.9	7.68±0.77
$1/Ca_{g,v}$	5,942±63	6,221±41	6,835±371	8,633±789	5,988±306	44,211±3,189	11,675±273	1,246±50	2,226±75
$1/Ca_{g,ae}$	5,831±107	6,220±41	6,807±375	8,582±855	5,829±228	43,379±4,045	11,455±336	1,170±32	2,156±48

† The number of replicates are subdivided into the number of replicates performed on separate days.

* This is the Reynolds number based on capillary length, Lc and is equal to $(Re/\sqrt{Bo})$

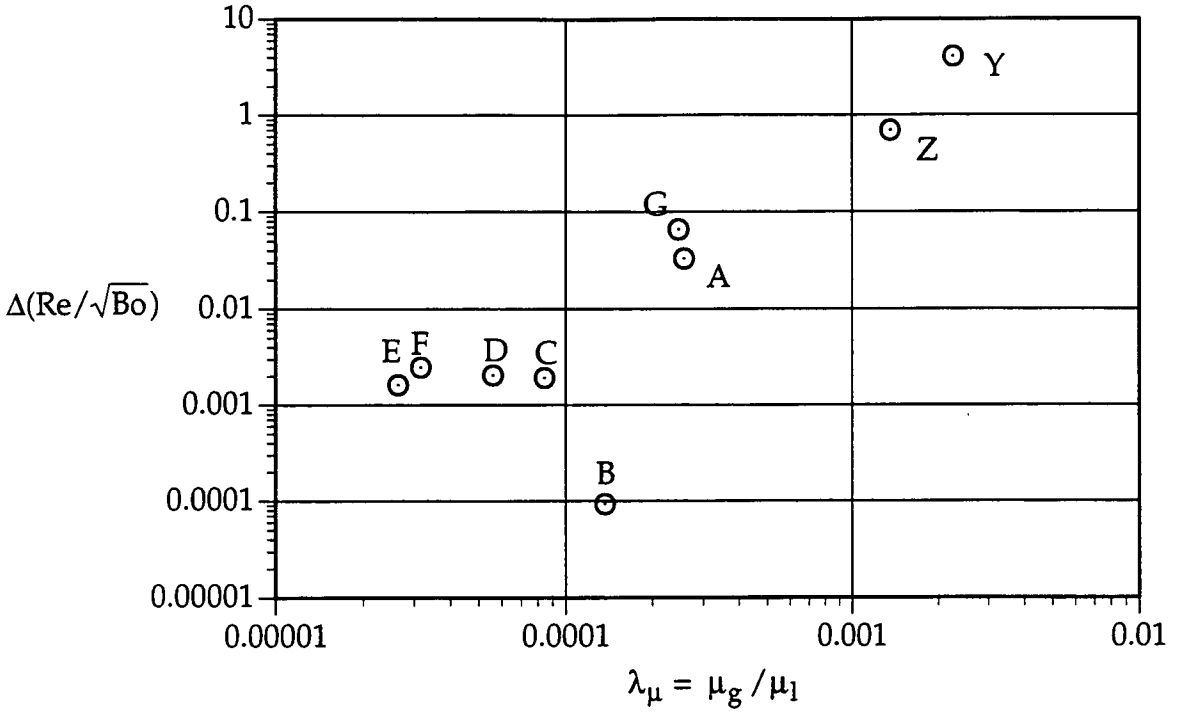

Figure 5.3. The interval between the Reynolds number over the square root of Bond number $\Delta(Re/\sqrt{Bo})$ for air film entrainment and formation in the side driven free surface cavity. Fluids F and G are glycerol water mixtures and the remainder are silicone oil.

words, detection of $\Delta(Re/\sqrt{Bo})<0.01$ is not possible by ramping the speed from below U_v to past U_{ae} with the apparatus described in Section 4.1. For all practical purposes the interval $\Delta(Re/\sqrt{Bo})$ for fluids B, C, D, E, and F will be considered zero. This will be statistically tested in the next section. The values for the second critical liquid capillary number, C_{ae}, are much less than unity for fluids A, G, Y, and Z. The parameters, Ca_{ae} and λ_μ, have been cited in the literature review of Section 2.5.1 as being successful in correlating critical air entrainment speeds in the plunging tape data. The interval $\Delta(Re/\sqrt{Bo})$ for fluid B does not follow the same pattern most likely due to the limited number of replicates.

The results will be tested in the next section with standard statistical procedures which will help clarify that fluids A, G, Y, and Z have finite intervals between initiation and entrainment for Ca, U, and $(Re/\sqrt{Bo})$.

5.4 Statistical Significance of the Data

Table 5.2 summarizes the t-test probabilities for a parameter, (.). This nomenclature, (.), represents any dimensional or dimensionless quantity tested under the hypothesis. The null hypothesis, H_o, that $(.)_v = (.)_{ae}$, was tested using a two tailed t-test with unequal sample variance. The equality or inequality of the sample variances was tested with a one-sided F-test.

TABLE 5.2. Two tailed t-test probabilities, %P of various null hypotheses.

	TEST FLUIDS								
H_o	A	B	C	D	E	F	G	Y	Z[1]
$(.)_v = (.)_{ae}$	Silicone oil 100 cs	Silicone oil 200 cs	Silicone oil 350 cs	Silicone oil 500 cs	Silicone oil 1000 cs	Glyceri ne 710 cs	Glyceri ne-water 90 cs	Silicone oil 10 cs	Silicone oil 20 cs
$U_v = U_{ae}$	0.1%	98.0%	87.9%	89.2%	31.5%	71.8%	35.0%	0.6%	8.1% (8.7, 1.9%)
$Ca_v = Ca_{ae}$	0.7%	98.4%	89.5%	89.8%	89.6%	73.6%	36.3%	3.9%	55.3% (11.5, 7.5%)
$(Re/\sqrt{Bo})_v = (Re/\sqrt{Bo})_{ae}$	1.8%	97.8%	86.8%	88.7%	59.9%	69.2%	34.5%	8.3%	17.8% (18.2, 2.5%)

(1) The probability in the brackets are for each data set tested independently. The number of replicates in each set was outlined in Table 5.1.

At a confidence interval (CI%) greater than 90%, where the CI% = 100% - P%, we can say that fluids A and Y have a difference in the first and second critical speed, Capillary, and $(Re/\sqrt{Bo})$ numbers. The confidence intervals for fluid Z are much lower because the seven replicate experiments were conducted in two sets with an average 6°C fluid temperature difference between sets. A temperature difference of

this magnitude decreases the density by 1.2%, surface tension by 1.7% and viscosity by 10.5%. Both the Capillary and $(Re/\sqrt{Bo})$ numbers are therefore not compared at the same properties with fluid Z. Thus, a discrepancy in the null hypothesis arises, namely that the sample set come from the same population. This discrepancy does not arise for the first and second critical speeds which are not calculated as a function of the fluid properties, although their magnitude is determined by a parameter set (λ_μ, ρ, γ, μ, U, V_e). When the data for fluid Z is tested independently for each replicate set, the null hypothesis probabilities for Capillary number are 11.5 and 7.5%, respectively, and 18.2 and 2.5% for $(Re/\sqrt{Bo})$ number. These values are shown in brackets below the probabilities in Table 5.2 for fluid Z.

Although not as evident from Fig. 5.3, fluid G, where $\lambda_\mu = 2.5 \times 10^{-4}$, has a confidence interval around 65% that the first and second critical parameters are different. This CI% is less than fluid A because of the fewer number of replicates.

Thus we can say with a high degree of confidence (> 90%) that, for $\lambda_\mu > 2 \times 10^{-4}$ an air film can be studied prior to entrainment when $U_v < U < U_{ae}$ for a given set of system parameters (λ_μ, ρ,....) and with $a_c \approx 1/3$. The cutoff between these two clearly defined regions, $\lambda_\mu \approx 2 \times 10^{-4}$, requires additional work to determine the exact transition value for λ_μ. The parameter $\Delta(Re/\sqrt{Bo})$ has been tested statistically to be equal to zero for fluids B, C, D, F, and E which indicates it is not detectable in our system.

Keep in mind that our objective was to identify the parameter set (λ_μ, ρ, γ, μ, U, V_e) where the air film can be studied at time scales > 50 ms. Meeting this objective was a prerequisite for undertaking the deflectometry experiments in Chapter VI because no information outside Veverka's (1991) limited work had clearly established that this "speed window" was finite. Summarizing the data up to 1993, Kistler (1993, p.340) states that , "The data available, do not indisputably establish that the speed at which visible bubbles are first entrained, U_{ae}, is the same as U_v". Thus, the conditions have been identified in this work for which $U_v \neq U_{ae}$. The technique was based on gradually accelerating the substrate velocity from well below U_v to above U_{ae} and visualizing the DCL with microscopic videography. The results may be better explained by numerical modeling which is an area suggested for future research.

5.5 Bulk Flow Effects in Delaying Air Entrainment

In order to show how the bulk flow effects of the main recirculating vortex influences Ca_{ae} between the silicone oils (fluids A - E, Y, Z) and glycerol-water mixtures (fluids F and G), we examine a plot of Ca_{ae} vs. λ_μ given in Fig. 5.4. The error bars in this figure represent the uncertainty in Ca_{ae} using the root sum square (RSS) method at 95% confidence interval and propagated using the ASME methodology discussed in Appendix XIII. Our results are compared against the

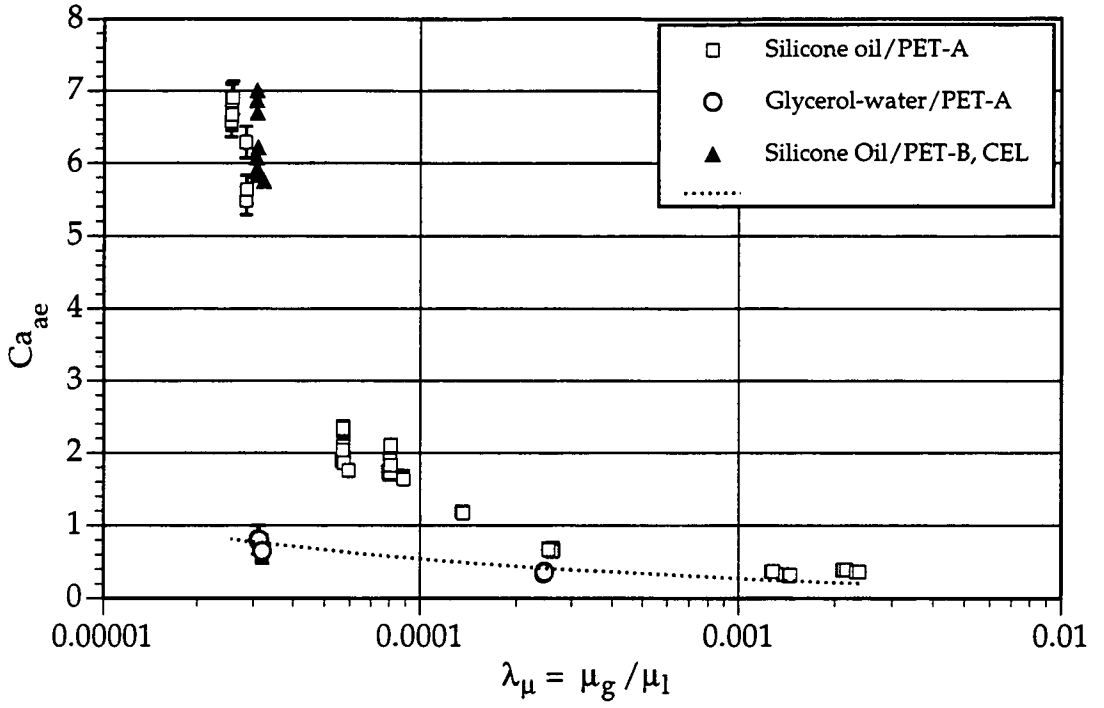

Figure 5.4. Variation in second critical capillary number for high and low surface tension fluids with three different substrate types. Coated PET-A (polyethyleneterephthlate), uncoated PET-B and cellulose acetate (CEL). The dashed line is Kistler's master correlation given in Eq. [2.3] for plunging tape experiments. The error bars represent the uncertainty at 95% confidence level.

master plunging tape equation[1] of Kistler previously given in Chapter II and which also spans the range $10^{-5} < \lambda_\mu < 10^{-2}$ for Ca_{ae}. When $Ca_{ae} < 1$ and $\lambda_\mu > 2 \times 10^{-4}$ the differences between the plunging-tape data and our system with a puddle-type coater are minimal. At the other extreme, for highly viscous liquids when $\lambda_\mu < 2 \times 10^{-4}$, the difference between the plunging tape experiments and our cavity flow results are quite significant leading up to a fivefold difference in Ca_{ae} at equivalent λ_μ. The main vortex interaction with the free surface in a low aspect ratio, confined cavity,

[1] Eq.[2.3] $Ca_{ae} = 0.034\lambda_\mu^{-0.30}$

$a_c = d_c/H_L$, is increased as the aspect ratio decreases. In plunging tape experiments this interaction is negligible because usually $a_c > 1$. The balance of normal stress at the interface involves the normal stress in the liquid which depends on the bulk liquid flow.

This interaction of the bulk flow field with the mechanics of air entrainment for low and high surface tension fluids has not been well documented.

In the next section, the physicochemical properties of four substrates, uncoated PET, coated PET, cellulose acetate, and paper, are tested to ascertain if these are influencing Ca_{ae} for $\lambda_\mu < 2 \times 10^{-4}$ in our system.

5.6 Substrate Surface Property Effect

Three other substrates, uncoated PET, cellulose acetate, and paper, were tested with the highly viscous fluid E using the constant acceleration ramping technique to identity U_v and U_{ae} discussed in Section 5.2. The additional data for U_v and U_{ae} with the silicone oil will be used to compare with the extensive data from the coated PET replicates. Table 5.3 summarizes the physicochemical relations of the four substrates that may be important for delaying air entrainment. As seen in this table there is no distinct influence of the substrate type on any of the hydrodynamic parameters despite the distinct chemical and physical substrate differences. By distinction, it means that the large differences in Ca_{ae} observed in Fig. 5.4 between the high viscosity silicone oil and glycerol are not manifested with dissimilar cellulose acetate and uncoated PET substrates. The data for cellulose acetate and uncoated PET are also plotted in Fig. 5.4.

Only one experiment performed with the paper substrate because the air entrainment speed was significantly higher (≈50 cm/s) and the DCL could not be clearly visualized. In this case the speed of air entrainment is estimated based on visible bubble evolution and not our usual criterion of using microscopic videography.

Table 5.3. Physicochemical properties summary for test substrates.

	SUBSTRATE TYPE			
	Coated PET	Uncoated PET	Cellulose Acetate	Paper base stock
TEST				
Roughness				
# Replicates	4	4	3	9
R_a, μm	1.09±0.30	1.45±0.48	0.57±0.07	5.53±0.90
R_q, μm	1.40±0.40	1.85±0.60	0.77±0.11	6.97±1.17
XPS				
Oxygen%	25	26	37	31
Carbon%	75	71	61	69
Silicon%	0	3	3	0
O/C	0.33	0.37	0.61	0.45
Surface Energy				
# Replicates	32	17	13	18
γ_s, dynes/cm	38.7±4.1	49.1±3.6	69.2±3.0	42.0±3.0
γ_s^d, dynes/cm	35.0±1.1	48.8±0.6	37.6±1.4	38.7±1.7
γ_s^n, dynes/cm	3.6±3.0	0.3±2.9	31.6±1.6	3.3±2.2
Surface Resistivity,				
# Replicates	10	10	10	10
Ω/square	6.9×10^{14} $\pm7.6\times10^{14}$	1.5×10^{15} $\pm1.2\times10^{15}$	2.9×10^{10} $\pm1.4\times10^{10}$	3.8×10^{11} $\pm1.4\times10^{11}$
# Replicates	11 = (5,3,3)	4	3	1
$\lambda_\mu \times 10^4$	0.26±0.01	0.31±0.01	0.31±0.01	0.31±0.01
N_{pp}	1,124±164	745.3±10.5	638.3±6.8	638.3±6.8
L_c (μm)	1534±3	1531±1	1534±1	1534±1
$(a_s/g) \times 10^4$	0.3172	0.3172	0.3172	0.3172
U_v (cm/s)	13.7±0.6	15.7±0.8	14.5±0.6	≈50
U_{ae} (cm/s)	13.8±0.6	15.7±0.8	14.5±0.2	≈50
Ca_v	6.47±0.51	6.70±0.34	5.94±0.10	
Ca_{ae}	6.50±0.53	6.70±0.34	5.94±0.10	
Re_v	0.19±0.01	0.25±0.01	0.235±0.01	
Re_{ae}	0.20±0.01	0.25±0.01	0.235±0.01	

The large air entrainment speed due to surface roughness of paper substrates has been explained by Scriven (1982) and investigated experimentally by Buonopane et al. (1986). Scriven (1982) reasoned that air escapes into the porous substrate and back through valleys created by the roughness. This confirms our limited paper substrate tests.

The experimental sets for uncoated PET and cellulose acetate in Table 5.3 have a comparable liquid physical property number, N_{pp}, and gas to liquid viscosity ratio, λ_{μ}. This should isolate the substrate property effect on air entrainment. By increasing the average roughness, R_a, from 0.57 to 1.45 μm between uncoated PET and cellulose acetate, a slight increase in the first and second critical speeds is observed. This increase is not significant because the standard deviations in the data are of equal magnitude to the difference in Ca, Re and U between the two substrates.

For a roughness change from 0.4 μm with polypropylene to 1.8 μm with polyethylene, the average increase in U_{ae} obtained by Buonopane et al. (1986) (see Table 2.3 in Chapter II) was much greater exhibiting a 300% increase. We don't have a satisfactory explanation for the discrepancy between our observations and Buonopane et al.'s 300% increase.

In summary, this section verifies for two additional smooth substrates that the air entrainment speed for the high viscosity silicone oil is comparable to our data with coated PET. The results are still much higher compared to the plunging tape data in the literature.

A qualitative analysis to explain the differences between our results and the plunging tape data will be discussed in the next section.

5.7 A Qualitative Analysis for Air Entrainment

It is necessary to get an idea of which forces are relevant for the onset of air entrainment and the effect of the "bulk flow" using a simple model. The normal stress difference across the gas liquid interface should be balanced by the action of surface tension, γ, with a radius of curvature, R, measured from inside the fluid phase. The surface tension is assumed to be uniform at the interface. This balance is given by

$$\frac{\gamma}{R} = \tau_{gn} - \tau_{ln} \qquad [5.3]$$

with τ_{gn} and τ_{ln} are the gas and liquid normal stresses, respectively. A schematic diagram of the simplified system is presented in Fig. 5.5. Near the onset of the air entrainment speed, the dynamic contact angle θ_d is close to 180° and the interface is almost parallel to the substrate. A wedge shaped region, with a spherical polar coordinate system and the origin at the DCL, is used to approximate the converging gas phase. The balance is for some angle, $\theta = \upsilon$, which is unknown but presumed to be small, and a distance r measured from the DCL. The gas normal stress, τ_{gn}, in Eq. [5.3] is expanded as

$$\tau_{gn} \approx -P_g + 2\mu_g \frac{Uf(\theta)}{r} \qquad [5.4]$$

where the term P_g represents the gas thermodynamic pressure above the atmospheric reference. The function $f(\theta)$ describes the gas normal stresses.

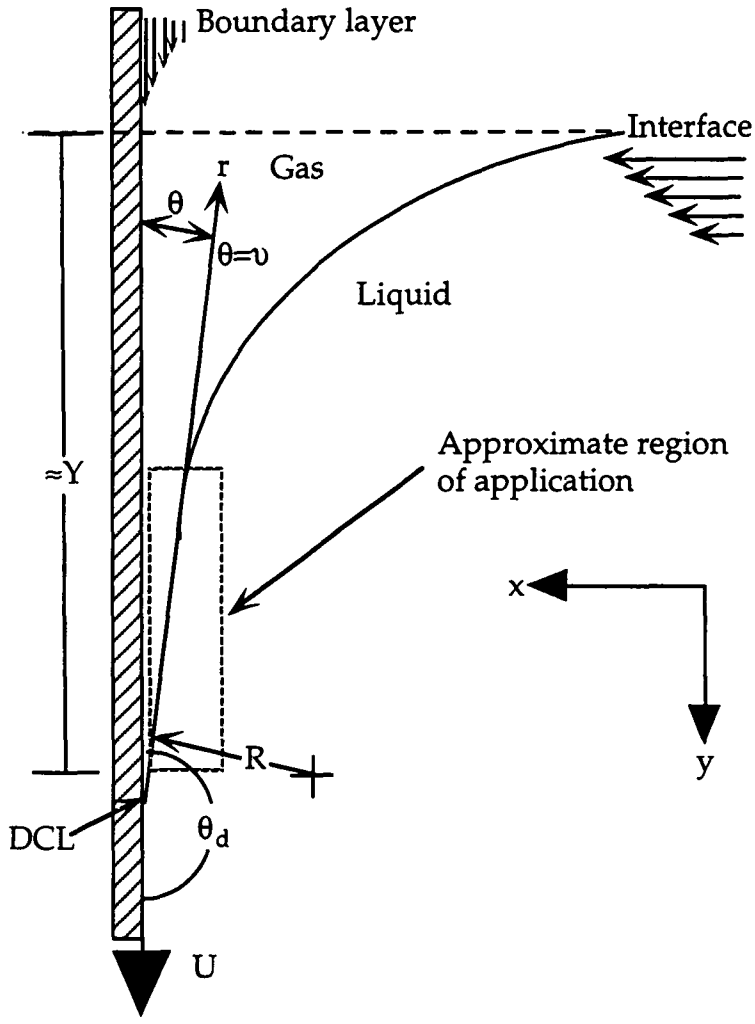

Figure 5.5. The basic setup for the qualitative analysis of air entrainment.

The form of the gas normal stress term, $2\mu_g \frac{Uf(\theta)}{r}$, for a converging gap with angle θ, is based on Moffat's (1964) or Huh and Scriven's (1971) solutions for creeping flow. The gas normal stress term $2\mu_g \frac{Uf(\theta)}{r}$ must be evaluated for $r > 0$ as discussed by Huh and Scriven (1971, p.93-95). We will not seek an explicit solution for $f(\theta)$ but rather simplify this function later. The liquid normal stress can be expanded as

$$\tau_{ln} = -\rho g Y - P_l + \mu\left(\frac{\partial u_i}{\partial x_j} + \frac{\partial u_j}{\partial x_i}\right) : \hat{n}\hat{n} \qquad [5.5]$$

with u_i the x_i-component of liquid velocity and Y, the liquid height measured from the contact line level. Because the interface is almost parallel to the substrate, we assume that $\hat{n} = n_x$. Substituting Eqs. [5.4] and [5.5] back into Eq. [5.3] we get a balance of the form

$$\frac{\gamma}{R} = -P_g + 2\mu_g \frac{Uf(\theta)}{r} + \rho g Y + P_l - 2\mu \frac{\partial u}{\partial x} \qquad [5.6]$$

where u is the x-component of liquid velocity . The liquid hydrostatic pressure term, ρgY, will be assumed to be negligible because the displacement depth is approximately 1-3 mm below the surface. At 1 mm depth, a 1 g/cm^3 fluid would have a hydrostatic pressure of 9.8 Pa (0.0014 psig). The capillary pressure term will be much greater than the hydrostatic pressure term. A 20-dyne/cm fluid and 100-μm radius of curvature, R, results in a capillary pressure of 200 Pa (0.029 psi). The estimate of R = 100 μm is not unreasonable considering that Mues et al. (1989) reported R to be smaller than 10 μm near the DCL.

The gas and liquid pressures, P_g and P_l, are nondimensionalized by $\mu_g U/L_c$ and $\mu U/L_c$ respectively, where L_c is the capillary length, $L_c = \sqrt{\gamma/\rho g}$, and U the substrate velocity. The result is given by

$$P_g^* = P_g \Big/ \left(\frac{\mu_g U}{L_c}\right), \text{ and } P_l^* = P_l \Big/ \left(\frac{\mu U}{L_c}\right) \qquad [5.7]$$

r, R, and x are nondimensionalized with respect to the capillary length scale, L_c, that is

$$r^* = r/L_c, \qquad R^* = R/L_c, \text{ and } x^* = x/L_c \qquad [5.8]$$

The x-component of liquid velocity, u, is nondimensionalized with respect to the substrate velocity, U

$$u^* = u/U \qquad [5.9]$$

Substituting the nondimensionalized variables back into Eq. [5.6], we get

$$\frac{\gamma}{R^{\cdot}L_c} = -\frac{\mu_g U}{L_c}P_g^{\cdot} + \frac{2\mu_g U}{r^{\cdot}L_c}f(\theta) + \frac{\mu U}{L_c}P_l^{\cdot} - \frac{2\mu U}{L_c}\frac{\partial u^{\cdot}}{\partial x^{\cdot}} \qquad [5.10]$$

By simplifying and writing the dimensionless groups, we get the form

$$\frac{1}{R^{\cdot}Ca_g} = -P_g^{\cdot} + \frac{2}{r^{\cdot}}f(\theta) + \frac{P_l^{\cdot}}{\lambda_\mu} - \frac{2}{\lambda_\mu}\frac{\partial u^{\cdot}}{\partial x^{\cdot}}$$

where $$Ca_g^{-1} = \frac{\gamma}{\mu_g U}, \text{ and } \lambda_\mu = \mu_g/\mu \qquad [5.11]$$

as previously described. For simplicity the term $2f(\theta)/r^*$ will be replaced by π^* and the gas terms will be grouped on the left hand side as

$$\left(P_g^{\cdot} - \pi^{\cdot}\right) + \left(\frac{1}{R^{\cdot}Ca_g}\right) = \frac{1}{\lambda_\mu}\left(P_l^{\cdot} - 2\frac{\partial u^{\cdot}}{\partial x^{\cdot}}\right) \qquad [5.12]$$

Each of the terms in Eq. [5.12] will have some unique set of values for a given parameter set and fluid properties in a particular geometry. The first term in brackets on the left hand side, (P_g^* - π^*), represents the gas normal stresses and will be assumed to be proportional to the substrate velocity, U. The function π^* is negative. The second term in brackets on the left-hand side is the capillary pressure term and the bracketed term on the right-hand side is the liquid pressure and normal stress term. The liquid decelerates in the x-direction as it approaches the DCL, therefore the sign of du^*/dx^* is negative.

Let us consider a short series of thought experiments to see if this simplistic approach can be used to explain the difference between the plunging tape data and the confined cavity setup from this work. The data comparing these systems was previously shown in Fig. 5.4 as a function of capillary number and λ_μ. In Fig. 5.6, the liquid viscosity and air entrainment speed, U_{ae}, are plotted for our data compared to the master plunging tape correlation given in Eq. [2.3]. Only two data sets for the glycerol-water fluids F and G are shown in Fig. 5.6, but this should not hinder our analysis. We will not complicate the analysis by considering changes in R* or P_l^*, but rather see if the trends correctly predict the data.

First, we will consider a low capillary pressure/high viscosity fluid. With the same fluid and substrate velocity, let us switch from a plunging tape system to the confined cavity setup used in this work. Thus, the importance of the liquid normal stress term on the right-hand side of Eq. [5.12] increases. To achieve a balance, the gas normal stress term can be increased. Since the gas normal stress term is proportional to substrate velocity, air entrainment is thereby delayed until a higher substrate velocity. This finding is confirmed by our experiments and graphically displayed in Fig. 5.6 when comparing U_{ae} for our data and the plunging tape data at low capillary pressures (20 dynes/cm) and large liquid viscosity (100 - 1000 cp). Thus, the balance in the case of our cavity is mainly between the gas and liquid normal stresses.

For a second example let us consider our confined cavity system with high viscosity liquids in Fig. 5.6. If we could suddenly increase the capillary pressure term in Eq. [5.12], the only term on the left-hand side that can decrease is the gas normal

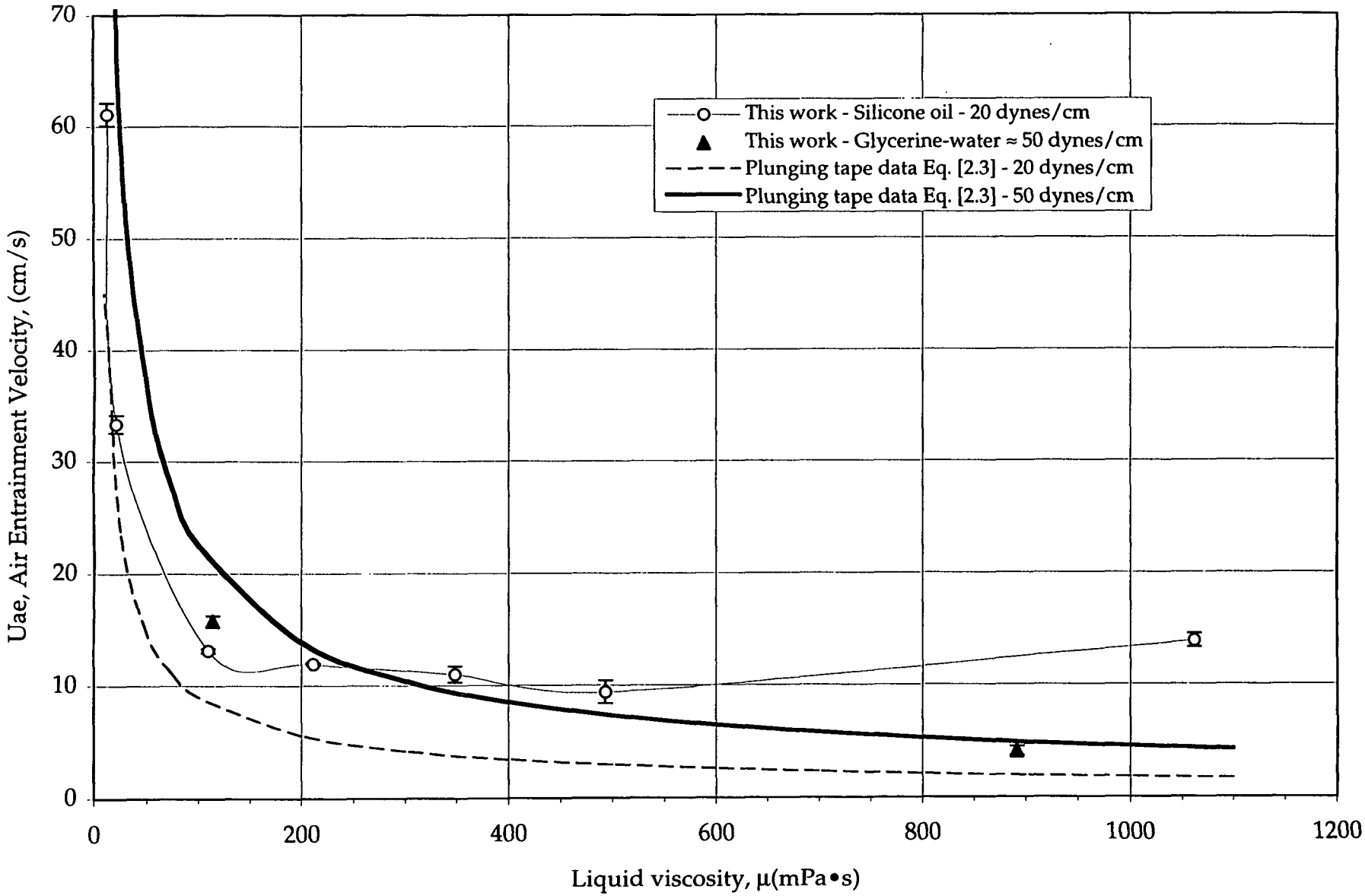

Figure 5.6. The second critical speed of air entrainment for confined cavity and plunging tape. The error bars are the standard deviation of the data.

stress term. Thus, by decreasing the substrate velocity, and thereby the gas normal stress term, we achieve a balance at a lower speed. Air entrainment is aided in this case which agrees with our results in Fig. 5.6 between the silicone oil and glycerol water data at high viscosity.

Comparing the data for the low viscosity silicone oil fluid A and glycerol-water fluid G in Table 5.4 we can see that for each fluid the capillary pressure, $1/Ca_g$, and $2/\lambda_\mu$ are comparable in magnitude. The gas normal stresses must also be of comparable magnitude and thus the air entrainment velocities are similar as seen in this work.

Table 5.4. Evaluation of qualitative analysis parameter differences for air film formation. Ca_g is evaluated at $U = U_v$.

		Parameter	
	Fluid	$1/Ca_g$	$2/\lambda_\mu$
Y	Silicone oil 10 cs	1,246	887
Z	Silicone oil 20 cs	2,226	1,466
A	Silicone oil 100 cs	5,942	7,785
B	Silicone oil 200 cs	6,221	14,667
C	Silicone oil 350 cs	6,835	23,668
D	Silicone oil 500 cs	8,633	35,756
E	Silicone oil 1000 cs	5,988	75,885
F	Glycerol 710 cs	44,211	63,297
G	Glycerol-water 90 cs	11,675	8,134

One result of this analysis is that simple correlations based on Ca and λ_μ are not satisfactory for explaining air entrainment results between different experiments. The estimation of the gas normal stress terms seems to be important in predicting air entrainment.

If we could obtain estimates of $\frac{2}{\lambda_\mu}\frac{\partial u^*}{\partial x^*}$ close to the DCL for the onset of air entrainment in plunging tape systems and a confined cavity with low aspect ratio, we can compare the significance of the liquid normal stress term. In Section 5.8, we will attempt to address this issue on the basis of the tape width and cavity dimensions for these two systems. An analytical 2-D solution will be used in Section 5.9 to obtain estimates of $\frac{2}{\lambda_\mu}\frac{\partial u^*}{\partial x^*}$.

5.8 The Difference in Normal Stresses

Let us focus in particular on the dimensionless term $\frac{2}{\lambda_\mu}\frac{\partial u^*}{\partial x^*}$ which represents the ratio of normal viscous stresses. The plunging tape and confined cavity in Figure 5.7 are two examples where the liquid normal stress acting at the DCL is different. First, in the side and front views of Figure 5.7 (a) and (b), a secondary recirculation with a viscous fluid is shown due to the fact that the tape usually occupies a fraction of the bath. This leads to a z-component of liquid velocity. Obtaining accurate estimates of $\frac{2}{\lambda_\mu}\frac{\partial u^*}{\partial x^*}$ for the plunging tape and the driven cavity is not possible with a 3-D analytical solution and would require computational simulation including surface tension effects and the cavity dimensions.

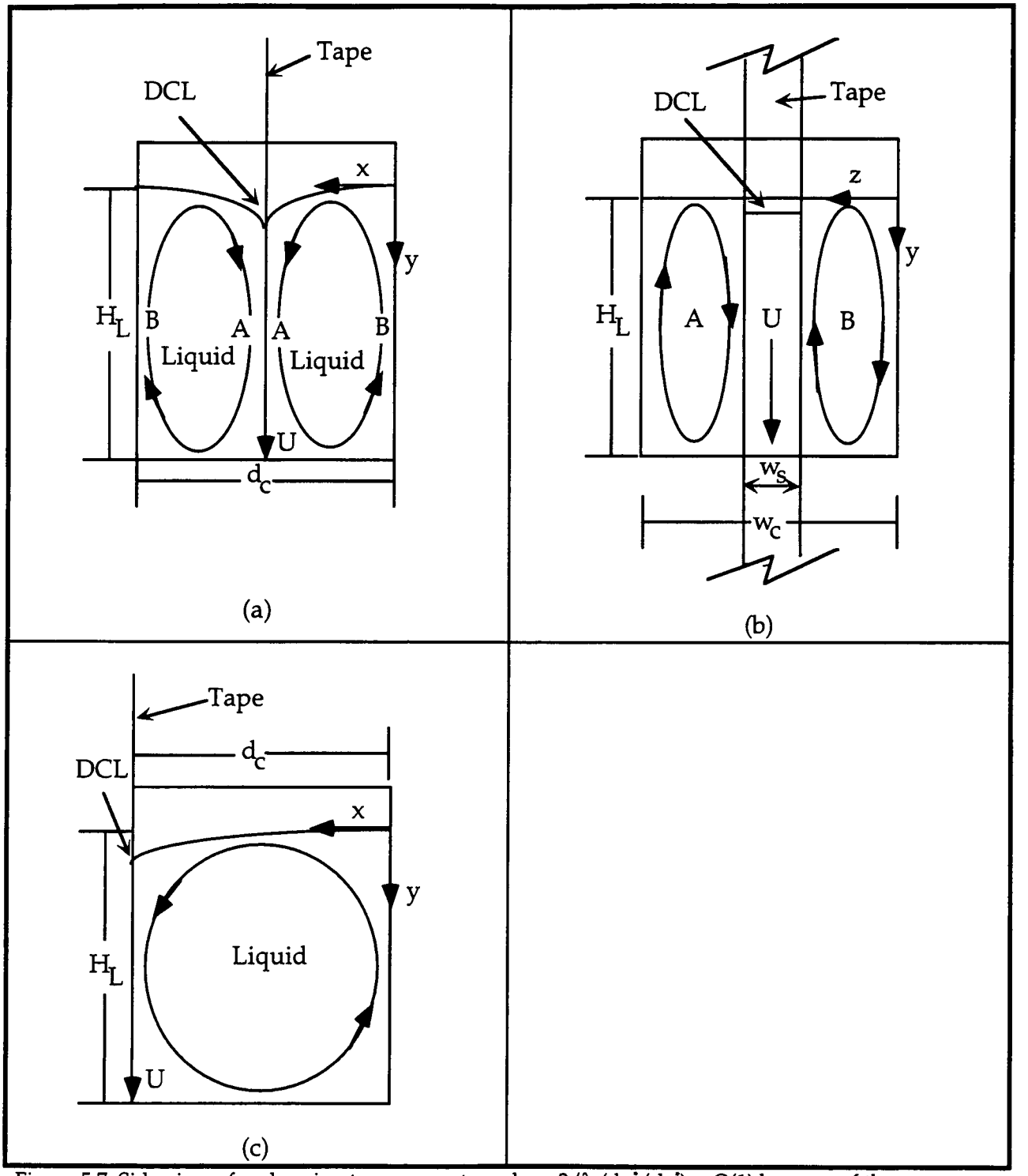

Figure 5.7. Side view of a plunging tape apparatus where $2/\lambda_\mu(du^*/dx^*)<<O(1)$ because of the recirculation seen in regions A and B. (b) Front view of plunging tape that occupies a fraction of the total cavity width. The secondary vortices are for locations A and B and are meant to depict the 3-D nature of the flow and there would be two secondary recirculations of similar to A and B on either side of the tape. c) Side view of a finite aspect ratio side driven free surface cavity.

We know that tape is usually much narrower than the width of the bath in most previous experiments. Perry (1967) for example, used 25-mm (1 in) tapes in a 10.16 x 7.62 x 10.16 cm (depth, d_c x height, h_c x width, w_c) tank for plunging tape experiments. The tape therefore only occupied 25% of the bath width, whereas in our system the tape spans the entire cavity width. Gutoff and Kendrick (1982) used a 16-mm tape in tank of dimensions 15.5 x 4.8 x 7.5 cm (depth, d_c x height, h_c x width, w_c) with a 16-mm tape. Thus, the tape occupies only a fraction of the bath in their system also.

In evaluating the upper limit for air entrainment speed the plunging tape system is not an acceptable apparatus for simulating the normal liquid stresses that may be present in actual operating systems. Even though we have treated the system on a continuum basis, we have pointed out some of the important parameters that should be measured, $\frac{2}{\lambda_\mu}\frac{\partial u^{\cdot}}{\partial x^{\cdot}}$, R^*, and $(P_g^*-\pi^*)$, when conducting air entrainment experiments. Unfortunately, during our experiments, measurement of these parameters was not undertaken because they are not easily accessible experimentally and represents detailed future experimental or modeling work.

Since we are not able to evaluate the full 3-D flow in the plunging tape or cavity, we will consider the limit when the depth of the cavity, d_c, is compared between our system and plunging tape cavity data. In Section 5.9 we will apply the analytical solution obtained by Canedo and Denson (1989) for the creeping flow limit (Stokes's flow). This dimensionless constrained solution of the stream function allows us to compare changes in liquid normal stresses with different cavity depths d_c

5.9 Estimating the Liquid Normal Stresses With an Analytical Solution

Canedo and Denson (1989) presented analytical solutions and experiments for creeping flow in a side driven open cavity with $a_c \leq 1$. (Note: $a_c = d_c/H_L$). Their experimental setup is similar to the cavity used in this work with the exception that they used a wetted roll for the moving side wall as opposed to our dry tape. In obtaining an analytical solution to compliment their experiments, they assumed that the upper free surface is flat, i.e. no surface tension effects, with free-slip. Due to of these limitations and the numerical convergence criteria, they were not able to obtain an accurate quantitative description of flow near the dynamic contact line. In effect, the DCL is pinned at the same location for all conditions using this model.

The asymptotic results from the creeping flow limit for the cavity flow given by

$$Re = U\rho d_c/\mu << 1, \qquad [5.13]$$

is used to compare the difference between the plunging tape and confined cavity at high viscosity. Using experimental measurements of the interfacial velocity profile and comparing them to the analytical solution, Canedo and Denson (1989) found good agreement up to cavity Re = 50 with cavity aspect ratios a_c = 1 and 2. Thus the creeping flow limit is applicable for our results with high viscosity fluids E and F where the cavity Reynolds numbers are 4.34 and 1.92 respectively. Figure 5.8 shows the simplified geometry and sets the nomenclature.

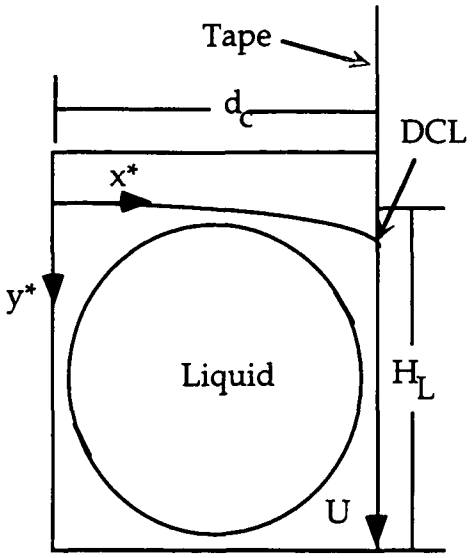

Figure 5.8. The simplified geometry and coordinate system used to estimate the liquid normal stress. The origin is different than Figure 5.7c so that the results can be interpreted with respect to Figure 5.9.

In the Stokes flow limit, the biharmonic equation of motion for the stream function is given by

$$\nabla^4 \psi_{sf} = 0 \qquad [5.14]$$

The partially constrained analytical model for $a_c \rightarrow 0$ is a function of the dimensionless coordinates, x* and y* defined by $x^*=x/d_c$ and $y^*=y/d_c$ over the domain $0 < x^* < 1$ and $0 < y^* < (1/a_c)$. The solution for the stream function with the appropriate boundary conditions is of the form

$$\psi_{sf} = -\frac{2}{\pi}\int_0^\infty F(x^*,\lambda)\frac{\sin\lambda y^*}{\lambda}d\lambda \qquad [5.15]$$

where λ is a parameter, $0 < \lambda < \infty$. Using the standard definition of the stream function in Cartesian coordinates, we can obtain a solution for the dimensionless x-component of velocity, u*, which has been scaled by U and is given by

$$u^* = -\frac{d\psi_{sf}}{dy^*} = \frac{2}{\pi}\int_0^\infty F(x^*,\lambda)\cos\lambda y^* d\lambda \qquad [5.16]$$

The dimensionless normal stress in the x* direction, τ^*_{xx}, is the derivative of Eq. [5.16] with respect to x* and is therefore

$$\tau^*_{xx} = 2\frac{du^*}{dx^*} = \frac{4}{\pi}\int_0^\infty F_x(x^*,\lambda)\cos\lambda y^* d\lambda \qquad [5.17]$$

The function $F(x^*, \lambda)$ and $F_x(x^*, \lambda)$ are hyperbolic functions given by

$$F = \frac{(1-x^*)\sinh\lambda\sinh\lambda x^* - \lambda x^*\sinh\lambda(1-x^*)}{\sinh^2\lambda - \lambda^2} \qquad [5.18]$$

$$F_x = \frac{\lambda^2 x^*\cosh(\lambda-\lambda x^*) + \lambda(1-x^*)\cosh(\lambda x^*)\sinh\lambda - \sinh\lambda\sinh(\lambda x^*) - \lambda\sinh(\lambda-\lambda x^*)}{\sinh^2\lambda - \lambda^2} \qquad [5.19]$$

The dimensionless normal stress τ^*_{xx}, in Eq. [5.17] is numerically integrated near the contact line region for $0.98 < x^* < 0.999$. The integral $\int_0^\infty(\cdot)d\lambda$ was numerically evaluated as $\int_{10^{-9}}^{5000}(\cdot)d\lambda$. The value of the integral outside this limit is negligible. Our numerical solution at the interface, τ^*_{xx} = 1.848, at x* =0.5 using Eq. [5.17], corresponds exactly to the solution obtained by Canedo and Denson (1989, Fig. 6).

The contour plot of the dimensionless normal stress, τ^*_{xx} is presented in Figure 5.9 for the region near the contact line. The line y*=1-x* represents the maximum normal stress for a given y* or x* coordinate. The results of Figure 5.9 will be used to estimate the effect of the cavity aspect ratio on the liquid normal stress.

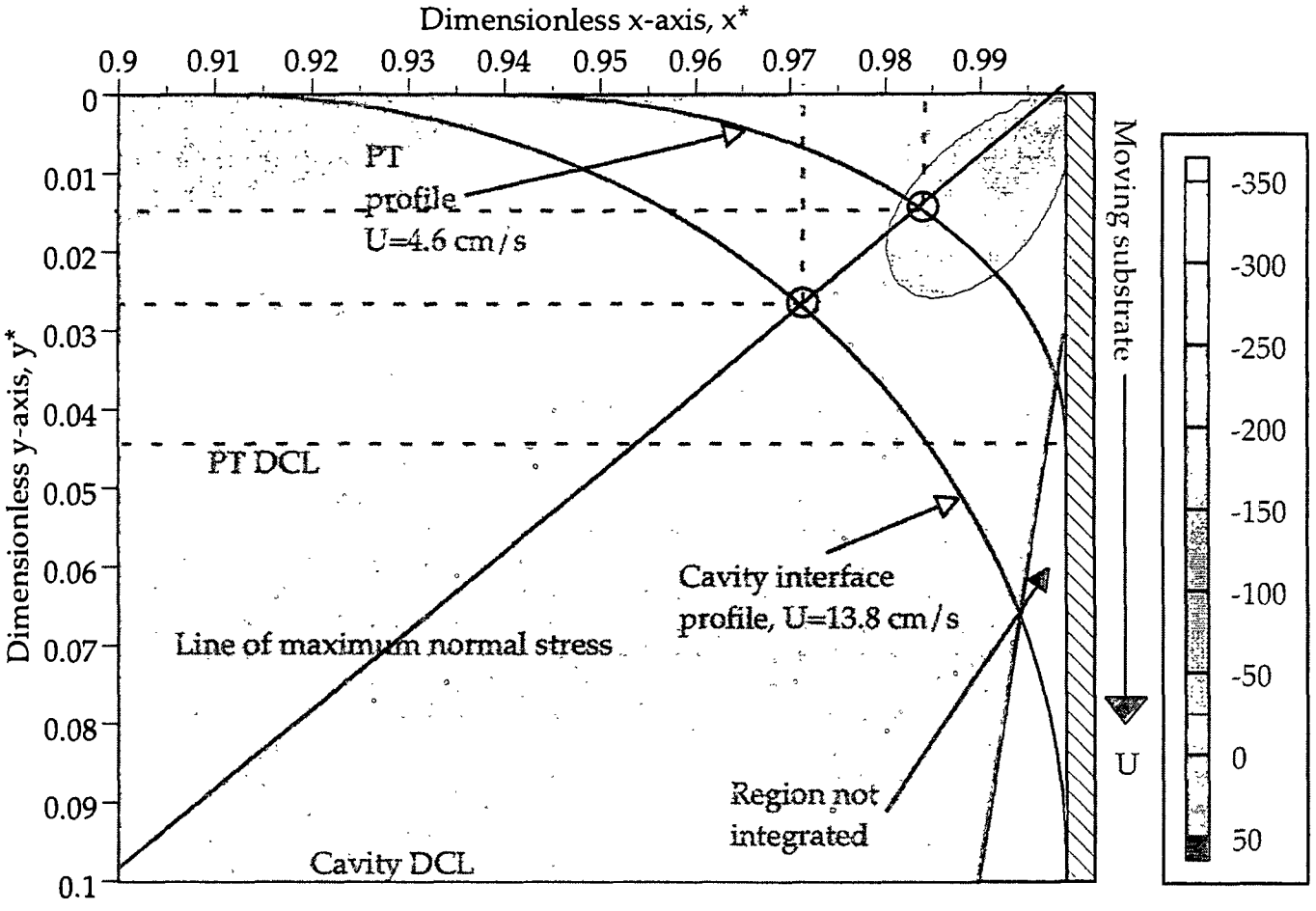

Figure 5.9. The dimensionless normal stress $\left(\pi/4\right)\tau^{*}_{xx}$ obtained from Eq. [5.17] for a cavity with an upper free surface and the side wall driven. The XYZ contour plot only represents the solution near the corner where the artificial DCL is located at $x^* = 1$ and $y^* = 0$. The grid spacing is 0.01 in both the x^* and y^* direction with a 0.002 grid applied in the region $0.98<x^*<0.999$ and $0<y^*<0.03$.

The position of the DCL for the cavity and the plunging tape is estimated at ($x^*=0$, $y^*= L_d/d_c$) for each system. The parameters L_d and d_c are contained in Table 5.5 with the Deryagin length, L_d, defined as $\sqrt{\frac{\mu U_{ae}}{\rho g}}$. At the same liquid viscosity ratio, it

already has been shown that the plunging tape exhibits a lower air entrainment velocity, U_{ae}. The position where the interface starts to deforming, (x*, y*=0), is

Table 5.5. Comparison of data between plunging tape and our free surface cavity for Fluid E (1000 cs silicone oil) when $U=U_{ae}$.

	L_d	d_c	U_{ae} cm/s	x* = 1-(0.3 cm/d_c)	y*	$(\pi/4)\dot{\tau}_{xx}$	τ_{xx} ‡ g/cm s^2
Our system	0.39 cm	3.51 cm	13.8	0.91	0.11	-18.02	-956
Perry(1966)	0.23 cm	5.08 cm†	4.6 §	0.94	0.044	-33.11	-405
Our system	0.23 cm	3.51 cm	4.6 ¶	0.91	0.064	-24.89	-440

† This is only 1/2 the total cavity depth because the tape divides the cavity into two sides.
‡ Note that 10 g/cm s^2 = 1 Pa; § Estimated from Eq. [2.2], ¶ This is not $U=U_{ae}$ but is used for comparison.

approximated from the experimental interface profiles of Burley and Kennedy (1977a) at a similar capillary number (Ca = 0.64). The interface coordinates x* and y* in Table 5.5 are used to approximate the starting points of gas/liquid interface profile as it deforms under forced wetting conditions. The approximated interface profile shape agrees with the experimental data of Burley and Kennedy (1977a).

The maximum *dimensionless* stress evaluated in Fig. 5.9 between the two systems is shown to be higher, i.e., $\dot{\tau}_{xx}^{PT} > \dot{\tau}_{xx}^{CAV}$, for the plunging tape (PT) vs. the free surface side driven cavity (CAV). The convention used is that negative normal stresses put the control volume in compression (Denn 1980, 149). By definition, the *dimensional* stress order will be reversed between the two systems because of the scaling by d_c and greater substrate velocity U prior to air entrainment. Equation [5.20] gives the definition for the dimensional stress.

$$\tau_{xx} = 2\mu\frac{\partial u}{\partial x} = 2\mu\frac{U}{d_c}\frac{\partial u^*}{\partial x^*} = \mu\frac{U}{d_c}\dot{\tau}_{xx} \qquad [5.20]$$

but

$$U_{ae}^{PT} < U_{ae}^{CAV} \text{ and } d_c^{PT} > d_c^{CAV} \qquad [5.21]$$

as shown by the data in Table 5.3 which leads to

$$\tau_{xx}^{PT} < \tau_{xx}^{CAV} \qquad [5.22]$$

The rationale for choosing the intersection of the approximate profiles with the line of maximum x-normal stress is that although the magnitude may be smaller, the order of τ_{xx}^{*} between the two systems will be the same near the contact line. The difference in the approximated profiles is due to the cavity depth, d_c, and the greater U_{ae} for our side driven cavity. The values for $(\pi/4)\tau_{xx}^{*}$ at the intersection of the line of maximum x-normal stress between the plunging tape and the side driven cavity are shown in Table 5.5. The last row in Table 5.5 also contains the estimated dimensionless stress for U=4.6 cm/s with our cavity dimensions. This profile is not shown in Fig. 5.9 but the data and sample calculations are in Appendix XVIII. This result also leads to the conclusion that $\tau_{xx}^{PT} < \tau_{xx}^{CAV}$.

The effect of a larger normal dimensional stress in the cavity is enhanced as the cavity depth, d_c, for the plunging tape system increases. Having a greater cavity depth, d_c, is more likely the case for the other plunging tape studies discussed in Chapter II. Perry's (1967) and Gutoff and Kendrick's (1982) works are two of the few references where the cavity dimensions are specified. The effect of the three-dimensional recirculation in the plunging tape system will additionally reduce the normal liquid stress acting on the interface near the DCL as discussed in Section 5.8. We have not investigated the effect of 3-D flow pattern generated by the plunging tape on the air entrainment speed. Therefore, it is not clear whether the 3-D flow

patterns are more significant than the differences in normal stress due to different aspect ratio cavities.

5.10 Summary

In summary, we have identified a parameter range when the triangular air film is stable according to the criteria identified in Section 5.2. The results were tested for statistical significance. For the stable parameter range, the confidence interval is greater than 90%. The difference in the importance of the liquid normal stress between the side driven free surface cavity and plunging tape studies is based on a qualitative analysis of the gas and liquid normal stresses with capillary pressure. We have given arguments about the 3-D flow in plunging tape systems leading to a lower air entrainment speed at high viscosity. With an available analytical 2-D solution in the creeping flow limit, the liquid normal stress near the DCL were estimated to be greater for the side driven free surface cavity compared to the plunging tape system.

The results in Chapter VI will now focus on the temporal and spatial behavior of the triangular air film using the deflectometry technique. It is applied to observe the behavior for the regions when $U_v < U < U_{ae}$ and also for $U > U_{ae}$. The necessary groundwork has been provided in Chapter V to conduct these experiments by determining under what conditions the triangular air film can be successfully studied.

CHAPTER VI

QUANTITATIVE RESULTS OF THE AIR FILM DIMENSIONS

6.1 Introduction to Results

The results obtained in Chapter VI are an extension of the results obtained in Chapter V for $U_v < U < U_{ae}$ and $U \approx U_{ae}$. Since these results are the first documented study of the temporal behavior of triangular air film structures, some new approaches to portraying the data will be used.

In Section 6.2 the results from Section 4.3.9 will be used to compare dimensions between substrate peaks and the average distance between entraining air fingers. No correlation is seen between these measurements. The deflectometry results are prefaced by an introduction in Section 6.3 to describe the data and visualization results presented in Section 6.4. Important observations summarized in Section 6.5 include: i) the long wave interfacial instability is supported by our time lapsed profile data, and ii) nucleation and air film retraction are usually preceded by an increase in the tip angle, $\varnothing_1$, and the thickness, h(0,y). The low viscosity fluids always have a greater out of plane thickness (up to 600 μm) compared to their high viscosity counterparts (as low as 10 μm).

The entire interface is geometry for a representative air film is reconstructed in Section 6.6. Section 6.7 discusses the influence of the gas Capillary and Weber numbers on the tip angles $\varnothing_1$ and $\varnothing_3$. Finally, in Section 6.8 a new type of flow structure is revealed that may be precursory to the "sawtooth" triangular air film

formation. Understanding of this precursor structure may give insight into the particular shape of the triangular air films.

6.2 Distance Between Triangular Air Films with 1000 cs Silicone Oil

Earlier the profilometer digital data was used with a fast Fourier transform (FFT) analysis. This FFT analysis resulted in an average wavelength, i.e. distance, between peaks on the substrate (see Section 4.3.9, Table 4.3). The wavelength results for the coated PET, the uncoated PET, and the cellulose acetate will be compared to the average experimental distance between the triangular air films (see Fig. 6.1)

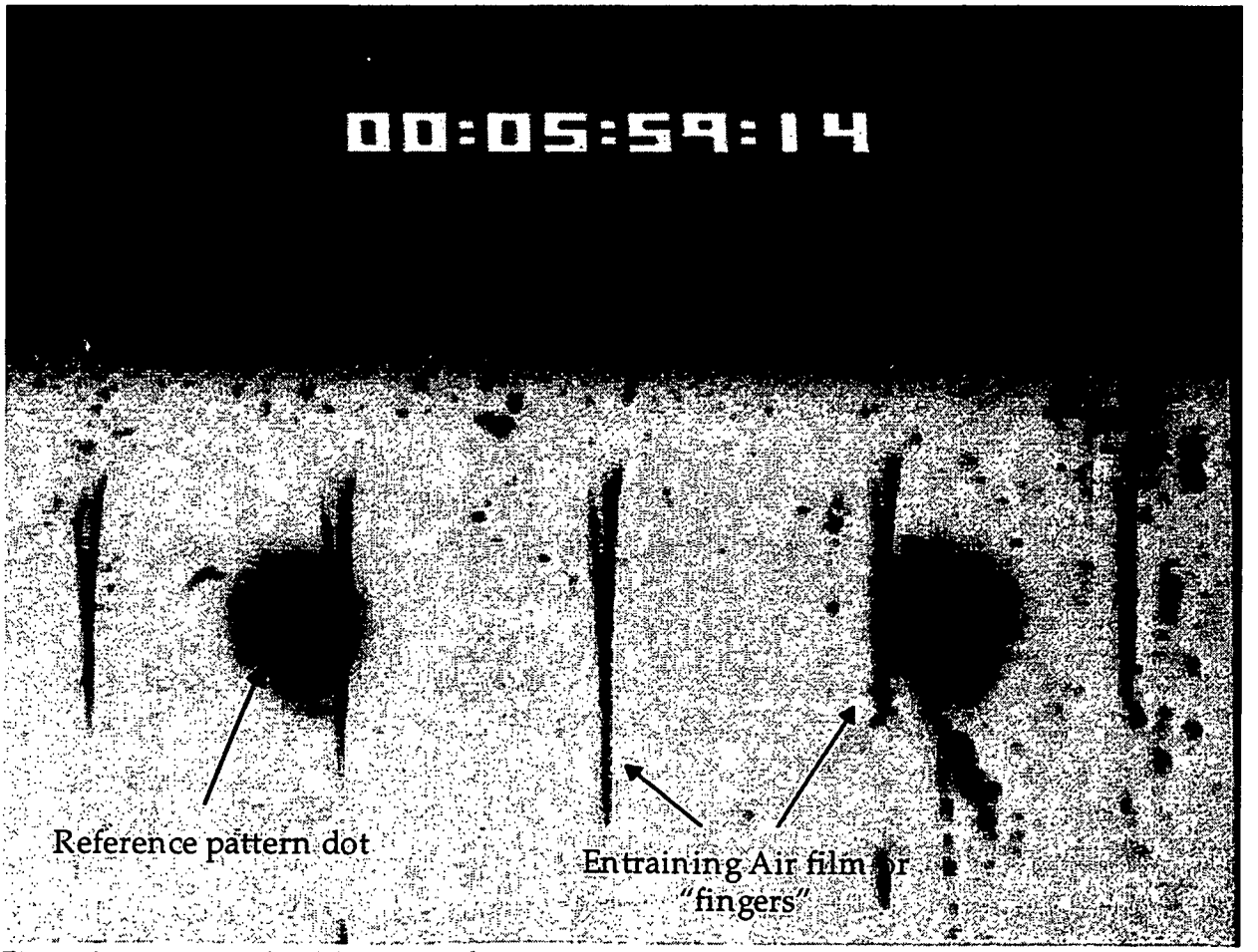

Figure 6.1. An example of the spacing between air pockets with the cellulose acetate. This experiment was run A07ERAM1 with the data file contained in Appendix VI in Table VI.6. The average distance between the two circular dot patterns is 1.6 mm. $U > U_{ae}$ and $Ca = 6.27$ with $\lambda_{\mu} = 0.32 \times 10^{-4}$.

using these same substrates. Only the 1000 cs silicone oil was tested.

The image shown in Fig. 6.1 is representative of the triangular air "fingers" seen with high viscosity silicone oil. The distance between the vertices of the air fingers was measured using image analysis on the experimental video data for $U > U_{ae}$. Table 6.1 contains the measurement statistics. The total number of samples measured was 498 between the coated PET, coated PET, and cellulose acetate. The paper substrate was not tested. The results show that there is no correlation between

Table 6.1. Average distance between vertices of air pockets

	Uncoated PET	**Coated PET**	**Cellulose Acetate**
Average distance (mm)	0.58	0.56	0.46
Standard Deviation (mm)	0.31	0.24	0.21
# Replicates	63	276	159
Table 4.3 Average substrate wavelength (mm)	8.9	11.0	10.8

the FFT substrate wavelengths and the distance between vertices of the entraining triangular air fingers. In fact, there is a 20-fold difference between these measurements. For example, coated PET had an average distance of 0.56 mm between fingers while the substrate peaks were 11.0 mm apart on average.

In order to verify that the FFT analysis represents the wavelength between peaks on the substrate, we need to reexamine Figs. 4.13 and 4.14. In these figures there are roughly 28-31 peaks that rise more than 0.5 μm above the mean profile. Dividing the sample length by the number of peaks above 0.5 μm gives an estimated

distance of 0.81 to 0.89 mm between peaks. This rough estimate is still a factor of two different from the air finger distance data (0.46 to 0.58 mm) in Table 6.1.

Another indication that the substrate roughness does not control the distance between air finger vertices is seen in comparison of the coated and uncoated PET data. Both of these substrates have different roughness, while the distance between air finger peaks is the same (0.58±0.31 vs. 0.56±0.24 mm).

These results seem to indicate that the air entrainment hydrodynamics control the distance between the triangular air fingers and not the substrate properties. Because only a single fluid (1000 cs silicone oil) was tested with this method, this result can only be stated for high viscosity. Later in Section 6.8, the precursor structures that form prior to the DCL will be surmised to control the distance between triangular air films.

In the next section we will discuss the measurement of the x, y, and z dimensions of the triangular air film as applied to the deflectometry results.

6.3 Overview of Deflectometry Results Presentation

The deflectometry technique outlined in the Section 4.2 was applied to observe the transient behavior of the axisymetric centerline profile during various cycles of air film formation, retraction, and nucleation. The substrate velocity for an individual case remained constant during these high-speed 16-mm microscope cinematography experiments. Images were digitized directly from the 16-mm film and analyzed using the previously mentioned methods described in Section 4.1.3

and in Appendix XVI.7. The spatio-temporal dynamics of the air film in all three dimensions are presented.

The air film length, ψ, and half-width, χ, were nondimensionalized by dividing the measurements, L_1 and $(W_1/2)$ by $20(L_c/Ca)$. This scaling parameter was used because the air film length and width are inversely proportional to the capillary number. The use of the symbol, ψ, to represent the air film length should not be confused with the stream function, ψ_{sf}, used in Section 5.9. The air film centerline thickness, h(0,y), was scaled by L_c and will be represented by $\zeta(0,\psi)$. Thus, the three dimensionless lengths χ, ψ, ζ are given by

$$\chi = \frac{\left(W_1/2\right)}{\left(20L_c/Ca\right)} = \left(\frac{W_1}{40}\right)\sqrt{\frac{\rho g U^2 \mu^2}{\gamma^3}}, \qquad [6.1]$$

$$\psi = \frac{L_1}{\left(20L_c/Ca\right)} = \left(\frac{L_1}{20}\right)\sqrt{\frac{\rho g U^2 \mu^2}{\gamma^3}}, \qquad [6.2]$$

and

$$\zeta = \frac{h}{L_c} = h\sqrt{\frac{\rho g}{\gamma}} \qquad [6.3]$$

The parameters χ, ψ, ζ are plotted with respect to the dimensionless time $\tau = t/t_{pp}$, where t_{pp} is a function of the fluid properties, $t_{pp} = \gamma/\mu g$. By representing the spatio-temporal behavior on χ, ψ, ζ plots, 3-D information can be inferred at various stages of the growth, nucleation, and retraction of a single air film. The axes for ψ

and χ on the χ, ψ, ζ plots are not scaled proportionally. Thus, the air film tip angle, $\varnothing_1$, the base angle of inclination, $\varnothing_2$, and the tip vertical angle, $\varnothing_3$ shown in Fig. 6.2 should not be inferred from the appearance of the dimensions that appear in Fig. 6.3 through Fig. 6.14. The two distinct regions, "air film" and "capillary tip", shown in Fig. 6.2 will be displayed more clearly from the deflectometry results in Section 6.4.

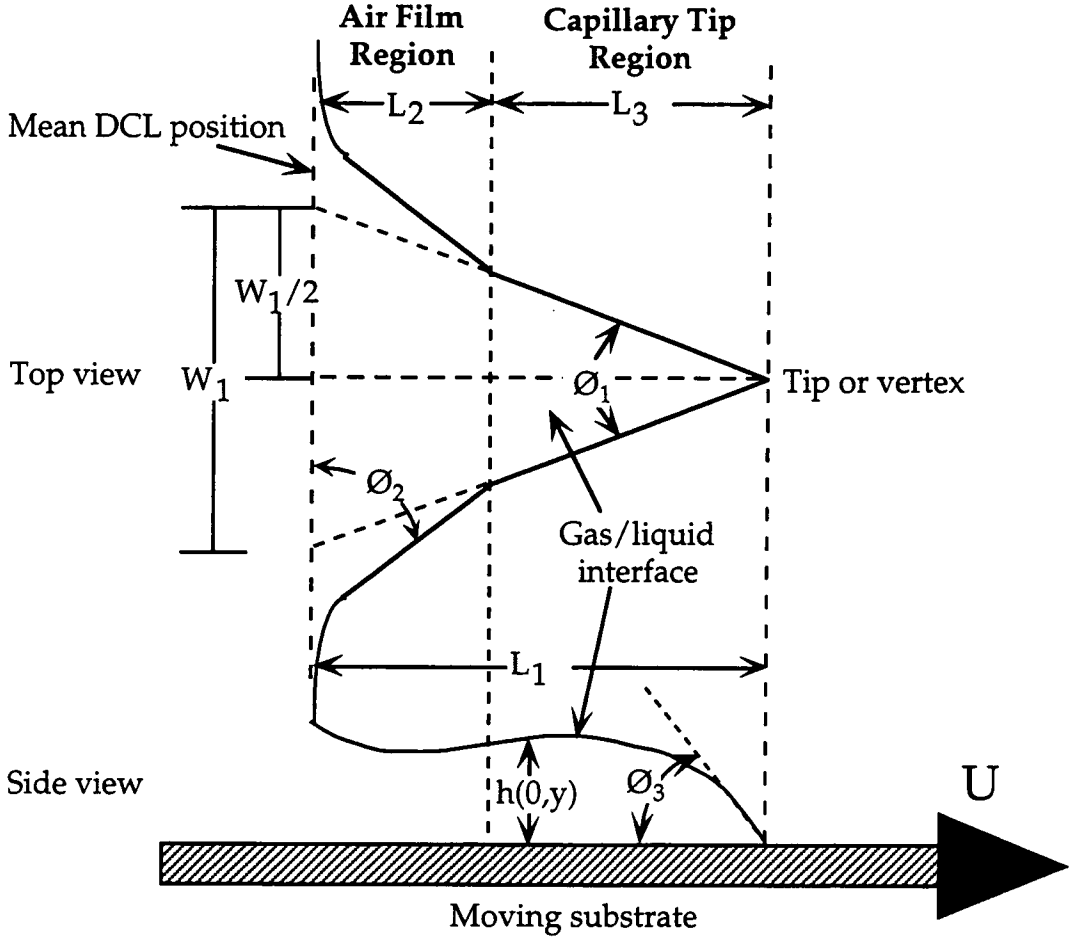

Figure 6.2. Defined top and side view dimensions for the triangular air film. Both of these axes will be projected onto the χ, ψ, ζ plots to show how the air film dimensions vary in time.

The angle $\varnothing_2$ is believed to be influenced by extensional flow and the local radius of curvature near the base of the air film, while $\varnothing_1$ and $\varnothing_3$ will be discussed in Section 6.7.

The experimental data for all of the cases is summarized in Table 6.2. Each case is defined as a separate set of images corresponding to a specific set of conditions.

The exact data files for the dimensional lengths, L_1 and L_2 as well as width, W_1, are contained in Appendix VIII for Cases #1-12. A full set of the images and data files for Case #11 with Fluid Z are contained in Appendix VII. Each case is presented with a short discussion in Section 6.4 of the salient features relevant to that case and how it may relate to the other cases. The graph(s) of χ, ψ, ζ versus $\tau = t/t_{pp}$ follow immediately after the discussion of each case. When more than a single figure is needed to present the time behavior of χ, ψ, and ζ, the time step from the previous figure is repeated so that comparison is simplified.

Some of the fluids, i.e. A, B and Z, have multiple cases at the same speed. The subcritical ($Ca < Ca_{ae}$) or supercritical ($Ca > Ca_{ae}$) state of the data is also presented in Table 6.2. The capillary number for the case was compared to the data from the ramping experiment results of Section 5.3 (Table 5.1) to determine if an air film once it formed: 1) would entrain, 2) was stable and would retract, or 3) was marginally stable where it may either entrain or retract. Thus, the data obtained in Chapter V was critical in locating when an air film would form in our deflectometry experiments. Without these results, the only other method would have been to make tedious step changes in the speed.

The thickness based on the calculated bubble volume, ζ_b, is also presented in Figs. 6.5, 6.8, and 6.9 as well as in Table 6.2. This bubble volume provides an

Table 6.2. Axisymetric Centerline Profile Case Parameters

	TEST FLUIDS								
	A	B		D	F	H	I	Y	Z
Type	Silicone oil 100 cc	Silicone oil 200 cs		Silicone oil 500 cs	Glycerin 400 cs	Glycerin-water 134 cs	Glycerin-water 48 cs	Silicone oil 10 cs	Silicone oil 20 cs
Case No.	1, 2	3, 4	5	6	7	8	9	10	11, 12
Description‡	(1) an, (2) ar	an	r	an	an/r	ar	ar	ar	r
Speed(cm/s)	12.8±0.2	12.1±0.1	12.1±0.01	12.9±0.2	5.17±0.21	15.50±0.03	36.15±0.76	60±0.8	34.5±0.2
Ca	0.66±0.02	1.17±0.03	1.17±0.03	2.82±0.07	0.60±0.08	0.53±0.01	0.48±0.05	0.36±0.02	0.34±0.01
$Ca > Ca_{ae}$?	Marginal	Marginal	Marginal	Yes	Yes	Marginal	Marginal	No	Marginal
$N_{pp} \times 10^4$	1498.0±99.4	19,015±1,238	18,517±1216	516,774±21,717	59,911±28,146	527.9±39.8	10.8±3.9	0.267±0.069	2.031±0.301
Re	1.70±0.04	0.85±0.02	0.86±0.02	0.39±0.01	0.24±0.03	2.31±0.04	14.5±1.4	69.6±4.5	24.1±0.9
L_c (μm)	1508.0±12.6	1495±12	1491.7±12	1544.0±15.0	1877.1±30.6	1995.8±7.1	1916.8±0.5	1468.6±7.1	1467.9±5.9
$\lambda_\mu \times 10^4$	1.92	1.06	1.07	0.43	0.43	1.33	3.87	18.1	10.6
t^* (ms)	19.93	10.51	10.57	4.68	8.84	29.76	77.05	170.24	102.48
G°	1)1.25°>0.90° 2) 0.90°	0.91° 0.91°	*1.60°	1.32°>0.93°	0.93°	0.90°	0.90°	0.89°	0.89°
η_4	1.4030	1.4032	1.4032	1.4034	1.4629	1.4539	1.4414	1.3989	1.4009
$1/P_f$ (μm)	100	80	80	100	100	100	200	200	200
ζ_b	1) 0.0011	3) 0.0273		0.0079	0.0044	-	-	-	-
ζ_{amp}	1) 0.0041 2) 0.0046	3) 0.0078 4) 0.0031				0.0022	0.0072	0.0346	10) 0.0828 11) 0.0556
τ_{per}	1) 0.387 2)0.392	3) 0.632 4) 0.551				0.258	0.078	0.0776	11) 0.1037 12) 0.0912
R^2	1) 0.335 2) 0.710	3) 0.347 4) 0.655				0.746	0.869	0.763	11) 0.740 12) 0.714
χ_{max}	1) -0.05 2) -0.035	3) -0.04 4) -0.055	-0.03	-0.035	-0.01	-0.03	-0.035	-0.04	11) -0.07 12) -0.06
Ψ_{max}	1) 0.03 2) 0.055	3) 0.08 4) 0.11	0.07	0.06	0.011	0.017	0.014	0.023	11) 0.065 12) 0.022
$\bar{\varnothing}_1$ (°)	1) 87.1 ± 17.9 2) 43.3 ± 6.9	3) 31.3 ± 4.2 4) 28.4 ± 4.6	21.4 ± 10.9	32.0 ± 4.2	39.6 ± 12.0 54.3 ± 6.7	70.6 ± 7.7	121.4 ± 15.4	124.5 ± 14.8	11) 90.3 ± 28 12)123.4 ±9.7
$\bar{\varnothing}_3$ (°)	1) 8.0 ± 3.1 2) 8.4 ± 1.2	3) 9.3 ± 1.3 4) 10.0 ± 2.0	9.9 ± 2.7	2.9 ± 1.4	5.3 ± 0.6 3.5 ± 1.1	7.7 ± 1.7	5.4 ± 3.9	8.4 ± 2.6	11) 16.3 + 8.7 12) 12.8 ± 3.2
$\bar{L}_1$ (μm)	1) 661 ± 271 2) 1835 ± 268	3) 1912 ± 46 4) 2634 ± 97	1494 ± 551	465 ± 122	650 ± 30 357 ± 40	1147 ± 169	1029 ± 478	1207 ± 344	11) 3124±2123 12) 1298 ± 629
$\bar{L}_2$ (μm)	1) 279 ± 139 2) 421 ± 139	3) 822 ± 124 4) 1426 ± 80	526 ± 353	178 ± 74	348 ± 62 179 ± 52	404 ± 124	288 ± 126	465 ± 101	11) 814 ± 378 12) 511 ± 225

* This value for G is much higher for Cases #3-5 because the special microscope/camera traversing apparatus had not been built yet leading to a greater error in aligning the optics perpendicular with the substrate surface. ‡ an - Advancing and nucleation, ar - Advancing and Retraction, and r - Retraction.

independent confirmation of the validity of the deflectometry technique. The bubble diameter was calculated in 4-5 successive time steps and the equilibrium diameter was used to calculate its volume. The dimensional centerline thickness, h(0,y), can be found by multiplying ζ by L_c. The maximum measured centerline thickness, h(0,y)=600 μm, is found for Case #11 with 20 cs silicone oil.

Based on the open literature, these results are the first data documenting how the air film dimensions vary both temporally and spatially.

6.4 Observations from the Deflectometry Cases

Each case contained in Table 6.2 is presented in this Section with a discussion followed by the plots of χ, ψ, and ζ vs. the time step, τ. The data points for each time step are contained at the top of each figure.

6.4.1 Case #1 - 100 cs Silicone Oil Triangular Air Film Profiles[1]

In this series (Fig. 6.3), a triangular air film grows due to an initial disturbance of a fiber passing near the DCL and the air film elongates at 3.2 cm/sec (one-fourth of U) until nucleation at τ = 2.057 occurs. The growth from τ = 0.000 to nucleation is very smooth with ζ increasing throughout the elongation and growth. $\varnothing_1$ remains constant around 75±5° with an increase beginning at τ = 2.057 and continuing until it reaches 115±5° at nucleation. The bubble that results from the nucleation and tip isolation can be used to calculate the mean thickness based on the bubble volume, ζ_b, and compared with the profile thickness. The bubble radius is calculated in 4-5 successive time steps using the equilibrium radius. For this case, ζ_b = 0.0011 and the film images after nucleation lead to the conclusion that a majority of the air volume escapes from the tip region before bubble formation. This is true when nucleation leads to a narrow strand near the vertex from which the air can percolate.

[1] Experimental file code U15ACA4 from 16-film times 401:18.846 to 401:18.887.

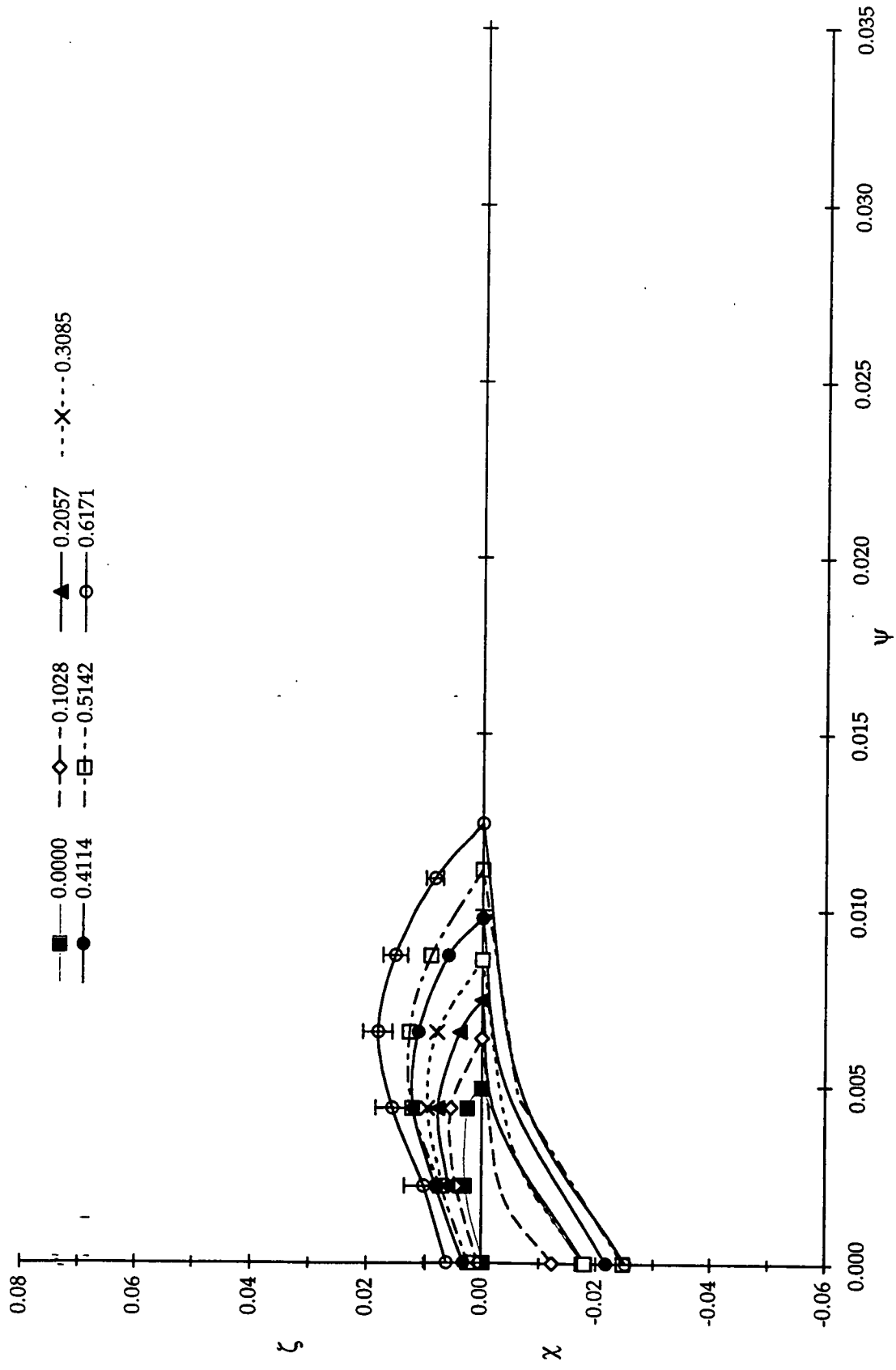

Figure 6.3. Case #1 - 100 cs Silicone Oil, Ca=0.66, U=12.8 cm/sec. (τ = 0.000 to 0.6171)

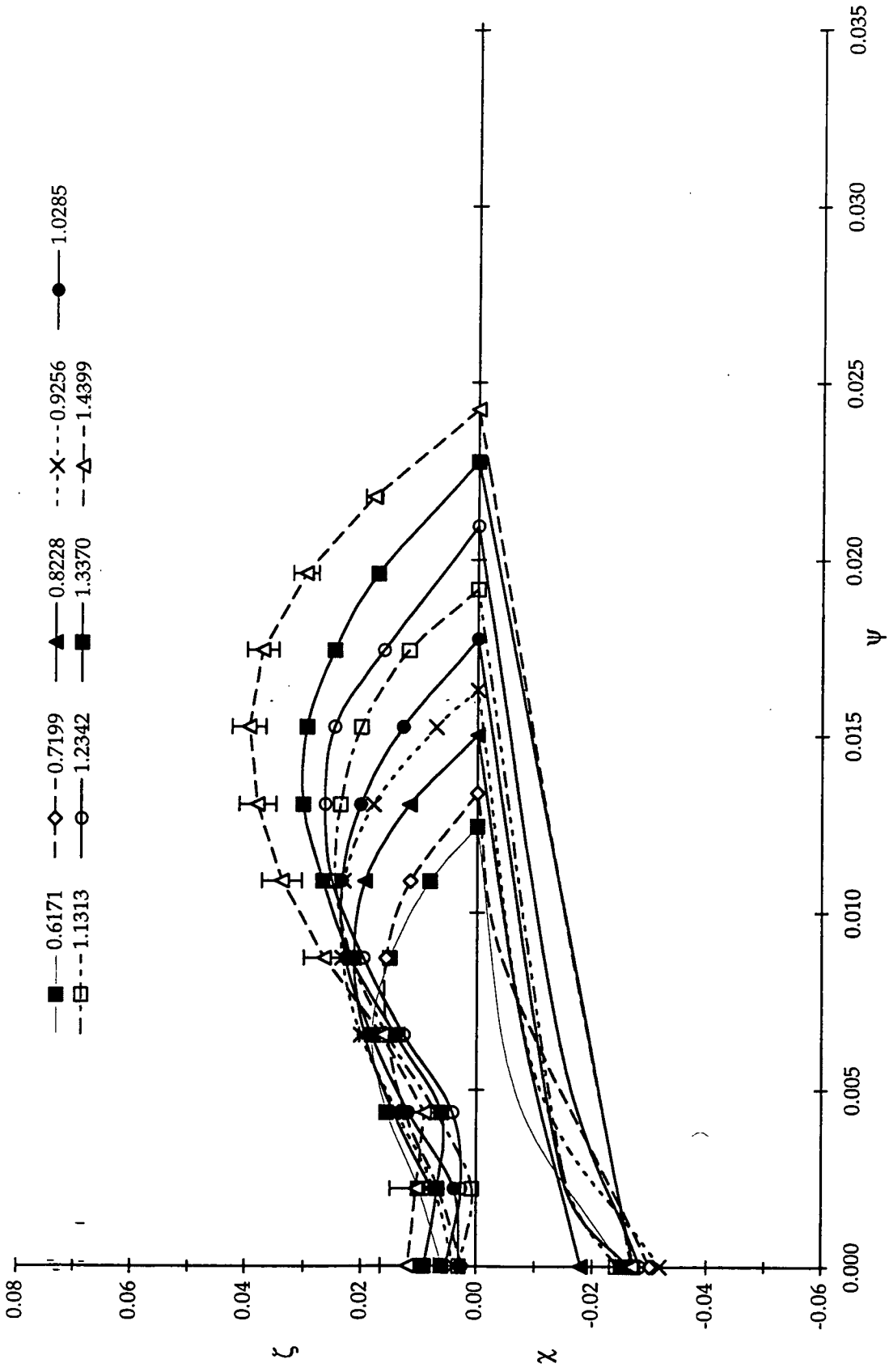

Figure 6.3. (Continued) (τ = 0.671 to 1.4399)

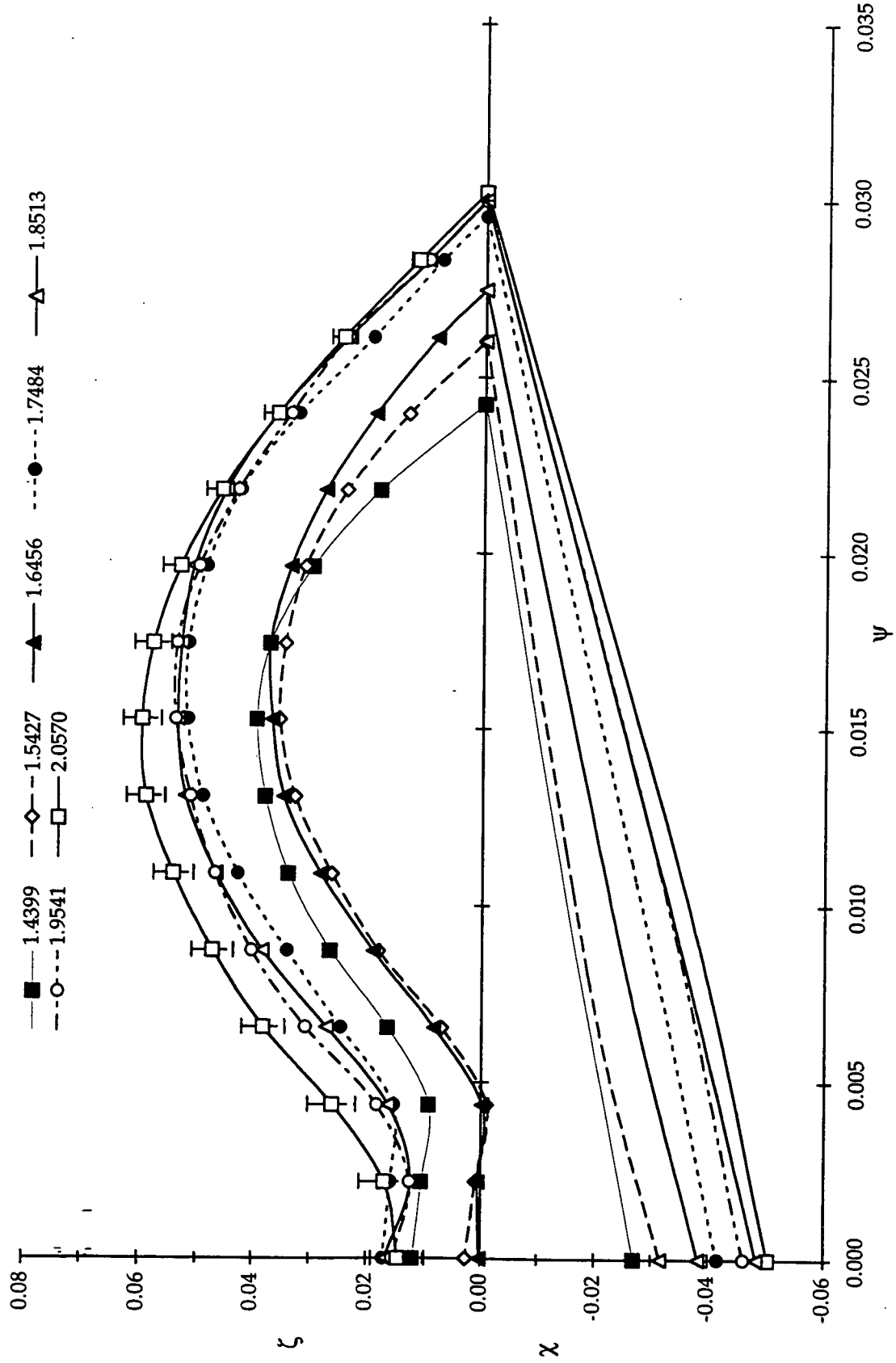

Figure 6.3. (Continued) (τ = 1.4399 to 2.0570)

6.4.2 Case #2 - Fluid A - 100 cs Silicone Oil Triangular Air Film Profiles[2]

In this case (Fig. 6.4), we have an air film forming and retracting at 4.4 cm/sec which is roughly one-third of U. The retraction starts at $\tau = 0.206$ with the decrease in ψ coinciding with decreases in ζ and $\varnothing_1$ during the retraction. For $\tau \geq 1.543$, $\varnothing_1$ begins to rise to 75±5° which is the same as the advancing values of $\varnothing_1 = 75\pm5°$ seen in Case #1 for Ca=0.66. Comparing the previous case to the current case, the maximum thickness, ζ_{max}, is of the same order. At $\tau = 0.000$ and $\tau = 0.103$ for $0.025 \leq \psi \leq 0.04$, there are two slight bumps in the profile. These slight rises were reproduced when the profiles were reexamined. In a plot of $\zeta(\psi=0.0065)$ as a function of τ, a slow decrease in thickness, ζ, occurs as the air film retracts.

[2] Experimental file code U15ACA4 from 16-mm film times 401:20.518 to 401:20.564.

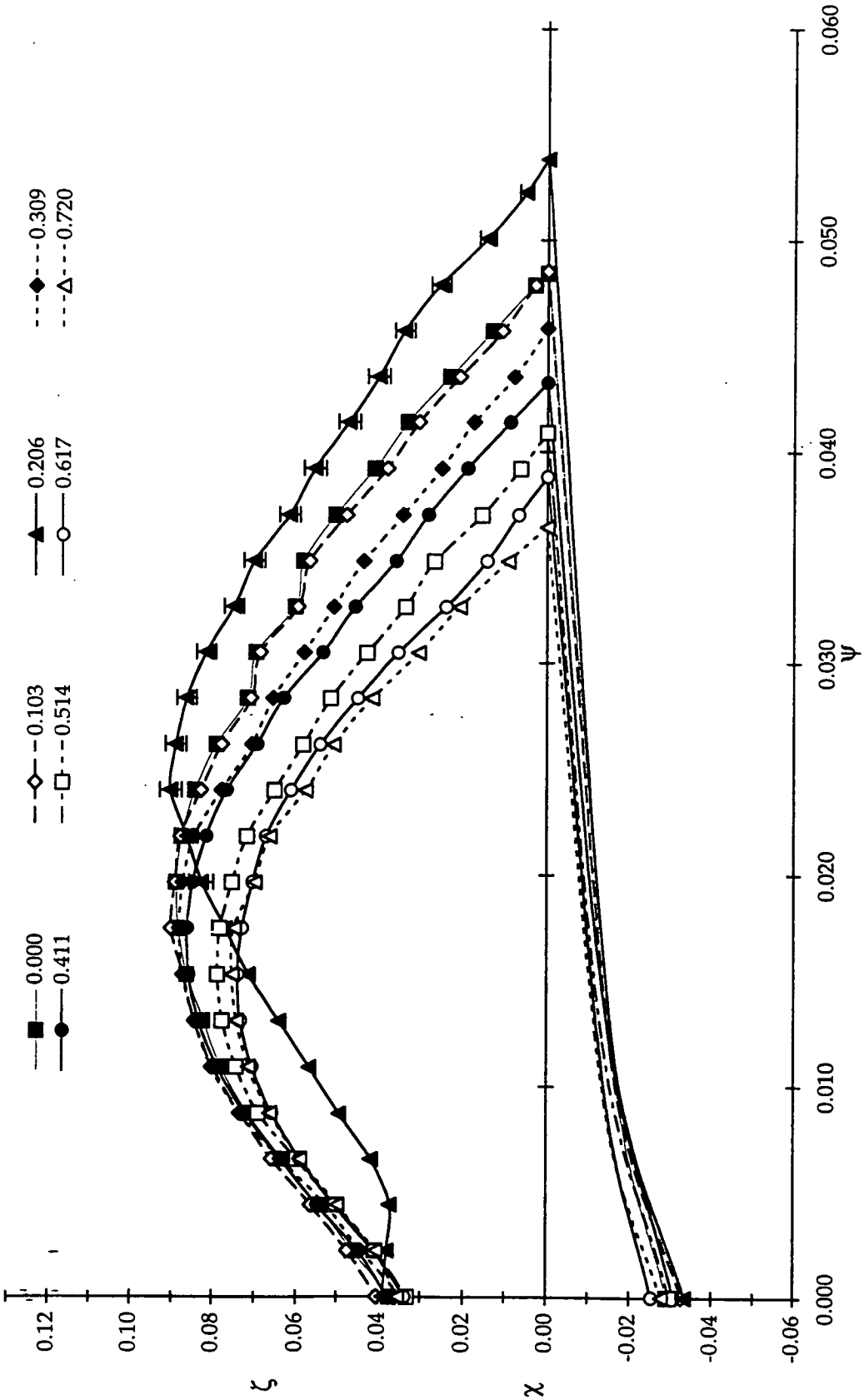

Figure 6.4. Case #2 - 100 cs Silicone Oil, Ca=0.66, U=12.8 cm/sec. (τ = 0.000 to 0.720)

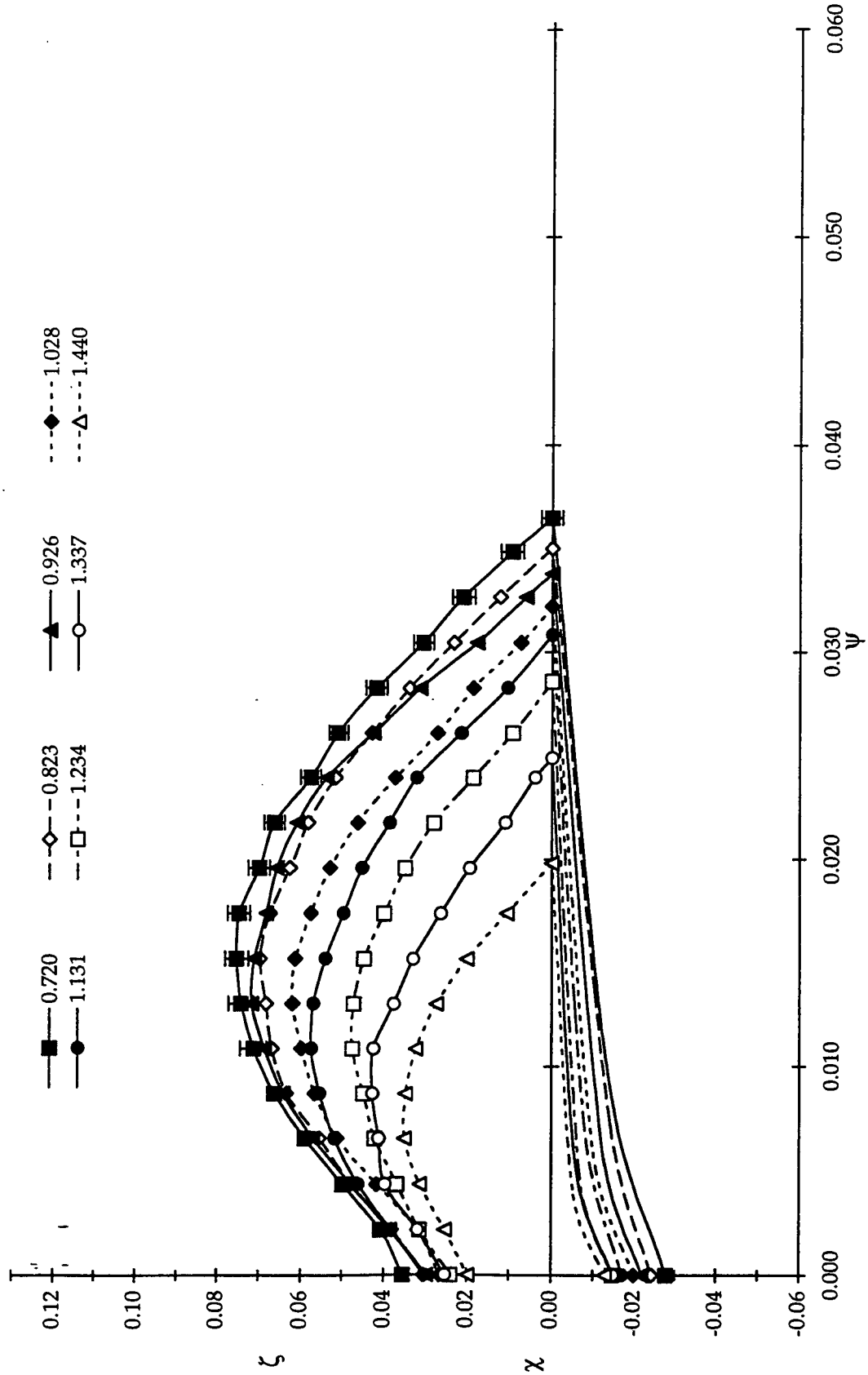

Figure 6.4. (Continued) (τ = 0.720 to 1.440)

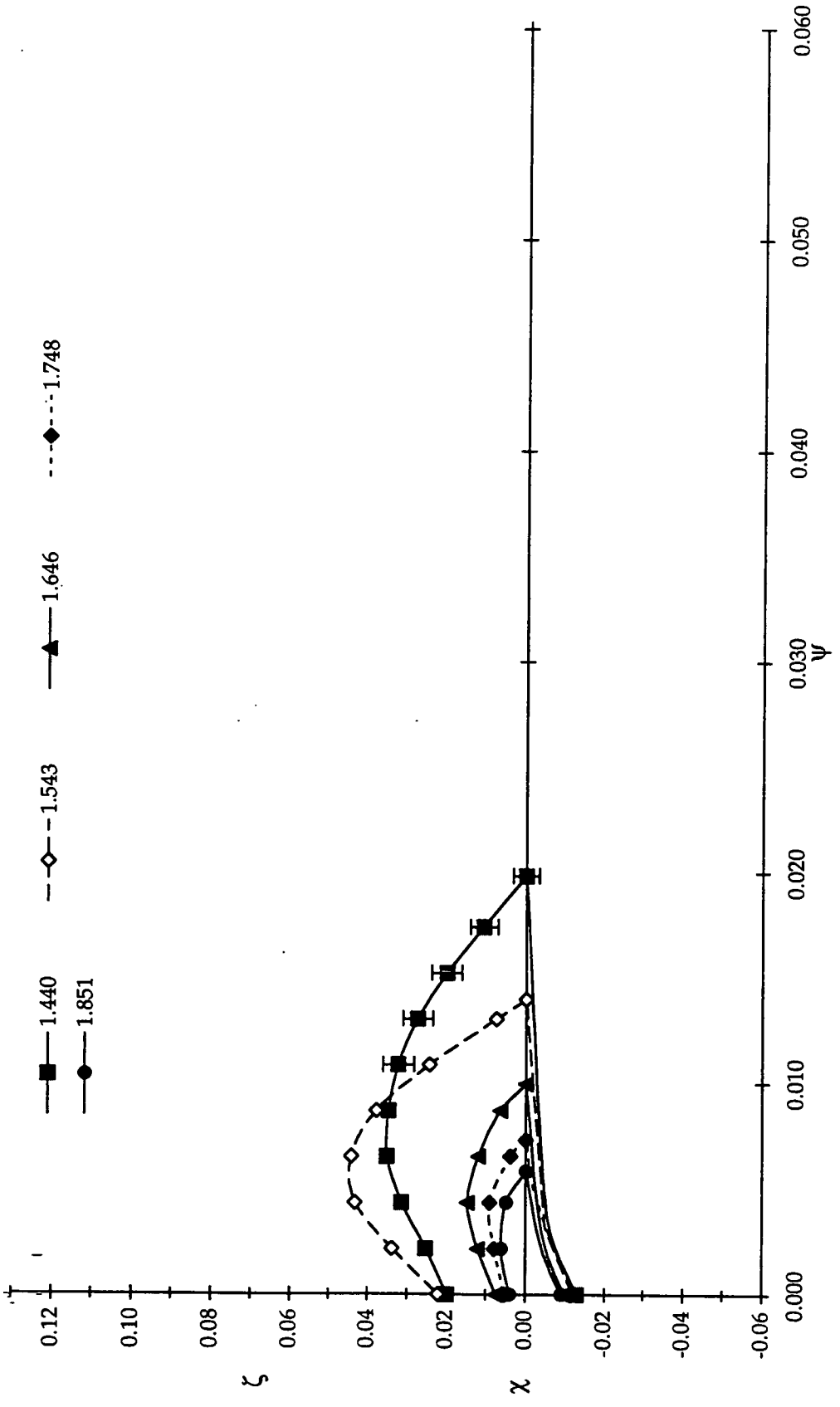

Figure 6.4. (Continued) (τ = 1.440 to 1.851)

6.4.3 Case #3 - Fluid B - 200 cs Silicone Oil Triangular Air Film Profiles[3]

Analysis of Fig. 6.5 begins with evolution of a triangular vertex at $\tau = 0.000$ and the vertex remains pinned at $\psi \approx 0.075$ until nucleation at $\tau = 2.774$. The equilibrium bubble volume that is ejected gives $\zeta_b = 0.0273$ which is representative of the mean thickness. The tip angle $\varnothing_1 = 30 \pm 5°$ for $\tau \leq 1.784$ after which it rises to $40 \pm 5°$ for $\tau = 2.774$.

The τ vs. $\zeta(\psi=0.0063)$ plot exhibits wavelike motion prior to nucleation. There is a large fluctuation in ζ at $\tau = 2.774$ immediately prior to nucleation which will also be seen in Case #4.

[3] Experimental file code M24BCA7#1. The time code generator was not operative during all of the experiments with Fluid B so the location of each "event" was marked on the film using a permanent marker. This presents considerable difficulty in archiving the 16 mm film to locate a sequence which may only last 20-30 frames out of 16,000 frames in a 400 foot roll of film.

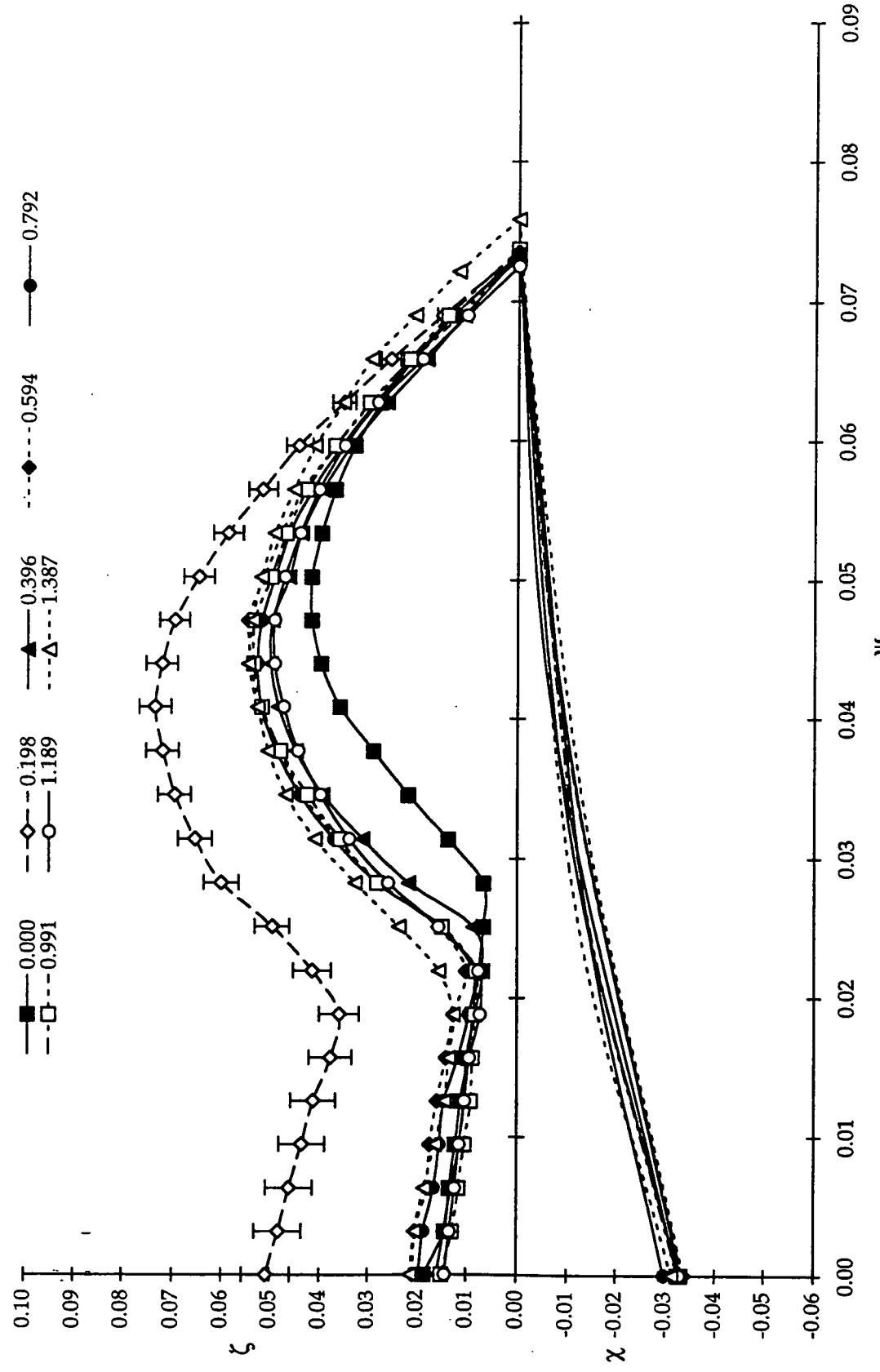

Figure 6.5. Case #3 - 200 cs Silicone Oil, Ca=1.17, U=12.1 cm/sec. (τ = 0.000 to 1.387)

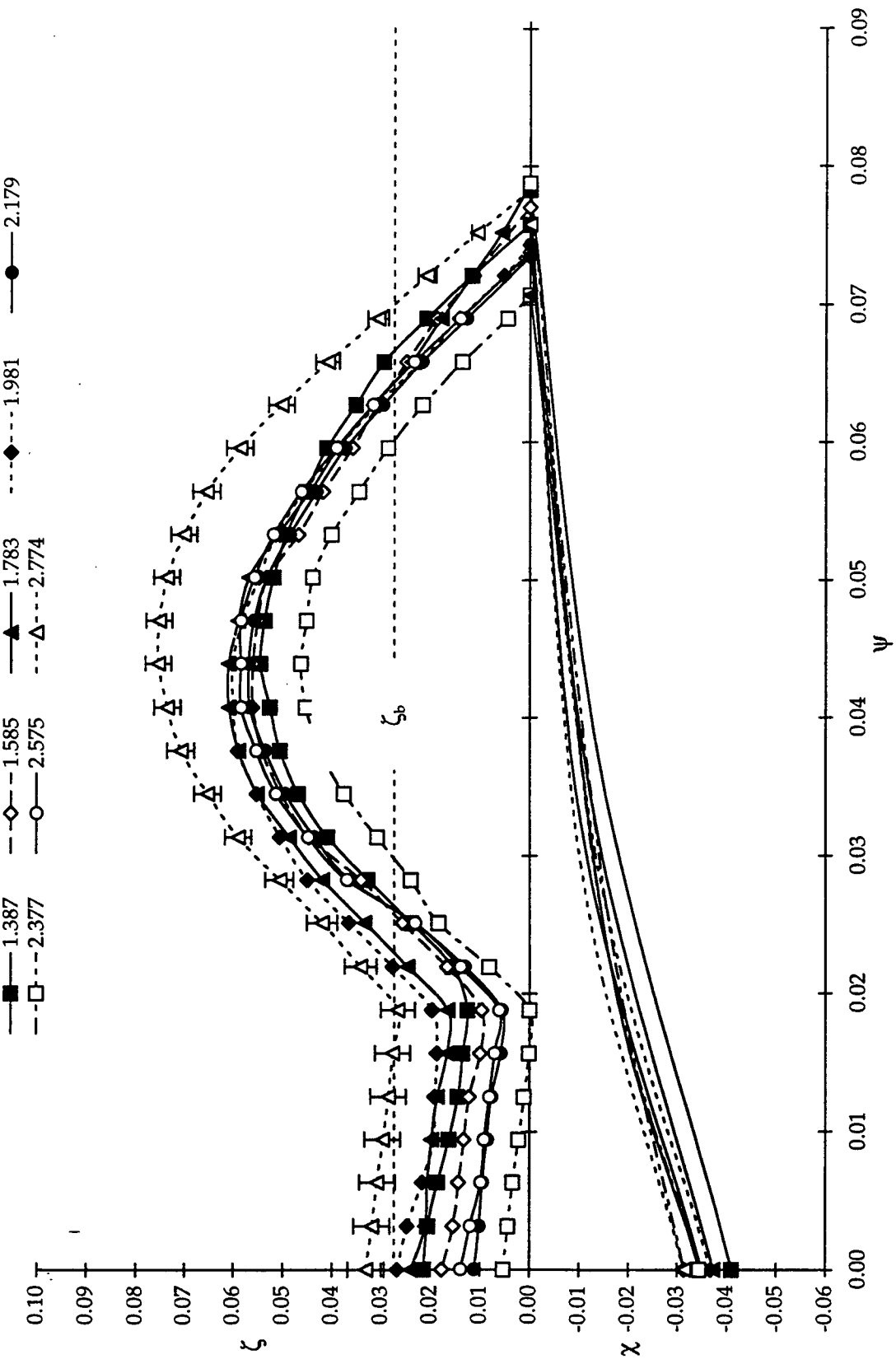

Figure 6.5. (Continued) (τ = 1.387 to 2.774)

6.4.4 Case #4 - Fluid B - 200 cs Silicone Oil Triangular Air Film Profiles[4]

In this case (Fig. 6.6), the air film achieves a triangular vertex at $\tau = 0.594$ and the air film nucleates at $\tau = 2.377$. The advancing tip region from $0.000 \leq \tau < 0.594$ is a blunt rather than a sharp vertex as seen in the χ, ψ, ζ, τ plot. $\varnothing_1$ increases from $25\pm5°$ for $\tau \leq 0.990$ to $35\pm5°$ immediately prior to nucleation. The thickness in the tail region increases from $\tau = 0.000$ to 0.991 after which the height remains essentially stationary exhibiting sinuous behavior for $\zeta(\psi=0.0063)$ vs. τ. It is not possible to measure ζ_b because of air percolation from the strand region.

The rise in the interface profile and $\varnothing_1$ prior to nucleation compliments the behavior seen in Case #3.

[4] Experimental file code M24BCA7#2.

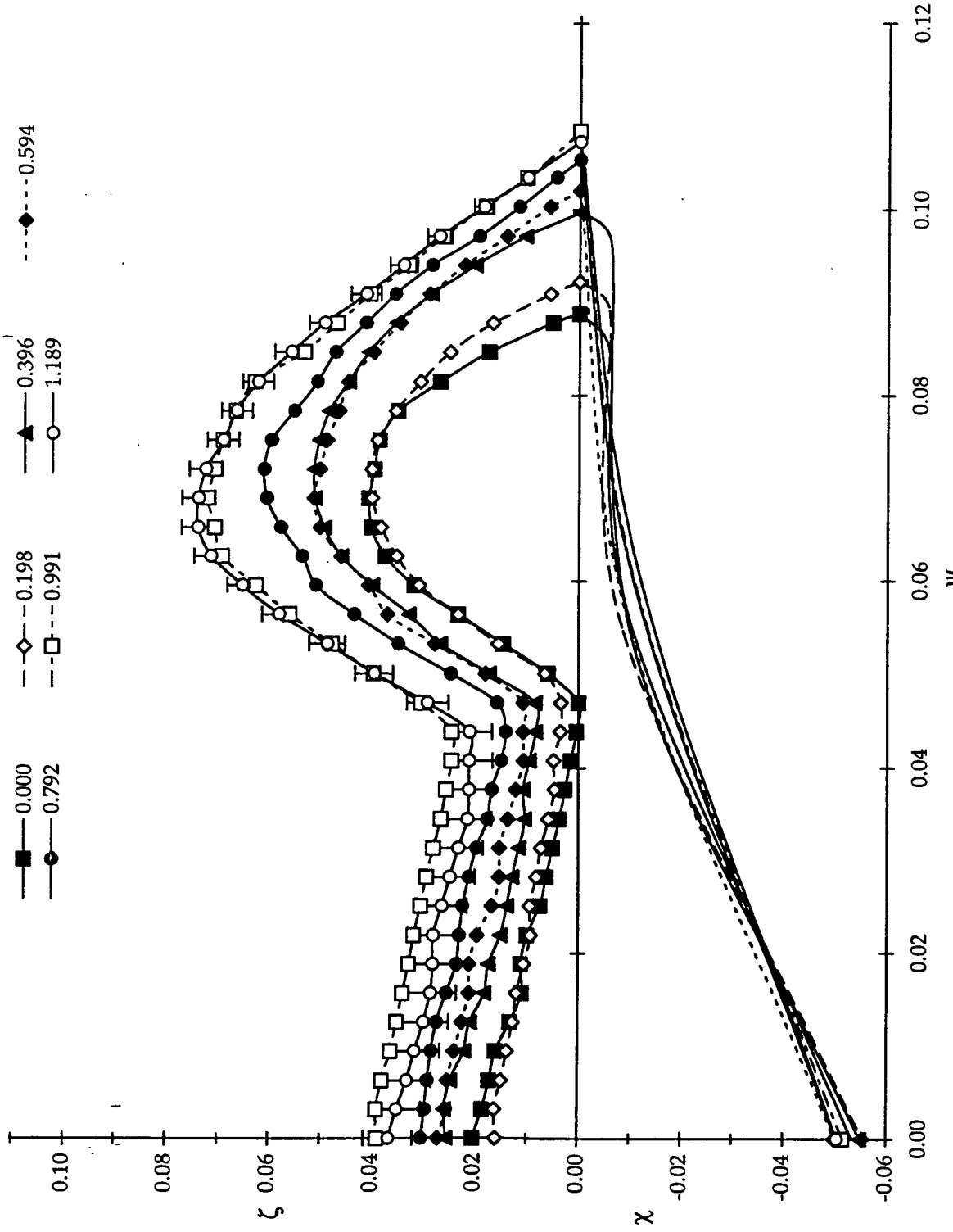

Figure 6.6. Case #4 - 200 cs Silicone Oil, Ca=1.17, U=12.1 cm/sec. (τ = 0.000 to 1.189)

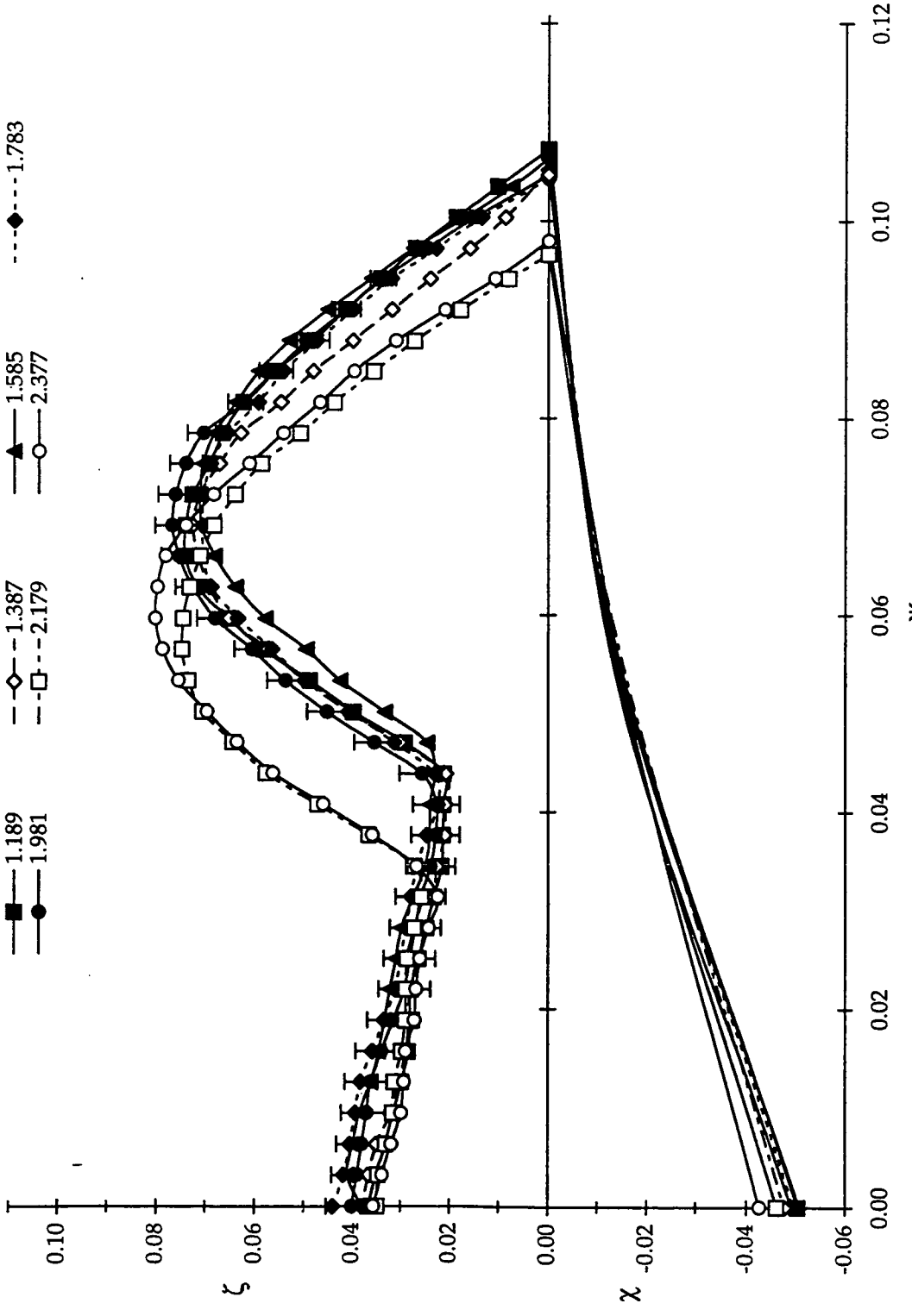

Figure 6.6. (Continued) (τ = 1.189 to 2.377)

6.4.5 Case #5 - Fluid B - 200 cs Silicone Oil Triangular Air Film Profiles[5]

In this case (Fig. 6.7), an air film retracts at a velocity one-third U (4 cm/sec). The retraction initiates at $\tau = 1.970$ when the air film centerline profile increases to a large value of ζ which seems to allow the pressure in the tip to be released. Thus it is possible that the surface tension forces act to minimize the interfacial area of the air film through retraction. The retraction is accompanied by narrowing of the air film with a tip angle from 30±5° at $\tau = 0$, decreasing to a minimum of 10±5° and then increasing to 60±5° as the film retracts further. The trend for $\varnothing_1$ complements the retraction in Case #2. The interface profiles were not measured for $\tau > 3.94$.

[5] Experimental file code M24BCA6.

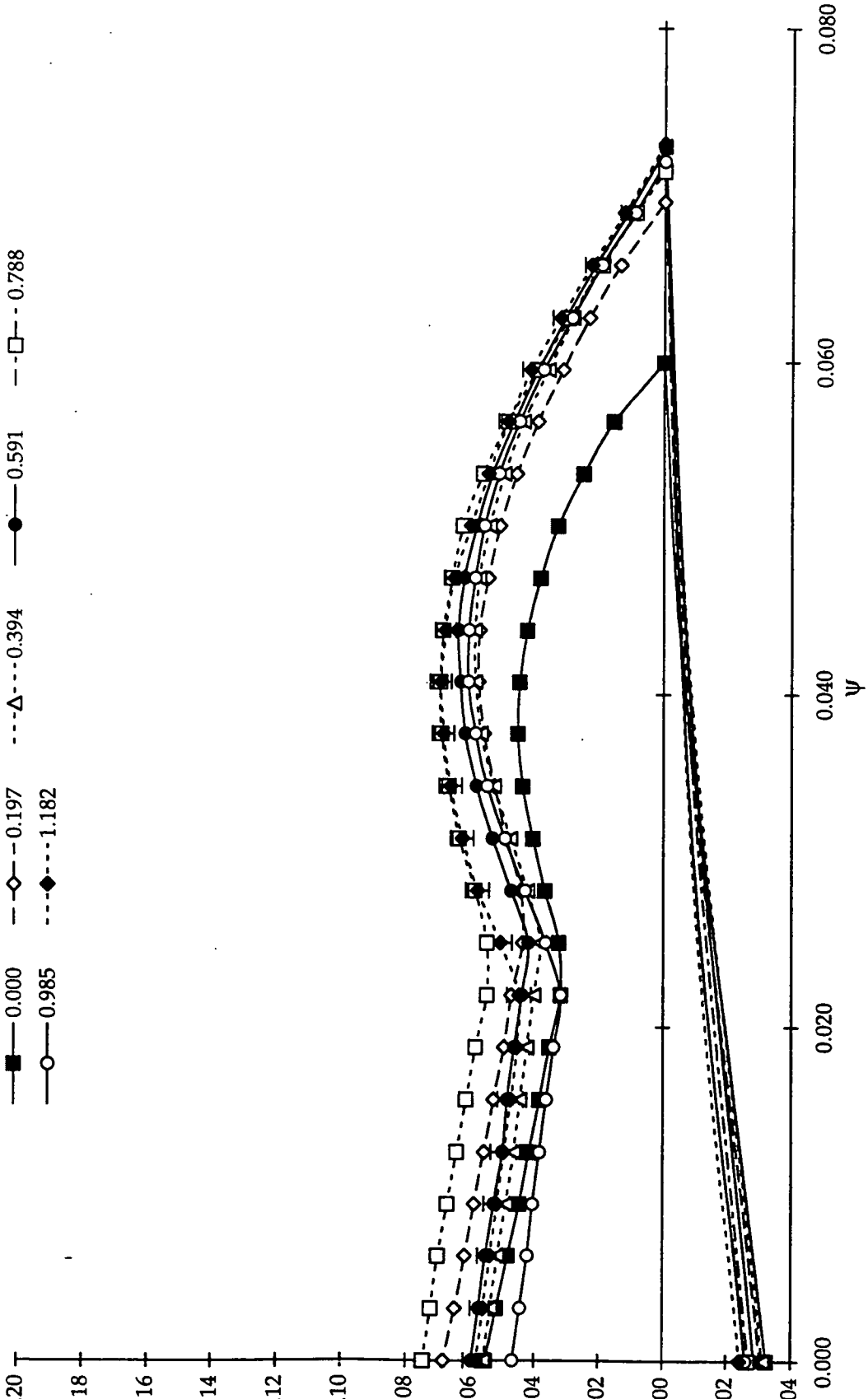

Figure 6.7. Case #5 - 200 cs Silicone Oil, Ca=1.17, U=12.1 cm/sec. (τ = 0.000 to 1.182)

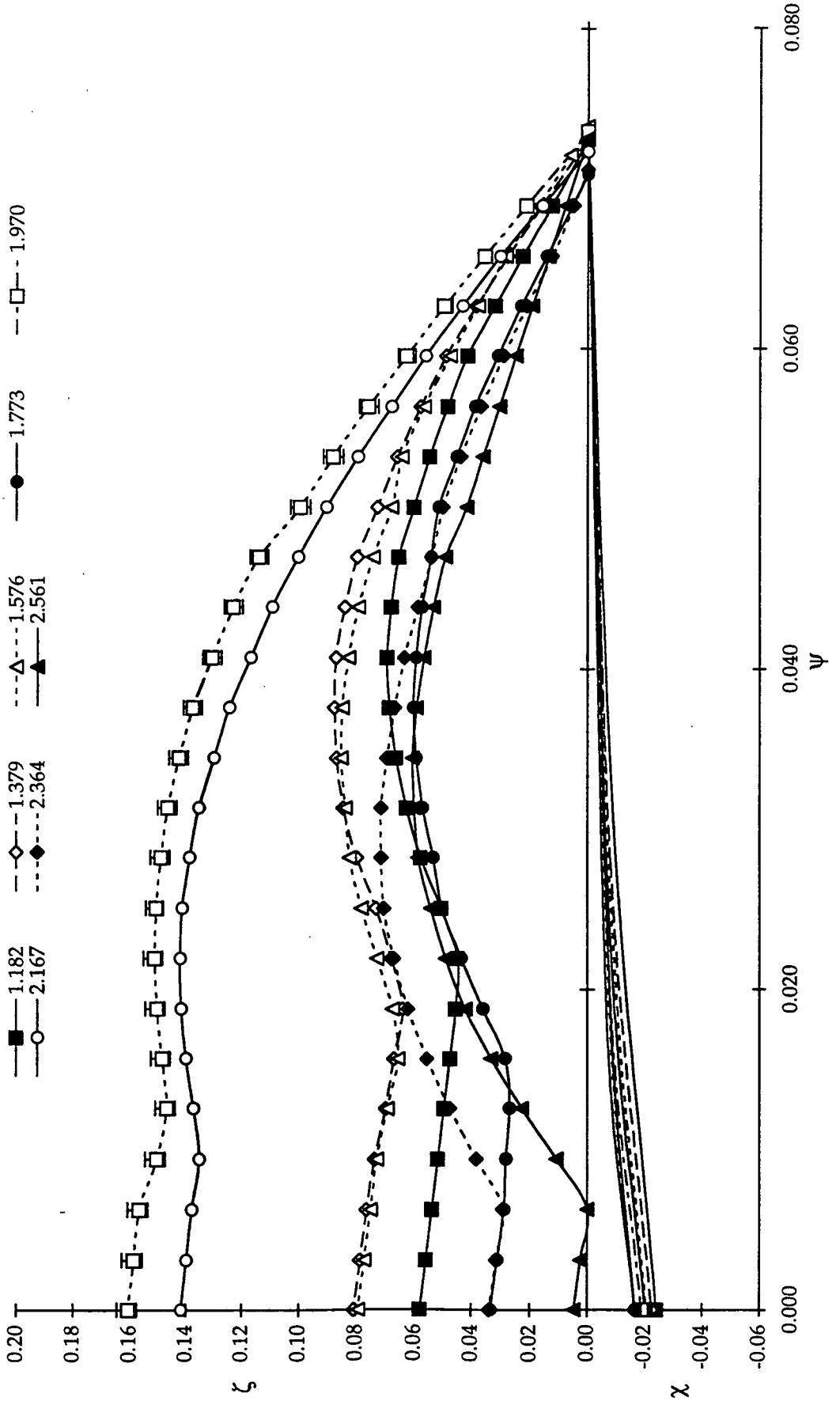

Figure 6.7. (Continued) (τ = 1.182 to 2.561)

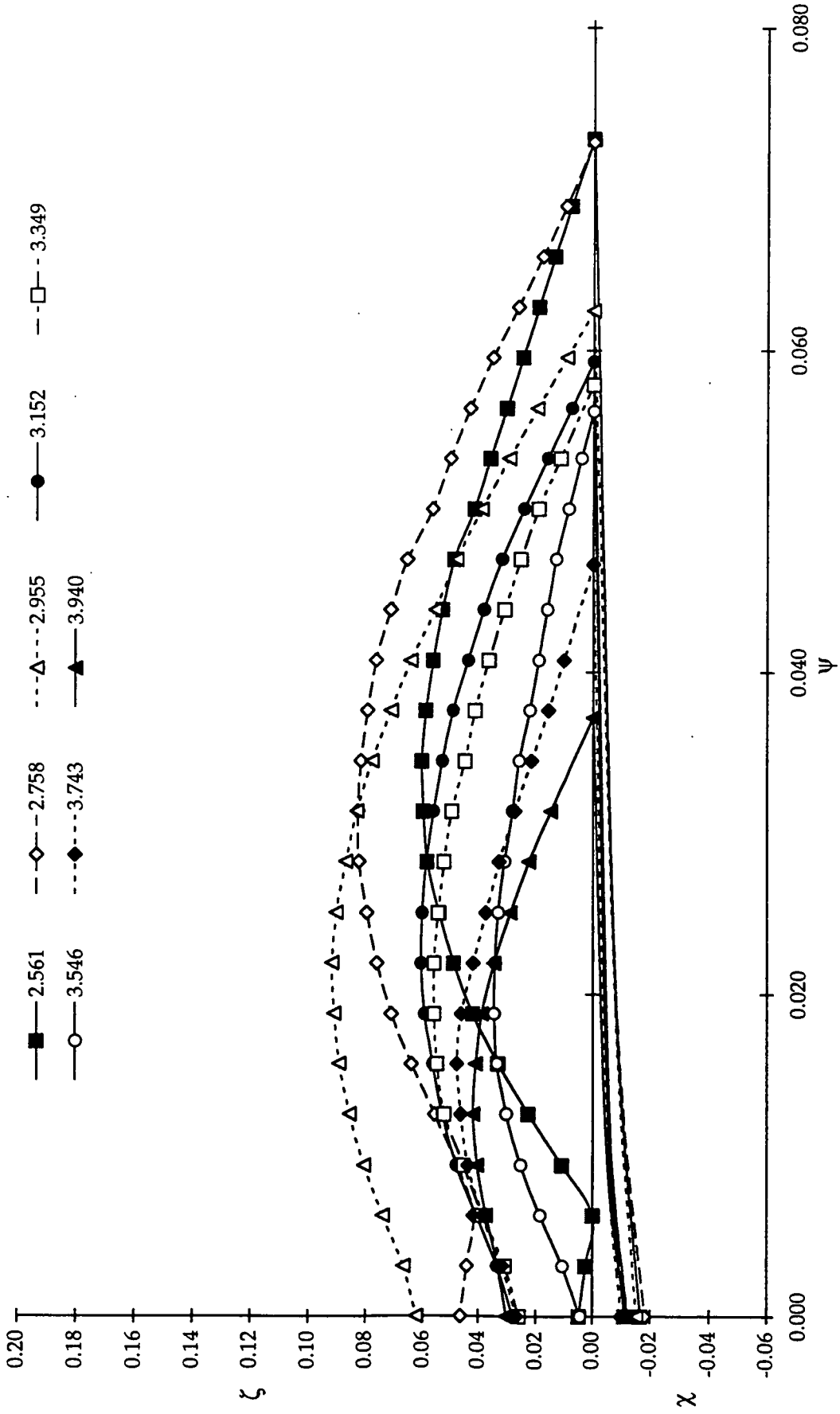

Figure 6.7. (Continued) (τ = 2.561 to 3.940)

6.4.6 Case #6 - Fluid D 500 cs Silicone Oil Triangular Air Film Profiles[6]

Case #6 (Fig. 6.8) with silicone oil is unique in that the thickness is much less than that for Case #8 at the same viscosity ratio, $\lambda_\mu \times 10^4 = 0.43$, but has a higher liquid Capillary number, 2.82 (Case #6) versus 0.60 (Case #8). The air film extends into the cavity at 3.2 cm/sec (25% U) up to $\psi = 0.059$, and then nucleates. The resulting bubble volume gives $\zeta_b = 0.0079$ which is very close to ζ_{max} (see Figure 6.8). This provides independent verification of the thickness. There is a rise in $\varnothing_1$ from 25±5° to 35±5° prior to nucleation. In a plot of ζ vs. $\tau(\psi=0.009)$, the result is difficult to interpret because of the extensional growth of the air film and the fact that the thickness is very close to $\zeta = 0$ near the tail.

Additionally, the maximum number of ruling lines measured was 6, which also means that the length is short. The deflectometry method is difficult to employ with a short air film. Under these conditions, either a finer ruling or another method should be used.

[6] Experimental file code G14DCA1 from 16-mm film times 215:00.484 to 215:00.494.

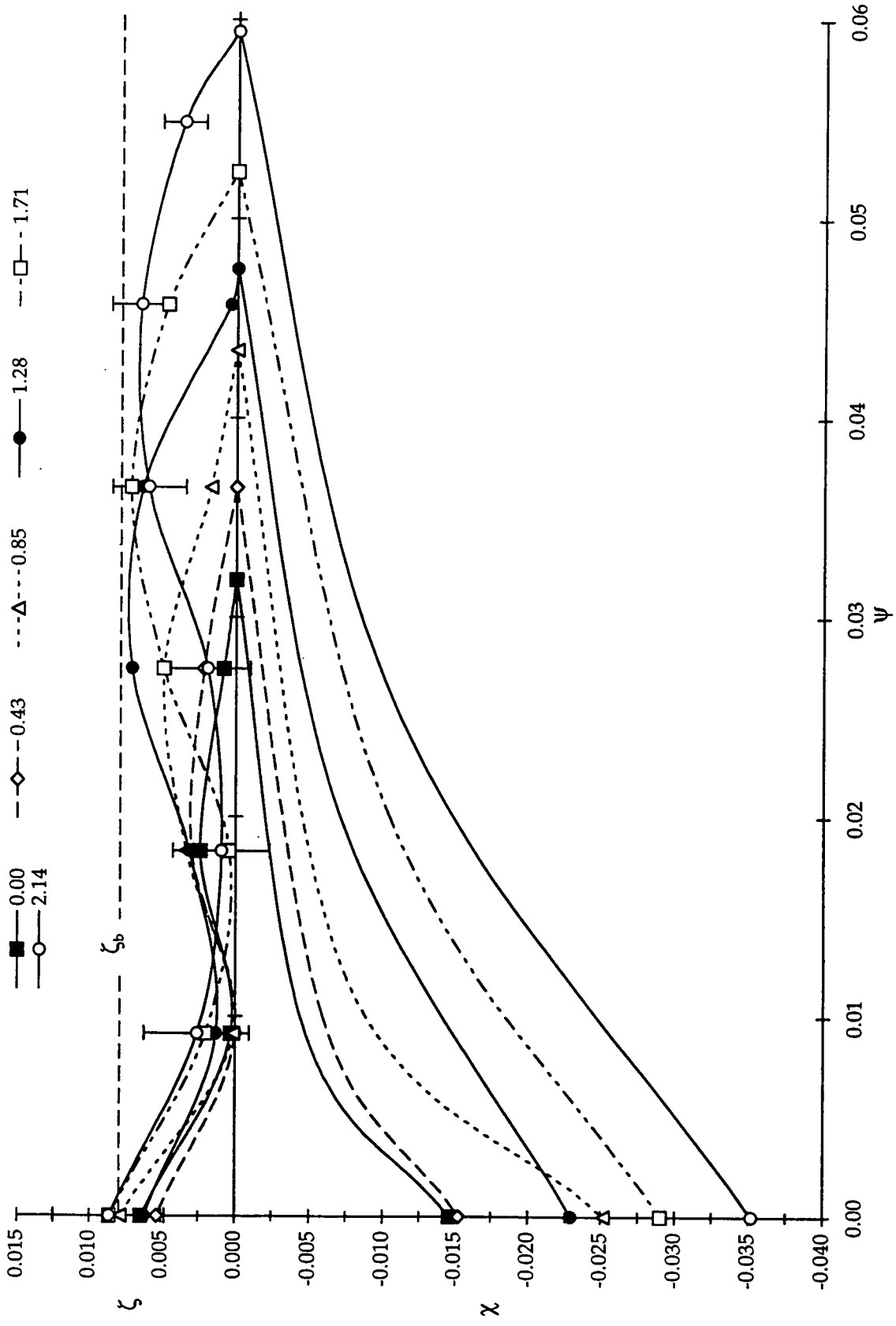

Figure 6.8. Case #6 - 500 cs Silicone Oil, Ca=2.82, U=12.9 cm/sec. (τ = 0.000 to 1.182)

6.4.7 Case#7 - Fluid F - 400 cs Glycerin-Water Triangular Air Film Profiles[7]

The air film with Fluid F in Fig. 6.9a,b is much narrower and shorter than the silicone oil results from Case #6. The profile remains fairly constant until at $\tau \geq 1.18$ the air film nucleates and a bubble is formed. Based on the entrained area, ζ_b = 0.0044. Comparing ζ_b to $\zeta(\tau)$, this value is reasonable and presents an independent confirmation of the thickness. Using $\tau = 0.000$ for the same air film after entrainment, it reestablishes the same length very quickly from $1.18 \leq \tau < 3.06$ and it begins retracting. Figure 6.9b presents the behavior for $\tau \geq 3.06$. Note also the extreme differences in ζ, which is almost 2 orders of magnitude less that the other cases. Compared at equal $\lambda_\mu = 0.43 \times 10^{-4}$, ψ_{max} is only 25% of the ψ_{max} for Fluid D in Case #6. When compared using dimensional scales, they extend the same distance, L_1, into the cavity.

[7] Experimental file code U26FCA1 from 16-mm film times 1:37.580 to 1:37.589.

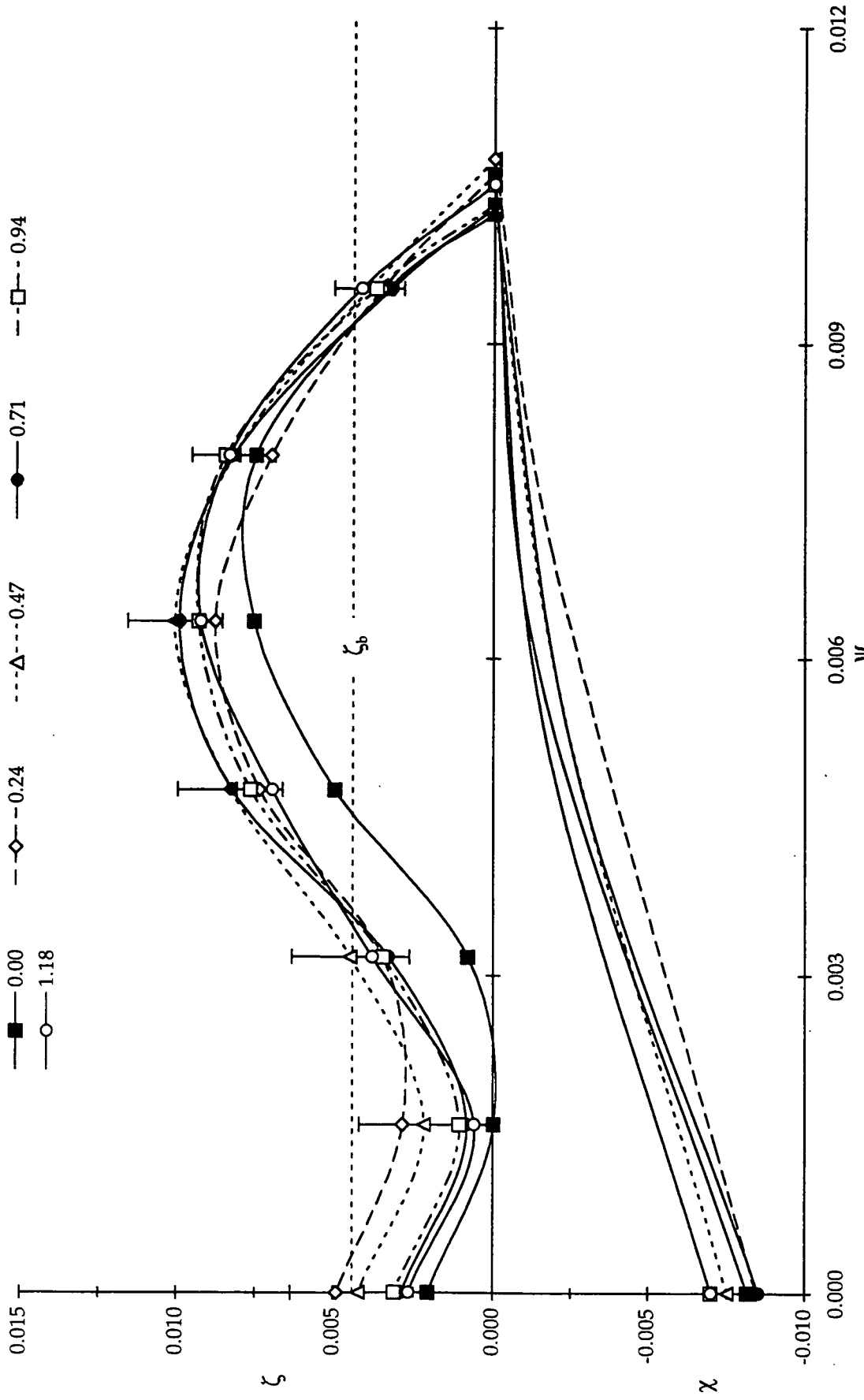

Figure 6.9a. Case #7 - 400 cs Glycerin, Ca=0.60, U=5.17 cm/sec. (τ = 0.000 to 1.18)

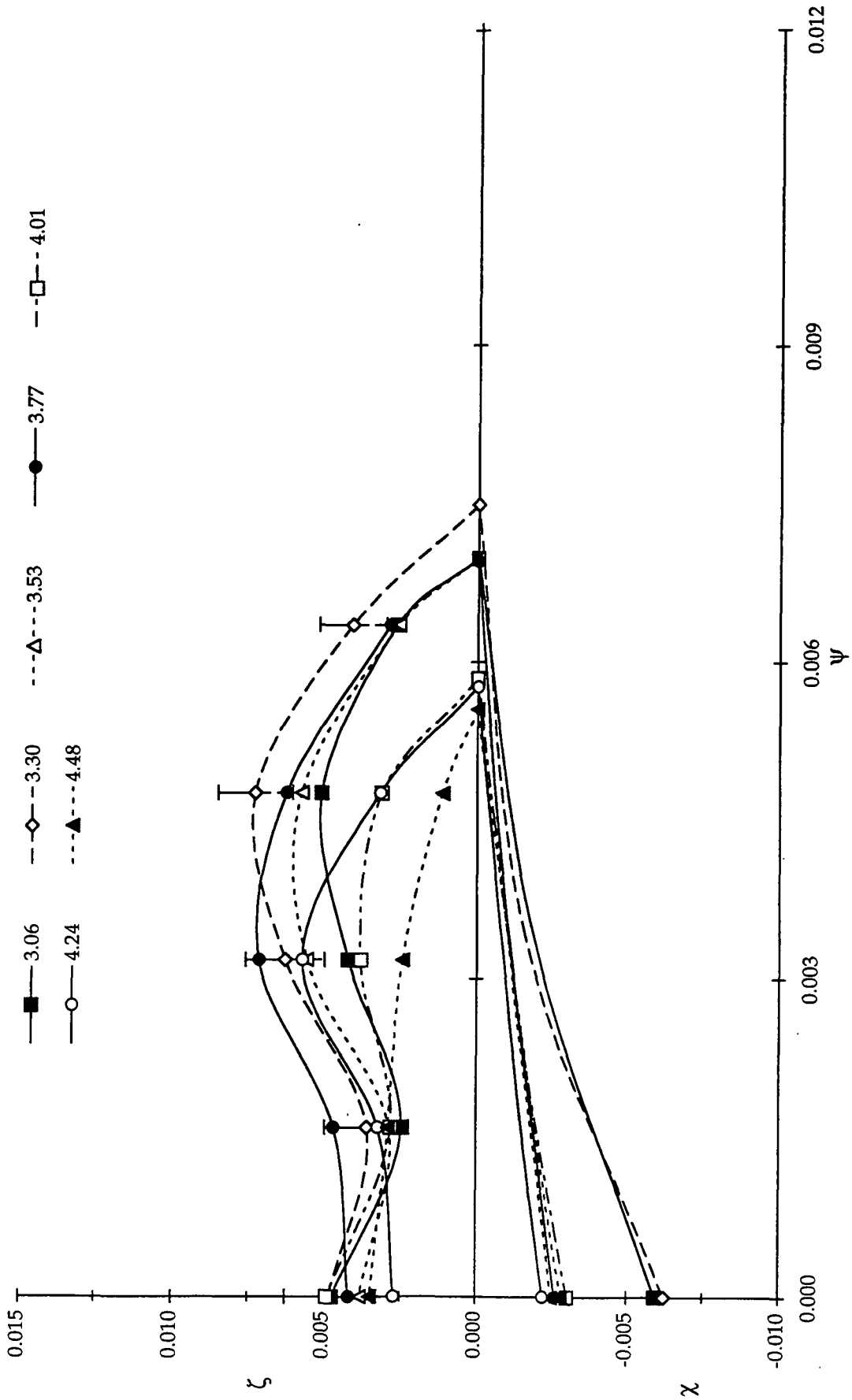

Figure 6.9b. Case #7 - 400 cs$_l$ Glycerin, Ca=0.60, U=5.17 cm/sec. (τ = 3.06 to 4.48)

6.4.8 Case #8 - Fluid H - 134 cs Glycerin-Water Triangular Air Film Profiles[8]

For this series, Fig. 6.10, represents an air film retracts at one-seventh of U, 2.3 cm/sec, with the retraction preceded by an increase in ζ at $\tau = 0.202$. This event seems to precede retraction as in Case #5. Graphs of $\zeta(\psi=0.001)$ vs. τ exhibit sinuous behavior for $\tau \leq 1.075$. There is no trend for $\varnothing_1$ that precedes retraction although a rise to 90±5° is seen as ψ approaches zero.

[8] Experimental file code L06HCA2 from 16-mm film times 21:15.594 to 21:15.613.

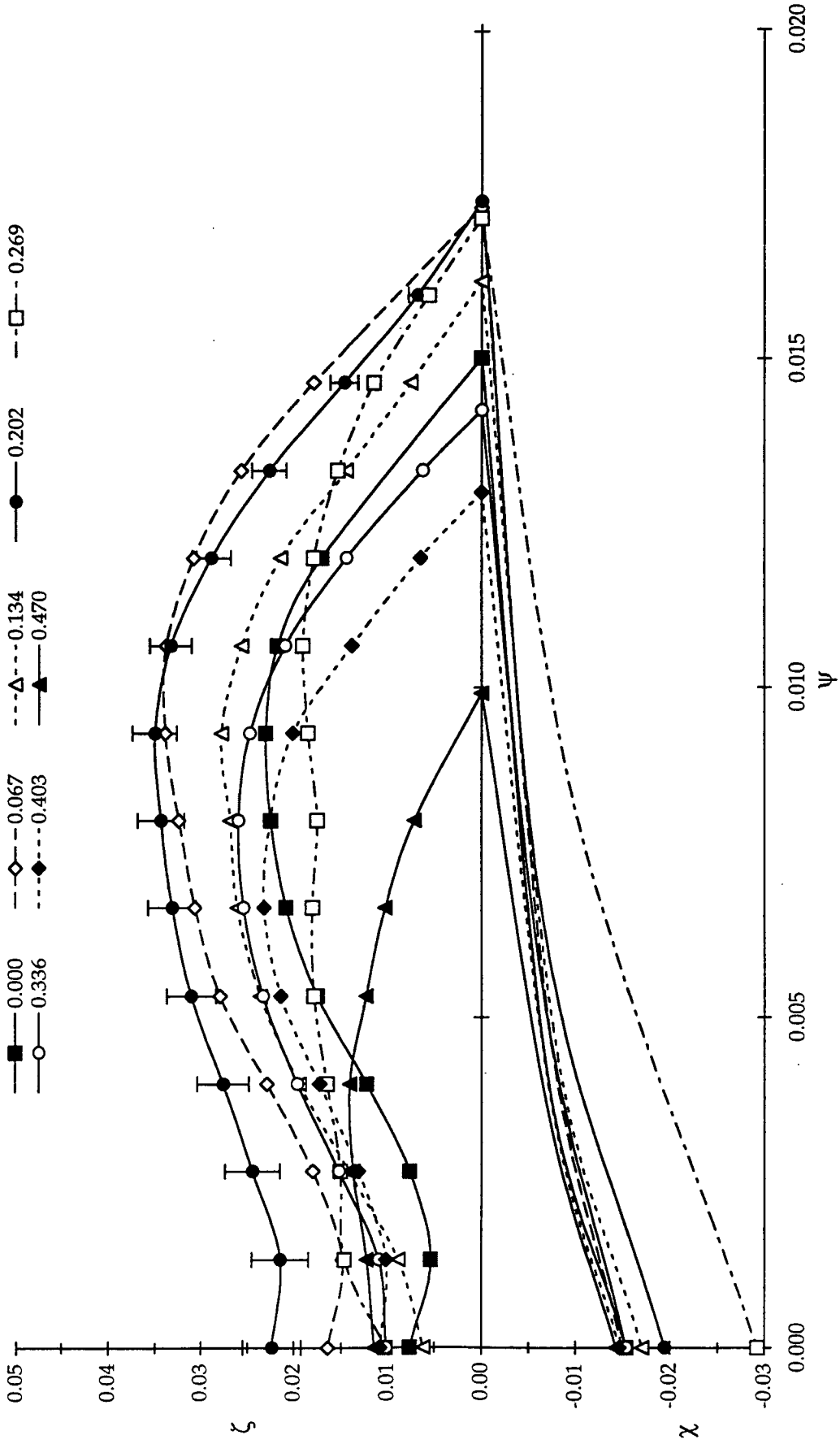

Figure 6.10. Case #8 - 134 cs Glycerine, Ca=0.53, U=15.5 cm/sec. (τ = 0.000 to 0.470)

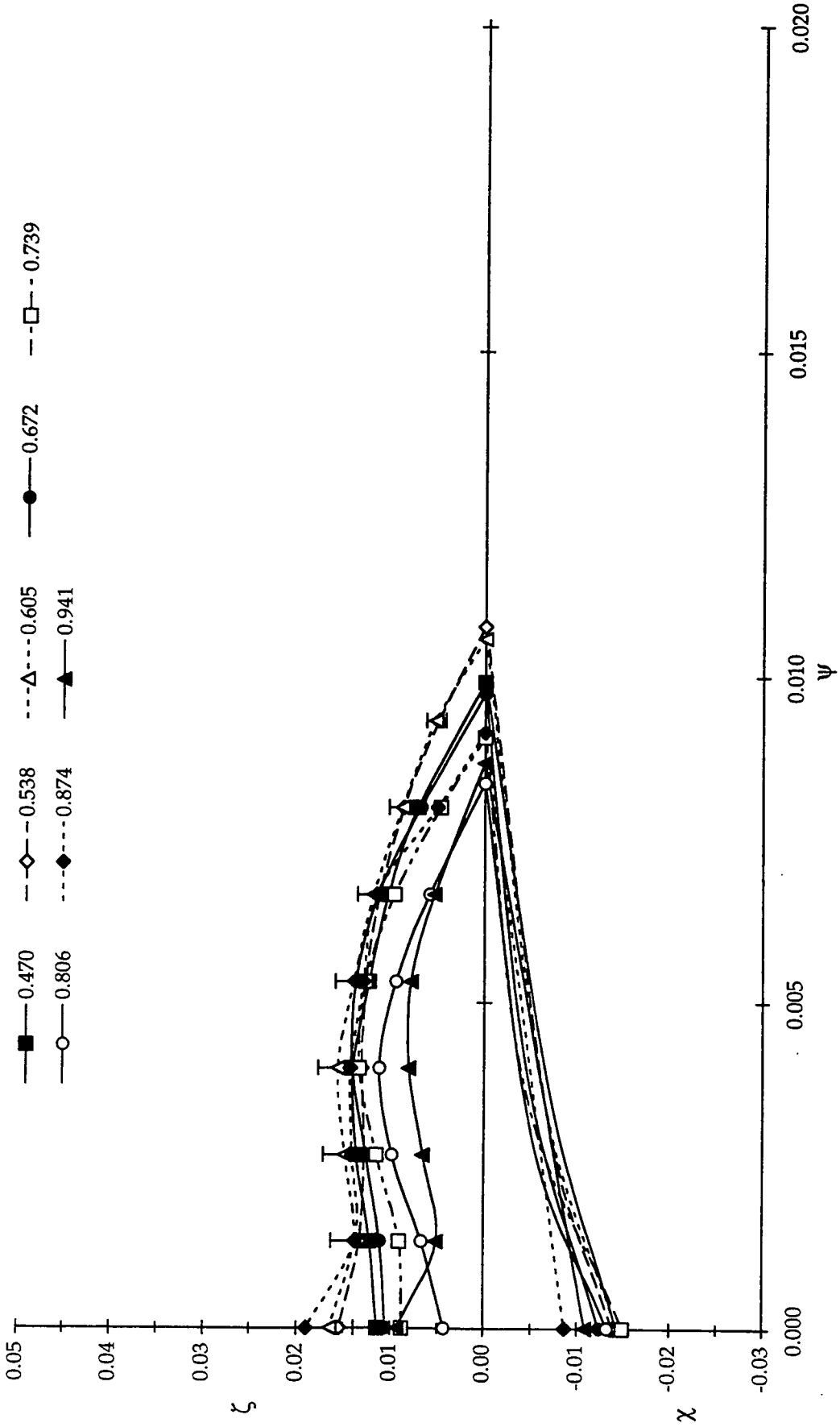

Figure 6.10 (Continued) (τ = 0.470 to 0.941)

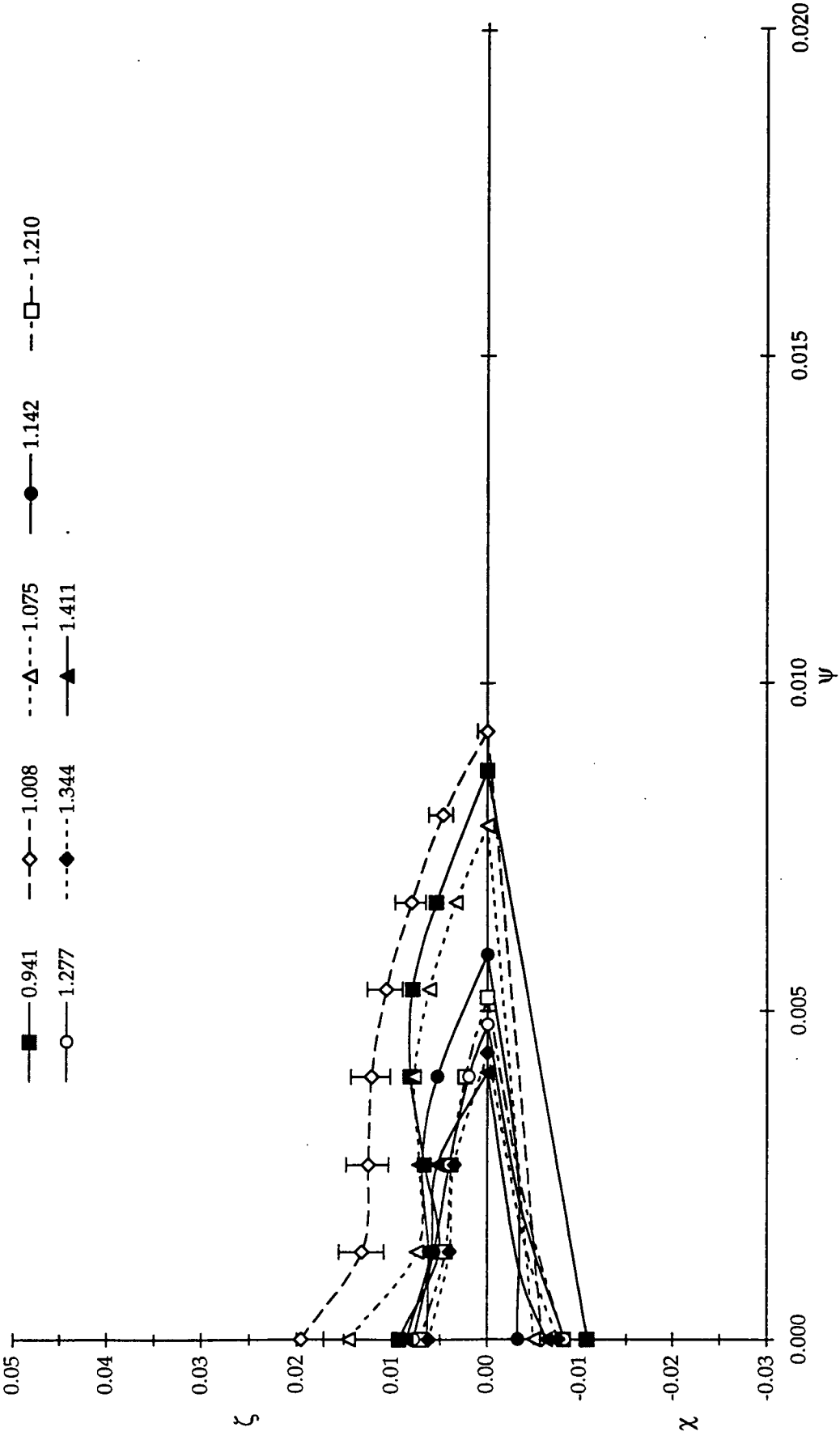

Figure 6.10 (Continued) (τ = 0.941 to 1.411)

6.4.9 Case #9 - Fluid I - 48 cs Glycerin-Water Triangular Air Film Profiles[9]

With Fluid I (Fig. 6.11) the triangular air film advances at a velocity one-third of U. The retraction occurs at one-half U for a single air film. The advance coincides with a decrease in $\varnothing_1$ to a minimum of 100±5° and, following the retraction, returns to the original value of 140±5°. The retraction is preceded by a slight rise in ζ at $\tau = 0.156$. During this process, the variation in $\zeta(\psi=0.001)$ with τ shows the extreme fluctuations in height and wavelike motion near the tail.

[9] Experimental file code LO7ICA2 from 16-mm film times 189:07.697 to 189:07.713.

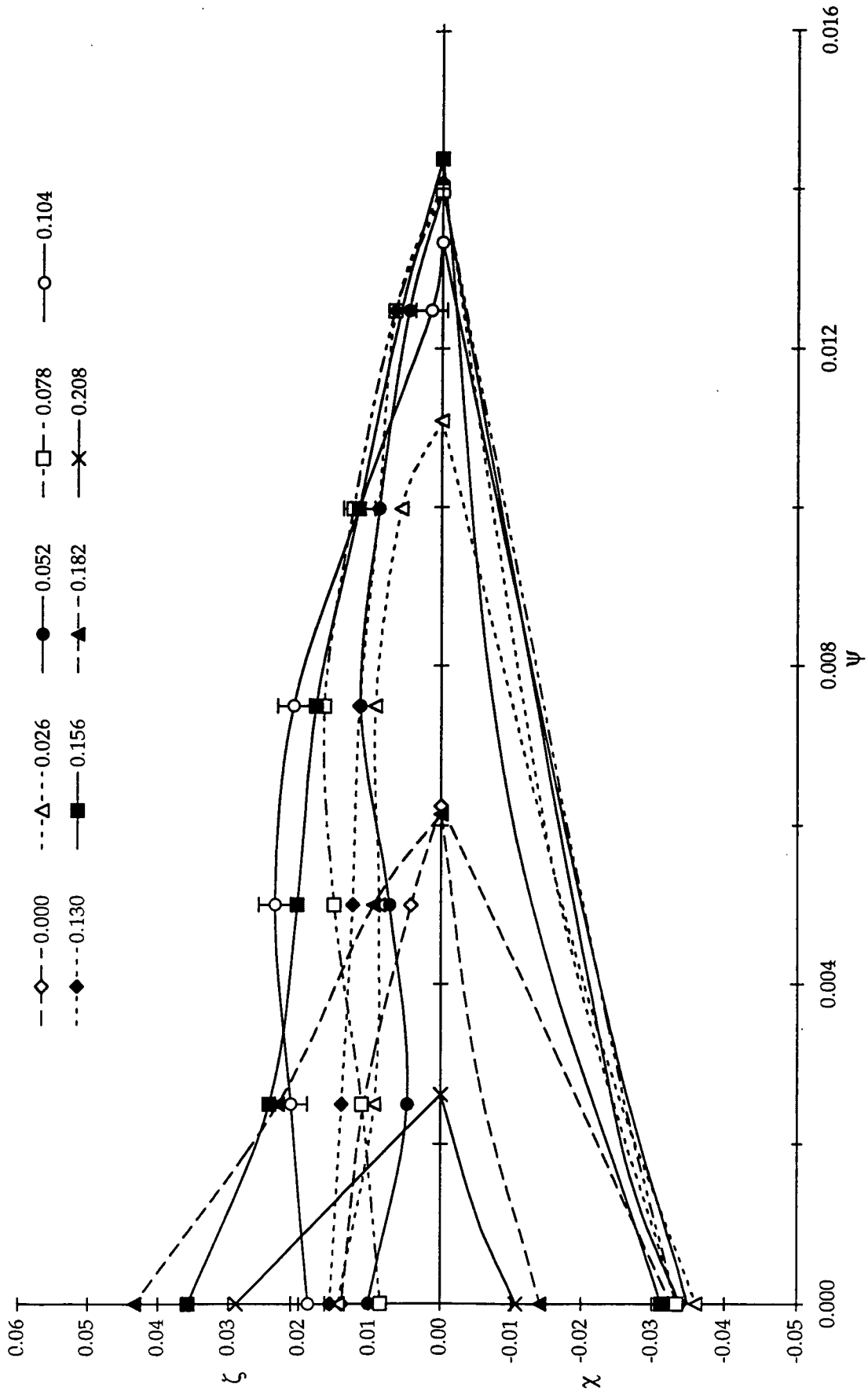

Figure 6.11. Case #9 - 48 cs Glycerine, Ca=0.48, U=36.15 cm/sec. (τ = 0.000 to 0.208)

6.4.10 Case #10 - Fluid Y - 10 cs Silicone Oil Triangular Air Film Profiles[10]

The documentation in Fig. 6.12 begins where the air film develops a vertex at $\tau = 0.000$. At which point it begins to retract at an average velocity of 4.1 cm/sec compared to the substrate velocity of 60 cm/sec. During the retraction, the initial slope remains fairly constant while the maximum height, ζ_{max}, and height near the tail is decreasing. For $\tau \geq 0.0705$, both ζ and ψ remain constant as $\varnothing_1$ increases and the air film forms an air sheet that nucleates. For $0.0587 \leq \tau < 0.1410$, the profile remains pinned at $\psi = 0.0125$ and keeps the same profile shape which may be necessary for the widening of the base to occur. At $\tau = 0.1410$, $\varnothing_1$ increases to a maximum of 140±5°.

[10] Experimental file code G12YCA1 from 16-mm film times 215:17.62 to 215:17.86.

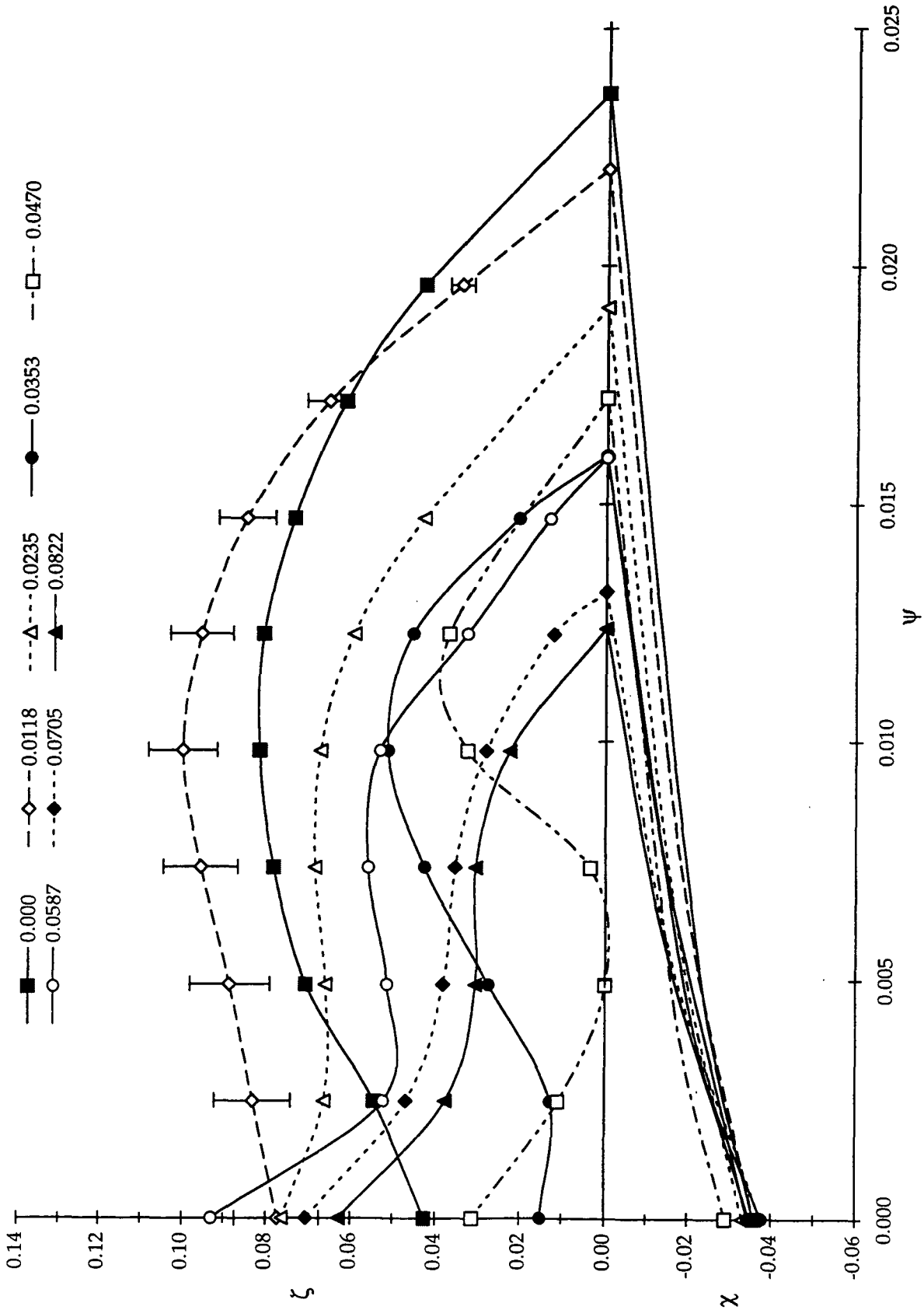

Figure 6.12. Case #10 - 10 cs Silicone oil, Ca=0.36, U=60 cm/sec. (τ = 0.000 to 0.0822)

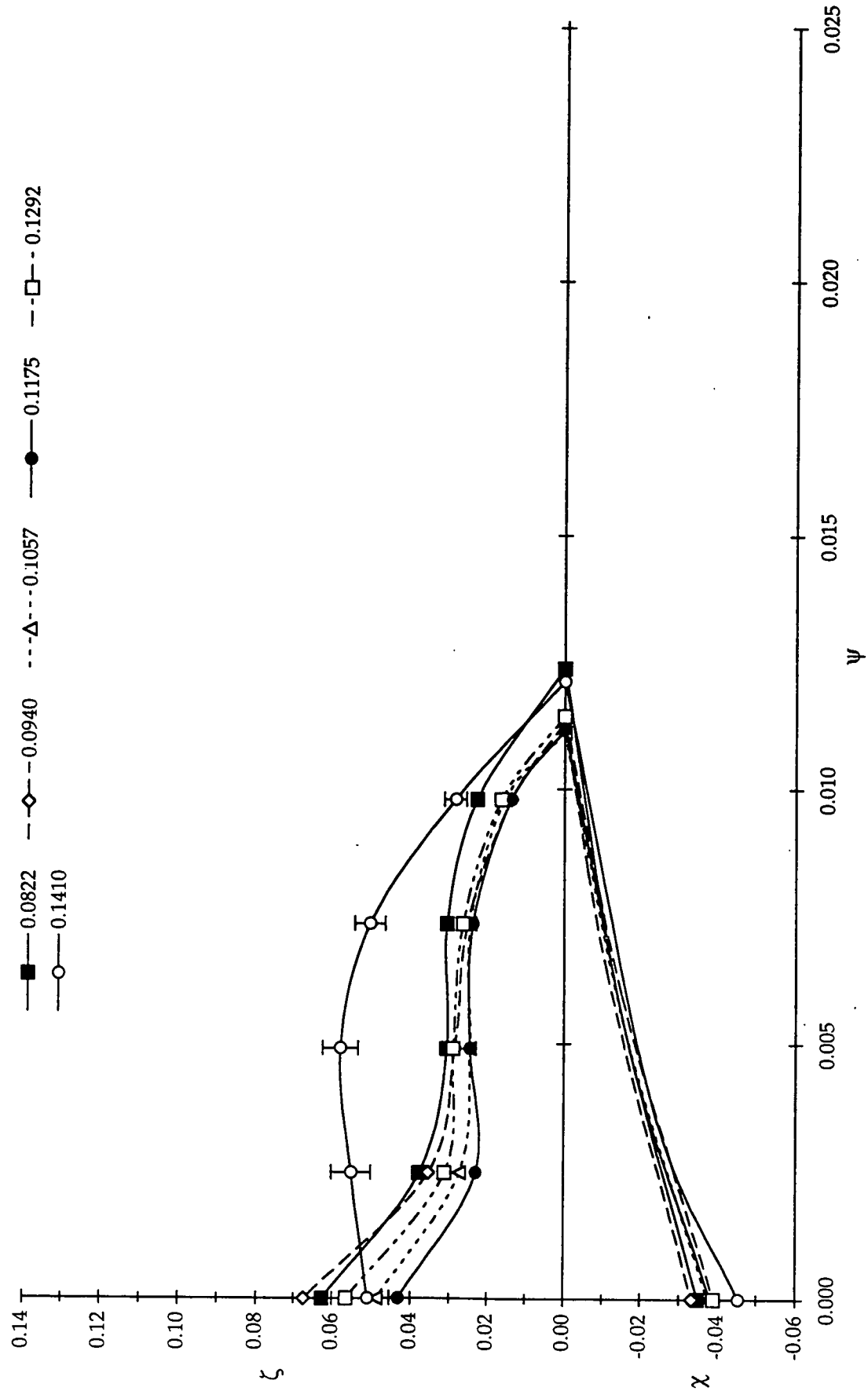

Figure 6.12. (Continued) (0.0822 to 0.1410)

6.4.11 Case #11 - Fluid Z - 20 cs Silicone Oil Triangular Air Film Profiles[11]

This case is at Ca = 0.34, (Fig. 6.13), which is marginally below Ca_{ae}, and leads to a thin air sheet which is followed by the formation of a precursor structure. The precursor structure and air sheet retracted inward to form a single triangular air film vertex at $\tau = 0.0000$. The centerline profile was analyzed as the air film started to retract at 75% of U (27.1 cm/sec vs. U = 34.8 cm/sec). For $\tau = 0.0203$ to 0.0610, the interface exhibits a change in inflection along the profile. The tail region also shows this large change in the plot of $\zeta(\psi=0.002)$ vs. τ. The wavelike behavior seen near the tail region is especially evident in the images and figures contained in Appendix XIV for Case #11. This is believed to verify the long wave interfacial instability hypothesized by Aidun et al. (1993) and verified analytically by Severtson and Aidun (1995).

The axisymetric profile at $\tau = 0.0407$ was verified with three independent analyses of the data, each showing the inflection change and contained in Tables VII.3 to VII.5 in the Appendix. Appendix VII contains a full set of images and data files for archival and comparison purposes.

[11] Experimental file code U22ZCA1 from 16-mm film times 4:34.811 to 4:34.831

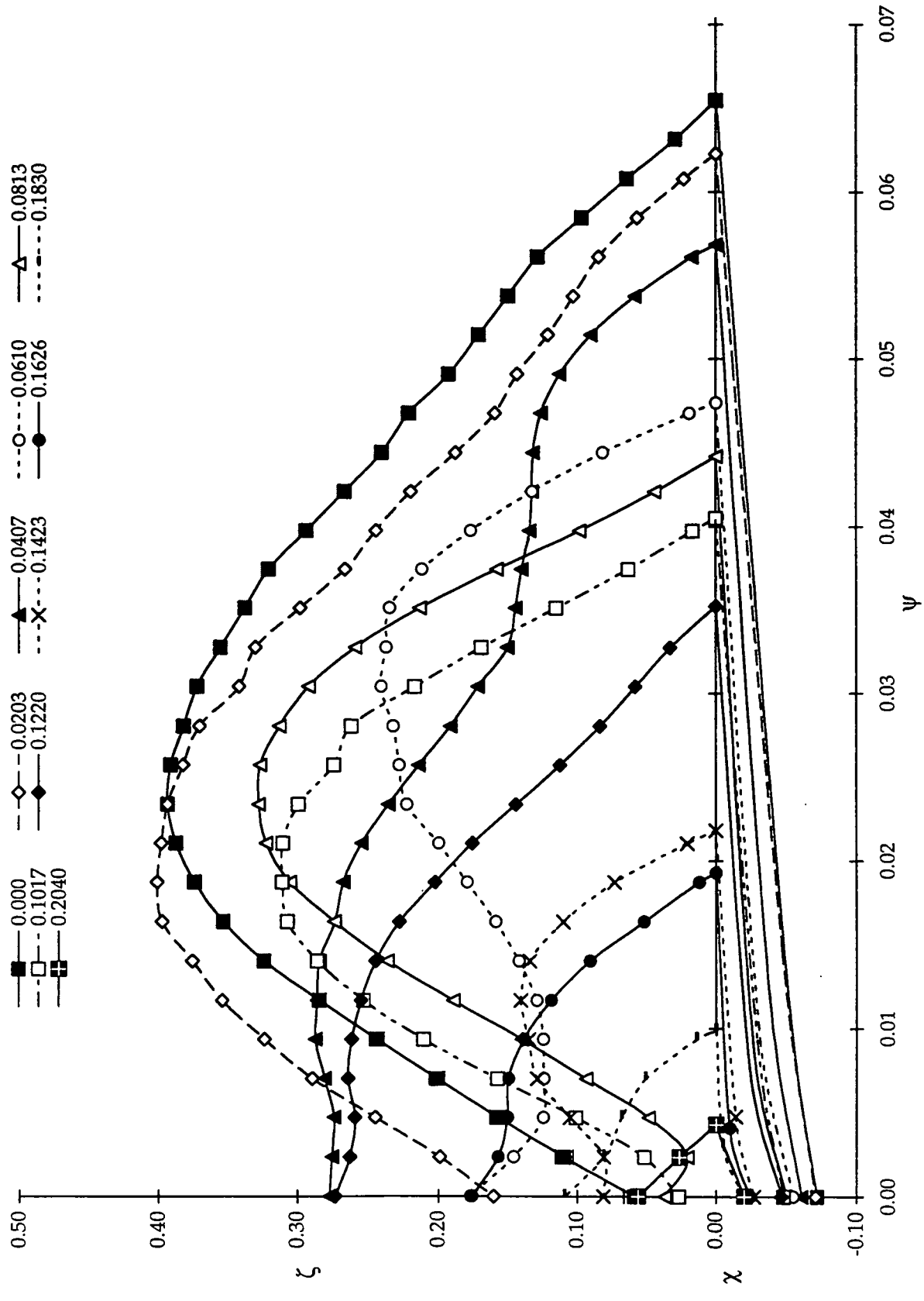

Figure 6.13. Case #11 - 20 cs Silicone oil, Ca=0.34, U=34.5 cm/sec. (τ = 0.000 to 0.2040)

6.4.12 Case #12 - Fluid Z - 20 cs Silicone Oil Triangular Air Film Profiles[12]

Case #12 (Fig. 6.14) represents the same conditions as Case #11 with Fluid Z for a retracting air pocket with velocity 18% of U. The triangular air film had originally formed from an air "sheet," At $\tau = 0.000$, a vertex is established and the centerline can be examined. This air film is much shallower, i.e. the length is much less than the previous case with Fluid Z. The value for ψ_{max} is 0.022 compared to 0.065 in Case #11. The retraction is preceded by an increase in $\emptyset_1$. Only slight variations in $\zeta(\psi=0.002)$ as a function of τ are seen as compared to Case #11 with the same fluid.

[12] Experimental file code U22ZCA2 from 16-mm film times 4:32.142 to 4:32.167

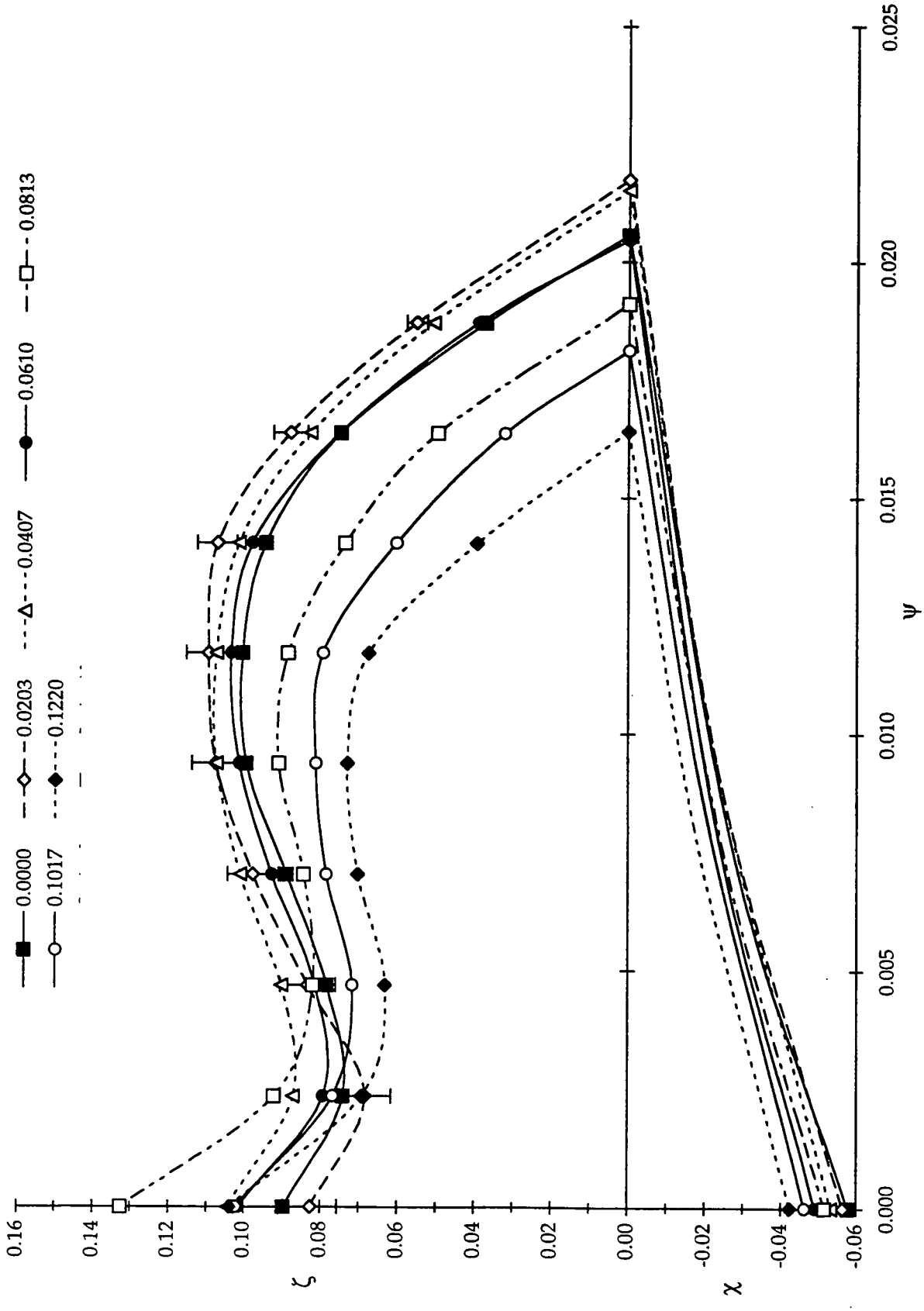

Figure 6.14. Case #12 - 20 cs Silicone oil, Ca=0.34, U=34.5 cm/sec. (τ = 0.000 to 0.1220)

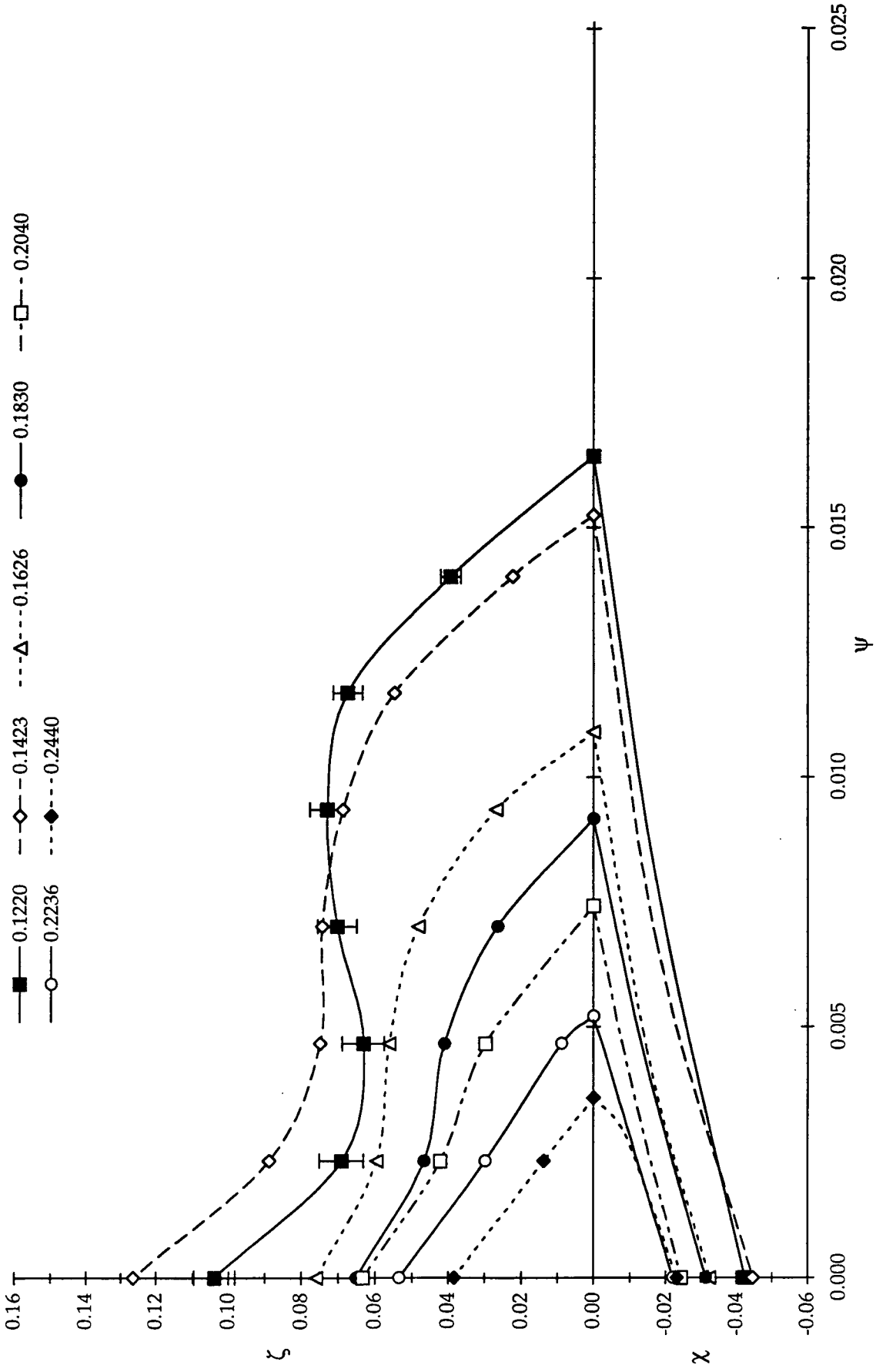

Figure 6.14. (Continued) (τ = 0.1220 to 0.2440)

6.5 Summary and Discussion of Deflectometry Observations

The deflectometry experiments have revealed that nucleation and the subsequent bubble formation is preceded by a defined increase in $\emptyset_1$ and ζ for Cases Nos. 1, 3, 6, and 7. Although Severtson and Aidun (1995) assumed (for simplicity in their stability analysis) a 2-D velocity field and an interface separating the two phases, visualization experiments (see Fig. 4 in Severtson and Aidun, 1995) have shown that the long waves also can propagate near the air film centerline $\psi(\chi=0)$. In our work the rise in ζ may be the crest of the wave traveling in the direction opposite to the substrate velocity U, with the trough leading to a nucleation site near the edges. Exact verification of the entire three-dimensional shape of the air film is difficult using the deflectometry technique over the entire air film surface. The difficulty comes from the image processing technique used for this work and the optical merging of the ronchi ruling lines due to large slopes for dh/dy or dh/dx. Temporally mapping the entire interface, not just the centerline, would provide full verification of the interfacial instability near the edges. A simplified geometric reconstruction of the interface is later presented in Section 6.6.

Retraction in Cases Nos. 5, 8, 9, 10 and 11 is preceded by a marked rise in ζ in the tail region of the air film. It is hypothesized that this provides a release of the excess pressure in the air film and results in the forces being out of balance. The surface tension forces, i.e., capillary pressure, counteract by minimizing the air film

interfacial surface area. The qualitative observations of the interface profiles for ζ and $\emptyset_1$ are summarized in Table 6.3.

Table 6.3. Summary of qualitative observations of axisymetric air film*.

RETRACTING			
Case# and Fluid	$\emptyset_1$	ζ	**$Ca > Ca_{ae}$?**
#2 Silicone Oil - 100 cs	↓ then ↑	↔ then retract	Marginal
#5 Silicone Oil 200 cs	↓ then ↑	↑ then retract	Marginal
#8 Glycerin-water 134 cs	↔	↑ then retract	Marginal
#9 Glycerin-water 48 cs	↓ then ↑	↑ then retract	Marginal
#10 Silicone Oil 10 cs	↔ then slight ↑	↑ then retract	No
#11 Silicone Oil 20 cs	↔ then slight ↑	↑ then retract	Marginal
#12 Silicone Oil 20 cs	↔ then slight ↑	↔ then retract	Marginal
NUCLEATION			
#1 Silicone Oil - 100 cs	↑	Slight ↑ then nucleation	Marginal
#3 Silicone Oil 200 cs	↑	Slight ↑ then nucleation	Marginal
#4 Silicone Oil 200 cs	↑	↔ then nucleation	Marginal
#6 Silicone Oil 500 cs	↑	↑ then nucleation	Yes
#7 Glycerine-water 400 cs	↑	↑ then nucleation	Yes

*Relative trend descriptors
↓ Decrease in the measured parameter.
↑ Increase in the measured parameter.
↔ Flat or no change in the measured parameter.

In order to partially quantify if waves are measurable near the tail edges of the triangular air film, a five-constant equation, Eq. [6.1], with both a trigonometric and linear term was used to estimate the values of $C_1=\tau_{per}$ and $B_1=\zeta_{amp}$ found in Table 6.2. Plots of $\zeta(\psi=0.01)$ vs. τ were used as the input data for each case with an example given in Figure VIII.13 contained in Appendix VIII.

$$\zeta = A_1 + B_1 \sin\left(\frac{2\pi\tau}{C_1} + D_1\right) + E_1\tau \qquad [6.4]$$

The limited data was fit to Eq. [6.1] using Gaussian elimination with a standard curve fitting package for a maximum of 100 iterations or a residual of less than 10^{-6} over 40 nodes. The major difficulty in estimating these parameters is the limited τ range that is used with approximately 10-15 data points to fit a five-constant equation. This type of an approach is clearly tenuous because any type of an equation could be fit to the data in a least-squares sense with enough parameters (Hornbeck, 1975). When τ_{per} for all of the cases in Table 6.2 are converted to dimensional time, $t = t_{pp}\tau_{per}$, the values for Fluid A, B, H and I are all approximately 6 ms, while $t = t_{pp}\tau_{per}$ for fluids Y and Z are 13.2 and 10.6 ms. This method also does not seem to be suitable for predicting the effect of surface tension on ζ_{amp} because we only have single cases to compare. Thus, our original hypothesis regarding the effect of surface tension on the interfacial waves stated in Chapter I cannot be rigorously tested.

The equivalent bubble thickness, ζ_b, provided an independent verification of the calculated thickness based on the deflectometry results.

The length and width of the air film for the DC200 fluids, when reduced to ψ and χ, vary in the range $0.023 \le \psi_{max} \le 0.11$ and $0.03 \le \chi_{max} \le 0.07$. The glycerin-water mixtures varied from $0.011 \le \psi_{max} \le 0.17$ and $0.01 \le \chi_{max} \le 0.035$. In the dimensional domain, variations in length, L_1, and width, W_1, are up to one order of magnitude different for the same range of liquid Capillary number, Ca, tested in this work. Taylor (1963), while studying cavitation in bearings, found that the length of the air

"fingers" extending from the meniscus was inversely proportional to the Capillary number, Ca. This result also corresponds to our results with silicone oils, i.e., lower Ca results in a wider and longer air film.

In Chapter V, considerable emphasis was placed on the effect of the liquid normal stresses delaying air entrainment for low surface tension silicone oils versus the glycerol-water mixtures. A form of the opposite effect is seen at low viscosity and low surface tension, that is, we form "thicker" and larger air films with Fluids Y and Z as the liquid normal stresses decrease. The dimensional thickness for Fluid I is less than that of Fluids Y and Z although the capillary number and viscosity are greater. Increased pressure on the interior of the air film, due to higher entrainment speed, as well as the lower surface tension (Fluids Y and Z) all combine to form a larger air film. Correspondingly, once air entrainment initiates, the bubble size will be greater and possibly the frequency of entrainment. Studying the bubble size and frequency of entrainment is much easier than studying the triangular air film. This could be another area of future research.

The thickness of the air film in this work is backed by Kennedy and Burley's (1977, 50) observation that the bubble size decreases(increases) as the viscosity increases(decreases). For our study the 20 cs silicone oil (Case #11) had a maximum dimensional centerline thickness, h(0,y), of 600 μm while the 500 cs silicone oil (Case #6) triangular air film thickness was only 10 μm. Correspondingly, for the glycerol-water mixtures the 48 cs fluid (Case #9) has a maximum dimensional centerline thickness of 50 μm while the 400 cs mixture (Case #7) has a 19 μm maximum thickness. The reduced dimensional thickness as the viscosity increases

for these fluids (silicone oil vs. glycerin) leads to a reduced speed window between U_v and U_{ae} as described in Chapter V. Out of the 12 cases documented, six (Nos. 1, 2, 9, 10, 11, and 12) were above the cutoff $\lambda_\mu > 2 \times 10^{-4}$ which we found in Chapter V.

The data contained in Figs. 6.3 through 6.14 represent the first data obtained regarding how the triangular air film behaves at different viscosities and surface tensions. Burley (1992a,b) has published schematic diagrams depicting his view of how a bubble is formed from a triangular air film. It is not stated in these articles whether this representation is based on actual experiments or speculation. We believe that our more comprehensive results support the interfacial long wave instability mode of air entrainment leading to a nucleation site and bubble formation as presented in Figure 2.6 of Section 2.4.

Some of the other more complicated modes of air entrainment when $U>>U_{ae}$ have not been discussed because these represent a regime where significant detrimental bubbles are produced. Thus, the macroscopic air entrainment phenomena was documented when $U \approx U_{ae}$ for 12 experimental cases with eight different fluids. The retraction and nucleation mechanisms were preceded by a rise in ζ and $\varnothing_1$. The next section will discuss the 3-D reconstruction of the air film shape using a simple geometric approach.

6.6 Using Multiple Rulings to Reconstruct a 3 D Interface Profile.

The previous section presented the results using a single ronchi ruling in a single direction parallel to the x-axis. By using a second ruling, we can get an independent estimate of the slope near the tail and the height at that location to calculate the correction angle between the substrate and optical axis, G. An example of an image grabbed from video for Fluid B with two rulings is represented by Fig. 6.15 and the ruling deflection in the x-direction near the triangular air film base gives the correction angle G = 0.65°.

The image resolution in Fig. 6.15 is not as clear because of the low number of video lines compared to 16-mm film which has much higher resolution. In order to reconstruct the entire surface of the air film, it was approximated as a segment of a circle of radius, R_{eq}, which was obtained from geometrical consideration of the centerline height, h(y), and the half width, $W_1/2$. With R_{eq} in hand, 10 points at each ruling line shown in the XYZ contour plot of Figure 6.16 were taken to reconstruct the surface. The methodology for the technique is outlined in Appendix XIV.

Figure 6.16 displays how the triangular air film rapidly rises to the peak at 100 μm height and quickly drops down to around 10 μm near the tail. Because the shape is reconstructed geometrically the validity is better near the tip than near the edges of the tail. From these analyses, we can conclude that nucleation is more likely to occur near the tail due to the reduced thickness in the "air film" region .

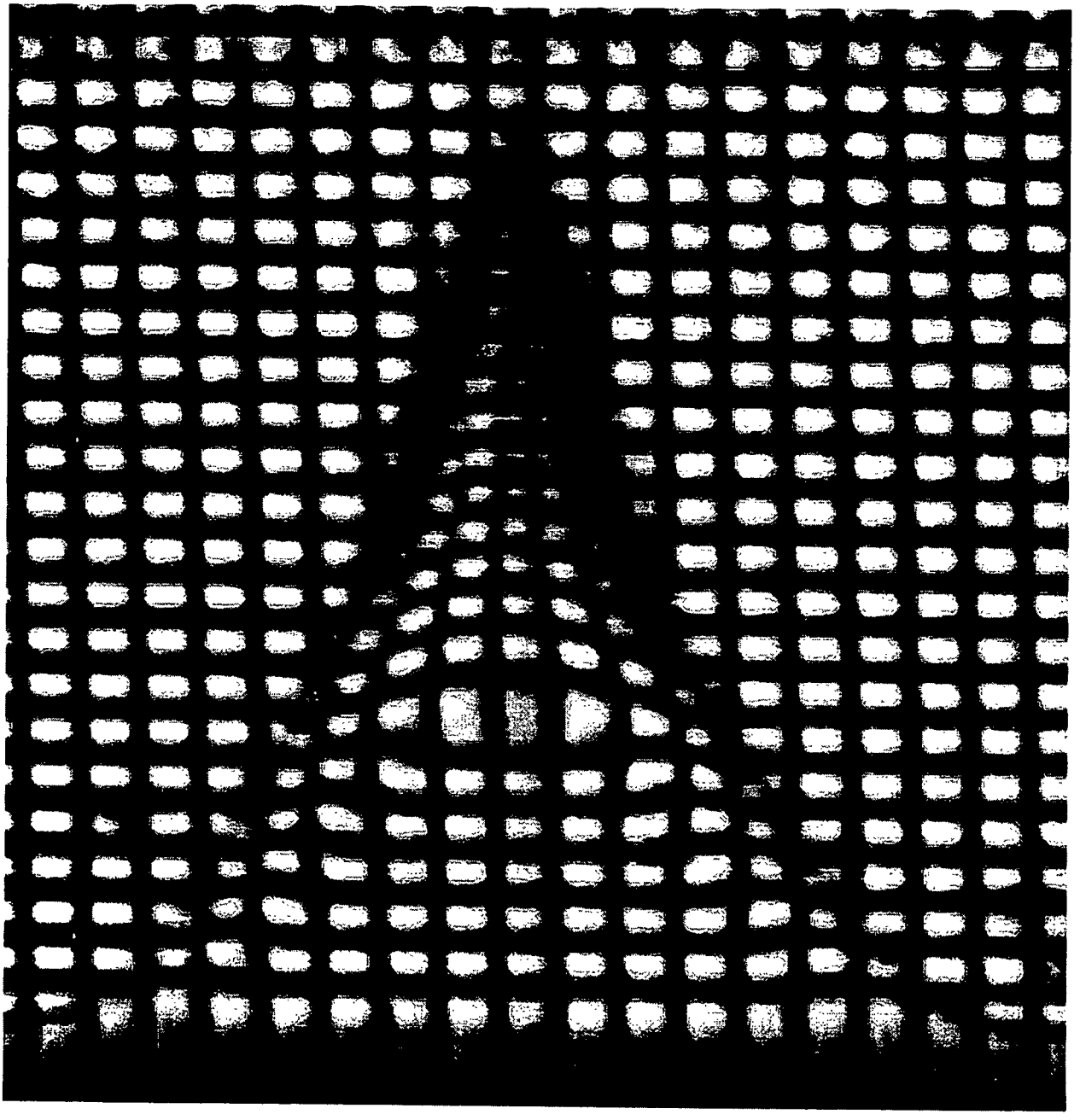

Figure 6.15. 200 cs silicone oil triangular air film from image U05RM620.TIF with run U05BRAM1.DAT at video time code 2:36:03. The substrate velocity is 12.23 cm/sec.(734 cm/min), Ca = 1.21 and λ_μ = 1.34 x 10^{-4}. The vertical and horizontal line spacing are 10 and 12.5 cycles/mm, respectively. G = 0.65°, Φ = -0.167°, η_4 = 1.4032, t_1 ,t_2 = 1588, 38.1 μm, η_1,η_2 = 1.515, 1.608.

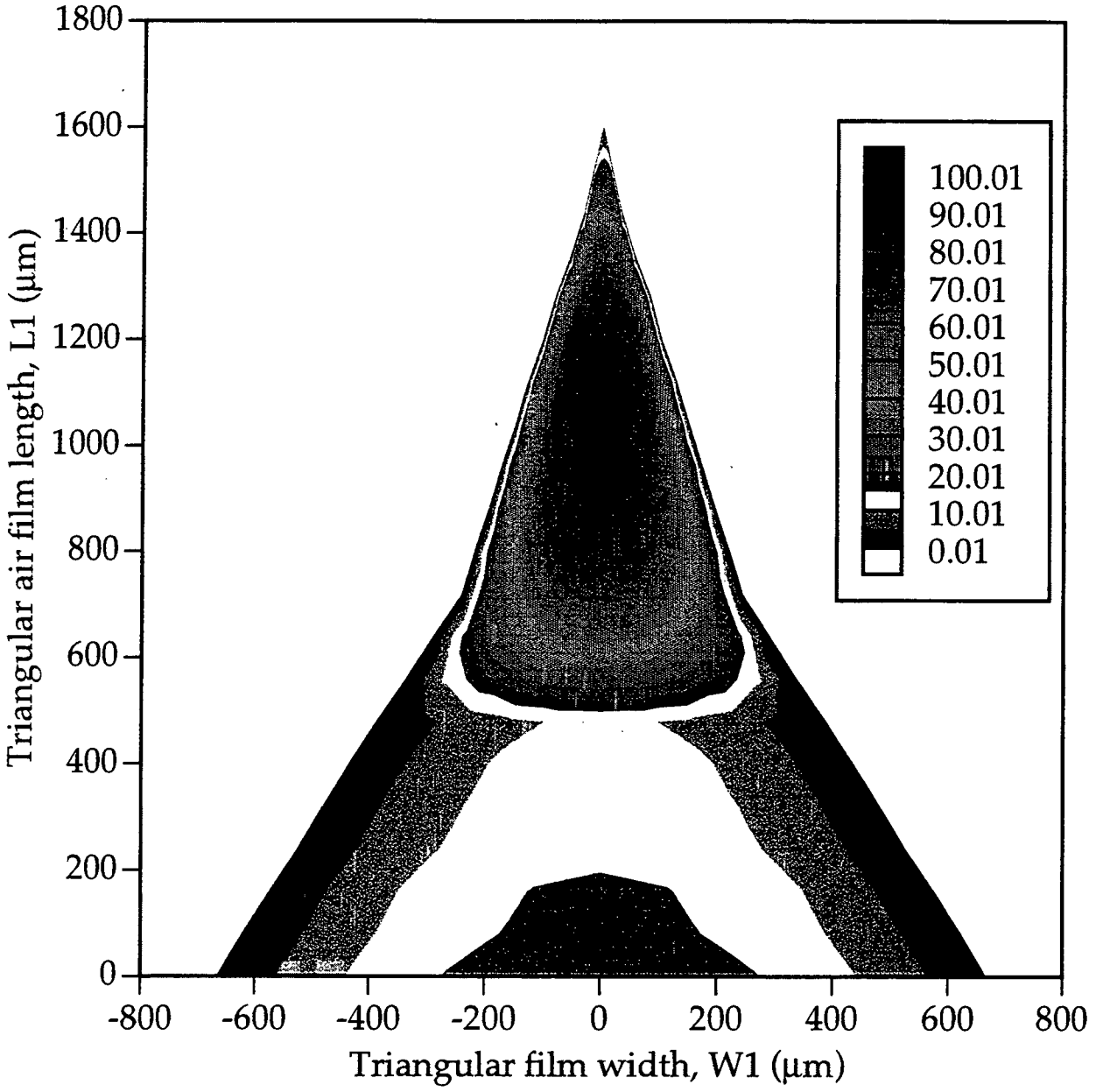

Figure 6.16. An XYZ contour plot of the double ruling triangular air film image from Figure 6.15. The data is calculated from the geometrical consideration of circle segment discussed in Appendix XIV.

This result supports the long wave interfacial instability of Aidun et al. (1993) and Severtson and Aidun (1995).

In Section 6.7 the dimensional data from Section 6.4 for $\varnothing_1$ and $\varnothing_3$ will be correlated with the gas Capillary and Weber numbers to estimate their influence.

6.7 Correlation of the Angles $\varnothing_1$ and $\varnothing_3$ with Air Film Dimensions

The data contained in the previous sections is unique in that it is the first limited data that considers all three dimensions of the air film. As previously shown in Fig. 6.2 and confirmed by the data in Section 6.4, we believe there exists two distinct regions for a triangular air film. The "capillary tip" region of length L_3, and the thin "air film" region of length L_2. The air film region thickness is usually thinner than the maximum in the capillary tip region. For this reason, the nucleation site occurs near the edges of the base due to the long wave interfacial instability. The tip angle can be measured from the initial slope of the centerline interface profiles. The measurements for L_1, L_2, and $\varnothing_3$ for each case are presented in Appendix VIII at each time step. Their averages are summarized in Table 6.2.

The tip vertical angle, $\varnothing_3$, can be thought of as the dynamic contact angle of the tip, $\varnothing_3 = (180° - \theta_d^{tip})$. The average tip vertical angle, $\overline{\varnothing}_3$, ranges from 16.3° (θ_d^{tip} = 163.7°) for Case #6 (500 cs silicone oil) to 2.9° (θ_d^{tip} = 177.1°) for Case #11 (20 cs silicone oil). The value of θ_d^{tip} is close to the 180° criteria for air entrainment.

The forces acting near the tip are from the gas pressure, the capillary pressure, and the viscous stresses. The buoyancy forces have been ignored but should be of

the same order for all of the cases. A dimensionless correlation of the gas Weber number (inertial/capillary forces) multiplied by the gas Capillary number (viscous/capillary forces) will be used. The characteristic length used in the gas Weber number will be the total length, L_1, measured from the experiments. Thus the dimensionless groups are

$$We_g = \frac{L_1 \rho_g U^2}{\gamma}, \qquad Ca_g = \frac{\mu_g U}{\gamma}, \text{ and} \qquad We_g Ca_g = \frac{\mu_g \rho_g L_1 U^3}{\gamma^2} \qquad [6.1]$$

The only liquid property in Eq. [6.1] is the surface tension, γ. Plots including the liquid Capillary number, $Ca = \frac{\mu U}{\gamma}$, multiplied by the gas Weber number were also tested vs. $Ø_3$. These did not exhibit significant correlation.

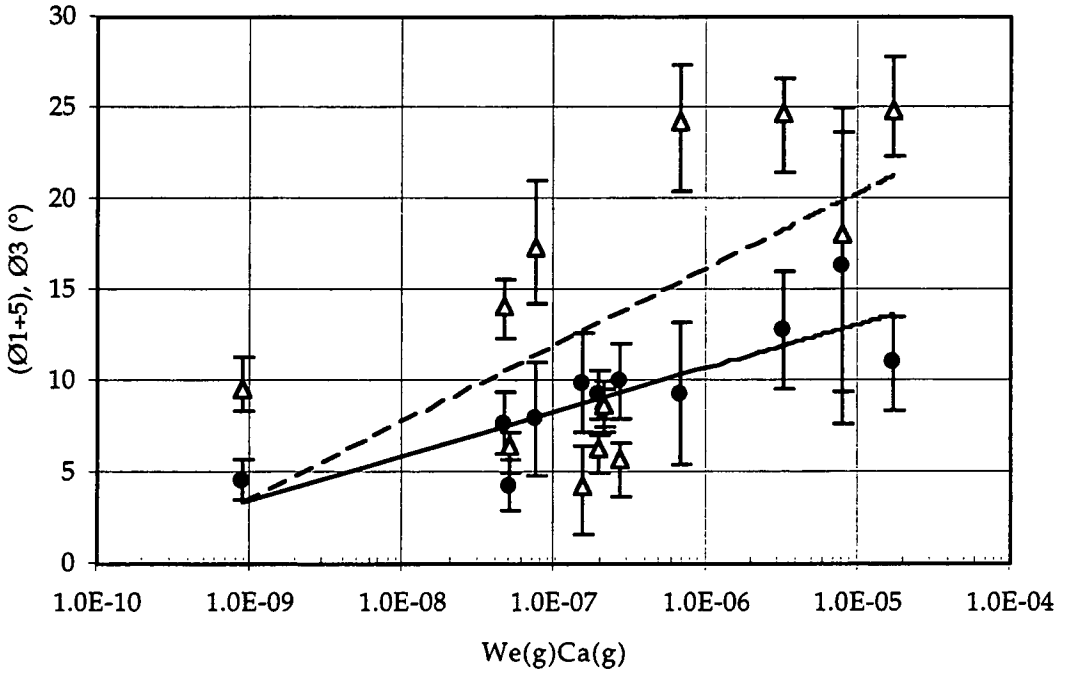

Figure 6.17. The average tip vertical angle •- $Ø_3$ and tip vertex angle Δ - $Ø_1$+5 from the triangular air film formation in Case Nos. 1 - 12. The air density used in We_g was taken to be 1.177×10^{-3} g/cm^3. The correlations through the data are $Ø_3 = 1.0359\ln(Ca_g We_g) + 25.035$, $R^2 = 0.70$ and $Ø_1 = 9.052\ln(Ca_g We_g) + 205.9$, $R^2 = 0.36$. The error bar represents the standard deviation of the data for each set of case measurements.

With the limited data set, Fig. 6.17 unfolds the trend that as the product We_gCa_g approaches a lower limit, the tip vertical angle, $\emptyset_3$, also approaches a lower limit. The tip vertex angle, $\emptyset_1$, also decreases with We_gCa_g but the data exhibit much more scatter due to the advancing and retraction of the air film which changes $\emptyset_1$. The case data for $\emptyset_1$ is limited which leads to the low correlation coefficient in the equations given below Fig. 6.17. A better criterion would be to measure $\emptyset_1$ when L_1 is at a maximum. This would require examining a significant number of cases to determine if any type of trend exists.

The narrow air tongue shown earlier in Fig. 6.1 represents another type of air entrainment which sometimes has been called "spitting." In this regime the traditional type of air entrainment outlined by Veverka et al. (1993) is no longer operable, but rather forms a continuous stream of bubbles. Because we have not made measurements with this fluid, the data in Figure 6.17 are outside the range of application for this type of air finger.

The rough analysis, discussed above should be applied within the context of the limited data set. Since the averages for $\emptyset_1$, $\emptyset_3$, L_1, and L_2 represent single case observations of the triangular air film, the results cannot be generalized but suggest another area for future experimental work. This work could systematically verify our data within the bounds that we have studied.

The next section will describe an interesting phenomenon first reported during this work. These phenomena are precursor structures at the gas liquid interface prior to the DCL.

6.8 Precursor Structures at Low Capillary Number and Liquid Viscosity

The deflectometry technique also revealed previously undocumented flow structures for our system when Ca<1 and We>>1 (note, We=Ca x Re with L_c as the characteristic length scale). Under these conditions, a thin flat air film forms at the contact line, during the ramping and the constant speed experiments. The width of the film of air, χ_s, is much larger than the triangular air pockets, i.e., $\chi_s >> \chi$. The sheet width was around 20-30 mm while the triangular air film was only on the order of 5-6 mm wide. This was confirmed by using dual CCD cameras slaved to the same time code generator. The two CCD cameras were interfaced with a stereo zoom microscope and a zoom lens, respectively. Ramping experiments (from below U_v to past U_{ae}) were conducted by focusing the two cameras on the same contact line position. A sample microscopic image from these experiments is shown in Fig. 6.18.

The precursor structure ruling line deflection in Fig. 6.18 reflects differences in the interface curvature that vary in both the x- and y directions. That is, the air sheet does not advance with the interface uniformly varying in thickness and rather localized differences are seen. These differences are the precursor structures. Another observation of the precursor structure detection is found in Appendix VII Figs. VII.8 and VII.9 for Case #11. The quantitative measurement of the profile using deflectometry shows that the precursor vertex is a low pressure region (Fig. VII.9). This is based on the concavity of the interface in this region. The region

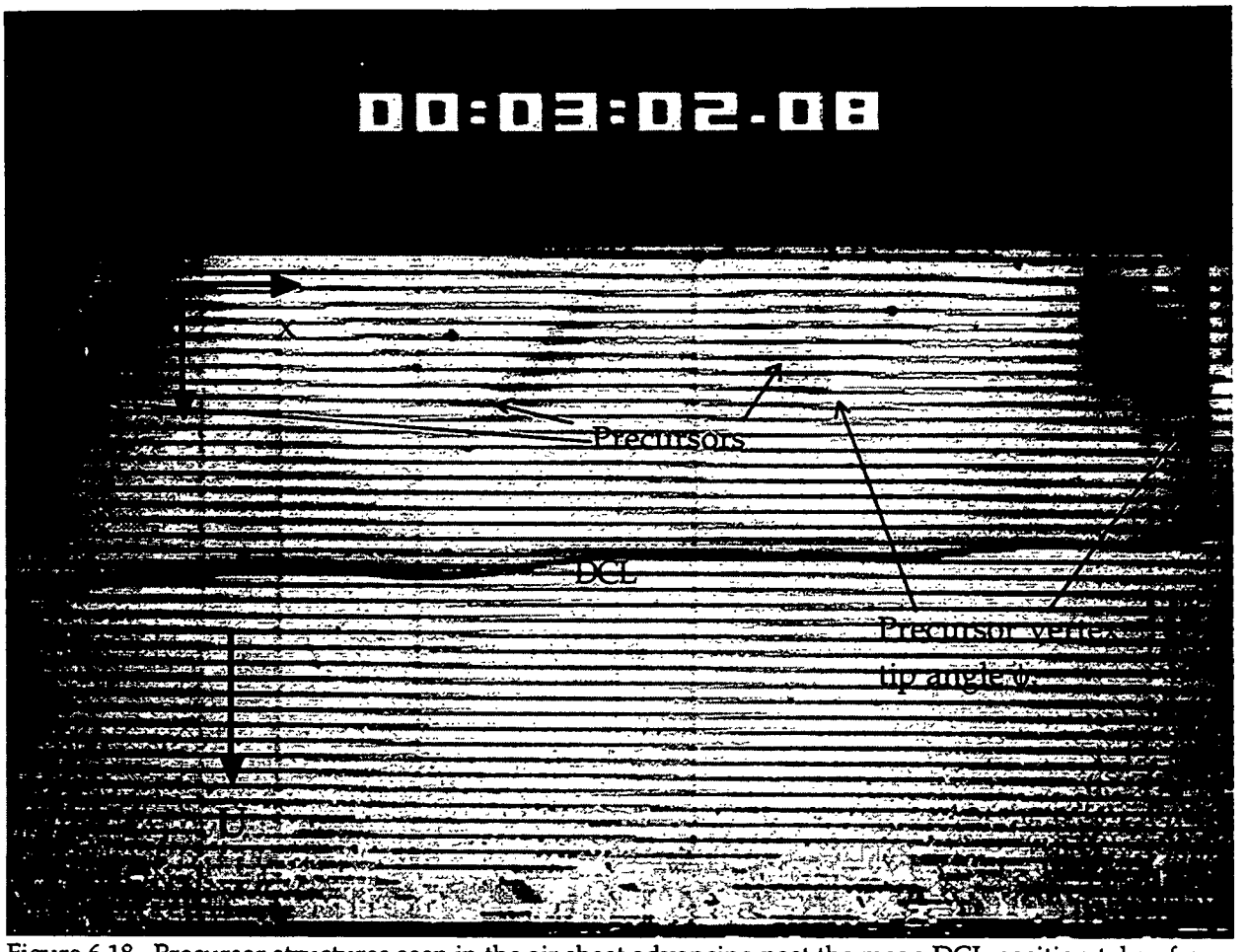

Figure 6.18. Precursor structures seen in the air sheet advancing past the mean DCL position taken from image U17ZRM39.TIF for experimental code U17ZRAM3. The substrate velocity was 35.0 cm/s and the liquid Capillary number 0.376 with $\lambda_\mu = 12.85 \times 10^{-4}$, and the distance between ruling lines was equal to 200 μm. Another example of an advancing air sheet with precursor structures is seen in Appendix VII for Case #11

from the DCL to the precursor vertex is presumed to be a high pressure region based on the profile concavity.

The precursor phenomena are not isolated. Many instances of these structures and the air sheet were seen with Fluids Y and Z (10 and 20 cs silicone oils). Without the use of the ronchi ruling in our flow visualization experiments, these structures could not have been easily detected. Once the sheet advances a maximum distance from the mean DCL position, the edges of the sheet collapse

inward, normal to the substrate velocity, until a triangular air film is formed. The precursor structures merge together as the sheet edges collapse.

It is hypothesized that these interface precursor structures are present before the DCL due to the gas velocity profile in this converging gap region. It is possible that the component of vorticity in the gas phase parallel to the dynamic contact line gives rise to a third velocity component creating a unique three-dimensional air flow that interacts with the free surface. These observation are insightful because it may provide the physical explanation for the triangular air film structures ("sawtooth" pattern) observed during air entrainment.

One possibility that the precursor structures have not been seen in previous experiments is that the plunging tape width is too narrrow for the air sheet to emerge. The tape edges "pin" a triangular air film as discussed in Section 2.6. In wetted roll studies, the thin liquid layer may change the gas boundary layer and prevent precusor formation.

The average tip angle, $\emptyset_1$, for the precursor structures was measured and compared to the average $\emptyset_1$ measurements of the air film with the same fluid (see Table 6.2). The precursor tip angle data is contained in Table 6.4. With Fluid Y (10 cs silicone oil), the average measured precursor vertex was $\emptyset_1$=85.2° while the corresponding triangular air film has an average of $\emptyset_1$=124.5°.
Fluid Z (20 cs silicone oil), has a precursor average of $\emptyset_1$=97.9° compared to the triangular air film average of 90.3° and 124.3° for Case Nos. 11 and 12 respectively. No other firm information can be garnered except that the values are of the same magnitude and may possibly be determining the angle of the triangular air film.

Table 6.4. Measurement of precursor structure vertex angle $\emptyset_1$

Image Name	Run Code	Time Code	$\emptyset_1$°	Precursor vertex distance from DCL (μm)
FLUID Y				
G12CA145	G12YCA1	215:15.255	77.5	2150
G12CA155	G12YCA1	215:18.474	94.0	1652
G11YRM11	G11YRAM1	2:22:11	88.2	3166
G11YRM12	G11YRAM1	2:24.23	82.5	1782
G11YRM31	G11YRAM3	1:17:12	80.4	1644
G11YRM61	G11YRAM6	54.29	80.3	-
G12YRM11	G12YRAM1	2:20:08	87.3	2183
2 precusors on image			91.6	1109
		Average	**85.2**	**Table 6.2 $\emptyset_1$°= 124.5°**
		Standard Deviation	**5.9**	
FLUID Z				
U22ZRAM3	U22ZRAM3	1:39.21	110.8	-
U19CA455	U19CA455.TIF	1:28.424	107.8	1840
3 precursors on image			101.6	1920
			100.1	1730
U22C1118	U22ZCA1	4:35.305	102.1	2189
U17ZRM38	U17ZRAM3	3:02:07	89.4	-
4 precursors on image			84.6	-
			86.4	-
			95.8	-
		Average	**97.9**	**Table 6.2 $\emptyset_1$°= 90.3°**
		Standard Deviation	**9.3**	**Table 6.2 $\emptyset_1$°= 124.3°**

If the base state is 2D parallel flow, then the first instability would be a 2-D state based on Squire's theorem (Squire 1933). Subsequent instabilities would then result in a 3-D state with the precusor structures shown in Fig. 6.18.

The two-dimensional instability shown by Severtson and Aidun (1995) and Aidun et al. (1993) may be more relevant to the formation of the precursor structures. It is however clear that the interfacial mode is the cause of instability and wave formation inside the triangular air films. The analysis regarding the origin

and physics of flow leading to the precursor structures are being pursued further in another thesis.

6.9 Summary of Chapter VI Results

The main results presented in Chapter VI include i) a detailed documentation of how the triangular air film dimensions evolve for $U_v < U < U_{ae}$, ii) the discovery of the precursor structures with low vicosity silicone oils when Ca < 1 in our side driven free surface cavity, iii) evidence that the distance between triangular air fingers is not dictated by substrate roughness giving more weight to idea that the interfacial precursor structures may determine the distance between triangular air films, and iv) qualitative evidence that the long wave interfacial instability is the mode that leads to nucleation and consequent air bubble entrainment.

CHAPTER VII

CONCLUSIONS

Several conclusions can be surmised with regard to variations and varying aspects of this research undertaken to study air entrainment at the dynamic contact line with a precision free surface coating cavity with $a_c \approx 1/3$. The precision experimental setup allowed us to isolate a regime where a triangular air film can remain stable without air entrainment. A quasi-steady state approach was used to determine the first and second critical speeds of air entrainment (i.e. U_v and U_{ae}, respectively). The specific conclusions from these experiments are as follows:

1) For air to liquid viscosity ratio, λ_μ, less than 2×10^{-4} and $Ca > 1$, the side driven cavity shows significant differences in the critical air entrainment speeds when compared to previous plunging tape experiments at the same fluid properties. There was no significant effect due to the surface properties of the tape that would explain the difference between the two systems. The major difference has been attributed to the bulk flow, and particularly, the smaller liquid normal stresses acting in the plunging tape system versus the cavity system studied here. A qualitative analysis was used to explain why in plunging tape systems, correlations of Capillary number and viscosity ratio would sufficiently predict the air entrainment speed. In a system where the bulk flow may affect the dynamic contact line, such as our confined cavity, the normal stresses must be included to correlate the air entrainment speed.

2) In the range $\lambda_\mu > 2 \times 10^{-4}$ and $Ca < 1$, a finite "window" exists where a triangular air film is stable. This is shown at greater than 90% confidence level with four different fluids of varying viscosities and surface tensions.

3) The mechanism of air entrainment first elucidated by Veverka (1991) using glycerine-water mixtures was verified using microscopic flow visualization in our cavity system. The same nucleation, isolation of tip, and bubble formation sequence (Veverka 1991) was observed at various viscosities with both silicone oils and glycerine-water mixtures and thus the mechanism is not system dependent.

An optical deflectometry technique was applied to analyze the centerline interface profile and the dynamics of the triangular air films. Some of the main conclusions learned about applying this technique to study thin film air entrainment include:

4) The alignment between the optical axis and the substrate must be carefully monitored and corrected to achieve an accurate interface profile height.

5) Results from two independent methods to estimate the thickness of the triangular air film, namely, the entrained bubble volume and the use of two perpendicular ronchi rulings, confirmed the results obtained in the single ruling optical deflectometry experiments.

When microscopic flow visualization using deflectometry was applied to study air entrainment, the following conclusions are reached:

6) A rise in the interface profile usually precedes both retraction and nucleation. This agrees with the results of Severtson and Aidun (1995) for the long wave interfacial instability resulting in surface waves and nucleation of wetting.

7) The increases in interface thickness leads to a finite speed window (see #2 above). In order for a nucleation site to initiate near the "air film" region at these conditions, the amplitude of the interfacial surface waves must be larger.

8) It is believed that the variations in the interface height near the base of the triangular air film can lead to either i) a release of the excess pressure in the air film leading to retraction or ii) a nucleation site via the trough of a surface wave touching the substrate.

9) Previously undocumented precursor structures for Ca < 1 and air to liquid viscosity ratio greater than 2×10^{-4} form when $U \approx U_{ae}$ as a sheet of air advances past the dynamic contact line position. This observation may provide the physical explanation for the triangular air film structures ("sawtooth" pattern) observed immediately prior to air entrainment. It is also concluded that under these conditions, the gas flow in the converging dynamic contact line region is not 2-D and should be studied further to understand the precursor phenomena.

10) No correlation was found between the peak spacing of the substrate roughness and the average spacing between air film vertices for $\lambda_\mu = 0.32 \times 10^{-4}$. This points to the fact that the contact line destabilization is of hydrodynamic origin not dictated by the substrate for the cases we have studied. This also supports the conclusion that the precursor structures may explain the sawtooth pattern (see #9 above).

11) The volume of air contained in the triangular air film is greater at low viscosity than at high viscosity. Correspondingly, the bubble volume should increase. Thus the severity of product defects due to this flow instability may be worsened when using a low viscosity coating fluid due to the larger bubbles.

CHAPTER VIII

FUTURE WORK AND SUGGESTIONS

8.1 Practical Implications for Air Entrainment and the Paper Industry

Air entrainment in the paper industry has only recently been recognized as causing runnability problems detrimental to quality and increased production speeds. The coating system used for our work is similar to a puddle coater used in the paper industry. It also has analogies to the apron size press (Justy 1982), the Beloit high-speed size applicator (Alheid 1983), the three roll two nip size press (Koski 1986) and the conventional size press (Aidun 1990). In a conventional size press there are *four* dynamic contact lines[1] where air entrainment is possible and may cause spitting in the pond at high speeds. Air entrainment in the short dwell coater and the current jet coaters also have been discussed. Any apparatus with a DCL is prone to air entrainment and the associated defects.

We have attributed the delay of air entrainment to the liquid normal stresses developed by the fluid acting on the liquid/air interface. A common trend to achieve higher running speeds is to use a nozzle type applicator with a metering blade. Teirfolk and Laaja (1995) demonstrated how a nozzle applicator could be run at speeds up to 2250 m/min while the short dwell coater produced skipping. Harrison (1994) discusses the future trends in coater design to achieve higher speeds. Other instabilities not withstanding the liquid normal stresses acting on the DCL must be increased in order to prevent air entrainment from occurring. At high

[1] One on either side of the sheet similar to the plunging tape system, and one at both sides where the rolls enter the pond reservoir.

viscosity, decreasing the surface tension increased the speed of air entrainment for our side driven free surface cavity. Applying this idea with coating colors, the heterogeneous nature of the mixture is questionable for lowering the surface tension through surfactant addition. Changing from a aqueous to solvent system is impractical for cost, flammability, and environmental reasons. Very high value added products may be able to justify a non-aqueous system but production rate is not usually a problem with these types of grades. The only alternative is to more effectively apply a force to counteract the factors that lead to air entrainment which we have attributed in Section 5.7, as arising from a stress balance on the interface near the DCL. As the dynamic contact angle approaches the assumed criteria of 180°, the "gas lubrication pressure" or "gas normal stress" dominates the other forces leading to the three-dimensional breakup of the DCL and air entrainment. Can incremental increases in the coater speed be achieved by altering the coating head delivery system? We believe so.

Aidun's (1994 a,b) alternatives to the SDC eliminate the central vortex recirculation that lead to 3-D instabilities. This design still has difficulty in sealing the overflow baffle from the air boundary and associated DCL at the gas/liquid/solid junction. A type of combination "liquid seal" is proposed for use with a vortex free coater design as shown in Figure 8.1. By varying the flow rate from the nozzle at the

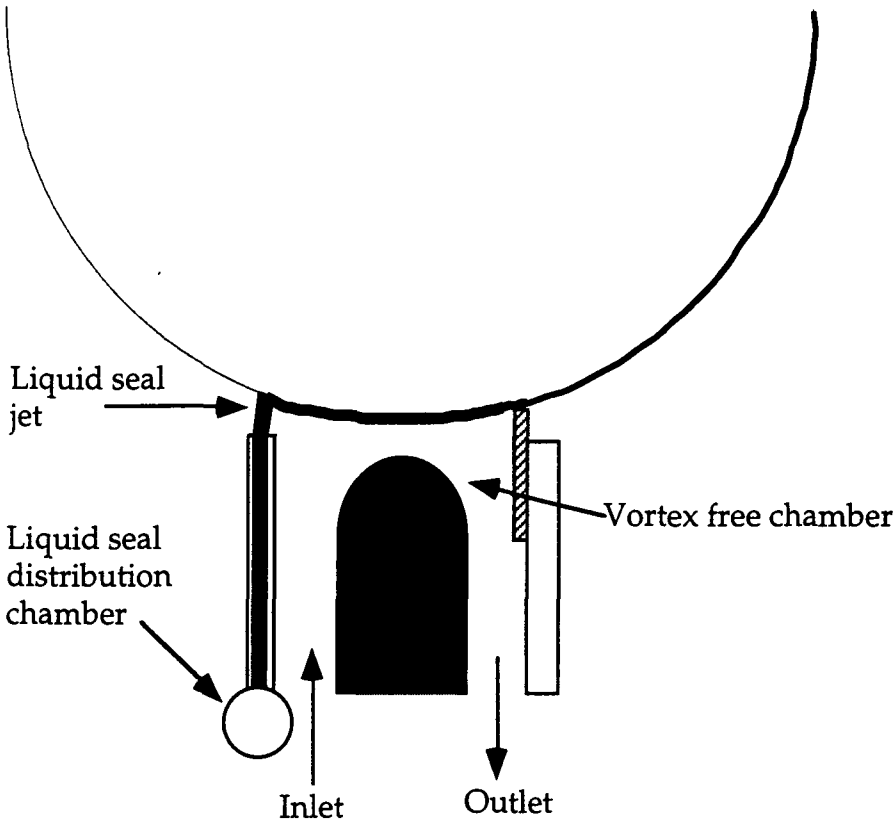

Figure 8.1. A simplified version of the combination vortex free coater with the "liquid seal" to prevent air entrainment at the dynamic contact line. The gap between the jet exit and the substrate as well as the flowrate to the distribution chamber would be control variables.

overflow baffle in Fig. 8.1, the normal force (or tangential momentum) of the fluid acting on the substrate is an additional control variable. Perry (1967) used a very simple approach similar to this and succeeded in delaying air entrainment. Analysis of the problem could begin using some of the work done by Blake, Clarke

and Ruchak (1994) for their "hydrodynamic assist" of dynamic wetting in a curtain coater.

By replacing the overflow baffle with this type of "liquid seal" in Fig. 8.1, any of the excess fluid would fall into a catch-all pan. A catch-all pan is currently installed on most coaters now so no additional modifications would be required. Some of the benefits of the system would be increased runnability at higher speed prior to air entrainment, and a compact design. It may also be possible to use a different coating color in the liquid seal jet that promotes sheet opacity while the primary coating layer from the cavity would have better print properties. This would only be true if the jet thickness was less than the blade gap which may be impractical. However, there are two apparent drawbacks to the proposed system. First, since the liquid seal jet is directed tangential to the web, significant absorption may occur as a pressure gradient exists driving liquid into the fibrous network. The short contact time, and reduced breaks, presumably due to less liquid absorption into the sheet, associated with the short dwell coater were its major selling points when introduced in the 1980's. The absorption might be overcome by pre-coating the sheet in a size press, although this also has limitations of added capital and possible air entrainment. Second, the possibility of misting from droplets of the jet being ejected near the DCL might also be increased leading to cleanliness problems in the application region of the paper machine.

A meaningful theory on why the DCL destabilizes into the triangular shapes has still not been developed although our results suggest that the flow in the converging gas phase near the DCL cannot be modeled as being two dimensional.

The flow visualization results with ronchi-rulings suggest a mechanism by which the DCL can destabilize due to spatial (in the CD direction) differences in gas flow and pressure. The shape of the free surface along the precursor centerline suggests a high pressure gas region exists past the tip of the precursor structure and up to the DCL position.

Thirdly, the results of the deflectometry experiments have provided a data set for future simulation of the behavior of the triangular air film over 2 decades in liquid viscosity variation. From these results we see that the low liquid viscosity triangular air film has a much greater total volume. Thus, by lowering liquid viscosity to prevent air entrainment larger bubbles will result. If undetected the defect severity may be increased during operation.

8.2 Suggestions for Future Work

The enhancement effect of the confined cavity versus the plunging tape was only studied for cavity aspect ratio $a_c = 1/3$. The working range of the stereo zoom microscope would have prevented increasing d_c and simultaneously viewing *through* the cavity. Thus studying $a_c \rightarrow 1$ and greater was not possible. Ramping experiments for $a_c \rightarrow \infty$ would have to be done by viewing from behind the coater shoe. Other aspect ratio cavities could have easily been used with the current system and improved techniques. These type of experiments would enable correlations similar to Eq. [2.3] taking into account bulk flow delay of air entrainment.

Simulation of the liquid normal stresses in cavities of varying dimensions is possible with commercially available computational fluid dynamics (CFD) programs. Some type of a slip model would be required to model the DCL. The gas phase flow should also be included as well as capillary pressure.

The precursor structures, previously undocumented should be further investigated as the mode by which the DCL breaks into the "sawtooth" configuration. This result is one of the newest significant discoveries regarding DCL instability. The question as to whether these structures are present at $\lambda_\mu < 2 \times 10^{-4}$ still needs to be answered although experimental verification may be impossible because $\Delta U \rightarrow 0$ for $\lambda_\mu < 2 \times 10^{-4}$

The thickness of the gap between the substrate and the gas liquid interface has been found to be around 200 μm for the image sequence found in Appendix VII at Ca=0.34. This sequence represent the formation of the triangular air film by way of the precursor structures. By seeding the gas boundary layer with 1-3 μm aerosol before it enters into the converging DCL region it may be possible to measure the gas flow in the plane of the substrate. This could be done with the mature LDV technique (Laser Doppler Velocimetry) on a point basis or PIV[2] (Particle Image Velocimetry) on a larger global basis. The LDV measuring volume can be as small as 40 μm if the proper optics are used (Mues et al. 1989). Computational work should be conducted parallel to develop a theory for the results.

---

[2] PIV was originally proposed for use on this thesis but the Coherent - Innova Model 70-4 CW Argon laser did not have sufficient power to scatter light from the 0.7 μm silicone oil aerosol droplets. See laboratory notebook page 6 for conditions tested with silicone oil and the TSI Model 1237 constant output atomizer.

The deflectometry technique used in this work was a compromise from the moiré technique based on interferometry. Better resolution might be achieved with an interferometry-based method now that data on the air tongue time and dimensional behavior is available.

8.3 Improvement to the Experimental Paper Film Coater

A number of improvements to the experimental system are offered for future reference:

1) The runnability at low viscosity is critically dependent on removing all of the liquid on the tape. "Telescoping" and wrapping at the rewind roll limited the running time to a few minutes (less than 5) versus hours for high viscosity liquids. This will require an analysis of the factors required to doctor low viscosity fluids of varying surface tension and implementing a new doctoring system.

2) The current fluid delivery system is cumbersome when changing fluids because of the requirement to flush and scrub the progressing cavity (Moyno) pump and change the lines. A simpler system might be based on a combination pressure/gravity feed system where the flowrate is regulated in a sealed vessel above the coating cavity. Two control loops, one for vessel pressure and another for a flow valve, could be used to regulate the flow. This system would also have the benefit of being vibration free.

3) The current control and data acquisition system for LABVIEW, although functional, should be optimized to collect data more rapidly plus be able to

electronically synchronize the video and data acquisition. That is, a master signal on any imaging device should be used to locate data exactly in the saved files.

4) Although a film based 16-mm system was used in this thesis, the advances in digital imaging will soon equal the film resolution to conduct deflectometry experiments. The tradeoff between field of view and resolution was discussed in the Chapter IV Section 4.1.3 and Appendix XVII. A digital camera with a 2K x 2K pixel array and minimum of 500 frames/second would be sufficient for this work. Other size pixel arrays may compromise obtaining accurate values for δy_i and δx_i.

5) The correction factor G was measured and found to alter the deflectometry measurements. Two immediate solutions to this problem are apparent. The first would be to reinforce the window shoe so that the deflection due to blade loading is minimized to less that 0.05°. The second would be to monitor the angle between the optics and substrate surface using either, i) digital levels which are commercially available or ii) an optics based system using triangulation of a beam of light (HeNe laser or diode laser) between the optical axis and the normal to the substrate. Both will achieve the result of minimizing G in deflectometry experiments.

6) Use of a combination time code generator with a data logger that electronically adds another signal such as substrate velocity onto the video system will facilitate locating an event in archived video tapes and should be incorporated.

CHAPTER IX

LITERATURE CITED

1) Abernathy, R.B., Benedict, R.P., and Dowdell, R.B. 1985. ASME Measurement Uncertainty. J. of Fluids Eng. 107(6):161-64.

2) Ablett, R. 1926. An Investigation of Contact Between Wax and Water. Phil. Mag. 46:244-256.

3) Aidun, C.K. 1990. Principles of Hydrodynamic Instability in Coating Systems. IPST Technical Paper Series. No. 346.

4) Aidun, C.K. 1991. Principles of Hydrodynamic Instabilty: Application in Coating Systems. Tappi J. Pt.1 74(2):213-219, Pt.2 74(3): 213-220, Pt.3 74(4):209-213.

5) Aidun, C.K., Veverka, P.J., and Scriven L.E. 1992. Onset of Air Entrainment - Paper 49a. AIChE Spring National Meeting, New Orleans, March 29-April 2.

6) Aidun, C.K., Veverka, P.J., and Scriven, L.E. 1993. The Mechanism for Excessive Air Entrainment in Coating Systems. 1993 TAPPI Coating Conference Proceedings, Minneapolis, MN, May 2-5. Atlanta, TAPPI Press, pp. 157-167.

7) Aidun, C.K. 1993. An Overview of Blade Coating Systems. IPST Technical Paper Series. No. 491.

8) Aidun, C.K. 1994a. Flotation Coating Device for Traveling Webs. U.S. Patent 5,354,376, Institute of Paper Science and Technology (Issued Oct. 11, 1994).

9) Aidun, C.K. 1994b. Coating Device for Traveling Webs. U.S. Patent 5,366,551, Institute of Paper Science and Technology (Issued Nov. 22, 1994).

10) Aidun, C.K., and Kovacs, A. 1995. A Vortex Free Pressurized Pond Coater. TAPPI 1995 Coating Conference, Dallas, TX, May 22-24. Atlanta, TAPPI Press, pp. 191-222.

11) Aidun, C.K., and Chen, Y. 1994. Instability of a Shear-Driven Air/Liquid Interface - Paper 5e. 1994 AIChE Spring National Meeting, Atlanta, April 17-21.

12) Aidun, C.K., and Triantafillopoulos, N. 1994. High Speed Blade Coating. IPST Technical Paper Series. No. 534. (Accepted for publication in Liquid Film Coating).

13) Alheid, R.J. 1983. Apparatus for High Speed Size Application. U.S. Patent 4,407,224 (Issued Oct. 4, 1983).

14) Berg, J.C., ed. 1993. Wettability - Surfactant Science Series: Vol. 49. New York, Marcel Dekker Inc.

15) Blake, T.D. 1966. The Contact Angle and Two-Phase Flow. Ph.D. Thesis, University of Bristol.

16) Blake, T.D., and Haynes, J.M. 1969. Kinetics of Liquid/Liquid Displacement. J. of Colloid Interface Sci. 3(3):421-23.

17) Blake, T.D., and Ruschak, K.J. 1979. A Maximum Speed of Wetting. Nature. 282:489-491.

18) Blake, T.D. 1988. Wetting Kinetics - How Do Wetting Lines Move? 1988 AIChE International Symposium on the Mechanics of Thin-Film Coating, March 6-10, New Orleans, Paper 1a.

19) Blake, T.D. 1993. Dynamic Contact Angles and Wetting Kinetics - Chapter 5 in Wettability - Surfactant Science Series. Berg, J.C., ed., v.49, New York, Marcel Dekker Inc.

20) Blake, T.D., Clarke, A., and Ruschak, K.J. 1994. Hydrodynamic Assist of Dynamic Wetting. AIChE J. 40(2):229-242.

21) Blake, T.D. 1995. Personal communication via letter dated January 18, 1995. Kodak Limited, Middlesex, England.

22) Blitshteyn, M. 1984. Measuring the Electric Field of Flat Surfaces with Electrostatic Fieldmeters. Evaluation Eng. 23(10):70-86

23) Bolton, B., and Middleman, S. 1980. Air Entrainment in a Roll Coating System. Chem. Eng. Sci. 35:597-601.

24) Booth, G.L. 1970. Coating Equipment and Processes. New York, Lockwood Publishing Co.

25) Born, M., and Wolf, E. 1980. Principles of Optics - Electromagnetic Theory of Propagation Interference and Diffraction of Light. Pergamon Press, Oxford.

26) Bracke, M., de Voeght, R., and Joos, P. 1989. The Kinetics of Wetting : The Dynamic Contact Angle. Prog. Coll. Polym. Sci. 79:142.

27) Brown, D.R. 1961. A Study of the Behavior of a Thin Sheet of Moving Liquid. J. Fluid Mech. 10:297-305.

28) Buonopane, R.A., Gutoff, E.B., and Rimore, M.M.T. 1986. Effect of Plunging Tape Surface Properties on Air Entrainment Velocity. AIChE J. 32(4):682-83.

29) Burley, R. 1971. Fluid Behavior Between Horizontal Pad Rollers. Textile Institute and Industry. 9:131-136.

30) Burley, R., and Brady, P.R. 1973. Displacement of an Air/Liquid Interface by a Moving Web of Fibers. J. Colloid Interface Sci. 42(1):131-136.

31) Burley, R., and Kennedy, B.S. 1976a. An Experimental Study of Air Entrainment at a Solid/Liquid/Gas Interface. Chem. Eng. Sci. 31:901-911.

32) Burley, R., and Kennedy, B.S. 1976b. A Study of the Dynamic Wetting Behaviour of Polyester Tapes. Brit. Polymer J. 8:140-143.

33) Burley, R., and Jolly, R.P.S. 1984. Entrainment of Air into Liquids by a High Speed Continuous Solid Surface. Chem. Eng. Sci. 39:1357-1372.

34) Burley, R. 1992a. Mechanisms and Mechanics of Air Entrainment in Coating Processes. Industrial Coating Research. 2:95-108.

35) Burley, R. 1992b. Air Entrainment and the Limits of Coatability. Surface Coatings International. 75(5):192-202.

36) Canedo, E.L., and Denson, C.D. 1989. Flow in Driven Cavities with a Free Surface. AIChE J. 35(1):129-138.

37) Cohen, E.D. and Gutoff, E.B. ed. 1992. Modern Coating and Drying Technology. - (Interfacial Engineering Series; V.1). New York, VCH Publishers Inc.

38) Cox, R.G. 1986. The Dynamics of the Spreading of Liquid on a Solid Surface. Part 1- Viscous Flow. J. Fluid Mech. 168:169-194.

39) deGennes, P.G., Hua, X., and Levinson, P. 1990. Dynamics of Wetting: Local Contact Angles. J. Fluid Mech. 212:55-63.

40) Deryagin, B. 1940. Zh. Fiz. Khim. 14:137.

41) Deryagin, B.V., and Levi, S.M. (Eichler, W.R., and Sutherns, E.A.), trans. 1964. Film Coating Theory. London, Focal Press Publishers. pp. 140-43, Translated from the original 1959 Russian text.

42) Dow Corning, 1991. Information About Silicone Oils. Information Form No. 22-927B-92 and 22-928B-92, Dow Corning Corp. Midland, MI.

43) Drazin, P.G., and Reid, W.H., 1981. Hydrodynamic stability. Cambridge University Press, New York. 525 p.

44) Ducey, M. J. 1984. New Short-Dwell Coaters Reduce Raw Materials and Downtime. Pulp and Paper. 56(6):102-4.

45) Durst, F., Melling, A., and Whitelaw, J.H. 1981. Principles and Practice of Laser-Doppler Anemometry. Academic Press Inc., New York.

46) Dussan, E.B. 1976. The Moving Contact Line: The Slip Boundary Condition. J. Fluid Mech. 77:665-84.

47) Dussan, E.B. 1979. On the Spreading of Liquids on Solid Surface: Static and Dynamic Contact Lines. Ann. Rev. Fluid Mech. 11:371-400.

48) Dussan, E.B, Ramé, E., and Garoff, S. 1991. On Identifying the Appropriate Boundary Conditions at a Moving Contact Line: An Experimental Investigation. J. Fluid Mech. 231:97-116.

49) Esmail, M.N., and Ghannam, M.T. 1990. Air Entrainment and Dynamic Contact Angles in Hydrodynamics of Liquid Coating. Canadian J. Chem. Eng. 68:197-203.

50) Flexel, Inc. 1989. Technical data sheet for PUT and PUT 002 cellulose film base sheet, Flexel, Inc., Atlanta, GA.

51) Freeman, G.B. 1994. Personal Communication August 3, 1994. Georgia Tech. Research Institute - Electro-Optics, Environment, and Materials Laboratory.

52) Fowkes, F.M. 1972. Donor-Acceptor Interactions at Interfaces. J. Adhesion. Vol. 4, p.155-59.

53) Ghannam, M.T., and Esmail, M.N. 1990. Effect of Substrate Entry Angle on Air Entrainment in Liquid Coating. AIChE Journal. 36(8):1283-1286.

54) Ghannam, M.T., and Esmail, M.N. 1992. The Effect of Pre-wetting on Dynamic Contact Angles. Canadian Journal of Chemical Engineering. 70(4):408-412.

55) Ghannam, M.T., and Esmail, M.N. 1993. Experimental Study of the Wetting of Fibers. AIChE J. 39(2):361-365.

56) Glasstone, S., Laidler, K.J. and Eyring, H.J. 1941. The Theory of Rate Processes. McGraw-Hill, New York.

57) Gutoff, E.B., and Kendrick, C.E. 1982. Dynamic Contact Angles. AIChE J. 28(3):459-66.

58) Gutoff, E.B., and Kendrick,C.E. 1987. Low Flow Limits of Coatability on a Slide Coater. AIChE J. 33(1): 141-145.

59) Gutoff, E.B. 1992. Personal communication via letter dated January 22, 1992. Consulting Chemical Engineer, Brookline, MA.

60) Hartman, R.L. High Speed Curtain Coating Process and Apparatus. International Patent. WO 89/05477, Publication date June 15,1989.

61) Higgins, T.V. 1994. All Rays Lead to Geometrical Optics. Laser Focus World. 4:89-97.

62) Hoffman, R.L. 1983. A Study of the Advancing Interface, II. Theoretical Prediction of the Dynamic Contact Angle in Liquid-Gas Systems. J. Colloid Interface Sci. 94(2):470-486.

63) Huh, Y., and Scriven, L.E. 1971. Hydrodynamic Model of Steady Movement of a Solid/Liquid/Fluid Contact Line. J. Colloid Interface Sci. 35:85-101.

64) ICI Americas, Inc. 1990. Technical data sheet for Melinex™ 453 and 454, ICI Films Unit, Wilminton, DE.

65) Inverarity, G. 1969. Dynamic Wetting of Glass Fibre and Polmer Fibre. British Polymer J. 1:245-251.

66) Ishimi, K., Hikita, H., and Esmail, M.N. 1986. Dynamic Contact Angles on Moving Plates. AIChE J. 32(3):486-492.

67) Ishizaki, K., Chino, N., and Fuchigami, S. 1982. Air Entrainment in Coating Processes. Fundamentals of Coating Operations, Winter National AIChE Meeting, Orlando, February 28 - March 3.

68) ISO Standard 4287/1. 1984. Surface roughness - Terminology - Part 1: Surface and its Parameters.

69) Harrison, A. 1994. New Coating Technologies Combine High Speeds with Higher Quality. Pulp and Paper. 68(5):60-64.

70) Janczuk, B., Wójcik, W., and Zdziennicka, A. 1993. Determination of the Components of the Surface Tension of Some Liquids from Interfacial Liquid-Liquid Tension Measurements. J. Colloid Interface Sci. 157:384-93.

71) Justus, E.J. 1982. High Speed Size Press. U.S. Patent 4,340,623 (Issued July 20, 1982).

72) Kapitsa, P.L., and Kapitsa, S.P. 1949. Wave Flow of Thin Layers of a Viscous Fluid. Zh. Eksp. Teor. Fiz. 19(2):105-120.

73) Kennedy, B.S. 1975. PhD Thesis, Heriot-Watt University, Edinburgh, Scotland.

74) Kennedy, B.S., and Burley, R. 1977. Dynamic Fluid Interface Displacement and Prediction of Air Entrainment. J. Colloid Interface Sci. 62(1):48-62.

75) Kheshgi, H.S., and Scriven, L.E. 1983. Measurement of Liquid Film Profiles by Moiré Topography. Chem. Eng. Sci. 38(4):525-534.

76) Kisler, S. 1991. Electrostatics, Thin Film Coatings - Topics in Coating and Drying Technology. AIChE Short Course, Minneapolis, June 27-28.

77) Kistler, S.F., and Scriven, L.E. 1982. Paper 45d. AIChE Winter National Meeting, Orlando, FL.

78) Kistler, S.F. 1984. The Fluid Mechanics of Curtain Coating and Related Viscous Surface Flows with Contact Lines. Ph.D. Thesis. University of Minnesota, Minneapolis.

79) Kistler, S.F., Hanauska, C.P. and Scriven, L.E. 1984. Impingement Flow and Air Entrainment in Curtain Coating - Paper 17a. AIChE Winter National Meeting, Atlanta, Symposium on Fundamental Advances in Coating Operations.

80) Kistler, S.F. 1993. Hydrodynamics of Wetting - Chapter 6 in Wettability - Surfactant Science Seriesl, V.49. Berg, J.C., ed. New York, Marcel Dekker Inc.

81) Kroschwitz, J.I., ed. 1990. Concise Encyclopedia of Polymer Science and Engineering. New York, John Wiley and Sons, pp.1052-59.

82) Kroschwitz, J.I., ed. 1991. Kirk-Othmer Encyclopedia of Chemical Technology - 4th Edition. New York, John Wiley and Sons, pp.314-343.

83) Koplik, J., Banavar, J.R. and Willemsen, J.F. 1989. Molecular dynamics of fluid flow at solid surfaces. Phys. Fluids A. 1(5):791-794.

84) Koski, E. 1986. Size Press. U.S. Patent 4,565,155 (Issued Jan. 21, 1986).

85) Levi, S.M., and Akulov, V.I. 1964. A Study of Kinetic Wetting During Coating of Photographic Emulsion. Zh. Nauchn. Prikl. Photogr. Kinematogr. 9:124-25.

86) Levi, S.M. 1966. The Influence of Coating Conditions on Kinetic Wetting of a Moving Substrate by Emulsion. Zh. Nauchn. Prikl. Photogr. Kinematogr. 11:401-2.

87) Li, A.C., and Burns, J.R. 1992a. Effects of Air Entrainment on Coat Weight Distributions with an Enclosed Pond Applicator. 1992 TAPPI Coating

Conference Proceedings, Orlando, FL, May 17-21. Atlanta, TAPPI Press, pp.173-184.

88) Li, A.C., and Burns, J.R. 1992b. Effects of Air Entrainment on Coat Weight Distributions with an Enclosed Pond Applicator. Tappi J. 75(10):151-59.

89) Lin, L.C., and Hopfe, H.H. 1986. A surface roughness characterization system. Wear. 109:79-85.

90) Lu, Y., and Aidun, C.K. 1995. A Method for Rheological Analysis of Coating Suspensions at High Shear. TAPPI 1995 Coating Fundamentals Symposium, Dallas, TX, May 18-20. Atlanta, TAPPI Press, pp. 153-160.

91) Miller, C.A., and Ruckenstein, E. 1974. The Origin of Flow During Wetting of Solids. J. Colloid Interface Sci. 48(3):368-373.

92) Miyamoto, K. and Scriven, L.E. 1982. Breakdown of an Air Film Entrained by Liquid Coated on a Web - Paper 106F. AIChE Annual Meeting, Los Angeles, November 1982.

93) Miyamoto, K. 1986. On the Nature of Entrained Air Bubbles in Coating. AIChE Spring National Meeting, New Orleans, April 7-10, 1986. Mechanics of Thin-Film Coating.

94) Miyamoto, K. 1989. U.S. Pat. 4,842,900 Method and Apparatus for Coating. (Filed February 27'th 1987).

95) Miyamoto, K. 1991. On the Mechanism of Air Entrainment. Industrial Coating Research. 1:71.

96) Miyamoto, K. 1992. On Competing Instabilities in Air Entrainment. Poster Presentation, AIChE Spring National Meeting, New Orleans, March 29-April 2.

97) Mason, E.A., and Monchick, L. 1963. Survey of the Equation of State and Transport Properties of Moist Gases - Vol. 3, Humidity and Moisture, 1963 International Symposium on Humidity and Moisture. New York, Reinhold Publishing Co., p. 266.

98) Moffat, H.K. 1964. Viscous and Resistive Eddies Near a Sharp Corner. J. Fluid Mech. 18(1):1-18.

99) Moffat, R.J. 1985. Using Uncertainty in the Planning of an Experiment. J. of Fluids Eng. 107(6):173-78.

100) Moore, A.D. 1973. Electrostatics and its Applications. New York, John Wiley and Sons.

101) Moran, B. 1995. Moving the Ball Down the Field. Paper Age. 111(5):24.

102) Mues, W., Hens, J., and Boiy, L. 1989. Observation of a Dynamic Wetting Process Using Laser-Doppler Velocimetry. AIChE J. 35(9):1521-26.

103) Nakajima, K., and Miyamoto, K. 1993. European Patent Application 93106390.3. Coating Method Employing Ultrasonic Waves (Filed April 20, 1993).

104) O'Connell, A. 1989. Observations of Air Entrainment and the Limits of Coatability. Ph.D. Thesis, Heriot-Watt University, Edinburgh, Scotland.

105) OMEGA, 1995. The Temperature Handbook™ - Vol. 29. Stamford, CT, Omega Engineering Inc.

106) OPTIMAS, Bioscan. 1992. Bioscan Optimas V4.02 Technical Reference Manual. Edmonds, WA, Bioscan Incorporated.

107) Pantano, C.G. 1981. Surface Analysis - Techniques for Characterizing Extremely Thin Surface Layers are Being Applied in Both Research and Industry. Earth and Mineral Sciences - Penn State University. 51(2):p.1,14-18.

108) Perry, R.T. 1967. Fluid Mechanics of Entrainment through Liquid-Liquid and Liquid-Solid Junctions. Ph.D. Thesis, University of Minnesota. 120 pgs.

109) Perry, R.H. 1984. Perry's Chemical Engineering Handbook. Perry, R.H., Green, D.H. and Maloney, J.O., ed. 6th edition. New York, McGraw-Hill Book Company.

110) Petrov, J.G., and Sedev, R.V. 1985. On the Existence of a Maximum Speed of Wetting. Colloids and Surfaces. 13:313-322.

111) Powell, R.E., Roseveare, W.E., and Eyring, H. 1941. J. Ind. Eng. Chem. 33:430.

112) Powell, R.L., Seymour, J.D., McCarthy, M.J. and McCarthy, K.L. 1995. Nuclear Magnetic Resonance Imaging Measurements of Spherical Particle Suspensions During Flow. Tappi Proceedings of the 1995 Coating Fundamentals Symposium, Dallas, May 18-19. Atlanta, GA, TAPPI Press, p.179-184.

113) Ramirez, R.W. 1975. The FFT: Fundamentals and Concepts. Beaverton, OR. Tektronix, Inc., 146 p.

114) Rudemillller, G.R. 1989. A Fundamental Study of Boiling Heat Transfer Mechanisms Related to Impulse Drying. Atlanta, GA, Institute of Paper Science and Technology, Ph.D. Thesis, 265 p.

115) Ruschak, K.J. 1985. Coating Flows. Ann. Rev. Fluid Mech. 17:65-89.

116) Satas, D.- ed. 1984. Web Processing and Converting Technology and Equipment. New York, Van Nostrand Reinhold Publishing Co.

117) Schlueter, G.E., and Gumpertz, W.E. 1976. The Stereomicroscope - Instrumentation and Techniques. American Laboratory. 4:61-64,66,68-71.

118) Schreiber, T.P. 1979. Coordinated Surface Analysis with Scanning Electron Microscopy, Electron Probe Microanalysis, and Electron Spectroscopy. American Laboratory. 3:43-51.

119) Scriven, L.E. 1982. How Does Air Entrain at Wetting Lines. 1982 AIChE National Meeting, Symposium on Fundamentals of Coating Operations, Orlando, Unpublished work.

120) Scriven, L.E., and Suszynski, W.J. 1990. Take a Closer Look at Coating Problems. Chem. Eng. Prog. 86(9):24-29.

121) Scriven, L.E. 1991. AIChE Coating Process Fundamental Short Course. University of Minnesota, June 24-26.

122) Sedev, R.V., and Petrov, J.G. 1988/89. Influence of Geometry of the Three-Phase System on the Maximum Speed of Wetting. Colloids and Surfaces. 34:197-201.

123) Severtson, Y.C., and Aidun, C.K. 1995. Stability of Two Layer Stratified Flow in Inclined Channels: Applications to Air Entrainment in Coating Systems. Accepted for publication in the Journal of Fluid Mechanics.

124) Shaw, D.J. 1980. Introduction to Colloid and Surface Chemistry, 3rd Edition, London, England, Butterworth & Co. Ltd., 273p.

125) Siddiqui, J. 1994. Personal conversation with Dr. Junaid Siddiqui, ICI Americas, Inc., Hopewell, VA., April, 1994.

126) Sigma, 1994. Biochemical Organic Compounds for Research and Diagnositic Reagents, Sigma Chemical Company, St. Louis, MO , p. 375.

127) Silvi, N., and Dussan, E.B. 1985. On the Rewetting of an Inclined Surface by a Liquid. Phys. Fluids. 28(1):5-7.

128) Sommer, H. 1988. Applicating Systems for Coating ULWC and MFP Papers. 1988 Tappi Coating Conference Proceedings. pp. 131-137.

129) Stephanopoulos, G. 1984. Chemical Process Control: An Introduction to Theory and Practice. Englewood Cliffs, NJ, Prentice-Hall, Inc., 696p.

130) Schwartz, A.M., and Tejada, S.B. 1972. Studies of Dynamic Contact Angles on Solids. J. Colloid Interface Sci. 38(2):359-375.

131) Schweizer, P.M. 1988. Visualization of Coating Flows. J. Fluid Mech. 193:285-302.

132) Squire, H.B. 1933. On the Stability of Three-Dimensional Distribution of Viscous Fluid Between Parallel Walls. Proc. Roy. Soc., ser. A, vol. 142, pp.621-628.

133) Ström, G., Fredricksson, M., and Stenius, P. 1990. Kinetics of Oil Displacement from a Solid Surface by an Aqueous Solution. J. Colloid and Interface Science. 134(1):117-121.

134) Su, C. 1994. Low Volatile Organic Compounds Coatings: Surface Energy Considerations. Tappi J. 77(5):209-14.

135) Taylor, G.I. 1963. Cavitation of a Viscous Fluid in a Narrow Passage. 16:595-619.

136) Taylor, G.I., and McEwan, A.D. 1964. The Stability of a Horizontal Fluid Interface in a Vertical Electric Field. J. Fluid Mech. 22:1-15.

137) Taylor, J.A. 1993. Making and Breaking Bubbles - CAS System. Black Clawson Tech Info. Sheet. Black Clawson Corp., South Fulton, NY.

138) Teirfolk, J.E., and Laaja, V. 1995. An Empirical Study of Blade Coating at 2250 m/min. TAPPI 1995 Coating Conference Proceedings. Dallas, May 22-24. Atlanta, GA, TAPPI Press, pp. 9-18.

139) Triantafillopoulus, N.K., and Farrington, T.E. 1988. Flash X-Ray Radiography for Visualizing Coating Flows. 1988 TAPPI Coating Conference Proceedings. Atlanta, GA, TAPPI Press, pp. 47-52.

140) O'Brien, J. 1992. Valmet-Appleton Surface Finishing Technology is a Total Process. PaperAge. 105(5):22-23,38.

141) Veverka, P.J. 1991. Dynamic Contact Line Instability and Air Entrainment in Coating Systems. A-190 Master's Project, Institute of Paper Science and Technology, Atlanta, 55p.

142) Veverka, P.J. and Aidun, C.K. 1991a. Using High-Speed Cinematography to Obtain Visual Evidence on Air Entrainment in Low-Speed Roll Coating. Tappi J. 74(9):203-210 and 74(11):14.

143) Veverka, P.J., and Aidun, C.K. 1991b. Flow Visualization of Air Entrainment and Dynamic Contact Line Instability in Low Speed Roll Coating. 1991 TAPPI Engineering Conference Proceedings, Nashville, TN, Sept. 30 - Oct. 3. Atlanta, TAPPI Press, pp. 719-725

144) Vosteen, W.E. 1986. A Review of Current Electrostatic Measurement Techniques and Their Limitations. Electrical Overstress Exposition. San Jose, CA, April 24-26.

145) Wagner, C.D. 1991. The NIST X-Ray Photoelectron Spectroscopy (XPS) Database. U.S. Department of Commerce. NIST Technical Note 1289.

146) Waldpole, R.E., and Meyers, R.H. 1989. Statistics for Scientists and Engineers. New York, Macmillan Publishing Company, 765p.

147) Walter, J.C. ed. 1993. The Coating Processes. Atlanta, GA, TAPPI Press.

148) Weast, R.C. ed. 1988. CRC Handbook of Chemistry and Physics - 69th edition. Boca Raton, FL., CRC Press, Inc.

149) Weiss, H.L. 1977/1983. Coating and Laminating Machines. Milwaukee, Converting Technology Co.

150) Wilkinson, W.L. 1975. Entrainment of Air by a Solid Surface Entering a Liquid/Air Interface. Chem. Eng. Sci. 30:1227-1230.

151) Wu, S. 1975. Polymer Handbook. Brandrup, J. and Immergut, E.H., eds. New York, Wiley-Interscience. pp.VI. 411-434.

152) Wu, S. 1978. Polymer Blends, Vol. 1. Paul, D.R. and Newman, S., eds. New York, Academic Press, pp. 243-293.

153) Zhang, T.Y., and Suen, C.Y. 1984. A Fast Parallel Algorithm for Thinning Digital Images. Comm. ACM, 27(3):236-239.

CHAPTER X

ACKNOWLEDGMENTS

First, I would like to thank God for giving me the stamina and resources to continue when the road seemed impossible. Second, I would like to thank my wonderful wife, Ann Maura, for helping me to keep going, and sacrificing much during the past 3-1/2 years while completing this thesis. I would also like to thank my children Lynn-Marie and Christopher for helping their father to stay balanced, always amuse and providing a dose of reality. Finally I would like to thank my parents whose support and encouragement has helped during the many changes over the past 29 years.

My primary thesis advisor, Dr. Cyrus K. Aidun has provided much encouragement and challenge to solving difficult problems. I appreciate his guidance immensely. I would like to thank my committee members past and present, Dr. Pierre Brodeur, Dr. Jeff Colwell and Dr. Yulin Deng, Dr. Jeff Lindsay and Dr. L.E. Scriven (U. of M.) for remarks and guidance as this project has progressed.

There are a number of people who have made contributions to completing this project and it would be a disservice not to mention them all:

- Mr. Dan Dyer of Vashaw for providing optical advice.
- Dr. Dana McCowan and 3M Corp. for donating the handheld static meter.
- Dr. Junaid Siddiqui and Linda Stall of ICI Americas Inc. for coordinating and approving donation of poly(ethyleneterephthlate) substrate.
- The entire design group and maintenance department for innumerable requests filled - Warren Davis, Jerry Kloth, Chris Knerr, John Welch, Jerry Nunn, Bruce, Conrad Davis, Robert Noland.

• Mr. Greg Smallwood of the National Research Council of Canada for the Mie scattering program and insight into particle image velocimetry, which proved we could not use this technique without a more powerful laser.
• Fife Corporation and Mike Flannigan, Ron Schmidt for web guidance equipment.
• Magpowr Inc. and Don Baldree for the web tension equipment.
• Tidland Corporation and Mr. Bill Leistritz for the safety chucks and air cores.
• Champion International Tech. Center and Mr. Dick Bowden, Gerard Closset for allowing me to use the Surfanalyzer and the paper samples.
• Dr. Roger Wygant and Dr. Phillip Jones for giving permission to use the profilometer in Sandersville.
• John Hudson and Tom Miller at IPST for the immeasurable video and photography assistance.
• The Polaroid Corporation Electrostatics Group, namely Dr. Semyon Kisler and Mr. George Mooza for advice on electrostatic effects.
• Dr. Derek Page for insight into microscopy, optics and the scientific method.
• Dr. Timothy Patterson for encouragement and advice when the the world seemed like it was ending and also for answering my phone calls.

Finally, I would like to thank the Institute of Paper Science and Technology and its member companies for providing the funds and opportunity to conduct independent graduate studies. My hope is that IPST will grow and flourish for many years to come.

"Science is, in its source eternal; in its scope, unmeasurable: in its problem, endless: in its goal, unattainable."

Von Baer

APPENDIX I

BLAKE MODEL OF ADSORPTION/DESORPTION KINETICS DURING LIQUID/GAS DISPLACEMENT

I.1 Adsorption/Desorption Models

Blake (1966) was the first to apply a simple molecular event model to the three phase dynamic contact line (DCL) with the goal of finding a relationship between the actual contact angle, θ, and the wetting velocity, v, of the system. It should be pointed out that the success of this molecular-kinetic theory is not a priori evidence of its validity (Blake and Haynes 1969; Blake 1988; Blake 1993). The wetting velocity can be thought of from a Lagrangian reference (e.g. [Silvi and Dussan 1985] a moving coordinate system with the DCL of a liquid sheet flowing down an inclined plane) or an Eulerian reference (e.g. typical wire or film coating operation). This statistical approach is based is based on Eyring's theory of absolute reaction rates as applied to transport processes (Glasstone, S., Laidler, K.J., and Eyring, H.J. 1941; Powell, R.E.; Roseveare,W.E. and Eyring, H. 1941). The contact angle as measured through fluid 2 into fluid 1 in Fig. I.1 can minimally be described as a function of the equilibrium contact angle, θ_{eq}, the liquid viscosity , μ, interfacial surface tension, γ_{12}, as well as the wetting velocity, v, and thus,

$$\theta = \theta\left(\theta_{eq}, \mu, \gamma_{12}, v, \ldots\right) \qquad [I.1]$$

The system to be modeled must first be described. When fluid 2 is displacing fluid 1 at the three phase DCL, this is considered the forward direction with a

frequency of $\kappa+$. Displacement of fluid 1 by fluid 2 is the reverse direction with frequency $\kappa-$. It is not essential for one phase to be completely displaced adjacent to the solid surface but because any entrained film is of molecular dimensions this is

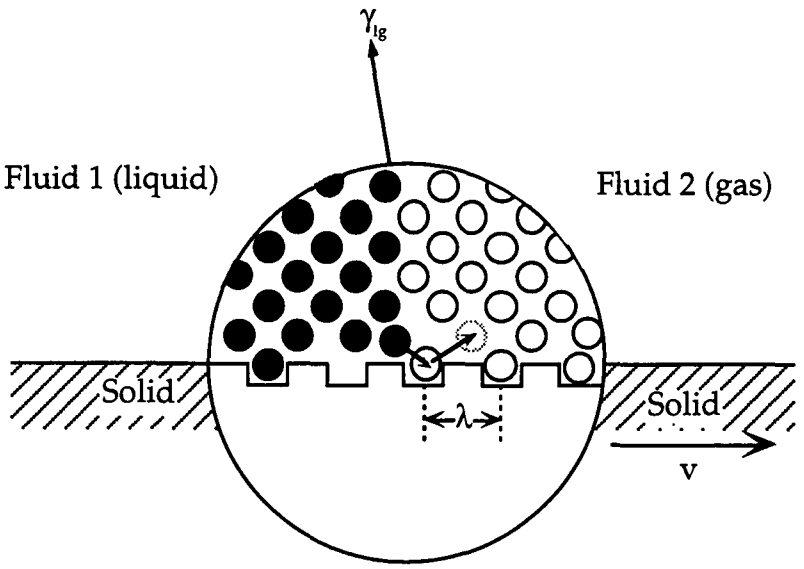

Figure I.1. Adsorption desorption model of molecular displacement within the three phase zone. Adapted from Blake (1993, p.266).

not considered to be macroscopic entrainment. The solid interface has n adsorption sites per unit area and the average length of each molecular displacement is λ as shown in Fig. I.1. At equilibrium, the net rate of displacement will be zero and thus,

$$\kappa+ = \kappa- = \kappa_w^\circ \qquad [I.2]$$

By using the Eyring's theory of absolute reaction rates we can relate the equilibrium frequency κ_w° to the molar activation free energy of wetting ΔG_w^* through the expression,

$$\kappa_w^\circ = \left(\frac{kT}{h}\right) exp\left(\frac{\Delta G_w^*}{NkT}\right) \qquad [I.3]$$

with k,T,h and N having their usual significance and defined in the notation section. Equation [I.3] could have also been written in terms of the partition functions and activation energy (Blake and Haynes 1969; Blake 1993). By applying a irreversible forward-directed shear stress to the molecules in the three phase zone, molecular displacements in the forward direction will be greater than in the reverse, i.e. $\kappa_+ > \kappa_-$, and the DCL will advance with respect to either reference frames previously mentioned. The irreversible shear stress per unit displacement of unit length of the DCL is w, and the work done on each site is w/n. With symmetrical energy barriers in the forward and reverse directions, w/2n is expended in each direction and thus,

$$\kappa_+ = \left(\frac{kT}{h}\right) exp\left(\frac{-\Delta G_w^*/N - w/2n}{kT}\right) \qquad [I.4]$$

$$\kappa_- = \left(\frac{kT}{h}\right) exp\left(\frac{-\Delta G_w^*/N + w/2n}{kT}\right) \qquad [I.5]$$

with the net frequency of molecular displacement as,

$$\kappa_w = \kappa_+ - \kappa_- = 2\kappa_w^\circ \, sinh(w/2nkT) \qquad [I.6]$$

By multiplying the net frequency of each molecular displacement by the average length, λ, the wetting velocity, v, is therefore,

$$v = 2\kappa_w^\circ \lambda \, sinh(w/2nkT) \qquad [I.7]$$

The next step is to achieve a tractable solution assuming that the irreversible shear stress is provided by out of balance interfacial tension forces given by,

$$w = \gamma_{12}(cos\theta_{eq} - cos\theta) \qquad [I.8]$$

Miller and Ruckenstein (1974) agree with this type of relationship as a driving force. The interfacial tension γ_{12} is assumed to remain constant and in general $\theta \neq \theta_{eq}$ (Blake 1993). Substitution of Eq. [I.8] into [I.7] results in the desired form of $v=v(\theta)$.

$$v = 2\kappa_w^{\circ}\lambda sinh\left[\frac{\gamma_{12}\left(cos\theta_{eq} - cos\theta\right)}{2nkT}\right] \qquad [I.9]$$

Two limiting cases of Eq. [I.9] exist dependent on the mathematical properties of the hyperbolic sine function. It follows that Eq. [I.10] becomes approximately valid if the argument of sinh in Eq. [I.9], i.e. the expression in brackets is sufficiently small and Eq. [I.11] becomes approximately valid if the argument of sinh in Eq. [I.9] is sufficiently large.

$$v = \kappa_w^{\circ}\lambda\gamma_{12}\frac{\left(cos\theta_{eq} - cos\theta\right)}{nkT} \because \gamma_{12}\left(cos\theta_{eq} - cos\theta\right) \ll 2nkT \qquad [I.10]$$

$$v = \kappa_w^{\circ}\lambda exp\left[\frac{\gamma_{12}\left(cos\theta_{eq} - cos\theta\right)}{2nkT}\right] \because \gamma_{12}\left(cos\theta_{eq} - cos\theta\right) \gg 2nkT \qquad [I.11]$$

Designating ($cos\theta_{eq}$ - $cos\theta$) as Δcos, Schwartz and Tejada (1972) called linear plots of v vs. Δcos as Haynes plots to indicate that Eq.[I.10] was operative. Linear plots of exp(Δcos) vs. v indicate Eq. [I.11] is operative.

I.2 Prediction of the Maximum Wetting Speed

A logical use of Eq. [I.9] relevant to air entrainment is the prediction of the maximum speed of wetting. The criteria that θ approaches 180° as a condition for

air entrainment has been discussed by many researchers (Deryagin and Levi 1964; Inverarity 1969; Burley and Kennedy 1976; Blake and Ruschak 1979; Gutoff and Kendrick 1982, 1987 Ghannam and Esmail 1990; Blake; Clark and Ruschak 1994) although there is still both experimental (Mues, Hens and Boiy 1989; Ghannam and Esmail 1992) and theoretical disagreement with this criteria. The maximum limit can be found by differentiating Eq. [I.9] with respect to θ. By substituting θ=180°, the maximum wetting velocity is,

$$v_{180^\circ} = 2\kappa_w^\circ \lambda \sinh\left[\frac{\gamma_{12}\left(\cos\theta_{eq}+1\right)}{2nkT}\right] \qquad [I.12]$$

The use of Eq.[I.12] still requires that either molecular parameters κ_w° and λ, κ_w° and n, or ΔG_w^* and n be calculated from experimental data since $\lambda \sim n^{-1/2}$ for an isotropic system and Eq.[I.3] gives $\kappa_w^\circ = \kappa_w^\circ(\Delta G_w^*)$.

Blake points out that the transition to macroscopic entrainment is quite abrupt (Blake 1966, 1988, 1993) because of the different length scales[1], as well as a displacement regime controlled by surface and capillary forces to one controlled by hydrodynamics.

I.3 Comparison with Experiment

Blake (1988,1993) compared Eq.[I.9] vs. the experimental data of Kennedy (1975) as well as Burley and Kennedy (1976 a,b) to show the utility of the molecular

[1] The length scale for the molecular displacement model is on the order of nanometers, whereas it is millimeters for macroscopic air entrainment.

kinetic theory of wetting. Equation [I.9] accounts of the dependence of θ on v at high and low velocities with the calculated value of $v_{180°}$ = 0.57 cm/sec close to the experimental value. The theoretical underpinnings of Blake (1966, 1988, 1993) and Blake and Haynes (1969) have not been proven a priori but the mathematical form that results appears to model the data well. For example, Cox (1976) analyzed displacement of one fluid with another using a three region matched expansion near the DCL. He assumed that inertial effects are negligible and slip must occur at distances of order s from the contact line to remove the non integratable stress. The perturbation parameter, ε=s/R, is much less than unity and it is also assumed that the surface tension effects dominate over viscous effects with λ_μ defined in Eq. [I.13].

$$\lambda_\mu \equiv \mu_2 / \mu_1 \qquad \text{[I.13]}$$

Cox's model with natural log, sin and $\sin^2$ terms achieves the same behavior for θ_m, the macroscopic contact angle, with $\lambda_\mu \ll 1$ as with Blake's adsorption/desorption model. Thus the mathematical form of the equation must contain some type of logarithmic dependance on θ to adequately model actual experimental data.

I.4 Combined Adsorption/Desorption and Viscous Flow Model

The adsorption/desorption step may not be the rate-determining step so it could be assumed that ΔG_w^* has both surface and viscous contributions (Hoffman 1983; Blake 1988). Invoking Eyring's theory again leads to,

$$\mu_i = \left(\frac{h}{V_i}\right) exp\left(\frac{\Delta G^*_{vis,i}}{NkT}\right) \qquad [I.14]$$

In Eq. [I.14], $\Delta G^*_{vis,i}$ and Vi are the molar activation free energy of bulk flow and Vi, the value of the "unit of flow" for phase i. For two phase displacement we write,

$$\Delta G^*_W = \Delta G^*_{vis,1} + \Delta G^*_{vis,2} + \Delta G^*_S \qquad [I.15]$$

By using the same analysis[2] used to solve Eqs. [I.2-9] and assuming that the displaced phase is a gas, i.e. $\Delta G^*_{vis,2} \approx 0$, we arrive at an expression with both surface and viscous terms relating v and θ.

$$v = 2\kappa_s^\circ \lambda \left(\frac{h}{\mu_1 V_1}\right) sinh\left[\frac{\gamma_{12}\left(cos\,\theta_{eq} - cos\,\theta\right)}{2nkT}\right] \qquad [I.16]$$

$$\kappa_w^\circ = \kappa_s^\circ \left(\frac{h^2}{\mu_1 V_1 \mu_2 V_2}\right) \qquad [I.17]$$

The term K_s° represents the frequency of molecular displacement at equilibrium when only retarded by surface forces and related to K_w° through Eq. [I.17]. It is important to note that Eq. [I.16] predicts that with all other factors held constant that decreasing the viscosity will lead to an increase in maximum velocity, $v_{180°}$, which is in accord with experimental observations.

---

[2] For a full derivation, see Blake (1988, 1993).

I.5 Combined Adsorption/Desorption Viscous and Hydrodynamic Model

The theories advanced thus far in Eq. [I.19] and [I.9] still do not explain that for certain flows θ' approaches 180° at velocities higher than expected (Blake 1988, 1993). Blake (1988) advanced the idea that the viscous drag of the liquid is able to act directly on the molecules of the three phase zone and that this stress is proportional to $\alpha_i^* \mu_i v$, where α_i is a numerical coefficient of order unity. The total wetting driving force is thus,

$$v = \gamma_{12}(\cos\theta^\circ - \cos\theta) + \left(\alpha_1^*\mu_1 - \alpha_2^*\mu_2\right)|v| \qquad [I.19]$$

The simplified equation linking v and θ and assuming that phase 2 (gas) viscosity is negligible is

$$v = 2\kappa_s^\circ\lambda\left(\frac{h}{\mu_1 V_1}\right)\sinh\left[\frac{\gamma_{12}\left(\cos\theta_{eq} - \cos\theta\right) + \alpha_1^*\mu_1|v|}{2nkT}\right] \qquad [I.20]$$

Macroscopic entrainment of the displaced phase is postponed according to Eq. [I.20] compared with Eq. [I.9] and [I.16] which is also in accord with experiment.

I.6 Summary of the Kinetic Theory of Wetting

The theory advanced by Blake (1966, 1988, 1993) and Blake and Haynes (1969) sucessfully accounts for the effect of :

- surface tension
- viscosity
- fluid flow hydrodynamics

Although their physical basis still has not been proven, they suggest the correct slip term is non linear and may be described in terms of molecular kinetics (Blake 1988, 1993). One difficulty with this theory is the strong sensitivity of θ to $\kappa_s^{\circ}\lambda h / V_1$ and nkT as well as the fact that $\theta=\theta(v)$ is a material function that needs to be measured for each liquid/solid system.

APPENDIX II

BLUEPRINTS FOR THE EXPERIMENTAL PAPER FILM COATER

This Appendix contains the computer assisted drafting (CAD) blueprints generated using the program FASTCAD V.2.72 from Evolution Computing, Tempe, AZ (602-967-8633).

The blueprint descriptions are as follows:

DWG. NO. A490-07-1D-01, FULLHD.FCD - Veverka coater head #1
DWG. NO. A490-07-1D-02, LRWALL.FCD - Veverka coater head #1
DWG. NO. A490-07-1D-03, BACK2.FCD - Veverka coater head #1
DWG. NO. A490-07-1D-04, BDBOT2.FCD - Veverka coater head #1
DWG. NO. A490-07-1D-05, FULLWIPE.FCD - Veverka wiper #1
DWG. NO. A490-07-1D-06, BLADE.FCD - Veverka wiper #1
DWG. NO. A490-07-1D-07, BLADHLD.FCD - Veverka wiper #1
DWG. NO. A490-07-1D-08, FULLSHOE.FCD - Veverka web delivery #1
DWG. NO. A490-07-1D-09, TRANSDUC.FCD - Veverka tension mounts
DWG. NO. A490-07-1D-10, TOPPREC.FCD - Veverka top precision bearings
DWG. NO. A490-07-1D-11, BOTPREC.FCD - Veverka bottom precision bearings
DWG. NO. A490-07-1D-12, GUSSET.FCD - Veverka gusset bracket/post caps
DWG. NO. A490-07-1D-13, ROLL.FCD - Veverka precision rolls
DWG. NO. A490-07-1D-14, WINPOS.FCD - Veverka window holder
DWG. NO. A490-07-1D-15, FRPOST.FCD - Veverka front right post
DWG. NO. A490-07-1D-16, FLPOST.FCD - Veverka front left post
DWG. NO. A490-07-1D-17, RRPOST.FCD - Veverka rear right post
DWG. NO. A490-07-1D-18, RLPOST.FCD - Veverka rear left post
DWG. NO. A490-07-1D-19, SHOEPLT.FCD - Veverka head shoe
DWG. NO. A490-07-1D-20, RUBROLL.FCD - Veverka rewind roll blanks
DWG. NO. A490-07-1D-21, WELDSTND.FCD - Veverka un/rewind stand
DWG. NO. A490-07-1D-22, MACHSTD.FCD - Veverka un/rewind stand machining
DWG. NO. A490-07-1D-23, MOTORPLT.FCD - Veverka motor/brake mounts
DWG. NO. A490-07-1D-24, BEARBRKT.FCD - Veverka bearing bracket
DWG. NO. A490-07-1D-25, SFTYMNT.FCD - Veverka bearing bracket
DWG. NO. A490-07-1D-26, MICROHLD.FCD - Veverka microscope mount
DWG. NO. A490-07-1D-27, PUMPWELD.FCD - Veverka pump base
DWG. NO. A490-07-1D-28, BLADMOD.FCD - Veverka wiper#2
DWG. NO. A490-07-1D-29, FIFE.FCD - Fife web guide bracket
DWG. NO. A490-07-1D-30, INSERT.FCD - Cavity insert
DWG. NO. A490-07-1D-31, BACK3.FCD - Veverka coater head#2
DWG. NO. A490-07-1D-32, BDBOT3.FCD - Veverka coater head#2

DWG. NO. A490-07-1D-33, FULLHD3.FCD - Veverka coater head#2
DWG. NO. A490-07-1D-34, LOCAMIC.FCD - Veverka microscope/LOCAM holder#1
DWG. NO. A490-07-1D-35, LOCAMIC2.FCD - Veverka microscope/LOCAM holder#2
DWG. NO. A490-07-1D-36, LOCAMIC3.FCD - Veverka microscope/LOCAM holder#3
DWG. NO. A490-07-1D-37, LOCAMIC4.FCD - Veverka microscope/LOCAM holder#4

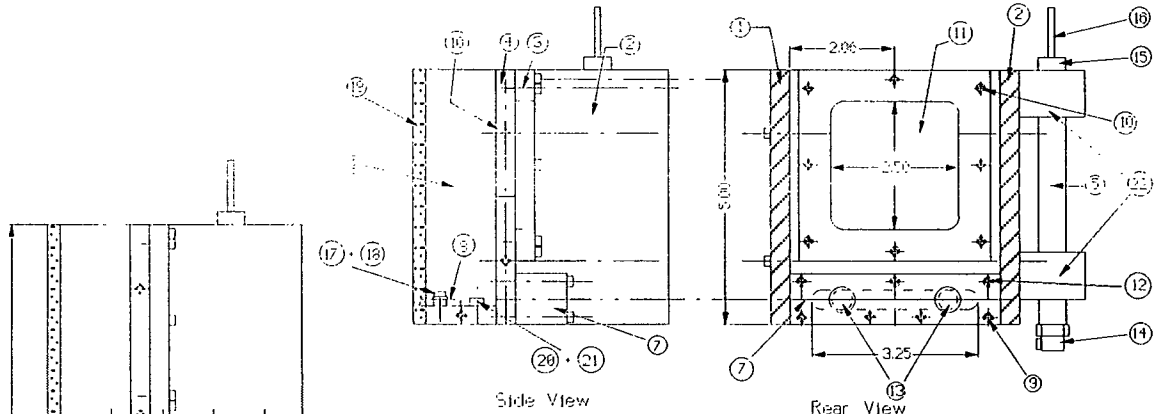

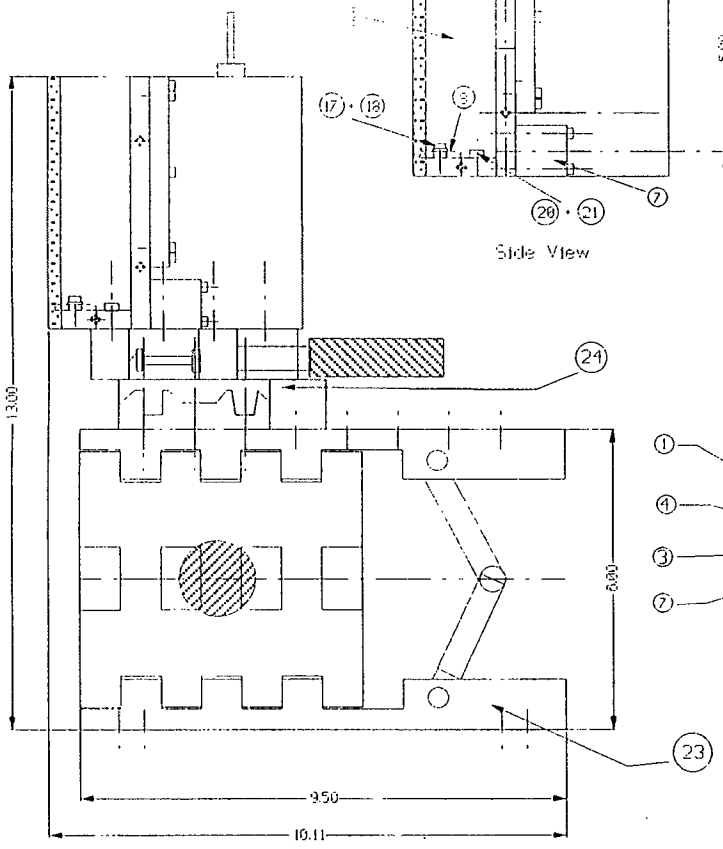

Side View w/x,y,z translators

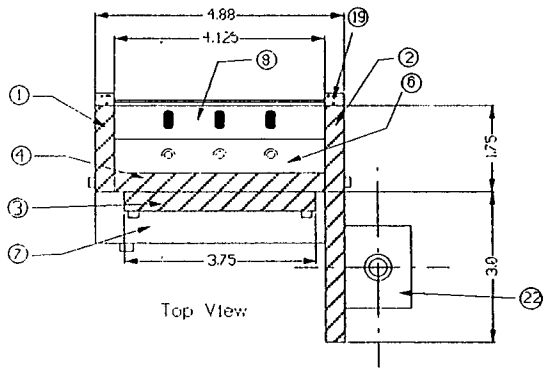

Top View

NOTES:
1) Horizontal translator part#23 can provide 23 lb. of force
2) Small letters indicate same socket head type
3) See additional drawings for individual parts
4) Part 25 can by any type of non-marring clamp and does not have to be size No.5

PART#	DESCRIPTION	MATERIAL	QTY
1	Left Wall	3/8" Acrylic	1
2	Right Wall	3/8" Acrylic	1
3	Glass Backing/Rear Wall	3/8" Acrylic	1
4	Rear Wall	3/8" Acrylic	1
5	Level Tube	1/4" Clr PVC	1
6	Bottom Wall	3/8" Acrylic	1
7	Distribution Chamber	1" Acrylic	1
8	Blade	1/4" Teflon	2
9	No.8x1-3/4" Socket HH	SS	4
10	No.8x3/4" Socket HH	SS	14
11	3"x3"x1/8",0.25"R Glass	SI-UVA Quartz	1
12	No.8x1-1/4" Socket HH	SS	3
13	1/4"MNPT Quick Connect	Delrin	2
14	1/8"MNPT Quick Connect	Delrin	2
15	Sensor Holder	3/4"D Acrylic	1
16	Fiber Optic Sensor	N/A	1
17	No.10x5/8" Socket HH	SS	3
18	No.10 Washer	SS	3
19	3/16"x3/8" Closed Cell	Vinyl	2
20	1/4"-20x3/4" Socket HH	SS	3
21	1/4" ID O-Ring	Butyl rubber	3
22	Pipe Clamp	Polypropulene	2
23	Newport Model 431-2	Exist	2
24	Lab Jack	Exist	1
25	No.5x1/2" Bolt	Nylon	1

REV	REVISIONS	DATE
A	FINAL DRAWING	12/14/92
	VEVERKA COATER HEAD	

UNLESS OTHERWISE SPECIFIED
DIMENSION STANDARD INCHES METRIC mm
TOLERANCES ON
3 PL DECIMALS ± .005
2 PL DECIMALS ± .010
ANGLES ± 0.5°
FRACTIONS ± 1/32
BREAK SHARP CORNERS
√ - SURFACE FINISH OF 125 OR BETTER

SIGNATURES
DRAWN P. VEVERKA 25/8/92
CHECKED
DESIGNER P. VEVERKA 8/92

CAD FILE #
\VEVPETA490\FULLHD\FCD\D

THE INSTITUTE OF PAPER SCIENCE AND TECHNOLOGY
575 14 "STREET N.W.
ATLANTA, GEORGIA 30318

VEVERKA COATER HEAD #1

SCALE ACT.
DWG NO A490-07-1D-01

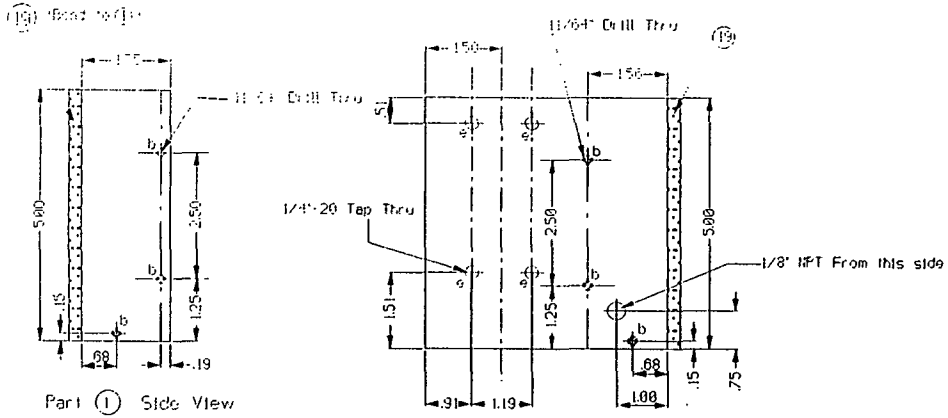

Part ② Side View

Part ① Side View

NOTES:
1) See drawing #1 in reference to No.5 tap on rail. 5 1/2 need for size of nylon bolt available at IPST. Used to position sensor vertically.

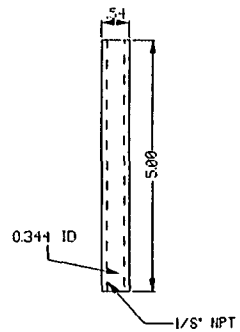

Part ⑤ Side View

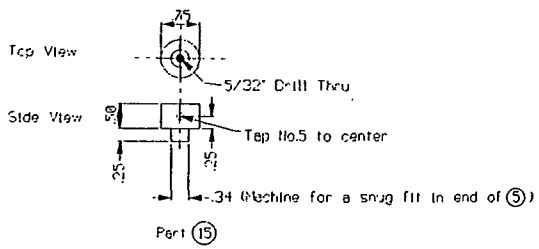

Part ⑮

REV	REVISIONS	DATE
A	FINAL DRAWING	12/15/92
	LEFT, RIGHT WALLS & LEVEL TUBE	

UNLESS OTHERWISE SPECIFIED
DIMENSION STANDARD
TOLERANCES ON
2 PL DECIMALS ± .00
3 PL DECIMALS ± .002
ANGLES ± .5°
FRACTIONS ± 1/32
BREAK SHARP CORNERS
√ - SURFACE FINISH OF 125 OR BETTER

SIGNATURES

DRAWN	P. VEVERKA	10/28/92
CHECKED		
DESIGNER	P. VEVERKA	9/92

CAD FILE #
\VEVPETA199\DRVALL.PCD/D

THE INSTITUTE OF PAPER SCIENCE AND TECHNOLOGY
575 14 "STREET N.W.
ATLANTA, GEORGIA 30318

VEVERKA COATER HEAD #1

SCALE ACT.
DWG NO A198-07-ID-02

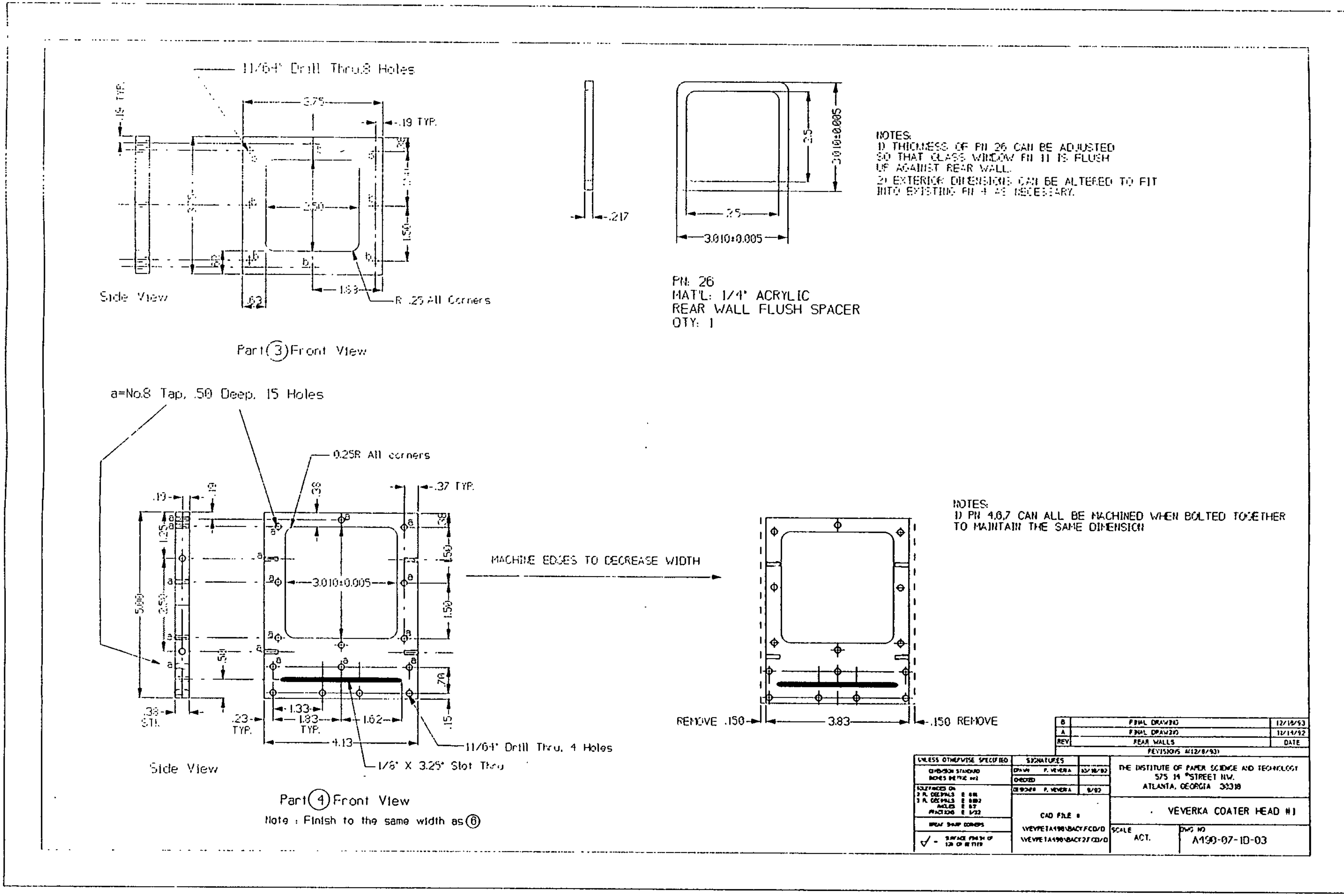
11/64" Drill Thru.8 Holes
.19 TYP.
R .25 All Corners
Side View
Part (3) Front View
PN: 26
MAT'L: 1/4" ACRYLIC
REAR WALL FLUSH SPACER
QTY: 1
NOTES:
1) THICKNESS OF PN 26 CAN BE ADJUSTED SO THAT GLASS WINDOW PN 11 IS FLUSH UP AGAINST REAR WALL.
2) EXTERIOR DIMENSIONS CAN BE ALTERED TO FIT INTO EXISTING PN 4 AS NECESSARY.
a=No.8 Tap, .50 Deep, 15 Holes
0.25R All corners
.37 TYP.
MACHINE EDGES TO DECREASE WIDTH
NOTES:
1) PN 4,6,7 CAN ALL BE MACHINED WHEN BOLTED TOGETHER TO MAINTAIN THE SAME DIMENSION
REMOVE .150
.150 REMOVE
11/64" Drill Thru, 4 Holes
1/8" X 3.25" Slot Thru
Side View
Part (4) Front View
Note : Finish to the same width as (6)
FINAL DRAWING
REAR WALLS
REVISIONS
THE INSTITUTE OF PAPER SCIENCE AND TECHNOLOGY
575 14 STREET NW.
ATLANTA, GEORGIA 30318
VEVERKA COATER HEAD #1
CAD FILE #
SCALE
ACT.
DWG NO
A190-07-10-03

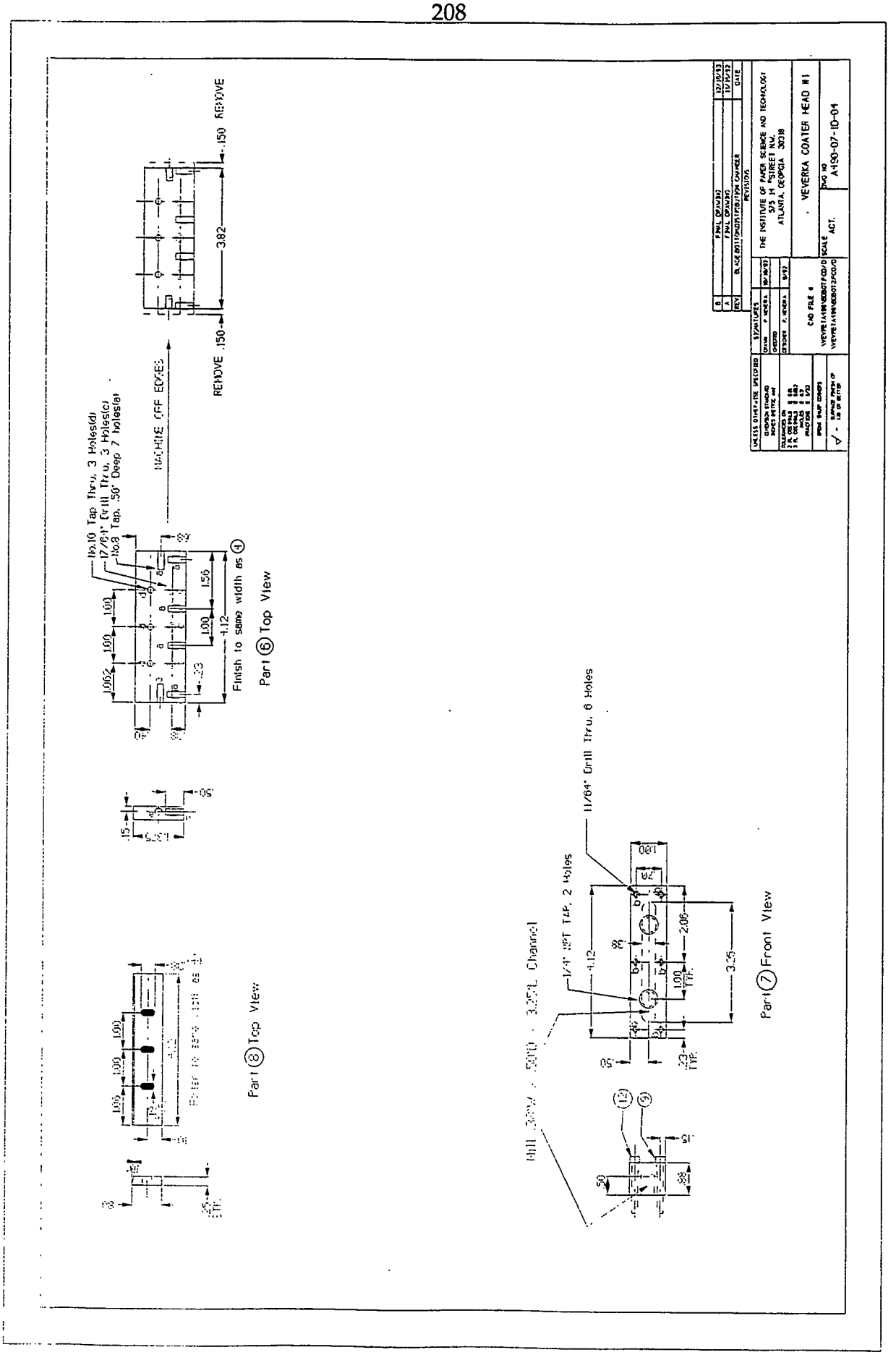
No.10 Tap Thru, 3 Holes(d)
17/64" Drill Thru, 3 Holes(c)
No.8 Tap, .50" Deep 7 Holes(e)
MACHINE OFF EDGES
REMOVE .150
.150 REMOVE
382
Finish to same width as 4
Part 6 Top View
Part 8 Top View
Part 7 Front View
1/4" NPT TAP, 2 Holes
11/64" Drill Thru, 6 Holes
3.25
2.06
4.12
1.00 TYP.
.23 TYP.
THE INSTITUTE OF PAPER SCIENCE AND TECHNOLOGY
575 14TH STREET N.W.
ATLANTA, GEORGIA 30318
VEVERKA COATER HEAD #1
A490-07-10-04

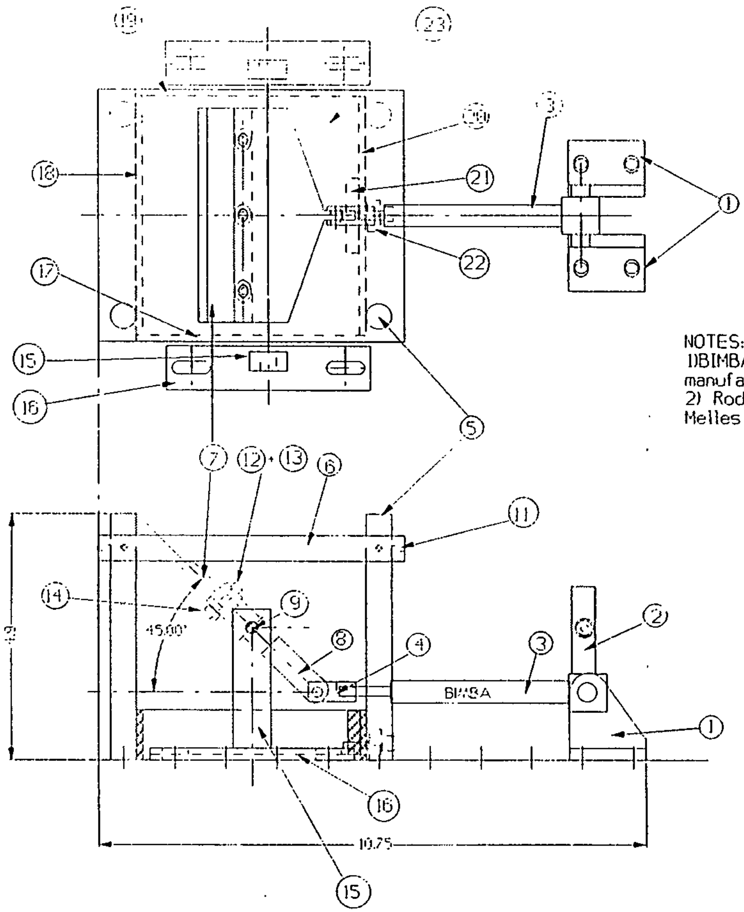

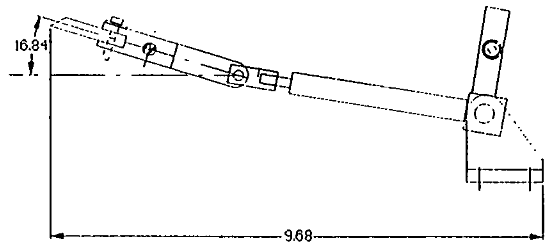

Wiper Blade In Retracted Position

NOTES:
1)BIMBA parts order directly from manufacturer
2) Rods for part 5 order from Melles Griot 07 REP 005

PART#	DESCRIPTION	MATERIAL	QTY
1	Trunnion Brackets	SS/BIMBA	1
2	FOPIK Flow Control	SS/BIMBA	1
3	7/16" Trunnion Air Cyl.	SS/BIMBA	1
4	D-850 Piston Rod Clevis	SS/BIMBA	1
5	.5" Mounting Post	SS	1
6	Blade Backing	1/2" Teflon	1
7	Blade	1/4" Teflon	2
8	Blade Holder	SS	1
9	Blade Holder Rod	1/4" OD SS	2
10			
11	No.8x3/8" Set Screw	SS	8
12	No.8x1" Socket HH	SS	3
13	No.8 Washer	SS	3
14	No.8 Hex Nut	SS	3
15	Blade Holder Arm	SS	1
16	Blade Holder Base	SS	1
17	Left Wall Pan	1/8" Acrylic	1
18	Front Wall Pan	1/8" Acrylic	1
19	Right Wall Pan	1/8" Acrylic	1
20	Rear Wall Pan	1/8" Acrylic	1
21	Connector Reinforce	1/4" Acrylic	1
22	1/8"MNPT Quick Connect	Delrin	1
23	Pan Bottom	1/8" Acrylic	1
24			
25			

REV	REVISIONS	DATE
A	PRELIMINARY DRAWING VEVERKA WIPER ASSEMBLY	11/27/92

THE INSTITUTE OF PAPER SCIENCE AND TECHNOLOGY
500 10th STREET NW.
ATLANTA, GEORGIA 30318

SIGNATURES: DRAWN P. VEVERKA 11/27/92; CHECKED G. ROTH; DESIGNER P. VEVERKA 8/92

VEVERKA WIPER #1

SCALE ACT. DWG NO A190-07-10-05

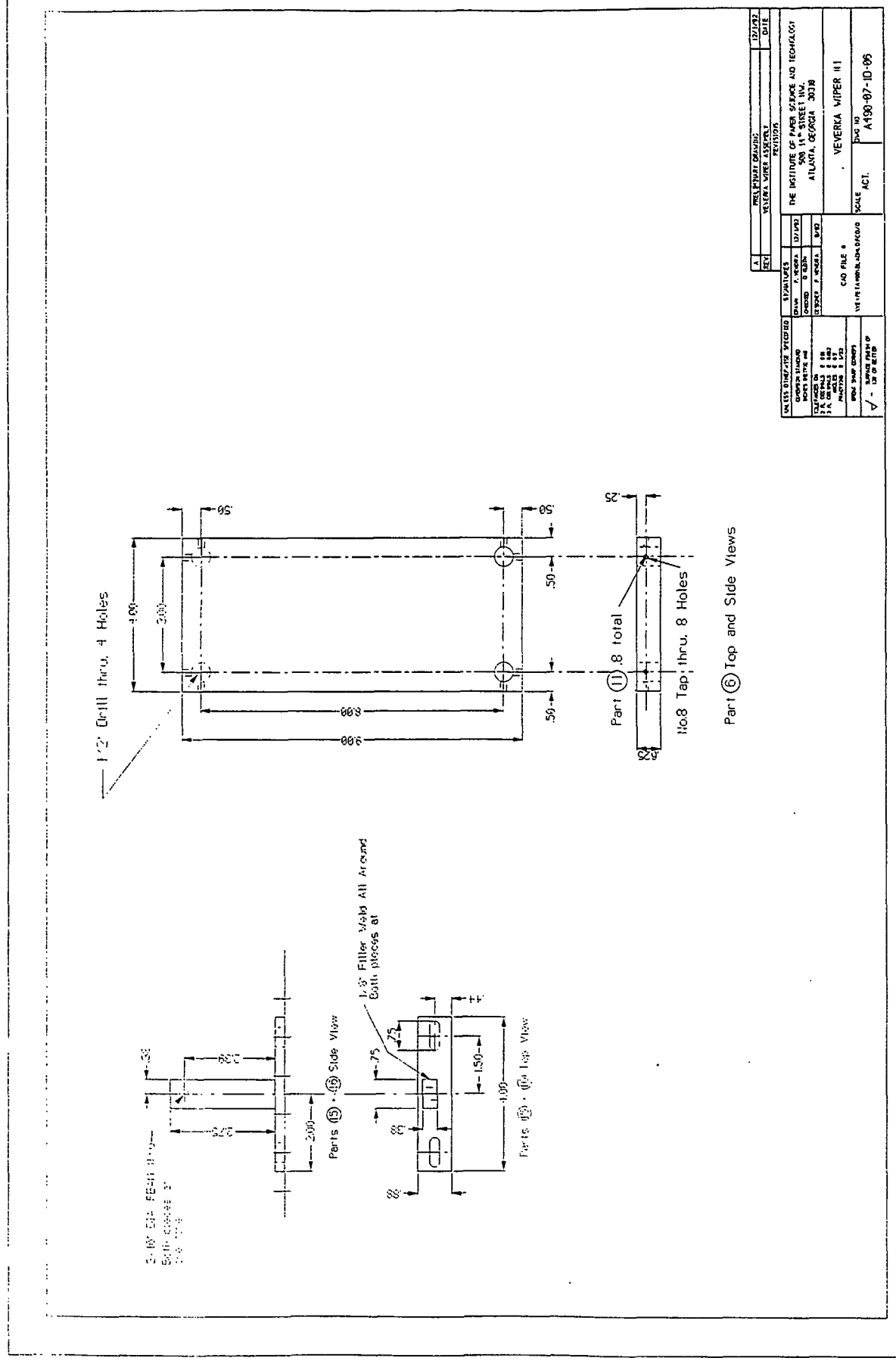
PRELIMINARY DRAWING
VEVERKA WIPER ASSEMBLY
REVISIONS
A
REV
12/1/92
DATE
UNLESS OTHERWISE SPECIFIED
SIGNATURES
DRAWN
CHECKED
ENGR APPR.
MFG APPR.
12/1/92
THE INSTITUTE OF PAPER SCIENCE AND TECHNOLOGY
500 14TH STREET NW.
ATLANTA, GEORGIA 30318
CAD FILE #
VEVERKA WIPER III
SCALE
ACT.
DWG NO
A190-07-ID-06
1/2" Drill thru, 4 Holes
Part (11) 8 total
No.8 Tap thru, 8 Holes
Part (6) Top and Side Views
Parts (15) Side View
1/8" Fillet Weld All Around Both pieces at
Parts (15) Top View

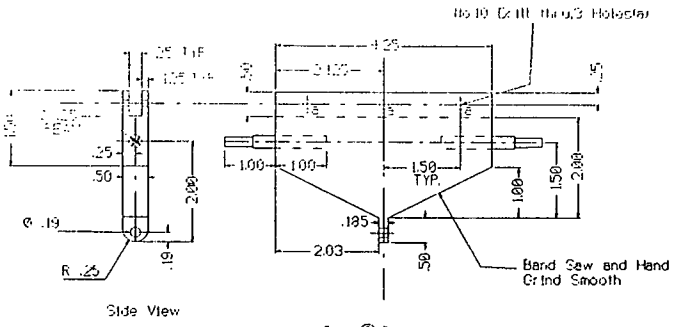

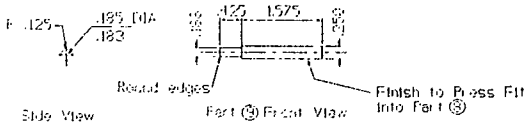

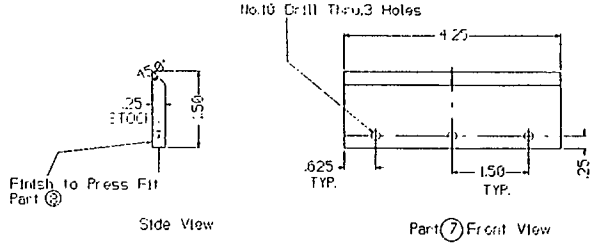

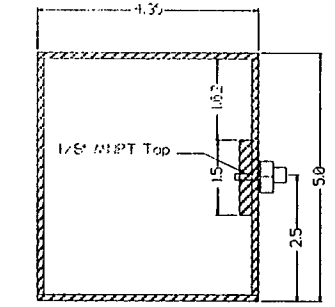

Notes:
1) Bond box together prior to tapping. Box must be watertight.

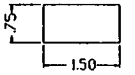

Part ㉑ Front View

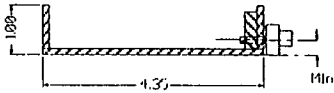

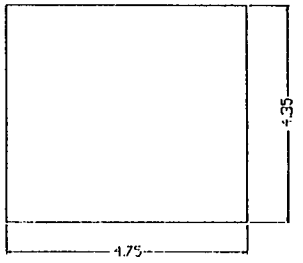

Part ㉓ Top View

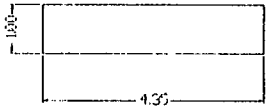

Part ⑰ and ⑲ Front View

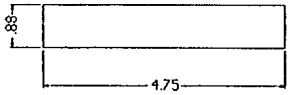

Part ⑱ and ⑳ Front View

A	PRELIMINARY DRAWING	12/7/02	
REV	VEVERKA WIPER ASSEMBLY	DATE	
	REVISIONS		

UNLESS OTHERWISE SPECIFIED DIMENSION STANDARD INCHES METRIC mm TOLERANCES ON 3 PL DECIMALS E ±.01 2 PL DECIMALS E ±.002 ANGLES E 0.5° FRACTIONS E 1/32 BREAK SHARP CORNERS √ - SURFACE FINISH OF 125 OR BETTER	SIGNATURES DRAWN P. VEVERKA 12/7/02 CHECKED G. ELOTH DESIGNER P. VEVERKA 9/02 CAD FILE # VEVERKAWIPERBLADEFCD#0	THE INSTITUTE OF PAPER SCIENCE AND TECHNOLOGY 500 10TH STREET NW. ATLANTA, GEORGIA 30318 VEVERKA WIPER #1 SCALE ACT. DWG NO A490-07-10-07

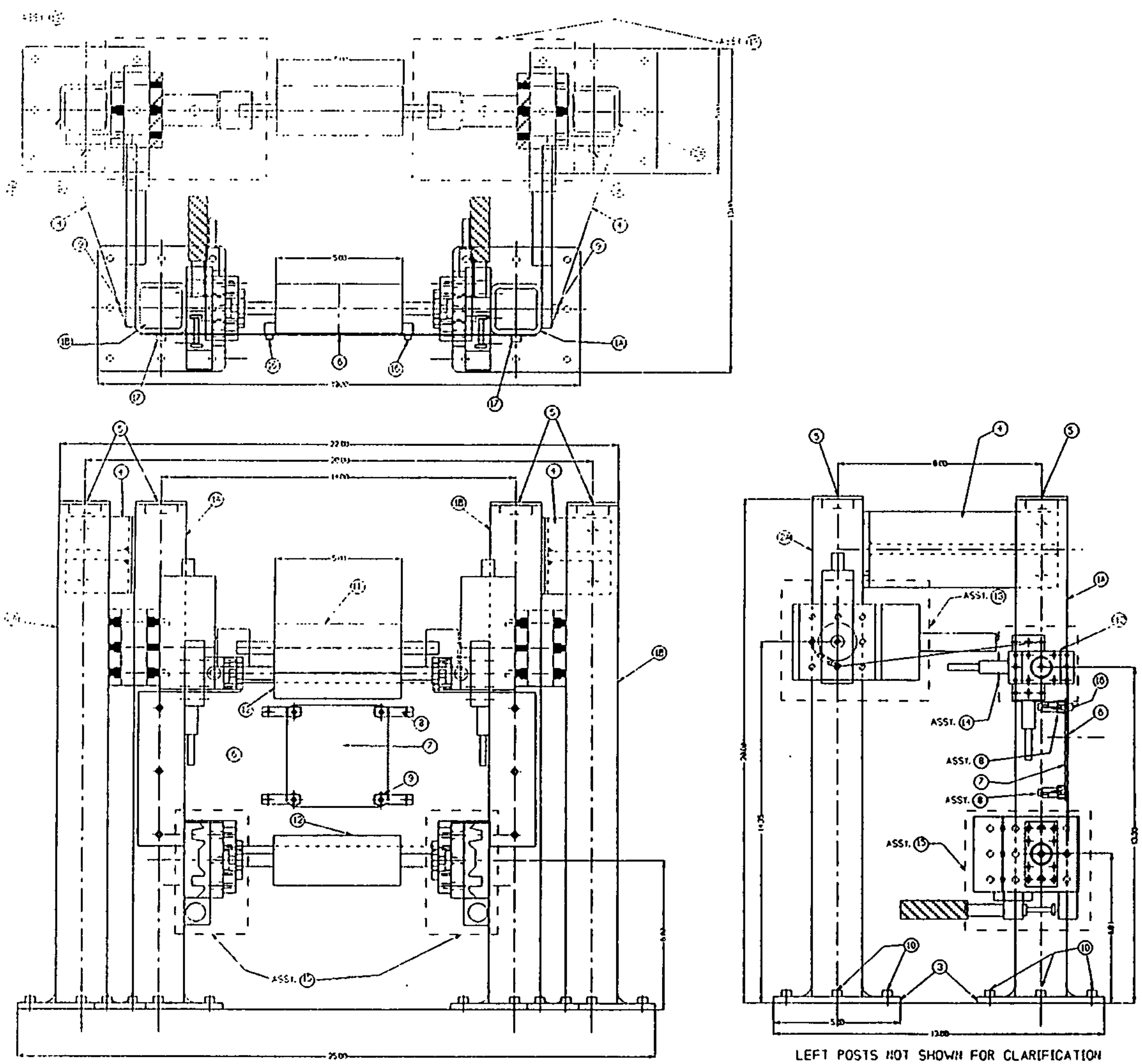

PART#	DESCRIPTION	MATERIAL	QTY
1A	Front Right Post	2"x2"x5.95H	1
1B	Front Left Post	2"x2"x5.55H	1
2A	Rear Right Post	2"x2"x5.55H	1
2B	Rear Left Post	2"x2"x5.95H	1
3	Post Support Base	HR Steel	4
4	Gusset Bracket	HR Steel	2
5	Post End Caps	Al	4
6	Shoe Plate	16 Gauge S/S	1
7	Quartz Glass Window	Exist	1
8	Window Positioner	Al	4
9	1/4-20x3/4" Socket HH	Exist	8
10	1/4-20x1/2" Socket HH	Exist	32
11	Rear Precision Roll	304L S/S	1
12	Front Precision Roll	304L S/S	3
13	See DWG NO. A490-07-10-09		1
14	See DWG NO. A490-07-10-10		1
15	See DWG NO. A490-07-10-11		1
16	No8-32x1" Socket HH	S/S	4
17	1/4-28x3/4" Socket HH	S/S	6
18			
19			
20			
21			
22			
23			

A	FINAL DRAWING	2/4/93
REV	VEVERKA WEB DELIVERY	DATE
	REVISIONS	

UNLESS OTHERWISE SPECIFIED

DIMENSION STANDARD

INCHES METRIC and

TOLERANCES ON

2 PL DECIMALS ± .01

3 PL DECIMALS ± .002

ANGLES ± 0.5

FRACTIONS ± 1/32

BREAK SHARP CORNERS

√ - SURFACE FINISH OF 125 OR BETTER

SIGNATURES		
DRAWN	P. VEVERKA	2/4/93
CHECKED		
DESIGNER	P. VEVERKA	1/93

CAD FILE #

VEVERKA490\PULLSHOE.CD/D

THE INSTITUTE OF PAPER SCIENCE AND TECHNOLOGY

500 10th STREET N.W.

ATLANTA, GEORGIA 30318

VEVERKA WEB DELIVERY #1

SCALE 12

DWG NO A490-07-10-08

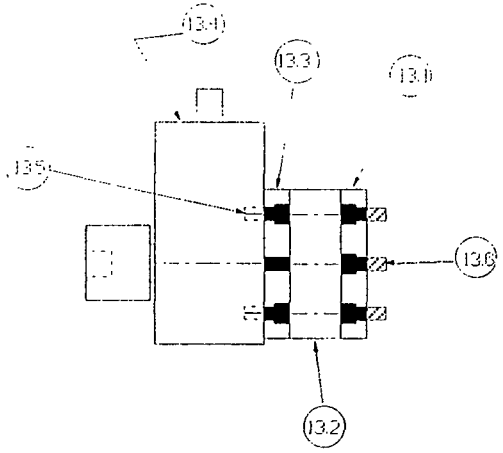

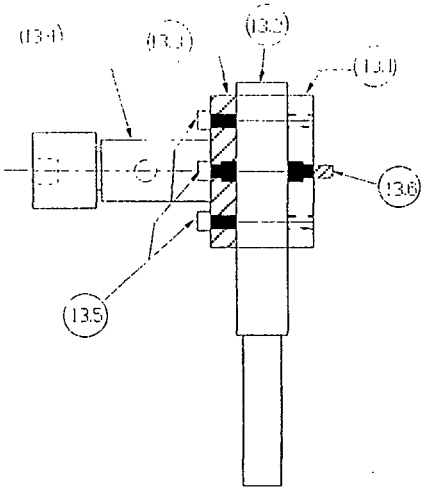

ASSY (13)

PART#	DESCRIPTION	MATERIAL	QTY
13.1	Translator/Post Adapt.	Al	2
13.2	CRITEL/[6021]	EXISTING EQ	2
13.3	Sensor/Translator Adapt	Al	2
13.4	Tapcon RHTSI-15	EXISTING EQ	8
13.5	1/4-20x2/8 Socket HH	Steel	16
13.6	1/4-20x5/8 Socket HH	Steel	10

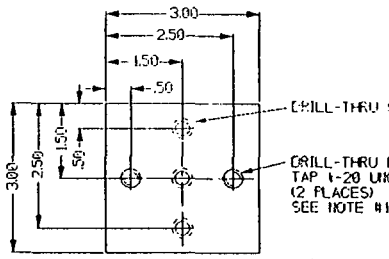

PN 13.1
TRANSLATOR POST ADAPTER
MATL: ALUMINUM
QTY: 2
SCALE: ACT.

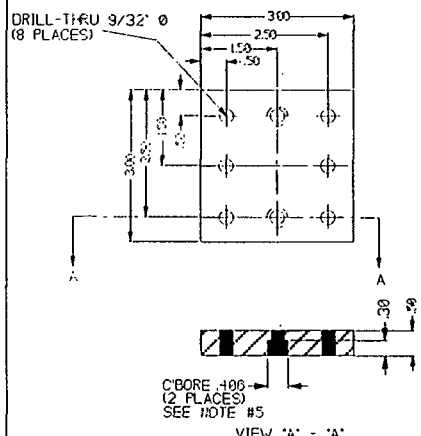

VIEW "A" - "A"

PN 13.3
SENSOR/TRANSLATOR ADAPTER
MATL: ALUMINUM
QTY: 2
SCALE: ACT.

NOTES:
1) Important to tap part 13.1 from bottom side.
2) Mounting holes in sensor are 1/4-20x3/8" Depth
3) Use part 13.6 to attach sensor to adapter and also 2x(3) for attaching to post
4) Use part 13.5 on rotating mounts
5) 13/32" ALSO ACCEPTABLE FOR COUNTER BORE

REV	DESCRIPTION	DATE
A	PRELIMINARY DRAWING	1/25/93
	REVISIONS	

UNLESS OTHERWISE SPECIFIED
DIMENSION STANDARD
BREAK SHARP CORNERS
√ - SURFACE FINISH OF 125 OR BETTER

SIGNATURES
DRAWN P. VEVERKA 1/25/93
CHECKED
DESIGNER P. VEVERKA 12/93

CAD FILE #
\VEVERKA\TRANSDUCER\D\0

THE INSTITUTE OF PAPER SCIENCE AND TECHNOLOGY
500 10TH STREET N.W.
ATLANTA, GEORGIA 30318

VEVERKA TENSION MOUNTS

SCALE ACT.
DWG NO A490-07-10-09

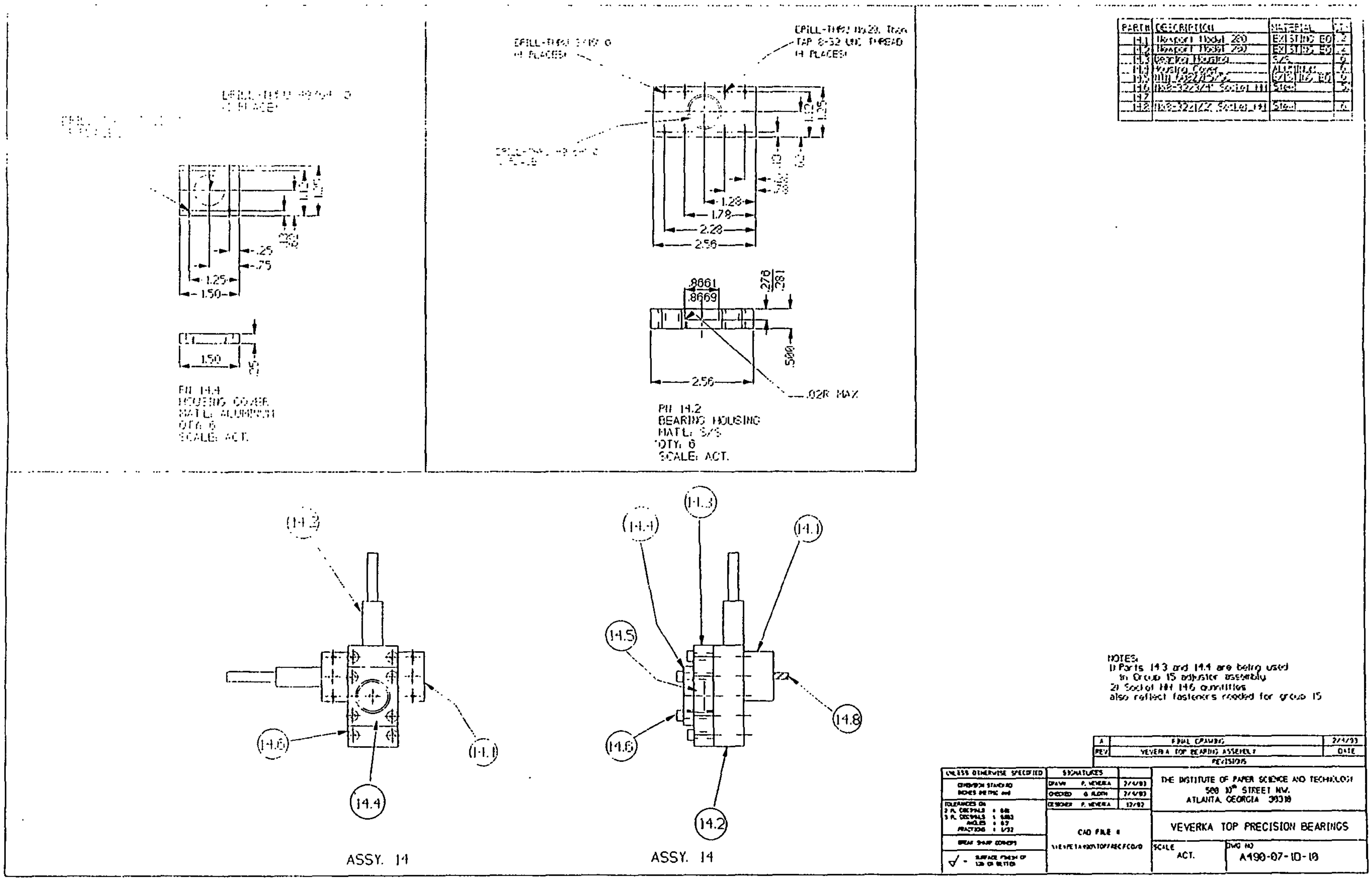
PART# DESCRIPTION MATERIAL
14.1 Newport Model 280 EXISTING EQ
14.2 Newport Model 290 EXISTING EQ
14.3 Bearing Housing S/S
14.4 Housing Cover ALUMINUM
14.6 Socket HH S/S
14.7
14.8 Steel
DRILL-THRU 1/4-20, TAP 8-32 UNC THREAD (4 PLACES)
DRILL-THRU (4 PLACES)
1.28
1.78
2.28
2.56
.8661
.8669
.278
.281
.500
2.56
.02R MAX
PN 14.2
BEARING HOUSING
MAT'L: S/S
QTY: 6
SCALE: ACT.
.25
.75
1.25
1.50
1.50
PN 14.4
HOUSING COVER
MAT'L: ALUMINUM
QTY: 6
SCALE: ACT.
14.1
14.2
14.3
14.4
14.5
14.6
14.8
ASSY. 14
ASSY. 14
NOTES:
1) Parts 14.3 and 14.4 are being used in Group 15 adjuster assembly
2) Socket HH 14.6 quantities also reflect fasteners needed for group 15
A FINAL DRAWING 2/4/93
REV VEVERKA TOP BEARING ASSEMBLY DATE
REVISIONS
UNLESS OTHERWISE SPECIFIED
SIGNATURES
DRAWN P. VEVERKA 2/4/93
CHECKED
DESIGNER P. VEVERKA 12/92
CAD FILE #
THE INSTITUTE OF PAPER SCIENCE AND TECHNOLOGY
500 10th STREET NW.
ATLANTA, GEORGIA 30318
VEVERKA TOP PRECISION BEARINGS
SCALE ACT.
DWG NO A490-07-10-10

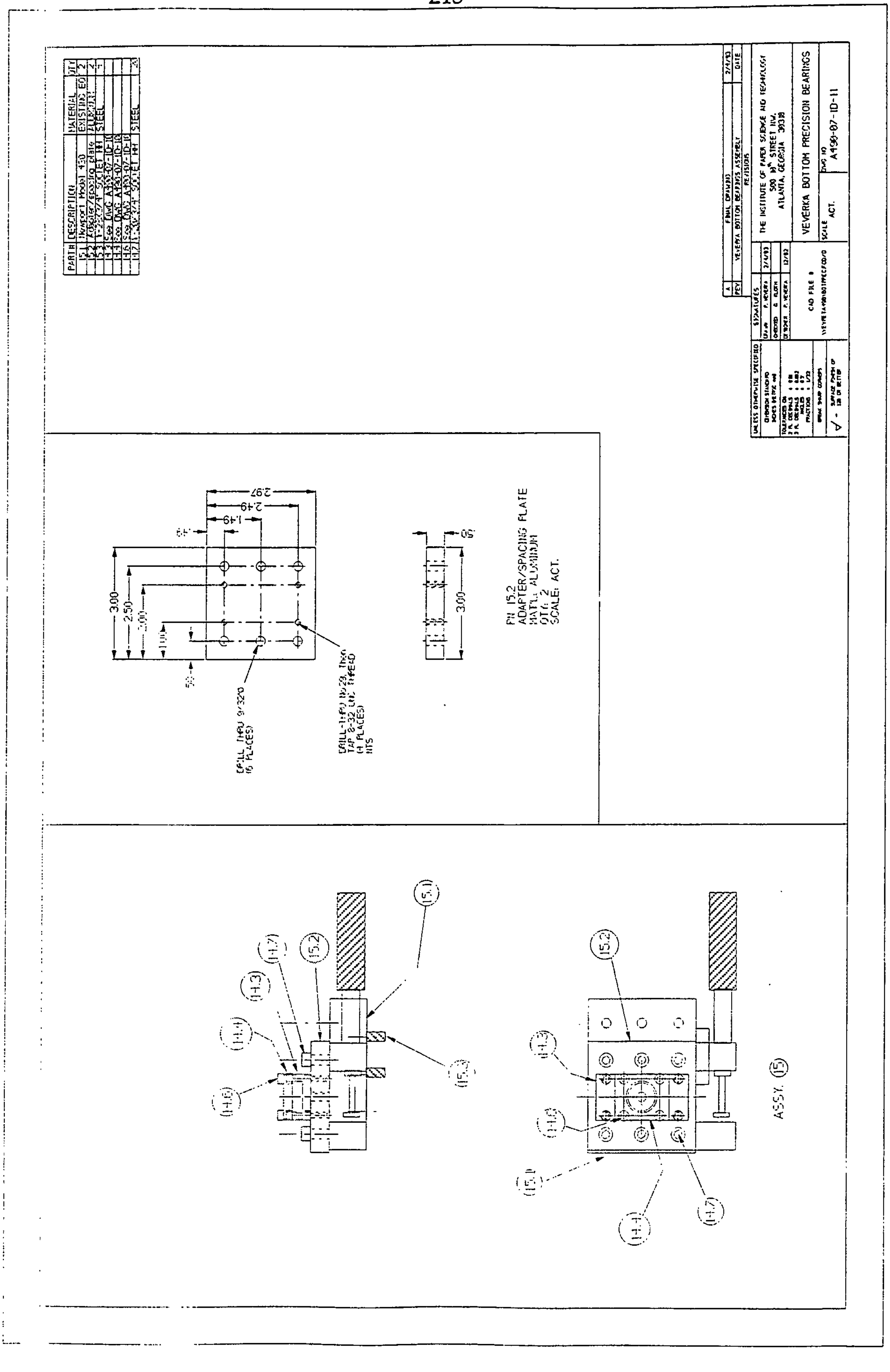

PART# DESCRIPTION MATERIAL QTY
15.1 Newport Model 430 EXISTING EQ 2
15.2 Adapter/spacing plate ALUMINUM 2
15.3 1-20x3/4" SOCKET HH STEEL 4
14.3 See DWG A490-07-ID-10
14.4 See DWG A490-07-ID-10
14.6 See DWG A490-07-ID-10
14.7 1-20x3/4" SOCKET HH STEEL 20
3.00
2.50
2.00
1.00
.50
1.49
2.49
2.97
DRILL THRU 9/32"Ø (6 PLACES)
DRILL-THRU No29, Then TAP 8-32 UNC THREAD (4 PLACES) NTS
PN 15.2
ADAPTER/SPACING PLATE
MAT'L: ALUMINUM
QTY: 2
SCALE: ACT.
ASSY. 15
A FINAL DRAWING 2/4/93
REV VEVERKA BOTTOM BEARINGS ASSEMBLY DATE
REVISIONS
UNLESS OTHERWISE SPECIFIED
SIGNATURES
THE INSTITUTE OF PAPER SCIENCE AND TECHNOLOGY
500 10th STREET NW.
ATLANTA, GEORGIA 30318
VEVERKA BOTTOM PRECISION BEARINGS
SCALE ACT.
DWG NO A490-07-ID-11

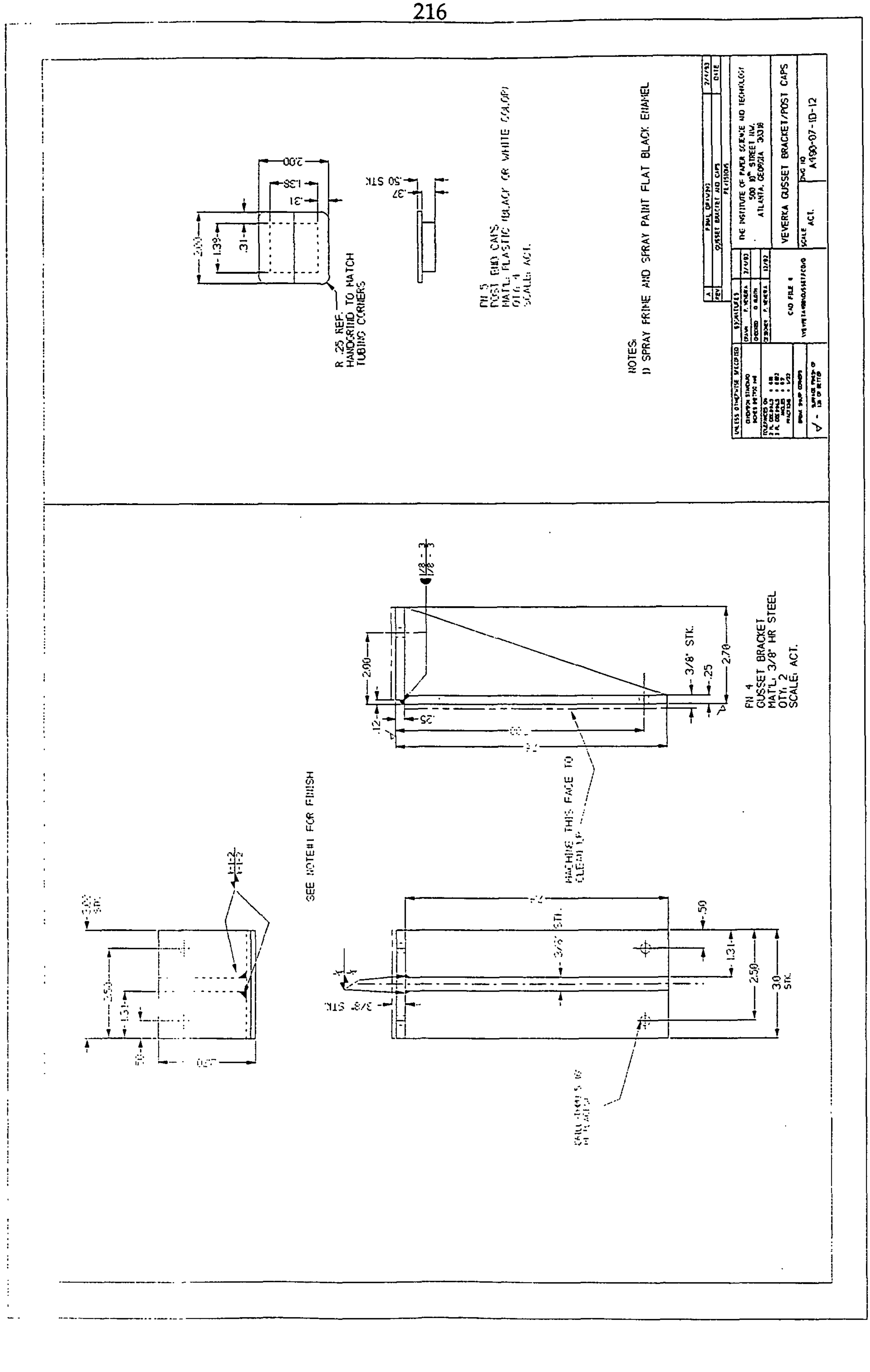
R .25 REF.
HANDGRIND TO MATCH
TUBING CORNERS
PN 5
POST END CAPS
MAT'L: PLASTIC (BLACK OR WHITE COLOR)
QTY: 4
SCALE: ACT.
NOTES:
1) SPRAY PRIME AND SPRAY PAINT FLAT BLACK ENAMEL
SEE NOTE#1 FOR FINISH
PN 4
GUSSET BRACKET
MAT'L: 3/8" HR STEEL
QTY: 2
SCALE: ACT.
THE INSTITUTE OF PAPER SCIENCE AND TECHNOLOGY
500 10th STREET NW.
ATLANTA, GEORGIA 30318
VEVERKA GUSSET BRACKET/POST CAPS
A190-07-1D-12

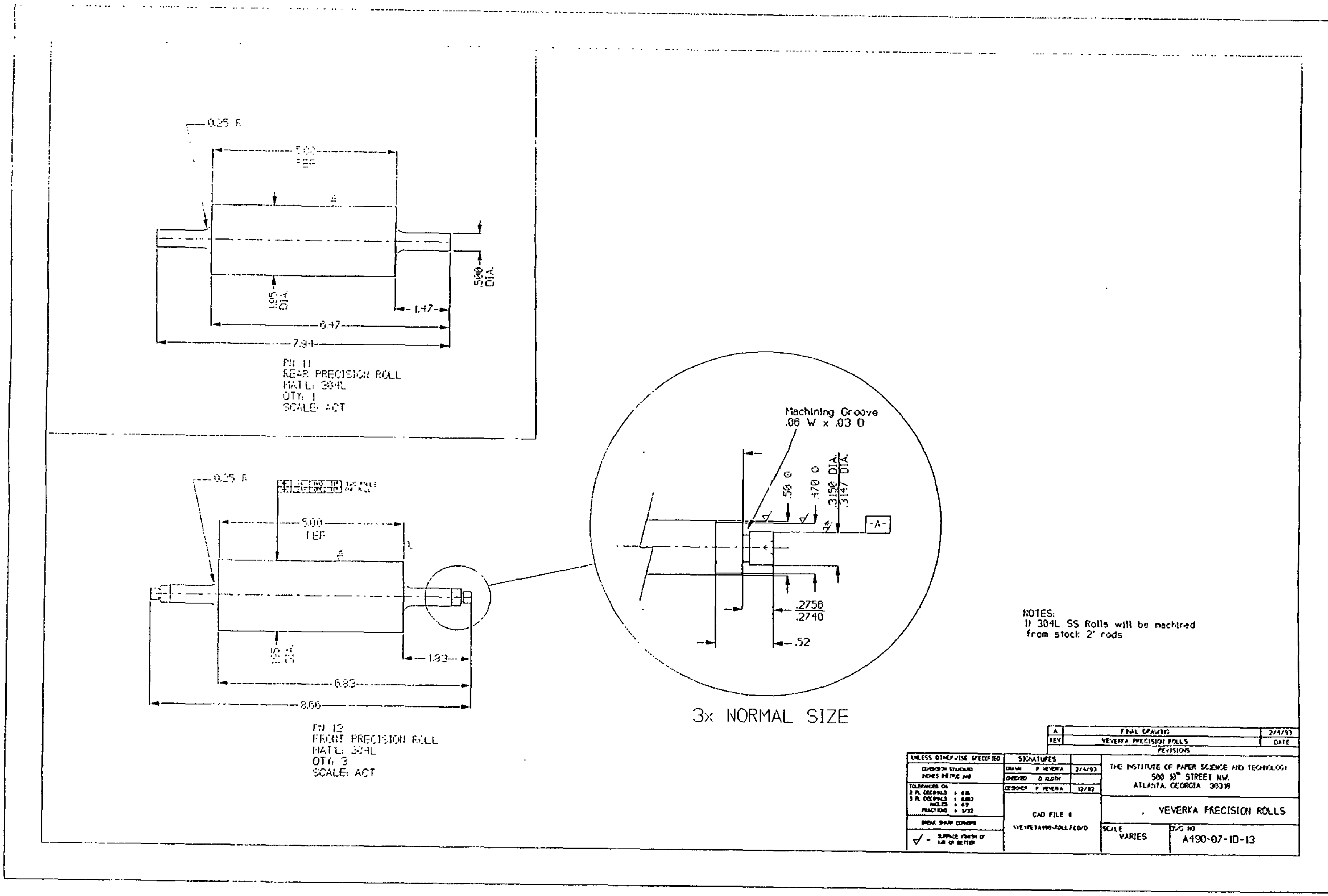
0.25 R
5.00 REF
.500 DIA.
1.47
6.47
7.94
PN 11
REAR PRECISION ROLL
MAT'L: 304L
QTY: 1
SCALE: ACT
0.25 R
5.00 REF
1.33
6.83
8.66
PN 12
FRONT PRECISION ROLL
MAT'L: 304L
QTY: 3
SCALE: ACT
Machining Groove
.06 W x .03 D
.50 ⌀
.470 ⌀
.3150 DIA.
.3147 DIA.
-A-
.2756
.2740
.52
3x NORMAL SIZE
NOTES:
1) 304L SS Rolls will be machined from stock 2" rods
A FINAL DRAWING 2/4/93
REV VEVERKA PRECISION ROLLS DATE
REVISIONS
UNLESS OTHERWISE SPECIFIED
SIGNATURES
THE INSTITUTE OF PAPER SCIENCE AND TECHNOLOGY
500 10th STREET NW.
ATLANTA, GEORGIA 30318
VEVERKA PRECISION ROLLS
CAD FILE #
SCALE
VARIES
DWG NO
A490-07-10-13

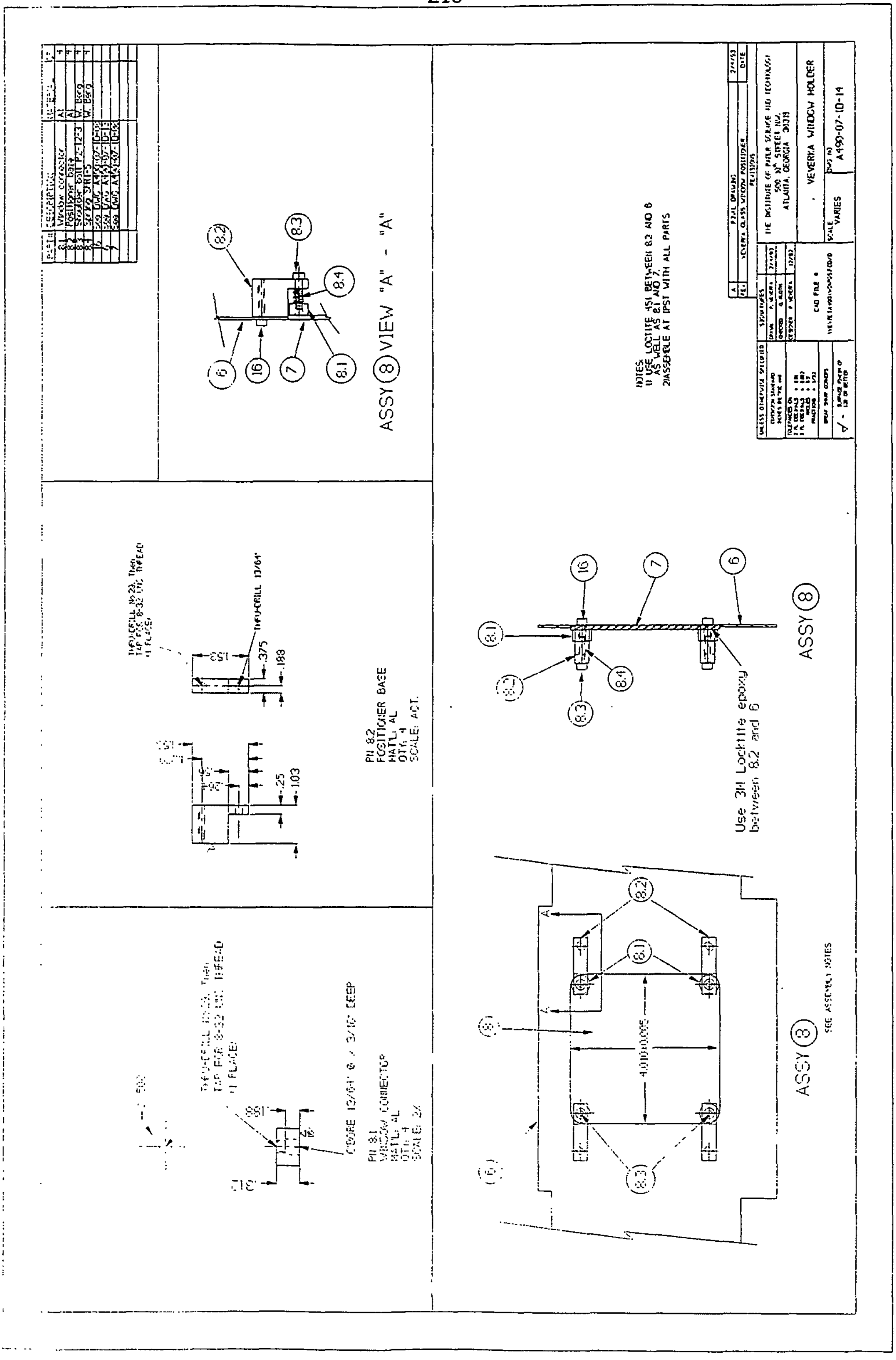
PART# DESCRIPTION
8.1 Window connector Al 4
8.2 Positioner base Al 4
8.3 Shoulder bolt PZ-12-3 W. Berg 4
8.4 Spring SRT-5 W. Berg 4
ASSY 8 VIEW "A" - "A"
NOTES
1) USE LOCTITE 451 BETWEEN 8.2 AND 6 AS WELL AS 8.1 AND 7.
2) ASSEMBLE AT IPST WITH ALL PARTS
FINAL DRAWING 2/4/93
VEVERKA GLASS WINDOW POSITIONER
REVISIONS
DATE
THE INSTITUTE OF PAPER SCIENCE AND TECHNOLOGY
500 10th STREET NW.
ATLANTA, GEORGIA 30318
VEVERKA WINDOW HOLDER
SCALE VARIES
DWG NO A493-07-10-14
SIGNATURES
CAD FILE #
UNLESS OTHERWISE SPECIFIED
THRU-DRILL 13/64"
.375
.188
.25
1.03
PN 8.2
POSITIONER BASE
MAT'L: AL
QTY: 4
SCALE: ACT.
ASSY 8
Use 3M Locktite epoxy between 8.2 and 6
4.000±0.005
SEE ASSEMBLY NOTES
.188
.312
C'BORE 13/64" ... 3/16" DEEP
PN 8.1
WINDOW CONNECTOR
MAT'L: AL
QTY: 4
SCALE: 2X

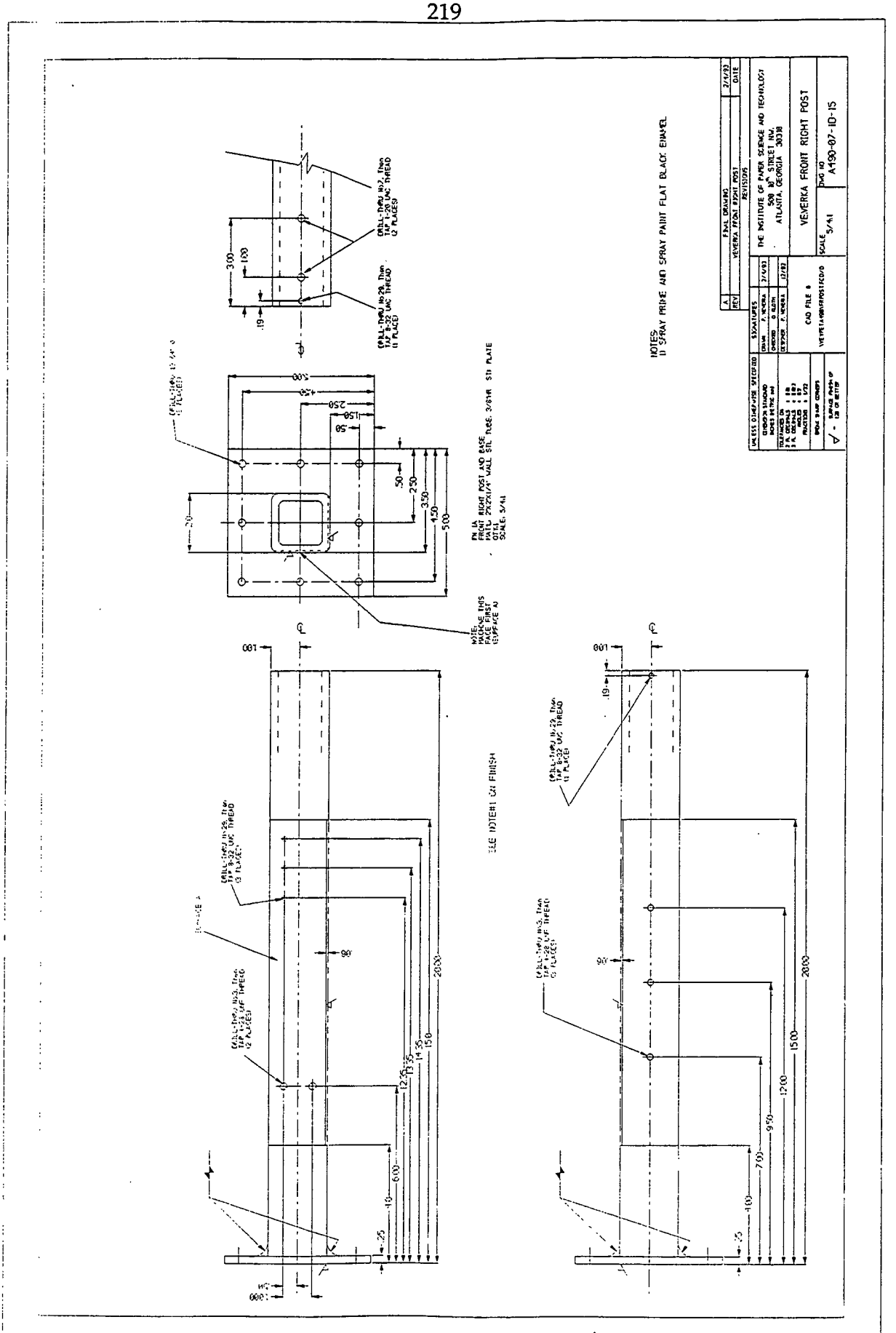
NOTES:
1) SPRAY PRIME AND SPRAY PAINT FLAT BLACK ENAMEL
FINAL DRAWING
VEVERKA FRONT RIGHT POST
REVISIONS
THE INSTITUTE OF PAPER SCIENCE AND TECHNOLOGY
500 10TH STREET, NW
ATLANTA, GEORGIA 30318
VEVERKA FRONT RIGHT POST
CAD FILE #
SCALE 1/4:1
DWG NO A-930-07-10-15
UNLESS OTHERWISE SPECIFIED
SIGNATURES
DRAWN
CHECKED
DESIGNER
SEE NOTE#1 FOR FINISH
FRONT RIGHT POST AND BASE
MATL: 2"X2"X1/4" WALL STL TUBE, 3/8"PL STL PLATE
SCALE: 1/4:1
NOTE: PACKAGE THIS FACE FIRST (SURFACE A)

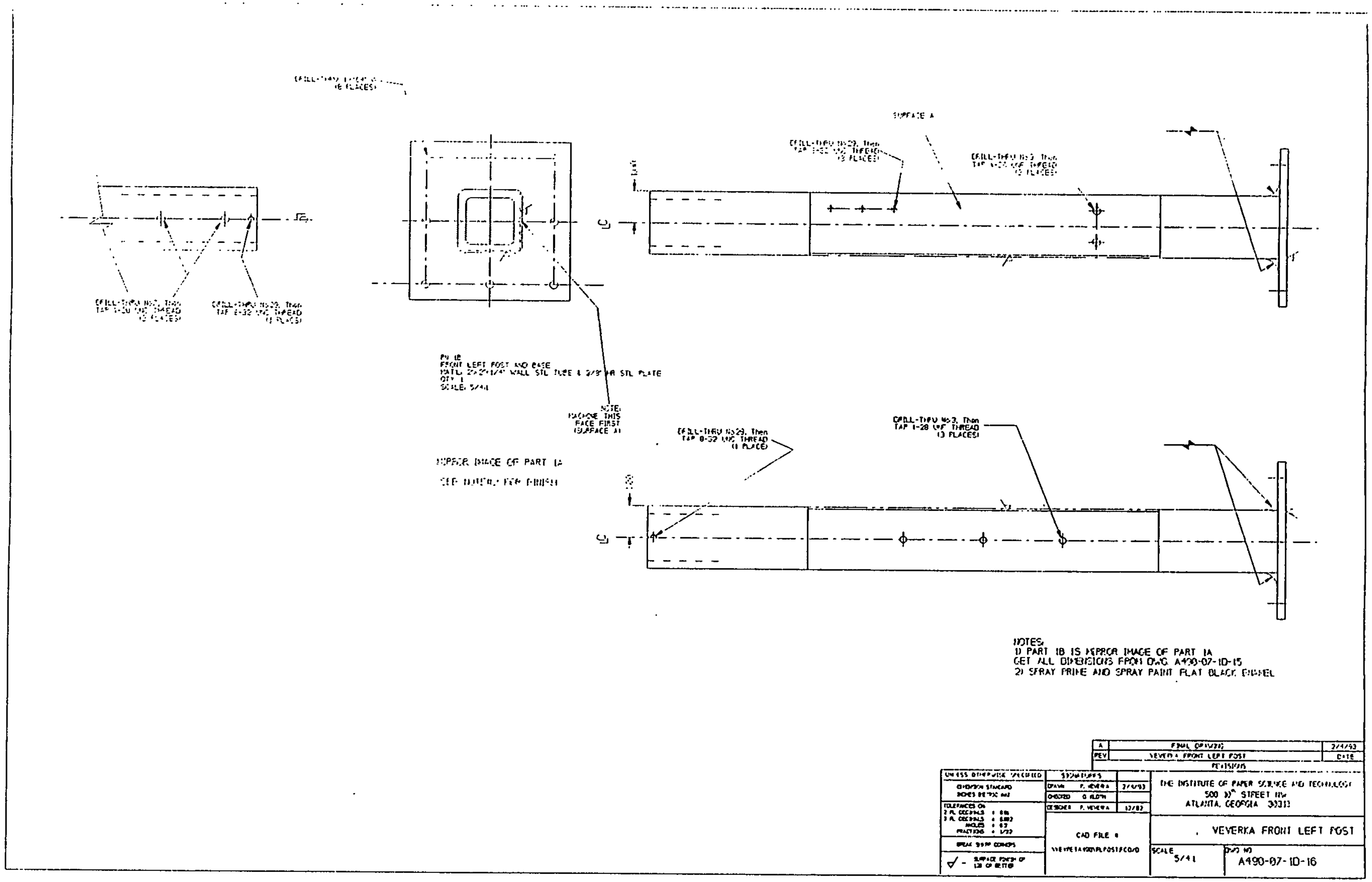
SURFACE A
FRONT LEFT POST AND BASE
MIRROR IMAGE OF PART 1A
NOTES:
1) PART 1B IS MIRROR IMAGE OF PART 1A
GET ALL DIMENSIONS FROM DWG. A490-07-1D-15
2) SPRAY PRIME AND SPRAY PAINT FLAT BLACK ENAMEL
FINAL DRAWING
VEVERKA FRONT LEFT POST
UNLESS OTHERWISE SPECIFIED
SIGNATURES
THE INSTITUTE OF PAPER SCIENCE AND TECHNOLOGY
ATLANTA, GEORGIA
CAD FILE #
VEVERKA FRONT LEFT POST
SCALE
5/41
A490-07-1D-16

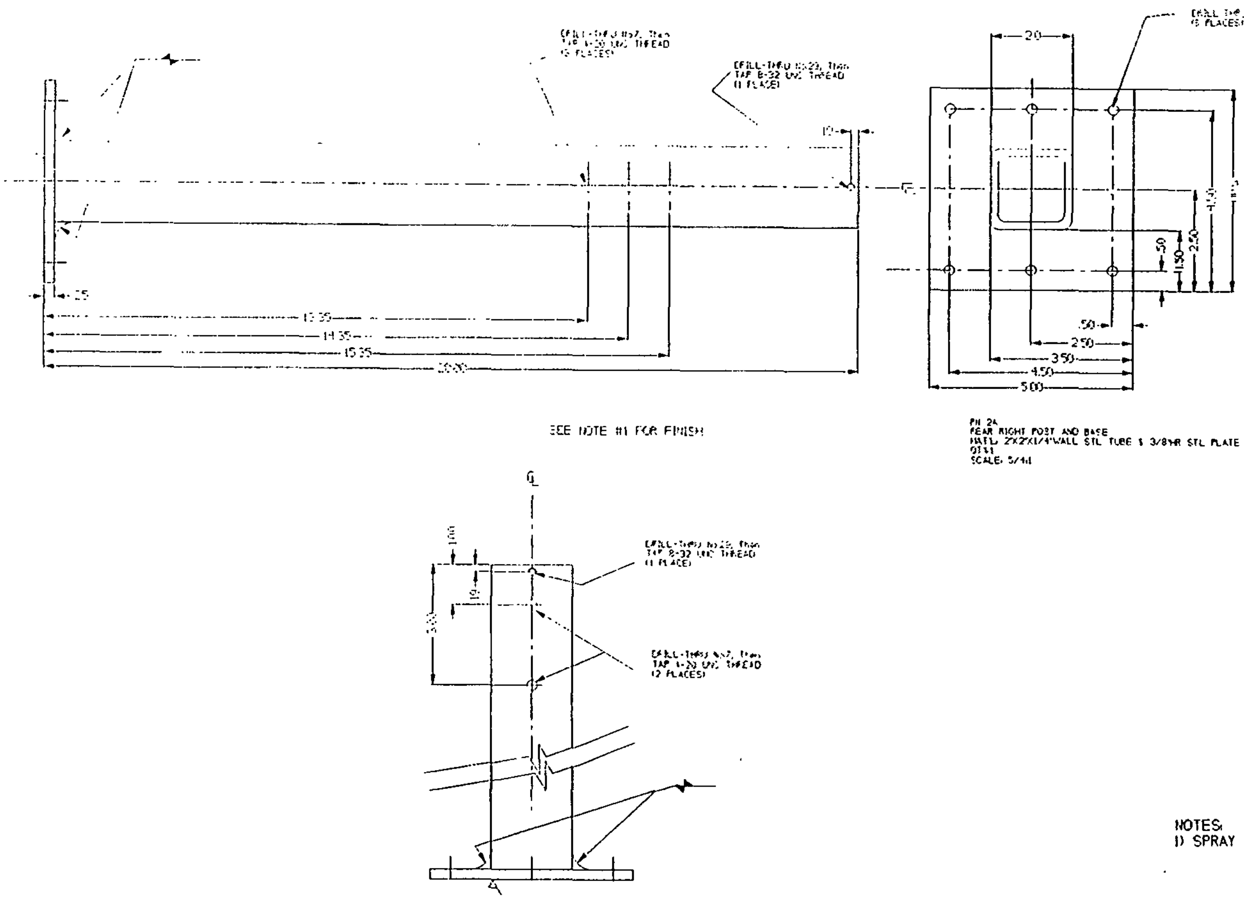

PN 24
REAR RIGHT POST AND BASE
MAT'L: 2"X2"X1/4"WALL STL TUBE & 3/8"HR STL PLATE
QTY 1
SCALE: 5/4

NOTES:
1) SPRAY PRIME AND SPRAY PAINT FLAT BLACK ENAMEL

A	FINAL DRAWING	2/4/93
REV	VEVERKA REAR RIGHT POST	DATE
	REVISIONS	

UNLESS OTHERWISE SPECIFIED	SIGNATURES			THE INSTITUTE OF PAPER SCIENCE AND TECHNOLOGY 500 10th STREET NW. ATLANTA, GEORGIA 30318	
	DRAWN	P. VEVERKA	2/4/93		
	CHECKED	G. ROTH			
	DESIGNER	P. VEVERKA	12/92		
	CAD FILE #			VEVERKA REAR RIGHT POST	
				SCALE ACT.	DWG NO A490-07-1D-17

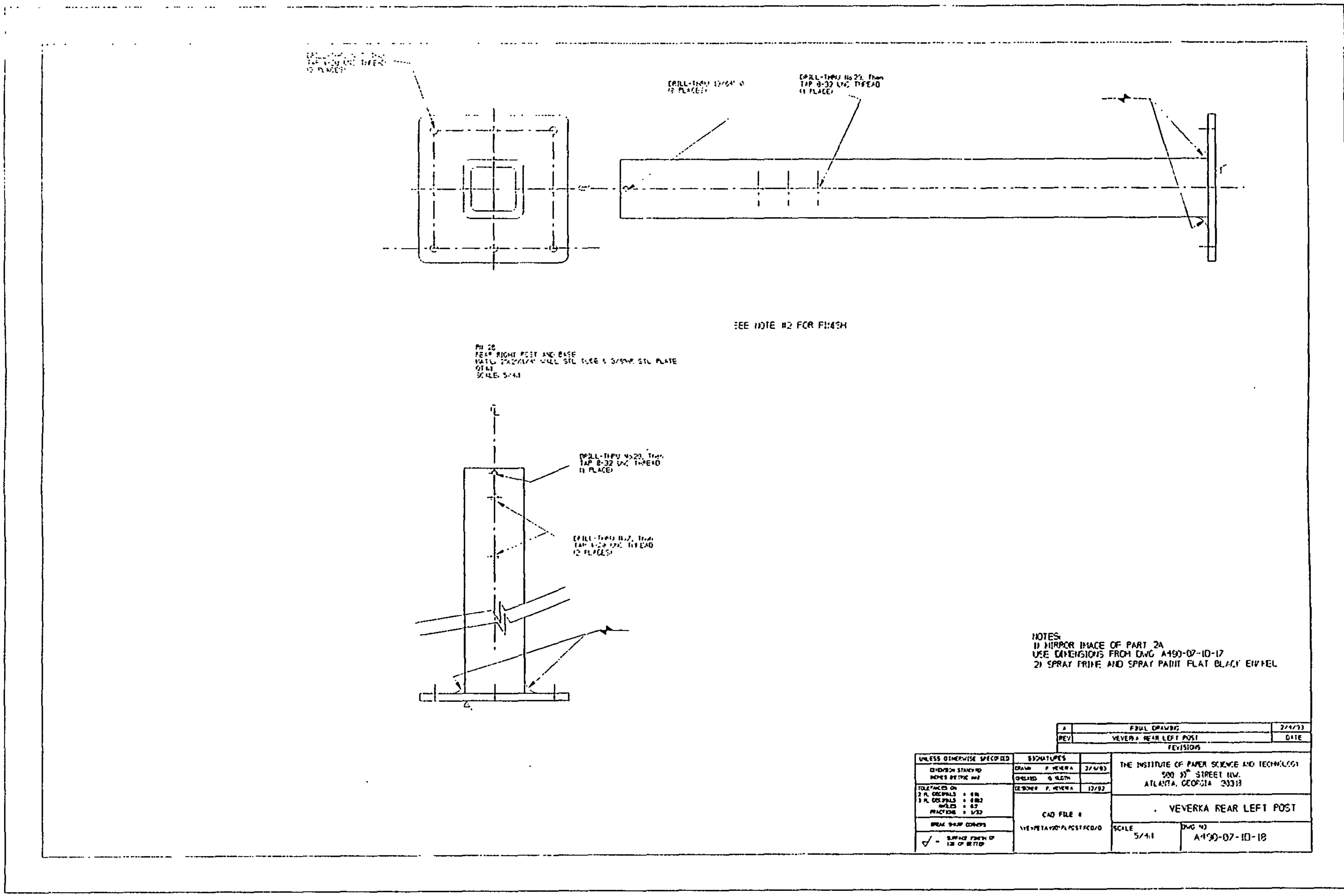
SEE NOTE #2 FOR FINISH
NOTES:
1) MIRROR IMAGE OF PART 2A
USE DIMENSIONS FROM DWG A490-07-10-17
2) SPRAY PRIME AND SPRAY PAINT FLAT BLACK ENAMEL
FINAL DRAWING
VEVERKA REAR LEFT POST
REVISIONS
UNLESS OTHERWISE SPECIFIED
SIGNATURES
THE INSTITUTE OF PAPER SCIENCE AND TECHNOLOGY
ATLANTA, GEORGIA
VEVERKA REAR LEFT POST
CAD FILE
SCALE
5/4:1
A490-07-10-18

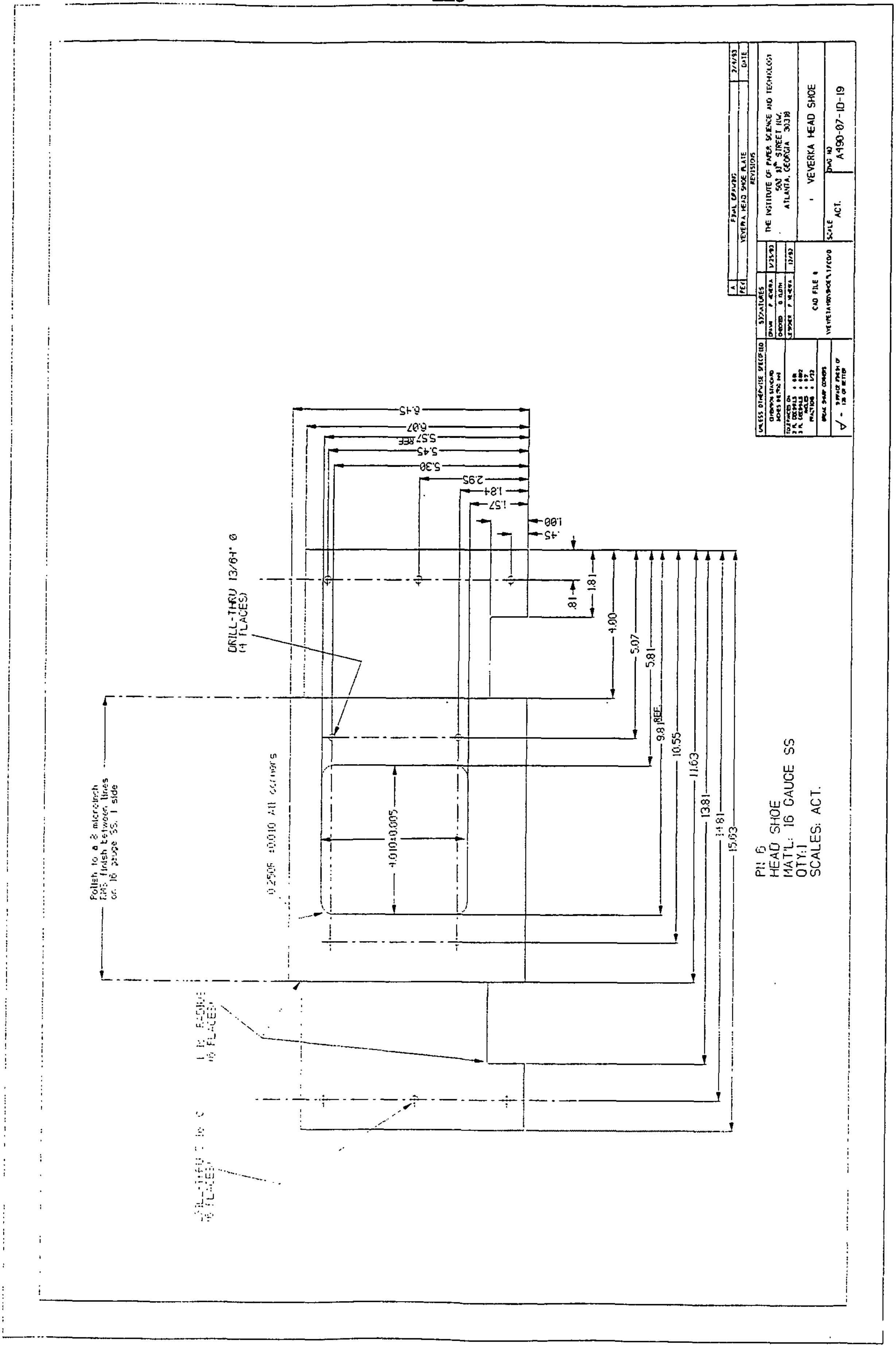
DRILL-THRU 13/64" Ø
(4 PLACES)
Polish to a 8 microinch
RMS finish between lines
on 16 gauge SS. 1 side
0.2505 ±0.010 All corners
4.010±0.005
.45
1.00
1.57
1.84
2.95
5.30
5.45
5.57 REF
6.07
6.45
.81
1.81
4.00
5.07
5.81
9.8 REF
10.55
11.63
13.81
14.81
15.63
PT. 6
HEAD SHOE
MAT'L: 16 GAUGE SS
QTY:1
SCALES: ACT.
THE INSTITUTE OF PAPER SCIENCE AND TECHNOLOGY
500 10th STREET NW.
ATLANTA, GEORGIA 30318
VEVERKA HEAD SHOE
SCALE ACT.
A190-07-10-19
REVISIONS
DATE
FINAL DRAWING
VEVERKA HEAD SHOE PLATE
UNLESS OTHERWISE SPECIFIED
SIGNATURES
CAD FILE #

NOTES:
1) .50" PRESTOCONDUCTIVE COVER TO BE SUPPLIED BY STOWE WOODWARD ON 3/21/93
BLANK WILL BE BROUGHT TO SW PLANT IN GRIFFIN, GA

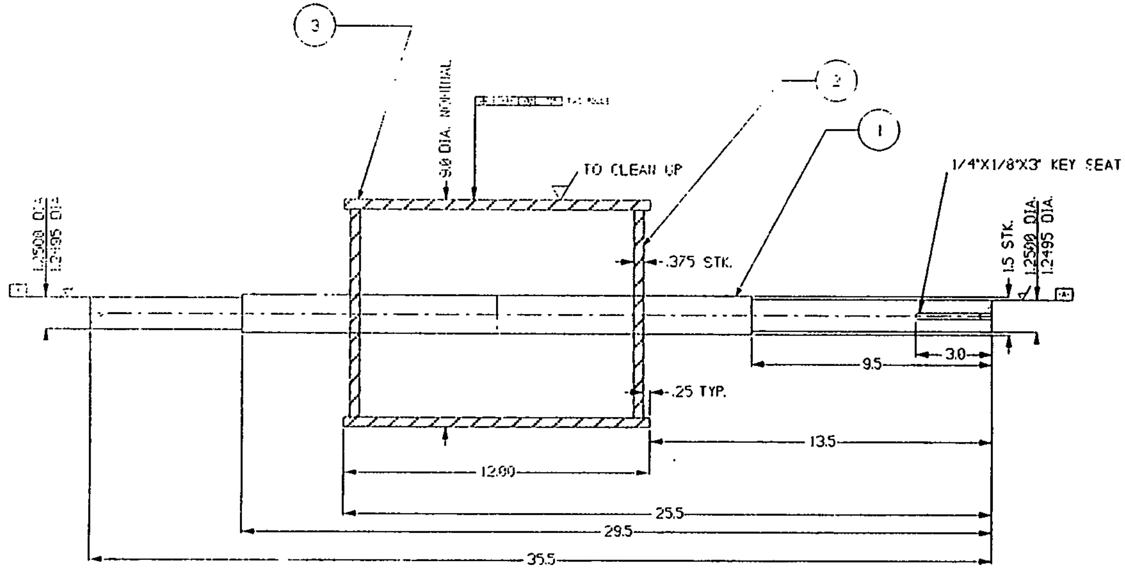

FN 2
RUBBER COVERED ROLL BLANK
QTY:2
PRIME AND PAINT FLAT BLACK ENAMEL EXCEPT ON MACHINED SURFACES

NO.	QTY	SIZE	MATERIAL
1	2	1.5 DIA.x35.5	STL STOCK
2	4	8.25 DIA.X.375	HR STL
3	2	9 O.D.X .375	ROUND STL TUBE

A	FINAL DRAWING	3/1/93
REV	VEVERKA RUBBER ROLL BLANKS	DATE
	REVISIONS	

THE INSTITUTE OF PAPER SCIENCE AND TECHNOLOGY
500 10th STREET NW.
ATLANTA, GEORGIA 30318

VEVERKA REWIND ROLL BLANKS

SCALE 1:2 — DWG NO A490-07-10-20

CAD FILE #

NOTES
1) 1/4" FILLET WELD ALL AROUND
2) PRIME AND PAINT FLAT BLACK EXCEPT ON MACHINED MOUNTING PADS

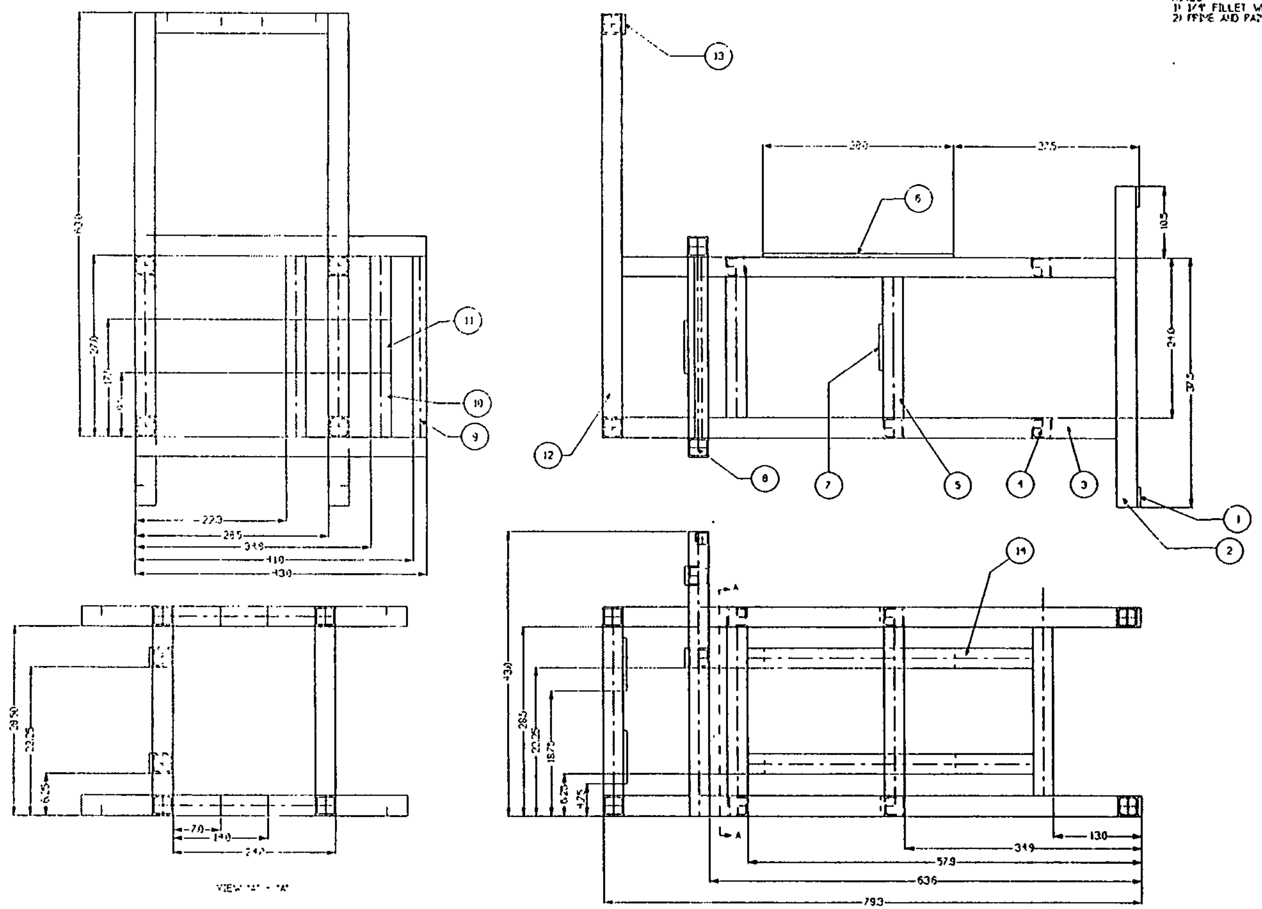

DT 1
UNWIND REWIND STAND
MATL: 3"X3"X1/4" WALL STL TUBE, 2"X2"X1/4" WALL STL TUBE & 1/4"R STL PLATE
QTY: 1
SCALE 1:7.5

NO	QTY	SIZE	MATERIAL
1	4	1/4x 3x3	HR STL
2	2	3/3x1/4x46	STL SQ TUBE
3	4	3/3/1/4/72.75	" "
4	8	3/3X1/4X25.5	" "
5	4	3X3X1/4X21	" "
6	2	1/4x3x28	HR STL
7	2	1/4X3X7	" "
8	2	3X3X1/4X43	STL SQ TUBE
9	1	2x2X1/4X27	" "
10	2	3x3X1/4X27	" "
11	2	1/4X3X8	HR STL
12	2	3X3X1/4X83	STL SQ TUBE
13	2	1/4x3x8	HR STL
14	2	[illegible]	STL SQ TUBE

A	FINAL DRAWING	3/17/93
REV	VEVERKA UNWIND REWIND STAND	DATE
	REVISIONS (3/17/93)	

UNLESS OTHERWISE SPECIFIED: DIMENSION STANDARD INCHES (METRIC mm); TOLERANCES ON 2 PL DECIMALS ± 0.01, 3 PL DECIMALS ± 0.002, ANGLES ± 0.5°, FRACTIONS ± 1/32; BREAK SHARP CORNERS; SURFACE FINISH OF 125 OR BETTER

SIGNATURES: DRAWN P. VEVERKA 2/27/93; CHECKED G. ROTH; DESIGNER P. VEVERKA 2/93

CAD FILE # \VEVERKA\490\VELOSTNDFCO/D

THE INSTITUTE OF PAPER SCIENCE AND TECHNOLOGY
500 10th STREET NW.
ATLANTA, GEORGIA 30318

VEVERKA UN/REWIND STAND

SCALE 1 : 7.5

DWG NO A490-07-ID-21

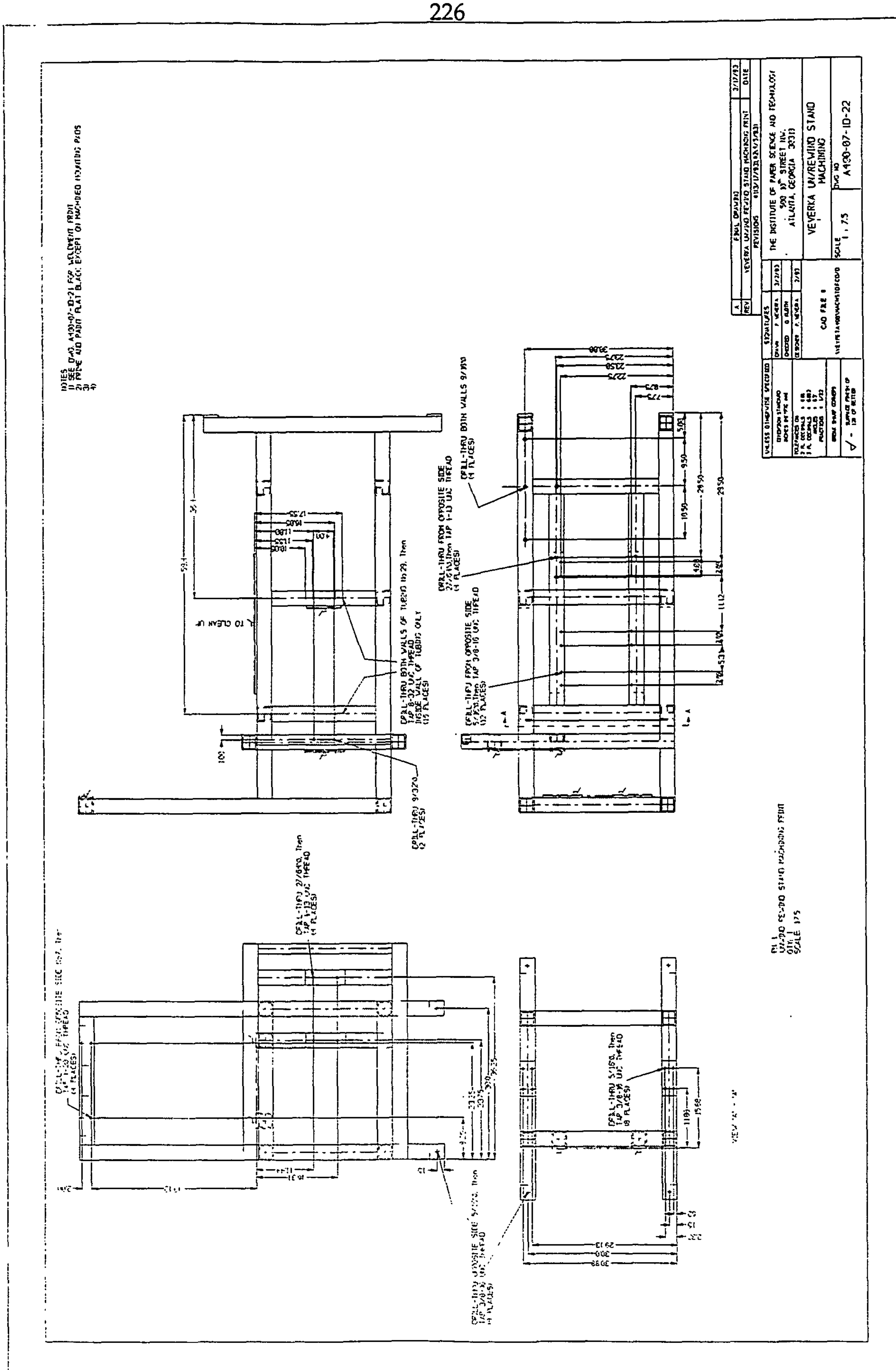
THE INSTITUTE OF PAPER SCIENCE AND TECHNOLOGY
VEVERKA UN/REWIND STAND MACHINING
A930-87-ID-22

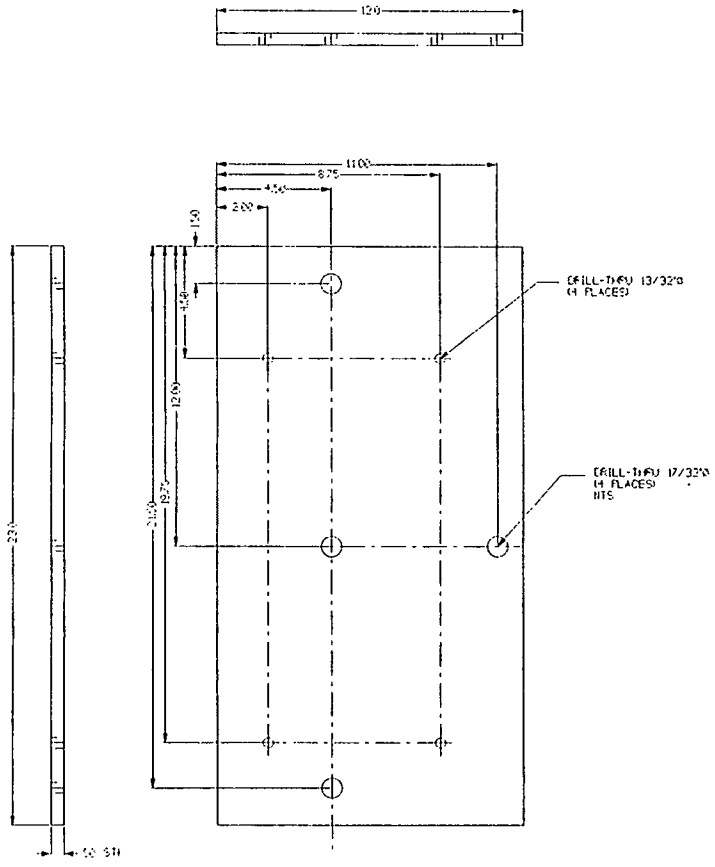

PN:3
MOTOR MOUNTING PLATE
MATL: 1/2" STEEL PLATE
QTY: 1
SCALE: 1:2

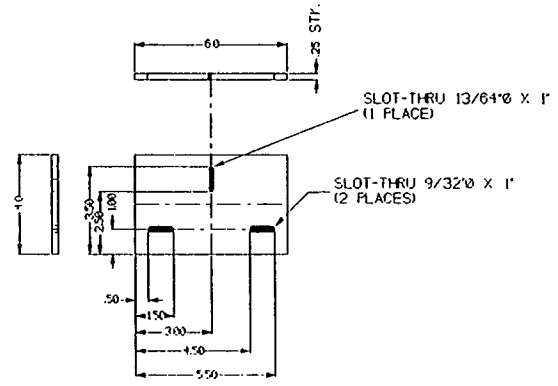

PN:4
BRAKE TORQUE PLATE
MATL: 1/4" STEEL OR AL PLATE
QTY: 1
SCALE: ACT.

NOTES:
1) FLAT BLACK FINISH ON STEEL SURFACES, LEAVE AL CLEAN

REV	REVISIONS	DATE
A	FINAL DRAWING	3/17/93

UNLESS OTHERWISE SPECIFIED	SIGNATURES	THE INSTITUTE OF PAPER SCIENCE AND TECHNOLOGY 500 10th STREET NW. ATLANTA, GEORGIA 30318
DIMENSION STANDARD INCHES [MILLIMETERS]	DRAWN P. VENEIRA 3/15/93	
TOLERANCES ON 2 PL. DECIMALS ± .01 3 PL. DECIMALS ± .005 ANGLES ± 0.5° FRACTIONS ± 1/32	CHECKED D. ROTH	
	DESIGNER P. VENEIRA 1/93	VEVERKA MOTOR/BRAKE MOUNTS
BREAK SHARP CORNERS	CAD FILE #	
✓ = SURFACE FINISH OF 125 OR BETTER	VEVPETA490MOTOPLT.PRO/D	SCALE: VARIES DWG NO: A490-07-1D-23

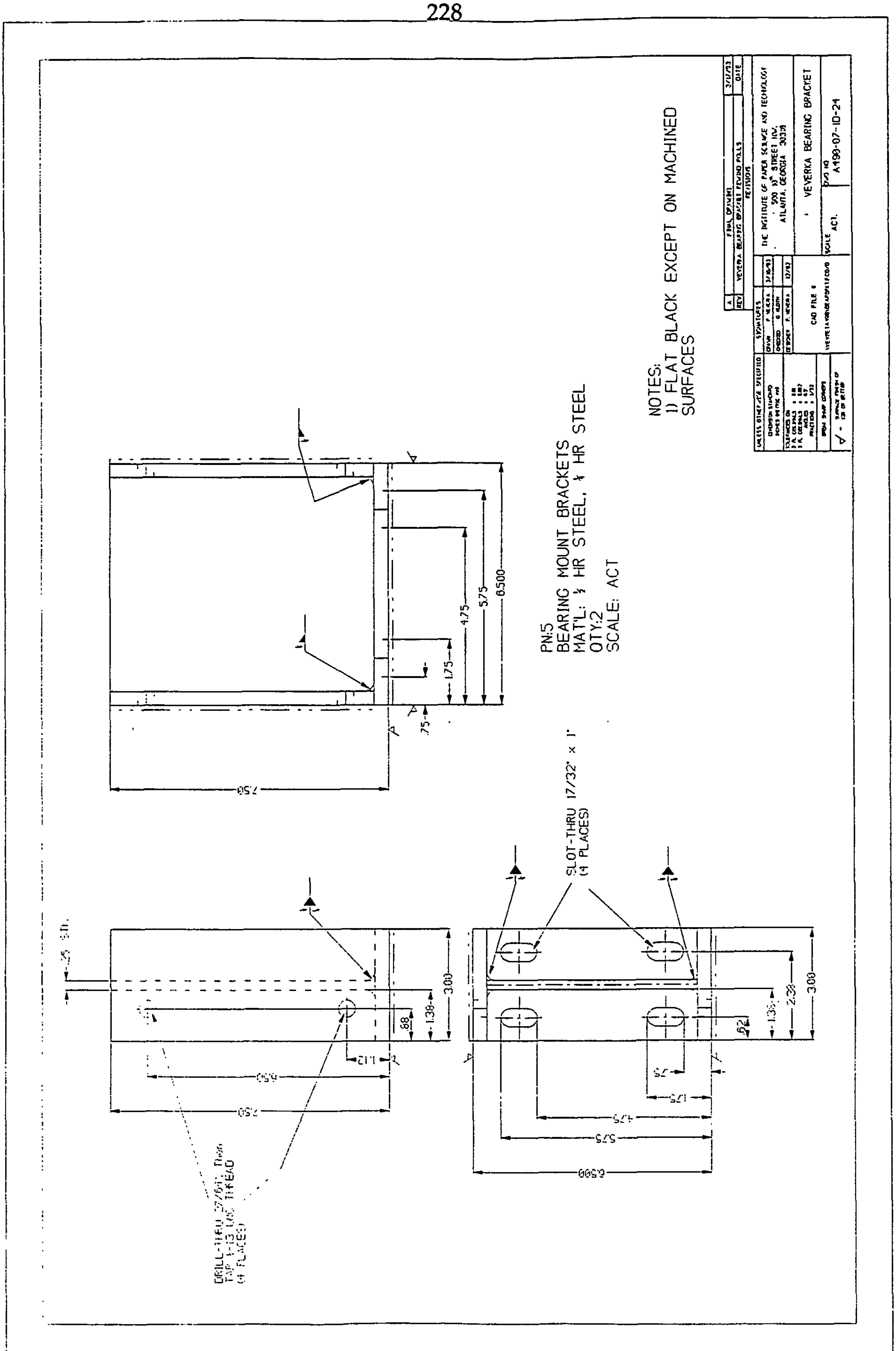
NOTES:
1) FLAT BLACK EXCEPT ON MACHINED SURFACES
PN:5
BEARING MOUNT BRACKETS
MAT'L: ½ HR STEEL, ¼ HR STEEL
QTY:2
SCALE: ACT
SLOT-THRU 17/32" x 1"
(4 PLACES)
6.500
5.75
4.75
1.75
7.50
3.00
2.38
1.38
.88
.62
1.12
.75
6.50
THE INSTITUTE OF PAPER SCIENCE AND TECHNOLOGY
ATLANTA, GEORGIA 30318
VEVERKA BEARING BRACKET
A499-07-10-24

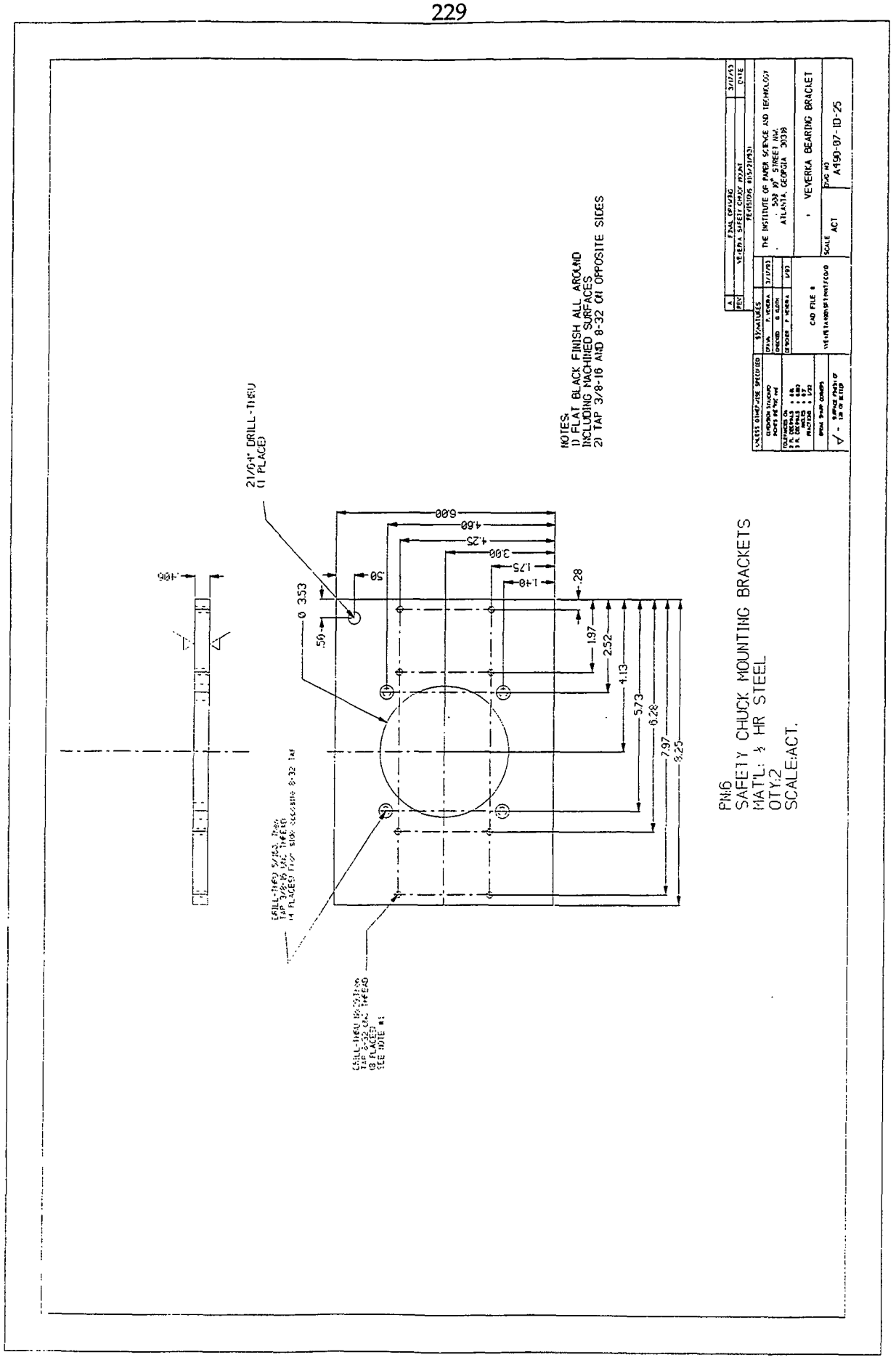
NOTES:
1) FLAT BLACK FINISH ALL AROUND
INCLUDING MACHINED SURFACES
2) TAP 3/8-16 AND 8-32 ON OPPOSITE SIDES
21/64" DRILL-THRU
(1 PLACE)
6.00
4.60
4.25
3.06
1.75
1.40
.28
.50
Ø .353
1.97
2.52
4.13
5.73
6.28
7.97
8.25
.106
PN:6
SAFETY CHUCK MOUNTING BRACKETS
MATL: ½ HR STEEL
QTY:2
SCALE:ACT.
VEVERKA BEARING BRACKET
THE INSTITUTE OF PAPER SCIENCE AND TECHNOLOGY
ACT
A490-07-ID-25

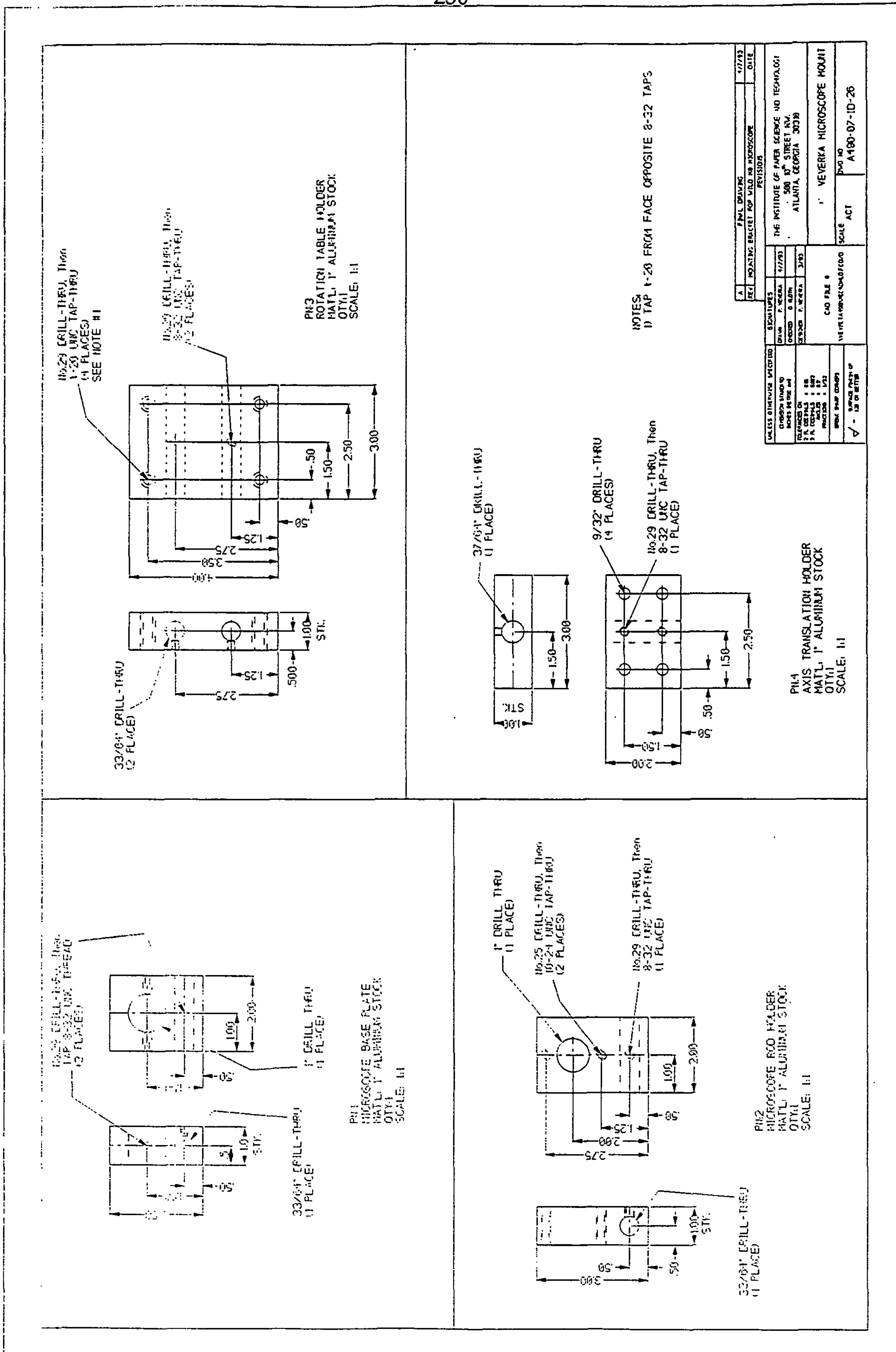
P/N3
ROTATION TABLE HOLDER
MAT'L: 1" ALUMINUM STOCK
QTY:1
SCALE: 1:1
No.29 DRILL-THRU, Then
1-20 UNC TAP-THRU
(4 PLACES)
SEE NOTE #1
33/64" DRILL-THRU
(2 PLACE)
NOTES:
1) TAP 1-20 FROM FACE OPPOSITE 8-32 TAPS
P/N4
AXIS TRANSLATION HOLDER
MAT'L: 1" ALUMINUM STOCK
QTY:1
SCALE: 1:1
37/64" DRILL-THRU
(1 PLACE)
9/32" DRILL-THRU
(4 PLACES)
No.29 DRILL-THRU, Then
8-32 UNC TAP-THRU
(1 PLACE)
P/N1
MICROSCOPE BASE PLATE
MAT'L: 1" ALUMINUM STOCK
QTY:1
SCALE: 1:1
1" DRILL THRU
(1 PLACE)
33/64" DRILL-THRU
(1 PLACE)
P/N2
MICROSCOPE ROD HOLDER
MAT'L: 1" ALUMINUM STOCK
QTY:1
SCALE: 1:1
1" DRILL THRU
(1 PLACE)
No.25 DRILL-THRU, Then
10-24 UNC TAP-THRU
(2 PLACES)
No.29 DRILL-THRU, Then
8-32 UNC TAP-THRU
(1 PLACE)
33/64" DRILL-THRU
(1 PLACE)
THE INSTITUTE OF PAPER SCIENCE AND TECHNOLOGY
500 10th STREET N.W.
ATLANTA, GEORGIA 30318
1" VEVERKA MICROSCOPE MOUNT
A190-07-1D-26

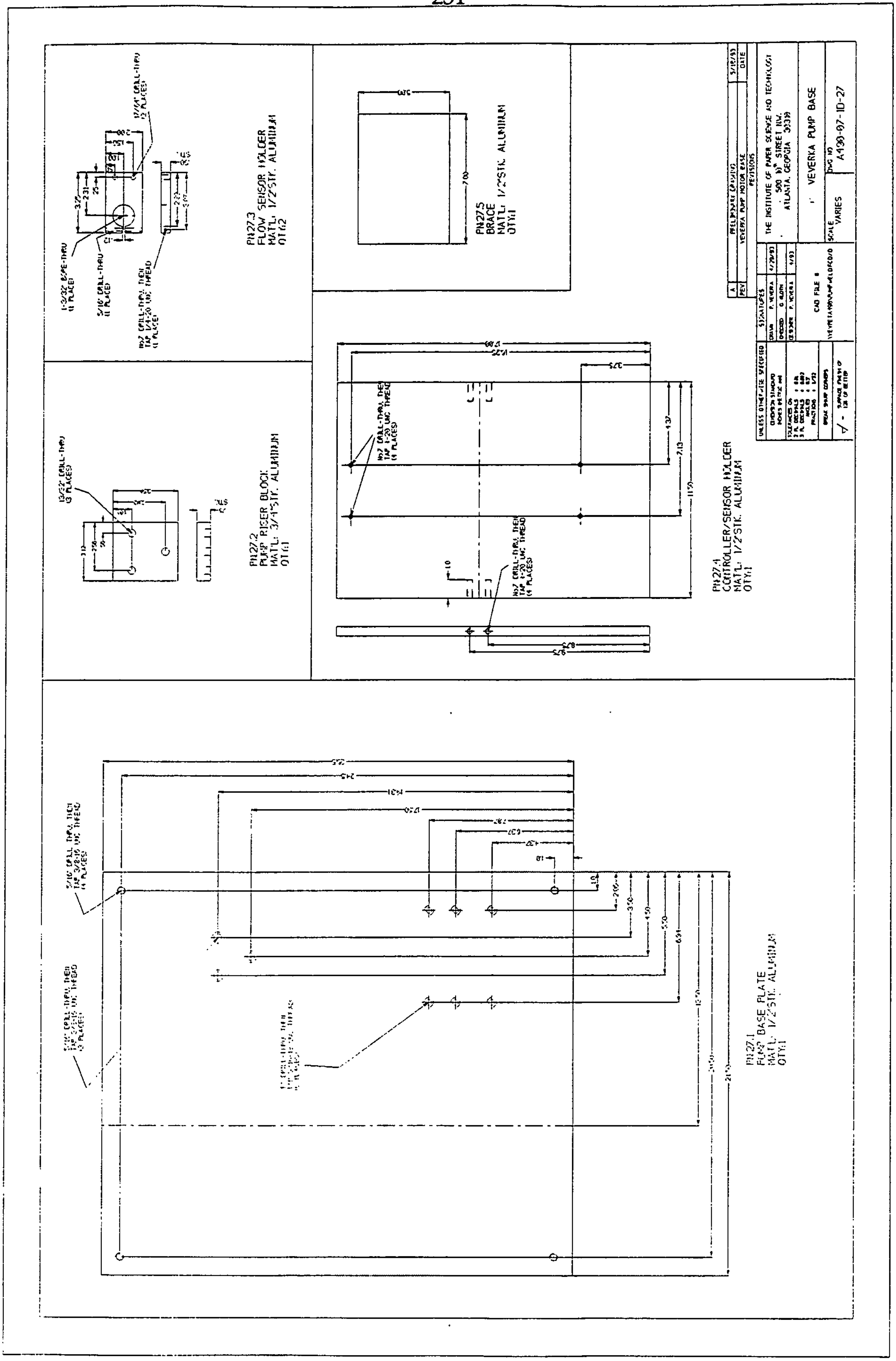

PN27.3
FLOW SENSOR HOLDER
MAT'L: 1/2"STK. ALUMINUM
PN27.5
BRACE
MAT'L: 1/2"STK. ALUMINUM
QTY:1
PN27.2
PUMP RISER BLOCK
MAT'L: 3/4"STK. ALUMINUM
QTY:1
PN27.4
CONTROLLER/SENSOR HOLDER
MAT'L: 1/2"STK. ALUMINUM
QTY:1
PN27.1
PUMP BASE PLATE
MAT'L: 1/2"STK. ALUMINUM
QTY:1
THE INSTITUTE OF PAPER SCIENCE AND TECHNOLOGY
ATLANTA, GEORGIA
VEVERKA PUMP BASE
VARIES

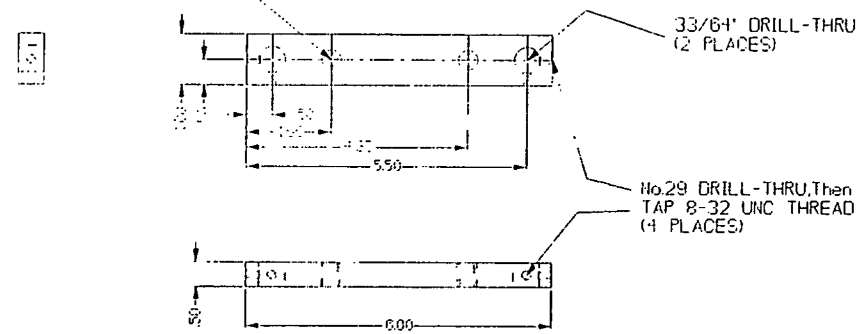

PN: 24
REVISED WIPER HOLDER
QTY: 2
MAT'L: AL OR CR?

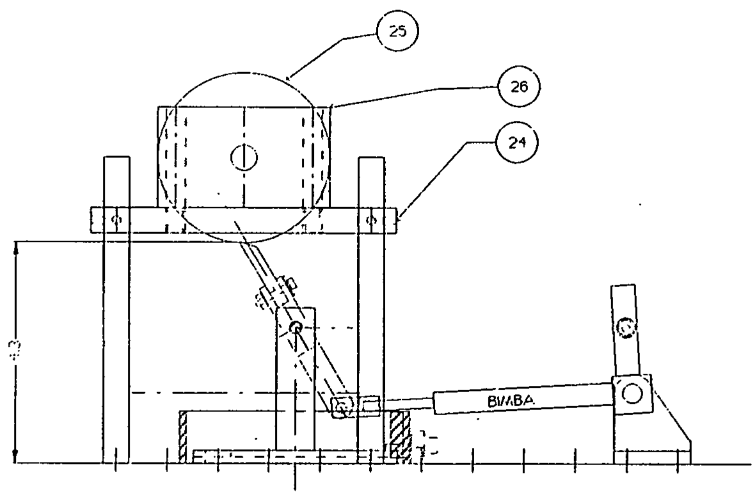

NOTES:
1) See DWG. A490-07-ID-05 for original wiper configuration
2) Use 8-32 set screws on PN24

PART#	DESCRIPTION	MATERIAL	QTY
24	Roll Bracket	AL OR CR?	2
25	Rubber Roll 3-3/8"	Exist	1
26	FAFNIR PBB	Exist	2

REV		DATE
A	FINAL DRAWING	6/17/93
	VEVERKA WIPER ASSEMBLY	
	REVISIONS	

THE INSTITUTE OF PAPER SCIENCE AND TECHNOLOGY
500 10th STREET NW.
ATLANTA, GEORGIA 30318

1" VEVERKA WIPER #2

SCALE: ACT.
DWG NO: A490-07-ID-28

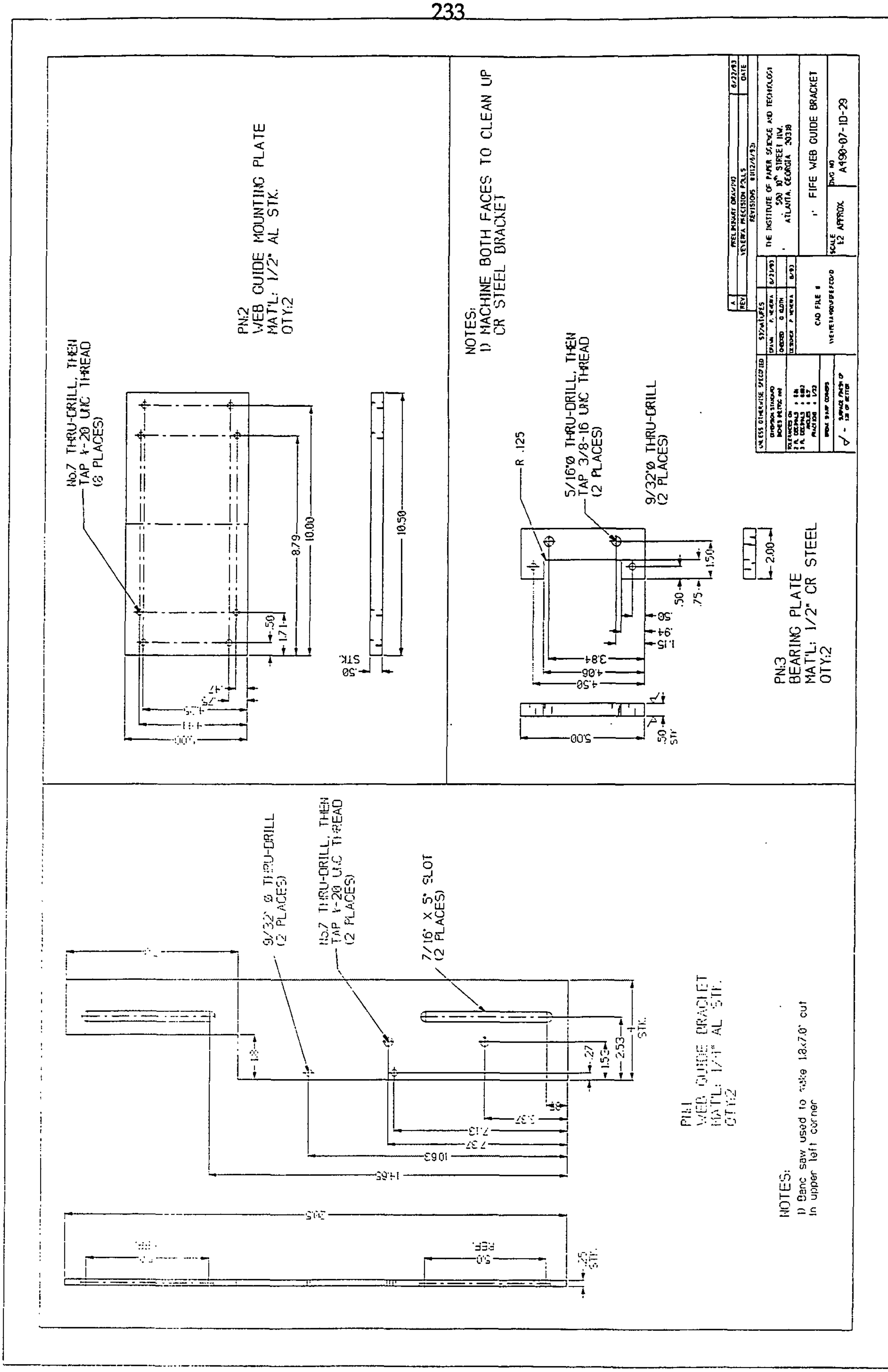
PN:2
WEB GUIDE MOUNTING PLATE
MAT'L: 1/2" AL STK.
QTY:2
No.7 THRU-DRILL, THEN TAP 1/4-20 UNC THREAD (8 PLACES)
10.00
8.79
10.50
.50 STK.
NOTES:
1) MACHINE BOTH FACES TO CLEAN UP CR STEEL BRACKET
R .125
5/16"Ø THRU-DRILL, THEN TAP 3/8-16 UNC THREAD (2 PLACES)
9/32"Ø THRU-DRILL (2 PLACES)
3.84
4.06
4.50
5.00
2.00
1.50
.50 STK
PN:3
BEARING PLATE
MAT'L: 1/2" CR STEEL
QTY:2
9/32" Ø THRU-DRILL (2 PLACES)
No.7 THRU-DRILL, THEN TAP 1/4-20 UNC THREAD (2 PLACES)
7/16" X 5" SLOT (2 PLACES)
2.53
1.53
.27
7.13
7.37
10.63
14.65
.25 STK.
PN:1
WEB GUIDE BRACKET
MAT'L: 1/4" AL STK.
QTY:2
NOTES:
1) Band saw used to make 1.8x7.0" cut in upper left corner
THE INSTITUTE OF PAPER SCIENCE AND TECHNOLOGY
500 10th STREET N.W.
ATLANTA, GEORGIA 30318
1" FIFE WEB GUIDE BRACKET
SCALE 1:2 APPROX.
DWG NO A490-07-ID-29

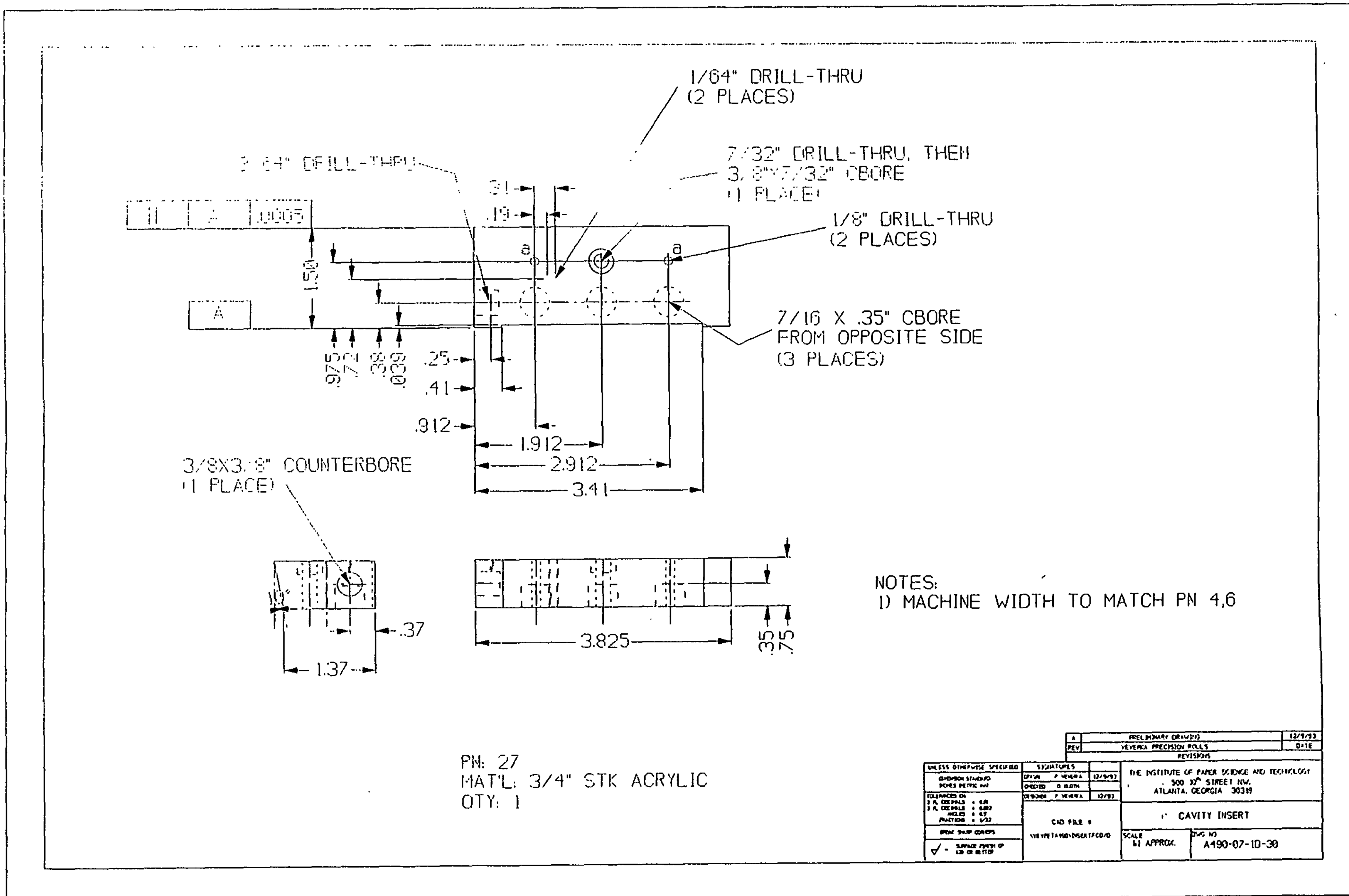
1/64" DRILL-THRU
(2 PLACES)
7/32" DRILL-THRU, THEN
3/8"X7/32" CBORE
(1 PLACE)
1/8" DRILL-THRU
(2 PLACES)
7/16 X .35" CBORE
FROM OPPOSITE SIDE
(3 PLACES)
3/64" DRILL-THRU
.0005
A
1.50
.975
.74
.38
.039
.31
.19
.25
.41
.912
1.912
2.912
3.41
a
3/8X3/8" COUNTERBORE
(1 PLACE)
.37
1.37
3.825
.35
.75
NOTES:
1) MACHINE WIDTH TO MATCH PN 4,6
PN: 27
MAT'L: 3/4" STK ACRYLIC
QTY: 1
PRELIMINARY DRAWING
YEVERKA PRECISION ROLLS
REVISIONS
REV
DATE
UNLESS OTHERWISE SPECIFIED
SIGNATURES
THE INSTITUTE OF PAPER SCIENCE AND TECHNOLOGY
500 10TH STREET NW.
ATLANTA, GEORGIA 30318
1" CAVITY INSERT
CAD FILE #
SCALE
1:1 APPROX.
DWG NO
A490-07-1D-30

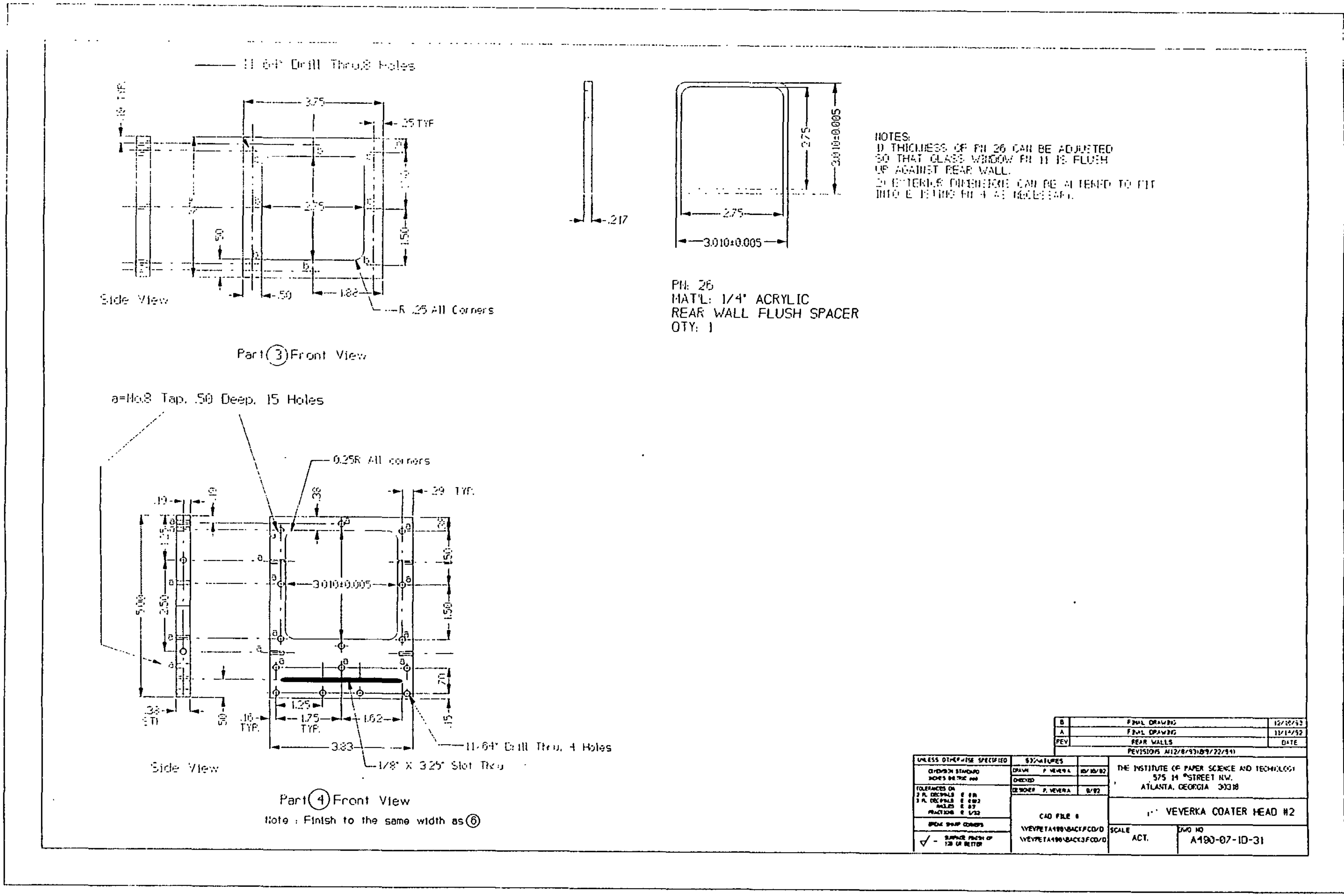

11/64" Drill Thru, 8 Holes
Side View
R .25 All Corners
Part (3) Front View
PN: 26
MAT'L: 1/4" ACRYLIC
REAR WALL FLUSH SPACER
QTY: 1
NOTES:
1) THICKNESS OF PN 26 CAN BE ADJUSTED SO THAT GLASS WINDOW PN 11 IS FLUSH UP AGAINST REAR WALL.
a=No.8 Tap. .50 Deep. 15 Holes
0.25R All corners
11/64" Drill Thru, 4 Holes
1/8" X 3.25" Slot Thru
Side View
Part (4) Front View
Note : Finish to the same width as (6)
FINAL DRAWING
REAR WALLS
THE INSTITUTE OF PAPER SCIENCE AND TECHNOLOGY
575 14 STREET N.W.
ATLANTA, GEORGIA 30318
VEVERKA COATER HEAD #2
A190-07-ID-31

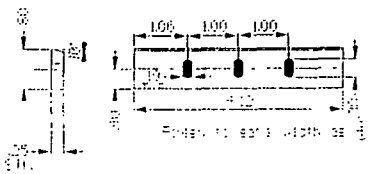

Part (8) Top View

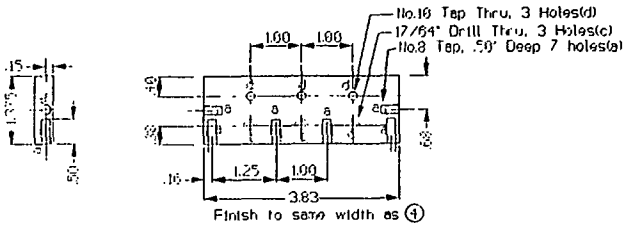

Part (6) Top View

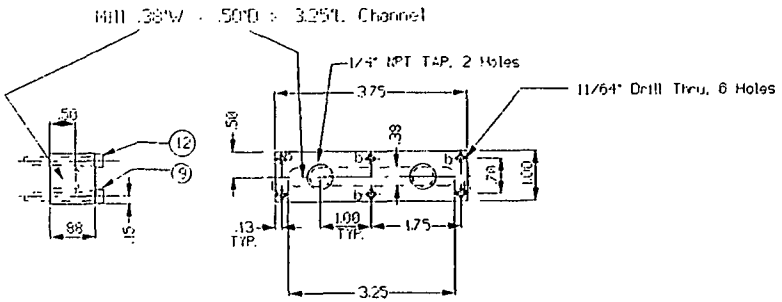

Part (7) Front View

REV	BLADE/BOTTOM DISTRIBUTION CHAMBER	DATE
B	FINAL DRAWING	12/10/93
A	FINAL DRAWING	10/15/93

REVISIONS 8/22/93

UNLESS OTHERWISE SPECIFIED
DIMENSION STANDARD
MOVES AS TYP. mm
TOLERANCES ON
2 PL DECIMALS ± .05
3 PL DECIMALS ± .030
ANGLES ± 0°
FRACTIONS ± 1/32
BREAK SHARP CORNERS
√ - SURFACE FINISH OF 125 OR BETTER

SIGNATURES

DRAWN	P. VEVERKA	10/20/93
CHECKED		
DESIGNED	P. VEVERKA	8/93

CAD FILE #
\VEVPETA190\ECB01PCD/D
\VEVPETA190\ECB013FCD/D

THE INSTITUTE OF PAPER SCIENCE AND TECHNOLOGY
575 14 TH STREET NW.
ATLANTA, GEORGIA 30318

TITLE: VEVERKA COATER HEAD #2

SCALE: ACT.

DWG NO: A190-07-ID-32

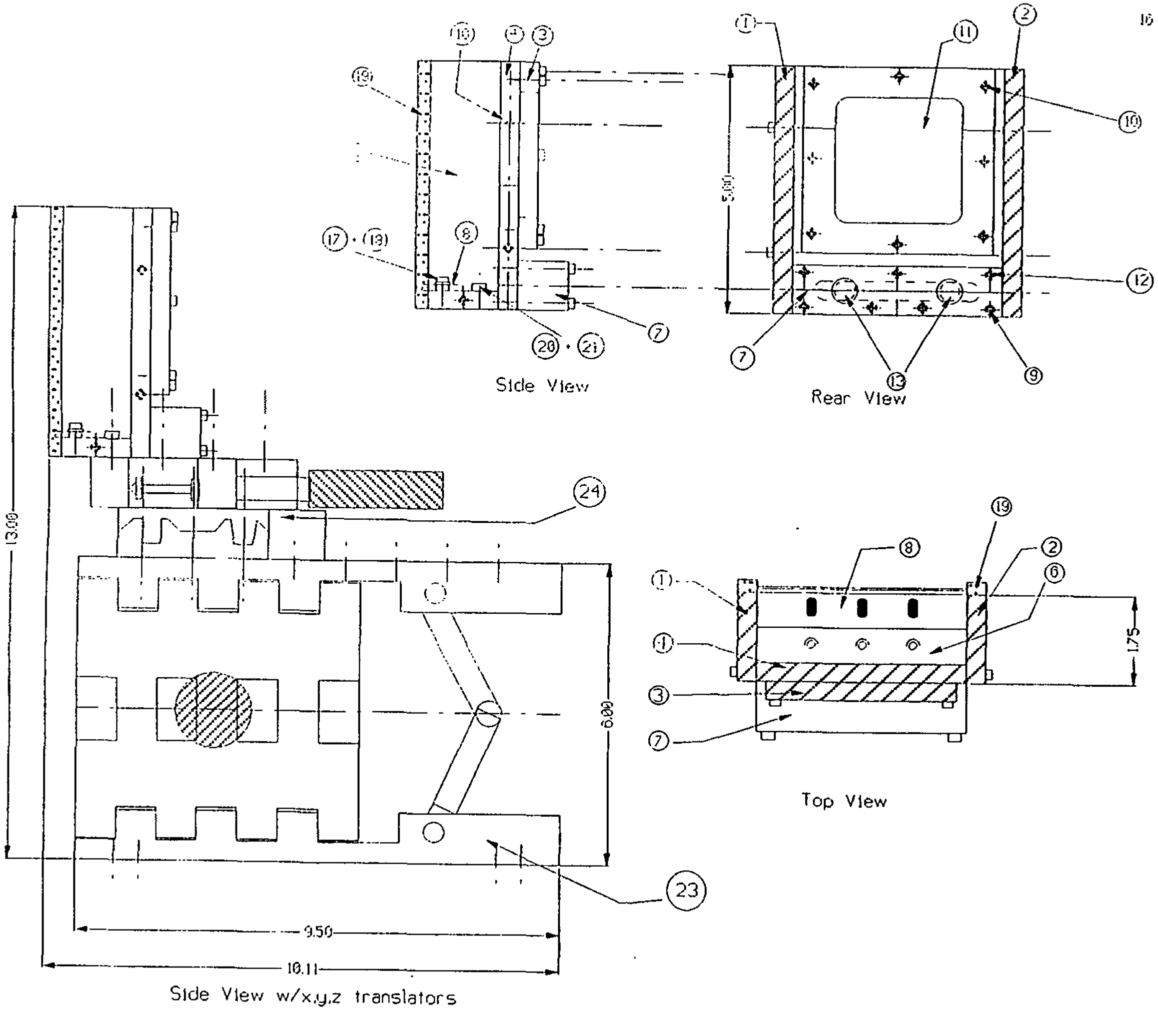

NOTES:
1) Horizontal translator part#23 can provide 23 lb. of force
2) Small letters indicate same socket head type
3) See additional drawings for individual parts
4) Part 25 can be any type of non-marring plastic and does not have to be size No.5

PART#	DESCRIPTION	MATERIAL	QTY
1	Left Wall	3/8" Acrylic	1
2	Right Wall	3/8" Acrylic	1
3	Glass Backing/Rear Wall	3/8" Acrylic	1
4	Rear Wall	3/8" Acrylic	1
6	Bottom Wall	3/8" Acrylic	1
7	Distribution Chamber	1" Acrylic	1
8	Blade	1/4" Acrylic	2
9	No.8x1-3/4" Socket HH	SS	4
10	No.8x3/4" Socket HH	SS	14
11	3"x3"x1/8" 0.25"R Glass	S1-UVA Quartz	1
12	No.8x1-1/4" Socket HH	SS	3
13	1/4"MNPT Quick Connect	Delrin	2
14	1/8"MNPT Quick Connect	Delrin	2
15			
16	Fiber Optic Sensor	N/A	1
17	No.10x5/8" Socket HH	SS	3
18	No.10 Washer	SS	3
19	3/16"x3/8" Closed Cell	Vinyl	2
20	1/4"-20x3/4" Socket HH	SS	3
21	1/4" ID O-Ring	Butyl rubber	3
			2
23	Newport Model 431-2	Exist	2
24	Lab Jack	Exist	1
25	No.5x1/2" Bolt	Nylon	1

REV		DATE
A	FINAL DRAWING	11/14/92
	VEVERKA COATER HEAD	
	REVISIONS 09/22/94	

UNLESS OTHERWISE SPECIFIED
SIGNATURES: DRAWN P. VEVERKA 10/8/92; CHECKED; DESIGNER P. VEVERKA 9/92
THE INSTITUTE OF PAPER SCIENCE AND TECHNOLOGY
575 14 STREET N.W.
ATLANTA, GEORGIA 30318
1" VEVERKA COATER HEAD #2
CAD FILE #
SCALE ACT.
DWG NO A499-07-10-33

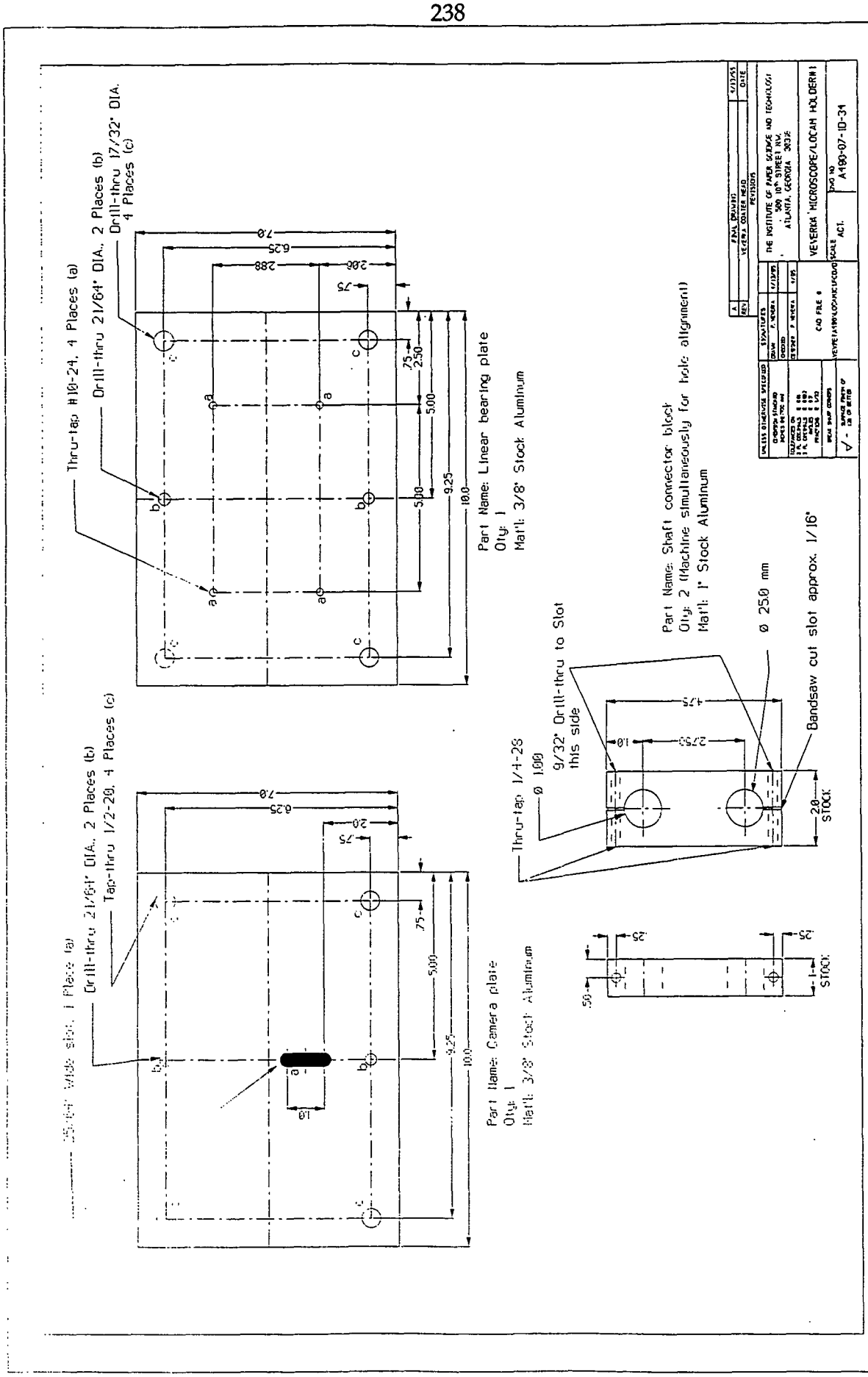
Thru-tap #10-24, 4 Places (a)
Drill-thru 21/64" DIA, 2 Places (b)
Drill-thru 17/32" DIA, 4 Places (c)
Part Name: Linear bearing plate
Qty: 1
Matl: 3/8" Stock Aluminum
Drill-thru 21/64" DIA, 2 Places (b)
Tap-thru 1/2-20, 4 Places (c)
Part Name: Camera plate
Qty: 1
Matl: 3/8" Stock Aluminum
Thru-tap 1/4-28
Ø .190
9/32" Drill-thru to Slot this side
Part Name: Shaft connector block
Qty: 2 (Machine simultaneously for hole alignment)
Matl: 1" Stock Aluminum
Ø 25.0 mm
Bandsaw cut slot approx. 1/16" wide
2.0 STOCK
1.0 STOCK
VELVERKA MICROSCOPE/LOCAM HOLDER #1
A190-07-ID-34
THE INSTITUTE OF PAPER SCIENCE AND TECHNOLOGY
500 10th STREET NW,
ATLANTA, GEORGIA 30318

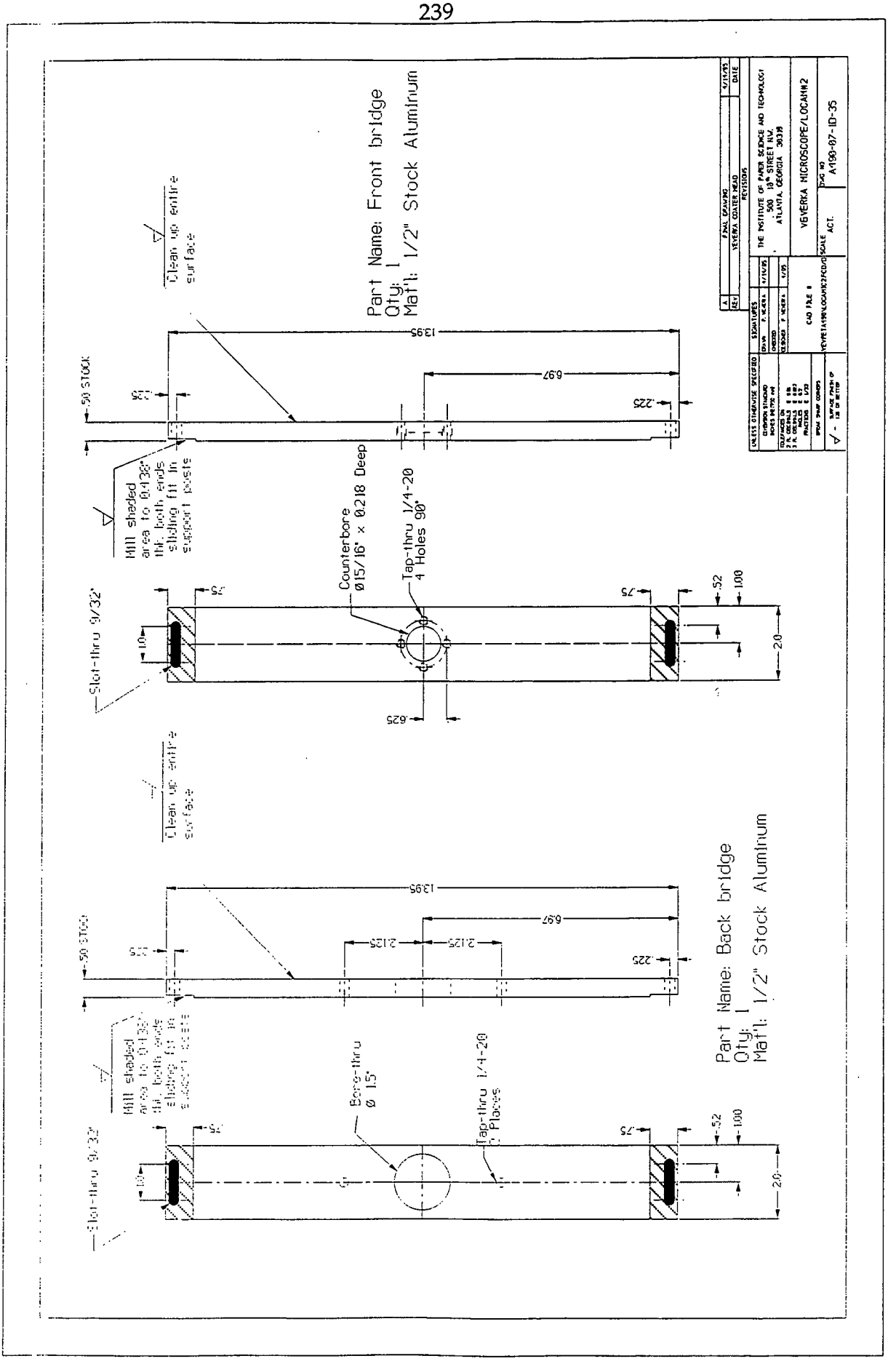
Part Name: Front bridge
Qty: 1
Matl: 1/2" Stock Aluminum
Clean up entire surface
Mill shaded area to 0.138" thk. both ends sliding fit in support posts
.50 STOCK
13.95
6.97
.225
Counterbore Ø15/16" × 0.218 Deep
Tap-thru 1/4-20 4 Holes 90°
Slot-thru 9/32"
.75
1.00
.52
2.0
.625
Part Name: Back bridge
Qty: 1
Matl: 1/2" Stock Aluminum
2.125
Bore-thru Ø .15"
Tap-thru 1/4-20 2 Places
FINAL DRAWING
VEVERKA COATER HEAD
REVISIONS
THE INSTITUTE OF PAPER SCIENCE AND TECHNOLOGY
500 10th STREET N.W.
ATLANTA, GEORGIA 30318
VEVERKA MICROSCOPE/LOCATOR2
CAD FILE #
SCALE
ACT.
DWG NO
A1993-07-ID-35

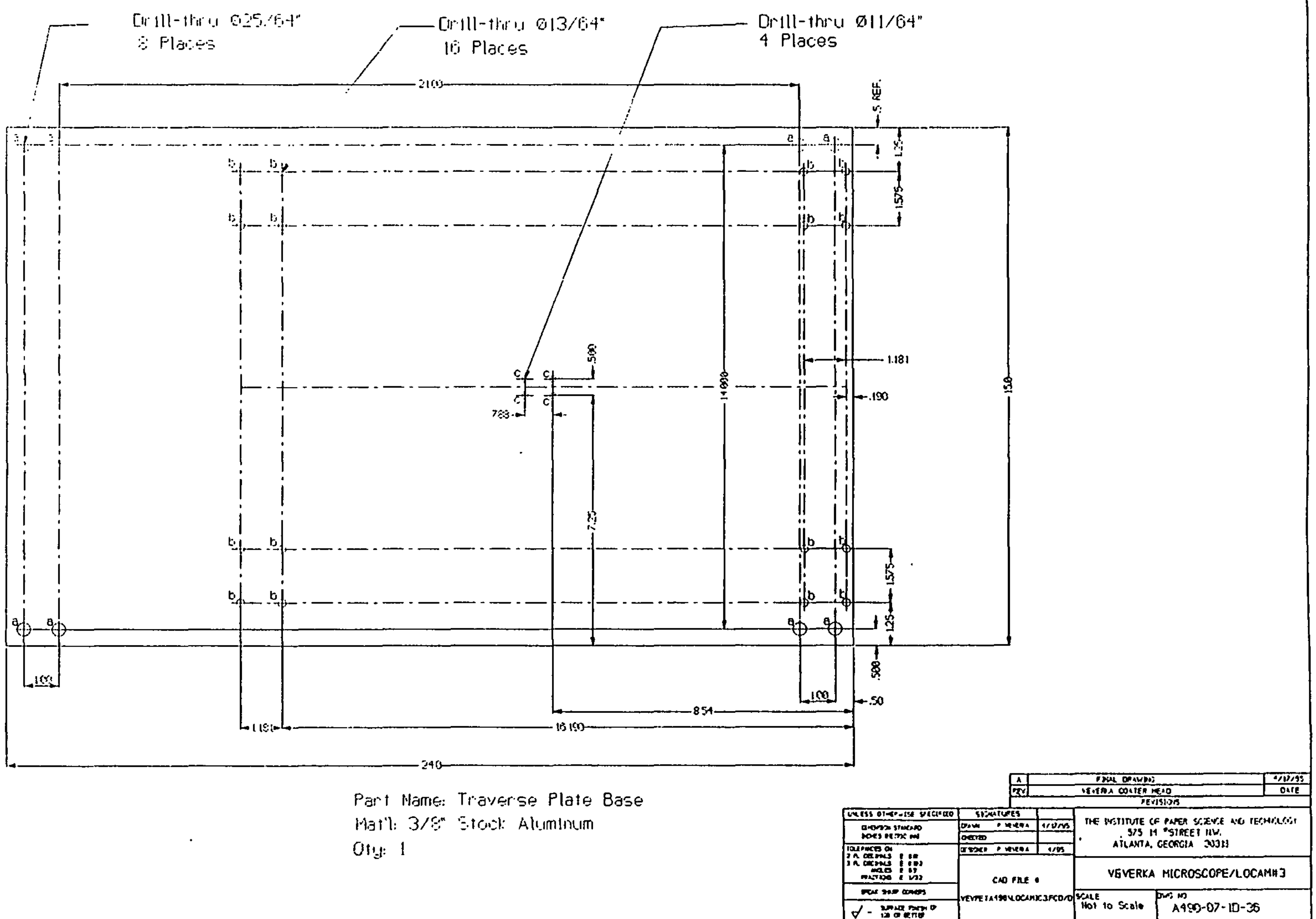
Drill-thru Ø25/64"
8 Places
Drill-thru Ø13/64"
16 Places
Drill-thru Ø11/64"
4 Places
2100
240
150
14.000
16.190
8.54
7.25
1.181
1.575
1.25
.5 REF.
.500
.50
.190
.783
1.00
Part Name: Traverse Plate Base
Mat'l: 3/8" Stock Aluminum
Qty: 1
THE INSTITUTE OF PAPER SCIENCE AND TECHNOLOGY
575 14 STREET NW.
ATLANTA, GEORGIA 30318
VEVERKA MICROSCOPE/LOCAM#3
Not to Scale
A490-07-10-36

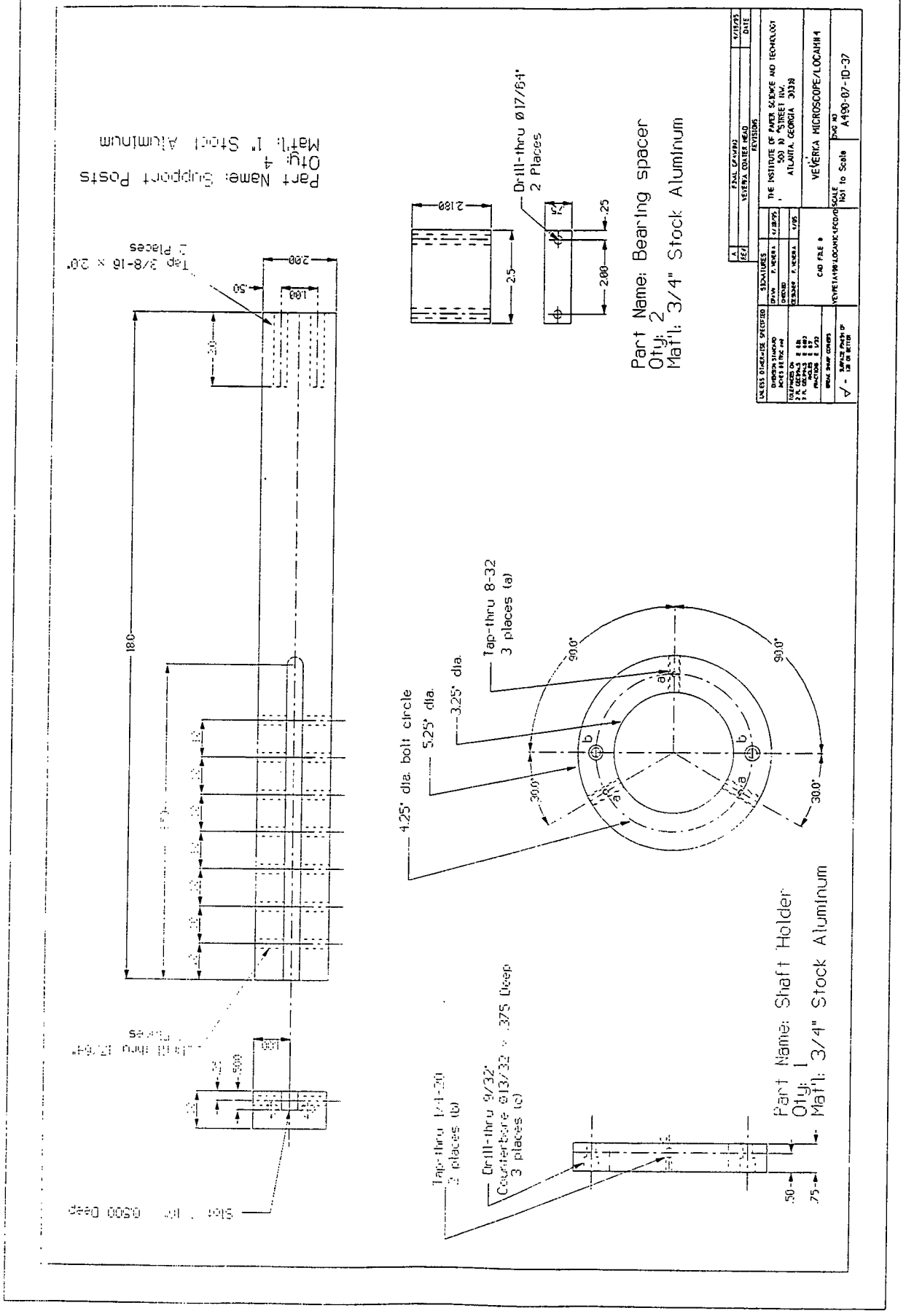
Part Name: Support Posts
Qty: 4
Matl: 1" Stock Aluminum
Tap 3/8-16 x .20" 2 Places
Drill-thru Ø17/64" 2 Places
Part Name: Bearing spacer
Qty: 2
Matl: 3/4" Stock Aluminum
4.25" dia. bolt circle
5.25" dia.
3.25" dia.
Tap-thru 8-32 3 places (a)
90.0°
30.0°
Tap-thru 1/4-20 3 places (b)
Drill-thru 9/32" Counterbore Ø13/32 x .375 Deep 3 places (c)
Part Name: Shaft Holder
Qty: 1
Matl: 3/4" Stock Aluminum
FINAL DRAWING
VEVERIA COLTER HEAD
REVISIONS
THE INSTITUTE OF PAPER SCIENCE AND TECHNOLOGY
500 10th STREET N.W.
ATLANTA, GEORGIA 30318
VEVERIA MICROSCOPE/LOCATOR
CAD FILE #
SCALE
Not to Scale
DWG NO
A490-07-ID-37

APPENDIX III

LISTING OF COMPONENTS, VENDORS, AND FABRICATORS FOR APPARATUS

This Appendix contains the main and secondary components used in all of the experiments and for construction of the experimental film coater. The part number and serial number have additionally been supplied for reference. The donated equipment is noted in the acknowledgements. The apparatus systems have been broken into subsystems as defined in the Chaper IV Section 4.1.

Table III.1. Summary of experimental systems components.

APPARATUS COMPONENT	DESCRIPTION OF COMPONENT	VENDOR
WEB TENSION CONTROL		
Tension Display and Control	Magpowr DIGITRAC with 90 VDC output power amplifier	Magnetic Power Systems, Inc. Fenton, MO 314-343-5550
Magnetic Particle Brake	Magpowr GLOBAL brake line model no. GBA, 5.5 ft-lb rated torque	
Tension Sensors	(2) Magpowr RMTS1-15, rotating modular tension sensors (1-15 lb) for live shaft rolls	
WEB GUIDANCE SYSTEM		
Signal Processor	FIFE Model No. CSP-01-06 signal processor with ISCT-03 servo center	Fife Corporation Oklahoma City, OK 405-755-1600
Sensor and Amplifier	FIFE Model No. SE-11-1T sensor assembly with M-17 mounting bracket; X10 Amplifier	
Web Guide	FIFE Model SYMAT 25 offset pivot guide assembly with 2.00" dia. x 6.30" face., Wrap Style 11	
Web guide mounting bracket	IPST drawing no. A490-07-1D-29	GTRI Mechanical Services Atlanta, GA 404-894-3680
DRIVE SYSTEM		
Motor/Power Supply	RELIANCE MinPak Plus VS Drive, 1725 rpm, 3/4 HP, model T56H1022, frame EF56C, Power Supply/Controller 14C10	Reliance Electric Cleveland, OH 216-266-7000

Table III.1(continued).

Motor mounting plate	IPST drawing no. A490-07-1D-29	IPST's machine shop
Digital Motor Speed Controller	FENNER M-Trim 2 with analog output	Fenner Industrial Controls Maple Grove, MN 612-424-7800
Proximity Feedback Sensor	RED LION proximity feedback sensor, Model ARCJ	J.W. Vaughn Co., Inc. Columbia, SC
Speed Reducer	Grove Flexline BMQ262-2 RS, 50:1 ratio	Grove Gear Corporation Union Grove, WI 414-878-1221
Adjustable Motor Mount Base	Sliding mount base for NEMA motors, Cat. no. 6531K12	McMaster-Carr Supply Co. Atlanta, GA 404-346-7000
HTD Sprockets	Wood's HTD sprocket nos., (3) P80-8M-30-SK, P38-8M-30-SH, (2) P36-8M-30-SH, P28-8M-30-QT	T.B. Wood's Sons Company Chambersburg, PA 717-264-7161
HTD Belts	Wood's HTD belt length & pitch code, (1) 2000-8M, (1) 2400-8M	
Surface Wind Drive Rolls	Blank rolls per IPST drawing no. A490-07-1D-20	GTRI Mechanical Services
Roll covering	Stowe Woodward PRESTO CONDUCTIVE, (1) O.D. 10.000", (1) O.D. 10.005"	Stowe Woodward Co. Griffin, GA 404-227-8000 Contact: Jack Robbins
Drive Roll Bearings	BrowNing rigid mount VPS-200 Series pillow block bearing, 1.25" bore., Cat. no. 5X694	W.W. Grainger, Inc. Atlanta, GA 404-355-1984
UNWIND/REWIND STAND		
Cantilevered Unwind Air Shaft	TIDLAND 300 Series 3" Pad Air Shaft, 31.25" overall length, end valve per sketch by Peter Veverka, Serial# 177975	Tidland Corporation Keene, NH 800-426-1000 Contact: Bill Leistritz
Canitlever Pillow Block Bearings	(2) Browning rigid mount VPS-200 Series pillow block bearing, 1.5" bore., Cat. no. 5X696	W.W. Grainger, Inc.
Safety Chuck	(2) BOSCH 22-30 FLO Safety Chucks, 1.25" square journal	Tidland Corporation Camas, WA 206-834-2345 Contact: Bill Leistritz
Rewind Air Shaft	TIDLAND 300 series 3" Pad Air Shaft w/ 1.25" square journals, 14" overall length per sketch by Peter Veverka, Serial# 177976	Tidland Corporation

Table III.1(continued).

Air Gun	TIDLAND high volume safety air gun w/ 10' recoiling air hose, Cat. no. 128052 and 128155	Tidland Corporation
Linear Bearings	(2) Thompson 24" double shaft end supported system, Cat. no. 1BB08BHO L24	Motion Industries, Inc. Austell, GA 404-948-5300
Unwind Roll Lift	BIMBA (2) 1-3/4" bore double acting pivot type air cylinder 11" stroke, model no. 2411-DP, (2) D-620-1 pivot brakcets, (2) FQP44K flow controls	Tool Systems, Inc. Atlanta, GA 404-491-0773
Precision Bearings	NTN TOYO bearing 608ZZ P5	NTN Bearing Corp. of America Norcross, GA 404-448-4710 Brownell Electro Inc. Forest Park, GA 404-362-9009
Ion Air Knife	Exair Model No. 7206 ionizing air knife 6" active area	Exair Corporation Cincinnati, OH 513-671-3322
Vibration Isolation Table		Technical Manufacturing Corp. Peabody, MA 508-532-6330
SENSORS		
Thermocouple	OMEGA Type T sub-miniature thermocouple, 0.020" sheath dia., special limits of error ±0.5°C or ±0.4% (ANSI MC96.1(1975)), Cat. no. TMQSS-020E-6-SLE	Omega Engineering, Inc. Stamford, CT 203-359-1660
Thermocouple Amplifier	OMEGA Omni-Amp IIB	
Thermocouple Wire	OMEGA 36" Glass braid thermocouple wire for Type T, 24 gauge, special limits of error	
Fiber Optic Displacement Sensor	PHILTEC Model LT88NE1 high performance fiber optic displacement transducer, LED light source 880 nm.	Philtec, Inc. Annapolis, MD 410-757-8138
Hand Held Static Sensor	3M Model 709 hand held static sensor, accuracy ±10%, low range to 1990 volts, high range to 19,900 volts	3M Austin Metrology Laboratory Austin, TX 800-328-1368
Electrostatic Volmeter	MONROE Isoprobe® Model 244A-2 electrostatic voltmeter, Series A2465	Monroe Electronics, Inc. Lyndonville, NY 716-765-2254
Electrostatic Probe	MONROE Model 1017S side looking miniature probe w/ 22 D gradient adapter	

Table III.1(continued).

Accelerometer	(2) Endevco Model 2217 Accelerometers, Ser. # CA03 and DE04	Endevco Corporation Pasedena, CA
Charge follower	(2) Columbia Research general purpose charge follower Model 4101, Serial# 108 and 109	Columbia Research Laboratories, Inc. Woodlyn, PA
Calibration Tachometer	SHIMPO DT-105 hand held digital tachometer	Shimpo America Corporation Lincolnwood, IL 708-679-6765
Gear Flow Transmitter	AW Company Model ZHM-01L with IG02H flmtr, Serial No. 312189	AW Company Racine, WI 414-884-9800
Gear Flow Display	AW Company FEM-02 LCD display	
Frequency to Voltage Convertor	ANALOG DEVICES Model 451J 10kHz frequency to voltage convertor	Analog Devices Norwood, MA 617-329-4700
COATING DELIVERY		
Coating Head	Puddle coater type coating head with cavity dimensions of 1.375x4.625x(4.00 to 3.83)". IPST drawing no. A490-07-1D-01(4" wide), A490-07-1D-33(3.83" wide)	IPST Machine Shop
Coating Head Edge Seal	ACE Open cell self-adhesive vinyl weather stripping, 3/8" width.	Ace Hardware Atlanta, GA 404-351-4240
Pump	MOYNO SP Pump 300 Series model no. 33104, 316 SS, 150 psig discharge pressure	Robbin & Myers, Inc. Fluids Handling Group Springfield, OH 513-327-3553
Pump Motor	RELIANCE ImPak Plus VS Drive, 1750 rpm, 3/4 HP, model T56H1022, frame EF56C, Controller 8C10	Reliance Electric Cleveland, OH 216-266-7000
Pump Motor Reducer	Grove Flexline BMQ175-2 XQ, 20:1 ratio	Grove Gear Corporation
Pump Base	IPST drawing no. A490-07-1D-27	IPST's machine shop
In-line Filters	Micro Separation Inc. polypropylene submicronic capsule filters, (1) 10 micron rating no. 43825K25, (1) 1.2 micron rating no. 43825K25	McMaster Carr Supply Co.
Tubing (delivery and recovery)	Tygothane® polyurethane tubing, 0.25"I.D., .125" wall	McMaster Carr Supply Co.
COATING RECOVERY		
Pump Head/Motor Drive	Masterflex ® L/S pump head Cat. no. 7017-20, drive cat. no. 7553-00, 1680 ml/min @ 600 rpm.	Cole Parmer Instrument Co. Chicago, IL 708-647-4340

Table III.1(continued).

Catchall Pan		
Wiper Blade (Rev. 1 & 2) and Pan	IPST drawing nos. A490-07-1D-05, A490-07-1D-06, A490-07-1D-07, A490-07-1D-28	IPST's machine shop
Trunnion air cylinder	BIMBA 7/16" bore trunnion mounted air cylinder, spring return, mod. no. BFT-011, TRB-1 trunnion bracket, FQP1K flow control	Tool Systems, Inc. Atlanta, GA 404-491-0773
DATA ACQUISITION		
Host Computer	IBM PS/2 77 DX2 computer w/ 500 Mb hard drive. 80486DX2 CPU w/ Microchannel architecture	International Business Machines
A/D Board	NATIONAL INSTRUMENTS MC-MIO-16L, Part# 180650-01 Rev. D, Serial# 3523	National Instruments Corporation Austin, TX 512-794-0100
Terminal Board	NATIONAL INSTRUMENTS SC-2070 general purpose termination breadboard, Part#180950-01 Rev. D, Serial# 00881	
Computer Control Software	NATIONAL INSTRUMENTS LabVIEW®for Windows, Ver. 2.5.2	
OPTICAL/IMAGING COMPONENTS		
Zoom stereomicroscope (SZM)	Wild M8 stereomicroscope with 1:8 zoom range; 1.6X and 0.4X additional objectives; Phototube HU with 40 mm eyepiece tube dia., Phototube A	Wild Heerbrugg Ltd. Heerbrugg, Switzerland (071) 703131 Local Representative: Vashaw Scientific, Norcross, GA 404-447-5632
Zoom Stereomicroscope Mount	IPST's drawing no. A490-07-1D-26	IPST's machine shop
16-mm Pin Register Camera	Redlake LOCAM II with A.N.D.S.(alpha numeric data system) film marking, capable of 500 full frames/sec max., Model#13-0200, Serial# 278	Redlake Corporation Morgan Hill, CA 408-779-6464
16 mm Film	Eastman-Kodak 7278 Tri-X Reversal Film, 400' and 100' reels, 3200K EI160/23°, daylight EI 200/240°, Cat. no. 164 3253	Chambless Cine Equipment Atlanta, GA 404-767-5210
Photographic Light Meter	Gossen Luna Pro	Gossen GmbH Mess-, Regelund Stromversorgungstechnik Erlangen, Germany 9131-8271

Table III.1(continued).

Ronchi Rulings	(1) 12.5 cycles/mm stock ronchi ruling 2"x2" image area, (1) 12.5 cycles/mm stock ronchi ruling 4"x4" image area, (1) 25 cycles/mm 1"x1" image area, (1) 5 cycles/mm 4"x4" image area, all line/space ratios 1:1 ± 4%	Applied Image, Inc. Rochester, NY 716-482-0300
Coater Head Glass Windows	(1) S-1 UVA Window 3" x 3" x 0.125", P/N ZQ130125, (1) S-1 UVA window 4" x 4" x 0.125", P/N ZQ140125R	Esco Products, Inc. Oak Ridge, NJ 201-697-3700
Color High Resolution RGB Video Camera	MicroImage Model I RGB video camera, C2051 Series	World Video Sales Co., Inc. Boyertown, PA 215-754-6800
External Time Code Generator	Horita II TG-50, Ver. T22, 9 Volt Power Supply	Horita Mission Viejo, CA 714-489-0240
Opal Glass	Flashed opal glass, 127 x 178 x 2.7-3.3 mm, Cat. no. 55.3150	Rolyn Optics Company Covina, CA 818-915-5717
B&W High Performance CCD Camera	4910 Series RS-170 and CCIR monochrome CCD camera, Model# 4915-3000/0000, Serial # 215520	Cohu, Inc. San Diego, CA 619-277-6700
Frame Grabber Board	DT2953 for the IBM PS/2	
Video Cassette Recorder	HR-S6600U	Jyoto Works Co., Ltd. Osaka, Japan
Plano-Convex Lenses	6.0 x 36.0 mm f.l. and 6.0 x 72.0 mm f.l. uncoated technical specification plano-convex lens, Stock# J32,848 and J32,850	Edmund Scientific Company Barrington, NJ 609-573-6250
Helium Neon Laser (HeNe)	Uniphase Novette 4 mW helium neon gas laser, Model # 7507-0, Serial # 721160	Uniphase Corporation San Jose, CA 408-434-1800
Precision Tilt Stage	Newport model F-91TS precision tilt stage, tilt stage component of model F-916 single mode fiber coupler	Newport Corporation Fountain Valley, CA 714-963-9811
PHYSICAL PROPERTY		
Viscometer	Rheometrics Fluids Spectrometer RFS II, Rheosource Series, Part # 706-00026-2 Rev.G, Ser.# BF011 with peripherals Control computer, Environmental control circulator, System control, Compressed air dryer and Rhios Plot and Tools Software	Rheometrics Inc. Piscataway, NJ 908-560-8550

Table III.1(continued).

Viscometer couette fixture	Rheometrics Couette fixture with 32 mm dia. bot and 34 mm dia. cup, bob length 33 mm	Rheometrics Inc.
Viscometer	Haake RV2 w/ PG142 controller and MK500 sensing head	Haake Buchler Instruments Saddle Brook, NJ 201-843-2320
Surface Tensiometer	Cahn Dynamic Contact Angle Analyzer DCA 312, Part # 93120-01 with computer control software. Cahn temperature control beaker, Part# 212225-02	Cahn Instruments, Inc. Cerritos, CA 90701-2275 310-926-3378
Tensiometer temperature control	Haake F3 temperature bath	
Tensiometer Wilhelmy plates	Fisher Fisherfinest Premium Cover Glass, 24 x 30 mm No.1, Cat. No. 1254856 VWR Selected Micro Cover Glasses, 22 x 3 mm No. 1, Cat. No. 48393-026	Fisher Scientific VWR Scientific Marietta, GA 30066 404-423-1354
Pycnometer	Hubbard-Carmick Specific Gravity Bottle, ASTM 25 ml stamped volume, 23.06 ml actual, Part# LX6268-1002	Lurex Manufacturing Co. Vineland, NJ 609-692-5600
Differential Scanning Calorimeter	SETARAM TG-DCS 111 Differential Scanning Calorimeter	Imported from SETARAM France by: Astra Scientific International, Inc. Pleasanton, CA 94566 510-426-6900
DSC Thermal Analysis Software	ASTRA + Thermal Analysis Software, Version 3.XX	Astra Scientific International, Inc.
Electrical Resistivity	Keithly Model 6105 Resistivity Adapter Ser.# 33738, 610 CR Meter Serial# 64739	Keithley Instruments, Inc. Cleveland, OH
Power supply	Model APH 2000DM high voltage power supply, Serial# 137906	Kepco Flushing, NY 718-461-7000
MATERIALS		
Polyester Film	Melinex™ 454/ 142 gauge polyester film. High clarity film with both sides pretreated to promote adhesion	ICI Films Hopewell, VA 804-530-9300
	Melinex™ 453/ 200 gauge polyester film. High clarity film with one side pretreated to promote adhesion	ICI Films

Table III.1(continued).

Regenerated Cellulose Film	PUT 002 Type 195 Uncoated regenerated cellulose film which normally contains water and a softening agent	Flexel, Inc. Atlanta, GA 30346 800-541-8682
Film converting	Slitting and winding, 25 rolls, 4"x 10,000' each on a 3" dia. core	Plastic Suppliers, Inc. Marietta, GA 404-424-0702
Roll cores	3" I.D. x 4" length x 1/4" wall open end tube	Trend-Pak of Atlanta, Inc. Atlanta, GA 404-768-9596
Silicone Oil	Dow Corning 200 ® Silicone Oil, 10 cs, 20 cs, 100 cs, 200 cs, 350 cs, 500 cs, 1000 cs	Chem Central Atlanta Atlanta, GA 404-448-7123
Glycerol	"Diamond Ultra" 99.7% refined glycerine, U.S.P. (edible) grade	The Dial Corporation Montgomery, IL 800-323-5385

APPENDIX IV

EXPERIMENTAL COATER WIRING DIAGRAM

This Appendix contains the wiring diagram for the process control and data acquisition system of the experimental film coater. More details concerning the data acquisition system are contained in Appendices V and XVI. The signal strength and channel configurations are discussed in Appendix XVI.

Many thanks to the design department for helping this setup to run smoothly.

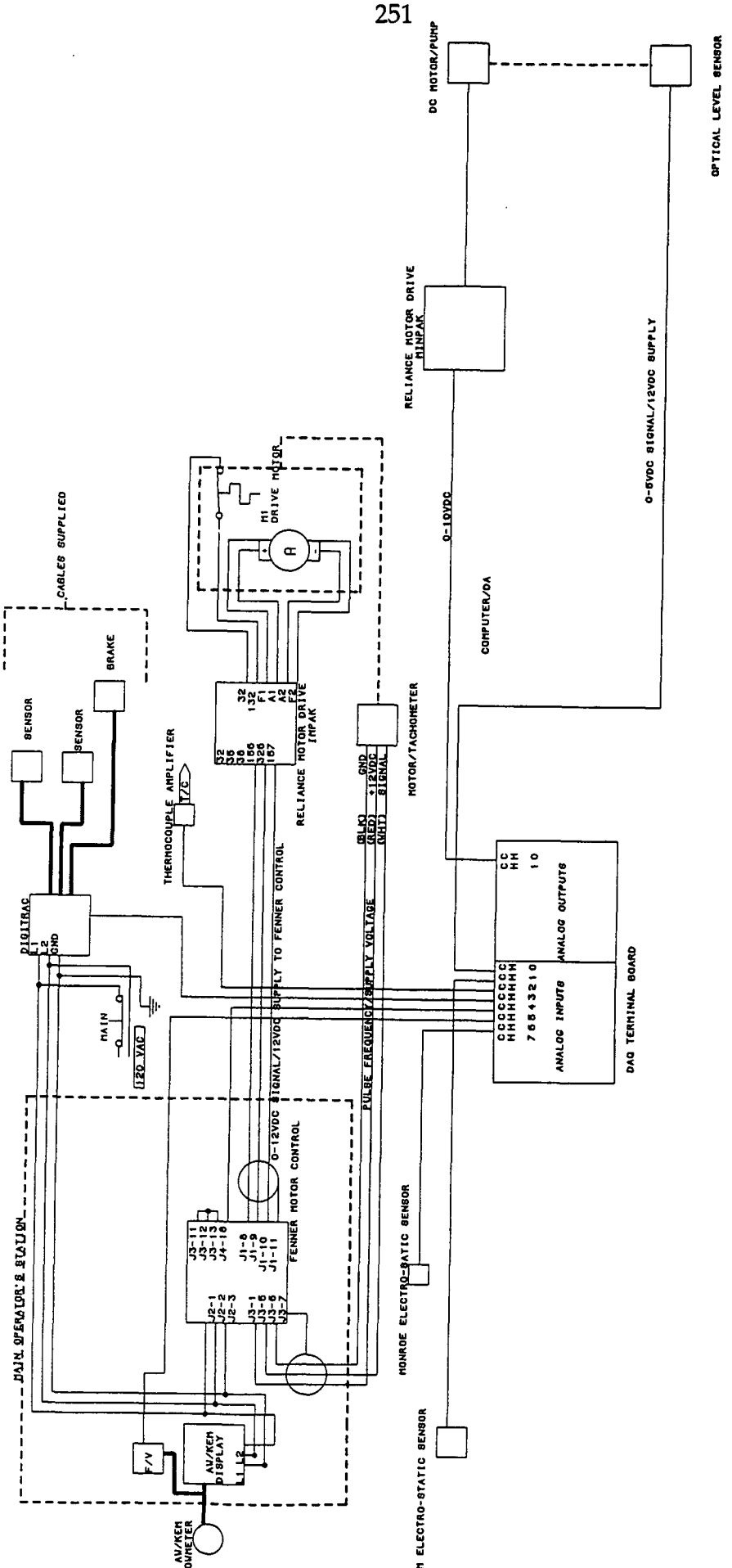
DC MOTOR/PUMP
OPTICAL LEVEL SENSOR
RELIANCE MOTOR DRIVE 3IMPAK
0-10VDC
COMPUTER/DA
0-5VDC SIGNAL/12VDC SUPPLY
CABLES SUPPLIED
M1 DRIVE MOTOR
BRAKE
SENSOR
SENSOR
THERMOCOUPLE AMPLIFIER
TYPE
RELIANCE MOTOR DRIVE 3IMPAK
MOTOR/TACHOMETER
GND
+12VDC
SIGNAL
(BLK)
(RED)
(WHT)
DIGITRAC
L1
L2
GND
MAIN
120 VAC
SUPPLY TO FENNER CONTROL
SUPPLY VOLTAGE
PULSE FREQUENCY
0-12VDC SIGNAL/12VDC
FENNER MOTOR CONTROL
ANALOG INPUTS
ANALOG OUTPUTS
DAQ TERMINAL BOARD
MONROE ELECTRO-STATIC SENSOR
3M ELECTRO-STATIC SENSOR
MAIN OPERATOR'S STATION
AV/KEM DISPLAY
F/V
AV/KEM FLOWMETER

APPENDIX V

LABVIEW DATA ACQUISITION DIAGRAMS AND INTERFACE PANELS

This appendix contains the virtual instrument (VI) diagrams and panels designed for control and data acquisition specifically for the experimental paper film coater used during this project. Descriptions of the five VI's are as follows:

• DATAACQ.VI - Configures the data acquisition board number, channel ranges, sampling rate per channel, and the rate at which data is saved to file. The PID control inputs are configured, and a sweep chart of the liquid height error signal is displayed. Additionally, the speed, temperature, 3M static voltage, and web tension are updated at 5 Hz. ASCII data are logged to a disk at 0.2 Hz. DATAACQ.VI calls on subVIs DATAUNIT.VI, PID.VI, and other LabVIEW library functions.

• DATAUNIT.VI - Configures the scaling and offset factors to convert the raw VDC input signals to the 3M electrostatic voltage, displacement sensor height, temperature, linear speed, web tension, and most importantly the liquid viscosity. The slope and intercept data for liquid viscosity must be entered in a function execution element. The DATAUNIT.VI calls on subVIs CAPILARY.VI, REYNOLDS.VI, and Convert Thermocouple Reading.VI.

• PID.VI - Computes the change in the previous controller signal using the so-called velocity form of the PID control algorithm for a discrete control system (Stephanopoulos 1984, 636). The current, E_n, and two past error signals, E_{n-1} and E_{n-2}, are stored for calculating the current difference in control signal, Δc_n. The velocity

form of the PID control algorithm is given in Eq. [V.1]. The parameters T, τ_I, τ_D, and K_c are the sampling period, integral constant, derivative constant and proportional gain respectively. The main advantages of the velocity over the position form are (a) it does not require initialization of the control signal; (b) it prevents saturation of the control signal due to integral "windup"; and (c) it protects the process against computer failure (Stephanopoulos 1984, 637).

$$\Delta c_n = K_c\left(1+\frac{T}{\tau_I}+\frac{\tau_D}{T}\right)E_n - K_c\left(1+\frac{2\tau_D}{T}\right)E_{n-1} + K_c\frac{\tau_D}{T}E_{n-2} \qquad [V.1]$$

• CAPILARY.VI - This VI takes the speed, viscosity, and temperature input to calculate the surface tension and capillary number. The slope and intercept data for liquid surface tension must be entered in a function execution element.

• REYNOLDS.VI - Takes the speed, viscosity, and temperature input to calculate the surface tension and liquid Reynolds number. The slope and intercept data for liquid viscosity must be entered in a function execution element.

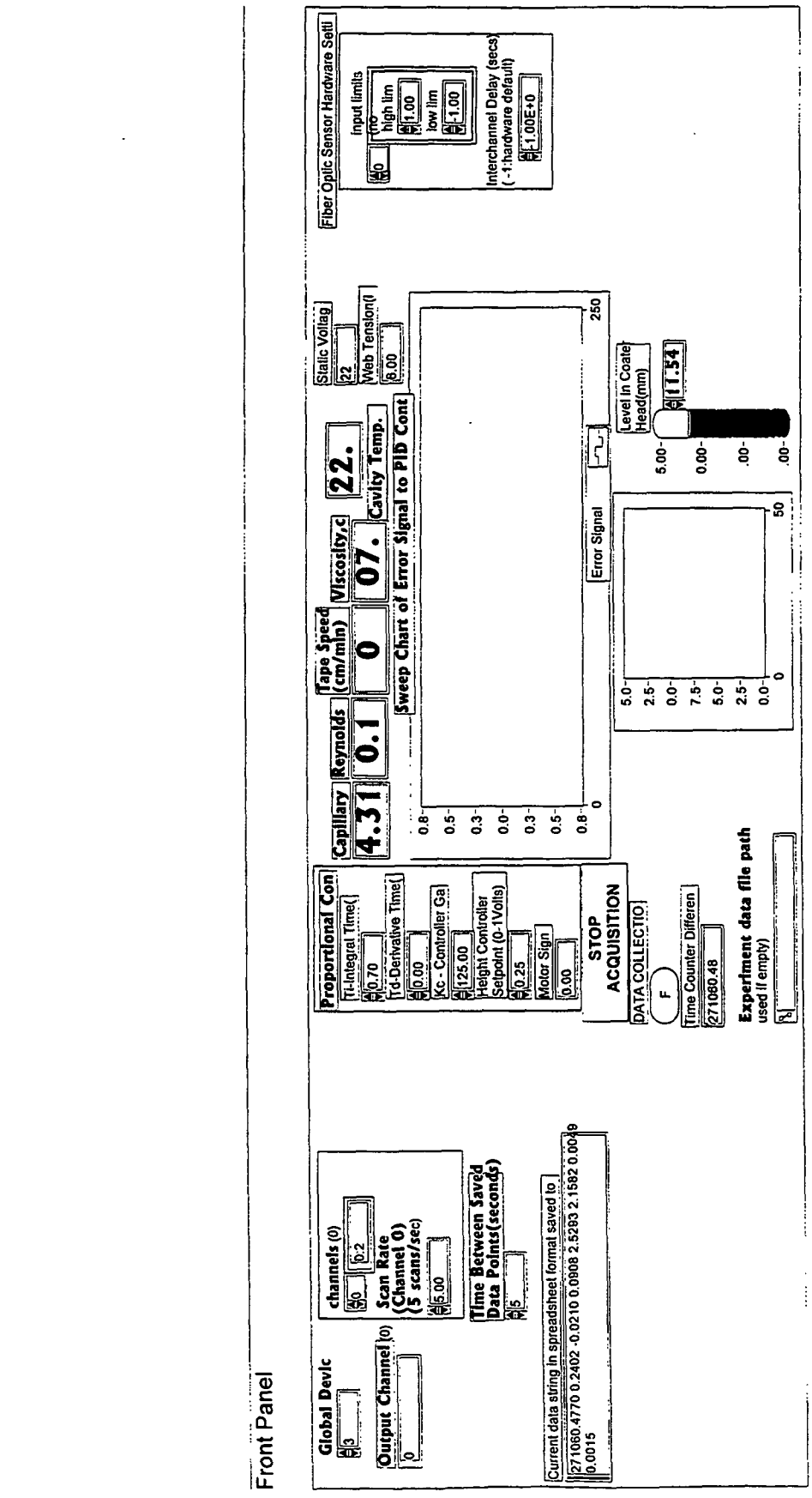

Figure V.1 - DATAACQ.VI Front Panel Diagram

Figure V.2 - DATAACQ.VI Block Diagram

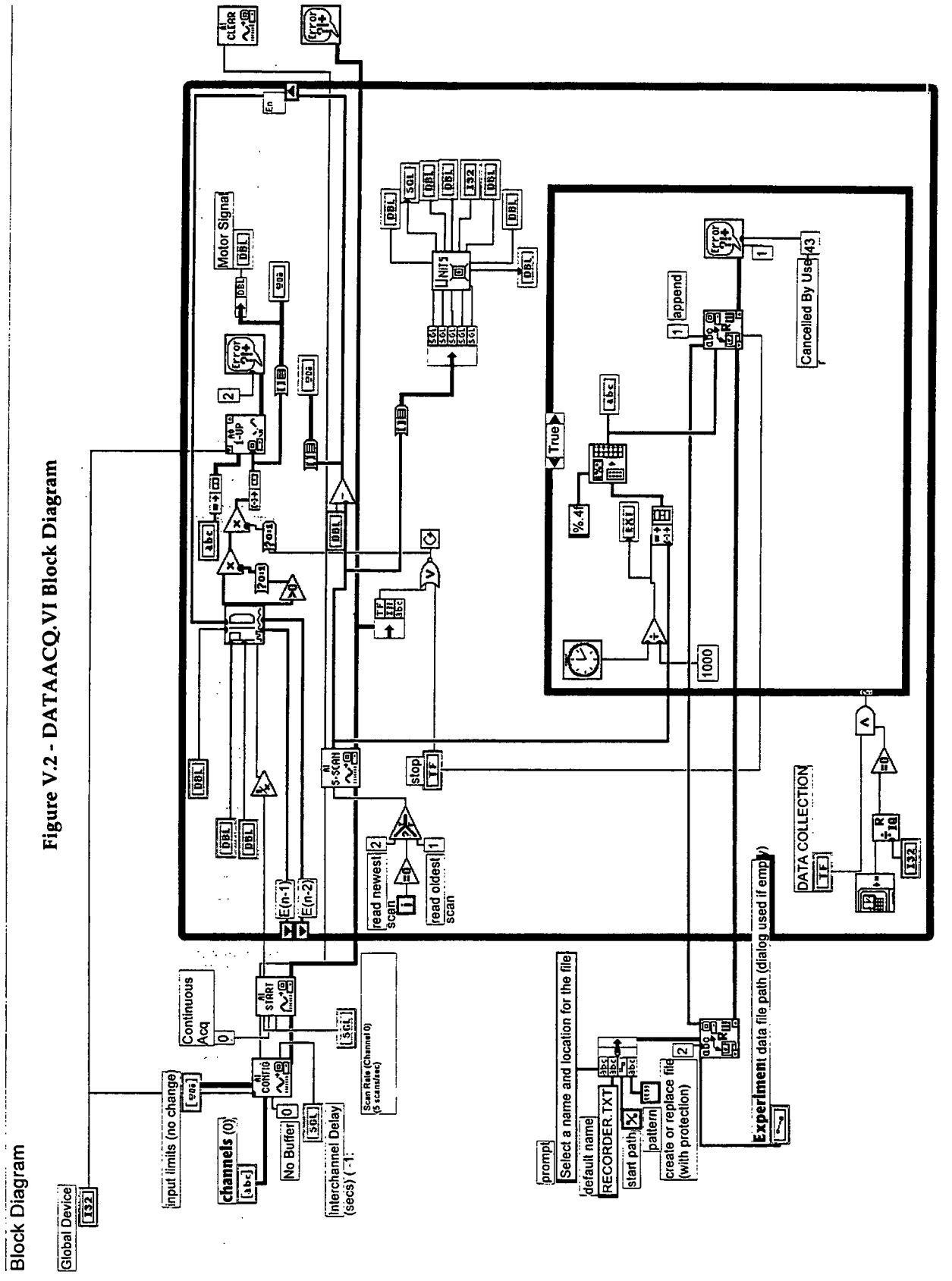

Front Panel

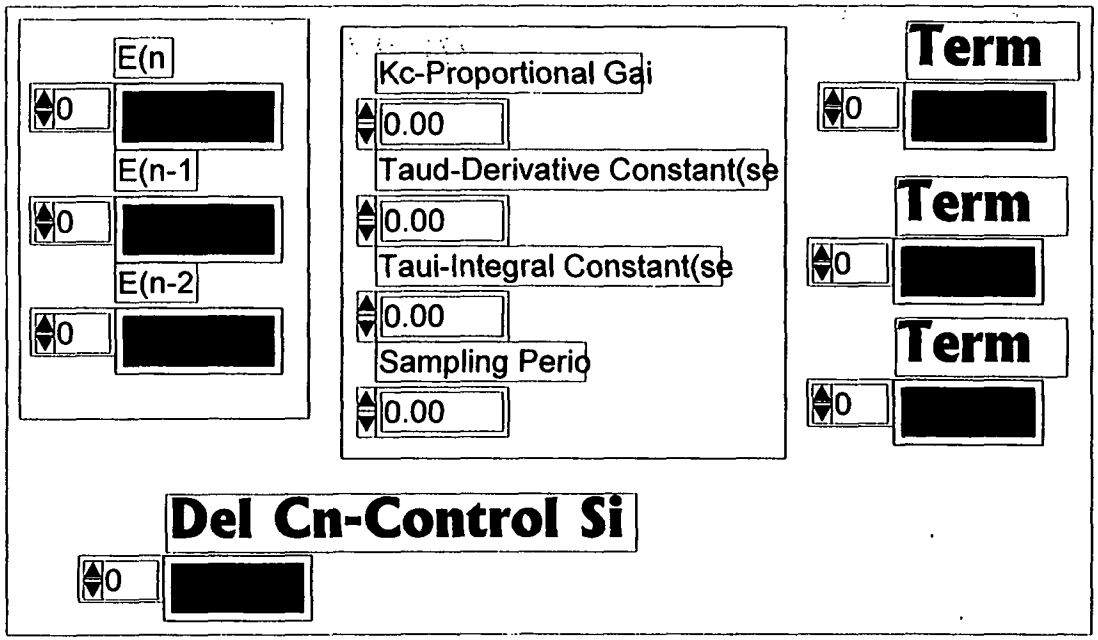

Figure V.3 - PID.VI Front Panel Diagram

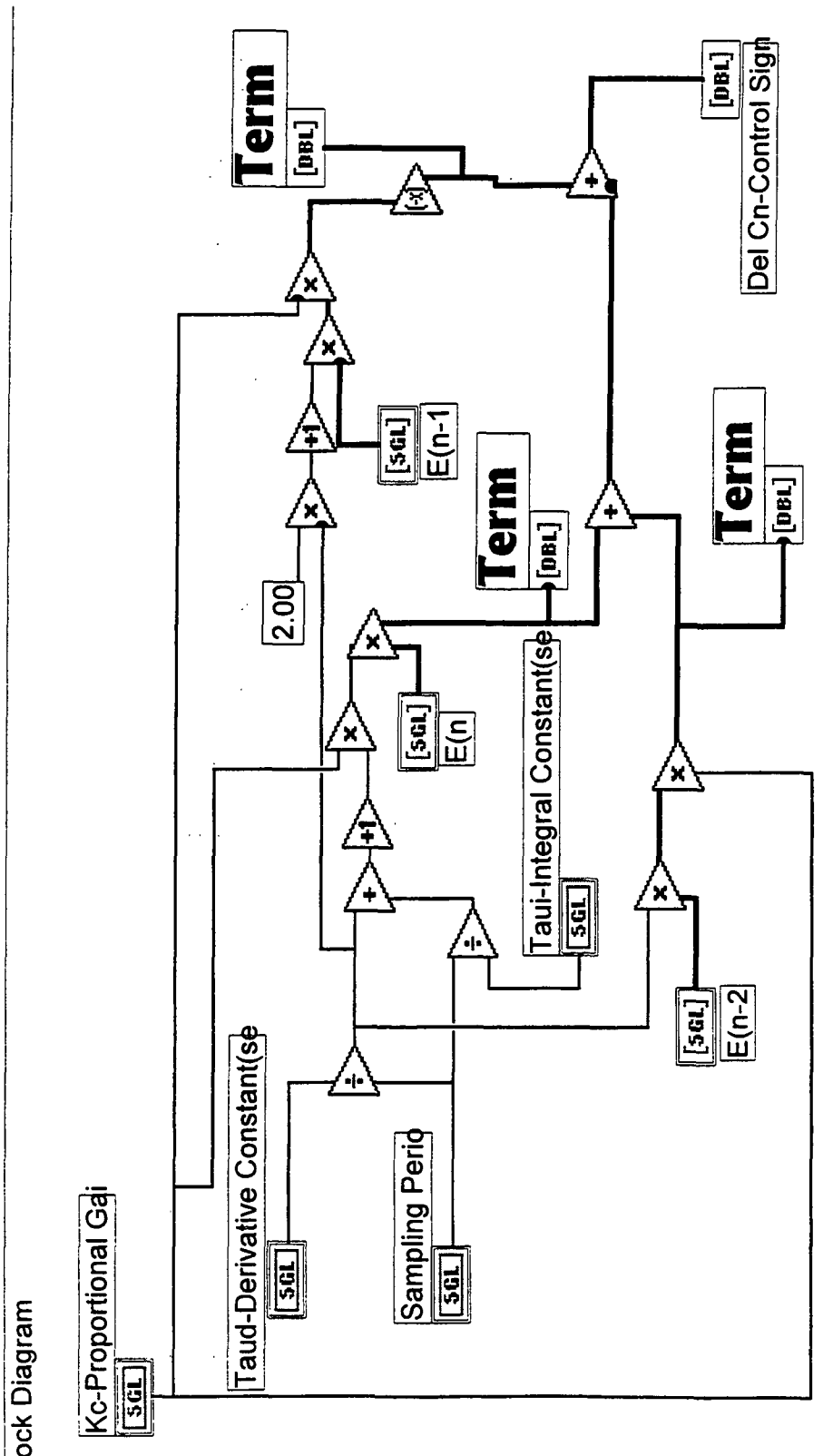

Figure V.4 - PID.VI Block Diagram

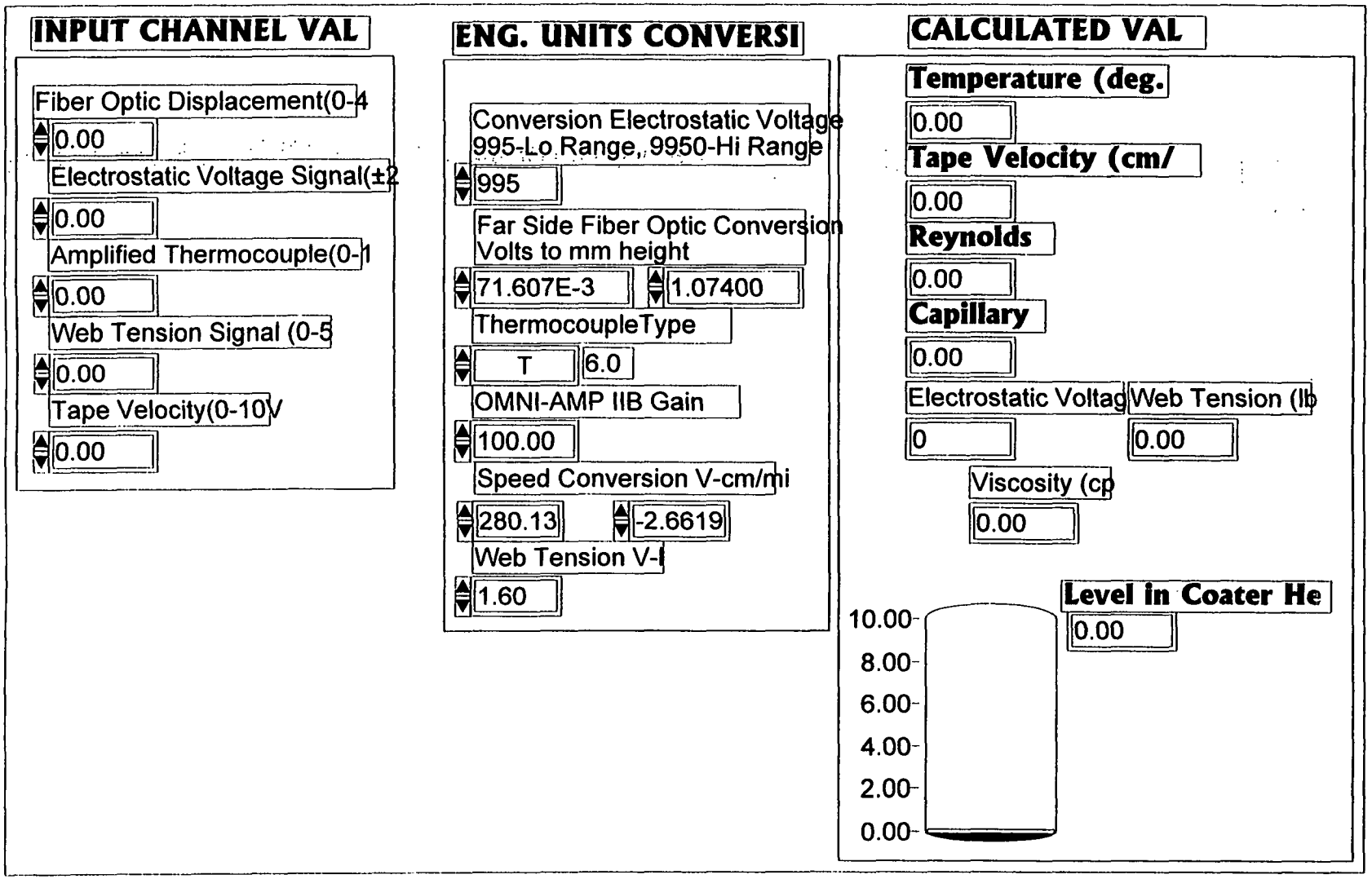

Figure V.5 - DATAUNIT.VI Front Panel Diagram

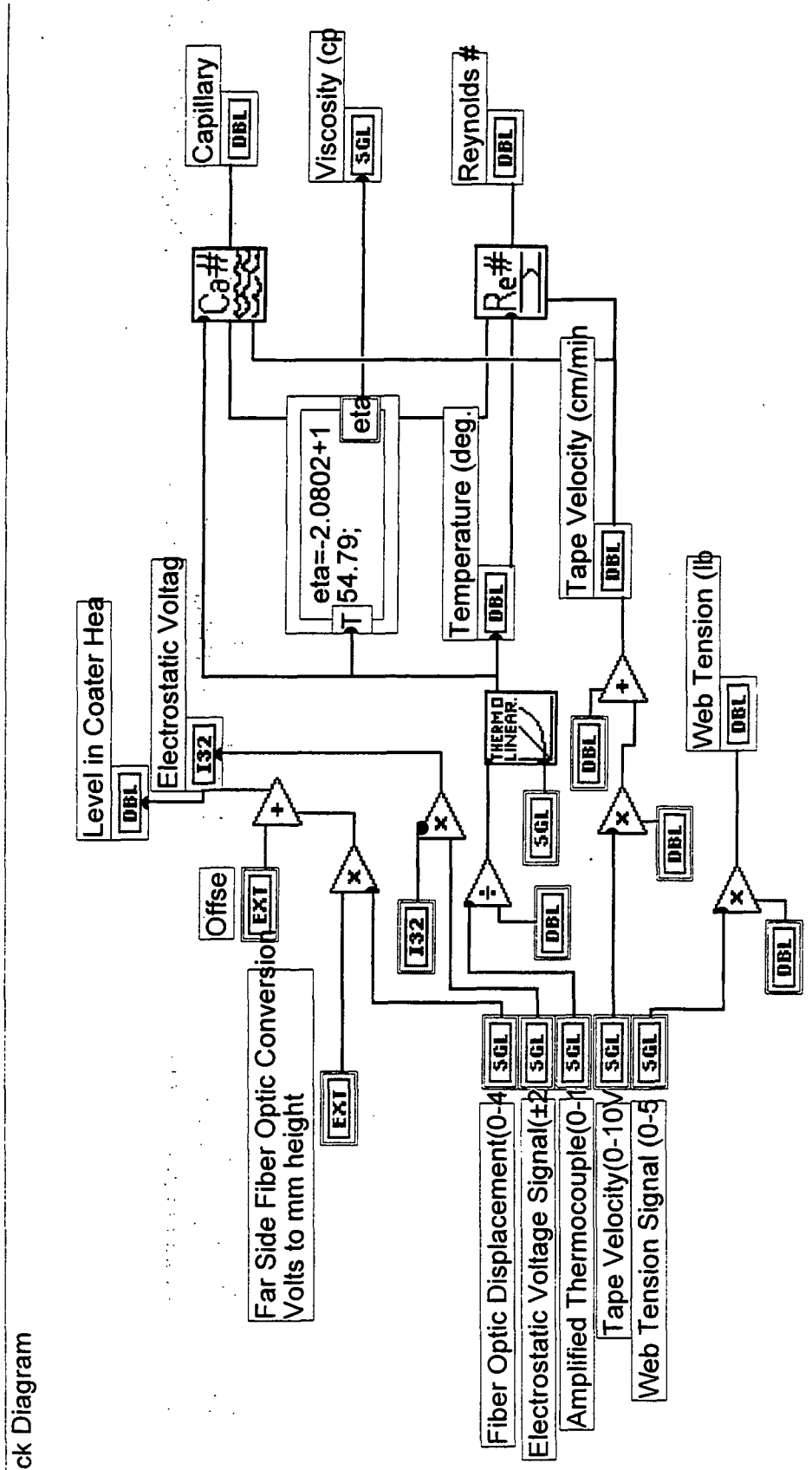

Figure V.6 - DATAUNIT.VI Block Diagram

Front Panel

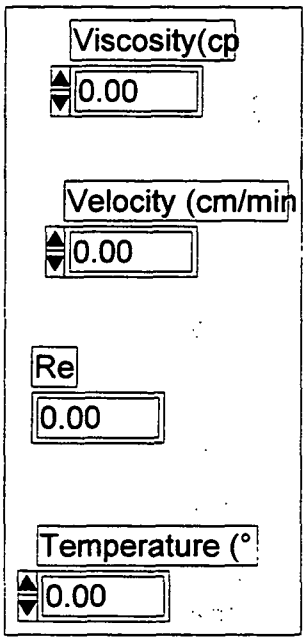

Block Diagram

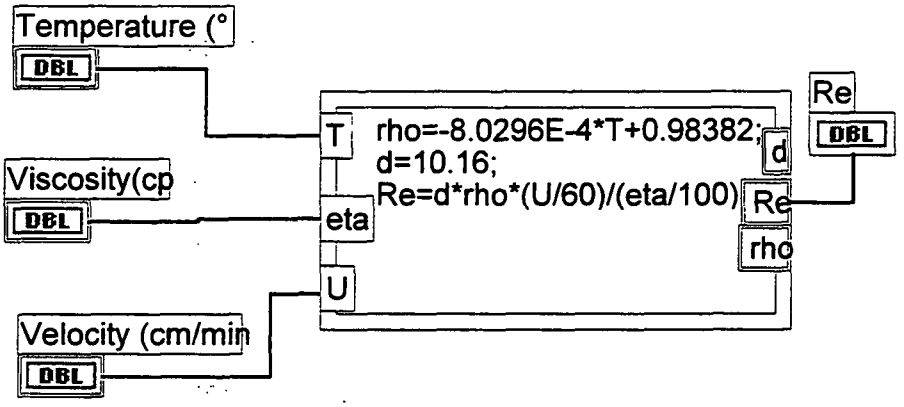

Figure V.7 - REYNOLDS.VI Front Panel and Block Diagram

Front Panel

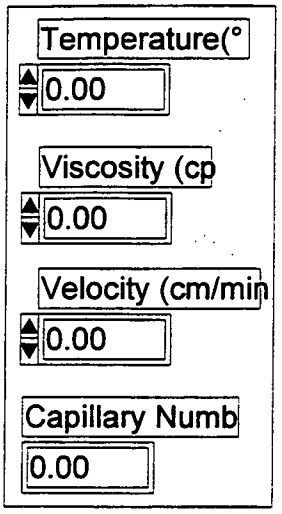

Block Diagram

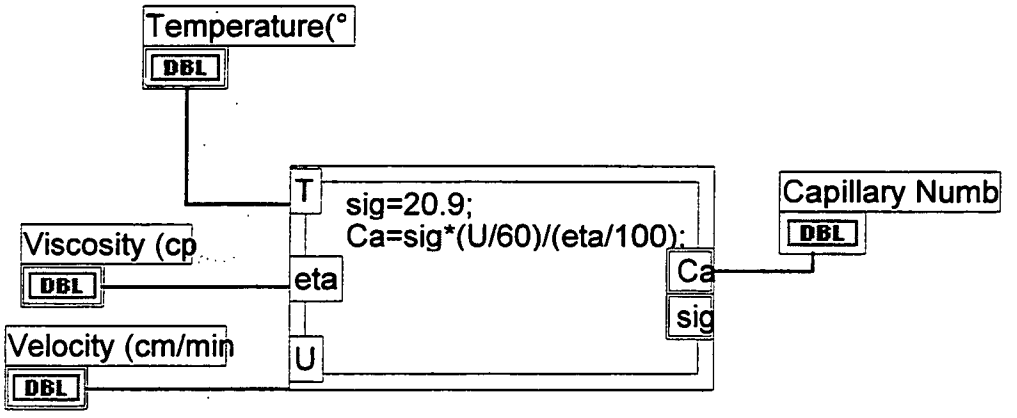

Figure V.8 - CAPILLARY.VI Front Panel and Block Diagram

APPENDIX VI

VI.1 Data for the Ramping Experiments

This appendix contains the reduced raw data files for all of the ramping experiments with 1) Melinex™454 - coated PET-A, 2) Melinex™453 - uncoated PET-B and 3) Flexel's PUT002 - cellulose acetate (CEL). The data file codes are discussed below. The elapsed time is based on the video time code generator, while the liquid physical properties are corrected for the temperature at the U_v and U_{ae}.

The electrostatic voltage data, 3M and Monroe, are contained at the end of each table and correspond to the average values at U_v.

VI.2 Data Acquisition File Codes

Data collection files consist of 8 characters followed by the extension XXXXXXXX.DAT. Each file is coded to contain the month (12 levels), day (31 levels max), fluid viscosity at 25°C (11 levels) and the run character (letters A-Z, 26 levels).

X	XX	X	XXX	X	.DAT
1	2	3	4	5	6

Position #1 - MONTH - The first letter of each month in the Julian calendar is used to code the files. An asterisk indicates that the file code letter is different from the first letter of the month.

J-January, **F**-February, **M**-March, **A**-April, **Y**-Ma**Y**(*), **U**-J**U**ne(*), **L**-Ju**L**y(*), **G**-Au**G**ust(*), **S**-September, **O**-October, **N**-November, **D**-December

Position #2 - DAY - The day in current month based on the Julian calendar.

Position #3 - VISCOSITY - A letter code designating viscosity range of the fluid being used.

A - DC200-100 cSt
B - DC200-200 cSt
C - DC200-350 cSt
D - DC200-500 cSt
E - DC200-1000 cSt
F - High viscosity glycerol/water mixture
G - Low viscosity glycerol/water mixture
H - Low viscosity glycerol/water mixture
I - Low viscosity glycerol/water mixture
Y - DC200-10 cSt
Z - DC200-20 cSt

Position #4 - EXPERIMENT TYPE - The type of experiment either RAMp type or constant CApillary number type.

Position #5 - RUN CODE - The number or letter of the current data file. Start first with single digit numbers 1-9 and proceed to letters A-Z if required.

TABLE VI.1 - Ramping Experiment Data for Fluid A - DC200-100 cs

Fluid A - DC200 - 100 cSt Silicone Oil

See laboratory notebook pages 70-71, 72, 74, 79-80

Characteristic length,cm	0.15
Gravity, cm/sec^2	980.7
Acceleration rate, cm/min^2	112.0

First Critical Speed Data

Experiment Code	Initial Speed (cm/min)	Elapsed minutes	Elapsed seconds	Elapsed fields	Time elapsed seconds	Uc1 Speed (cm/sec)	Uc1 Speed (cm/min)	Liquid Temp. (C°)	Liquid surface tension (mN/cm)	Liquid density (g/cm^3)	Liquid viscosity (cp)	Liquid Npp	Liquid Capillary Number	Liquid Reynolds Number	Gas Temp. (C°)	Gas Capillary Number
F05ARAM1	300	4	10	24.0	250.80	12.80	768.2	21.6	21.4	0.9665	107.4	0.139	0.644	1.73	23.0	1.69E-04
F05ARAM2	300	4	11	22.5	251.75	12.83	769.9	21.2	21.4	0.9669	108.3	0.142	0.649	1.72	23.0	1.69E-04
F05ARAM3	300	4	10	2.5	250.08	12.78	766.8	21.3	21.4	0.9668	108.1	0.141	0.645	1.72	23.0	1.69E-04
F16ARAM1	300	4	12	2.5	252.08	12.84	770.6	20.9	21.5	0.9671	108.9	0.144	0.652	1.71	22.7	1.68E-04
F16ARAM2	300	4	8	20.0	248.67	12.74	764.2	20.6	21.5	0.9673	109.5	0.147	0.649	1.69	22.7	1.66E-04
F16ARAM3	300	4	12	26.5	252.88	12.87	772.0	21.3	21.4	0.9668	108.1	0.141	0.650	1.73	22.7	1.69E-04
F16ARAM4	500	2	29	23.0	149.77	12.99	779.6	22.0	21.3	0.9662	106.6	0.136	0.650	1.77	22.7	1.71E-04
F16ARAM5	600	1	28	25.0	88.83	12.76	765.8	21.4	21.4	0.9667	107.9	0.140	0.644	1.72	22.7	1.68E-04
M17ARAM1	650	0	54	13.0	54.43	12.53	751.6	21.1	21.4	0.9669	110.9	0.156	0.648	1.64	22.8	1.64E-04
M17ARAM2	650	0	58	8.0	58.27	12.65	758.8	21.1	21.4	0.9669	110.9	0.156	0.654	1.66	22.8	1.66E-04
M17ARAM3	650	1	2	10.5	62.35	12.77	766.4	21.1	21.4	0.9669	110.9	0.156	0.661	1.67	22.8	1.68E-04
M17ARAM4	650	1	6	24.0	66.80	12.91	774.7	21.0	21.4	0.9670	111.1	0.157	0.669	1.69	22.8	1.69E-04
M17ARAM5	650	1	10	7.0	70.23	13.02	781.1	21.1	21.4	0.9669	110.9	0.156	0.674	1.71	22.8	1.71E-04
M17ARAM6	650	1	6	7.5	66.25	12.89	773.7	21.1	21.4	0.9669	110.9	0.156	0.667	1.69	22.8	1.69E-04
M17ARAM7	650	1	7	7.5	67.25	12.93	775.5	21.0	21.4	0.9670	111.1	0.157	0.670	1.69	22.8	1.70E-04
M17ARAM8	650	1	1	17.5	61.58	12.75	765.0	21.1	21.4	0.9669	110.9	0.156	0.660	1.67	22.8	1.67E-04
					Average	**12.82**	**769.0**	**21.2**	**21.4**	**0.9669**	**109.5**	**0.149**	**0.655**	**1.70**		**1.68E-04**
					Standard Deviation	**0.12**	**7.5**					**0.008**	**0.010**	**0.03**		**1.8E-06**
					Standard Error	0.97%	0.97%					5.38%	1.52%	1.88%		1.05%

TABLE VI.1(continued) - Ramping Experiment Data for Fluid A - DC200-100 cs

Fluid A - DC200 - 100 cSt Silicone Oil

Second Critical Speed Data

Experiment Code	Initial Speed (cm/min)	Elapsed minutes	Elapsed seconds	Elapsed fields	Time elapsed seconds	Uc2 Speed (cm/sec)	Uc2 Speed (cm/min)	Liquid Temp. (C°)	Liquid surface tension (mN/cm)	Liquid density (g/cm^3)	Liquid viscosity (cp)	Liquid Npp	Liquid Capillary Number	Liquid Reynolds Number	Gas Temp. (C°)	Gas Capillary Number
F05ARAM1	300	4	40	8.5	280.28	13.72	823.2	21.6	21.4	0.9665	107.4	0.139	0.690	1.85	23.0	1.81E-04
F05ARAM2	300	4	13	22.0	253.73	12.89	773.6	21.2	21.4	0.9669	108.3	0.142	0.652	1.73	23.0	1.70E-04
F05ARAM3	300	4	10	4.5	250.15	12.78	766.9	21.3	21.4	0.9668	108.1	0.141	0.645	1.72	23.0	1.69E-04
F16ARAM1	300	4	14	0.5	254.02	12.90	774.2	20.8	21.5	0.9672	109.1	0.145	0.655	1.72	22.7	1.69E-04
F16ARAM2	300	4	18	7.5	258.25	13.03	782.1	20.6	21.5	0.9673	109.5	0.147	0.664	1.73	22.7	1.70E-04
F16ARAM3	300	4	17	22.0	257.73	13.02	781.1	21.4	21.4	0.9667	107.9	0.140	0.656	1.75	22.7	1.71E-04
F16ARAM4	500	2	34	18.5	154.62	13.14	788.6	22.0	21.3	0.9662	106.6	0.136	0.658	1.79	22.7	1.73E-04
F16ARAM5	600	1	34	15.0	94.50	12.94	776.4	21.3	21.4	0.9668	108.1	0.141	0.653	1.74	22.7	1.70E-04
M17ARAM1	650	1	4	15.5	64.52	12.84	770.4	21.1	21.4	0.9669	110.9	0.156	0.664	1.68	22.8	1.69E-04
M17ARAM2	650	1	9	13.0	69.43	12.99	779.6	21.1	21.4	0.9669	110.9	0.156	0.672	1.70	22.8	1.71E-04
M17ARAM3	650	1	8	3.0	68.10	12.95	777.1	21.2	21.4	0.9669	110.7	0.155	0.669	1.70	22.8	1.70E-04
M17ARAM4	650	1	19	7.5	79.25	13.30	797.9	21.0	21.4	0.9670	111.1	0.157	0.689	1.74	22.8	1.74E-04
M17ARAM5	650	1	18	25.0	78.83	13.29	797.2	21.1	21.4	0.9669	110.9	0.156	0.687	1.74	22.8	1.74E-04
M17ARAM6	650	1	13	9.0	73.30	13.11	786.8	21.0	21.4	0.9670	111.1	0.157	0.679	1.72	22.8	1.72E-04
M17ARAM7	650	1	16	4.5	76.15	13.20	792.1	21.0	21.4	0.9670	111.1	0.157	0.684	1.73	22.8	1.73E-04
M17ARAM8	650	1	7	0.5	67.02	12.92	775.1	21.1	21.4	0.9669	110.9	0.156	0.668	1.69	22.8	1.70E-04
					Average	**13.07**	**783.9**	**21.2**	**21.4**	**0.9669**	**109.5**	**0.149**	**0.668**	**1.73**		**1.72E-04**
					Standard Deviation	**0.23**	**13.9**					**0.008**	**0.014**	**0.04**		**3.3E-06**
					Standard Error	1.77%	1.77%					5.37%	2.16%	2.38%		1.90%

Empty values indicate that 3M meter or data acquisition malfunctioned or Monroe meter unavailable

Experiment Code	ΔU=Uc2-Uc1 (cm/min)	3M Static Volt @ Uc1 (7 pt.)	3M stdev	Normalized 3M @ Uc1	Avg. Monroe Static Volt	Monroe stdev.	Norm. Monroe Static @ Uc1
F05ARAM1	55.0	110.5	5.1	1.62			
F05ARAM2	3.7	31.2	7.2	0.46			
F05ARAM3	0.1	62.4	8.2	0.92			
F16ARAM1	3.6	42.0	8.0	0.49			
F16ARAM2	17.9	144.8	9.7	1.68			
F16ARAM3	9.1	65.3	6.2	0.76			
F16ARAM4	9.1	140.1	3.0	1.62			
F16ARAM5	10.6	39.9	5.9	0.46			
M17ARAM1	18.8	66.0	33.5	0.89	-2939.0	473.0	1.18
M17ARAM2	20.8	189.9	31.1	2.56	-1261.0	769.0	0.51
M17ARAM3	10.7	-16.2	15.3	-0.22	-3472.0	23.0	1.39
M17ARAM4	23.2	68.3	12.8	0.92			
M17ARAM5	16.1	67.1	12.9	0.90	-3251.0	203.0	1.31
M17ARAM6	13.2				-3396.0	174.0	1.36
M17ARAM7	16.6	5.6	20.2	0.08	-2973.0	450.0	1.19
M17ARAM8	10.1	138.9	12.8	1.87	-137.0	41.0	0.06

TABLE VI.2 - Ramping Experiment Data for Fluid B - DC200-200 cs

Fluid B - DC200-200 cSt Silicone Oil

See laboratory notebook pages 125-126

Characteristic length,cm	0.15
Gravity, cm/sec^2	980.7
Acceleration rate, cm/min^2	112.0

First Critical Speed Data

Experiment Code	Initial Speed (cm/min)	Elapsed minutes	Elapsed seconds	Elapsed fields	Time elapsed seconds	Uc1 Speed (cm/sec)	Uc1 Speed (cm/min)	Liquid Temp. (C°)	Liquid surface tension (mN/cm)	Liquid density (g/cm^3)	Liquid viscosity (cp)	Liquid Npp	Liquid Capillary Number	Liquid Reynolds Number	Gas Temp. (C°)	Gas Capillary Number
N24BRAM1	600	1	2	13.0	62.43	11.94	716.5	21.2	21.4	0.9685	212.6	2.12	1.19	0.8	24.2	1.61E-04
N24BRAM2	550	1	30	12.0	90.40	11.98	718.7	21.5	21.3	0.9683	211.3	2.08	1.19	0.8	24.2	1.62E-04
N24BRAM3	625	0	44	12.0	44.40	11.80	707.9	21.7	21.3	0.9682	210.5	2.06	1.17	0.8	24.2	1.60E-04
N24BRAM4	650	0	36	3.0	36.10	11.96	717.4	21.7	21.3	0.9682	210.5	2.06	1.18	0.8	24.2	1.62E-04
N24BRAM5	650	0	31	23.5	31.78	11.82	709.3	21.6	21.3	0.9682	210.9	2.07	1.17	0.8	24.2	1.60E-04
					Average	**11.9**	**714.0**	**21.5**	**21.3**	**0.9683**	**211.2**	**2.08**	**1.18**	**0.8**		**1.61E-04**
					Standard Deviation	**0.1**	**5.0**					**0.03**	**0.01**	**0.0**		**1.1E-06**
					Standard Error	0.70%	0.70%					1.26%	0.86%	0.64%		0.66%

Second Critical Speed Data

Experiment Code	Initial Speed (cm/min)	Elapsed minutes	Elapsed seconds	Elapsed fields	Time elapsed seconds	Uc2 Speed (cm/sec)	Uc2 Speed (cm/min)	Liquid Temp. (C°)	Liquid surface tension (mN/cm)	Liquid density (g/cm^3)	Liquid viscosity (cp)	Liquid Npp	Liquid Capillary Number	Liquid Reynolds Number	Gas Temp. (C°)	Gas Capillary Number
N24BRAM1	600	1	2	14.5	62.48	11.94	716.6	21.2	21.4	0.9685	212.6	2.12	1.19	0.8	24.2	1.61E-04
N24BRAM2	550	1	30	15.0	90.50	11.98	718.9	21.5	21.3	0.9683	211.3	2.08	1.19	0.8	24.2	1.62E-04
N24BRAM3	625	0	44	13.0	44.43	11.80	707.9	21.7	21.3	0.9682	210.5	2.06	1.17	0.8	24.2	1.60E-04
N24BRAM4	650	0	36	3.5	36.12	11.96	717.4	21.7	21.3	0.9682	210.5	2.06	1.18	0.8	24.2	1.62E-04
N24BRAM5	650	0	31	24.0	31.80	11.82	709.4	21.6	21.3	0.9682	210.9	2.07	1.17	0.8	24.2	1.60E-04
					Average	**11.9**	**714.1**	**21.5**	**21.3**	**0.9683**	**211.2**	**2.08**	**1.18**	**0.8**		**1.61E-04**
					Standard Deviation	**0.1**	**5.0**					**0.03**	**0.01**	**0.0**		**1.1E-06**
					Standard Error	0.70%	0.70%					1.26%	0.87%	0.64%		0.66%

Experiment Code	ΔU=Uc2-Uc1 (cm/min)	3M Static Volt @ Uc1 (7 pt.)	3M stdev	Normalized 3M @ Uc1	Avg. Monroe Static Volt	Monroe stdev.	Norm. Monroe Static @ Uc1
N24BRAM1	0.0933	3.7	97.9	-0.88	2.9	4.2	0.20
N24BRAM2	0.1867	-89.1	93.3	21.32	0.8	43.2	0.06
N24BRAM3	0.0622	-4.7	105.8	1.13	32.6	71.5	2.29
N24BRAM4	0.0311	28.6	83.1	-6.85	6.7	12.7	0.47
N24BRAM5	0.0311	40.6	42.5	-9.72	28.1	19.0	1.98

TABLE VI.3 - Ramping Experiment Data for Fluid C - DC200-350 cs

Fluid C - DC200-350 cSt Silicone Oil

See laboratory note pages 117,123-124

Characteristic length,cm	0.15
Gravity, cm/sec^2	980.7
Acceleration rate, cm/min^2	112.00

First Critical Speed Data

Experiment Code	Initial Speed (cm/min)	Elapsed minutes	Elapsed seconds	Elapsed fields	Time elapsed seconds	Ucl Speed (cm/sec)	Ucl Speed (cm/min)	Liquid Temp. (C°)	Liquid surface tension (mN/cm)	Liquid density (g/cm^3)	Liquid viscosity (cp)	Liquid Npp	Liquid Capillary Number	Liquid Reynolds Number	Gas Temp. (C°)	Gas Capillary Number
O17CRAM1	600	0	19	21.5	19.72	10.61	636.8	21.3	22.1	0.9715	361.5	16.1	1.739	0.4	24.0	1.38E-04
O17CRAM2	400	1	58	6.5	118.22	10.34	620.7	21.7	22.0	0.9712	358.6	15.7	1.685	0.4	24.0	1.35E-04
O17CRAM3	400	2	40	14.0	160.47	11.66	699.5	21.9	22.0	0.9710	357.2	15.5	1.894	0.5	24.0	1.52E-04
O17CRAM4	350	2	33	7.5	153.25	10.60	636.1	22.1	22.0	0.9709	355.7	15.3	1.717	0.4	24.0	1.39E-04
O17CRAM5	350	3	45	15.5	225.52	12.85	771.0	22.2	22.0	0.9708	355.0	15.2	2.078	0.5	24.0	1.68E-04
O17CRAM6	500	1	35	22.0	95.73	11.31	678.7	22.2	22.0	0.9708	355.0	15.2	1.829	0.5	24.0	1.48E-04
N17CRAM1	400	2	9	3.0	129.10	10.68	641.0	24.4	21.7	0.9690	339.1	13.1	1.670	0.5	26.7	1.48E-04
N17CRAM2	400	2	6	9.5	126.32	10.60	635.8	24.4	21.7	0.9690	339.1	13.1	1.657	0.5	26.7	1.47E-04
N17CRAM3	400	2	7	12.5	127.42	10.63	637.8	24.4	21.7	0.9690	339.1	13.1	1.662	0.5	26.7	1.47E-04
N17CRAM4	400	2	8	16.5	128.55	10.67	640.0	24.4	21.7	0.9690	339.1	13.1	1.668	0.5	26.7	1.48E-04
N17CRAM5	400	2	4	24.0	124.80	10.55	633.0	24.5	21.7	0.9689	338.4	13.0	1.647	0.5	26.7	1.46E-04
N17CRAM6	400	2	2	28.0	122.93	10.49	629.5	24.5	21.7	0.9689	338.4	13.0	1.638	0.5	26.7	1.45E-04
					Average	**10.9**	**655.0**	**23.2**	**21.8**	**0.9700**	**348.0**	**14.3**	**1.740**	**0.46**		**1.47E-04**
					Standard Deviation	**0.7**	**42.7**					**1.3**	**0.132**	**0.03**		**8.4E-06**
					Standard Error	6.52%	6.52%					8.82%	7.58%	5.94%		5.71%

TABLE VI.3(continued) - Ramping Experiment Data for Fluid C - DC200-350 cs

Second Critical Speed Data

Experiment Code	Initial Speed (cm/min)	Elapsed minutes	Elapsed seconds	Elapsed fields	Time elapsed seconds	Uc2 Speed (cm/sec)	Uc2 Speed (cm/min)	Liquid Temp. (C°)	Liquid surface tension (mN/cm)	Liquid density (g/cm^3)	Liquid viscosity (cp)	Liquid Npp	Liquid Capillary Number	Liquid Reynolds Number	Gas Temp. (C°)	Gas Capillary Number
O17CRAM1	600	0	20	14.0	20.47	10.64	638.2	21.3	22.1	0.9715	361.5	16.1	1.74	0.4	24.0	1.38E-04
O17CRAM2	400	2	0	27.0	120.90	10.43	625.7	21.7	22.0	0.9712	358.6	15.7	1.70	0.4	24.0	1.36E-04
O17CRAM3	400	2	40	14.0	160.47	11.66	699.5	21.9	22.0	0.9710	357.2	15.5	1.89	0.5	24.0	1.52E-04
O17CRAM4	350	2	35	1.5	155.05	10.66	639.4	22.1	22.0	0.9709	355.7	15.3	1.73	0.4	24.0	1.39E-04
O17CRAM5	350	3	50	14.0	230.47	13.00	780.2	22.2	22.0	0.9708	355.0	15.2	2.10	0.5	24.0	1.70E-04
O17CRAM6	500	1	35	22.0	95.73	11.31	678.7	22.2	22.0	0.9708	355.0	15.2	1.83	0.5	24.0	1.48E-04
N17CRAM1	400	2	12	22.5	132.75	10.80	647.8	24.4	21.7	0.9690	339.1	13.1	1.69	0.5	26.7	1.49E-04
N17CRAM2	400	2	6	18.5	126.62	10.61	636.4	24.4	21.7	0.9690	339.1	13.1	1.66	0.5	26.7	1.47E-04
N17CRAM3	400	2	7	12.5	127.42	10.63	637.8	24.4	21.7	0.9690	339.1	13.1	1.66	0.5	26.7	1.47E-04
N17CRAM4	400	2	8	18.5	128.62	10.67	640.1	24.4	21.7	0.9690	339.1	13.1	1.67	0.5	26.7	1.48E-04
N17CRAM5	400	2	7	17.0	127.57	10.64	638.1	24.5	21.7	0.9689	338.4	13.0	1.66	0.5	26.7	1.47E-04
N17CRAM6	400	2	3	15.0	123.50	10.51	630.5	24.5	21.7	0.9689	338.4	13.0	1.64	0.5	26.7	1.46E-04
					Average	**11.0**	**657.7**	**23.2**	**21.8**	**0.9700**	**348.0**	**14.3**	**1.75**	**0.46**		**1.47E-04**
					Standard Deviation	**0.7**	**44.0**					**1.3**	**0.14**	**0.03**		**8.6E-06**
					Standard Error	6.69%	6.69%					8.82%	7.74%	6.11%		5.86%

Experiment Code	ΔU=Uc2-Uc1 (cm/min)	3M Static Volt @ Uc1 (7 pt.)	3M stdev	Normalized 3M @ Uc1	Avg. Monroe Static Volt	Monroe stdev.	Norm. Monroe Static @ Uc1
O17CRAM1	1.4	64.7	16.9	0.84	6.3	21.9	-1.62
O17CRAM2	5.0	25.1	11.5	0.33	6.2	37.4	-1.60
O17CRAM3	0.0	23.8	11.3	0.31	-30.2	42.9	7.78
O17CRAM4	3.4	62.7	21.8	0.81	5.4	108.4	-1.40
O17CRAM5	9.2	107.2	9.5	1.39	-5.4	4.6	1.38
O17CRAM6	0.0	178.5	6.8	2.32	-5.6	4.7	1.45
N17CRAM1	6.8	-5.3	8.9	-0.08	16.7	20.6	1.32
N17CRAM2	0.6	34.2	7.5	0.54	9.0	4.4	0.71
N17CRAM3	0.0	45.1	1.4	0.71	5.9	3.7	0.46
N17CRAM4	0.1	67.9	3.3	1.07	8.9	15.7	0.70
N17CRAM5	5.2	97.9	5.9	1.54	7.6	21.8	0.60
N17CRAM6	1.1	142.2	10.0	2.23	28.2	46.8	2.22

TABLE VI.4 - Ramping Experiment Data for Fluid D - DC200-500 cs

Fluid D - DC200-550 cSt Silicone Oil
See labororatory notebook pages 177-78

Characteristic length,cm	0.15
Gravity, cm/sec^2	980.7
Acceleration rate, cm/min^2	Varies

First Critical Speed

Experiment Code	Initial Speed (cm/min)	Acceler. (cm/min^2)	Elapsed minutes	Elapsed seconds	Elapsed fields	Time elapsed seconds	Uc1 Speed (cm/sec)	Uc1 Speed (cm/min)	Liquid Temp. (C°)	Liquid surface tension (mN/cm)	Liquid density (g/cm^3)	Liquid viscosity (cp)	Liquid Npp	Liquid Capillary Number	Liquid Reynolds Number	Gas Temp. (C°)	Gas Capillary Number
G13DRAM2	500.0	224.0	0	4	27.0	4.90	8.64	518.3	24.2	22.8	0.9715	500.2	53.5	1.90	0.3	23.3	1.08E-04
G13DRAM3	400.0	224.0	0	58	5.0	58.17	10.29	617.2	24.7	22.7	0.9711	495.1	51.6	2.24	0.3	23.3	1.28E-04
G13DRAM5	500.0	112.0	0	7	12.5	7.42	8.56	513.8	24.7	22.7	0.9711	495.1	51.6	1.86	0.3	23.5	1.07E-04
G13DRAM1	500.0	112.0	0	41	3.5	41.12	9.61	576.8	24.7	22.7	0.9711	495.1	51.6	2.09	0.3	23.2	1.20E-04
G13DRAM2	500.0	224.0	0	16	4.5	16.15	9.34	560.3	24.6	22.7	0.9712	496.1	52.0	2.04	0.3	23.2	1.16E-04
G13DRAM3	500.0	896.0	0	9	7.5	9.25	10.64	638.1	24.6	22.7	0.9712	496.1	52.0	2.32	0.3	23.2	1.33E-04
G13DRAM4	100.0	896.0	0	26	24.0	26.80	8.34	500.2	26.6	22.6	0.9695	475.7	45.1	1.76	0.3	23.2	1.05E-04
						Average	**9.3**	**560.7**	**24.9**	**22.7**	**0.9709**	**493.4**	**51.1**	**2.03**	**0.28**		**1.17E-04**
						Standard Deviation	**0.9**	**53.4**					**2.7**	**0.20**	**0.03**		**1.1E-05**
						Standard Error	9.52%	9.52%					5.33%	10.09%	8.99%		9.34%

Second Critical Speed

Experiment Code	Initial Speed (cm/min)	Acceler. (cm/min^2)	Elapsed minutes	Elapsed seconds	Elapsed fields	Time elapsed seconds	Uc2 Speed (cm/sec)	Uc2 Speed (cm/min)	Liquid Temp. (C°)	Liquid surface tension (mN/cm)	Liquid density (g/cm^3)	Liquid viscosity (cp)	Liquid Npp	Liquid Capillary Number	Liquid Reynolds Number	Gas Temp. (C°)	Gas Capillary Number
G13DRAM2	500.0	224.0	0	5	0.0	5.00	8.64	518.7	24.2	22.8	0.9715	500.2	53.5	1.90	0.3	23.3	1.08E-04
G13DRAM3	400.0	224.0	1	4	7.0	64.23	10.66	639.8	24.7	22.7	0.9711	495.1	51.6	2.32	0.3	23.3	1.33E-04
G13DRAM5	500.0	112.0	0	7	12.5	7.42	8.56	513.8	24.7	22.7	0.9711	495.1	51.6	1.86	0.3	23.5	1.07E-04
G14DRAM1	500.0	112.0	0	41	3.5	41.12	9.61	576.8	24.7	22.7	0.9711	495.1	51.6	2.09	0.3	23.2	1.20E-04
G14DRAM2	500.0	224.0	0	16	13.0	16.43	9.36	561.4	24.6	22.7	0.9712	496.1	52.0	2.04	0.3	23.2	1.17E-04
G14DRAM3	500.0	896.0	0	9	17.5	9.58	10.72	643.1	24.6	22.7	0.9712	496.1	52.0	2.34	0.3	23.2	1.34E-04
G14DRAM4	100.0	896.0	0	26	24.0	26.80	8.34	500.2	26.6	22.6	0.9695	475.7	45.1	1.76	0.3	23.2	1.05E-04
						Average	**9.4**	**564.8**	**24.9**	**22.7**	**0.9709**	**493.4**	**51.1**	**2.04**	**0.29**		**1.18E-04**
						Standard Deviation	**1.0**	**58.9**					**2.7**	**0.22**	**0.03**		**1.2E-05**
						Standard Error	10.43%	10.43%					5.33%	10.97%	9.92%		10.27%

Empty values indicate that 3M meter of data acquisition malfunctioned of Monroe meter unavailable

Experiment Code	ΔU=Uc2-Uc1 (cm/min)	3M Static Volt @ Uc1 (7 pt.)	3M stdev	Normalized 3M @ Uc1	Avg. Monroe Static Volt	Monroe stdev.	Norm. Monroe Static @ Uc1
G13DRAM2	0.3733	-27.6	57.2	0.50			
G13DRAM3	22.6489	-61.2	48.7	1.11	18.6	31.2	2.44
G13DRAM5	0.0000	-86.2	43.8	1.57	2.9	14.9	0.38
G14DRAM1	0.0000	-17.9	21.0	0.33	16.7	59.0	2.19
G14DRAM2	1.0578	-86.9	53.6	1.58	-2.4	54.9	-0.32
G14DRAM3	4.9778			0.00	15.0	23.2	1.97
G14DRAM4	0.0000	-50.6	38.3	0.92	-5.1	73.5	-0.67

TABLE VI.5 - Ramping Experiment for Fluid E with coated PET-A - DC200-1000 cs

Fluid E - DC200-1000 cSt Silicone Oil
See laboratory notebook pages 82-86,173

Characteristic length,cm	0.15
Gravity, cm/sec^2	980.7
Acceleration rate, cm/min^2	112.0

Notes
1) Data from all experiments on A10 are edge data and not representative of DCL instability.
2) Data for experiments with PET-B and CEL are in TABLES VI.6 and VI.7.
3) The data for runs A07ERAM1#2 and A07ERAM3#2 are repeat analysis on lab notebook page 173.

First Critical Speed with PET-A Substrate

Experiment Code	Initial Speed (cm/min)	Elapsed minutes	Elapsed seconds	Elapsed fields	Time elapsed seconds	Uc1 Speed (cm/sec)	Uc1 Speed (cm/min)	Liquid Temp. (C°)	Liquid surface tension (mN/cm)	Liquid density (g/cm^3)	Liquid viscosity (cp)	Liquid Npp	Liquid Capillary Number	Liquid Reynolds Number	Gas Temp. (C°)	Gas Capillary Number
M30ERAM1	600	2	15	25.0	135.83	14.23	853.6	19.5	22.6	0.9778	1092.4	1233.1	6.87	0.20	22.2	1.75E-04
M30ERAM2	600	1	53	18.0	113.60	13.53	812.1	19.3	22.6	0.9780	1096.6	1249.8	6.56	0.19	22.2	1.66E-04
M30ERAM3	600	2	7	5.0	127.17	13.96	837.4	19.5	22.6	0.9778	1092.4	1233.1	6.74	0.19	22.2	1.72E-04
M30ERAM4	600	1	57	19.0	117.63	13.66	819.6	19.5	22.6	0.9778	1092.4	1233.1	6.59	0.19	22.2	1.68E-04
M30ERAM5	600	2	11	21.5	131.72	14.10	845.9	19.5	22.6	0.9778	1092.4	1233.1	6.81	0.19	22.2	1.73E-04
A02ERAM1	700	1	23	29.0	83.97	14.28	856.7	19.7	22.6	0.9776	1088.3	1216.5	6.87	0.20	21.9	1.75E-04
A02ERAM2	700	1	28	19.0	88.63	14.42	865.4	20.2	22.6	0.9771	1077.9	1175.8	6.88	0.20	21.9	1.77E-04
A02ERAM3	700	1	5	23.5	65.78	13.71	822.8	Thermocouple malfunction							21.9	
A07ERAM1#2	100	5	44	16.0	344.53	12.39	743.1	24.1	22.4	0.9732	996.7	889.7	5.52	0.19	23.1	1.57E-04
A07ERAM2	100	5	54	13.0	354.43	12.69	761.6	24.3	22.3	0.9730	992.6	876.5	5.64	0.19	23.1	1.61E-04
A07ERAM3#2	200	5	37	9.5	337.32	13.83	829.7	24.0	22.4	0.9733	998.8	896.3	6.18	0.21	23.1	1.75E-04
A07ERAM1	100	5	41	2.5	341.08	12.28	736.7	24.1	22.4	0.9732	996.7	889.7	5.47	0.18	23.1	1.55E-04
A07ERAM3	200	4	48	14.0	288.47	12.31	738.5	24.0	22.4	0.9733	998.8	896.3	5.50	0.18	23.1	1.56E-04
A10ERAM1	100	3	23	18.0	203.60	8.00	480.1	22.9	22.4	0.9744	1021.7	971.9	3.64	0.12	22.8	1.00E-04
A10ERAM2	100	3	1	7.5	181.25	7.31	438.3	22.9	22.4	0.9744	1021.7	971.9	3.33	0.11	22.8	9.16E-05
A10ERAM3	200	1	56	13.5	116.45	6.96	417.4	22.9	22.4	0.9744	1021.7	971.9	3.17	0.10	22.8	8.72E-05
					Average w/o A10	**13.7**	**822.5**	**21.0**	**22.5**	**0.9763**	**1062.1**	**1123.7**	**6.47**	**0.19**	**22.3**	**1.70E-04**
					Standard Deviation	**0.6**	**38.6**					**164.2**	**0.51**	**0.01**	**0.5**	**6.8E-06**
					Standard Error	4.70%	4.70%					14.61%	7.95%	3.52%	2.1%	4.02%

TABLE VI.5(continued) - Ramping Experiment for Fluid E with coated PET-A - DC200-1000 cs

Second Critical Speed with PET-A Substrate

Experiment Code	Initial Speed (cm/min)	Elapsed minutes	Elapsed seconds	Elapsed fields	Time elapsed seconds	Uc2 Speed (cm/sec)	Uc2 Speed (cm/min)	Liquid Temp. (C°)	Liquid surface tension (mN/cm)	Liquid density (g/cm^3)	Liquid viscosity (cp)	Liquid Npp	Liquid Capillary Number	Liquid Reynolds Number	Gas Temp. (C°)	Gas Capillary Number
M30ERAM1	600	2	15	25.5	135.85	14.23	853.6	19.5	22.6	0.9778	1092.4	1233.1	6.87	0.20	22.2	1.75E-04
M30ERAM2	600	1	55	0.0	115.00	13.58	814.7	19.3	22.6	0.9780	1096.6	1249.8	6.58	0.19	22.2	1.67E-04
M30ERAM3	600	2	9	21.0	129.70	14.04	842.1	19.5	22.6	0.9778	1092.4	1233.1	6.78	0.19	22.2	1.73E-04
M30ERAM4	600	2	2	15.5	122.52	13.81	828.7	19.5	22.6	0.9778	1092.4	1233.1	6.67	0.19	22.2	1.70E-04
M30ERAM5	600	2	16	15.0	136.50	14.25	854.8	19.5	22.6	0.9778	1092.4	1233.1	6.88	0.20	22.2	1.75E-04
A02ERAM1	700	1	23	29.0	83.97	14.28	856.7	19.7	22.6	0.9776	1088.3	1216.5	6.87	0.20	21.9	1.75E-04
A02ERAM2	700	1	30	4.5	90.15	14.47	868.3	20.2	22.6	0.9771	1077.9	1175.8	6.91	0.20	21.9	1.77E-04
A02ERAM3	700	1	18	2.5	78.08	14.10	845.8	Thermocouple malfunction							21.9	
A07ERAM1#2	100	5	49	16.5	349.55	12.54	752.5	25.1	22.3	0.9722	975.9	824.9	5.49	0.19	23.1	1.59E-04
A07ERAM2	100	5	54	13.0	354.43	12.69	761.6	24.3	22.3	0.9730	992.6	876.5	5.64	0.19	23.1	1.61E-04
A07ERAM3#2	200	5	45	16.0	345.53	14.08	845.0	24.0	22.4	0.9733	998.8	896.3	6.29	0.21	23.1	1.78E-04
A07ERAM1	100	6	32	2.5	392.08	13.86	831.9	24.1	22.4	0.9732	996.7	889.7	6.18	0.21	23.1	1.75E-04
A07ERAM3	200	5	42	24.0	342.80	14.00	839.9	24.0	22.4	0.9733	998.8	896.3	6.25	0.21	23.1	1.77E-04
A10ERAM1	100	3	23	18.0	203.60	8.00	480.1	22.9	22.4	0.9744	1021.7	971.9	3.64	0.12	22.8	1.00E-04
A10ERAM2	100	3	1	7.5	181.25	7.31	438.3	22.9	22.4	0.9744	1021.7	971.9	3.33	0.11	22.8	9.16E-05
A10ERAM3	200	1	56	13.5	116.45	6.96	417.4	22.9	22.4	0.9744	1021.7	971.9	3.17	0.10	22.8	8.72E-05
					Average w/o A10	**13.8**	**829.4**	**21.1**	**22.5**	**0.9762**	**1060.0**	**1117.2**	**6.50**	**0.20**	**22.3**	**1.71E-04**
					Standard Deviation	**0.6**	**38.6**					**175.3**	**0.53**	**0.01**	**0.5**	**6.8E-06**
					Standard Error	4.65%	4.65%					15.69%	8.12%	3.55%	2.1%	3.97%

Missing value indicate that 3M meter or data acquisition malfunctioned or Monroe meter unavailable

Experiment Code	ΔU=Uc2-Uc1 (cm/min)	3M Static Volt @ Uc1 (7 pt.)	3M stdev	Normalized 3M @ Uc1	Avg. Monroe Static Volt	Monroe stdev.	Norm. Monroe Static @ Uc1
M30ERAM1	0.031	24.6	24.1	0.46	-853.4	627.5	3.05
M30ERAM2	2.6	1.9	22.9	0.03	-1543.5	740.2	5.51
M30ERAM3	4.7	26.2	32.3	0.49	-198.1	592.2	0.71
M30ERAM4	9.1	91.0	18.3	1.70	1379.2	818.6	-4.93
M30ERAM5	8.9	123.5	41.8	2.31	-184.0	808.2	0.66
A02ERAM1	0.0	32.9	11.1	1.83	-36.1	35.2	1.30
A02ERAM2	2.8	17.3	10.7	0.96	-52.5	33.8	1.89
A02ERAM3	23.0	3.6	1.8	0.20	5.4	22.9	-0.20
A07ERAM1#2	9.4				-113.8	46.7	3.59
A07ERAM2	0.0	6.6	68.7	-5.10	64.6	41.8	-2.04
A07ERAM3#2	15.3	-9.2	81.8	7.10	-45.9	37.1	1.45

TABLE VI.6 - Ramping Experiments for Fluid E with PET-B and CEL - DC200-1000 cs

Fluid E - DC200-1000 cSt Silicone Oil

See notebook page 106 for L27ERAM* data, page 101, 104 for L07ERAM* and L08ERAM* data.

Characteristic length,cm	10.16
Gravity, cm/sec^2	980.7
Acceleration rate, cm/min^2	112.0

First Critical Speed Data

CEL - PUT 002

Experiment Code	Initial Speed (cm/min)	Elapsed minutes	Elapsed seconds	Elapsed fields	Time elapsed seconds	Ucl Speed (cm/sec)	Ucl Speed (cm/min)	Liquid Temp. (C°)	Liquid surface tension (mN/cm)	Liquid density (g/cm^3)	Liquid viscosity (cp)	Liquid Npp	Liquid Capillary Number	Liquid Reynolds Number	Gas Temp. (C°)	Gas Capillary Number
L07ERAM1	500	3	19	11.5	199.38	14.54	872.2	23.6	22.4	0.9737	887.6	557.0	5.76	16.2	23.9	1.86E-04
L08ERAM1	700	1	40	13.5	100.45	14.79	887.5	21.6	22.5	0.9757	924.4	644.0	6.08	15.9	23.2	1.86E-04
L08ERAM2	700	1	26	6.0	86.20	14.35	860.9	21.6	22.5	0.9757	924.4	644.0	5.89	15.4	23.2	1.81E-04
L08ERAM3	800	0	37	10.0	37.33	14.49	869.7	21.8	22.5	0.9755	920.7	634.9	5.93	15.6	23.2	1.82E-04
L08ERAM4	800	0	30	22.5	30.75	14.29	857.4	21.9	22.5	0.9754	918.9	630.4	5.84	15.4	23.2	1.80E-04
					Average	**14.49**	**869.5**	**22.1**	**22.5**	**0.9752**	**915.2**	**622.0**	**5.90**	**15.69**	**23.3**	**1.83E-04**
					Standard Deviation	**0.20**	**11.7**				**15.6**	**36.8**	**0.12**	**0.34**		**3.0E-06**
					Standard Error	1.35%	1.35%					5.92%	1.98%	2.18%		1.64%

PET-B - Melinex™ 453

L27ERAM1	600	3	26	6.0	206.20	16.42	984.9	23.6	22.4	0.9737	956.1	749.9	7.01	17.0	25.4	2.16E-04
L27ERAM2	800	0	42	24.5	42.82	14.67	879.9	23.9	22.4	0.9734	949.5	731.6	6.22	15.3	25.4	1.93E-04
L27ERAM3	800	1	27	22.5	87.75	16.06	963.8	23.5	22.4	0.9738	958.3	756.1	6.87	16.6	25.4	2.11E-04
L27ERAM4	800	1	17	1.0	77.03	15.73	943.8	23.7	22.4	0.9736	953.9	743.8	6.70	16.3	25.4	2.07E-04
					Average	**15.72**	**943.1**	**23.7**	**22.4**	**0.9736**	**954.4**	**745.3**	**6.70**	**16.29**	**25.4**	**2.07E-04**
					Standard Deviation	**0.76**	**45.3**				**3.7**	**10.5**	**0.34**	**0.73**		**9.8E-06**
					Standard Error	4.81%	4.81%					1.41%	5.11%	4.49%		4.77%

TABLE VI.6(continued) - Ramping Experiments for Fluid E with PET-B and CEL - DC200-1000 cs

Second Critical Speed Data

CEL - PUT 002

Experiment Code	Initial Speed (cm/min)	Elapsed minutes	Elapsed seconds	Elapsed fields	Time elapsed seconds	Uc2 Speed (cm/sec)	Uc2 Speed (cm/min)	Liquid Temp. (C°)	Liquid surface tension (mN/cm)	Liquid density (g/cm^3)	Liquid viscosity (cp)	Liquid Npp	Liquid Capillary Number	Liquid Reynolds Number	Gas Temp. (C°)	Gas Capillary Number
L07ERAM1	500	3	19	11.5	199.38	14.54	872.2	23.6	22.4	0.9737	887.6	557.0	5.76	16.2	23.9	1.86E-04
L08ERAM1	700	1	41	13.5	101.45	14.82	889.4	21.6	22.5	0.9757	924.4	644.0	6.09	15.9	23.2	1.86E-04
L08ERAM2	700	1	28	3.5	88.12	14.41	864.5	21.6	22.5	0.9757	924.4	644.0	5.92	15.5	23.2	1.81E-04
L08ERAM3	800	0	37	10.0	37.33	14.49	869.7	21.8	22.5	0.9755	920.7	634.9	5.93	15.6	23.2	1.82E-04
L08ERAM4	800	0	30	22.5	30.75	14.29	857.4	21.9	22.5	0.9754	918.9	630.4	5.84	15.4	23.2	1.80E-04
					Average	**14.51**	**870.6**	**22.1**	**22.5**	**0.9752**	**915.2**	**622.0**	**5.91**	**15.71**	**23.3**	**1.83E-04**
					Standard Deviation	**0.20**	**11.9**				**15.6**	**36.8**	**0.12**	**0.33**		**3.0E-06**
					Standard Error	1.37%	1.37%					5.92%	2.06%	2.12%		1.62%

PET-B - Melinex™ 453

L27ERAM1	600	3	26	6.0	206.20	16.42	984.9	23.6	22.4	0.9737	956.1	749.9	7.01	17.0	25.4	2.16E-04
L27ERAM2	800	0	42	24.5	42.82	14.67	879.9	23.9	22.4	0.9734	949.5	731.6	6.22	15.3	25.4	1.93E-04
L27ERAM3	800	1	27	22.5	87.75	16.06	963.8	23.5	22.4	0.9738	958.3	756.1	6.87	16.6	25.4	2.11E-04
L27ERAM4	800	1	17	1.0	77.03	15.73	943.8	23.7	22.4	0.9736	953.9	743.8	6.70	16.3	25.4	2.07E-04
					Average	**15.72**	**943.1**	**23.7**	**22.4**	**0.9736**	**954.4**	**745.3**	**6.70**	**16.29**	**25.4**	**2.07E-04**
					Standard Deviation	**0.76**	**45.3**					**10.5**	**0.34**	**0.73**		**9.8E-06**
					Standard Error	4.81%	4.81%					1.41%	5.11%	4.49%		4.77%

TABLE VI.7 - Ramping Experiments for Fluid F and G -Glycerine/Water Mixtures

Fluid F - 99.7% Glycerol
Fluid G - Diluted Glycerol
See laboratory notebook pages 88-91

Characteristic length,cm	10.16
Gravity, cm/sec^2	980.7
Acceleration rate, cm/min^2	112.00

First Critical Speed Data

Experiment Code	Initial Speed (cm/min)	Elapsed minutes	Elapsed seconds	Elapsed fields	Time elapsed seconds	Uc1 Speed (cm/sec)	Uc1 Speed (cm/min)	Liquid Temp. (C°)	Liquid surface tension (mN/cm)	Liquid density (g/cm^3)	Liquid viscosity (cp)	Liquid Npp	Liquid Capillary Number	Liquid Reynolds Number	Gas Temp. (C°)	Gas Capillary Number
A14FRAM1	100	1	19	9.5	79.32	4.13	248.1	23.1	49.5	1.2602	908.5	43.7	0.759	5.83	22.9	2.36E-05
A14FRAM2	100	1	10	25.5	70.85	3.87	232.3	23.4	49.5	1.2601	882.9	39.0	0.690	5.61	22.9	2.21E-05
A14FRAM3	100	1	24	8.5	84.28	4.29	257.3	23.2	49.5	1.2602	899.9	42.1	0.780	6.10	22.9	2.44E-05
A14FRAM4	100	1	4	11.5	64.38	3.67	220.2	23.5	49.5	1.2600	874.3	37.5	0.648	5.37	22.6	2.08E-05
A15GRAM1	900	0	1	1.0	1.03	15.03	901.9	24.1	50.3	1.2329	113.6	1.04E-02	0.340	165.8	22.6	8.38E-05
A15GRAM2	600	2	55	13.0	175.43	15.46	927.5	24.0	50.3	1.2330	114.3	1.07E-02	0.351	169.4	22.6	8.61E-05
A15GRAM3	600	2	46	6.0	166.20	15.17	910.2	24.0	50.3	1.2330	114.3	1.07E-02	0.345	166.2	22.6	8.45E-05
A15GRAM4	600	3	8	4.5	188.15	15.85	951.2	24.1	50.3	1.2329	113.6	1.04E-02	0.358	174.9	22.6	8.83E-05
					Average	**4.0**	**239.5**	**23.3**	**49.5**	**1.2601**	**891.4**	**40.6**	**0.72**	**5.73**	**22.8**	**2.27E-05**
					Standard Deviation	**0.3**	**16.5**					**2.8**	**0.06**	**0.31**		**1.6E-06**
					Standard Error	6.89%	6.89%					6.9%	8.44%	5.41%		7.12%
					Average	**15.4**	**922.7**	**24.1**	**50.3**	**1.2329**	**114.0**	**1.05E-02**	**0.35**	**169.1**	**22.6**	**8.57E-05**
					Standard Deviation	**0.4**	**21.8**					**1.6E-04**	**0.01**	**4.2**		**2.0E-06**
					Standard Error	2.36%	2.36%					1.5%	2.31%	2.47%		2.36%

TABLE VI.7(continued) - Ramping Experiments for Fluid F and G -Glycerine/Water Mixtures

Second Critical Speed Data

Experiment Code	Initial Speed (cm/min)	Elapsed minutes	Elapsed seconds	Elapsed fields	Time elapsed seconds	Uc2 Speed (cm/sec)	Uc2 Speed (cm/min)	Liquid Temp. (C°)	Liquid surface tension (mN/cm)	Liquid density (g/cm^3)	Liquid viscosity (cp)	Liquid Npp	Liquid Capillary Number	Liquid Reynolds Number	Gas Temp. (C°)	Gas Capillary Number
A14FRAM1	100	1	26	8.5	86.28	4.35	261.1	23.0	49.5	1.2603	917.0	45.3	0.806	6.08	22.9	2.48E-05
A14FRAM2	100	1	10	25.5	70.85	3.87	232.3	23.4	49.5	1.2601	882.9	39.0	0.690	5.61	22.9	2.21E-05
A14FRAM3	100	1	28	15.5	88.52	4.42	265.2	23.2	49.5	1.2602	899.9	42.1	0.804	6.29	22.9	2.52E-05
A14FRAM4	100	1	4	11.5	64.38	3.67	220.2	23.5	49.5	1.2600	874.3	37.5	0.648	5.37	22.6	2.08E-05
A15GRAM1	900	0	39	17.0	39.57	16.23	973.9	24.0	50.3	1.2330	114.3	1.07E-02	0.369	177.8	22.6	9.04E-05
A15GRAM2	600	2	55	13.0	175.43	15.46	927.5	24.0	50.3	1.2330	114.3	1.07E-02	0.351	169.4	22.6	8.61E-05
A15GRAM3	600	2	46	6.0	166.20	15.17	910.2	24.1	50.3	1.2329	113.6	1.04E-02	0.343	167.3	22.6	8.45E-05
A15GRAM4	600	3	8	4.5	188.15	15.85	951.2	24.1	50.3	1.2329	113.6	1.04E-02	0.358	174.9	22.6	8.83E-05
					Average	**4.1**	**244.7**	**23.3**	**49.5**	**1.2601**	**893.5**	**41.0**	**0.74**	**5.84**	**22.8**	**2.32E-05**
					Standard Deviation	**0.4**	**21.9**					**3.5**	**0.08**	**0.42**		**2.1E-06**
					Standard Error	8.97%	8.97%					8.4%	10.85%	7.18%		9.19%
					Average	**15.7**	**940.7**	**24.1**	**50.3**	**1.2329**	**114.0**	**1.05E-02**	**0.36**	**172.3**	**22.6**	**8.74E-05**
					Standard Deviation	**0.5**	**27.8**					**1.6E-04**	**0.01**	**4.8**		**2.6E-06**
					Standard Error	2.95%	2.95%					1.5%	3.13%	2.81%		2.94%

Experiment Code	ΔU=Uc2-Uc1 (cm/min)	3M Static Volt @ Uc1 (7 pt.)	3M stdev	Normalized 3M @ Uc1	Avg. Monroe Static Volt	Monroe stdev.	Norm. Monroe Static @ Uc1
A14FRAM1	13.0	8.76	2.72	1.14	-31.58	31.12	1.32
A14FRAM2	0.0	11.59	9.70	1.50	-14.94	1.75	0.63
A14FRAM3	7.9	1.25	5.49	0.16	-17.23	3.10	0.72
A14FRAM4	0.0	9.25	5.60	1.20	-31.76	9.62	1.33
A15GRAM1	71.9	18.85	16.61	1.81	-41.42	27.57	1.54
A15GRAM2	0.0	-3.25	9.03	-0.31	-26.93	16.08	1.00
A15GRAM3	0.0	12.57	13.41	1.21	-8.71	42.66	0.32
A15GRAM4	0.0	13.53	61.95	1.30	-30.76	20.31	1.14

TABLE VI.8 - Ramping Experiment Data for Fluid Y - Dc200-10 cs

Fluid Y - DC200-10 cSt Silicone Oil
See laboratory notebook pages 174-175

Characteristic length,cm	0.15
Gravity, cm/sec^2	980.7
Acceleration rate, cm/min^2	Varies

First Critical Speed Data

Experiment Code	Initial Speed (cm/min)	Acceler. (cm/min^2)	Elapsed minutes	Elapsed seconds	Elapsed fields	Time elapsed seconds	Uc1 Speed (cm/sec)	Uc1 Speed (cm/min)	Liquid Temp. (C°)	Liquid surface tension (mN/cm)	Liquid density (g/cm^3)	Liquid viscosity (cp)	Liquid Npp	Liquid Capillary Number	Liquid Reynolds Number	Gas Temp. (C°)	Gas Capillary Number
G11YRAM1	2000.0	713.6	1	58	26.0	118.87	56.90	3413.8	19.4	20.3	0.9380	13.2	3.7E-05	0.368	60.2	22.2	7.79E-04
G11YRAM2	2000.0	951.5	1	34	5.0	94.17	58.22	3493.3	19.6	20.3	0.9378	13.1	3.7E-05	0.376	61.8	22.6	8.03E-04
G11YRAM3	2000.0	1427.2	0	59	24.5	59.82	57.05	3422.9	20.1	20.3	0.9374	13.0	3.6E-05	0.366	60.9	23.2	7.96E-04
G11YRAM4	3000.0	951.5	0	16	11.0	16.37	54.33	3259.5	24.6	20.1	0.9334	12.2	2.9E-05	0.330	61.7	23.6	7.69E-04
G11YRAM5	3000.0	1427.2	0	26	28.5	26.95	60.68	3641.1	25.8	20.1	0.9323	12.0	2.7E-05	0.362	70.0	23.8	8.65E-04
G11YRAM6	3000.0	713.6	0	35	3.0	35.10	56.96	3417.5	26.1	20.1	0.9320	11.9	2.6E-05	0.339	66.0	23.6	8.09E-04
						Average	57.4	3441.3	22.6	20.2	0.9351	12.6	3.2E-05	0.357	63.4		8.04E-04
						Standard Deviation	2.1	124.3					5.3E-06	0.018	3.8		3.4E-05
						Standard Error	3.61%	3.61%					16.4%	5.15%	6.04%		4.20%

Second Critical Speed Data

Experiment Code	Initial Speed (cm/min)	Acceler. (cm/min^2)	Elapsed minutes	Elapsed seconds	Elapsed fields	Time elapsed seconds	Uc2 Speed (cm/sec)	Uc2 Speed (cm/min)	Liquid Temp. (C°)	Liquid surface tension (mN/cm)	Liquid density (g/cm^3)	Liquid viscosity (cp)	Liquid Npp	Liquid Capillary Number	Liquid Reynolds Number	Gas Temp. (C°)	Gas Capillary Number
G11YRAM1	2000.0	713.6	2	14	4.0	134.13	59.92	3595.3	19.4	20.3	0.9380	13.2	3.7E-05	0.388	63.4	22.2	8.20E-04
G11YRAM2	2000.0	951.5	1	46	12.5	106.42	61.46	3687.6	19.6	20.3	0.9378	13.1	3.7E-05	0.397	65.2	22.6	8.48E-04
G11YRAM3	2000.0	1427.2	1	10	6.5	70.22	61.17	3670.3	20.1	20.3	0.9374	13.0	3.6E-05	0.393	65.3	23.2	8.54E-04
G11YRAM4	3000.0	951.5	0	37	28.0	37.93	60.03	3601.6	24.6	20.1	0.9334	12.2	2.9E-05	0.364	68.1	23.6	8.50E-04
G11YRAM5	3000.0	1427.2	0	31	14.5	31.48	62.48	3748.9	25.8	20.1	0.9323	12.0	2.7E-05	0.373	72.1	23.8	8.91E-04
G11YRAM6	3000.0	713.6	0	56	11.5	56.38	61.18	3670.6	26.1	20.1	0.9320	11.9	2.6E-05	0.364	70.9	23.6	8.69E-04
						Average	61.0	3662.4	22.6	20.2	0.9351	12.6	3.2E-05	0.380	67.5		8.55E-04
						Standard Deviation	1.0	57.4					5.3E-06	0.015	3.5		2.4E-05
						Standard Error	1.57%	1.57%					16.4%	3.85%	5.15%		2.75%

Experiment Code	ΔU=Uc2-Uc1 (cm/min)	3M Static Volt @ Uc1 (7 pt.)	3M stdev	Normalized 3M @ Uc1	Avg. Monroe Static Volt	Monroe stdev.	Norm. Monroe Static @ Uc1
G11YRAM1	181.6	-50.9	84.5	0.80	14.4	19.8	0.92
G11YRAM2	194.3	-46.4	61.2	0.73	16.0	20.2	1.02
G11YRAM3	247.4	-70.9	58.0	1.12	8.0	22.9	0.51
G11YRAM4	342.0	-96.6	101.7	1.53	19.7	41.5	1.26
G11YRAM5	107.8	-22.0	28.6	0.35	20.8	12.5	1.33
G11YRAM6	253.1	-93.2	52.0	1.47	15.0	23.2	0.96

TABLE VI.9 - Ramping Experiment Data for Fluid Z - DC200 - 20 cs

Fluid Z - DC200-20 cSt Silicone Oil

See laboratory notebook pages 153, 155 and 171-172

Characteristic length,cm	0.15
Gravity, cm/sec^2	980.7
Acceleration rate, cm/min^2	251.48

First Critical Speed Data

Experiment Code	Initial Speed (cm/min)	Elapsed minutes	Elapsed seconds	Elapsed fields	Time elapsed seconds	Uc1 Speed (cm/sec)	Uc1 Speed (cm/min)	Liquid Temp. (C°)	Liquid surface tension (mN/cm)	Liquid density (g/cm^3)	Liquid viscosity (cp)	Liquid Npp	Liquid Capillary Number	Liquid Reynolds Number	Gas Temp. (C°)	Gas Capillary Number
U17ZRAM1	995.0	4	4	27.5	244.92	33.69	2021.5	19.4	20.3	0.9554	22.3	3.0E-04	0.369	21.2	22.9	4.67E-04
U17ZRAM2	1492.4	2	0	4.0	120.13	33.27	1996.0	19.6	20.3	0.9552	22.2	3.0E-04	0.363	21.1	22.9	4.62E-04
U17ZRAM3	1492.4	2	2	9.5	122.32	33.42	2005.1	20.1	20.3	0.9548	22.0	2.9E-04	0.361	21.4	22.9	4.64E-04
U22ZRAM1	1800.0	0	26	12.5	26.42	31.85	1910.7	24.6	20.1	0.9513	20.0	2.0E-04	0.317	22.2	22.6	4.43E-04
U22ZRAM2	1800.0	0	9	5.5	9.18	30.64	1838.5	25.8	20.1	0.9504	19.5	1.9E-04	0.298	21.9	22.6	4.28E-04
U22ZRAM3	1900.0	0	0	0.0	0.00	31.67	1900.0	26.1	20.1	0.9501	19.4	1.8E-04	0.306	22.8	22.6	4.42E-04
U22ZRAM4	1900.0	0	0	0.0	0.00	31.67	1900.0	26.3	20.1	0.9500	19.3	1.8E-04	0.305	22.9	22.6	4.42E-04
					Average	**32.3**	**1938.8**	**23.1**	**20.2**	**0.9525**	**20.7**	**2.3E-04**	**0.331**	**21.9**		**4.50E-04**
					Standard Deviation	**1.1**	**68.8**					**5.8E-05**	**0.032**	**0.7**		**1.5E-05**
					Standard Error	3.55%	3.55%					24.87%	9.53%	3.40%		3.28%

Second Critical Speed Data

Experiment Code	Initial Speed (cm/min)	Elapsed minutes	Elapsed seconds	Elapsed fields	Time elapsed seconds	Uc2 Speed (cm/sec)	Uc2 Speed (cm/min)	Liquid Temp. (C°)	Liquid surface tension (mN/cm)	Liquid density (g/cm^3)	Liquid viscosity (cp)	Liquid Npp	Liquid Capillary Number	Liquid Reynolds Number	Gas Temp. (C°)	Gas Capillary Number
U17ZRAM1	995.0	4	10	25.0	250.83	34.10	2046.3	19.4	20.3	0.9554	22.3	3.0E-04	0.373	21.5	22.9	4.73E-04
U17ZRAM2	1492.4	2	5	12.0	125.40	33.63	2018.0	19.6	20.3	0.9552	22.2	3.0E-04	0.367	21.3	22.9	4.67E-04
U17ZRAM3	1492.4	2	14	20.5	134.68	34.28	2056.9	20.1	20.3	0.9548	22.0	2.9E-04	0.371	21.9	22.9	4.76E-04
U22ZRAM1	1800.0	0	49	4.0	49.13	33.43	2005.9	24.6	20.1	0.9513	20.0	2.0E-04	0.333	23.3	22.6	4.65E-04
U22ZRAM2	1800.0	0	27	11.0	27.37	31.91	1914.7	25.8	20.1	0.9504	19.5	1.9E-04	0.310	22.8	22.6	4.45E-04
U22ZRAM3	1900.0	0	20	23.5	20.78	33.12	1987.1	26.1	20.1	0.9501	19.4	1.8E-04	0.320	23.8	22.6	4.62E-04
U22ZRAM4	1900.0	0	17	1.5	17.05	32.86	1971.5	26.3	20.1	0.9500	19.3	1.8E-04	0.316	23.8	22.6	4.59E-04
					Average	**33.3**	**2000.1**	**23.1**	**20.2**	**0.9525**	**20.7**	**2.3E-04**	**0.342**	**22.6**		**4.64E-04**
					Standard Deviation	**0.8**	**48.3**					**5.8E-05**	**0.028**	**1.1**		**1.0E-05**
					Standard Error	2.42%	2.42%					24.87%	8.17%	4.72%		2.19%

Experiment Code	ΔU=Uc2-Uc1 (cm/min)	3M Static Volt @ Uc1 (7 pt.)	3M stdev	Normalized 3M @ Uc1	Avg. Monroe Static Volt	Monroe stdev	Norm. Monroe Static @ Uc1
U17ZRAM1	24.8	138.0	38.6	0.61	24.3	12.7	1.08
U17ZRAM2	22.1	300.9	55.8	1.32	23.6	19.5	0.10
U17ZRAM3	51.8	244.0	51.6	1.07	19.4	39.8	0.09
U22ZRAM1	95.2	89.5	210.9	0.44	42.1	35.8	1.07
U22ZRAM2	76.2	126.5	57.3	0.62	35.8	32.6	0.91
U22ZRAM3	87.1	252.8	68.7	1.25	29.0	14.6	0.74
U22ZRAM4	71.5	341.5	70.3	1.69	50.3	25.3	1.28

APPENDIX VII

FULL SET OF DEFLECTOMETRY IMAGES AND DATA TABLES FOR CASE#11

This Appendix is intended to include a set of laser printed images and the corresponding analysis files for archival and comparison purposes. The distance between the ruling lines in all the images is 200 μm. For Fluid Z, DC200-20 cs, case#11, an air sheet is formed and advances at 7.94 cm/sec with a substrate velocity of 34.48 cm/sec and Ca = 0.34±0.01, as shown in Figure VII.1. The sheet edges move inward, forming an air tongue which then retracts. Images from the advancing and retracting sequences have been included.

The first set of images from the TIFF[1] files display the advance from the mean dynamic contact line position, i.e., prior to advance, until film time 4:34.811 (τ = 0.000). The deflectometry analysis was initiated at this film time because the triangular air tongue had reached a maximum length, the tip was well defined, the shape was axisymetric, and the retraction sequence was starting. For the images from 4:34.811 to 4:34.831, the experimental data for δy_i, calculated error, dh(i), and interface height, h(i) (μm), are found in Tables VII.1 to VII.14. The tables are after the respective images so that a comparison between the experimentally measured deflection and the "apparent" deflection in the images can be made.

---

[1] A bitmap graphics file using the LZW compression algorithm. TIFF stands for "tagged image file format."

There are a number of important features to note in the image series. In Figure VII.6 an inflection point at the interface can be seen at the left-hand edge which is then enlarged in Figure VII.7.

The images in Figures VII.4 to VII.8 show two precursor structures that combine to a larger precursor, with the air film developing in the same location at film time 4:34.809. The interface profile along line ABC in Figure VII.8 was calculated and is presented in Figure VII.9. The vertex of the precursor represents a localized minima in the profile. The analysis of the sheet profile is more difficult because reference lines are not available on either side of the air tongue for computing δy_i and Φ. Additionally, the axisymetric criteria is not satisfied, and thus, the profile has a greater error.

The image file for $\tau = 0.0407$ (see Figures VII.18 and VII.19) was twice reanalyzed[2] to verify the inflection in the interface profile. Each analysis revealed the same shape with the biggest differences in height occurring near the tail. The differences near the tail for retest#1 and #2 are still within ±10% of the original analysis. At $\tau = 0.0813$, the image was also reanalyzed to confirm the results. This validation was almost identical with the worst case 20 μm different in h(i) from the original analysis.

[2] Compare original analysis in Table VII.3 vs reanalyses in Table VII.4 and VII.5.

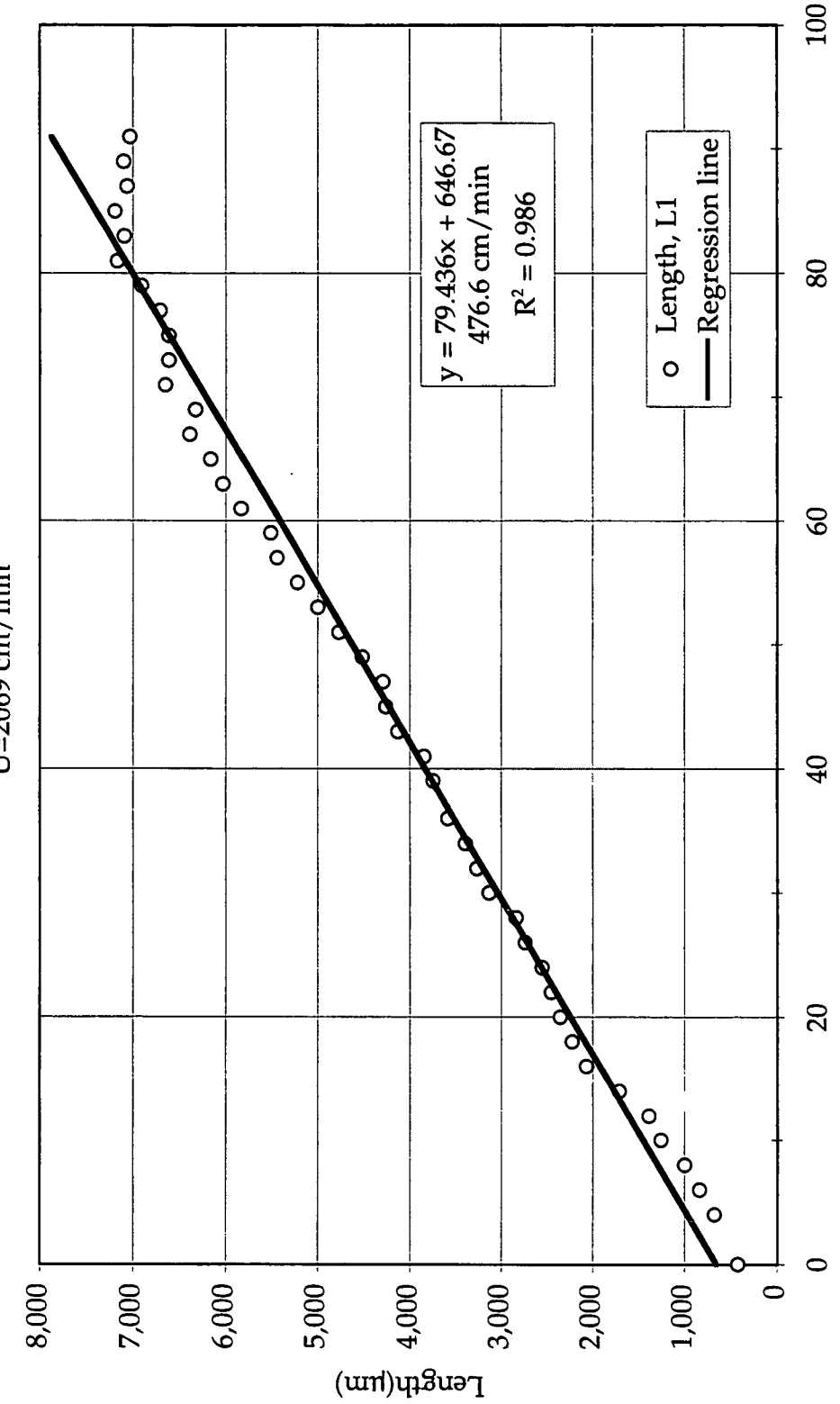

Figure VII.1 - Advancing Air Sheet for DC200-20 cSt Run U22ZCA1 4:34.710 to 4:34.809 - U=2069 cm/min

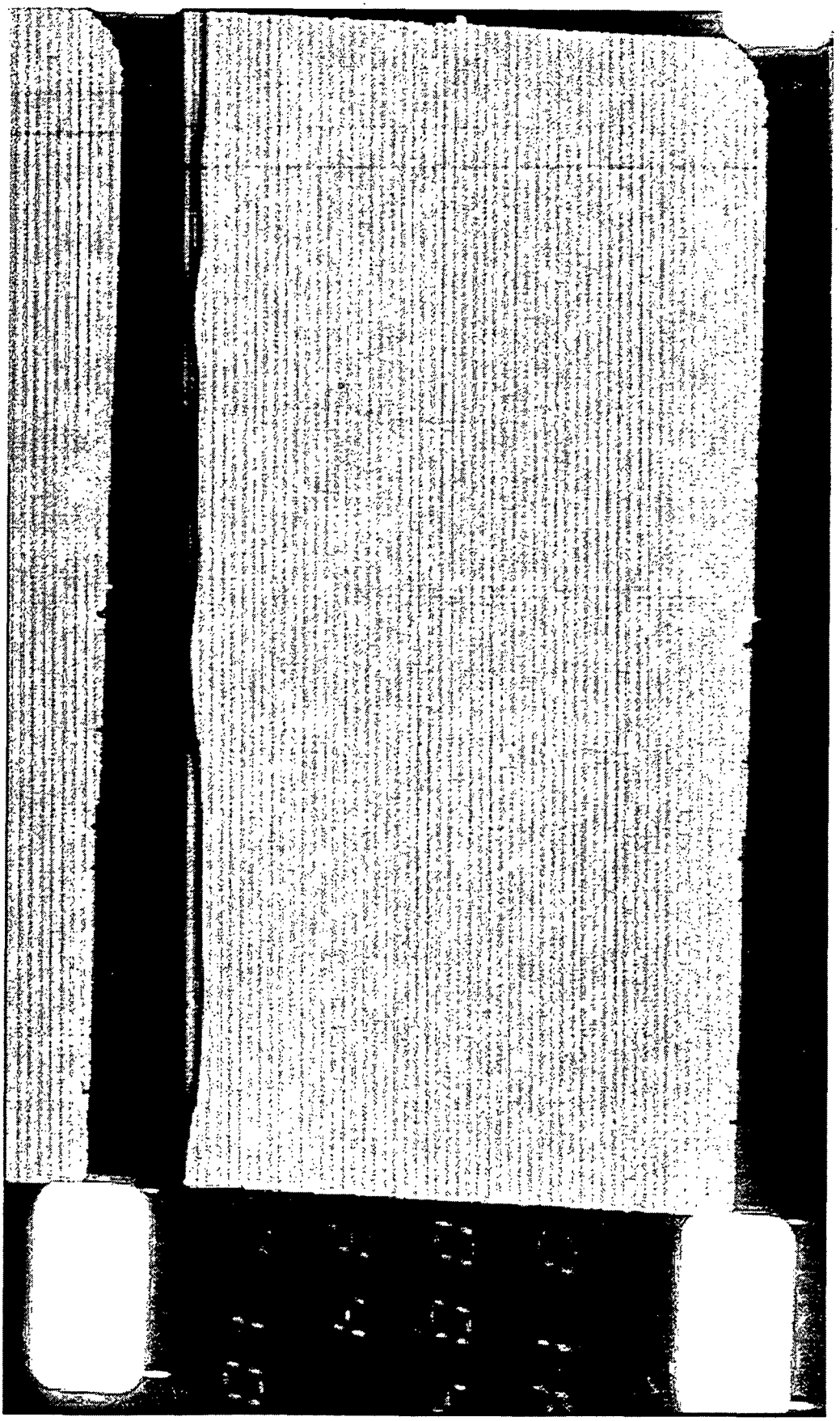

Figure VII.2 Image U22C1201.TIF at time 4:34.710. The air sheet begins advancing past the mean DCL position

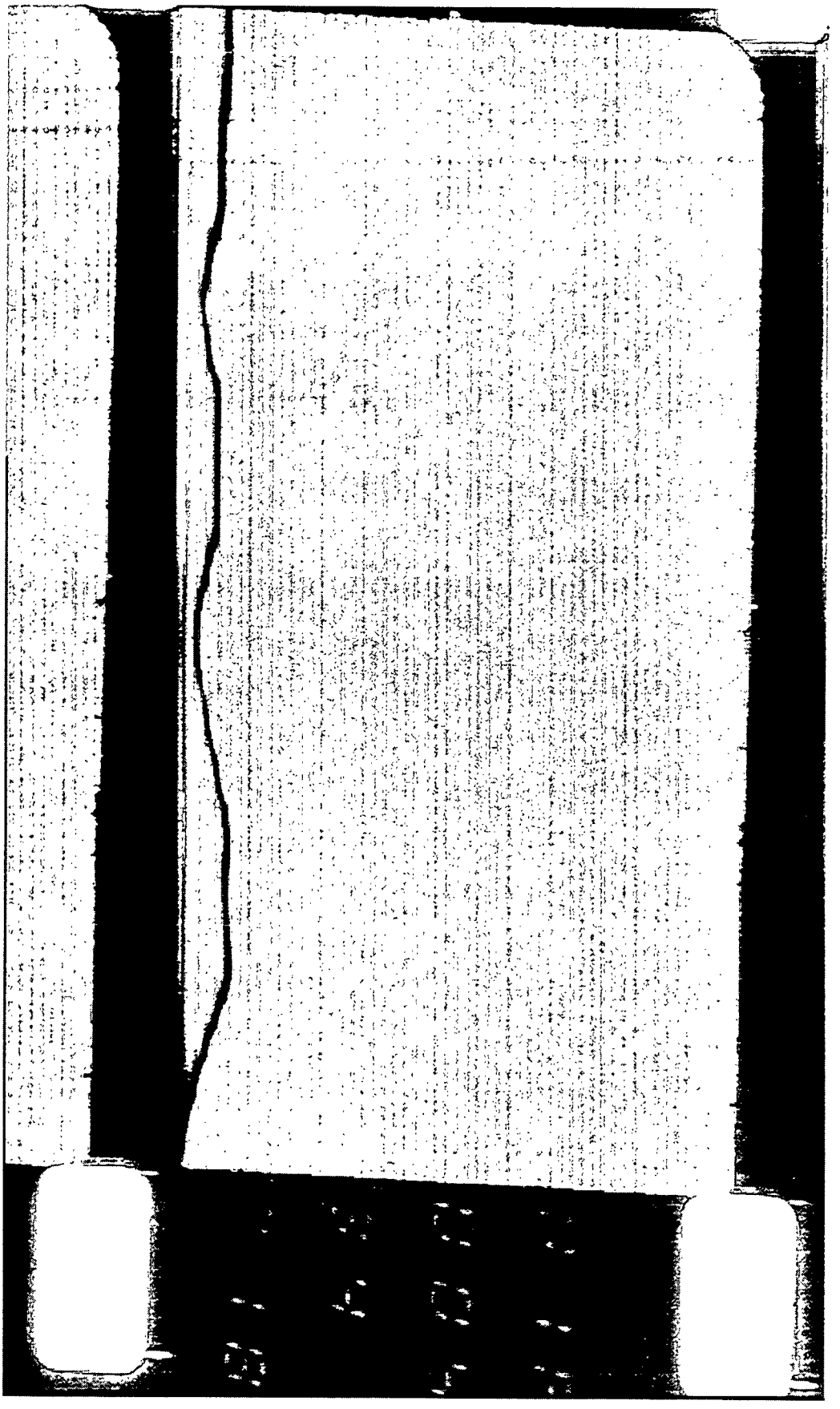

Figure VII.3 Image U22C1204.TIF at time 4:34.718. Air sheet continues advancing at 7.94 cm/sec.

Figure VII.4 Image U22C1217.TIF at time 4:34.744. Two triangular precursor structures are shown near the mean DCL position.

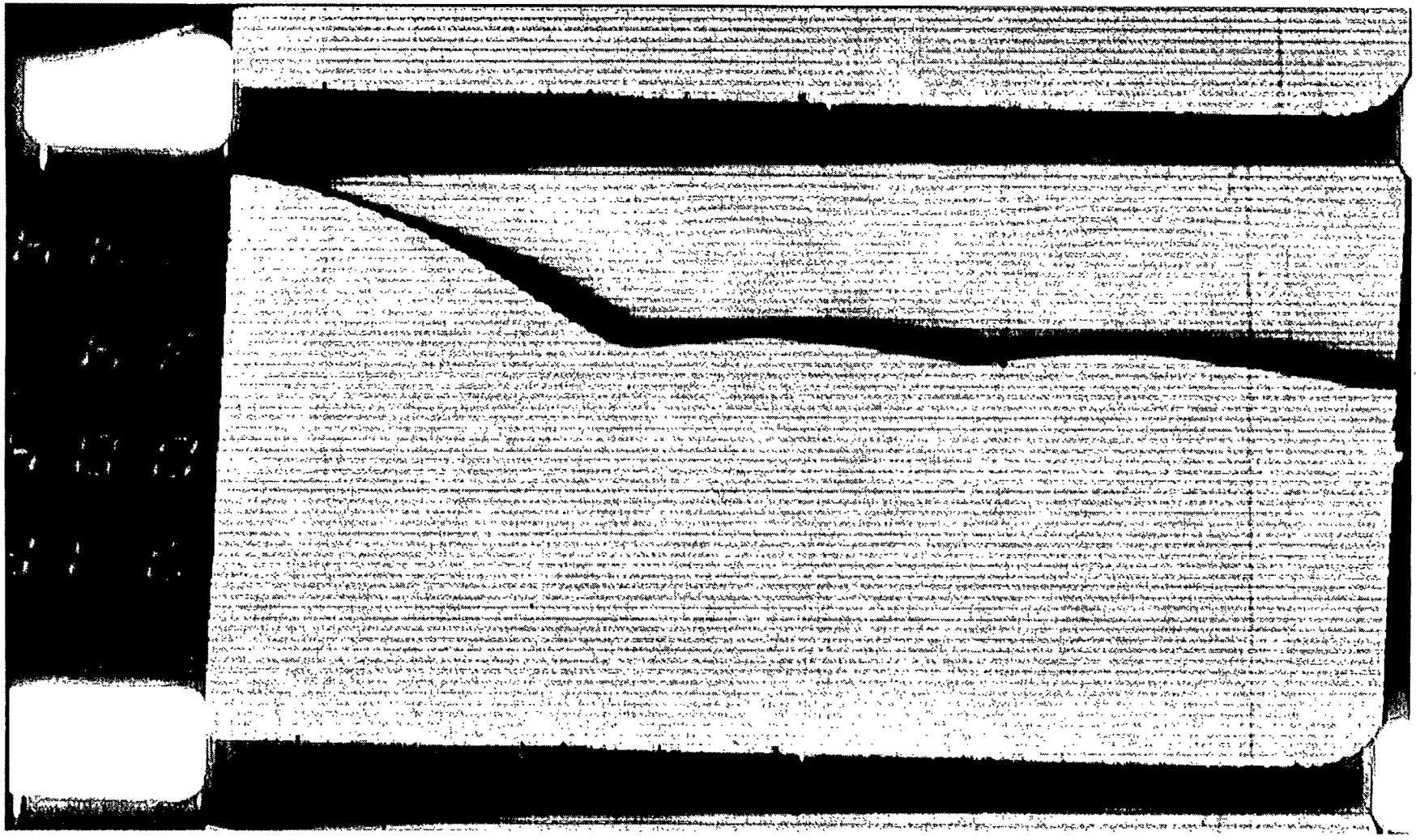

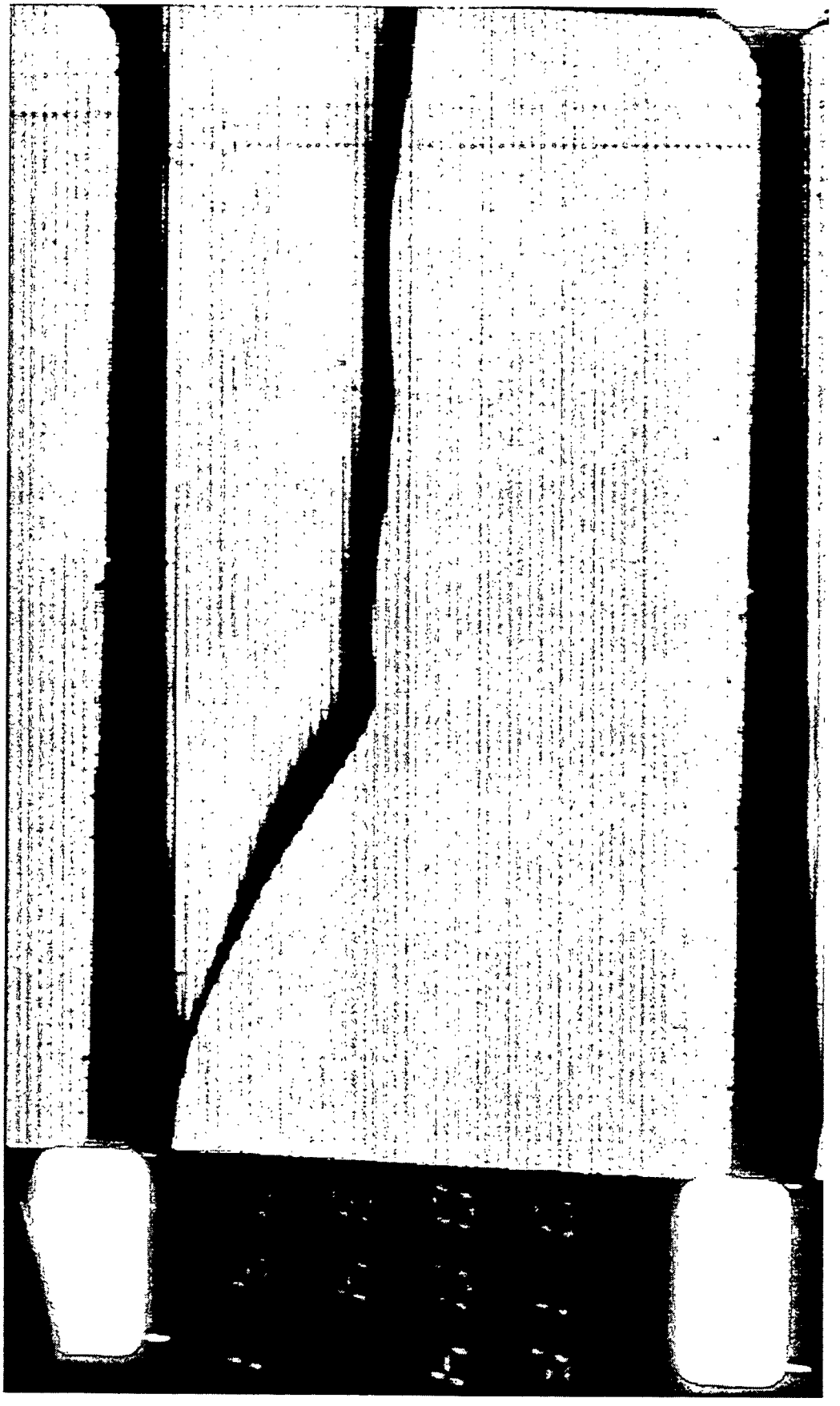

Figure VII.5 Image U22C1220.TIF at time 4:34.751. The triangular precursor structures have begun to merge.

Figure VII.6 Image U22C1225.TIF at time 4:34.761. A localized disturbance near the left edge can be qualitatively be seen as a localized increase in height in that location. The precursor structures have merged to a single triangular precursor.

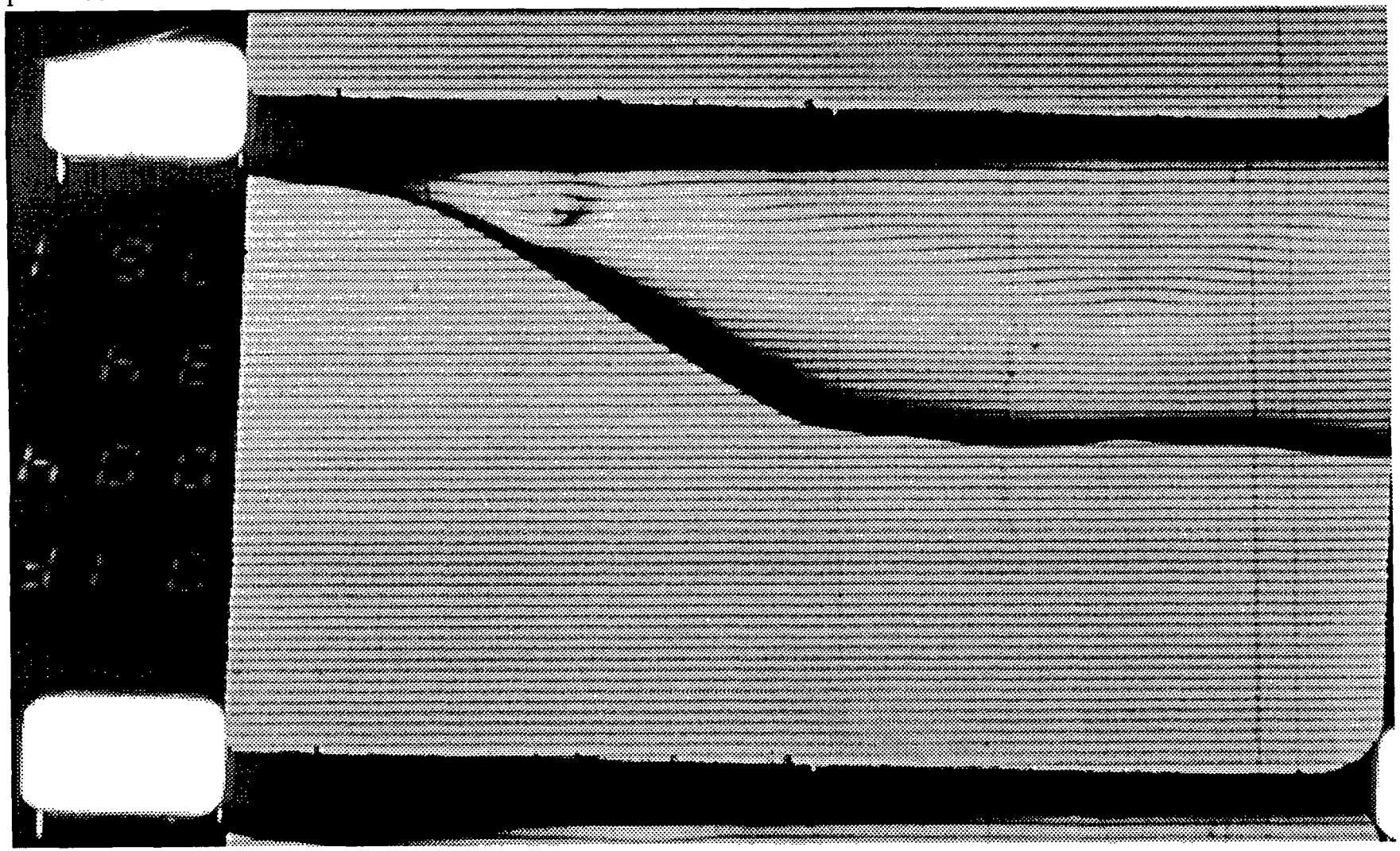

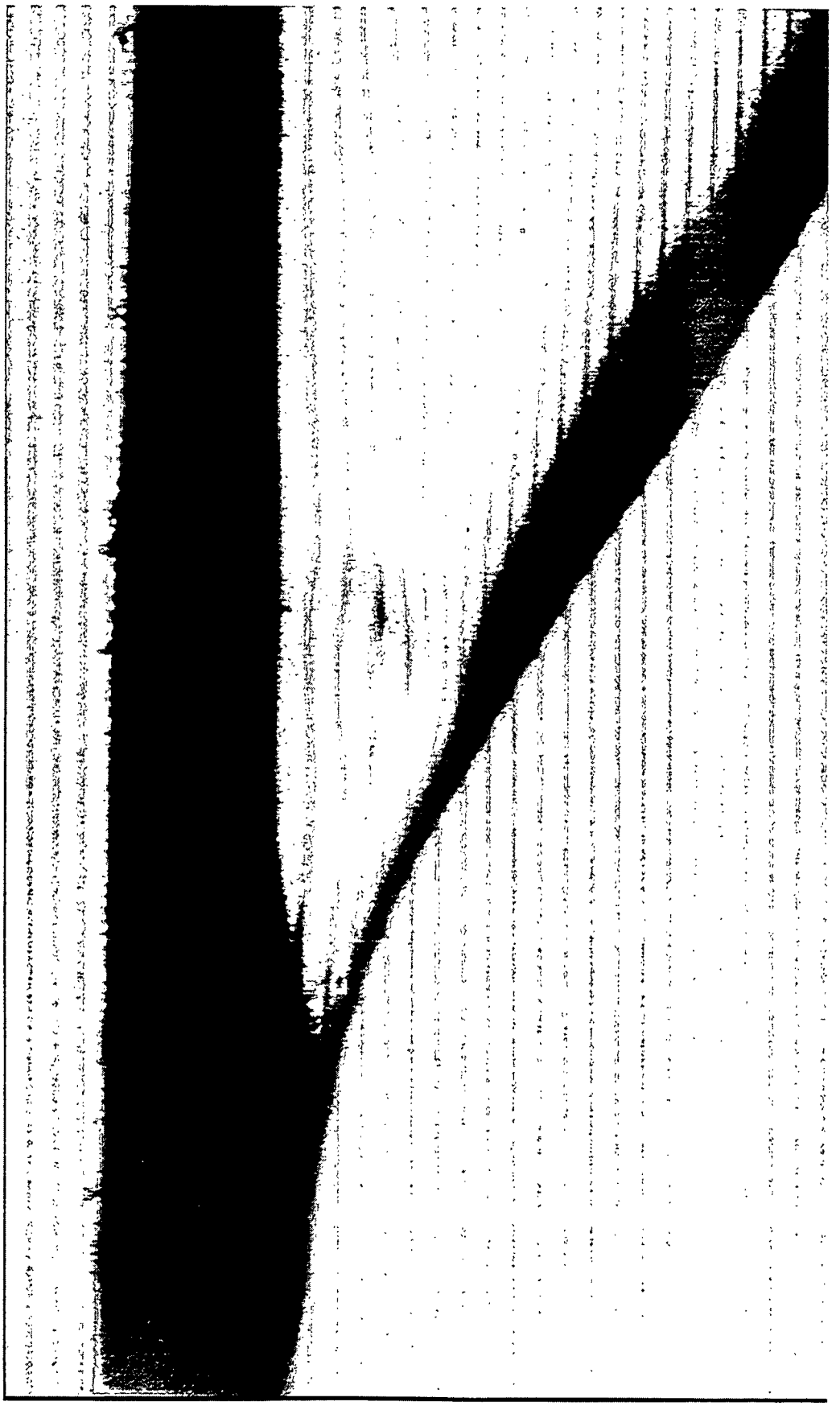

Figure VII.7 Image U22C1226.TIF at time 4:34.761. Close up of disturbance near left edge.

Figure VII.8 Image U22C1227.TIF at time 4:34.763. Disturbance finished and single precursor. The interface profile is given in the next image.

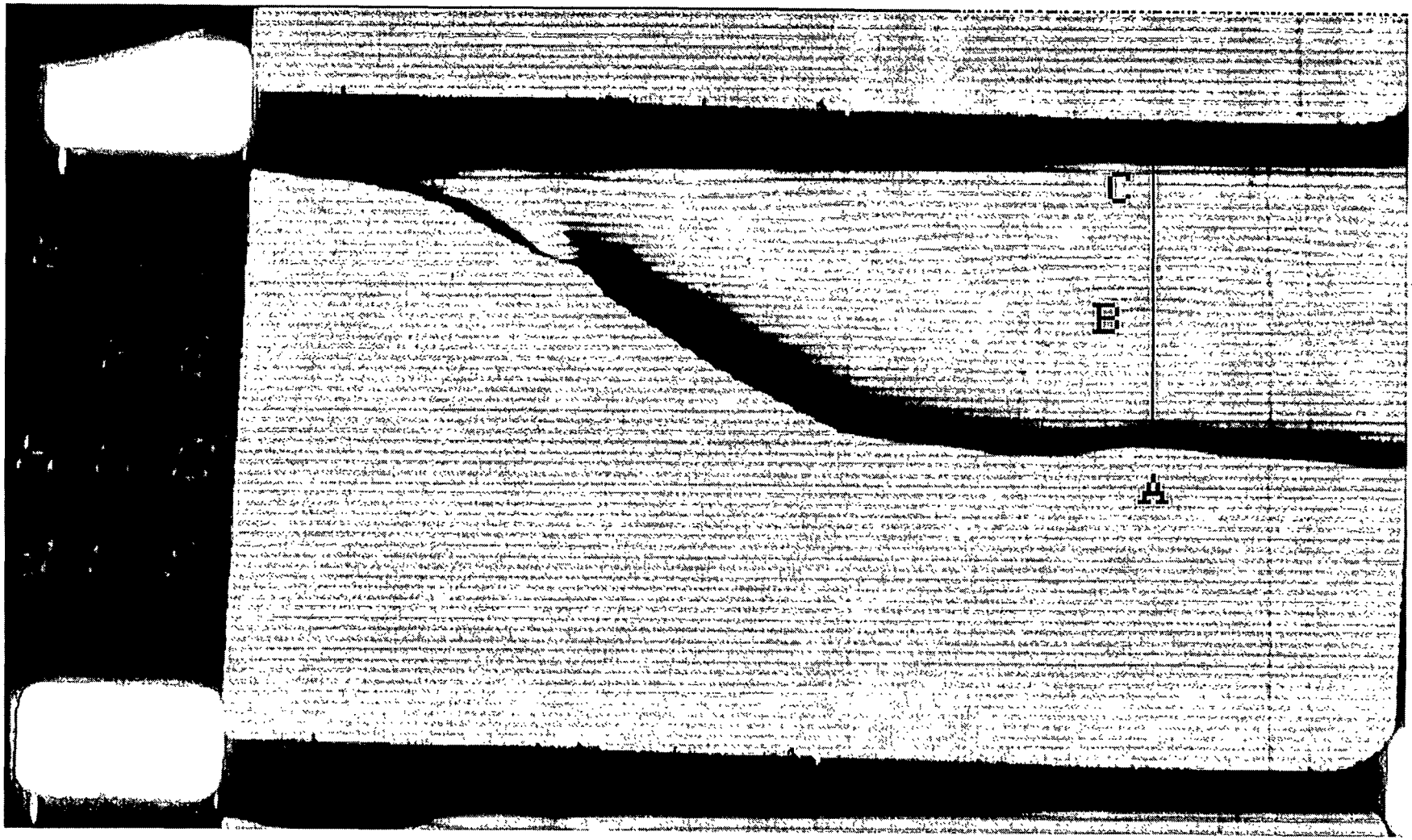

Figure VII.9 Dimensional graph of the interface profile at time 4:34.763 from deflection data along line ABC. A correction of 8.5 μm has been added to the deflection data equivalent to G = 1.47°. This is greater than can be accounted for by the correction determined from the blade loading.

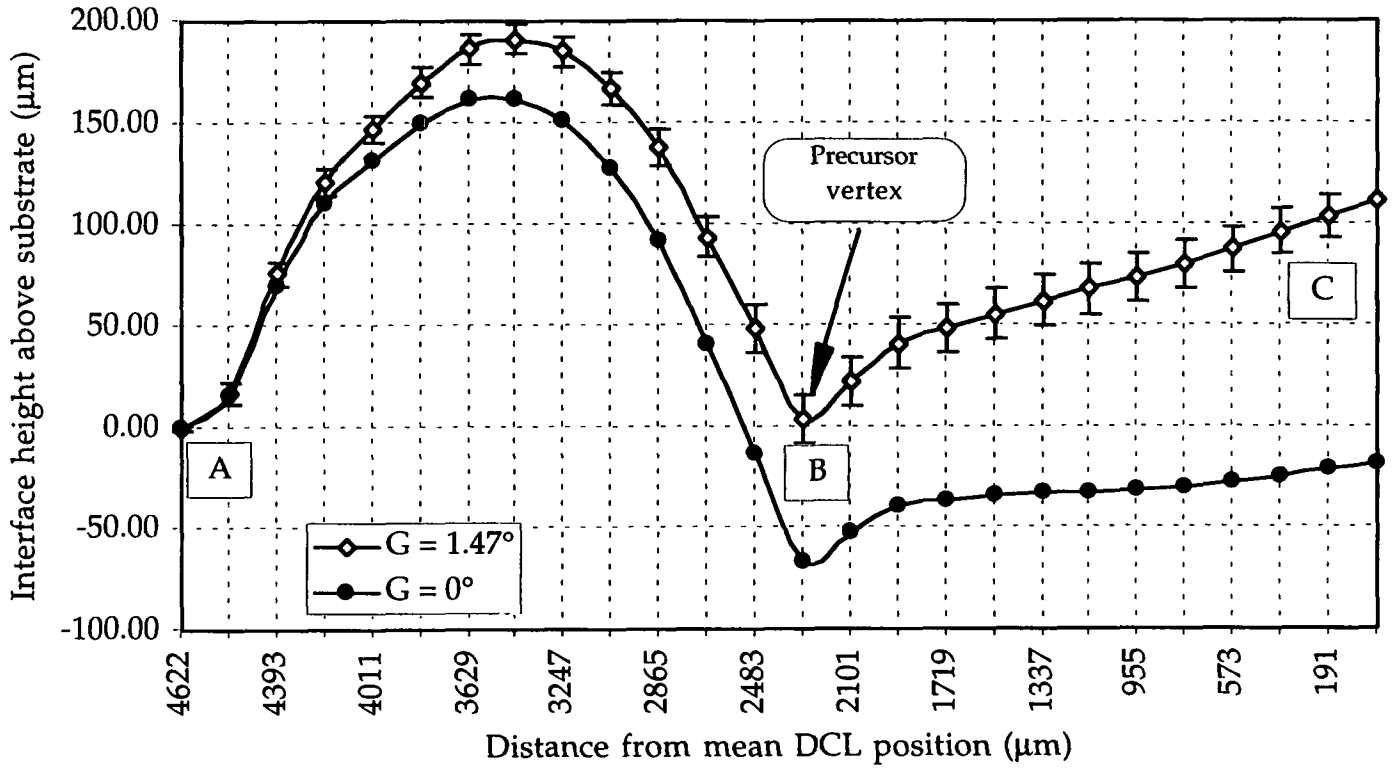

Figure VII.10 Image U22C1231.TIF at time 4:34.771. The tip angle, $\varnothing_1$ = 105±5° of the precursor has decreased from the value of $\varnothing_1$ = 119±5° in previous figure with U22C1257.TIF.

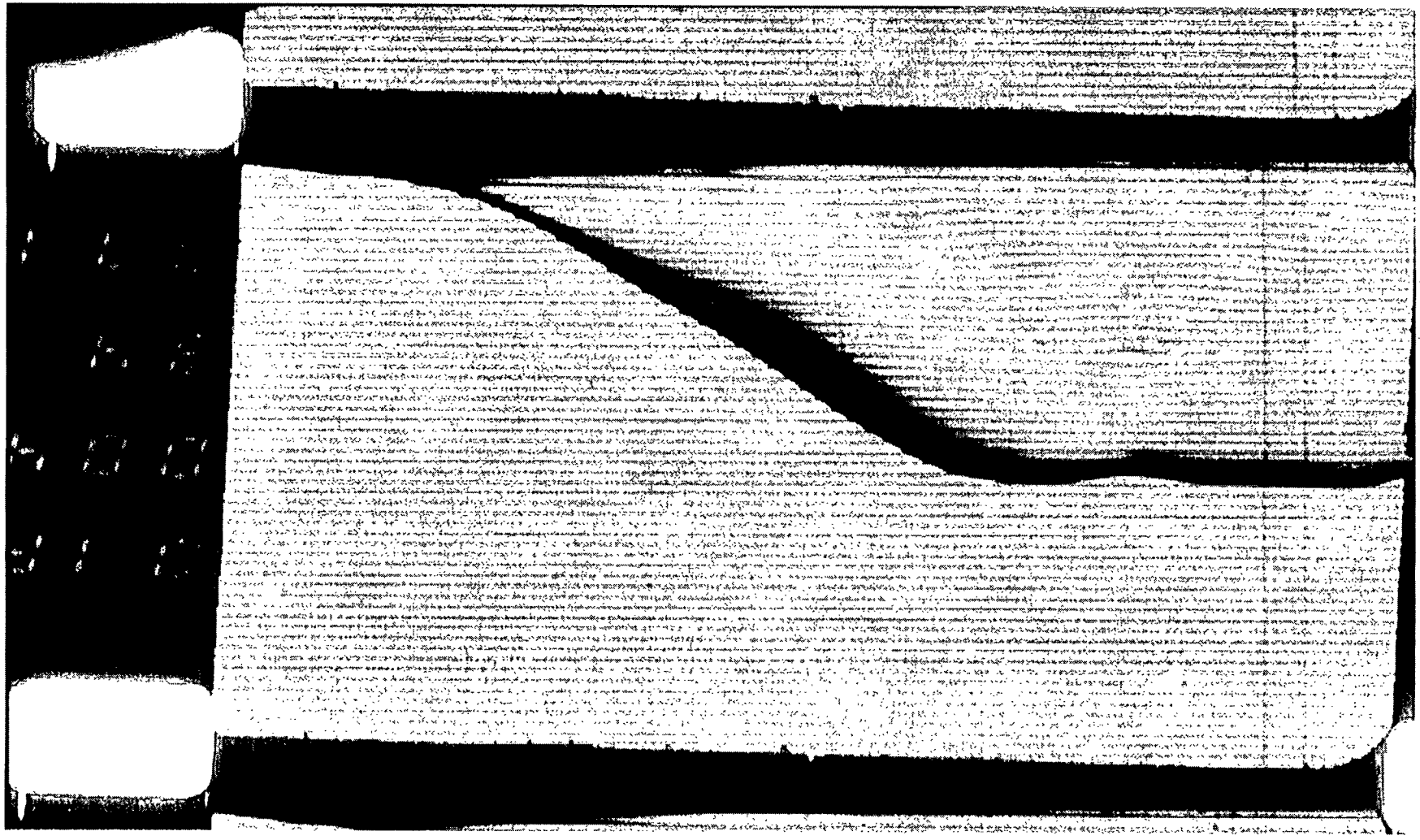

Figure VII.11 Image U22C1234.TIF at time 4:34.777. $\varnothing_1 = 93\pm5°$. The dark area on the image near the precursor structure is a piece of dust on the film and not present during the actual experiment.

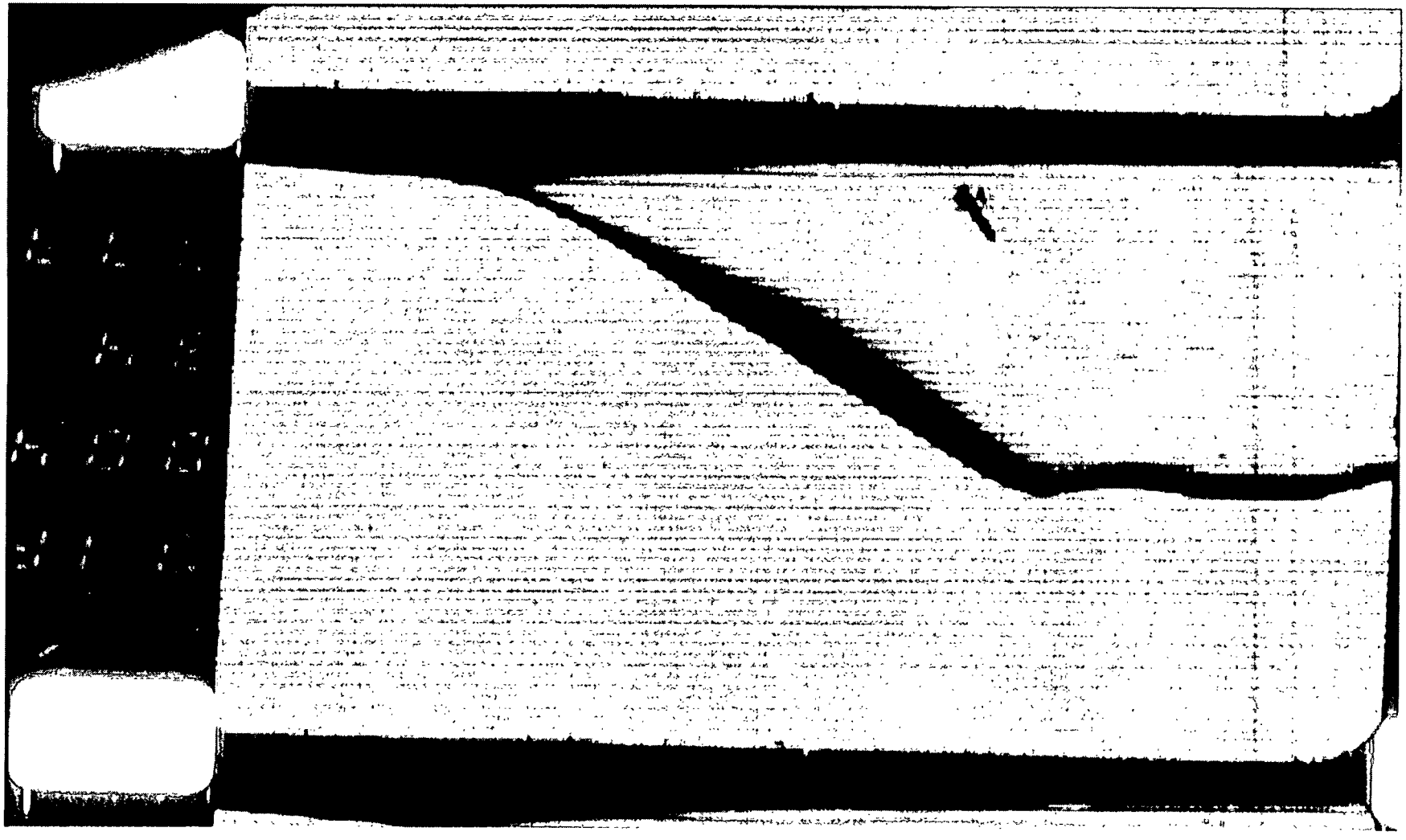

Figure VII.12 Image U22C1240.TIF at time 4:34.789. The precursor structure has been disrupted as the triangular air tongue develops.

Figure VII.13 Image U22C1243.TIF at time 4:34.795. The base of the air sheet continues to narrow and the tip of the air tongue continues to develop. The precursor structure is visible again.

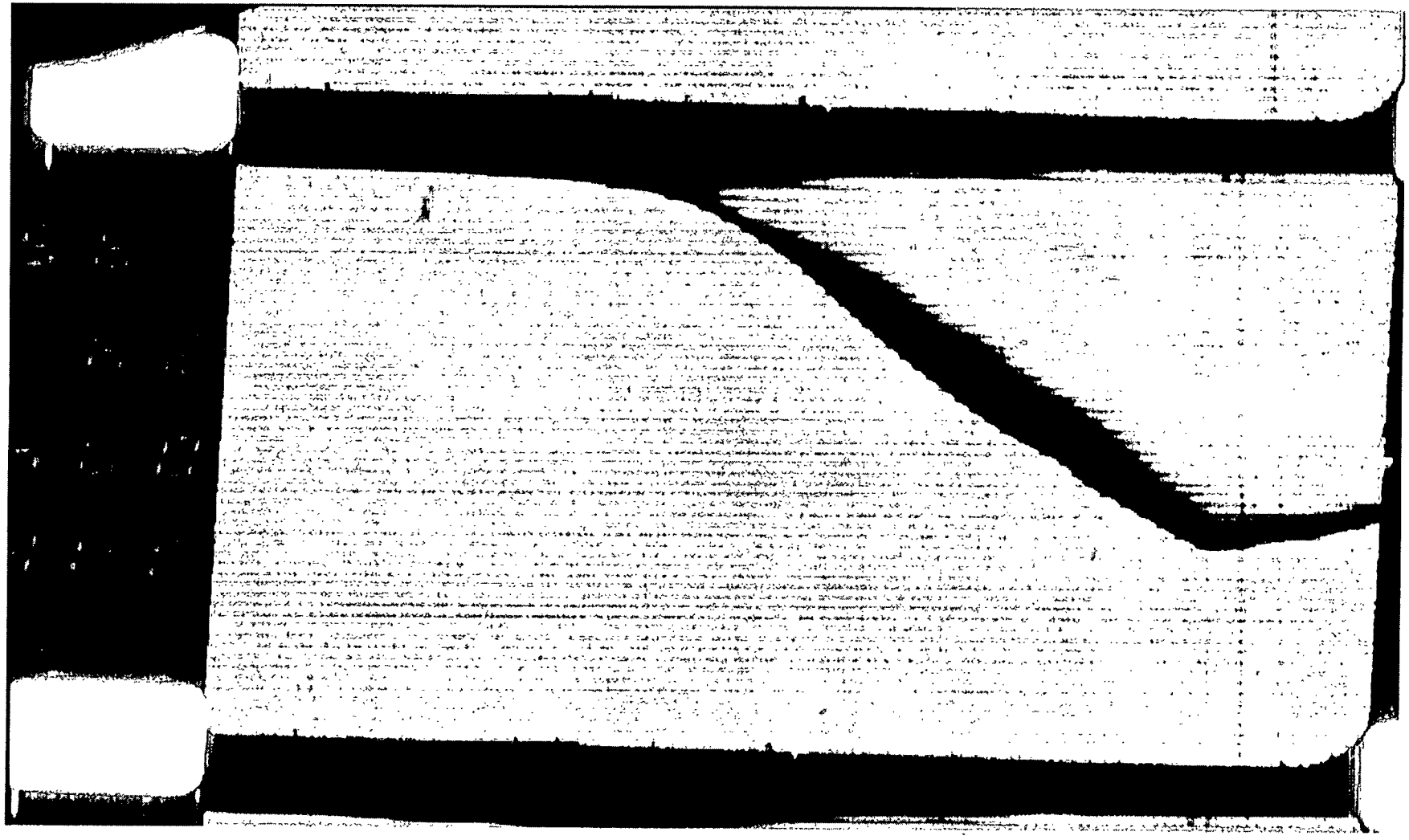

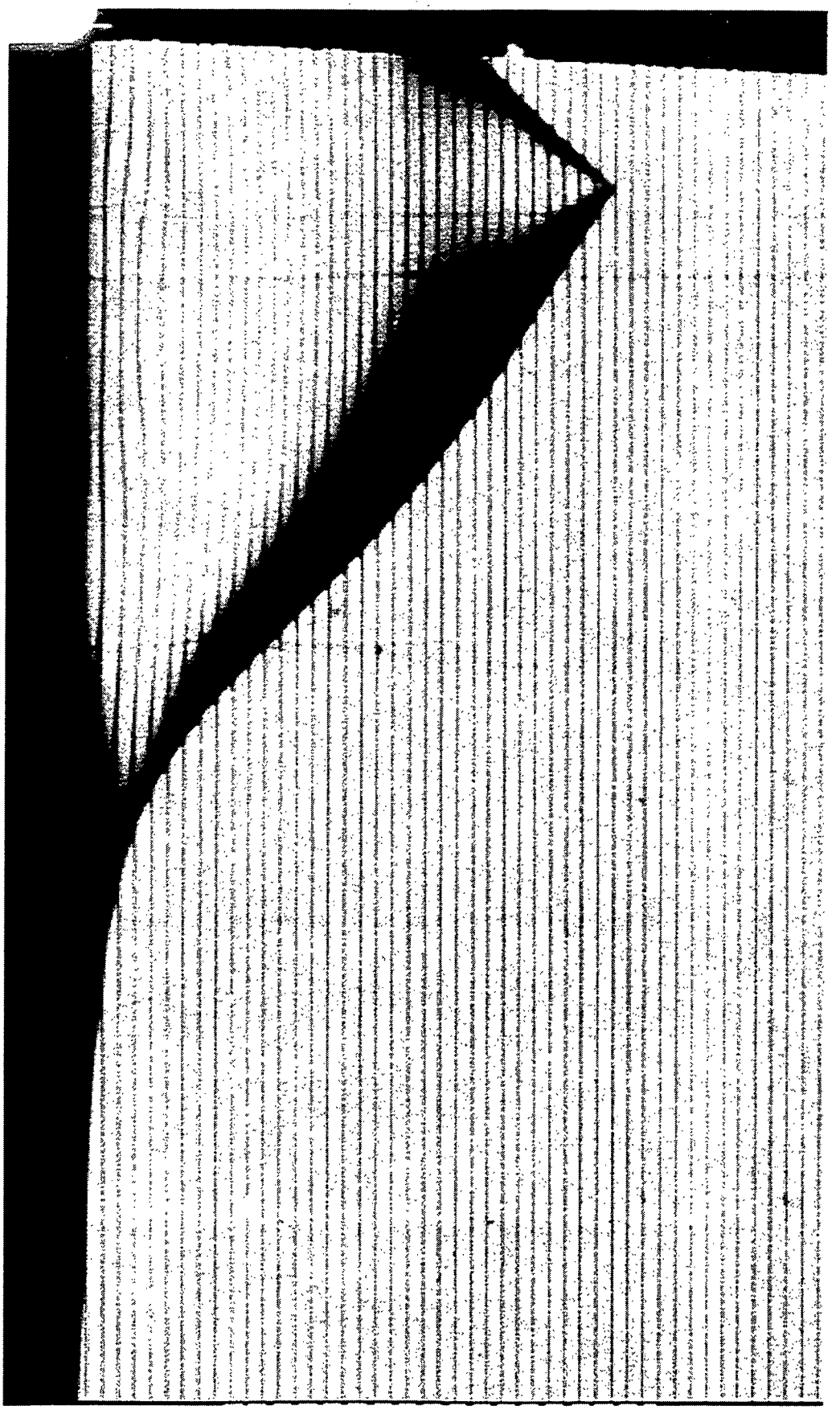

Figure VII.14 Image U22C1251.TIF at time 4:34.809. No deflectometry measurements were made because the air tongue is not axisymetric.

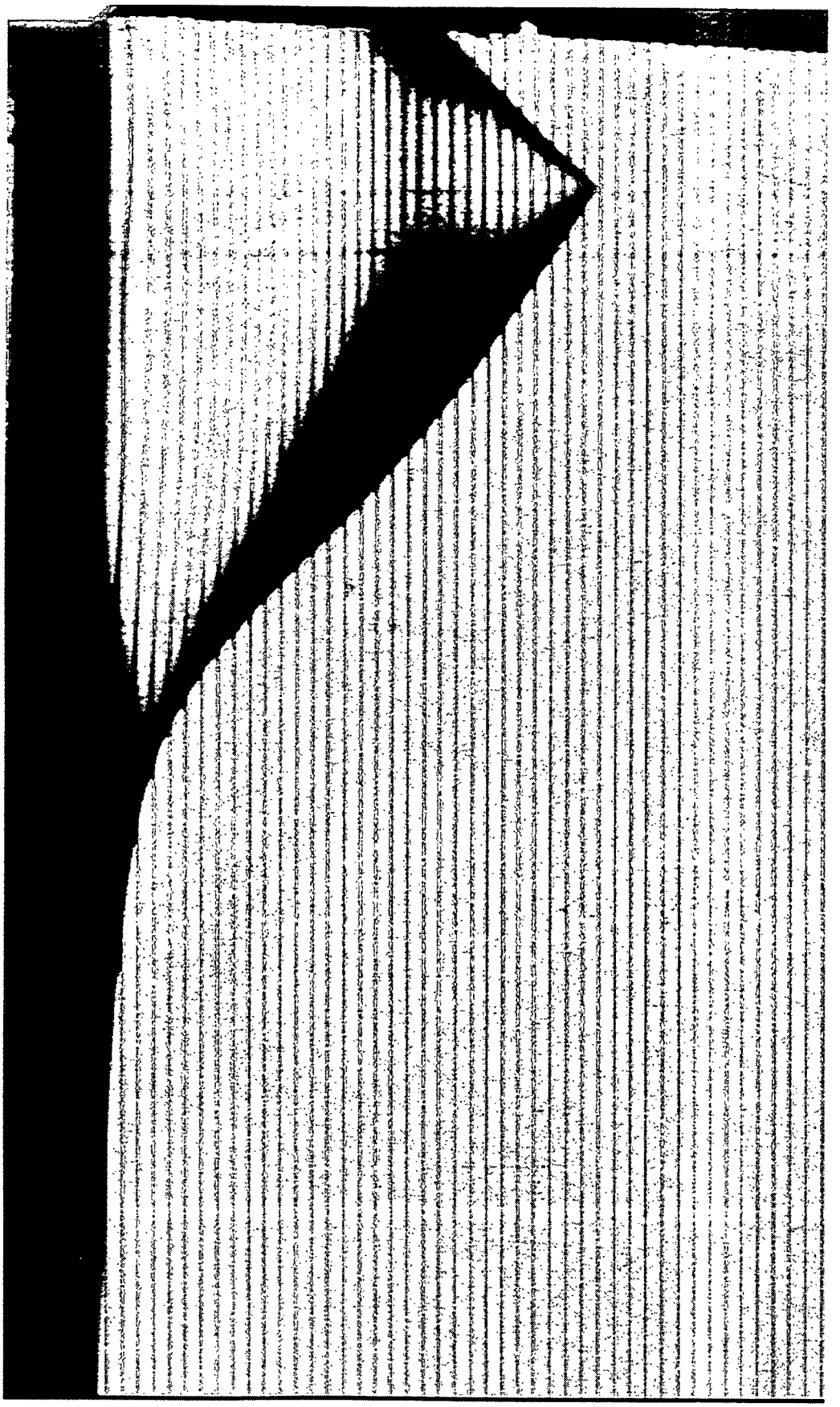

Figure VII.15 Image U22C1252.TIF at time 4:34.811 (t = 0.000) for deflectometry analysis. The data file and analyzed data are contained in Table VII.1.

TABLE VII.1 - Image U22C1252.TIF Case#11 with DC200-10 cs.

Film Time 4:34.811, τ = 0.000

			Thickness	Refractive index	
Angular Misalignment, Φ	0.0188°	Window	1588	1.515	b*(μm)= 1071.88
Magnification factor in dimensions	8	Substrate	38.1	1.608	c*(μm)= 698.88
Distance between fringes $1/P_f$, (μm)	200	Liquid		1.4009	
Distance(μm) from tip to first fringe d_t =	200	Air Gap	0	1.003	
		Errors			
		Window,1	4.4	0.005	
		Substrate,2	1.6	0.005	
		Liquid,4		0.005	
		dδy(i)=d(y(i)-y(i-1)), (μm)		7	

Correction(μm, °)	5.94	0.89	deg.		Error	Error	Error	Error	Error		Quadratic		
i	δy(i)	δy(i)+corr.	b	c	dh(i)/db	dh(i)/dc	db	dc	dh(i)	Δ dh(i)	h(i), (μm)	y(μm)	dh/dy
0											**0.0**	0	
1	62.3	68.3	1071.9	-47,700	-0.037	-8.64E-04	4.0	4892.1	4.2	4.23	**42.8**	200	0.214
2	79.9	85.9	1029.1	-105,886	-0.077	-8.21E-04	5.8	6855.3	5.6	1.42	**94.3**	400	0.257
3	78.0	84.0	977.6	-159,733	-0.113	-7.92E-04	6.9	8052.6	6.4	0.78	**142.6**	600	0.242
4	78.7	84.6	929.3	-211,978	-0.145	-7.64E-04	7.5	8698.5	6.7	0.31	**189.5**	800	0.234
5	51.6	57.6	882.4	-243,317	-0.167	-7.56E-04	7.8	8989.4	6.9	0.18	**220.6**	1000	0.156
6	52.9	58.8	851.3	-277,554	-0.186	-7.38E-04	8.0	9034.2	6.8	-0.08	**251.7**	1200	0.155
7	54.8	60.7	820.2	-312,160	-0.204	-7.21E-04	7.9	8982.8	6.7	-0.15	**283.0**	1400	0.157
8	77.4	83.4	788.9	-361,558	-0.226	-6.95E-04	7.8	8876.4	6.4	-0.26	**324.7**	1600	0.209
9	51.0	56.9	747.2	-387,797	-0.243	-6.89E-04	7.5	8791.8	6.3	-0.09	**352.6**	1800	0.140
10	76.8	82.7	719.3	-435,767	-0.261	-6.65E-04	7.5	8613.7	6.1	-0.27	**392.1**	2000	0.197
11	79.3	85.2	679.8	-479,859	-0.280	-6.48E-04	7.2	8546.4	5.9	-0.15	**431.7**	2200	0.198
12	79.9	85.9	640.2	-522,770	-0.298	-6.32E-04	7.1	8477.3	5.8	-0.13	**470.6**	2400	0.195
13	52.2	58.2	601.2	-545,120	-0.311	-6.27E-04	7.0	8419.6	5.7	-0.05	**496.6**	2600	0.130
14	54.1	60.1	575.3	-574,226	-0.323	-6.17E-04	6.9	8272.5	5.6	-0.14	**522.9**	2800	0.132
15	51.6	57.6	549.0	-600,687	-0.333	-6.08E-04	6.8	8206.2	5.5	-0.09	**547.7**	3000	0.124
16	27.1	33.0	524.2	-610,155	-0.341	-6.07E-04	6.8	8162.0	5.5	-0.02	**561.8**	3200	0.071
17	26.4	32.4	510.0	-624,845	-0.346	-6.02E-04	6.7	8090.3	5.4	-0.06	**575.6**	3400	0.069
18	1.3	7.2	496.3	-621,970	-0.350	-6.05E-04	6.7	8062.0	5.4	0.01	**578.6**	3600	0.015
19	-26.4	-20.5	493.3	-605,886	-0.349	-6.12E-04	6.7	8044.8	5.5	0.04	**569.9**	3800	-0.044
20	-51.0	-45.0	502.0	-579,377	-0.343	-6.24E-04	6.7	8093.0	5.6	0.10	**550.5**	4000	-0.097
21	-76.2	-70.2	521.4	-540,983	-0.333	-6.41E-04	6.8	8216.6	5.7	0.18	**519.7**	4200	-0.154
22	-103.2	-97.3	552.2	-489,017	-0.316	-6.65E-04	7.0	8436.5	6.0	0.29	**475.7**	4400	-0.220
23	-129.7	-123.7	596.2	-423,454	-0.292	-6.99E-04	7.2	8792.8	6.5	0.46	**417.7**	4600	-0.290
24	-129.0	-123.1	654.2	-361,672	-0.261	-7.30E-04	7.6	9317.1	7.1	0.60	**357.5**	4800	-0.301
25	-127.8	-121.8	714.4	-298,039	-0.226	-7.66E-04	8.1	9747.0	7.7	0.60	**295.2**	5000	-0.311
26	-126.5	-120.6	776.7	-232,161	-0.186	-8.08E-04	8.7	10207.3	8.4	0.71	**230.5**	5200	-0.324
27	-128.4	-122.5	841.4	-161,491	-0.138	-8.59E-04	9.3	10788.5	9.4	0.96	**161.1**	5400	-0.347
28	-129.0	-123.1	910.8	-86,646	-0.080	-9.22E-04	10.2	11647.5	10.8	1.41	**86.9**	5600	-0.371

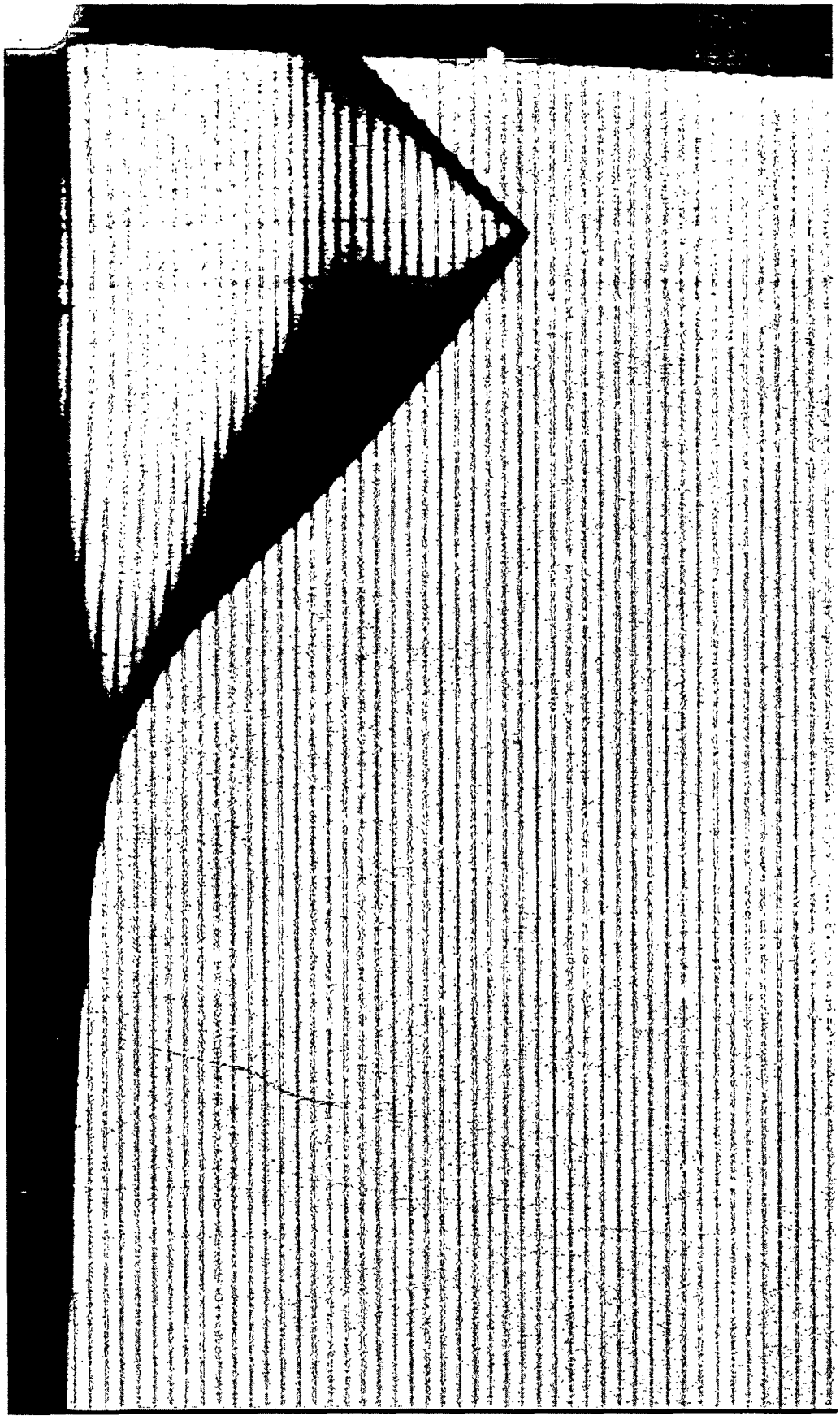

Figure VII.16 Image U22C1253.TIF at time 4:34.813 (τ = 0.0203) for deflectometry analysis. The data file and analyzed data are contained in Table VII.2.

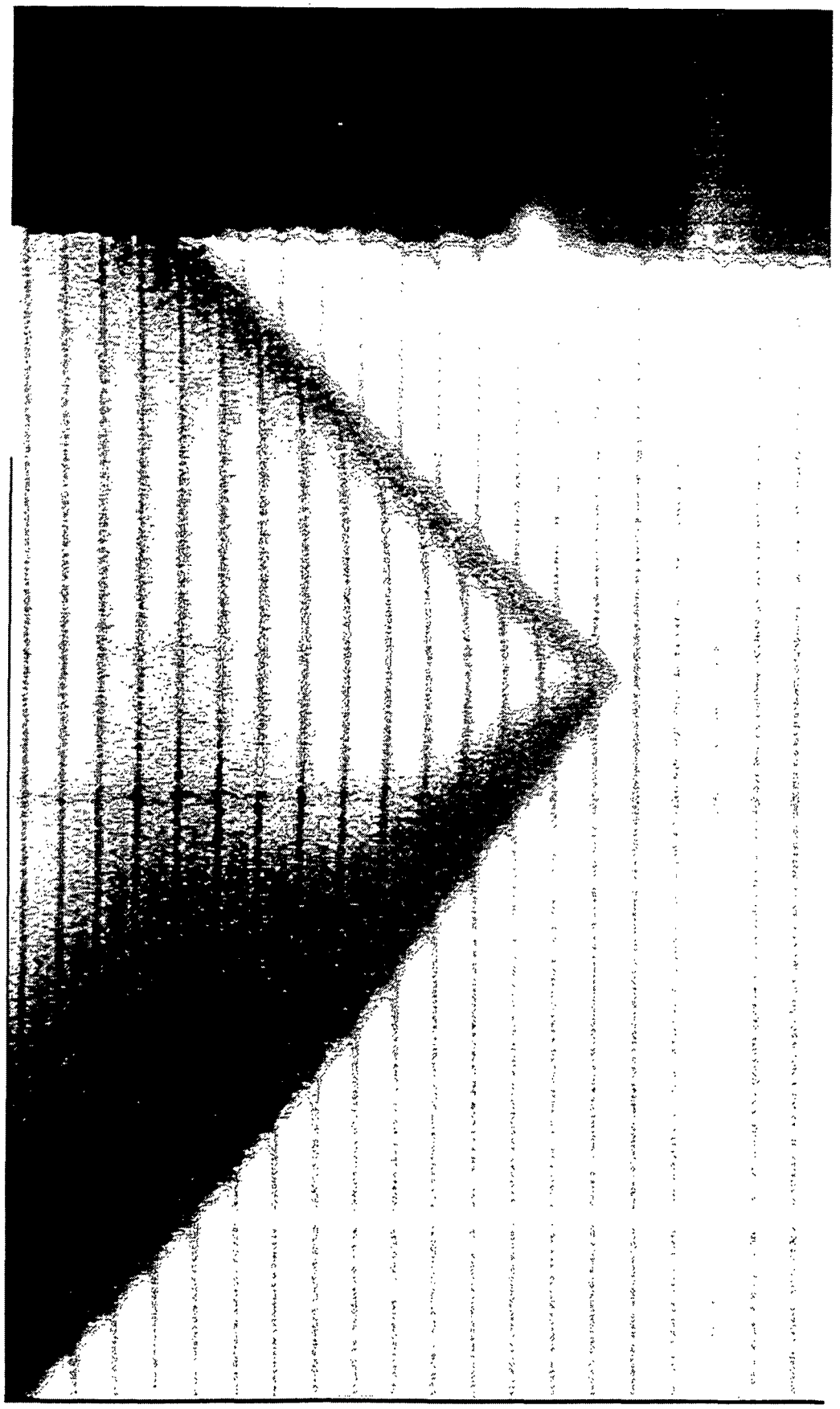

Figure VII.17 Image U22C1254.TIF at time 4:34.813 (τ = 0.0203) close up of tip region for deflectometry.

TABLE VII.2 - Image U22C1253.TIF and U22C1254.TIF Case#11 with DC200-10 cs.

			Thickness	Refractive index	
Film Time 4:34.813, t = 0.0203					
Angular Misalignment Φ	-0.037 and -0.086°	Window	1588	1.515	b*(μm)= 1071.88
Magnification factor in dimensions	8	Substrate	38.1	1.608	c*(μm)= 698.88
Distance between fringes $1/P_t$, (μm)	200	Liquid		1.4009	
Distance(μm) from tip to first fringe d_t =	126.3	Air Gap	0	1.003	
		Errors			
		Window,1	4.4	0.005	
		Substrate,2	1.6	0.005	
		Liquid,4		0.005	
		dδy(i)=d(y(i)-y(i-1))		7	

Correction (μm, °)	5.94	0.89	deg.		Error	Error	Error	Error	Error		360.6 Quadratic		
i	δy(i)	δy(i)+corr.	b	c	dh(i)/db	dh(i)/dc	db	dc	dh(i)	Δ dh(i)	h(i), (μm)	y(μm)	dh/dy
0											0.0	0	
1	78.5	84.5	1071.9	-37,283	-0.030	-8.78E-04	4.0	3089.4	2.7	2.71	33.7	126.3	0.267
2	76.2	82.2	1038.2	-93,567	-0.069	-8.30E-04	4.8	6029.1	5.0	2.30	83.4	326.3	0.249
3	65.0	70.9	988.5	-138,969	-0.101	-8.08E-04	6.4	7528.1	6.1	1.10	124.8	526.3	0.207
4	41.3	47.2	947.1	-166,797	-0.121	-8.00E-04	7.3	8361.0	6.7	0.63	151.8	726.3	0.135
5	42.1	48.1	920.1	-196,306	-0.140	-7.83E-04	7.8	8818.2	7.0	0.25	178.7	926.3	0.134
6	53.4	59.3	893.2	-232,979	-0.160	-7.60E-04	8.0	9048.3	7.0	0.01	211.0	1126.3	0.162
7	62.9	68.9	860.9	-256,556	-0.176	-7.52E-04	8.0	9109.9	7.0	0.00	234.3	1326.3	0.116
8	74.8	80.7	837.6	-307,515	-0.199	-7.20E-04	8.0	9159.0	6.8	-0.22	276.1	1526.3	0.209
9	86.6	92.6	795.8	-360,648	-0.224	-6.94E-04	7.9	9052.8	6.5	-0.26	322.5	1726.3	0.232
10	111.2	117.1	749.4	-397,373	-0.245	-6.82E-04	7.6	8935.7	6.4	-0.15	358.6	1926.3	0.181
11	103.1	109.0	713.2	-432,532	-0.262	-6.68E-04	7.5	9011.5	6.3	-0.04	391.5	2126.3	0.164
12	95.0	100.9	680.4	-490,201	-0.281	-6.42E-04	7.5	8948.9	6.1	-0.21	438.2	2326.3	0.234
13	98.5	104.4	633.6	-542,694	-0.302	-6.24E-04	7.3	8765.4	5.9	-0.23	485.1	2526.3	0.234
14	33.2	39.1	586.8	-547,320	-0.316	-6.28E-04	7.1	8662.9	5.9	-0.01	502.5	2726.3	0.087
15	92.7	98.6	569.4	-607,517	-0.328	-6.03E-04	7.1	8357.0	5.5	-0.34	545.1	2926.3	0.213
16	34.6	40.6	526.8	-612,633	-0.341	-6.05E-04	6.8	8434.0	5.6	0.06	562.4	3126.3	0.087
17	32.5	38.4	509.4	-629,744	-0.347	-6.00E-04	6.9	8222.7	5.5	-0.13	578.7	3326.3	0.081
18	9.8	15.8	493.2	-631,353	-0.352	-6.01E-04	6.8	8139.9	5.4	-0.04	585.4	3526.3	0.033
19	3.5	9.4	486.5	-634,034	-0.354	-6.01E-04	6.7	8082.0	5.4	-0.03	589.3	3726.3	0.020
20	-18.5	-12.5	482.5	-622,937	-0.354	-6.06E-04	6.7	8059.1	5.4	0.02	584.0	3926.3	-0.026
21	-79.4	-73.4	487.8	-574,700	-0.347	-6.28E-04	6.7	8080.6	5.6	0.16	552.4	4126.3	-0.158
22	-78.0	-72.0	519.4	-541,823	-0.334	-6.41E-04	6.8	8383.8	5.8	0.25	520.8	4326.3	-0.158
23	-107.7	-101.8	551.0	-487,167	-0.316	-6.66E-04	7.1	8528.5	6.1	0.27	474.9	4526.3	-0.230
24	-112.7	-106.7	597.0	-434,419	-0.294	-6.91E-04	7.3	8886.5	6.5	0.40	425.0	4726.3	-0.249
25	-141.0	-135.0	646.8	-361,220	-0.263	-7.33E-04	7.6	9190.1	7.0	0.52	359.1	4926.3	-0.330
26	-136.7	-130.8	712.8	-293,495	-0.225	-7.71E-04	8.1	9799.9	7.8	0.75	292.1	5126.3	-0.335
27	-112.0	-106.0	779.8	-238,978	-0.188	-8.00E-04	8.7	10346.7	8.4	0.66	235.4	5326.3	-0.283

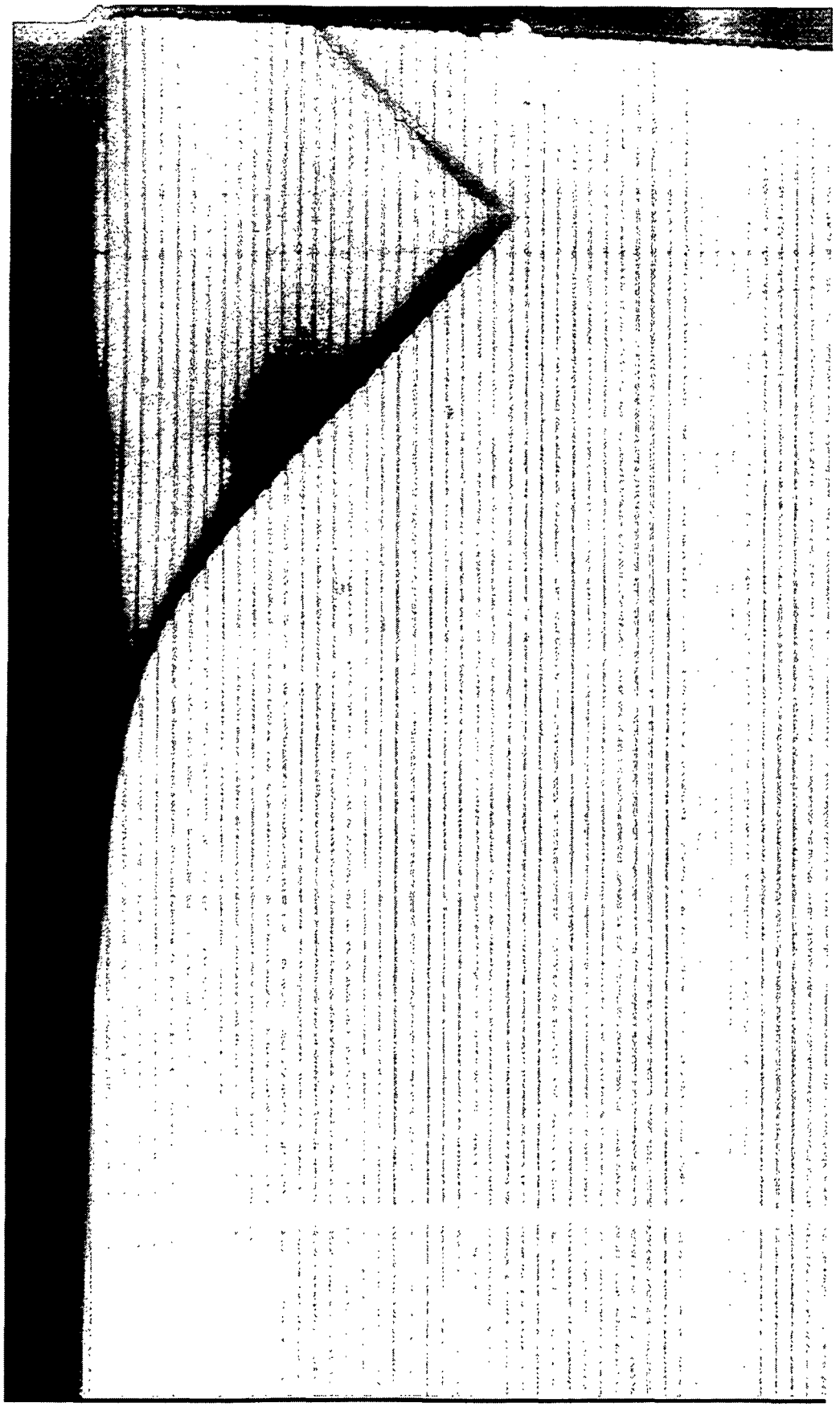

Figure VII.18 Image U22C1255.TIF at time 4:34.815 (τ = 0.0407) for deflectometry analysis. The data file and analyzed data are contained in Table VII.3.

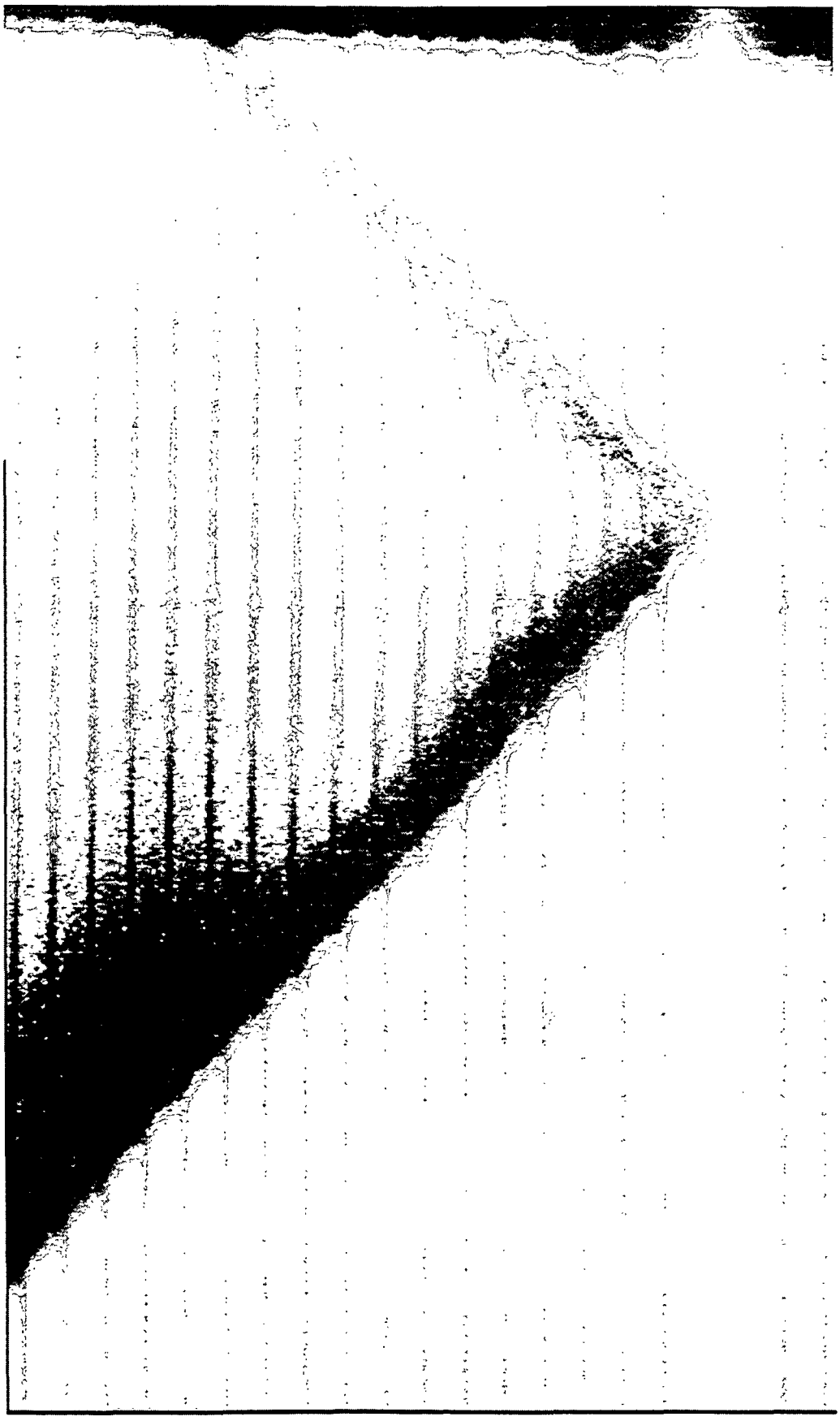

Figure VII.19 Image U22C1256.TIF at time 4:34.815 (τ = 0.0407) close up of tip region for deflectometry.

TABLE VII.3 - Image U22C1255.TIF and U22C1256.TIF Case#11 with DC200 - 10 cs.

Film Time 4:34.815, τ = 0.0407

			Thickness	Refractive index		
Angular Misalignment, Φ	-0.1268	Window	1588	1.515	b*(μm)=	1071.8788
Magnification factor in dimensions	8	Substrate	38.1	1.608	c*(μm)=	698.87753
Distance between fringes $1/P_t$, (μm)	200	Liquid		1.4009		
Distance(μm) from tip to first fringe d_t =	64.9	Air Gap	0			
		Errors				
		Window,1	4.4	0.005		
		Substrate,2	1.6	0.005		
		Liquid,4		0.005		
		dδy(i)=d(y(i)-y(i-1))		7		

Correction	5.94	0.89	deg.		Error	Error	Error	Error	Error		Quadratic		
i	δy(i)	δy(i)+corr.	b	c	dh(i)/db	dh(i)/dc	db	dc	dh(i)	Δ dh(i)	h(i), (μm)	y(μm)	dh/dy
0											**0.0**	0	
1	117.0	123.0	1071.9	-27,884	-0.023	-8.91E-04	4.0	1587.5	1.4	1.42	**25.4**	64.9	0.392
2	94.9	100.8	1046.5	-97,684	-0.071	-8.20E-04	4.2	5914.0	4.9	3.44	**86.2**	264.9	0.304
3	74.6	80.5	985.6	-148,694	-0.106	-7.99E-04	6.3	7547.9	6.1	1.21	**132.9**	464.9	0.233
4	53.2	59.1	938.9	-183,814	-0.131	-7.86E-04	7.2	8375.7	6.7	0.59	**166.3**	664.9	0.167
5	29.7	35.7	905.6	-203,188	-0.146	-7.83E-04	7.7	8786.8	7.0	0.31	**186.1**	864.9	0.099
6	9.2	15.1	885.8	-210,049	-0.153	-7.85E-04	8.0	9001.4	7.2	0.20	**194.5**	1064.9	0.042
7	-0.9	5.1	877.4	-209,579	-0.154	-7.89E-04	8.2	9154.7	7.3	0.16	**195.4**	1264.9	0.005
8	-1.4	4.5	876.5	-212,577	-0.156	-7.86E-04	8.3	9298.0	7.4	0.09	**197.9**	1464.9	0.013
9	9.1	15.1	874.0	-222,628	-0.160	-7.77E-04	8.4	9384.4	7.4	0.00	**206.1**	1664.9	0.041
10	31.3	37.2	865.8	-229,373	-0.165	-7.75E-04	8.4	9388.3	7.4	-0.02	**212.7**	1864.9	0.033
11	41.3	47.3	859.2	-238,692	-0.170	-7.69E-04	8.4	9406.2	7.4	-0.03	**221.0**	2064.9	0.041
12	52.9	58.9	850.9	-277,995	-0.186	-7.38E-04	8.4	9404.5	7.1	-0.26	**252.0**	2264.9	0.155
13	50.8	56.7	819.8	-309,824	-0.204	-7.23E-04	8.1	9230.6	6.9	-0.23	**281.4**	2464.9	0.147
14	59.8	65.7	790.5	-347,502	-0.222	-7.04E-04	7.9	9035.4	6.6	-0.28	**314.5**	2664.9	0.166
15	57.1	63.1	757.4	-381,165	-0.239	-6.90E-04	7.7	8855.9	6.4	-0.22	**345.6**	2864.9	0.155
16	52.4	58.3	726.3	-411,180	-0.254	-6.78E-04	7.5	8682.5	6.2	-0.19	**373.8**	3064.9	0.141
17	33.8	39.7	698.1	-428,415	-0.265	-6.74E-04	7.3	8527.2	6.1	-0.12	**392.7**	3264.9	0.095
18	13.5	19.4	679.1	-434,530	-0.271	-6.74E-04	7.2	8382.4	6.0	-0.08	**401.9**	3464.9	0.046
19	27.8	33.7	669.9	-454,394	-0.277	-6.64E-04	7.2	8285.0	5.9	-0.13	**417.8**	3664.9	0.079
20	-1.3	4.6	654.1	-451,015	-0.281	-6.69E-04	7.1	8216.4	5.8	-0.01	**419.9**	3864.9	0.011
21	-1.3	4.6	652.0	-453,329	-0.282	-6.68E-04	7.1	8184.7	5.8	-0.03	**422.1**	4064.9	0.011
22	-27.1	-21.2	649.8	-437,622	-0.280	-6.78E-04	7.0	8166.4	5.9	0.06	**412.1**	4264.9	-0.050
23	-27.1	-21.2	659.8	-426,934	-0.275	-6.83E-04	7.1	8231.1	6.0	0.07	**402.1**	4464.9	-0.050
24	-1.3	4.6	669.8	-434,199	-0.273	-6.76E-04	7.1	8278.7	5.9	-0.02	**404.3**	4664.9	0.011
25	0.0	5.9	667.6	-437,467	-0.275	-6.75E-04	7.1	8237.1	5.9	-0.04	**407.1**	4864.9	0.014

TABLE VII.4 - Image U22C1255.TIF and U22C1256.TIF Case#11 RETEST#1 with DC200-10 cs.

Film Time 4:34.815, τ = 0.0407

			Thickness	Refractive index		
Angular Misalignment, Φ	-0.1268	Window	1588	1.515	b*(μm)=	1071.8788
Magnification factor in dimensions	8	Substrate	38.1	1.608	c*(μm)=	698.87753
Distance between fringes $1/P_f$, (μm)	200	Liquid		1.4009		
Distance(μm) from tip to first fringe d_t =	71.9	Air Gap	0			
		Errors				
		Window,1	4.4	0.005		
		Substrate,2	1.6	0.005		
		Liquid,4		0.005		
		dδy(i)=d(y(i)-y(i-1))		7		

Correction	5.94	0.89	deg.		Error	Error	Error	Error	Error		Quadratic		
i	δy(i)	δy(i)+corr.	b	c	dh(i)/db	dh(i)/dc	db	dc	dh(i)	Δ dh(i)	h(i), (μm)	y(μm)	dh/dy
0											**0.0**	0	
1	112.7	118.6	1071.9	-29,800	-0.024	-8.88E-04	4.0	1758.7	1.6	1.56	**27.1**	71.9	0.377
2	90.1	96.1	1044.8	-96,210	-0.070	-8.23E-04	4.3	5903.3	4.9	3.30	**85.1**	271.9	0.290
3	66.0	71.9	986.7	-141,513	-0.102	-8.06E-04	6.3	7515.7	6.1	1.22	**127.1**	471.9	0.210
4	45.1	51.0	944.8	-171,836	-0.124	-7.96E-04	7.3	8347.1	6.7	0.61	**156.1**	671.9	0.145
5	21.7	27.6	915.8	-186,629	-0.136	-7.94E-04	7.8	8794.7	7.1	0.36	**171.6**	871.9	0.078
6	0.0	5.9	900.3	-188,113	-0.140	-8.00E-04	8.1	9067.3	7.3	0.28	**175.0**	1071.9	0.017
7	-11.5	-5.6	896.9	-186,123	-0.140	-8.03E-04	8.3	9300.7	7.6	0.22	**173.8**	1271.9	-0.006
8	-12.6	-6.7	898.1	-181,637	-0.137	-8.08E-04	8.5	9507.1	7.8	0.20	**170.1**	1471.9	-0.019
9	-0.3	5.7	901.8	-186,237	-0.139	-8.01E-04	8.7	9693.9	7.9	0.09	**173.2**	1671.9	0.016
10	22.8	28.7	898.6	-192,910	-0.142	-7.96E-04	8.8	9774.7	7.9	0.02	**179.0**	1871.9	0.029
11	40.1	46.1	892.9	-203,449	-0.148	-7.88E-04	8.8	9811.6	7.8	-0.04	**188.2**	2071.9	0.046
12	44.0	49.9	883.7	-236,601	-0.164	-7.61E-04	8.8	9815.0	7.6	-0.23	**215.3**	2271.9	0.135
13	44.2	50.2	856.6	-265,839	-0.181	-7.46E-04	8.6	9623.5	7.3	-0.26	**242.0**	2471.9	0.133
14	56.6	62.5	829.9	-303,094	-0.199	-7.25E-04	8.3	9401.8	7.0	-0.33	**274.5**	2671.9	0.162
15	51.9	57.9	797.4	-334,632	-0.216	-7.12E-04	8.1	9174.7	6.8	-0.26	**303.9**	2871.9	0.147
16	32.2	38.1	768.0	-352,319	-0.228	-7.07E-04	7.8	8949.7	6.6	-0.18	**322.9**	3071.9	0.095
17	33.8	39.7	748.9	-373,930	-0.239	-6.97E-04	7.7	8748.3	6.4	-0.21	**342.6**	3271.9	0.098
18	13.5	19.4	729.3	-380,765	-0.246	-6.98E-04	7.5	8590.1	6.3	-0.10	**352.1**	3471.9	0.048
19	27.8	33.7	719.8	-400,975	-0.253	-6.86E-04	7.4	8476.8	6.1	-0.16	**368.5**	3671.9	0.082
20	-1.3	4.6	703.4	-398,176	-0.257	-6.92E-04	7.3	8383.1	6.1	-0.02	**370.7**	3871.9	0.011
21	-1.3	4.6	701.2	-400,569	-0.258	-6.91E-04	7.3	8340.6	6.1	-0.04	**372.9**	4071.9	0.011
22	-27.1	-21.2	698.9	-384,941	-0.255	-7.02E-04	7.2	8313.3	6.1	0.06	**362.6**	4271.9	-0.052
23	-27.1	-21.2	709.3	-373,885	-0.249	-7.07E-04	7.3	8382.5	6.2	0.08	**352.2**	4471.9	-0.052
24	-1.3	4.6	719.7	-380,773	-0.248	-7.00E-04	7.4	8440.3	6.2	-0.02	**354.5**	4671.9	0.011
25	0.0	5.9	717.4	-384,122	-0.250	-6.98E-04	7.3	8399.6	6.1	-0.04	**357.4**	4871.9	0.015

TABLE VII.5 - Image U22C1255.TIF and U22C1256.TIF Case#11 RETEST#2 with DC200-10 cs.

Film Time 4:34.815, τ = 0.0407

			Thickness	Refractive index		
Angular Misalignment, Φ	-0.1214	Window	1588	1.515	b*(μm)=	1071.8788
Magnification factor in dimensions	8	Substrate	38.1	1.608	c*(μm)=	698.87753
Distance between fringes $1/P_f$, (μm)	200	Liquid		1.4009		
Distance(μm) from tip to first fringe d_t =	77	Air Gap	0			
		Errors				
		Window,1	4.4	0.005		
		Substrate,2	1.6	0.005		
		Liquid,4		0.005		
		dδy(i)=d(y(i)-y(i-1))		7		

Correction	5.94	0.89	deg.		Error	Error	Error	Error	Error		Quadratic		
i	δy(i)	δy(i)+corr.	b	c	dh(i)/db	dh(i)/dc	db	dc	dh(i)	Δ dh(i)	h(i), (μm)	y(μm)	dh/dy
0											**0.0**	0	
1	123.5	129.5	1071.9	-34,835	-0.028	-8.81E-04	4.0	1883.5	1.7	1.66	**31.6**	77	0.410
2	99.6	105.5	1040.3	-107,565	-0.077	-8.13E-04	4.3	6070.6	4.9	3.28	**94.8**	277	0.316
3	77.3	83.2	977.1	-159,718	-0.113	-7.92E-04	6.3	7652.3	6.1	1.16	**142.6**	477	0.239
4	43.8	49.7	929.2	-187,654	-0.134	-7.87E-04	7.3	8424.8	6.7	0.60	**170.6**	677	0.140
5	32.9	38.9	901.3	-210,047	-0.149	-7.78E-04	7.8	8797.5	6.9	0.24	**192.1**	877	0.107
6	9.8	15.7	879.8	-216,915	-0.157	-7.80E-04	8.0	8987.8	7.1	0.18	**200.8**	1077	0.043
7	9.5	15.5	871.1	-219,340	-0.159	-7.82E-04	8.2	9121.0	7.2	0.12	**204.0**	1277	0.016
8	-1.6	4.3	867.9	-221,685	-0.161	-7.81E-04	8.3	9232.5	7.3	0.08	**206.4**	1477	0.012
9	9.8	15.7	865.5	-232,197	-0.166	-7.72E-04	8.3	9305.8	7.3	-0.02	**214.9**	1677	0.043
10	32.9	38.9	857.0	-240,819	-0.171	-7.67E-04	8.3	9299.2	7.3	-0.04	**223.0**	1877	0.040
11	44.9	50.9	848.9	-252,702	-0.177	-7.60E-04	8.3	9302.7	7.2	-0.06	**233.5**	2077	0.052
12	56.1	62.0	838.4	-293,591	-0.194	-7.30E-04	8.2	9289.4	7.0	-0.26	**265.9**	2277	0.162
13	65.3	71.2	806.0	-334,743	-0.214	-7.09E-04	8.0	9121.1	6.7	-0.27	**302.1**	2477	0.181
14	68.3	74.3	769.8	-375,710	-0.234	-6.91E-04	7.8	8947.0	6.4	-0.25	**338.9**	2677	0.184
15	55.8	61.7	733.0	-406,382	-0.251	-6.80E-04	7.6	8778.5	6.3	-0.18	**368.8**	2877	0.150
16	52.2	58.1	703.1	-435,946	-0.265	-6.68E-04	7.4	8596.2	6.1	-0.19	**396.5**	3077	0.138
17	33.8	39.7	675.4	-452,755	-0.276	-6.64E-04	7.2	8449.5	6.0	-0.12	**415.2**	3277	0.093
18	13.5	19.4	656.7	-458,563	-0.282	-6.64E-04	7.2	8313.7	5.9	-0.08	**424.2**	3477	0.045
19	27.8	33.7	647.7	-478,281	-0.288	-6.55E-04	7.1	8223.1	5.8	-0.12	**439.8**	3677	0.078
20	-1.3	4.6	632.1	-474,654	-0.292	-6.60E-04	7.0	8164.3	5.8	0.00	**441.9**	3877	0.011
21	-1.3	4.6	629.9	-476,935	-0.293	-6.59E-04	7.0	8136.6	5.7	-0.02	**444.1**	4077	0.011
22	-27.1	-21.2	627.8	-461,194	-0.290	-6.68E-04	7.0	8121.5	5.8	0.06	**434.2**	4277	-0.049
23	-27.1	-21.2	637.6	-450,664	-0.286	-6.73E-04	7.0	8184.4	5.9	0.07	**424.4**	4477	-0.049
24	-1.3	4.6	647.5	-458,089	-0.284	-6.66E-04	7.1	8228.0	5.8	-0.02	**426.5**	4677	0.011
25	0.0	5.9	645.4	-461,321	-0.285	-6.65E-04	7.1	8186.1	5.8	-0.04	**429.3**	4877	0.014

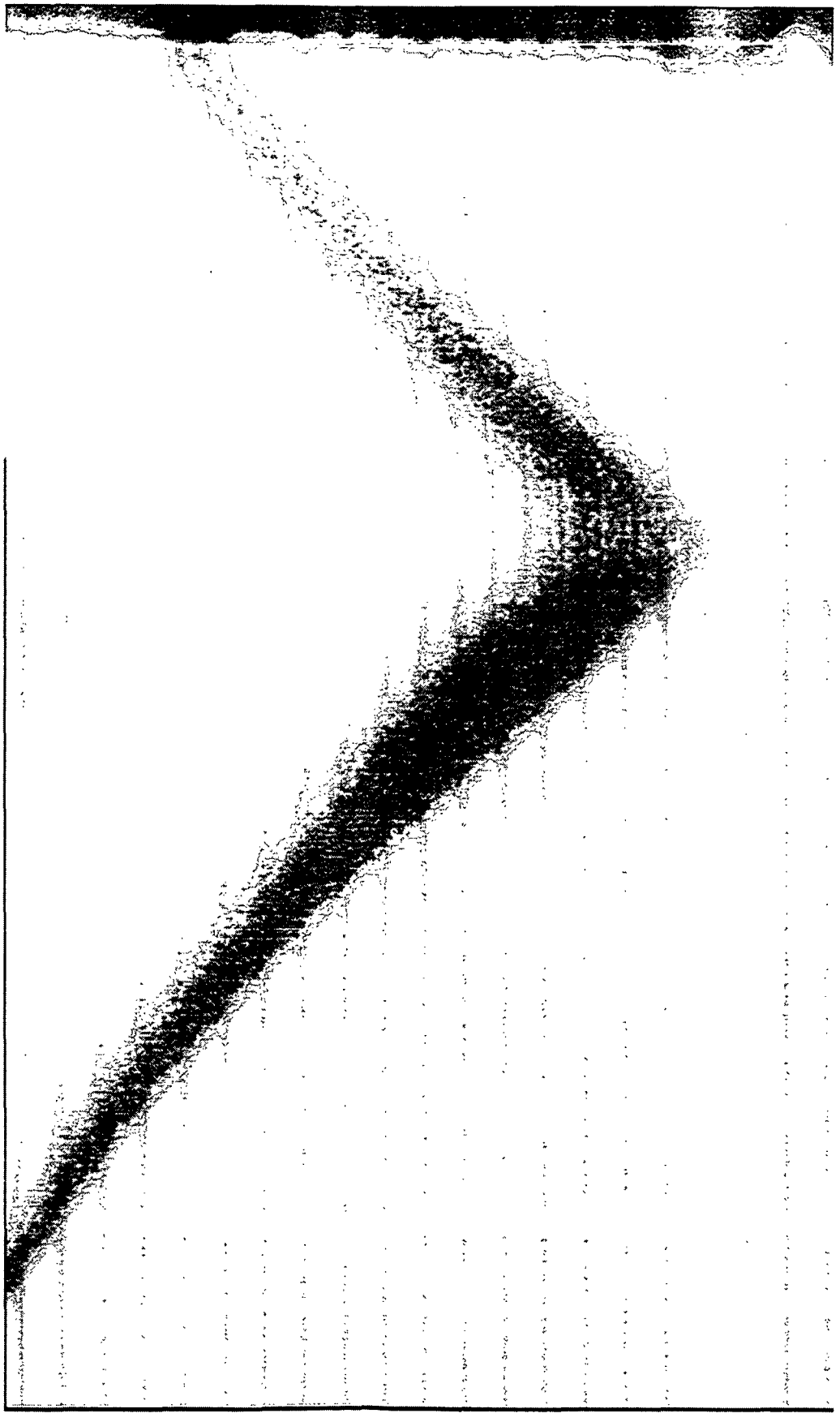

Figure VII.20 Image U22C1258.TIF at time 4:34.817 (τ = 0.0610) close up of tip region for deflectometry. The data file and analyzed data are contained in Table VII.6.

TABLE VII.6 - Image U22C1257.TIF and U22C1258.TIF Case#11 with DC200-10 cs.

Film Time 4:34.817, τ = 0.0610

			Thickness	Refractive index	
Angular Misalignment, Φ	0.051 and -0.078°	Window	1588	1.515	b*(μm)= 1071.88
Magnification factor in dimensions	8	Substrate	38.1	1.608	c*(μm)= 698.88
Distance between fringes $1/P_f$, (μm)	200	Liquid		1.4009	
Distance(μm) from tip to first fringe d_t =	55	Air Gap	0		
		Errors			
		Window,1	4.4	0.005	
		Substrate,2	1.6	0.005	
		Liquid,4		0.005	
		dδy(i)=d(y(i)-y(i-1)), (μm)		7	

Correction	5.94	0.89	deg.		Error	Error	Error	Error	Error		Quadratic		
i	δy(i)	δy(i)+corr.	b	c	dh(i)/db	dh(i)/dc	db	dc	dh(i)	Δ dh(i)	h(i), (μm)	y(μm)	dh/dy
0											**0.0**	0	
1	152.9	158.9	1071.9	-30,531	-0.025	-8.87E-04	4.0	1345.3	1.2	1.20	**27.8**	55	0.505
2	152.1	158.0	1044.1	-140,206	-0.094	-7.78E-04	4.1	6363.4	5.0	3.77	**120.4**	255	0.463
3	130.1	136.0	951.5	-224,135	-0.146	-7.45E-04	6.4	8205.5	6.2	1.21	**195.4**	455	0.375
4	116.6	122.6	876.5	-295,145	-0.186	-7.16E-04	7.3	8913.4	6.5	0.35	**259.8**	655	0.322
5	96.0	102.0	812.1	-349,702	-0.217	-6.97E-04	7.6	9112.0	6.6	0.03	**311.3**	855	0.258
6	61.7	67.6	760.6	-380,925	-0.238	-6.90E-04	7.7	9021.1	6.5	-0.08	**344.7**	1055	0.167
7	20.5	26.4	727.2	-374,500	-0.245	-7.02E-04	7.6	8785.8	6.4	-0.04	**348.2**	1255	0.018
8	4.3	10.2	723.7	-380,379	-0.247	-6.99E-04	7.6	8632.2	6.3	-0.13	**353.2**	1455	0.025
9	-30.6	-24.7	718.7	-361,347	-0.243	-7.14E-04	7.5	8513.8	6.3	0.03	**341.0**	1655	-0.061
10	-52.4	-46.4	730.9	-356,594	-0.239	-7.14E-04	7.5	8558.9	6.4	0.02	**334.7**	1855	-0.032
11	-61.1	-55.2	737.2	-348,106	-0.235	-7.19E-04	7.5	8641.4	6.5	0.09	**327.1**	2055	-0.038
12	-71.6	-65.6	744.8	-304,705	-0.220	-7.51E-04	7.6	8745.9	6.8	0.32	**293.5**	2255	-0.168
13	-63.1	-57.1	778.4	-274,641	-0.202	-7.66E-04	7.8	9043.9	7.1	0.33	**263.6**	2455	-0.149
14	-62.5	-56.6	808.3	-242,979	-0.183	-7.84E-04	8.1	9272.0	7.4	0.32	**233.3**	2655	-0.151
15	-51.0	-45.0	838.6	-218,571	-0.166	-7.96E-04	8.4	9534.5	7.7	0.30	**208.7**	2855	-0.123
16	-39.4	-33.5	863.2	-200,293	-0.153	-8.04E-04	8.7	9745.4	7.9	0.23	**190.2**	3055	-0.093
17	-18.0	-12.1	881.7	-195,392	-0.147	-8.01E-04	8.9	9914.0	8.0	0.10	**183.4**	3255	-0.034
18	-7.3	-1.3	888.4	-195,687	-0.146	-7.98E-04	9.0	9962.3	8.1	0.01	**182.7**	3455	-0.004
19	-5.0	1.0	889.2	-196,512	-0.146	-7.96E-04	9.0	9958.7	8.0	-0.01	**183.2**	3655	0.003
20	52.1	58.0	888.6	-236,951	-0.163	-7.59E-04	9.0	9945.1	7.7	-0.35	**214.7**	3855	0.158
21	79.5	85.5	857.1	-289,927	-0.189	-7.27E-04	8.6	9721.0	7.2	-0.44	**259.6**	4055	0.224

Figure VII.21 Image U22C1259.TIF at time 4:34.819 (τ = 0.0813) for deflectometry analysis. The data file and analyzed data are contained in Table VII.7 and rechecked with another analysis in Table VII.8.

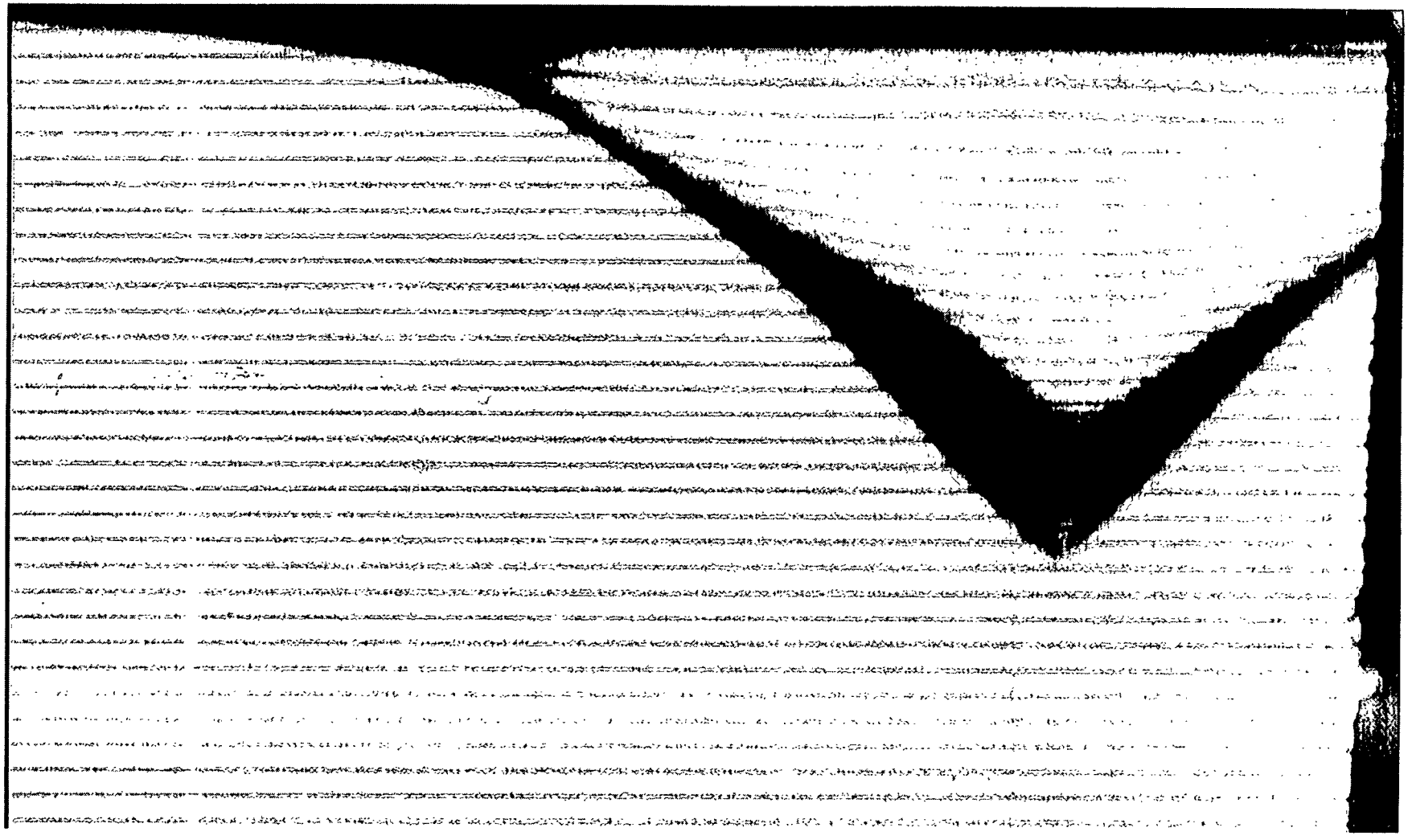

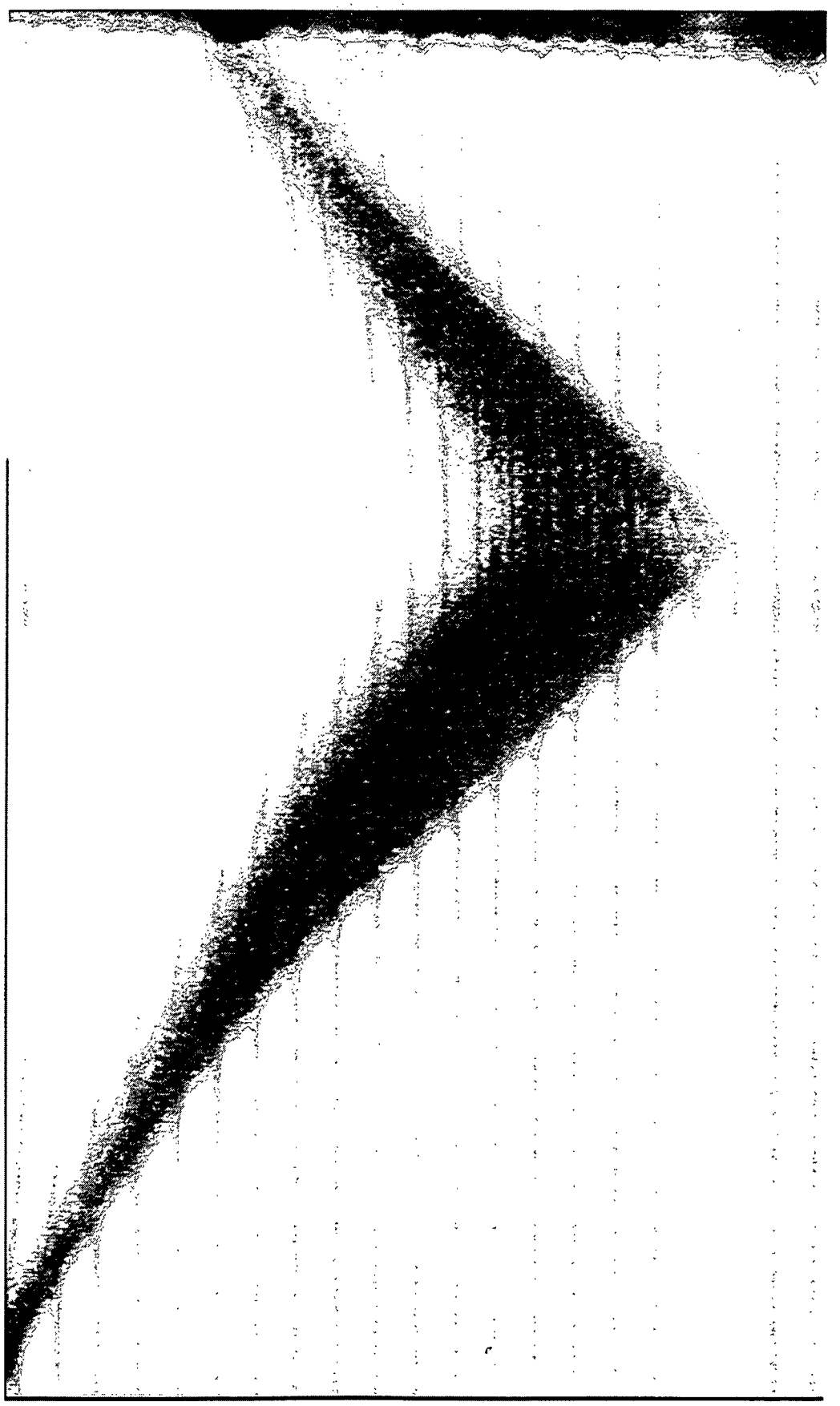

Figure VII.22 Image U22C1260.TIF at time 4:34.819 (τ = 0.0813) close up of tip region for deflectometry.

TABLE VII.7 - Image U22C1259.TIF and U22C1260.TIF Case#11 with DC200-10 cs.

Film Time 4:34.819, τ = 0.0813

			Thickness	Refractive index	
Angular Misalignment, Φ	-0.123	Window	1588	1.515	b*= 1071.88
Magnification factor in dimensions	8	Substrate	38.1	1.608	c*= 698.88
Distance between fringes $1/P_{\mu}$ (μm)	200	Liquid		1.4009	
Distance(μm) from tip to first fringe d_t =	181.7	Air Gap	0		
		Errors			
		Window,1	4.4	0.005	
		Substrate,2	1.6	0.005	
		Liquid,4		0.005	
		dδy(i)=d(y(i)-y(i-1)), (μm)		7	

Correction		5.94	0.89	deg.		Error	Error	Error	Error	Error		Quadratic		
	i	δy(i)	δy(i)+corr.	b	c	dh(i)/db	dh(i)/dc	db	dc	dh(i)	Δ dh(i)	h(i), (μm)	y(μm)	dh/dy
	0											**0.0**	0	
	1	110.2	116.1	1071.9	-73,739	-0.054	-8.32E-04	4.0	4444.5	3.7	3.70	**64.9**	181.7	0.357
	2	133.8	139.8	1007.0	-167,214	-0.112	-7.71E-04	5.4	6894.2	5.3	1.64	**145.1**	381.7	0.401
	3	156.4	162.3	926.7	-268,996	-0.167	-7.19E-04	6.7	8286.4	6.1	0.71	**232.1**	581.7	0.435
	4	155.0	160.9	839.8	-361,276	-0.214	-6.82E-04	7.2	9102.3	6.4	0.34	**313.3**	781.7	0.406
	5	133.3	139.2	758.6	-433,135	-0.250	-6.58E-04	7.5	9399.6	6.5	0.07	**380.3**	981.7	0.335
	6	99.5	105.4	691.6	-481,330	-0.277	-6.45E-04	7.6	9295.3	6.4	-0.11	**429.4**	1181.7	0.245
	7	66.5	72.4	642.5	-506,254	-0.294	-6.40E-04	7.5	8975.0	6.2	-0.20	**459.4**	1381.7	0.150
	8	39.6	45.5	612.4	-524,262	-0.305	-6.36E-04	7.3	8648.9	5.9	-0.22	**479.9**	1581.7	0.102
	9	-2.5	3.5	592.0	-516,848	-0.310	-6.43E-04	7.1	8387.9	5.8	-0.11	**481.5**	1781.7	0.008
	10	-25.0	-19.1	590.4	-503,992	-0.308	-6.50E-04	7.0	8242.6	5.8	-0.05	**473.7**	1981.7	-0.039
	11	-66.5	-60.6	598.2	-469,249	-0.300	-6.69E-04	7.0	8219.3	5.9	0.10	**448.4**	2181.7	-0.126
	12	-103.6	-97.7	623.5	-412,337	-0.282	-7.00E-04	7.1	8417.7	6.2	0.34	**402.1**	2381.7	-0.232
	13	-118.7	-112.8	669.8	-352,139	-0.254	-7.34E-04	7.4	8874.5	6.8	0.55	**346.5**	2581.7	-0.278
	14	-138.2	-132.3	725.4	-278,942	-0.217	-7.80E-04	7.8	9393.8	7.5	0.75	**278.0**	2781.7	-0.342
	15	-137.7	-131.7	793.9	-205,914	-0.171	-8.29E-04	8.5	10140.8	8.5	1.01	**205.9**	2981.7	-0.360
	16	-123.9	-118.0	865.9	-138,288	-0.121	-8.76E-04	9.4	10981.9	9.7	1.15	**137.8**	3181.7	-0.341
	17	-115.1	-109.2	934.1	-71,362	-0.066	-9.29E-04	10.5	11914.2	11.1	1.41	**71.0**	3381.7	-0.334
	18	-71.0	-65.1	1000.9	-30,634	-0.028	-9.43E-04	11.8	13186.0	12.4	1.35	**29.7**	3581.7	-0.206
	19	37.3	43.2	1042.2	-59,315	-0.047	-8.69E-04	13.1	14316.7	12.5	0.02	**54.1**	3781.7	0.122

TABLE VII.8 - Image U22C1259.TIF and U22C1260.TIF Case#11 RETEST#1 with DC200-10 cs.

Film Time 4:34.819, τ = 0.0813

			Thickness	Refractive index	
Angular Misalignment, Φ	-0.123	Window	1588	1.515	b*= 1071.88
Magnification factor in dimensions	8	Substrate	38.1	1.608	c*= 698.88
Distance between fringes $1/P_f$, (μm)	200	Liquid		1.4009	
Distance(μm) from tip to first fringe d_i =	181.7	Air Gap	0	1.003	
		Errors			
		Window,1	4.4	0.005	
		Substrate,2	1.6	0.005	
		Liquid,4		0.005	
		dδy(i)=d(y(i)-y(i-1)), (μm)		7	

Correction	5.94	0.89	deg.		Error	Error	Error	Error	Error		Quadratic		
i	δy(i)	δy(i)+corr.	b	c	dh(i)/db	dh(i)/dc	db	dc	dh(i)	Δ dh(i)	h(i), (μm)	y(μm)	dh/dy
0											**0.0**	0	
1	105.4	111.3	1071.9	-70,670	-0.052	-8.36E-04	4.0	4444.5	3.7	3.72	**62.3**	181.7	0.343
2	127.3	133.2	1009.6	-159,872	-0.108	-7.76E-04	5.4	6854.9	5.4	1.63	**139.2**	381.7	0.384
3	148.9	154.8	932.7	-257,370	-0.162	-7.26E-04	6.7	8222.3	6.1	0.71	**222.7**	581.7	0.418
4	148.1	154.0	849.1	-346,397	-0.207	-6.89E-04	7.2	9018.8	6.4	0.33	**301.1**	781.7	0.392
5	127.5	133.5	770.7	-416,056	-0.244	-6.65E-04	7.5	9316.4	6.5	0.07	**366.0**	981.7	0.324
6	94.8	100.8	705.9	-462,731	-0.270	-6.52E-04	7.6	9228.7	6.4	-0.11	**413.4**	1181.7	0.237
7	61.6	67.5	658.5	-486,009	-0.286	-6.49E-04	7.5	8931.6	6.2	-0.18	**441.7**	1381.7	0.142
8	29.9	35.9	630.1	-498,576	-0.296	-6.47E-04	7.3	8623.5	6.0	-0.19	**458.1**	1581.7	0.082
9	-2.0	4.0	613.7	-493,849	-0.300	-6.52E-04	7.2	8375.6	5.9	-0.12	**460.0**	1781.7	0.009
10	-34.9	-29.0	611.9	-474,612	-0.297	-6.63E-04	7.1	8249.2	5.9	-0.01	**447.8**	1981.7	-0.061
11	-56.5	-50.6	624.0	-447,905	-0.289	-6.77E-04	7.1	8275.3	6.0	0.10	**426.4**	2181.7	-0.107
12	-88.5	-82.5	645.5	-399,384	-0.273	-7.05E-04	7.2	8409.9	6.2	0.27	**386.9**	2381.7	-0.198
13	-111.1	-105.2	685.0	-341,165	-0.247	-7.38E-04	7.4	8765.7	6.7	0.49	**334.6**	2581.7	-0.261
14	-132.2	-126.3	737.3	-270,395	-0.211	-7.84E-04	7.8	9282.4	7.5	0.74	**268.8**	2781.7	-0.329
15	-143.8	-137.9	803.1	-191,723	-0.162	-8.42E-04	8.4	10032.0	8.6	1.09	**192.6**	2981.7	-0.381
16	-132.0	-126.0	879.3	-118,327	-0.106	-8.96E-04	9.4	11043.3	9.9	1.39	**118.6**	3181.7	-0.370
17	-111.1	-105.2	953.3	-53,584	-0.050	-9.44E-04	10.7	12201.8	11.5	1.58	**53.2**	3381.7	-0.327
18	-35.6	-29.6	1018.6	-36,348	-0.032	-9.19E-04	12.2	13583.0	12.5	0.97	**34.5**	3581.7	-0.094
19	37.3	43.2	1037.4	-64,449	-0.051	-8.66E-04	13.1	14286.9	12.4	-0.11	**58.8**	3781.7	0.121

Figure VII.23 Image U22C1261.TIF at time 4:34.821 (τ = 0.1016) for deflectometry analysis. The data file and analyzed data are contained in Table VII.9.

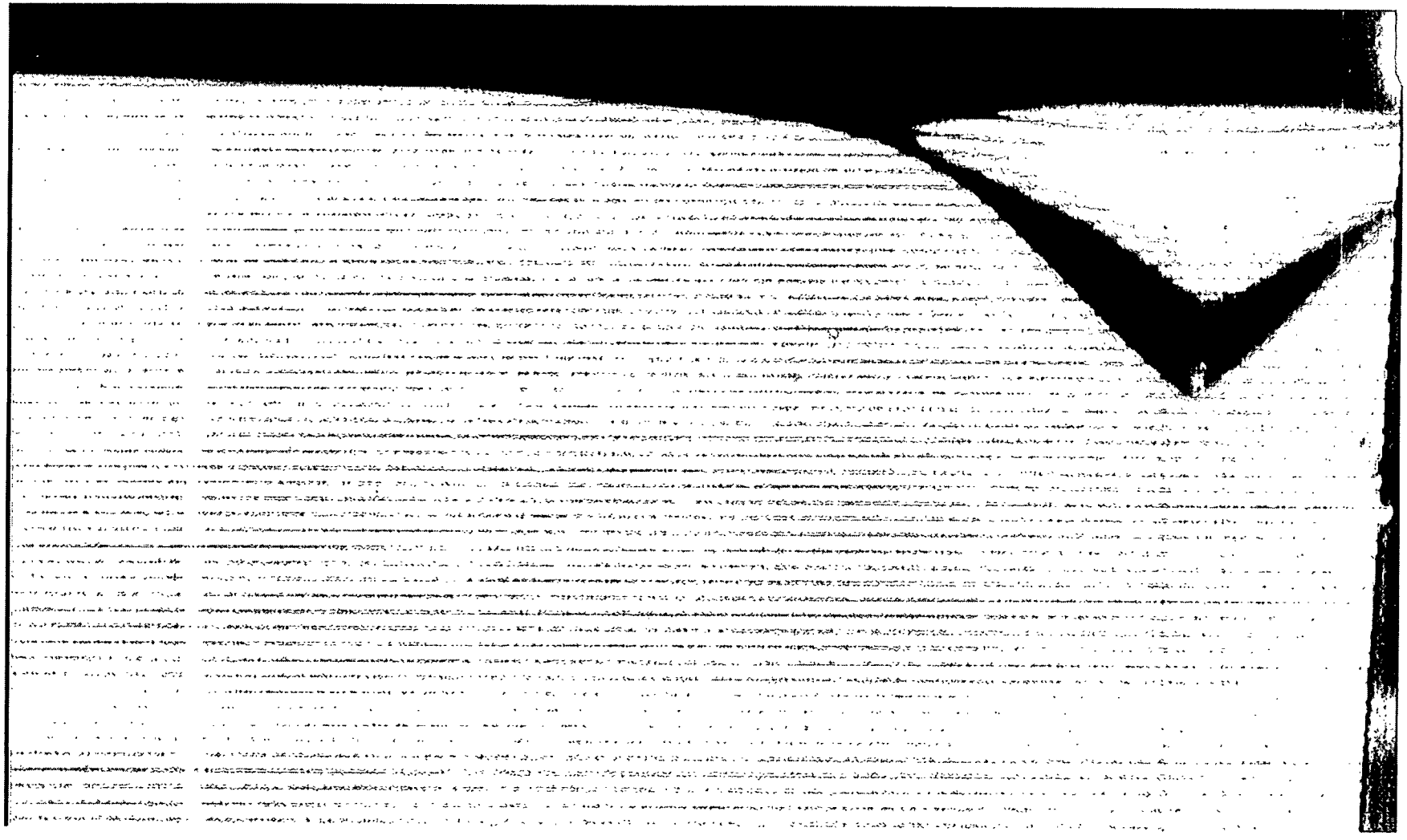

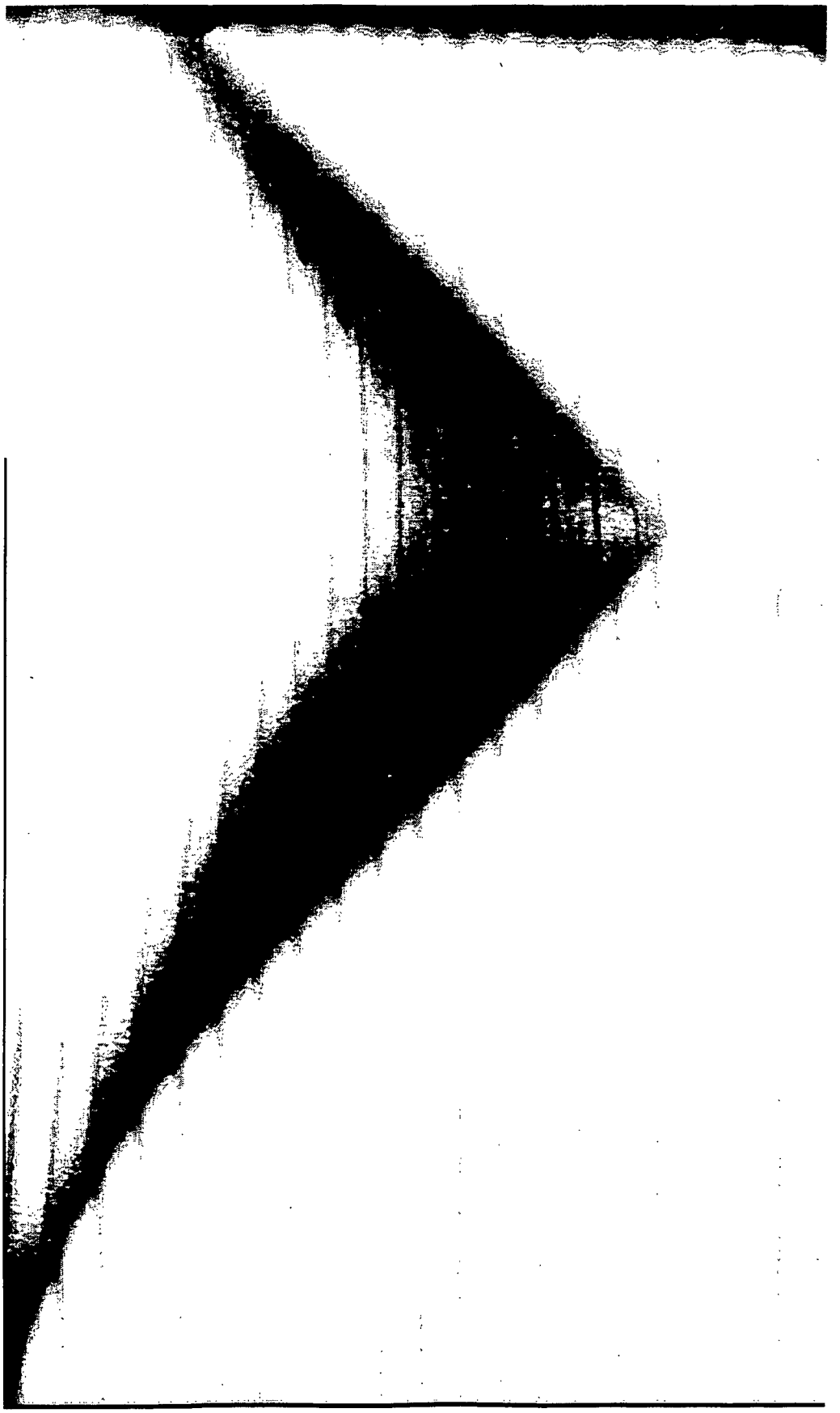

Figure VII.24 Image U22C1262.TIF at time 4:34.821 (τ = 0.1016) close up of tip region for deflectometry.

TABLE VII.9 - Image U22C1262.TIF Case#11 with DC200-10 cs.

Film Time 4:34.821, τ = 0.1016

			Thickness	Refractive index	
Angular Misalignment, Φ	0.07°	Window	1588	1.515	b*(μm)= 1071.88
Magnification factor in dimensions	8	Substrate	38.1	1.608	c*(μm)= 698.88
Distance between fringes $1/P_t$, (μm)	200	Liquid		1.4009	
Distance(μm) from tip to first fringe d_t =	66.2	Air Gap	0		
		Errors			
		Window,1	4.4	0.005	
		Substrate,2	1.6	0.005	
		Liquid,4		0.005	
		dδy(i)=d(y(i)-y(i-1)), (μm)		7	

Correction	5.94	0.89	deg.		Error	Error	Error	Error	Error		Quadratic		
i	δy(i)	δy(i)+corr.	b	c	dh(i)/db	dh(i)/dc	db	dc	dh(i)	Δ dh(i)	h(i), (μm)	y(μm)	dh/dy
0											**0.0**	0	
1	108.5	114.4	1071.9	-26,465	-0.022	-8.93E-04	4.0	1619.3	1.4	1.45	**24.1**	66.2	0.365
2	108.7	114.7	1047.7	-106,029	-0.075	-8.11E-04	4.2	5818.0	4.7	3.28	**93.0**	266.2	0.344
3	130.7	136.7	978.9	-195,145	-0.129	-7.58E-04	6.2	7571.1	5.8	1.07	**169.9**	466.2	0.385
4	142.0	147.9	902.0	-285,465	-0.177	-7.15E-04	7.0	8604.3	6.3	0.48	**248.2**	666.2	0.392
5	134.3	140.2	823.7	-364,036	-0.218	-6.84E-04	7.4	9131.0	6.5	0.18	**318.7**	866.2	0.352
6	131.5	137.5	753.2	-437,663	-0.253	-6.57E-04	7.6	9245.6	6.4	-0.09	**384.6**	1066.2	0.330
7	108.5	114.4	687.2	-438,754	-0.270	-6.70E-04	7.5	9203.1	6.5	0.12	**402.6**	1266.2	0.090
8	74.1	80.1	669.3	-487,476	-0.284	-6.46E-04	7.6	9126.1	6.3	-0.21	**439.6**	1466.2	0.185
9	29.6	35.5	632.3	-496,039	-0.295	-6.48E-04	7.4	8764.9	6.1	-0.19	**455.9**	1666.2	0.081
10	-4.5	1.5	616.0	-488,966	-0.298	-6.54E-04	7.3	8454.4	5.9	-0.14	**456.1**	1866.2	0.001
11	-39.4	-33.4	615.8	-481,130	-0.297	-6.59E-04	7.1	8303.8	5.9	-0.07	**451.0**	2066.2	-0.025
12	-72.6	-66.7	620.9	-436,812	-0.287	-6.85E-04	7.1	8296.5	6.0	0.17	**419.8**	2266.2	-0.156
13	-105.3	-99.4	652.1	-380,464	-0.266	-7.17E-04	7.2	8538.1	6.4	0.38	**371.6**	2466.2	-0.241
14	-129.8	-123.8	700.2	-311,792	-0.234	-7.59E-04	7.5	9012.0	7.1	0.65	**309.0**	2666.2	-0.313
15	-150.9	-145.0	762.9	-229,814	-0.189	-8.16E-04	8.1	9695.1	8.1	1.00	**231.2**	2866.2	-0.389
16	-150.7	-144.7	840.7	-146,641	-0.130	-8.79E-04	9.0	10686.7	9.5	1.41	**148.3**	3066.2	-0.415
17	-125.4	-119.5	923.6	-75,446	-0.070	-9.31E-04	10.3	11911.9	11.1	1.64	**75.5**	3266.2	-0.364
18	-64.5	-58.6	996.4	-40,014	-0.036	-9.31E-04	11.8	13260.4	12.4	1.25	**38.7**	3466.2	-0.184

Figure VII.25 Image U22C1263.TIF at time 4:34.823 (τ = 0.1220) for deflectometry analysis. The data file and analyzed data are contained in Table VII.10.

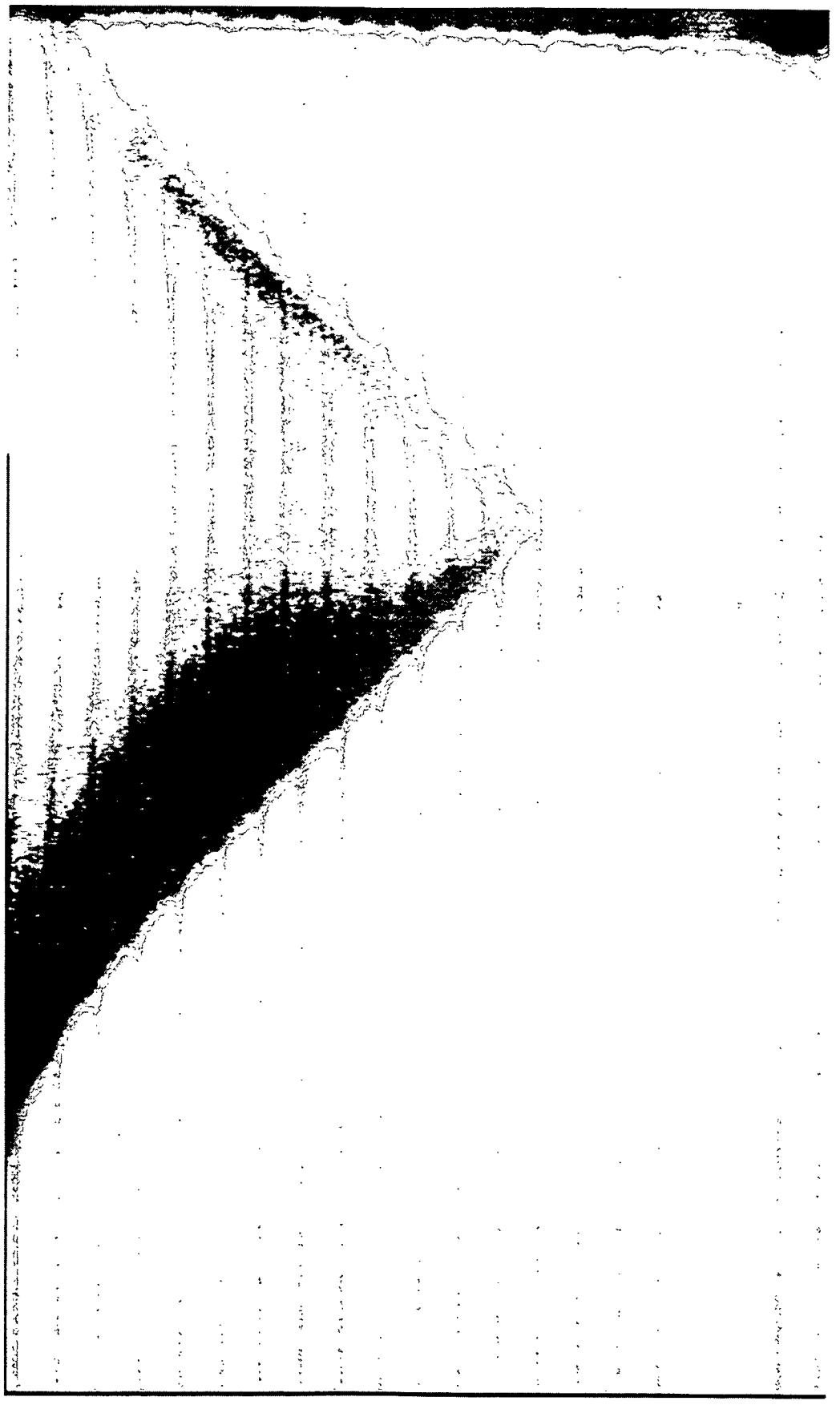

Figure VII.26 Image U22C1264.TIF at time 4:34.823 (τ = 0.1220) close up of tip region for deflectometry.

TABLE VII.10 - Image U22C1264.TIF Case#11 with DC200-10 cs.

Film Time 4:34.823, τ = 0.1220

			Thickness	Refractive index	
Angular Misalignment, Φ	-0.032°	Window	1588	1.515	b*(μm)= 1071.88
Magnification factor in dimensions	8	Substrate	38.1	1.608	c*(μm)= 698.88
Distance between fringes $1/P_t$, (μm)	200	Liquid		1.4009	
Distance(μm) from tip to first fringe d_t =	210	Air Gap	0		
		Errors			
		Window,1	4.4	0.005	
		Substrate,2	1.6	0.005	
		Liquid,4		0.005	
		dδy(i)=d(y(i)-y(i-1)), (μm)		7	

Correction	5.94	0.89	deg.		Error	Error	Error	Error	Error		Quadratic		
i	δy(i)	δy(i)+corr.	b	c	dh(i)/db	dh(i)/dc	db	dc	dh(i)	Δ dh(i)	h(i), (μm)	y(μm)	dh/dy
0											**0.0**	0	
1	67.3	73.3	1071.9	-53,753	-0.041	-8.56E-04	4.0	5136.7	4.4	4.40	**48.0**	210	0.229
2	56.6	62.5	1023.9	-95,151	-0.072	-8.37E-04	5.9	7009.0	5.9	1.48	**85.8**	410	0.189
3	57.7	63.6	986.1	-136,383	-0.100	-8.12E-04	7.1	8114.0	6.6	0.74	**123.0**	610	0.186
4	69.2	75.2	948.9	-184,343	-0.129	-7.81E-04	7.7	8762.5	6.9	0.30	**165.4**	810	0.212
5	79.7	85.6	906.5	-237,152	-0.159	-7.52E-04	8.0	9087.2	6.9	0.03	**212.0**	1010	0.233
6	81.0	87.0	859.8	-288,065	-0.187	-7.27E-04	8.0	9186.2	6.8	-0.10	**257.8**	1210	0.229
7	67.3	73.2	814.1	-330,030	-0.211	-7.10E-04	7.9	9130.9	6.7	-0.15	**297.0**	1410	0.196
8	68.4	74.3	774.9	-370,326	-0.231	-6.93E-04	7.8	8956.0	6.5	-0.23	**334.0**	1610	0.185
9	44.8	50.7	737.9	-393,424	-0.246	-6.87E-04	7.6	8791.7	6.3	-0.14	**358.7**	1810	0.124
10	24.7	30.7	713.1	-407,029	-0.256	-6.84E-04	7.5	8596.4	6.2	-0.14	**374.3**	2010	0.078
11	13.2	19.1	697.6	-415,229	-0.262	-6.82E-04	7.3	8440.9	6.1	-0.11	**383.9**	2210	0.048
12	1.9	7.8	687.9	-417,011	-0.265	-6.83E-04	7.2	8340.6	6.0	-0.06	**387.7**	2410	0.019
13	-21.2	-15.2	684.2	-404,903	-0.263	-6.92E-04	7.2	8289.4	6.0	0.03	**380.4**	2610	-0.037
14	5.0	10.9	691.5	-415,339	-0.264	-6.84E-04	7.2	8322.1	6.0	-0.04	**385.6**	2810	0.026
15	27.0	32.9	686.3	-436,337	-0.270	-6.72E-04	7.2	8275.7	5.9	-0.11	**401.2**	3010	0.078

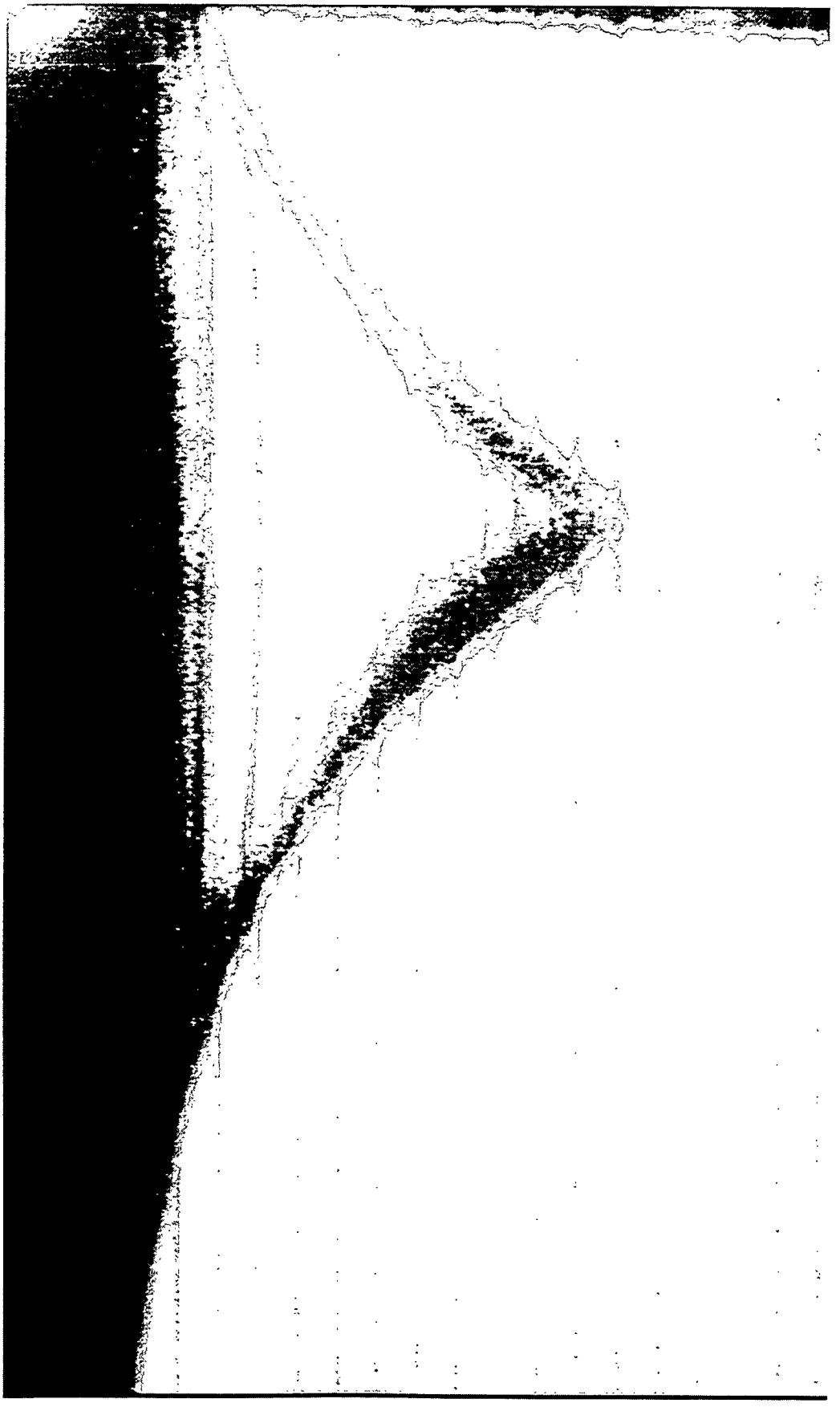

Figure VII.27 Image U22C1265.TIF at time 4:34.825 (τ = 0.1423) for deflectometry analysis. The data file and analyzed data are contained in Table VII.11.

TABLE VII.11 - Image U22C1265.TIF Case#11 with DC200-10 cs.

Film Time 4:34.825, τ = 0.1423

			Thickness	Refractive index	
Angular Misalignment, Φ	-0.0167	Window	1588	1.515	b*(μm)= 1071.88
Magnification factor in dimensions	8	Substrate	38.1	1.608	c*(μm)= 698.88
Distance between fringes $1/P_f$, (μm)	200	Liquid		1.4009	
Distance(μm) from tip to first fringe d_t =	66.3	Air Gap	0		
		Errors			
		Window,1	4.4	0.005	
		Substrate,2	1.6	0.005	
		Liquid,4		0.005	
		dδy(i)=d(y(i)-y(i-1)), (μm)		7	

Correction	5.94	0.89	deg.		Error	Error	Error	Error	Error		Quadratic		
i	δy(i)	δy(i)+corr.	b	c	dh(i)/db	dh(i)/dc	db	dc	dh(i)	Δ dh(i)	h(i), (μm)	y(μm)	dh/dy
0											**0.0**	0	
1	137.5	143.4	1071.9	-33,221	-0.027	-8.83E-04	4.0	1621.7	1.4	1.44	**30.1**	66.3	0.455
2	124.3	130.2	1041.7	-123,309	-0.085	-7.96E-04	4.2	6193.4	4.9	3.51	**107.3**	266.3	0.386
3	90.7	96.7	964.6	-182,593	-0.126	-7.76E-04	6.3	7879.4	6.2	1.22	**162.1**	466.3	0.274
4	58.3	64.3	909.8	-218,622	-0.151	-7.66E-04	7.3	8568.5	6.7	0.49	**197.4**	666.3	0.177
5	11.3	17.3	874.4	-223,700	-0.161	-7.76E-04	7.7	8826.1	7.0	0.30	**206.9**	866.3	0.047
6	-21.1	-15.2	865.0	-211,148	-0.157	-7.92E-04	8.0	8980.2	7.2	0.26	**198.5**	1066.3	-0.042
7	-53.3	-47.3	873.3	-201,841	-0.152	-7.98E-04	8.2	9222.5	7.5	0.24	**189.8**	1266.3	-0.043
8	-67.5	-61.6	882.0	-160,433	-0.130	-8.39E-04	8.4	9515.3	8.1	0.60	**154.7**	1466.3	-0.176
9	-67.3	-61.3	917.1	-122,999	-0.103	-8.66E-04	9.0	10099.8	8.8	0.74	**118.7**	1666.3	-0.180
10	-2.1	3.8	953.1	-128,153	-0.100	-8.39E-04	9.6	10770.8	9.1	0.29	**119.5**	1866.3	0.004

Figure VII.28 Image U22C1266.TIF at time 4:34.827 (τ = 0.1626) for deflectometry analysis. The data file and analyzed data are contained in Table VII.12.

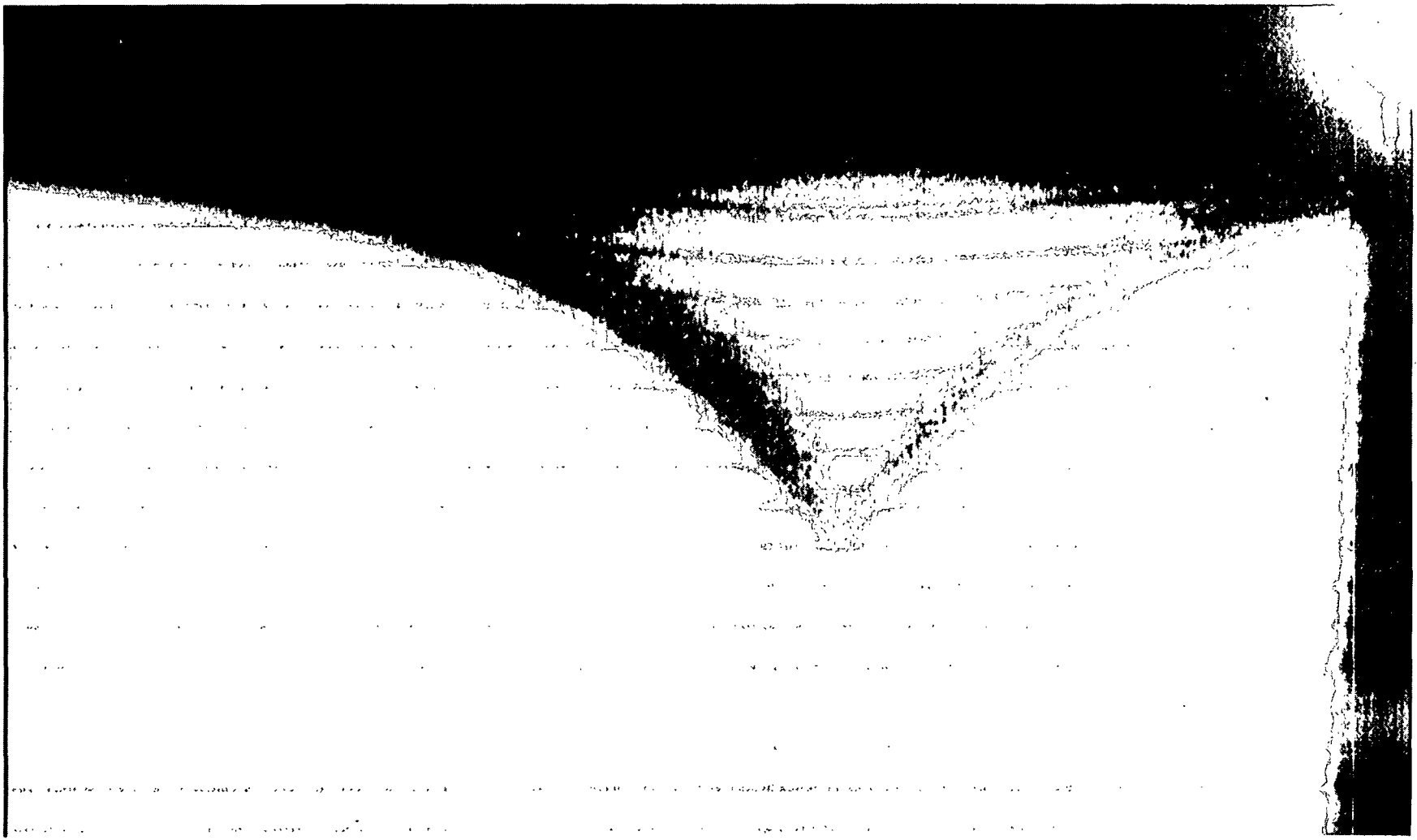

TABLE VII.12 -Image U22C1266.TIF Case#11 with DC200-10 cs.

Film Time 4:34.827, τ = 0.1626

			Thickness	Refractive index	
Angular Misalignment, Φ	-0.03615	Window	1588	1.515	b*(μm)= 1071.88
Magnification factor in dimensions	8	Substrate	38.1	1.608	c*(μm)= 698.88
Distance between fringes $1/P_f$, (μm)	200	Liquid		1.4009	
Distance(μm) from tip to first fringe d_t =	50	Air Gap	0		
		Errors			
		Window,1	4.4	0.005	
		Substrate,2	1.6	0.005	
		Liquid,4		0.005	
		dδy(i)=d(y(i)-y(i-1)), (μm)		7	

Correction	5.94	0.89	deg.		Error	Error	Error	Error	Error		Quadratic		
i	δy(i)	δy(i)+corr.	b	c	dh(i)/db	dh(i)/dc	db	dc	dh(i)	Δ dh(i)	h(i), (μm)	y(μm)	dh/dy
0											**0.0**	0	
1	103.1	109.1	1071.9	-19,056	-0.016	-9.03E-04	4.0	1223.0	1.1	1.11	**17.5**	50	0.350
2	91.0	97.0	1054.4	-86,525	-0.063	-8.28E-04	4.1	5667.6	4.7	3.59	**76.5**	250	0.295
3	92.1	98.1	995.4	-150,552	-0.106	-7.92E-04	6.1	7398.1	5.9	1.20	**133.4**	450	0.284
4	68.0	73.9	938.5	-194,609	-0.136	-7.76E-04	7.1	8347.5	6.6	0.65	**174.8**	650	0.207
5	46.8	52.7	897.1	-224,222	-0.156	-7.67E-04	7.7	8766.2	6.8	0.27	**203.7**	850	0.144
6	24.0	29.9	868.2	-239,251	-0.168	-7.65E-04	7.9	8929.9	7.0	0.13	**219.9**	1050	0.081
7	1.5	7.4	852.0	-236,982	-0.171	-7.73E-04	8.0	8995.0	7.1	0.13	**220.9**	1250	0.005
8	12.2	18.1	851.0	-249,416	-0.176	-7.62E-04	8.1	9091.8	7.1	-0.01	**230.6**	1450	0.049
9	46.2	52.2	841.3	-283,645	-0.190	-7.37E-04	8.1	9091.7	6.9	-0.20	**258.0**	1650	0.137

Figure VII.29 Image U22C1267.TIF at time 4:34.829 (τ = 0.1830) for deflectometry analysis. The data file and analyzed data are contained in Table VII.13.

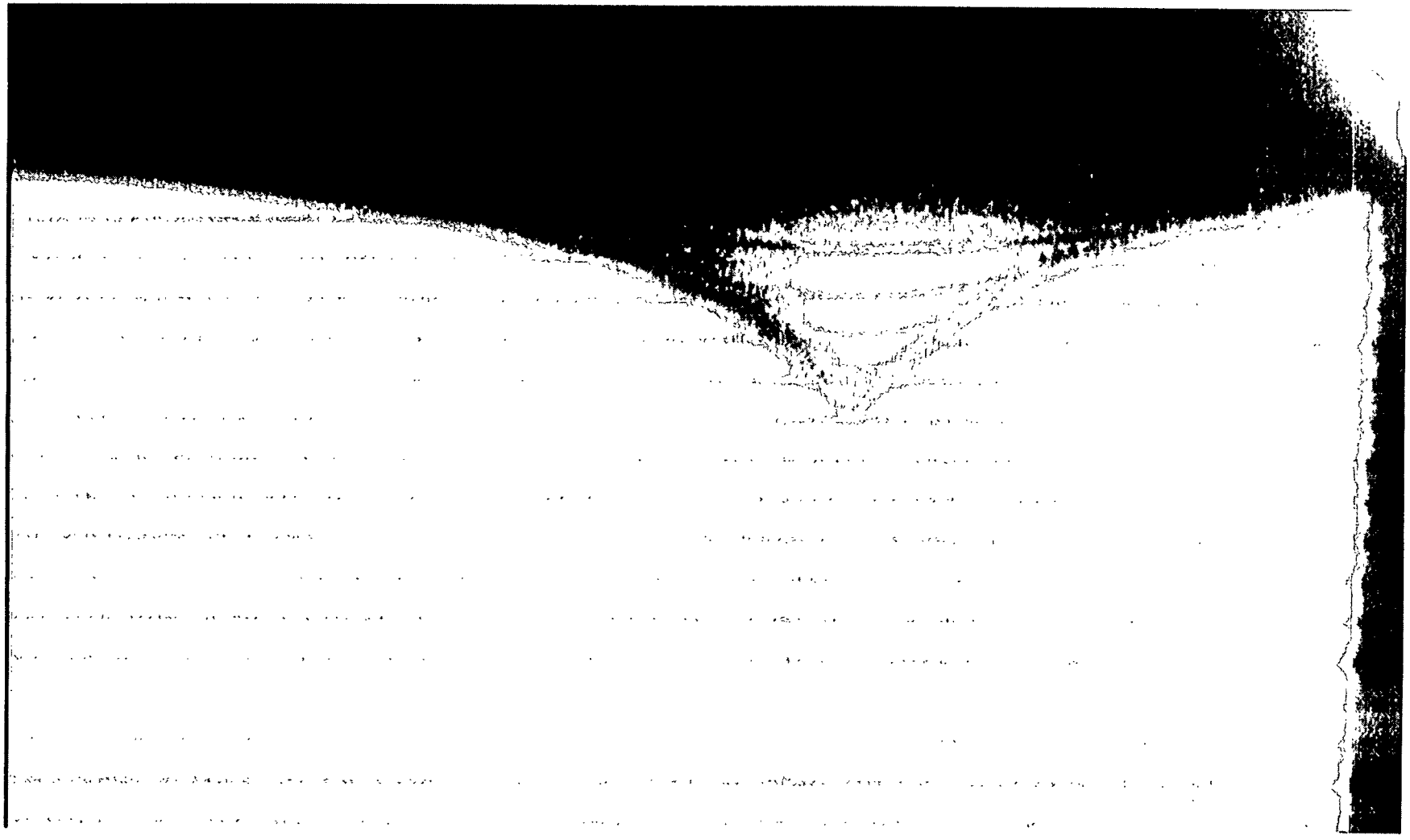

TABLE VII.13-Image U22C1267.TIF Case#11 with DC200-10 cs.

			Thickness	Refractive index	
Film Time 4:34.829, τ = 0.1830					
Angular Misalignment, Φ	-0.113°	Window	1588	1.515	b*(μm)= 1071.88
Magnification factor in dimensions	8	Substrate	38.1	1.608	c*(μm)= 698.88
Distance between fringes $1/P_f$, (μm)	200	Liquid		1.4009	
Distance(μm) from tip to first fringe d_t =	47	Air Gap	0		
		Errors			
		Window,1	4.4	0.005	
		Substrate,2	1.6	0.005	
		Liquid,4		0.005	
		dδy(i)=d(y(i)-y(i-1)), (μm)		7	

Correction	5.94	0.89	deg.		Error	Error	Error	Error	Error		Quadratic		
i	δy(i)	δy(i)+corr.	b	c	dh(i)/db	dh(i)/dc	db	dc	dh(i)	Δ dh(i)	h(i), (μm)	y(μm)	dh/dy
0											**0.0**	0	
1	127.5	133.5	1071.9	-21,923	-0.018	-8.99E-04	4.0	1149.7	1.0	1.04	**20.1**	47	0.427
2	82.5	88.4	1051.8	-83,311	-0.062	-8.33E-04	4.1	5961.4	5.0	3.94	**74.0**	247	0.270
3	37.4	43.3	997.9	-109,615	-0.083	-8.35E-04	6.4	7538.0	6.3	1.34	**99.9**	447	0.129
4	26.1	32.1	972.0	-129,453	-0.098	-8.27E-04	7.5	8418.9	7.0	0.68	**118.7**	647	0.094
5	67.4	73.3	953.2	-178,447	-0.126	-7.85E-04	8.0	8997.8	7.1	0.14	**160.3**	847	0.208

Figure VII.30 Image U22C1268.TIF at time 4:34.831 (τ = 0.2040) for deflectometry analysis. The data file and analyzed data are contained in Table VII.14.

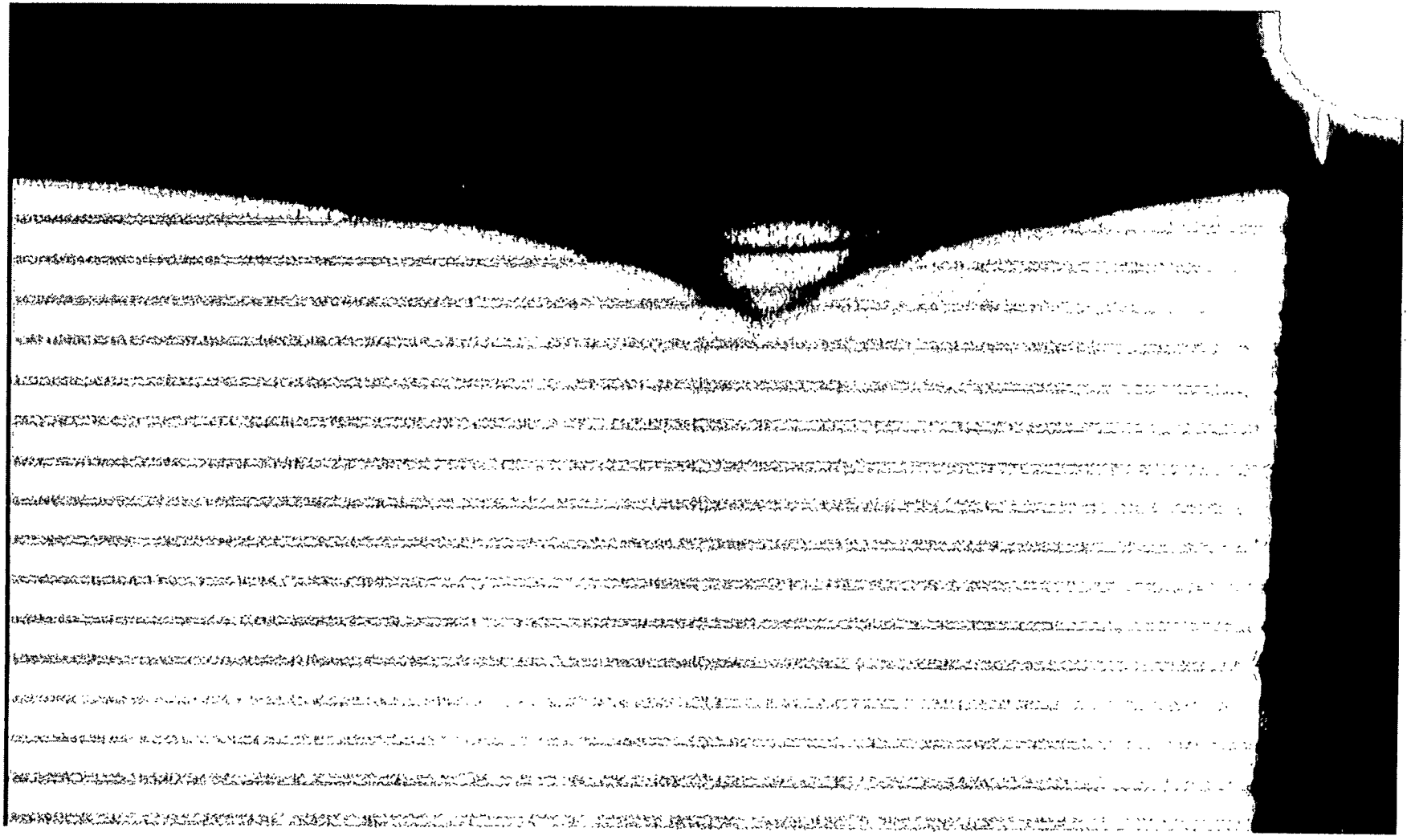

TABLE VII.14 - Image U22C1268.TIF Case#11 with DC200-10 cs.

			Thickness	Refractive index	
Film Time 4:34.831, τ = 0.2040					
Angular Misalignment (degrees)	0.00°	Window	1588	1.515	b*(μm)= 1071.88
Magnification factor in dimensions	8	Substrate	38.1	1.608	c*(μm)= 698.88
Distance between fringes	200	Liquid		1.4009	
Distance(μm) from tip to first fringe =	164.7	Air Gap	0		
		Errors			
		Window,1	4.4	0.005	
		Substrate,2	1.6	0.005	
		Liquid,4		0.005	
		dδy(i)=d(y(i)-y(i-1)), (μm)		7	

Correction		5.94	0.89	deg.		Error	Error	Error	Error	Error		Quadratic		
	i	δy(i)	δy(i)+corr.	b	c	dh(i)/db	dh(i)/dc	db	dc	dh(i)	Δ dh(i)	h(i), (μm)	y(μm)	dh/dy
	0											**0.0**	0	
	1	67.6	73.5	1071.9	-42,326	-0.033	-8.71E-04	4.0	4028.7	3.5	3.51	**38.1**	164.7	0.232
	2	67.6	73.5	1033.7	-92,268	-0.069	-8.34E-04	5.3	6406.3	5.4	1.84	**82.6**	364.7	0.223

Figure VII.31 Image U22C1269.TIF at time 4:34.833 for deflectometry analysis.

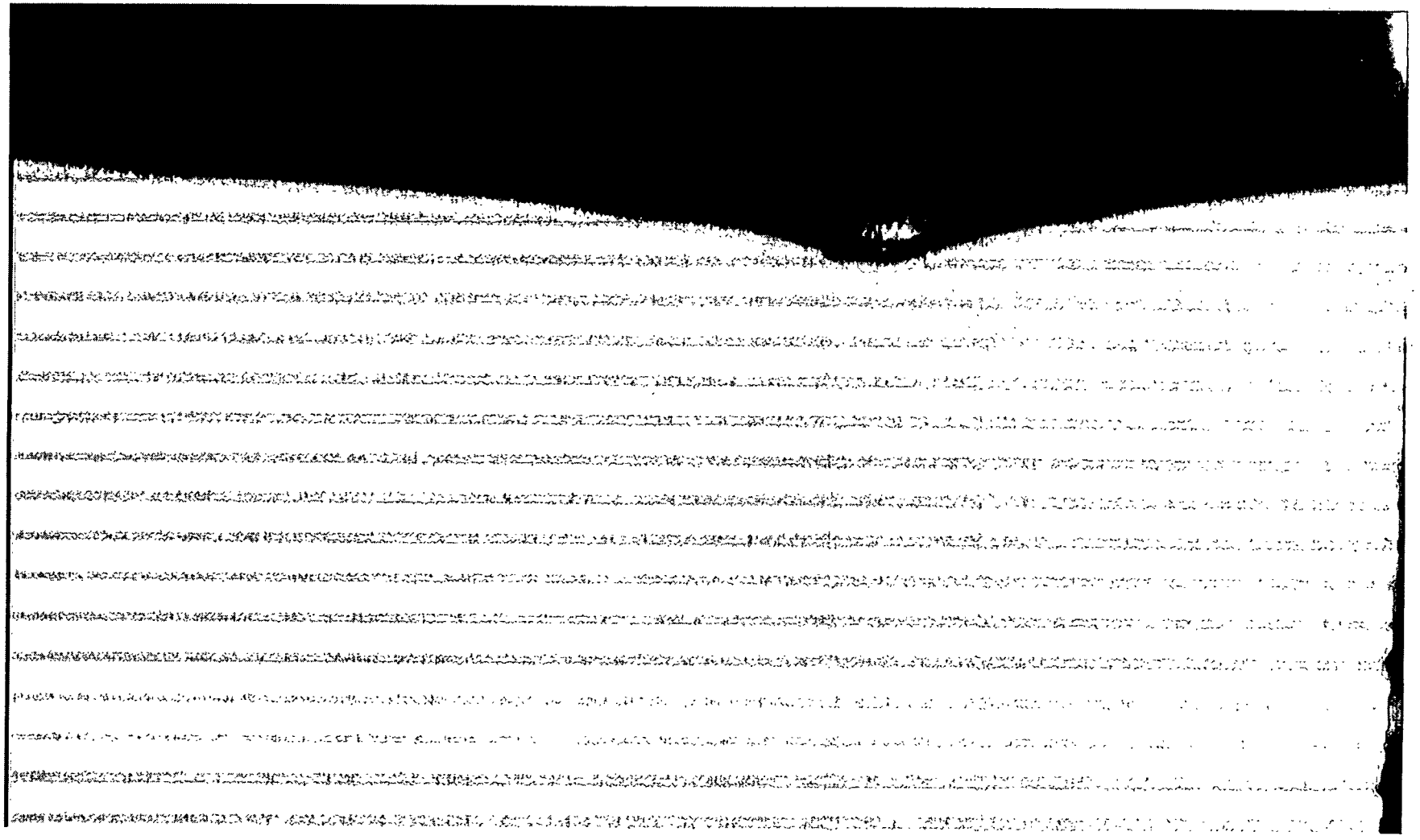

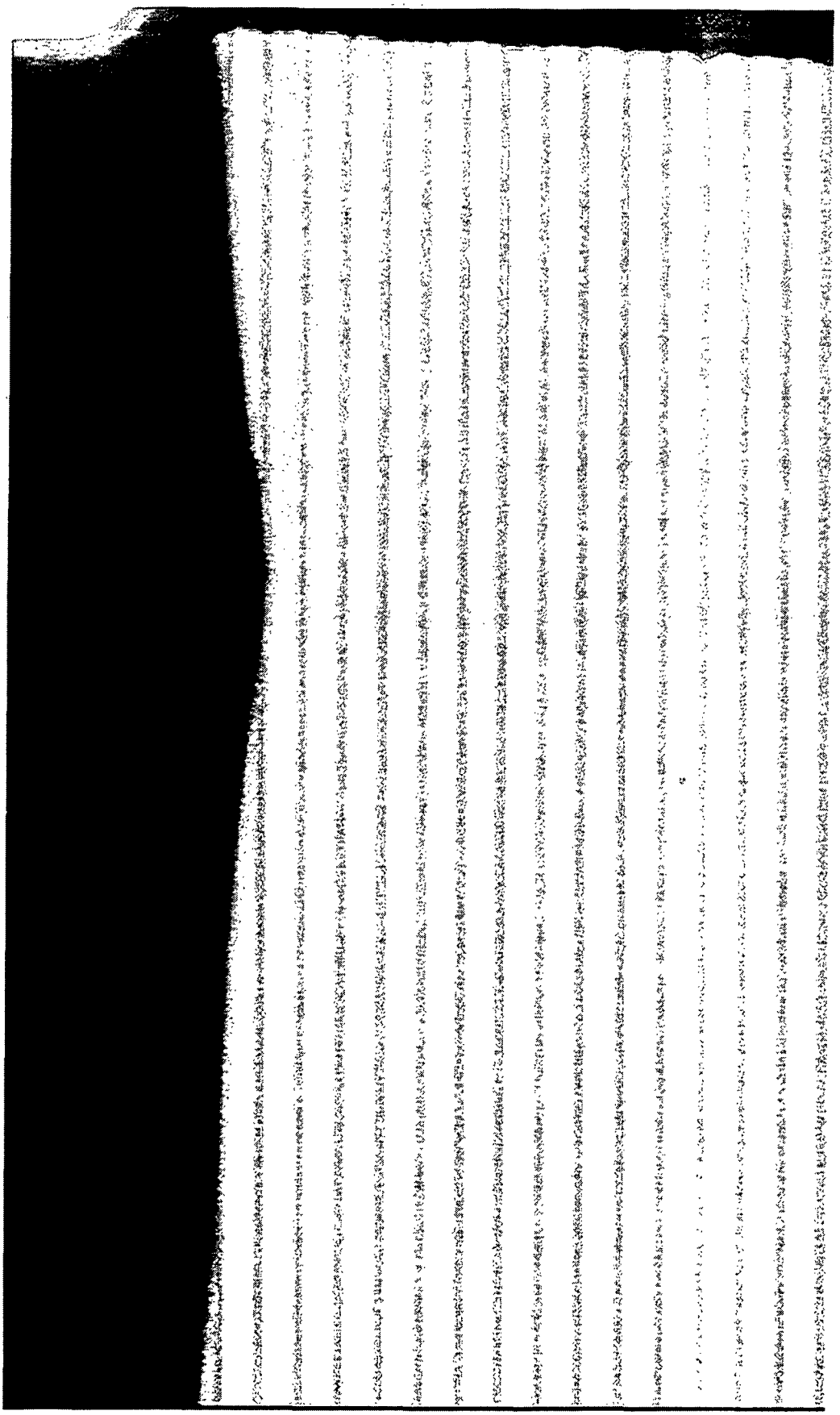

Figure VII.32 Image U22C1270.TIF at time 4:34.835 for deflectometry analysis.

APPENDIX VIII

LENGTH, WIDTH, AND Ø1 DATA FOR AIR FILM CASES

This Appendix includes the triangular air film lengths, L1 and L2, width, W1, tip angles, $Ø_1$, $Ø_2$ and $Ø_3$, in Tables VIII.1 through VIII.12. These were measured for the cases previously reported in Section VI. The advancing and retracting velocities are reported for the applicable cases along with the correlation coefficient.

The dimensionless time, τ, is plotted with respect to L1, L2, W1 and Ø1 and Ø3 in Figs. VIII.1 through VIII.12. The dimension $Ø_3$ in Figs. VIII.1 through VIII.12 has been multiplied five times to keep it on the same scale as $Ø_1$.

TABLE VIII.1 - Time vs. Length, Width, and Angle Data for Air Tongue - Fluid A

Experiment Code U15ACA4
Case #1 = DC200 - 100cs Silicone Oil
Film time from 401:20.828 to 401:20.879
Calibration Magnification (X) = 1.0
Distance between fringes (μm) 100.0

Time (ms)	Tau	L1 Length(μm)	W1 Width (μm)	L2 Length2(μm)	Tip Angle Ø1(°)	Base Angle Ø2(°)	Tip Vert. Angle Ø3(°)
846.0	0.0000	294	808	126	119.6	13.8	1.6
848.0	0.1028	309	904	97	70.7	13.4	2.0
850.0	0.2057	380	928	180	66.6	14.5	4.4
852.0	0.3085	447	1282	147	79.7	14.3	4.1
854.0	0.4114	512	1260	227	68.4	15.8	6.1
857.0	0.5142	573	1528	214	77.5	14.2	5.2
859.0	0.6171	640	1841	226	72.6	14.9	7.4
861.0	0.7199	714	1732	380	70.8	18.3	6.4
863.0	0.8228	780	2088	313	79.4	19.7	8.7
865.0	0.9256	854	2270	246	74.8	13.8	10.2
867.0	1.0285	1014	2412	114	74.3	12.1	8.1
869.0	1.1313	1000	2439	127	75.6	16.3	9.5
871.0	1.2342	1080	2111	280	79.9	23.8	8.1
873.0	1.3370	1174	2296	118	92.0	35.9	8.8
875.0	1.4399	1193	2289	480	86.1	40.1	12.0
877.0	1.5427	1307	2328	353	85.4	31.9	10.5
879.0	1.6456	1380	2016	372	98.5	32.3	10.0
881.0	1.7484	1406	1834	493	107.5	36.6	10.6
883.0	1.8513	1427	1808	387	115.1	33.5	11.5
885.0	1.9541	1427	1762	500	114.7	36.8	11.6
887.0	2.0570	1447	1684	486	118.9	35.5	11.2
Average		**661**	**1791**	**279**	**87.1**	**23.2**	**8.0**
Standard Deviation		**271**	**510**	**139**	**17.9**	**10.2**	**3.1**
Standard Error		**41.0%**	**28.5%**	**49.7%**	**20.6%**	**43.8%**	**39.1%**

Advancing Velocity (cm/min)	**190.8**	**R^2 = 0.9876**
(cm/sec)	**3.2**	
Substrate Velocity(cm/sec)	**12.8**	

Figure VIII.1 - Case #1 - Fluid A

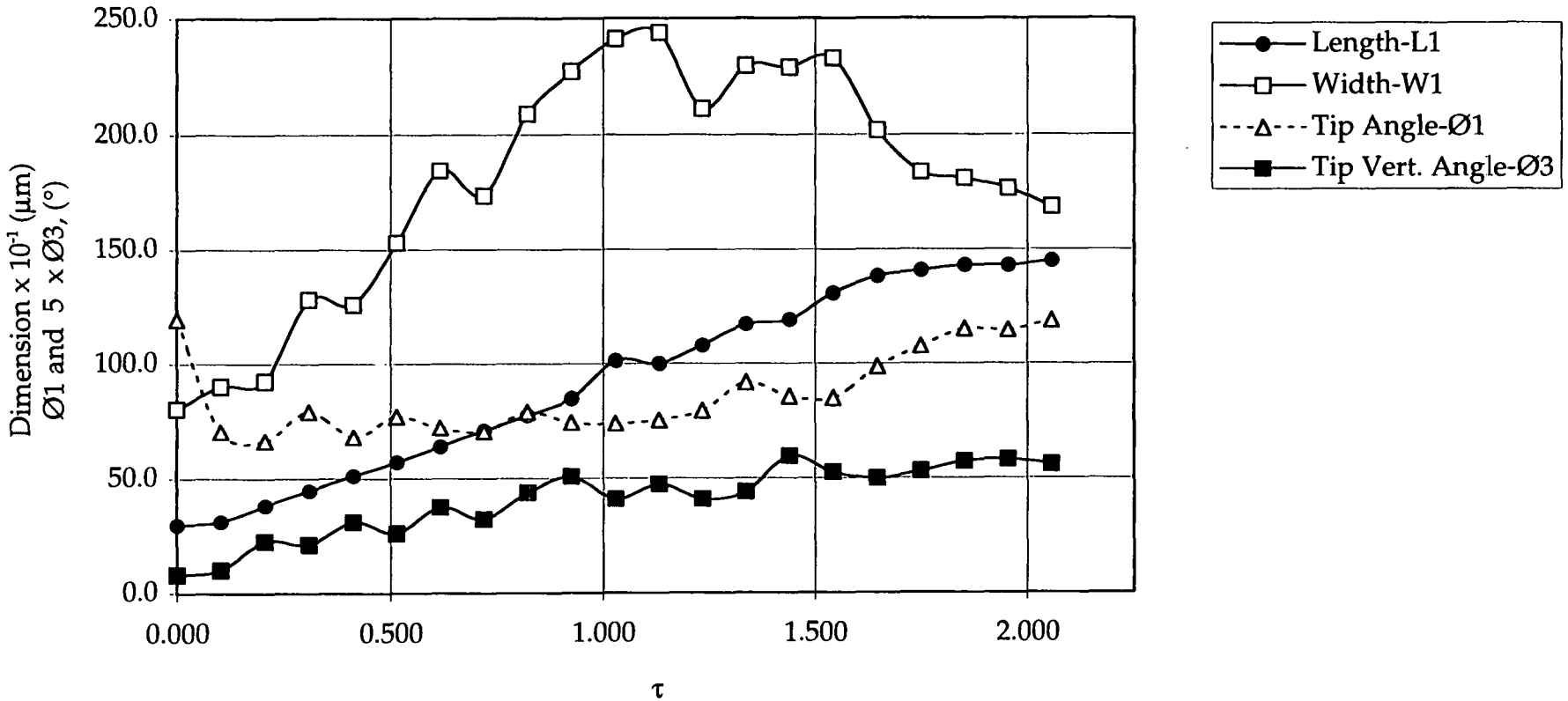

TABLE VIII.2 - Time vs. Length, Width, and Angle Data for Air Tongue - Fluid A

Experiment Code U15ACA4
Case #2 - DC200 - 100cs
Film time from 401:20.518 to 401:20.564
Calibration Magnification (X) = 1.0
Distance between fringes (μm) 100.0

Time (ms)	Tau	L1 Length(μm)	W1 Width (μm)	L2 Length2(μm)	Tip Angle Ø1(°)	Base Angle Ø2(°)	Tip Vert. Angle Ø3(°)
518	0.000	2285	1961	496	45.0	39.9	9.0
521	0.103	2279	1982	516	44.5	33.5	7.1
523	0.206	2274	2274	558	45.6	34.4	7.3
526	0.309	2179	1890	516	47.1	36.6	7.4
528	0.411	2084	1818	642	47.1	39.5	8.8
531	0.514	1968	1695	568	46.7	36.6	7.6
533	0.617	1842	1715	474	48.5	41.1	6.9
536	0.720	1801	1684	421	49.6	33.6	10.2
538	0.823	1748	1561	337	48.8	35.5	9.6
541	0.926	1684	1325	285	43.3	32.7	10.1
543	1.028	1632	1119	284	36.9	31.6	8.9
546	1.131	1547	914	326	33.4	38.4	8.5
548	1.234	1421	770	221	29.2	31.3	7.5
551	1.337	1242	647	253	29.8	31.6	6.5
554	1.440	1000	575	190	32.7	28.2	8.2
556	1.543	747	544	148	40.7	24.3	14.4
559	1.646	558	452	148	46.3	29.0	6.3
561	1.748	432	503	201	62.7	25.6	5.5
564	1.851	347	524	105	74.6	24.3	3.0
Average		**1835**	**1524**	**421**	**43.3**	**35.6**	**8.4**
Standard Deviation		**268**	**449**	**139**	**6.9**	**3.2**	**1.2**
Standard Error		**14.6%**	**29.5%**	**33.1%**	**16.0%**	**9.1%**	**14.1%**

Retraction Velocity (cm/min)	**262.4**	**R^2 = 0.943**
(cm/sec)	**4.4**	
Substrate Velocity (cm/sec)	**12.8**	

Figure VIII.2 - Case #2 - Fluid A

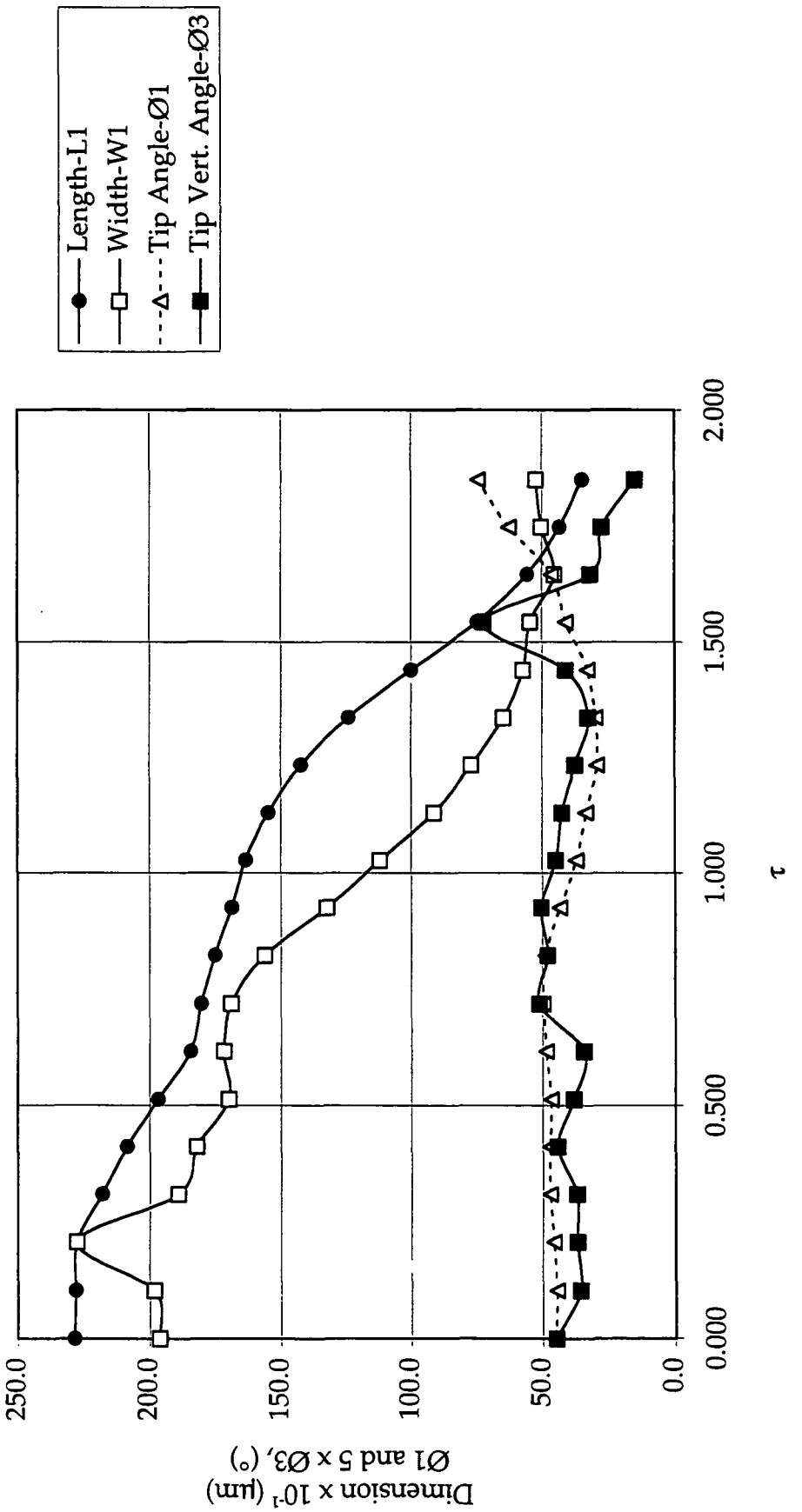

TABLE VIII.3 - Time vs. Length, Width, and Angle Data for Air Tongue - Fluid B

Experiment Code M24BCA7.1
Case #3 - DC200 - 200cs Silicone Oil
Film time from 0 to 29.2 ms
Calibration Magnification (X) = 8.0
Distance between fringes (μm) 80.0

Time (ms)	Tau	L1 Length(μm)	W1 Width(μm)	L2 Length2(μm)	Tip Angle Ø1(°)	Base Angle Ø2(°)	Tip Vert. Angle Ø3(°)
0.00	0.000	1805	1732	1013	26.1	57.3	9.8
2.08	0.198	1902	1714	1013	29.9	58.7	11.1
4.17	0.396	1914	1685	981	31.1	59.2	8.2
6.25	0.595	1890	1667	894	36.0	58.9	9.4
8.33	0.793	1914	1685	713	31.1	59.2	9.3
10.41	0.990	1884	1685	769	30.8	55.8	9.3
12.50	1.189	1902	1755	832	27.1	55.2	9.6
14.58	1.387	1914	1797	750	25.6	54.3	10.1
16.67	1.586	1974	1885	826	25.9	52.8	7.7
18.75	1.784	2010	1885	694	30.0	52.9	5.9
20.83	1.982	1956	2080	631	32.3	51.7	8.9
22.92	2.181	1888	2064	769	33.7	52.1	9.4
25.00	2.379	1908	2073	831	34.6	53.5	9.4
27.08	2.577	1890	1667	675	36.0	58.9	9.7
29.17	2.775	1926	1720	938	39.8	53.7	11.1
Average		**1912**	**1806**	**822**	**31.3**	**55.6**	**9.3**
Standard Deviation		**46**	**154**	**124**	**4.2**	**2.8**	**1.3**
Standard Error		**2.4%**	**8.5%**	**15.0%**	**13.3%**	**5.1%**	**14.0%**

Figure VIII.3 - Case #3 - Fluid B

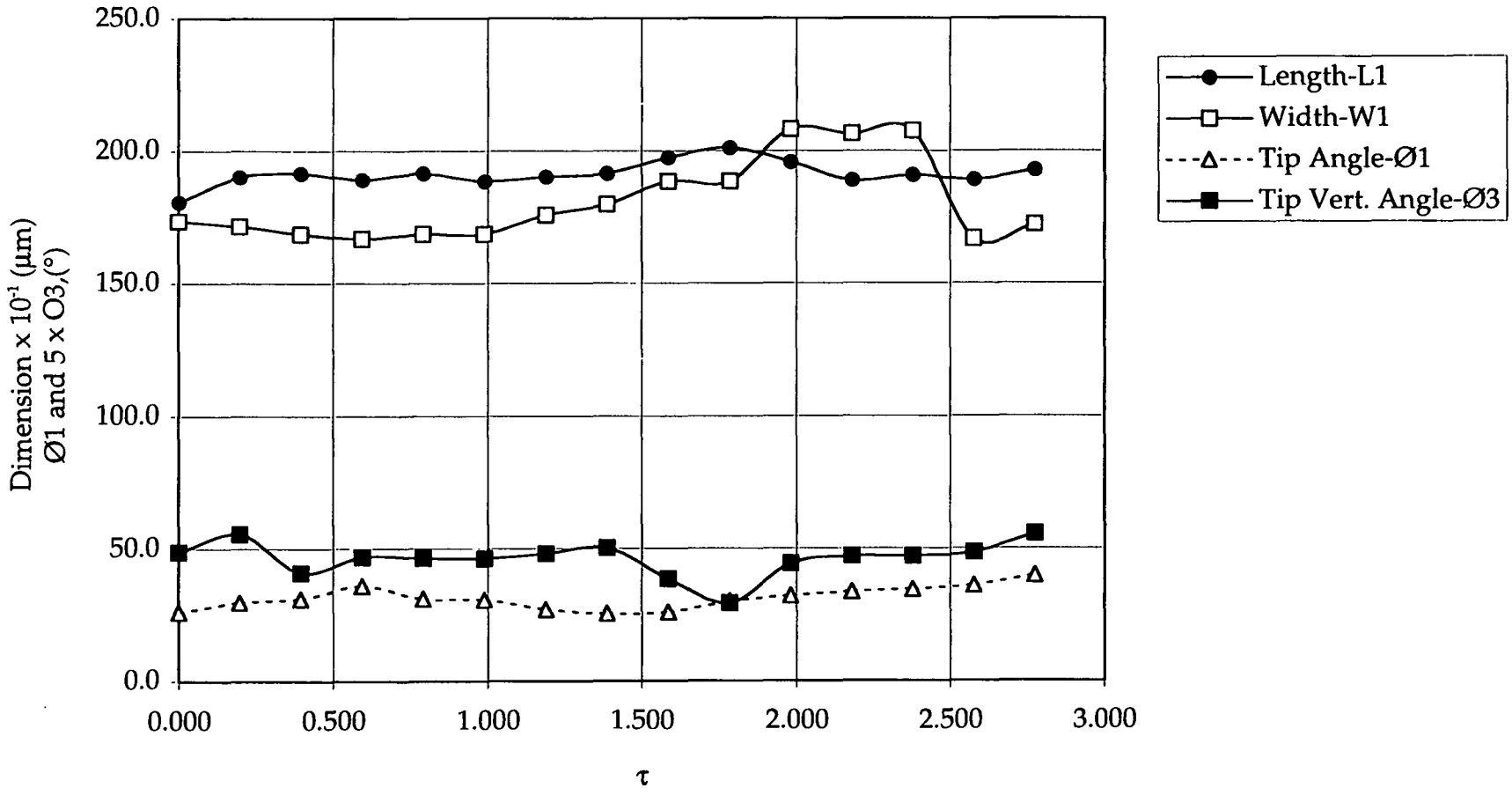

TABLE VIII.4 -Time vs. Length, Width, and Angle Data for Air Tongue - Fluid B

Experiment Code M24BCA7.2
Case #4 - DC200 - 200cs Silicone Oil
Film time from 0 to 25 ms
Calibration Magnification (X) = 8.0
Distance between fringes (μm) 80.0

Time (ms)	Tau	L1 Length(μm)	W1 Width(μm)	L2 Length(μm)	Tip Angle Ø1(°)	Base Angle Ø2(°)	Tip Vert. Angle O3(°)
0.00	0.000	2385	2720	1404	24.3	30.9	13.7
2.08	0.198	2534	2823	1396	21.8	32.5	12.4
4.17	0.396	2727	2797	1331	23.0	32.4	11.7
6.25	0.595	2615	2551	1420	22.9	32.5	9.6
8.33	0.793	2726	2567	1518	25.7	32.5	7.8
10.41	0.990	2742	2629	1518	25.8	33.3	7.5
12.50	1.189	2686	2575	1527	29.8	32.4	9.0
14.58	1.387	2702	2590	1429	30.8	32.1	6.6
16.67	1.586	2599	2536	1478	33.2	31.6	9.4
18.75	1.784	2599	2513	1356	32.2	30.7	10.7
20.83	1.982	2639	2436	1519	33.0	30.1	10.9
22.92	2.181	2663	2359	1323	32.3	28.3	10.4
25.00	2.379	2631	2174	1316	34.2	24.8	9.9
Average		**2634**	**2559**	**1426**	**28.4**	**31.1**	**10.0**
Standard Deviation		**97**	**174**	**80**	**4.6**	**2.3**	**2.0**
Standard Error		**3.7%**	**6.8%**	**5.6%**	**16.0%**	**7.5%**	**20.1%**

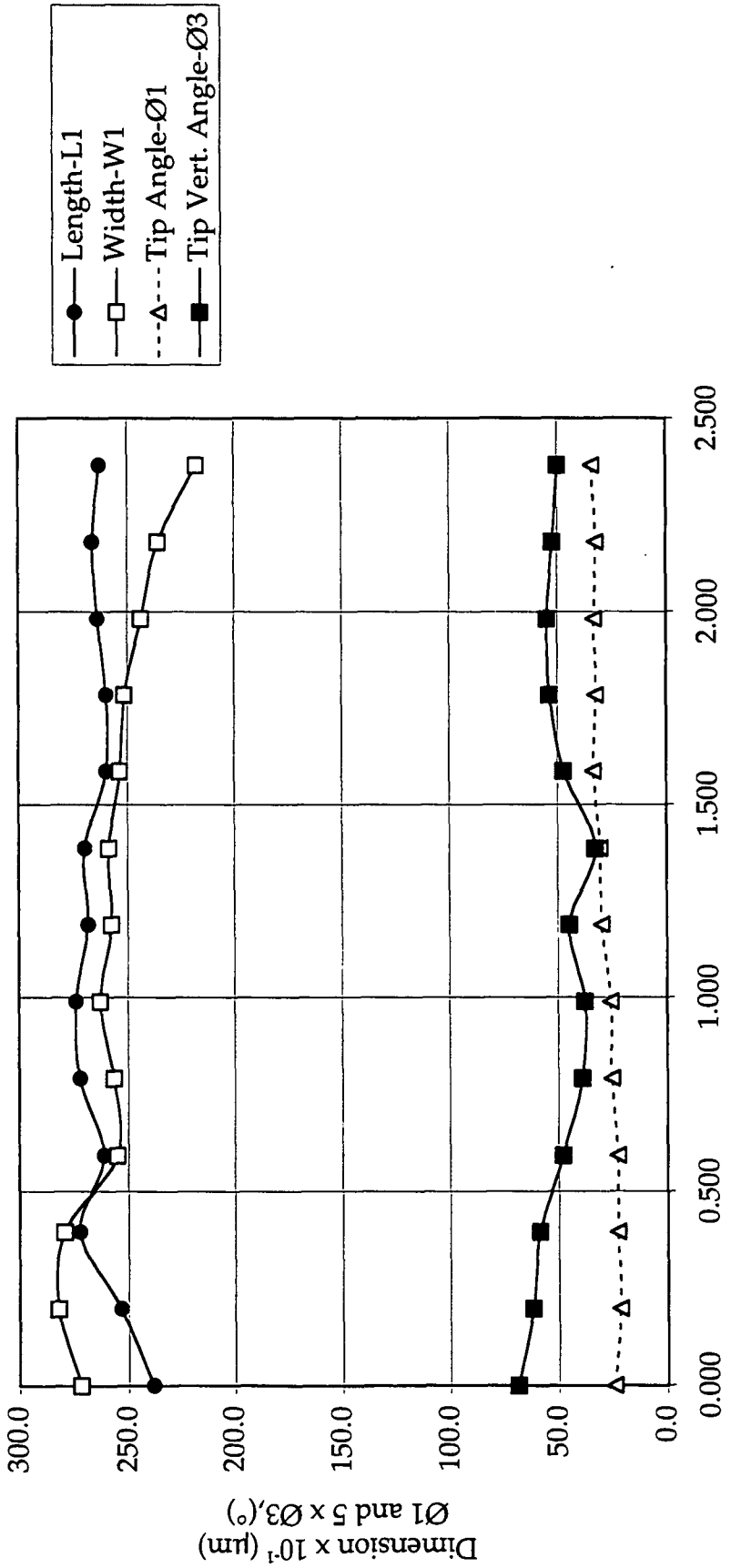

Figure VIII.4 - Case #4 - Fluid B

TABLE VIII.5 - Time vs. Length, Width, and Angle Data for Air Tongue - Fluid B

Experiment Code M24BCA6
Case #5 - DC200 - 200cs Silicone Oil
Film time from 0 to 41.7 ms - Alpha Numeric Data System not installed
Calibration Magnification (X) = 1.0
Distance between fringes (μm) 80.0

Time (ms)	Tau	L1 Length(μm)	W1 Width(μm)	L2 Length2(μm)	Tip Angle Ø1(°)	Base Angle Ø2(°)	Tip Vert. Angle Ø3(°)
0.00	0.000	1642	1034	1043	32.8	58.0	12.3
2.08	0.197	1772	1014	998	27.2	59.2	11.2
4.17	0.394	1902	994	1002	29.5	60.8	9.6
6.25	0.591	1869	950	923	28.7	62.1	10.2
8.33	0.788	1837	927	872	26.2	62.4	11.4
10.41	0.985	1868	832	832	24.3	62.3	10.4
12.50	1.182	1921	785	759	22.2	63.1	10.5
14.58	1.379	1930	712	772	20.1	64.6	12.5
16.67	1.576	1925	658	699	19.2	65.6	11.7
18.75	1.773	1930	608	621	17.3	63.2	9.3
20.83	1.970	1941	554	575	15.7	63.1	15.1
22.92	2.167	1874	476	478	13.8	62.0	15.3
25.00	2.364	1843	511	391	14.8	58.9	7.8
27.09	2.561	1830	511	391	15.5	59.9	6.2
29.17	2.758	1770	507	322	15.9	51.4	8.3
31.26	2.955	1647	457	129	15.6	35.6	10.8
33.34	3.152	1553	328	180	11.9	47.7	8.8
35.43	3.349	1511	311	138	11.3	43.7	8.3
37.51	3.546	1456	324	180	11.6	50.0	4.8
39.60	3.743	1272	291	161	12.5	50.8	5.7
41.68	3.940	987	274	147	16.0	40.2	8.4
43.77	4.137	876	255	152	16.6	38.6	*
45.85	4.334	767	259	147	18.4	44.1	*
47.94	4.531	442	212	1138	19.8	44.2	*
50.02	4.728	290	191	90	36.5	42.6	*
52.11	4.925	186	229	*	63.4	58.3	*
Average		**1494**	**546**	**526**	**21.4**	**54.3**	**9.9**
Standard Deviation		**551**	**280**	**353**	**10.9**	**9.4**	**2.7**
Standard Error		**36.9%**	**51.3%**	**67.2%**	**51.1%**	**17.3%**	**27.4%**

Retraction Velocity (cm/min)	**240.5**	**R^2=0.906**
(cm/sec)	**4.0**	
Substrate Velocity	**12.1**	

Figure VIII.5 - Case #5 - Fluid B

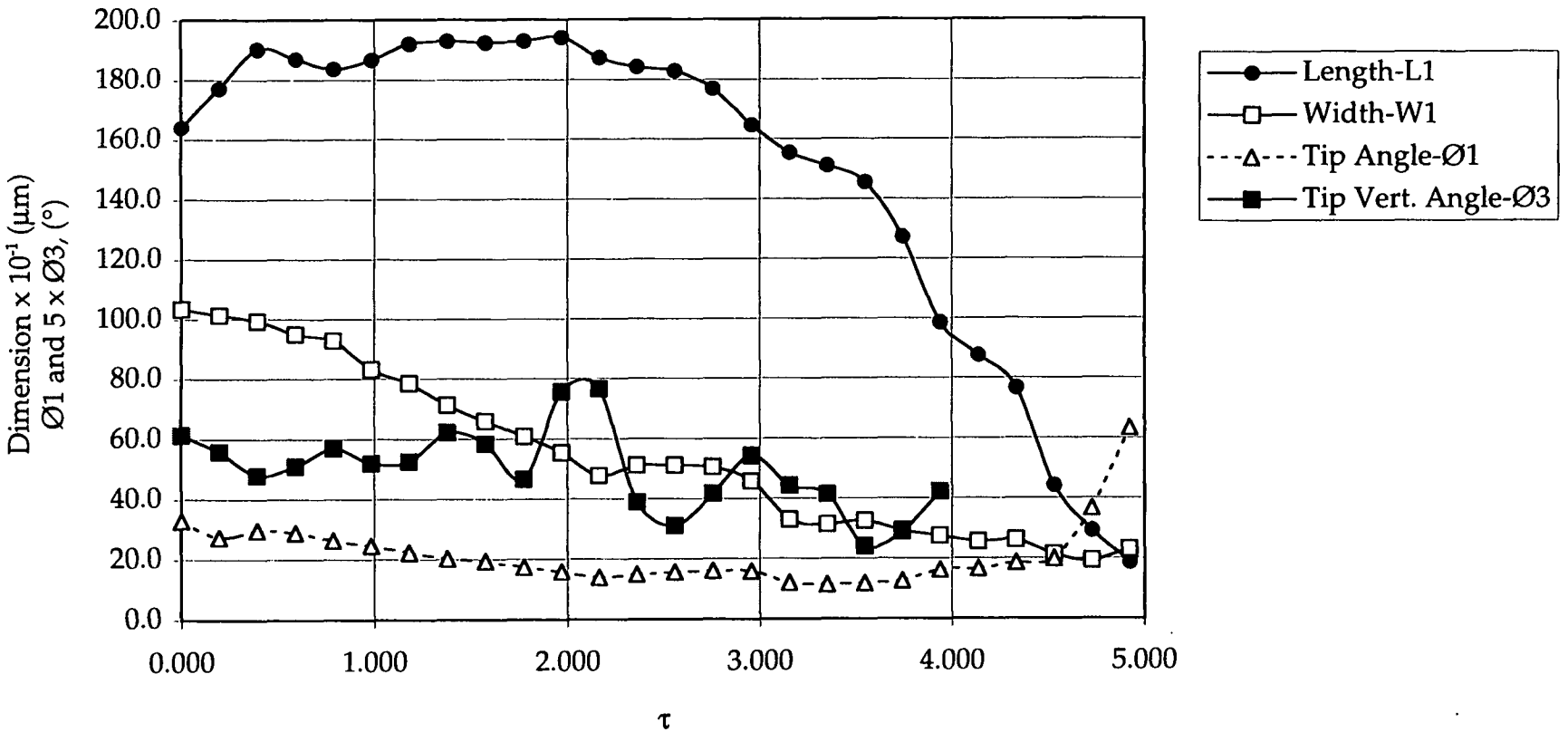

TABLE VIII.6 - Time vs. Length, Width, and Angle Data for Air Tongue - Fluid D

Experiment Code G14DCA1
Case #6 - DC200 - 500cs Silicone Oil
Film time from 215:00.484 to 215:00.494
Calibration Magnification (X) = 1.0
Distance between fringes (μm) 100.0

Time (ms)	Tau	L1 Length(μm)	W1 Width(μm)	L2 Length2(μm)	Tip Angle Ø1(°)	Base Angle Ø2(°)	Tip Vert. Angle Ø3(°)
484.0	0.00	323	170	100	26.1	42.9	1.4
486.0	0.43	361	187	111	28.7	47.2	1.3
488.0	0.85	421	242	131	31.5	34.2	2.5
490.0	1.28	481	279	221	32.8	51.8	4.9
492.0	1.71	558	376	221	37.0	47.2	3.6
494.0	2.14	644	423	283	35.8	46.5	3.7
Average		**465**	**279**	**178**	**32.0**	**44.9**	**2.9**
Standard Deviation		**122**	**102**	**74**	**4.2**	**6.0**	**1.4**
Standard Error		**26.2%**	**36.5%**	**41.7%**	**13.0%**	**13.3%**	**48.3%**

Advancing Velocity(cm/min)	**193.5**	$R^2 = 0.9843$
(cm/sec)	**3.2**	
Substrate Velocity (cm/min)	**12.9**	

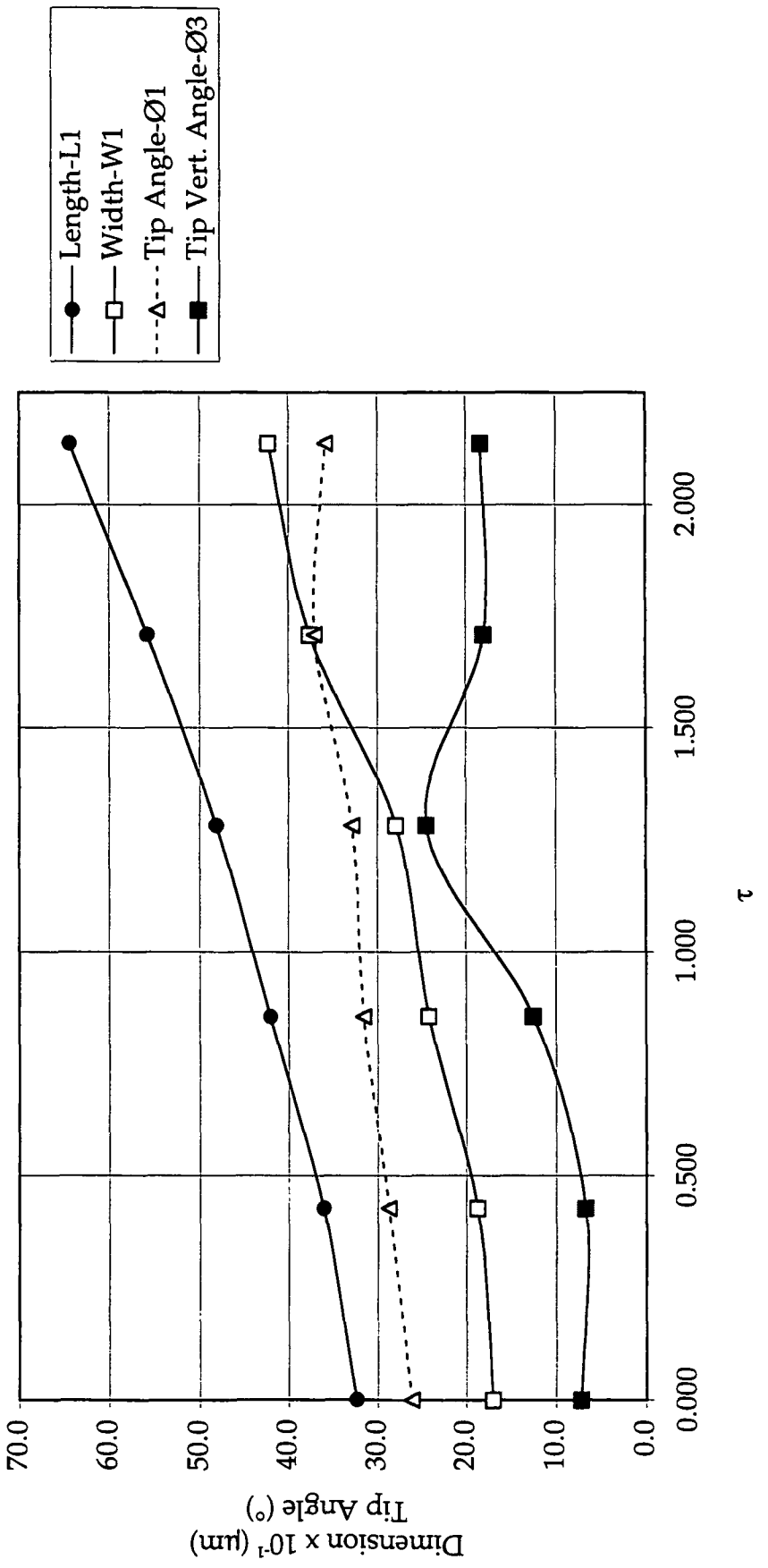

Figure VIII.6 - Case #6 - Fluid D

TABLE VIII.7 - Time vs. Length, Width, and Angle Data for Air Tongue - Fluid F

Experiment Code U26FCA1
Case #7 - Glycerin-water ≈ 500 cp
Film time from 1:37.418 to 1:37.597
Calibration Magnification (X) = 1.0
Distance between fringes (μm) 100

Time (ms)	Tau	L1 Length(μm)	W1 Width(μm)	L2 Length2(μm)	Tip Angle Ø1(°)	Base Angle Ø2(°)	Tip Vert. Angle Ø3(°)
554	0.00	616	596	253	39.5	33.6	5.4
556	0.24	684	467	374	32.4	41.4	4.4
558	0.47	690	395	442	22.3	42.4	4.9
560	0.71	637	626	358	51.7	46.7	5.8
562	0.94	637	662	321	54.4	40.6	5.9
564	1.18	637	488	342	37.3	45.0	5.4
580	3.06	401	554	211	65.1	39.8	3.7
582	3.30	413	436	215	54.0	36.4	4.5
585	3.53	367	351	225	47.0	66.5	4.2
587	3.77	361	379	225	49.5	65.2	4.6
589	4.01	329	369	150	56.7	57.4	2.3
591	4.24	315	340	125	48.0	66.0	3.7
593	4.48	312	411	100	60.1	60.0	1.7
Average (554-564)		**650**	**539**	**348**	**39.6**	**41.6**	**5.3**
Standard Deviation		**30**	**104**	**62**	**12.0**	**4.5**	**0.6**
Standard Error		**4.6%**	**19.4%**	**17.9%**	**30.3%**	**10.9%**	**10.7%**
Average (580-593)		**357**	**406**	**179**	**54.3**	**55.9**	**3.5**
Standard Deviation		**40**	**73**	**52**	**6.7**	**12.6**	**1.1**
Standard Error		**11.3%**	**18.1%**	**29.4%**	**12.4%**	**22.6%**	**31.5%**

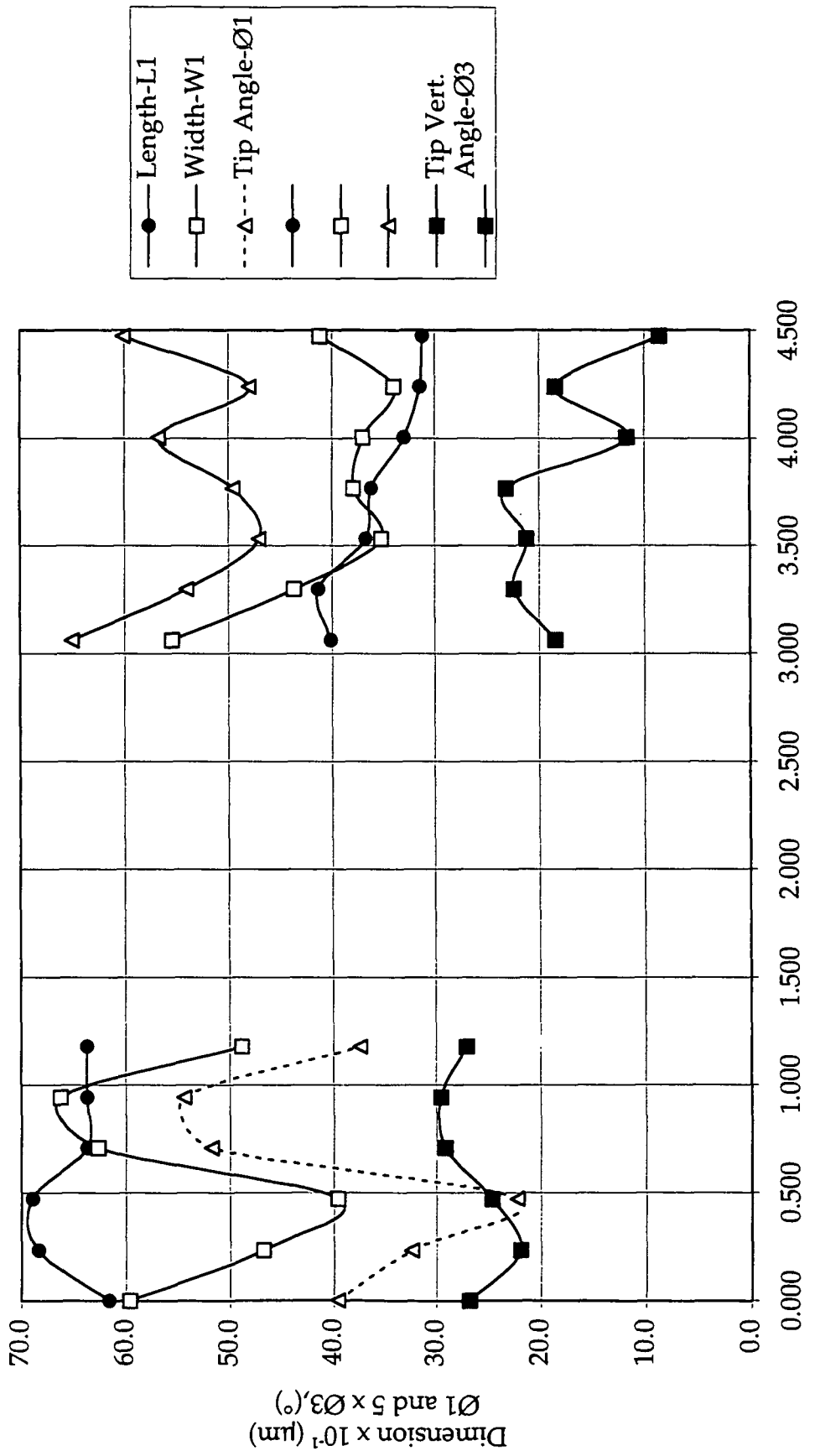

Figure VIII.7 - Case #7 - Fluid F

Table VIII.8 - Time vs. Length, Width, and Angle Data for Air Tongue - Fluid H

Experiment Code L06HCA2
Case #8 - Glycerin-water ≈ 165 cp
Film time from 21:15.594 to 21:15.643
Calibration Magnification (X) = 8.0
Distance between fringes (μm) 100.0

Time (ms)	Tau	L1 Length	W1 Width	L2 Length2	Tip Angle Ø1(*)	Base Angle Ø2(°)	Tip Vert. Angle Ø3(°)
594.0	0.000	1224	1846	322	59.7	26.9	7.7
596.0	0.067	1296	1707	400	58.9	33.0	9.8
598.0	0.134	1319	1712	364	62.0	27.1	7.6
600.0	0.202	1325	1613	484	60.7	26.6	8.1
602.0	0.269	1215	1579	603	77.2	22.8	7.0
604.0	0.336	1104	1544	400	70.7	31.4	9.7
606.0	0.403	1009	1520	299	74.0	27.9	9.0
608.0	0.470	910	1503	272	79.0	26.5	4.9
610.0	0.538	812	1485	245	83.9	25.1	4.7
613.0	0.605	842	1293	275	78.8	24.4	3.8
615.0	0.672	752	1142	293	73.8	26.7	5.7
617.0	0.739	734	1083	275	70.9	19.1	6.0
619.0	0.806	657	1159	221	82.5	20.0	4.8
621.0	0.874	630	1237	*	91.9	*	4.5
623.0	0.941	619	1237	*	74.6	*	3.6
625.0	1.008	717	972	*	63.5	*	4.6
627.0	1.075	630	821	*	61.4	*	3.7
629.0	1.142	524	843	196	72.6	*	3.4
631.0	1.210	472	861	174	84.3	26.3	2.3
633.0	1.277	407	883	158	91.4	23.3	2.9
635.0	1.344	385	828	113	94.1	21.7	2.1
637.0	1.411	335	649	88	88.4	20.5	3.3
Average		**1147**	**1578**	**404**	**70.6**	**27.1**	**7.7**
Standard Deviation		**169**	**77**	**124**	**7.7**	**2.8**	**1.7**
Standard Error		**14.7%**	**4.9%**	**30.6%**	**10.9%**	**10.2%**	**22.2%**

*Not possible to make measurement due geometric considerations.

Retraction Velocity(cm/min)	**138.8**	**R^2=0.9463**
(cm/sec)	**2.3**	
Substrate Velocity(cm/sec)	**15.5**	

Figure VIII.8 - Case #8 - Fluid H

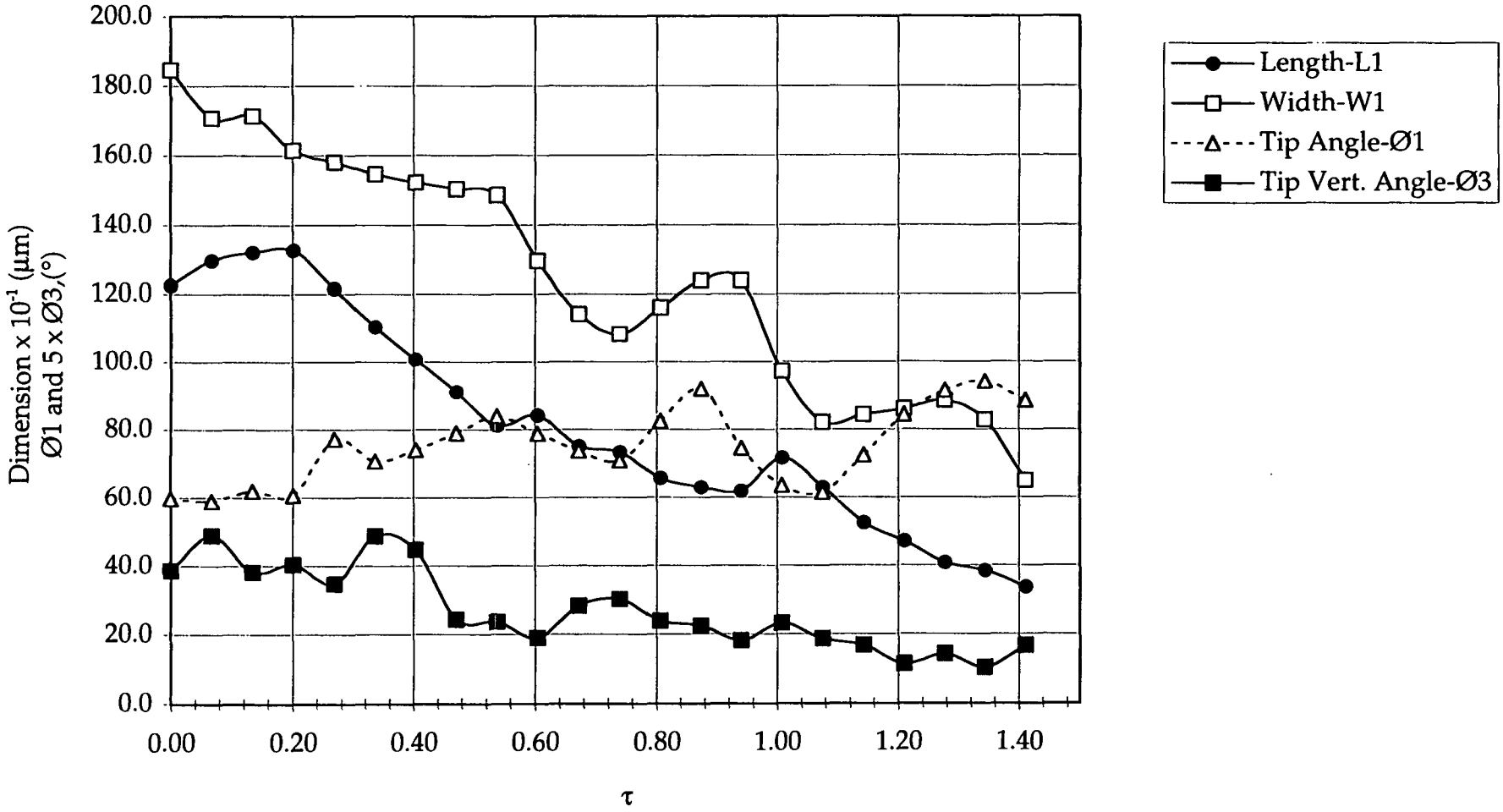

TABLE VIII.9 - Time vs. Length, Width, and Angle Data for Air Tongue - Fluid I

Experiment Code L07ICA2
Case #9 - Glycerin-water ≈ 58 cp
Film time from 189:07.695 to 189:07.713
Calibration Magnification (X) = 8.0
Distance between fringes (μm) 100.0

Time (ms)	Tau	L1 Length(μm)	W1 Width(μm)	L2 Length2(μm)	Tip Angle Ø1(°)	Base Angle Ø2(°)	Tip Vert. Angle Ø3(°)
697.0	0.000	668	4533	252	144.7	10.9	3.9
699.0	0.026	997	6575	318	135.0	14.3	3.3
701.0	0.052	1217	6650	176	125.5	14.3	2.9
703.0	0.078	1447	6629	285	116.8	20.0	4.2
705.0	0.104	1633	4416	318	108.0	17.9	5.0
707.0	0.130	1469	3528	428	102.6	17.3	2.8
709.0	0.156	1107	2897	504	103.4	16.1	3.6
711.0	0.182	476	1598	227	118.8	17.6	8.4
713.0	0.208	243	1150	87	138.2	11.2	14.8
Average		**1029**	**4220**	**288**	**121.4**	**15.5**	**5.4**
Standard Deviation		**478**	**2119**	**126**	**15.4**	**3.1**	**3.9**
Standard Error		**46.5%**	**50.2%**	**43.6%**	**12.7%**	**19.9%**	**71.9%**

Advancing Velocity(cm/min)	**713.5**	**R^2=0.9891**
(cm/sec.)	**11.9**	
Retracting Velocity(cm/min)	**1131.4**	**R^2=0.9628**
(cm/sec.)	**18.9**	
Substrate Velocity(cm/sec)	**36.2**	

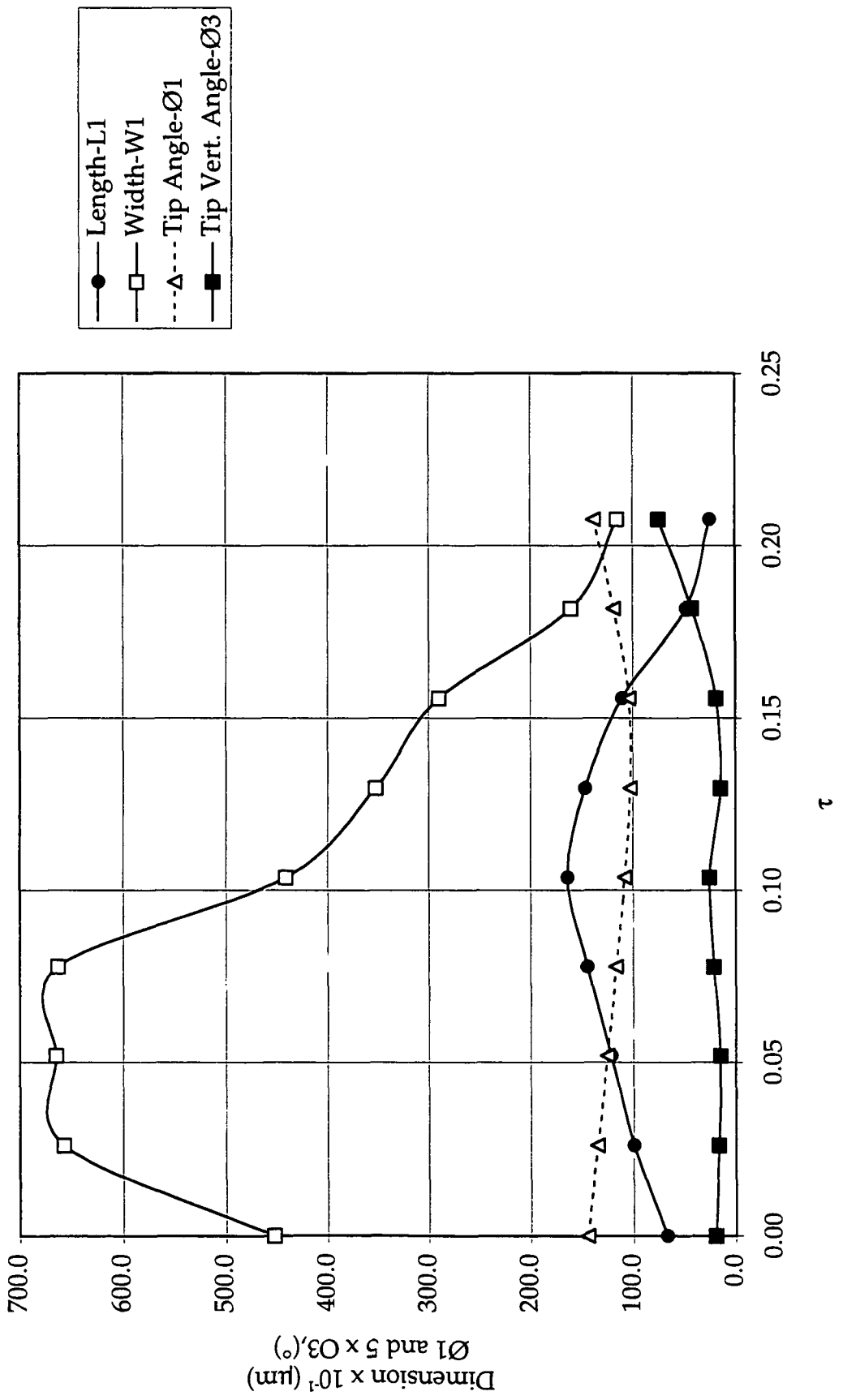

Figure VIII.9 - Case #9 - Fluid I

TABLE VIII.10 - Time vs. Length, Width, and Angle Data for Air Tongue - Fluid Y

Experiment Code G12YCA1
Case #10 - DC200 - 10 cs
Film time from 215:17.62 to 215:17.86
Calibration Magnification (X) = 8.0
Distance between fringes (μm) 100.0

Time (ms)	Tau	L1 Length(μm)	W1 Width(μm)	L2 Length2(μm)	Tip Angle Ø1(°)	Base Angle Ø2(°)	Tip Vert Angle Ø3(°)
62.0	0.0000	1902	5028	446	102.9	22.1	9.8
64.0	0.0118	1797	4440	603	102.8	22.8	13.5
66.0	0.0235	1534	4120	551	107.3	21.9	9.0
68.0	0.0353	1351	3993	643	114.5	20.6	12.0
70.0	0.0470	1167	4062	367	119.1	20.0	5.0
72.0	0.0587	1155	4697	341	128.6	13.8	8.9
74.0	0.0705	1128	4096	459	124.0	14.3	8.3
76.0	0.0822	1085	4014	489	124.1	15.8	6.3
78.0	0.0940	963	3919	529	128.0	16.1	6.4
80.0	0.1057	936	4622	448	137.1	13.9	6.3
82.0	0.1175	879	5173	381	142.5	12.9	6.2
84.0	0.1292	918	5133	485	141.2	14.0	6.5
86.0	0.1410	879	5837	302	146.3	9.5	10.8
	Average	**1207**	**4549**	**465**	**124.5**	**16.8**	**8.4**
	Standard Deviation	**344**	**597**	**101**	**14.8**	**4.2**	**2.6**
	Standard Error	**28.5%**	**13.1%**	**21.7%**	**11.9%**	**25.4%**	**31.0%**

Average Retraction Velocity (cm/min)	**245.2**	**R^2 =0.859**
(cm/sec)	**4.1**	
Retraction Velocity(62-74 ms) (cm/min)	**425.7**	**R^2 =0.924**
(cm/sec)	**7.1**	
Retraction Velocity(74-86 ms) (cm/min)	**125.0**	**R^2 =0.826**
(cm/sec)	**2.1**	
Substrate Velocity(cm/sec)	**60.0**	

Figure VIII.10 - Case #10 - Fluid Y

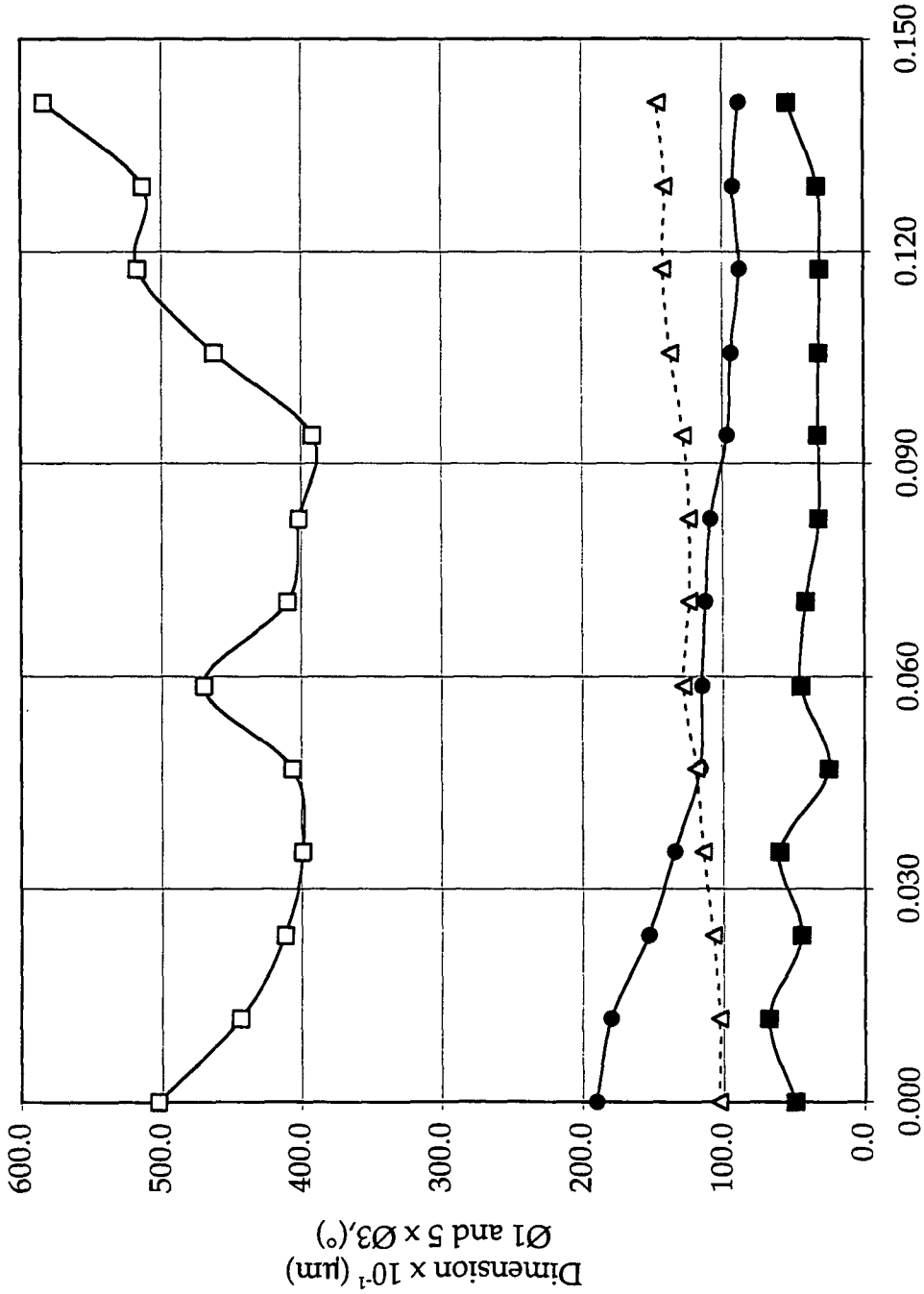

TABLE VIII.11 - Time vs. Length, Width, and Angle Data for Air Tongue - Fluid Z

Experiment Code U22ZCA1
Case #11 - DC200 - 20 cs Silicone Oil
Film time from 4:34.811 to 4:34.835
Calibration Magnification (X) = 8.0
Distance between fringes (μm) 200.0

Time (ms)	Tau	L1 Length(μm)	W1 Width (μm)	L2 Length2(μm)	Tip Angle Ø1(°)	Base Angle Ø2(°)	Tip Vert. Angle Ø3(°)
811	0.0000	6294	10496	1046	79.2	29.7	13.5
813	0.0203	5930	10090	1217	80.4	30.2	13.4
815	0.0407	5338	8278	1238	76.1	32.1	15.9
817	0.0610	4758	6976	1238	72.4	30.8	23.3
819	0.0813	4105	6203	1206	75.7	31.2	21.0
821	0.1016	3882	6378	874	79.2	29.0	19.9
823	0.1220	3414	5418	918	77.8	25.3	11.3
825	0.1423	2493	3234	657	66.1	31.3	19.2
827	0.1626	1786	2779	716	75.4	30.8	16.4
829	0.1830	1121	2046	641	83.1	26.9	12.5
831	0.2040	682	2165	421	114.4	18.0	12.8
833	0.2236	472	2350	236	137.0	10.0	*
835	0.2440	337	3049	170	157.1	6.6	*
Average		**3124**	**5343**	**814**	**90.3**	**25.5**	**16.3**
Standard Deviation		**2123**	**3006**	**378**	**27.9**	**8.5**	**8.7**
Standard Error		**68.0%**	**56.2%**	**46.4%**	**30.9%**	**33.4%**	**53.4%**

Retraction Velocity (cm/min)	**1625**	**R^2=0.988**
(cm/sec)	**27.1**	
Substrate Velocity(cm/min)	**34.8**	

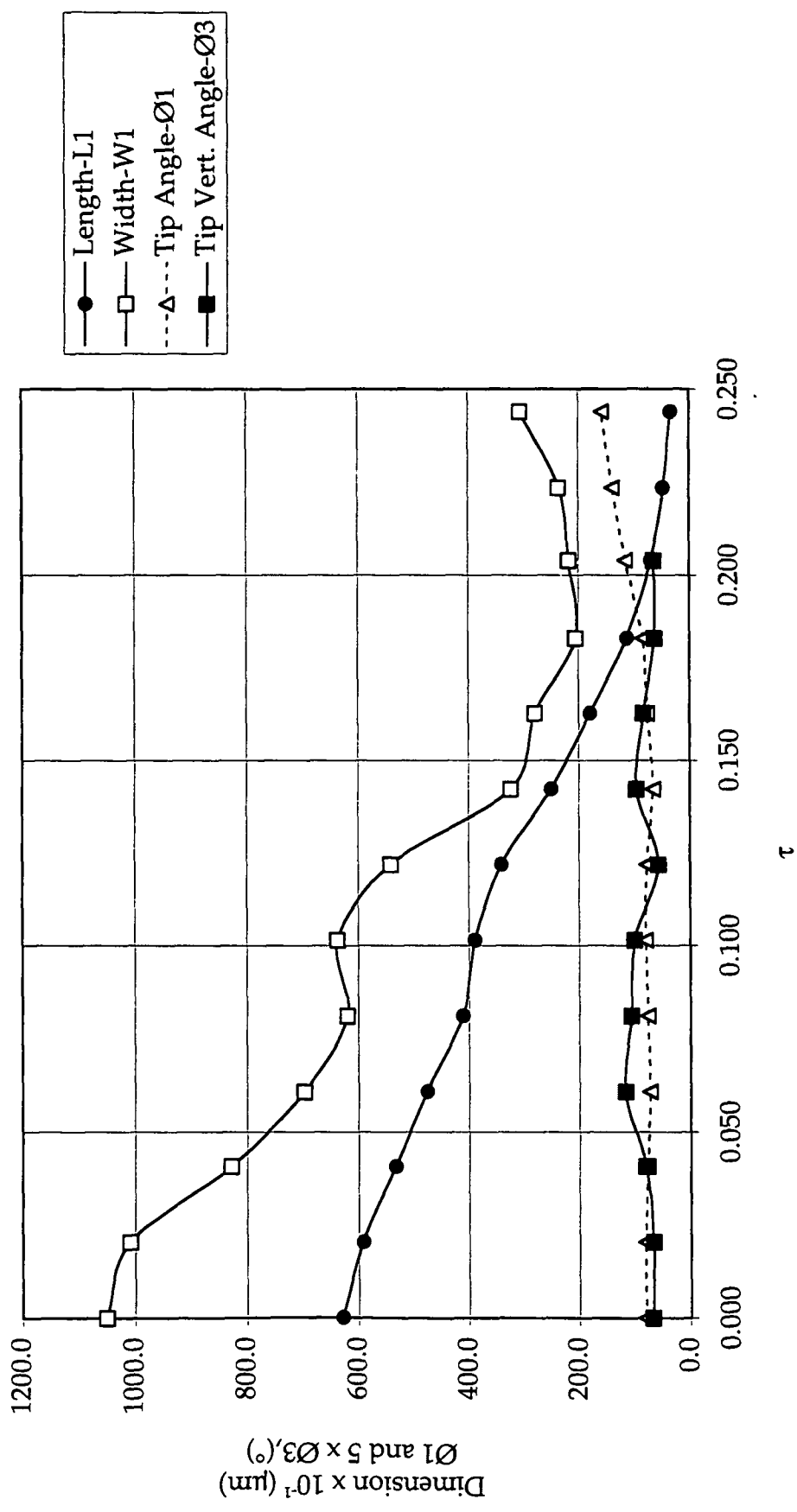

Figure VIII.11 - Case #11 - Fluid Z

TABLE VIII.12 - Time vs. Length, Width, and Angle Data for Air Tongue - Fluid Z

Experiment Code U22ZCA1
Case #12 - DC200 - 20 cs Silicone Oil
Film time from 4:32.098-4:32.167
Calibration Magnification (X) = 8.0
Distance between fringes (μm) 200.0

Time (ms)	Tau	L1 Length(μm)	W1 Width (μm)	L2 Length2(μm)	Tip Angle Ø1(°)	Base Angle Ø2(°)	Tip Vert. Angle Ø3(°)
142	0.0000	1866.3	7899	660.9	124.4	14.0	17.0
144	0.0203	2058.6	6533	795.9	115.1	15.6	15.8
146	0.0407	2031.7	6453	823.1	115.6	17.3	15.5
148	0.0610	1921.4	6051	686.1	115.5	17.0	17.3
150	0.0813	1893.9	6212	659.2	118.2	15.6	14.1
152	0.1016	1756.7	5784	714.1	117.8	17.7	9.9
155	0.1220	1565.3	5275	686.7	118.1	17.7	13.8
157	0.1423	1454.6	4846	577.0	118.9	13.9	14.6
159	0.1626	1146.8	3692	389.2	117.9	14.3	11.8
161	0.1830	1028.0	3586	401.3	121.7	14.4	8.9
163	0.2033	800.2	2920	348.3	122.9	15.3	8.2
165	0.2236	629.8	2616	274.1	127.3	13.2	9.7
167	0.2440	540.8	2573	244.6	136.0	11.0	10.4
169	0.2643	450.5	1867	219.3	130.8	11.7	*
171	0.2846	318.6	2457	177.9	151.1	8.8	*
Average		**1298**	**4584**	**511**	**123.4**	**14.5**	**12.8**
Standard Deviation		**629**	**1879**	**225**	**9.7**	**2.6**	**3.2**
Standard Error		**48.4%**	**41.0%**	**44.0%**	**7.9%**	**17.8%**	**24.8%**

Retraction Velocity (cm/min)	**391**	**R^2=0.946**
(cm/sec)	**6.5**	
Substrate Velocity(cm/min)	**34.8**	

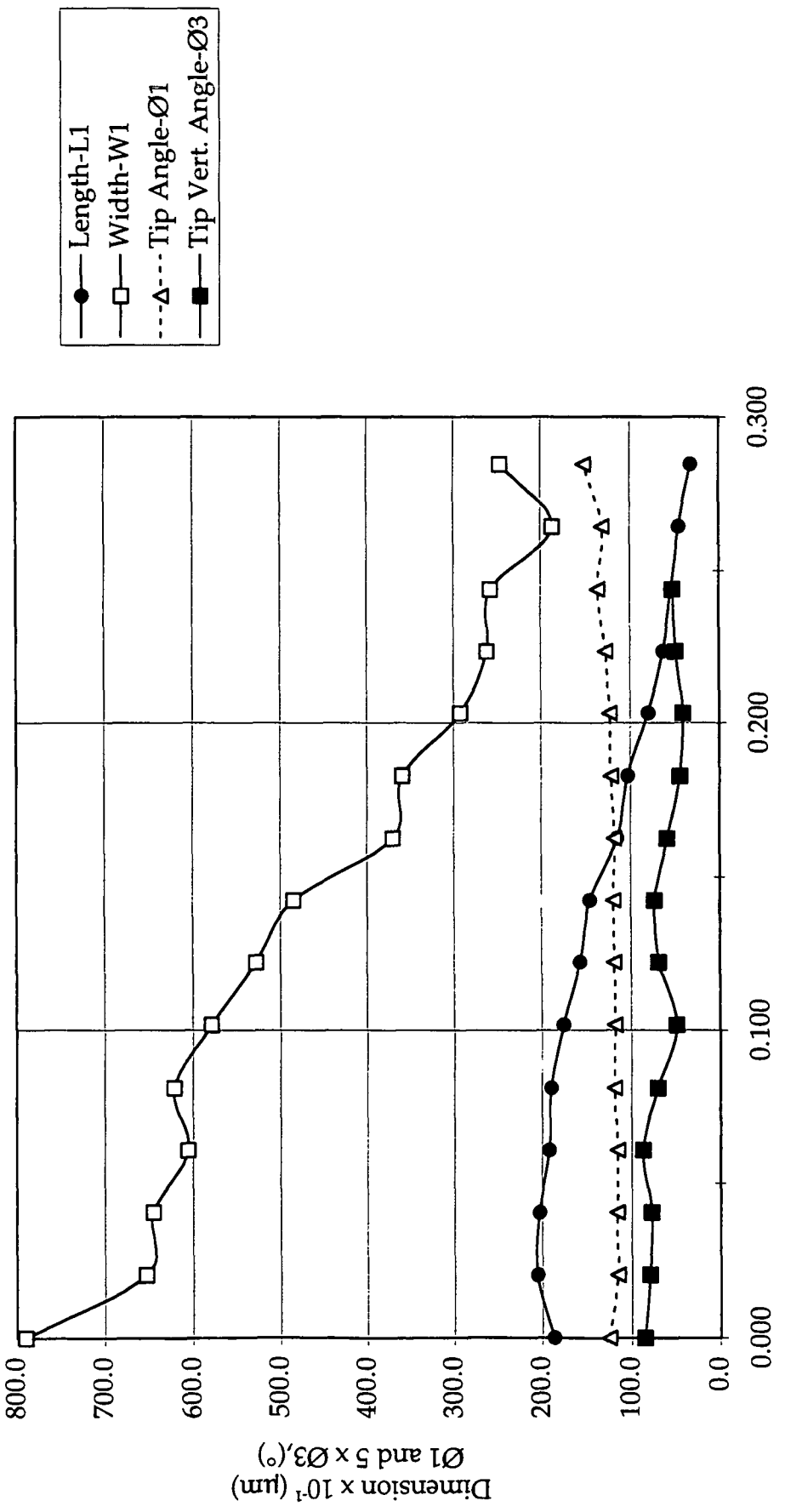

Figure VIII.12 - Case #12 - Fluid Z

Figure VII.13 - Input Data and Regression Model for Eq. [6.4] Section 6.4 from Data for Case #8.

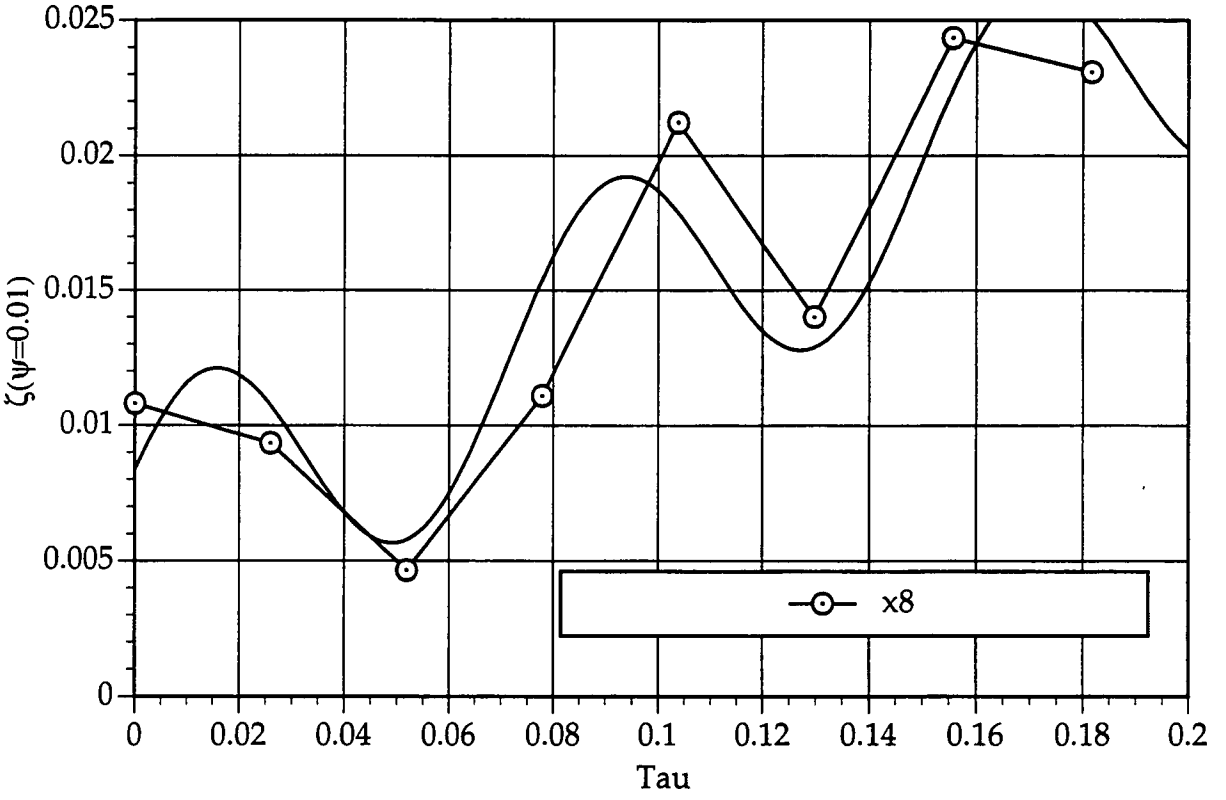

APPENDIX IX

SOLID AND LIQUID CONTACT ANGLE AND SURFACE ENERGY MEASUREMENTS

Appendix IX is designed to outline the theory behind the dispersion and nondispersion components of surface tension in appendix Section IX.1 and the technique used to measure them covered in appendix Section IX.2. The average measurements for the substrate are contained in appendix Section IX.3 while appendix Section IX.4 contains the liquid components. The remainder of the data files are given in appendix Section IX.5

IX.1 Solid and Liquid Dispersive and Nondispersive Components of Surface Tension

According to Fowkes (1972), the liquid surface tension or solid surface free energy can be expressed as the sum of the parts of a variety of interactions,

$$\gamma = \gamma^d + \gamma^i + \gamma^p + \gamma^h + \gamma^\pi + \gamma^{ad} + \gamma^e \qquad \text{[IX.1]}$$

where superscript d refers to London dispersion forces, i to induced dipole-dipole, p to dipole-dipole, h to hydrogen bonding, π to pi bonding, ad to acceptor-donor, and e to electrostatic interactions. This can be written in more practical terms by breaking the total surface tension into the nondispersion, superscript n, and dispersion components,

$$\gamma = \gamma^d + \gamma^n \qquad \text{[IX.2]}$$

The nondispersion component can also be referred to as the "polar" interaction (Berg 1993), and, if the same geometric mixing rule for the dispersion force interaction is assumed, the interfacial tension can be expressed as,

$$\gamma_{sl} = \gamma_s + \gamma_l - 2\sqrt{\gamma_s^d \gamma_l^d} - 2\sqrt{\gamma_s^n \gamma_l^n} \qquad [IX.3]$$

where the indices S and L (when used singly) refer to two immiscible phases in contact with their own vapor, and the index SL refers to two phases being in contact with each other after equilibrium (Janczuk, Wójcik, and Zdsiennicka 1993).

By using contact angle measurements and pairs of probes, γ^n and γ^d can be determined for many liquids and solids (Janczuk, Wójcik and Zdsiennicka, 1993). By assuming that the liquid film on the solid surface does not change its surface energy from the Young equation,

$$cos\theta_{eq} = \frac{\gamma_{sg} - \gamma_{sl}}{\gamma_{lg}} \qquad [IX.4]$$

where θ_{eq} represents the equilibrium contact angle between the solid and liquid and subscripts sg, lg, sl represent surface tensions of solid/gas, liquid/gas and solid/liquid respectively. The surface tension of γ_{lg} is approximately equal to the surface energy γ_l. Furthermore, if the gas which contacts the solid does not strongly adsorb to the solid surface $\gamma_{sg} \approx \gamma_s$ can also be used. Thus, the interfacial free energy can be then be rewritten as,

$$\gamma_l cos\theta_{eq} = -\gamma_l + 2\sqrt{\gamma_s^d \gamma_l^d} + 2\sqrt{\gamma_s^n \gamma_l^n} \qquad [IX.5]$$

By using apolar liquids, such as methylene iodide, which has $\gamma_l^n = 0$, the solid dispersion component, γ_s^d, can easily be calculated as:

$$\gamma_s^d = \frac{\gamma_l^2(cos\theta_{eq} + 1)^2}{4\gamma_l^d} \qquad [IX.6]$$

where l and s refer to the liquid and solid, respectively. Water has been studied extensively for the "polar" and dispersion components. By substituting the value for γ_s^d from the methylene iodide system, and measuring θ_{eq} of water against the solid substrate, the polar component, γ_s^n, of the solid surface free energy can be solved. A similar approach is use to evaluate the liquid γ_l^d and γ_l^n using surfaces with known energy components applied in this Appendix section IX.4.

Once the dispersion and nondispersion components of a solid surface have been determined, a common application is to match the "polarity" of the adhesive and adherent to optimize adhesion (Janczuk, Wójcik, and Zdsiennicka 1993). An example of this type of "polarity matching" was used by Su (1994) to study the printability ("orange peel appearance") of different coatings with water-based ink formulations[1]. Ström et al. (1990) used γ_s^d to characterize the degree of treatment a surface had received for a wetting kinetics study. Ishizaki et al. (21) attempted to correlate the air entrainment velocity, U_{ae}, with γ_s^d in a gelatine/water coating system. They were coating on polyethylene terephtalate, triacetyl cellulose, and polyethylene. The data revealed only a slight difference in U_{ae}.

---

[1] Su(1994) mixed the disepersion and polar componenents of water, p.211

IX.2 Technique

The contact angles for uncoated PET, coated PET, cellulose acetate and paper were measured with a modified goniometer instrument. The camera method in Appendix A.2.3 of Tappi Test Method T 458 om-89 was used. A COHU 4910 CCD video camera with a 25 mm f.l. lens and 15 mm of extension tube was used to magnify the 4 µl drop delivered by a Rainin 1-100 µl automatic pipette. A Horita time code generator superimposed a time code for each field of video displayed and thus permitted accurate identification in the 5 second time specified by T458 om-89 for measuring the apparent contact angle. The droplet image at 5 seconds was digitized (8-bit compression) with the DT2953 frame grabber board and the apparent contact angle measured with OPTIMAS V4.1 image analysis software. By using a 4X zoom on the left and right hand sides of the droplet, the precision of the test was increased to ±0.01° for the angle measured.

For the initial sample, uncoated PET (Melinex™ 454), 30 data individual contact angles were measured. This was to determine the reproducibility of the method. Occasionally, excess liquid would be left at the end of the pipette tip, adding to the volume of the droplet being dispensed. The effective droplet volume was greater than 4 µl. T 458 om-89 specifies that the volume should be within ±0.4 µl. This was not the case for droplets that had combined. By measuring the diameter of

the surface of contact of the droplet[2] for all measurements, it was found that a bimodal distribution existed and all the contact angles for droplets above a certain diameter were discarded.

IX.3 Measurements and Results for Substrate Surface Energy

Based on the error analysis, it can be seen that uncoated PET, and the paper base sheet have a zero polar component, while the coated PET has a slight polar component. The highest polar component as expected is from the highly

Table IX.1. Surface energy (dynes/cm) data for substrates.

	Total±Error	γ_s^d Dispersive±Error	γ_s^n Polar±Error
coated PET	45.8±3.1	35.0±1.1	10.8±2.0
uncoated PET	53.0±2.5	48.8±0.6	4.2±1.9
cellulose acetate	71.3±2.6	37.6±1.4	33.7±1.1
paper	42.0±3.9	38.7±1.7	3.3±2.2

hydrophilic regenerated cellulose, cellulose acetate. The experimental values of γ_s for uncoated PET was compared with Wu's (1978) data at γ_s = 42.1 dynes/cm for polyetheleneterephthlate. The published data for cellulose acetate from Wu (1975) is at 45.9 dynes/cm with 29.6% polar fraction which is lower than our measured value for cellulose acetate of γ_s=71.3 dynes/cm and 47.3% polar fraction. It is possible that the softening agents change the surface energy. Since the adhesion pretreatment for coated PET is proprietary, we do not have a comparison database.

---

[2] See Fig. 4 in T 458 om89 for definition.

IX.4 Liquid Equilibrium Contact Angles and Dispersion and Polar Components

The static contact angles of the silicone oils and glycerol were measured on both coated PET and cellulose acetate. The liquid dispersive and polar components were calculated using the previously determined values of γ_s^d and γ_s^n and assuming that $\gamma_l=\gamma_l^d+\gamma_l^n$ is not known a priori. The simultaneous equations can therefore be solved for the solid surface components. The calculated values of γ_l^d and γ_l^n are normalized so that their sum equals γ_l. Table IX.2 contains a summary of the data with $\gamma_l^n \approx 0$ for the silicone oils which is in accord with their hydrocarbon nature. The dispersive and polar components for glycerol very different. For the silicone oils, the static contact angle, $\theta_{eq} \pm \sigma$, ranged from 9.4 to 32.3° with very little difference between substratescoated PET and cellulose acetate. Glycerol had a value of 29.3° on cellulose acetate and 72.6° on the coated PET indicative of the polar nature of glycerol.

Table IX.2. Static contact angle and liquid surface tension components.

Test Fluid	μ(cp.) @ 23.9°C	cellulose acetate θ_{eq}(°)	coated PET-A θ_{eq}(°)	γ_l^d (dynes/cm)	γ_l^n (dynes/cm)
DC200-20	20.3	9.4±2.9	9.6±2.4	20.06	0.14
DC200-100	105.1	14.4±1.7	14.1±2.8	20.84	0.16
(1)DC200-200	201.5	16.2±2.3	17.2±1.2	20.91	0.13
(2)DC200-200	201.5	18.1±2.6	18.3±3.2	20.89	0.15
DC200-350	342.7	23.9±2.7	20.9±1.7	21.45	0.25
DC200-545	503.3	21.6±1.8	20.8±2.4	21.82	0.18
DC200-1000	949.5	30.6±3.9	32.3±2.1	22.30	0.10
Glycerol	840.2	29.3±3.4	72.6±2.9	8.22	41.25

IX.5 Data Tables

Tables IX.3 - IX.6 contain the left and right contact angles on coated PET, uncoated PET, cellulose acetate and paper measured for each drop along with the base length in uncalibrated units. The left and right angles were averaged, thus eliminating any tilt errors that may have occurred from the goniometer or imaging instrumentation.

Tables IX.7 - IX.14 are the calculated spreadsheet files for silicone oils and glycerol to evaluate the polar and dispersive energies. Prior to normalization the sum of the components is greater than the measured total surface tension which violates Fowkes (1972) assumption.

TABLE IX.3 - Contact Angle and Surface Energy Data for uncoated PET-A

Surface Energy in dynes/cm

Fluid	Total Surface Energy	Dispersion Component	Polar Component	Average Contact Angle°	Standard Deviation (±°)
Water	72.8	21.8	51	66.17	4.46
Methylene iodide	50.8	50.8		48.60	2.05
Melinex 454™					
Surface Energy	45.8	35.0	10.8		
Errors	3.1	1.1	2.0		

Water Contact Angle

Original Data

	Left(°)	Right(°)	Base Length
P1D1	71.0	114.2	15.8
P1D2	65.2	117.3	17.1
P1D3	65.6	123.5	16.7
P1D3	66.0	117.3	16.6
P1D4	67.7	119.0	16.8
P1D5	67.8	125.7	16.8
P1D5	63.2	124.7	17.0
P1D6	62.4	121.6	16.1
P1D7	68.1	115.4	17.4
P1D8	65.3	115.8	16.3
P1D9	70.7	116.4	16.6
P1D10	62.5	120.1	16.2
P1D11	67.6	113.5	15.6
P1D12	68.4	119.0	15.0
P1D13	68.5	119.1	16.4
P1D14	65.3	118.4	17.4
P1D15	71.0	112.6	16.3
P1D16	70.9	113.6	16.9
PID17	65.1	116.3	15.6
P1D18	72.4	111.5	16.0
P1D19	73.4	109.6	16.0
P1D20	80.8	109.1	15.7
P2D1	68.9	112.1	16.8
P2D2	70.5	114.2	16.9
P2D3	66.0	115.0	17.0
P2D4	66.0	115.6	17.0
P2D5	68.1	115.6	16.7
P2D6	70.4	116.4	17.1
P2D7	71.6	110.8	16.5
P2D8	71.6	110.3	15.5
P2D9	68.5	114.5	16.2
P2D10	69.2	115.9	16.9
P2D11	69.7	118.0	17.3
Average	68.5	63.9	
Standard Deviation	3.6	4.1	

Total Average
66.2
4.5

Methylene Iodide Contact Angle Data

Original Data

	Left(°)	Right(°)	Base Length
P1D1	45.4	134.3	19.9
P1D2	51.7	131.3	20.0
P1D3	49.5	132.1	20.3
P1D4	50.5	128.8	19.4
P2D5	47.0	132.1	18.1
P1D5	49.9	133.5	20.5
P1D6	50.1	133.5	18.3
P1D7	49.5	130.7	20.8
P1D8	48.1	128.9	19.9
P1D9	49.0	133.0	19.5
P1DA	44.5	132.7	17.6
P1DB	45.3	133.0	23.1
P1DC	51.2	130.9	14.8
P2D2	48.0	132.2	21.6
P2D3	46.4	134.7	21.4
P2D4	47.4	133.1	18.9
P2D5	48.1	127.2	19.5
P2D6	47.9	131.3	20.0
P2D7	47.5	127.1	20.0
P2D8	49.8	128.2	19.8
P2D9	50.0	127.2	19.1
P2DA	41.2	137.3	22.1
P3D1	49.7	130.7	18.9
P3P2	49.0	132.1	19.7
P3P3	48.2	131.4	20.2
P3D4	49.4	135.2	19.3
P3D5	31.9	141.6	22.6
P3D6	32.4	148.2	23.5
P3D7	45.7	134.1	19.5
P3D8	35.1	143.2	23.0
P3D9	46.5	131.4	18.8
P3DA	51.4	129.3	20.3
Average	46.8	47.2	
Standard Deviation	5.0	4.5	

Total Average
47.0
4.7

TABLE IX.3(Continued) - Contact Angle and Surface Energy Data for uncoated PET-A

Methylene Iodide Contact Angle Data
Bimodal Removed Data

	Left(°)	Right(°)	Base Length
P1D1	45.4	134.3	19.9
P1D2	51.7	131.3	20.0
P1D3	49.5	132.1	20.3
P1D4	50.5	128.8	19.4
P2D5	47.0	132.1	18.1
P1D5	49.9	133.5	20.5
P1D6	50.1	133.5	18.3
P1D7	49.5	130.7	20.8
P1D8	48.1	128.9	19.9
P1D9	49.0	133.0	19.5
P1DA	44.5	132.7	17.6
P1DC	51.2	130.9	14.8
P2D4	47.4	133.1	18.9
P2D5	48.1	127.2	19.5
P2D6	47.9	131.3	20.0
P2D7	47.5	127.1	20.0
P2D8	49.8	128.2	19.8
P2D9	50.0	127.2	19.1
P3D1	49.7	130.7	18.9
P3P2	49.0	132.1	19.7
P3P3	48.2	131.4	20.2
P3D4	49.4	135.2	19.3
P3D7	45.7	134.1	19.5
P3D9	46.5	131.4	18.8
P3DA	51.4	129.3	20.3
P3DC	47.6	131.4	18.9
P3DD	44.9	130.2	17.4
P3DE	49.5	132.8	17.5
P3DF	46.9	132.2	17.9
	48.5	48.7	
	1.9	2.2	

Total Average
48.6
2.0

TABLE IX.4 - Contact Angle and Surface Energy Data for uncoated PET-B

Surface Energy in dynes/cm

Fluid	Total Surface Energy	Dispersion Component	Polar Component	Average Contact Angle°	Standard Deviation (±°)
Water	72.8	21.8	51	72.54	3.57
Methylene iodide	50.8	50.8		16.17	2.54
Melinex 453™ Untreated Side					
Surface Energy	53.0	48.8	4.2		
Errors	2.5	0.6	1.9		

Water Contact Angle

Original Data

	Left(°)	Right(°)	Base Length
1	71.1	111.5	12.4
2	68.9	111.3	12.3
3	70.4	109.4	12.5
4	72.6	110.4	12.4
5	69.9	109.8	12.3
6	75.6	109.3	12.6
7	72.4	107.8	12.4
8	70.5	113.1	12.2
9	73.9	107.7	12.1
10	71.3	108.5	12.4
11	74.4	105.0	12.4
12	70.2	106.6	12.5
13	74.3	106.6	12.3
14	70.1	106.0	12.4
15	76.7	109.0	12.5
16	85.9	100.9	12.4
17	74.2	103.2	11.7
Average	73.1	72.0	12.2
Standard Deviation	4.0	3.1	

Total Average
72.5
3.6

Methylene Iodide Contact Angle Data

Original Data

	Left(°)	Right(°)	Base Length
1	21.5	158.8	18.4
2	14.3	162.9	18.1
3	11.9	164.2	22.4
4	13.7	163.2	18.2
5	17.2	162.0	18.3
6	18.3	161.4	20.7
7	12.5	165.5	20.9
8	10.9	165.2	19.9
9	15.0	163.7	21.1
10	13.4	162.1	19.5
11	12.4	164.1	20.6
12	17.7	162.9	17.0
13	18.5	159.7	14.7
14	17.0	164.7	20.3
15	14.2	162.9	20.2
16	13.0	163.3	18.9
17	14.6	161.3	20.1
18	15.6	161.8	20.2
Average	15.1	17.3	
Standard Deviation	2.8	1.8	

Total Average
16.2
2.5

TABLE IX.5 - Contact Angle and Surface Energy Data for Cellulose Acetate

Surface Energy in dynes/cm

Fluid	Total Surface Energy	Dispersion Component	Polar Component	Average Contact Angle°	Standard Deviation (±°)
Water	72.8	21.8	51	22.33	5.17
Methylene iodide	50.8	50.8		43.92	2.72
Extruded Viscose					
Surface Energy	71.3	37.6	33.7		
Errors	2.6	1.4	1.1		

Water Contact Angle

Original Data

	Left(°)	Right(°)	Base Length
1	18.6	163.5	22.2
2	19.4	159.5	21.7
3	17.0	163.5	24.1
4	18.1	165.7	24.6
5	18.1	162.2	23.7
6	23.1	159.0	20.9
7	21.2	154.6	18.5
8	31.4	153.1	18.5
9	29.8	143.4	18.8
10	25.1	153.9	15.8
11	25.3	155.0	16.9
12	21.9	156.8	18.2
13	22.6	160.9	19.9
Average	22.4	22.2	
Standard Deviation	4.5	5.9	

Total Average
22.3
5.2

Methylene Iodide Contact Angle Data

Original Data

	Left(°)	Right(°)	Base Length
1	45.1	135.2	17.1
2	45.1	129.4	17.2
3	42.2	135.5	15.7
4	45.3	135.1	14.9
5	44.7	139.0	15.6
6	46.1	135.5	15.4
7	41.8	135.6	15.6
8	42.4	133.4	15.1
9	43.1	139.5	14.1
10	42.9	134.5	14.7
11	40.8	138.9	17.2
12	41.7	134.1	14.9
13	41.7	134.9	14.9
14	45.7	135.5	15.2
15	47.2	138.2	14.7
16	41.6	138.7	12.7
17	47.9	133.3	13.5
18	50.4	134.9	14.6
19	43.0	140.3	15.9
20	41.6	141.9	17.0
Average	44.0	43.8	
Standard Deviation	2.6	2.9	

Total Average
43.9
2.7

TABLE XL6 - Contact Angle and Surface Energy Data for Paper Substrate

Surface Energy in dynes/cm

Fluid	Total Surface Energy	Dispersion Component	Polar Component	Average Contact Angle°	Standard Deviation (±°)
Water	72.8	21.8	51	81.05	4.42
Methylene iodide	50.8	50.8		41.83	3.25
LWC Base					
Surface Energy	42.0	38.7	3.3		
Errors	3.9	1.7	2.2		

Water Contact Angle

	Original Data Left(°)	Right(°)	Base Length
1	85.2	103.9	15.5
2	81.4	101.9	12.4
3	74.3	107.4	12.8
4	82.7	101.4	12.4
5	80.1	101.7	13.7
6	86.7	97.0	11.6
7	93.9	92.9	13.1
8	83.6	96.4	11.7
9	77.6	103.9	11.7
10	78.8	106.2	11.6
11	77.3	102.7	11.2
12	79.7	101.9	11.1
13	83.4	98.9	12.3
14	87.0	97.3	11.4
15	83.4	99.0	12.4
16	83.3	101.1	10.9
17	86.2	101.2	10.2
18	82.8	94.5	10.0
	82.6	79.5	
	4.5	3.9	

Total Average
81.1
4.4

Methylene Iodide Contact Angle Data

	Original Data Left(°)	Right(°)	Base Length
P1D1	42.8	38.9	14.2
P1D2	41.3	43.6	13.5
P1D3	46.2	45.3	11.8
P1D4	44.0	44.1	12.9
P2D5	36.3	44.0	14.0
P1D5	36.8	40.2	17.0
P1D6	44.1	40.0	11.3
P1D7	45.2	41.4	12.9
P1D8	37.9	38.2	11.7
P1D9	45.5	44.1	13.7
P1DA	42.7	44.8	12.4
P1DC	42.8	41.8	11.5
P2D4	43.3	40.9	12.4
P2D5	38.8	34.7	14.8
P2D6	39.3	44.6	13.3
P2D7	44.0	39.3	11.8
P2D8	37.2	47.5	12.4
P2D9	38.9	36.5	12.2
P3D1	43.8	45.7	13.5
P3P2	40.8	46.0	12.3
	41.6	42.1	
	3.1	3.4	

Total Average
41.8
3.2

TABLE IX.7 - Contact Angle and Surface Tension Components for DC200-20 cs Silicone Oil

DC200-20 Silicone Oil
Surface Tension @23.9°C 20.2 dynes/cm

Solid Surface	Total Surface Energy	Dispersion Component	Polar Component	Average Contact Angle°	Standard Deviation (±°)
PUT 002	**71.3**	**37.6**	**33.7**	**9.41**	2.85
Melinex 454™	**45.8**	**35**	**10.8**	**9.63**	2.36

A= 1.99 D= 1.99
B= 12.26 E= 11.83
C= 11.61 F= 6.57

Common factor	-0.56	Normalized Components	
Surface tension(d)=	**31.77**	**20.06**	**dynes/cm**
Surface tension(n)=	**0.23**	**0.14**	**dynes/cm**

Liquid on CEL Substrate

	Original Data Left(°)	Right(°)	Base Length
P1D1	11.2	172.6	19.1
P1D2	11.5	172.7	19.0
P1D3	8.7	174.3	18.9
P1D3	13.8	174.7	18.1
P1D4	11.5	173.6	18.8
P1D5	14.6	172.7	18.5
P1D5	11.8	172.4	19.0
P1D7	11.5	172.5	19.0
P1D8	12.3	172.0	18.5
Average	11.9	7.0	
Standard Deviation	1.7	0.9	

Total Average
9.41
2.85

Liquid on PET-B Substrate

	Original Data Left(°)	Right(°)	Base Length
P1D1	9.4	6.6	24.3
P1D2	10.2	6.8	21.7
P1D3	9.4	8.3	20.5
P1D4	9.3	7.7	22.0
P2D5	14.9	7.9	20.3
P1D5	10.4	9.4	19.5
P1D6	7.4	12.9	19.8
P1D7	10.0	11.3	19.7
P1D8	10.8	10.5	20.7
P1D9	7.8	9.3	21.0
P1DA	10.0	7.8	20.5
P1DB	15.9	7.0	20.8
Average	10.5	8.8	
Standard Deviation	2.5	2.0	

Total Average
9.63
2.36

TABLE XL8 - Contact Angle and Surface Tension Components for DC20-100 cs Silicone Oil

DC200-100 Silicone Oil

Surface Tension @23.9°C 21 dynes/cm

Solid Surface	Total Surface Energy	Dispersion Component	Polar Component	Average Contact Angle°	Standard Deviation (±°)
PUT 002	**71.3**	**37.6**	**33.7**	**14.43**	1.71
Melinex 454™	**45.8**	**35**	**10.8**	**14.14**	2.84

A= 1.97 D= 1.97

B= 12.26 E= 11.83

C= 11.61 F= 6.57

Common factor	-0.57	**Normalized Components**	
Surface tension(d)=	**32.19**	**20.84**	**dynes/cm**
Surface tension(n)=	**0.24**	**0.16**	**dynes/cm**

CEL Contact Angle Data

	Original Data Left(°)	Right(°)	Base Length
P1D1	14.4	163.3	17.3
P1D2	14.6	167.1	16.3
P1D3	17.1	165.5	17.3
P1D3	15.8	165.7	17.2
P1D4	16.9	165.3	16.3
P1D5	15.2	165.8	17.2
P1D5	15.4	166.5	16.7
P1D6	14.8	165.6	13.1
P1D7	16.5	166.3	16.3
P1D8	14.7	168.9	14.4
P1D9	14.4	167.4	14.9
P1D10	16.5	168.8	16.1
P1D11	14.5	169.4	16.6
	15.4	13.4	
	1.0	1.7	

Total Average

14.43

1.71

PET-A Contact Angle Data

	Original Data Left(°)	Right(°)	Base Length
P1D1	11.8	6.3	17.1
P1D2	11.2	10.3	16.4
P1D3	14.2	11.6	17.2
P1D4	14.6	13.5	16.2
P2D5	17.1	17.3	14.6
P1D5	18.1	12.8	17.1
P1D6	17.8	14.6	16.9
P1D7	15.9	12.8	17.4
P1D8	16.1	11.1	16.3
P1D9	18.7	14.5	16.7
P1DA	16.1	13.8	17.5
P1DB	14.5	13.5	16.6
P1DC	17.0	12.5	17.8
	15.6	12.7	
	2.3	2.6	

Total Average

14.14

2.84

TABLE IX.9 - Contact Angle and Surface Tension Components for DC200-200 cs Silicone Oil

DC200-200 Silicone Oil
Surface Tension @23.9°C 21.04 dynes/cm

Solid Surface	Total Surface Energy	Dispersion Component	Polar Component	Average Contact Angle°	Standard Deviation (±°)
PUT 002	**71.3**	**37.6**	**33.7**	**16.23**	**2.34**
Melinex 454™	**45.8**	**35**	**10.8**	**17.20**	**1.25**

A= 1.96 D= 1.96
B= 12.26 E= 11.83
C= 11.61 F= 6.57

Common factor	-0.59	Normalized Components	
Surface tension(d)=	**33.01**	**20.91**	**dynes/cm**
Surface tension(n)=	**0.21**	**0.13**	**dynes/cm**

CEL Contact Angle Data

	Original Data Left(°)	Right(°)	Base Length
P1D1	15.8	163.1	17.3
P1D2	19.4	158.3	16.3
P1D3	14.5	160.1	17.3
P1D3	18.1	163.0	17.2
P1D4	16.6	164.3	16.3
P1D5	18.9	166.5	17.2
P1D5	15.9	166.2	16.7
P1D6	15.9	164.2	13.1
P1D7	16.4	162.6	16.3
P1D8	16.3	163.3	14.4
P1D9	17.5	163.7	14.9
P1D10	13.2	162.5	16.1
P1D11	18.1	160.8	16.6
P1D12	18.4	164.6	16.5
P1D13	15.1	166.4	16.4
P1D14	12.3	171.4	16.8
P1D15	16.1	163.1	16.7
P1D16	12.6	164.8	17.0
PID17	16.3	162.6	16.5
P1D18	16.3	163.0	17.0
	16.2	16.3	
	2.0	2.7	

Total Average
16.23
2.34

PET-A Contact Angle Data

	Left(°)	Right(°)	Base Length
P1D1	15.4	15.8	17.1
P1D2	16.4	17.6	16.4
P1D3	16.6		17.2
P1D4	16.9	16.4	16.2
P2D5	16.4	16.3	14.6
P1D5	17.3	17.3	17.1
P1D6	18.5	18.9	16.9
P1D7	17.1	16.5	17.4
P1D8	17.7	16.9	16.3
P1D9	15.9	17.0	16.7
P1DA	17.0	17.3	17.5
P1DB	19.7	18.7	16.6
P1DC	17.8	17.0	17.8
P2D2	16.1	16.6	16.5
P2D3	19.6	19.5	17.5
P2D4	18.9	18.5	17.5
P2D5	16.7	16.4	16.9
P2D6	14.2	18.1	17.5
	17.1	17.3	
	1.4	1.1	

Total Average
17.20
1.25

TABLE IX.10 - Contact Angle and Surface Tension Components for DC200-200 cs Silicone Oil

DC200-200 Silicone Oil (Repeat)

Surface Tension @23.9°C 21.04 dynes/cm

Solid Surface	Total Surface Energy	Dispersion Component	Polar Component	Average Contact Angle°	Standard Deviation (±°)
PUT 002	**71.3**	**37.6**	**33.7**	**18.14**	1.78
Melinex 454™	**45.8**	**35**	**10.8**	**18.32**	2.83

A= 1.95 D= 1.95

B= 12.26 E= 11.83

C= 11.61 F= 6.57

Common factor	-0.59	**Normalized Components**	
Surface tension(d)=	**32.99**	**20.89**	**dynes/cm**
Surface tension(n)=	**0.24**	**0.15**	**dynes/cm**

PUT 002 Contact Angle Data

	Original Data Left(°)	Right(°)	Base Length
P1D1	22.2	162.2	17.3
P1D2	18.3	164.9	16.3
P1D3	15.5	162.3	17.3
P1D3	19.6	164.4	17.2
P1D4	19.1	164.0	16.3
P1D5	20.4	163.6	17.2
P1D5	19.3	164.3	16.7
P1D6	20.6	162.1	13.1
P1D7	23.7	160.8	16.3
P1D8	17.1	164.6	14.4
P1D9	17.7	163.3	14.9
P1D10	20.2	161.5	16.1
	19.5	16.8	
	2.2	1.3	

Methylene Iodide Contact Angle Data

	Left(°)	Right(°)	Base Length
P1D1	21.8	17.8	17.1
P1D2	24.3	18.1	16.4
P1D3	20.0	16.0	17.2
P1D4	18.4	17.5	16.2
P2D5	20.3	21.5	14.6
P1D5	15.1	17.0	17.1
P1D6	25.7	17.0	16.9
P1D7	19.9	13.9	17.4
P1D8	22.1	15.0	16.3
P1D9	15.9	13.0	16.7
P1DA	15.4	19.0	17.5
P1DB	18.1	16.6	16.6
	19.8	16.9	
	3.4	2.3	

TABLE XI.11 - Contact Angle and Surface Tension Components for DC200-350 cs

DC200-350 Silicone Oil
Surface Tension @23.9°C 21.7 dynes/cm

Solid Surface	Total Surface Energy	Dispersion Component	Polar Component	Average Contact Angle°	Standard Deviation (±°)
PUT 002	**71.3**	**37.6**	**33.7**	**23.93**	2.72
Melinex 454™	**45.8**	**35**	**10.8**	**20.94**	1.67

A= 1.91 D= 1.93
B= 12.26 E= 11.83
C= 11.61 F= 6.57

Common factor	-0.58	Normalized Components
Surface tension(d)=	**32.30**	**21.45** **dynes/cm**
Surface tension(n)=	**0.38**	**0.25** **dynes/cm**

CEL Contact Angle Data

Original Data

	Left(°)	Right(°)	Base Length
P1D1	19.7	154.8	17.3
P1D2	22.4	154.0	16.3
P1D3	26.3	152.5	17.3
P1D3	23.8	159.0	17.2
P1D4	21.6	155.9	16.3
P1D5	22.4	152.6	17.2
P1D5	25.5	153.4	16.7
P1D6	24.0	155.4	13.1
P1D7	24.0	155.9	16.3
P1D8	20.9	155.7	14.4
P1D9	24.7	155.9	14.9
P1D10	25.2	156.7	16.1
P1D11	21.8	149.8	16.6
P1D12	20.9	154.1	16.5
P1D13	27.9	156.5	16.4
P1D14	17.6	160.6	16.8
	23.0	24.8	
	2.7	2.6	

Total Average
23.93
2.72

PET-A Contact Angle Data

	Left(°)	Right(°)	Base Length
P1D1	20.6	19.8	8.2
P1D2	19.1	22.0	9.0
P1D3	19.6	23.0	9.9
P1D4	19.2	23.1	9.6
P2D5	21.1	24.7	9.9
P1D5	22.3	22.2	9.4
P1D6	19.9	22.1	10.0
P1D7	23.1	19.9	9.6
P1D8	21.7	24.3	10.2
P1D9	19.8	20.9	9.0
P1DA	19.6	21.3	8.5
P1DB	18.5	21.0	9.4
P1DC	17.8	21.3	9.3
P2D2	20.2	19.1	9.2
P2D3	19.9	21.3	9.0
	20.2	21.7	
	1.4	1.6	

Total Average
20.94
1.67

TABLE IX.12 - Contact Angle and Surface Tension Components for DC200-545 cs Silicone Oil

DC200-545 Silicone Oil
Surface Tension @23.9°C 22 dynes/cm

Solid Surface	Total Surface Energy	Dispersion Component	Polar Component	Average Contact Angle°	Standard Deviation (±°)
PUT 002	**71.3**	**37.6**	**33.7**	**21.58**	1.71
Melinex 454™	**45.8**	**35**	**10.8**	**20.84**	2.43

A= 1.93 D= 1.93
B= 12.26 E= 11.83
C= 11.61 F= 6.57

Common factor	-0.59	Normalized Components	
Surface tension(d)=	**33.17**	**21.82**	**dynes/cm**
Surface tension(n)=	**0.27**	**0.18**	**dynes/cm**

CEL Contact Angle Data

	Original Data Left(°)	Right(°)	Base Length
P1D1	23.5	157.7	12.6
P1D2	21.2	157.1	11.9
P1D3	22.6	158.4	14.2
P1D3	22.5	158.3	14.4
P1D4	21.9	158.3	14.8
P1D5	23.0	157.5	14.9
P1D5	21.9	157.1	15.4
P1D6	23.0	157.5	14.7
P1D7	19.3	161.2	15.2
P1D8	20.0	159.3	15.4
P1D9	21.4	156.7	15.1
P1D10	20.8	159.8	10.3
P1D11	19.4	160.9	11.0
P1D12	20.1	160.6	11.0
P1D13	17.9	159.0	11.0
P1D14	22.4	158.0	14.7
P1D15	22.5	158.3	15.0
P1D16	27.1	157.9	15.5
	21.7	21.4	
	2.0	1.3	

Total Average
21.6
1.7

PET-A Contact Angle Data

	Left(°)	Right(°)	Base Length
P1D1	22.6	17.1	3.5
P1D2	20.5	17.8	3.0
P1D3	16.9	17.3	7.3
P1D4	19.6	16.5	7.5
P2D5	19.6	18.2	7.7
P1D5	17.4	18.0	7.2
P1D6	22.5	22.8	6.9
P1D7	22.1	22.7	7.0
P1D8	21.0	21.9	7.2
P1D9	24.6	20.1	7.6
P1DA	23.6	21.6	7.1
P1DB	22.2	22.1	7.6
P1DC	22.4	21.1	7.7
P2D2	23.7	24.2	7.6
P2D3	22.3	23.0	7.4
	21.4	20.3	7.6
	2.2	2.6	7.7

Total Average
20.8
2.4

TABLE IX.13 - Contact Angle and Surface Tension Components for DC200-1000 cs Silicone oil

DC200-1000 Silicone Oil
Surface Tension @23.9°C 22.4 dynes/cm

Solid Surface	Total Surface Energy	Dispersion Component	Polar Component	Average Contact Angle°	Standard Deviation (±°)
PUT 002	**71.3**	**37.6**	**33.7**	**30.59**	**3.88**
Melinex 454™	**45.8**	**35**	**10.8**	**32.25**	**2.09**

A= 1.86 D= 1.85
B= 12.26 E= 11.83
C= 11.61 F= 6.57

Common factor	-0.67	**Normalized Components**	
Surface tension(d)=	**37.75**	**22.30**	**dynes/cm**
Surface tension(n)=	**0.17**	**0.10**	**dynes/cm**

CEL Contact Angle Data

	Original Data Left(°)	Right(°)	Base Length
P1D1	26.6	157.1	17.3
P1D2	23.9	159.4	16.3
P1D3	26.6	150.8	17.3
P1D3	27.9	147.6	17.2
P1D4	29.5	147.8	16.3
P1D5	30.7	152.5	17.2
P1D5	33.1	147.4	16.7
P1D6	31.3	146.4	13.1
P1D7	28.5	146.3	16.3
P1D8	34.3	148.4	14.4
P1D9	34.7	147.3	14.9
P1D10	32.5	143.4	16.1
P1D11	32.6	150.0	16.6
P1D12	35.8	147.5	16.5
	30.6	30.6	
	3.5	4.3	

Total Average
30.6
3.9

PET-A Contact Angle Data

	Left(°)	Right(°)	Base Length
P1D1	29.5	29.4	17.1
P1D2	31.0	34.8	16.4
P1D3	31.2	32.9	17.2
P1D4	31.3	32.0	16.2
P2D5	31.9	34.0	14.6
P1D5	31.4	33.9	17.1
P1D6	31.1	36.0	16.9
P1D7	28.9	34.9	17.4
P1D8	34.5	33.1	16.3
P1D9	33.1	34.2	16.7
P1DA	28.5	31.7	17.5
	31.1		
	1.7		

Total Average
32.2
2.1

TABLE IX.14 - Contact Angle and Surface Energy Data for Glycerol

99.7% Glycerol

Surface Tension @23.9°C 49.47 dynes/cm

Solid Surface	Total Surface Energy	Dispersion Component	Polar Component	Average Contact Angle°	Standard Deviation (±°)
PUT 002	**71.3**	**37.6**	**33.7**	**29.31**	3.44
Melinex 454™	**45.8**	**35**	**10.8**	**72.61**	2.91

A= 1.87 D= 1.30

B= 12.26 E= 11.83

C= 11.61 F= 6.57

Common factor	-1.22	Normalized Components	
Surface tension(d)=	**11.54**	**8.22**	**dynes/cm**
Surface tension(n)=	**57.91**	**41.25**	**dynes/cm**

PUT 002 Contact Angle Data

	Original Data Left(°)	Right(°)	Base Length
P1D1	32.7	155.9	17.3
P1D2	32.5	150.1	16.3
P1D3	31.8	153.0	17.3
P1D3	36.4	151.6	17.2
P1D4	31.6	155.6	16.3
P1D5	34.1	152.0	17.2
P1D5	30.5	154.3	16.7
P1D6	34.0	152.6	13.1
P1D7	34.2	154.6	16.3
P1D8	31.2	154.5	14.4
P1D9	30.2	155.9	14.9
P1D10	28.0	151.9	16.1
P1D11	31.4	153.0	16.6
P1D12	31.2	154.3	16.5
	32.1	26.5	
	2.1	1.8	

Total Average

29.3

3.4

Methylene Iodide Contact Angle Data

	Original Data Left(°)	Right(°)
P1D1	73.4	72.6
P1D2	77.1	76.2
P1D3	74.2	76.4
P1D4	73.6	71.0
P2D5	70.5	72.8
P1D5	66.5	67.2
P1D6	72.3	71.8
P1D7	70.6	76.2
P1D8	74.6	72.6
P1D9	73.9	76.1
P1DA	68.0	73.0
P1DB	68.9	73.1
	72.0	73.2
	3.1	2.7

Total Average

72.6

2.9

APPENDIX X

SUBSTRATE ESCA SPECTRA AND ELECTRICAL PROPERTIES

This Appendix gives additional details about the ESCA (Section X.1) technique as well as a more detailed discussion of the ESCA results (Section X.2). The electrical properties are also discussed and summarized (Section X.3).

X.1 Additional Background on ESCA

Once the sample is irradiated by soft x-rays, measurements of the energy distribution of emitted photoelectrons (from which the binding information or core electrons is obtained) permits elemental identification within the sample volume. A very precise, or high resolution, determination of the electron binding energy can reveal "chemical shifts" caused by changes in the chemical structure or oxidation state relative to the reference state (Pantano, 1981). The analysis depth is in the 5-50 Å range (Schreiber, 1979). The surface sensitivity of ESCA is derived from the limited escape depth, or inelastic mean path of photoelectrons produced within the sample volume. (Pantano, 1981) Thus, only photoelectrons originating near the surface escape without perturbation of their characteristic energy.

Surface analysis such as ESCA must be carried out at very low vacuum, typically 10^{-6} to 10^{-8} Pascal , in order to minimize electron scattering and surface contamination by residual hydrocarbons and adsorbed atmospheric gases (Pantano, 1981). One drawback of ESCA when examining bulk insulating materials, e.g. glasses, ceramics, and polymers, is the emission of electrons that can cause "charging" of the surface (Pantano, 1981). This can prevent the analysis, complicate

the interpretation, and damage the sample. One successful method to alleviate this problem is to cool the sample with liquid nitrogen during the analysis, thus reducing the diffusivity of the mobile species and allowing for more time prior to beam induced perturbation (Pantano, 1981). Another method to combat charging is to heat the sample thus increasing carrier mobility and thereby assisting charge recombination (Freeman, 1994). When charging of a sample does occur, the high resolution carbon 1s peaks are shifted. The C-C and C-H peak is present at the lowest binding energy of 284.9 eV [1] and all values are shifted to bring that peak back to its reference chemical state (Freeman, 1994 and Wagner, 1991).

X.2 ESCA Results

The samples were analyzed on 7/29/94 at Georgia Tech Research Institute, Electro-Optics, Environment, and Materials Laboratory - Materials Analysis Center under reference MSA#315S51900A0. The untreated side of uncoated PET was tested for comparison to the treated coated PET. Peak smearing and charge shifting of the high resolution carbon 1s peaks occurred for the coated PET, cellulose acetate, and paper substrates, although this does not affect the semiquantitative data for oxygen carbon and silicon atomic percentages. The full survey spectra and high resolution spectra are contained in Figures X.1 through X.8. The semiquantitative data are given in Table X.1.

[1] ±0.5 eV as based on hexane (C6H6)

Table X.1. Semiquantitative ESCA data (atomic percents) and electrical properties.

	O%	C%	Si%	O/C	Surface Resistivity (Ω/square)	Volume Resistivity (Ω-cm)
coated PET-A	25	75	0	0.33	6.91E14	1.65E9
uncoated PET-B	26	71	3	0.37	1.48E15	1.05E11
cellulose acetate	37	61	3	0.61	2.93E10	4.46E11
paper	31	69	0	0.45	3.83E11	3.12E9

Based on the carbon and oxygen atomic percents, the base substrate for both the coated PET and uncoated PET was reconfirmed to be *polyethylene terephthalate,* $(C_{10}H_8O_4)_n$. The adhesion pretreatment coating is an acrylic-based hydrophilic compound. The hydrophilicity of the coated PET is confirmed by the polar surface energy, γ_s^n, component discussed in Section 4.3 and Appendix IX, when compared to the untreated side of uncoated PET (10.8 vs. 4.2 dynes/cm). Based on some of the commercially produced acrylic polymers (Kroschwitz 1991) and the ESCA data, it is hypothesized that the polymer coating is *n-Butyl acrylate, sec-Butyl acrylate,* or *tert-Butyl acrylate* $(C_7H_{10}O_2)_n$. The atomic percentages for oxygen, and carbon for this compound are 22.2% and 77.8% with an O/C ratio of 0.29. The ESCA technique can only measure the atomic percentage within ±1% which easily leaves room for the differences in the percents and O/C ratio. No further work was conducted to determine the exact proprietary coating compound.

Interestingly, the most easily identified compound, cellulose acetate (CEL), which is almost pure α-cellulose, $(C_6H_{10}O_5)_n$, did not have oxygen or carbon atomic mass percentages close to the ideal of 45.5%, and 54.6% respectively. It is possible that some of the additives may preferentially be present at the surface.

X.3 Electrical Properties of the Substrates

The electrical properties are a function of the chemical nature and structure of the substrate. The dissolution of electrical surface charge, i.e., surface resistivity, and the charge transfer through the bulk material, i.e., volume resistivity, were measured with equipment specified in Appendix III. All samples were preconditioned at 23.8°C and 50% RH. Data for these tests are also summarized in Table X.1. The atomic percent oxygen was a good indicator of the surface resistivity (see Figure X.1).

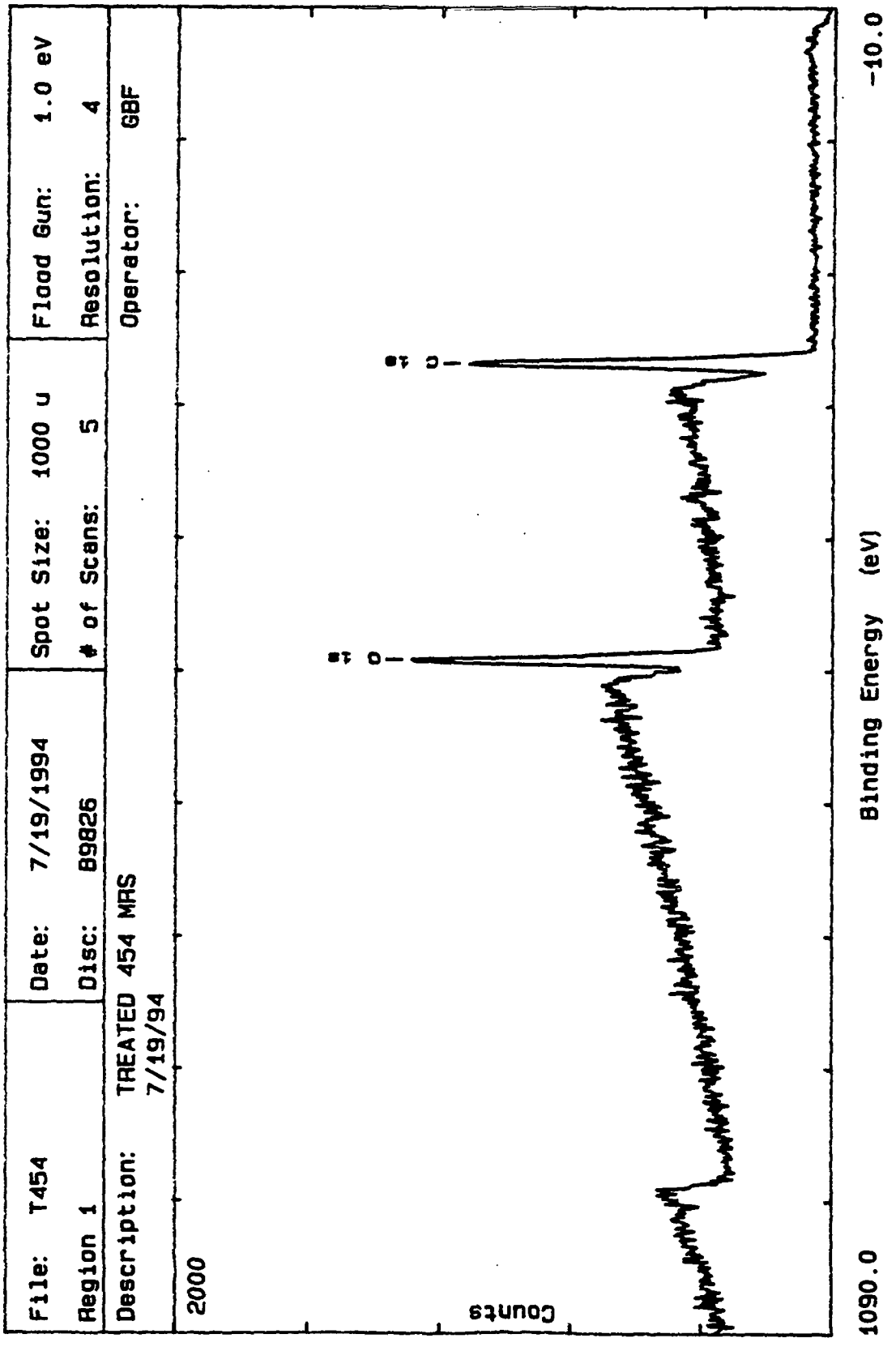

Figure X.1. ESCA survey spectra for PET-A, ICI Americas - Melinex®454

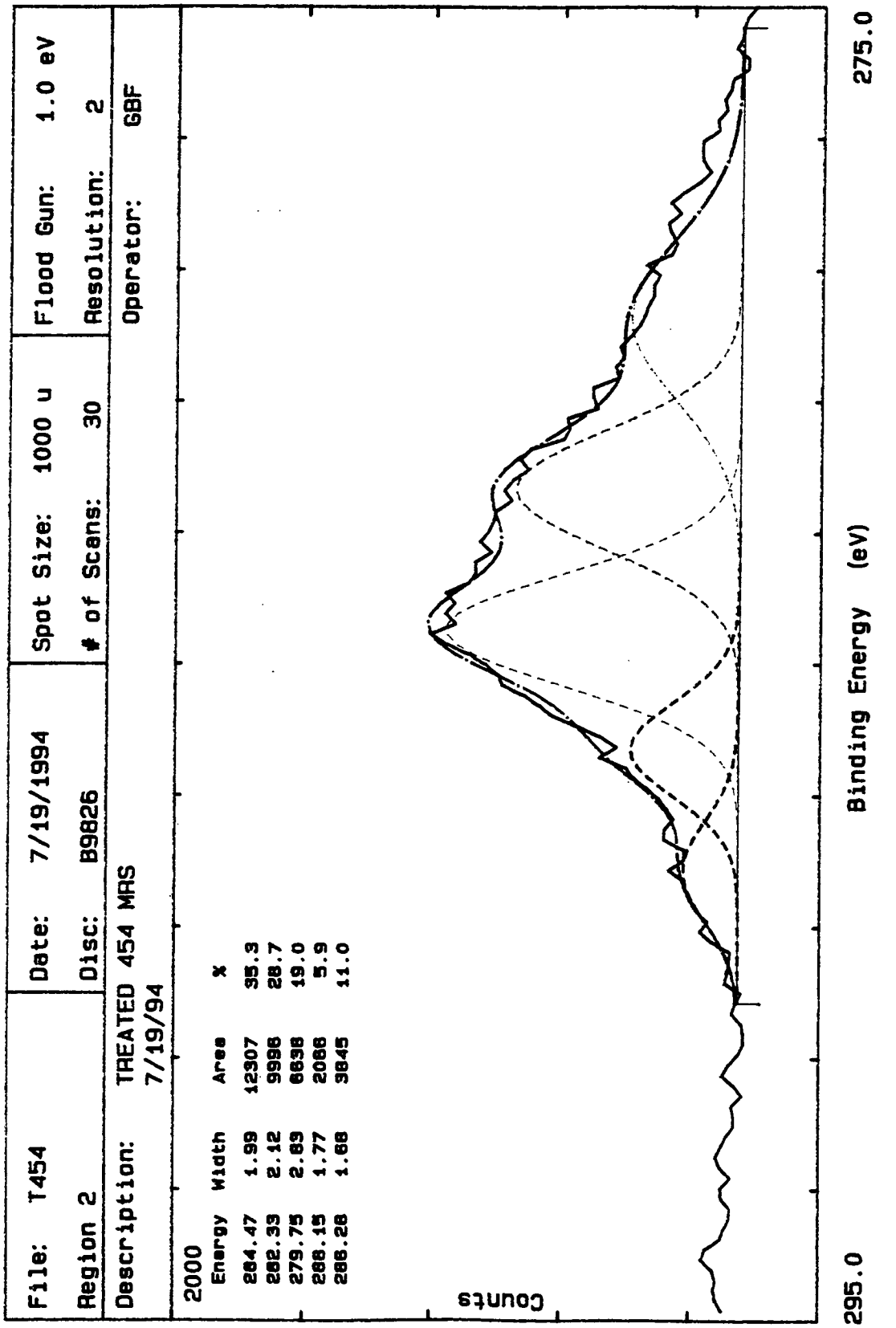

Figure X.2. ESCA high resolution carbon survey spectra for PET-A, ICI Americas - Melinex®454. The survey has been resolved for the C-O, C=O and O-C-O by shifting the lowest energy C-C peak to 284.9 eV.

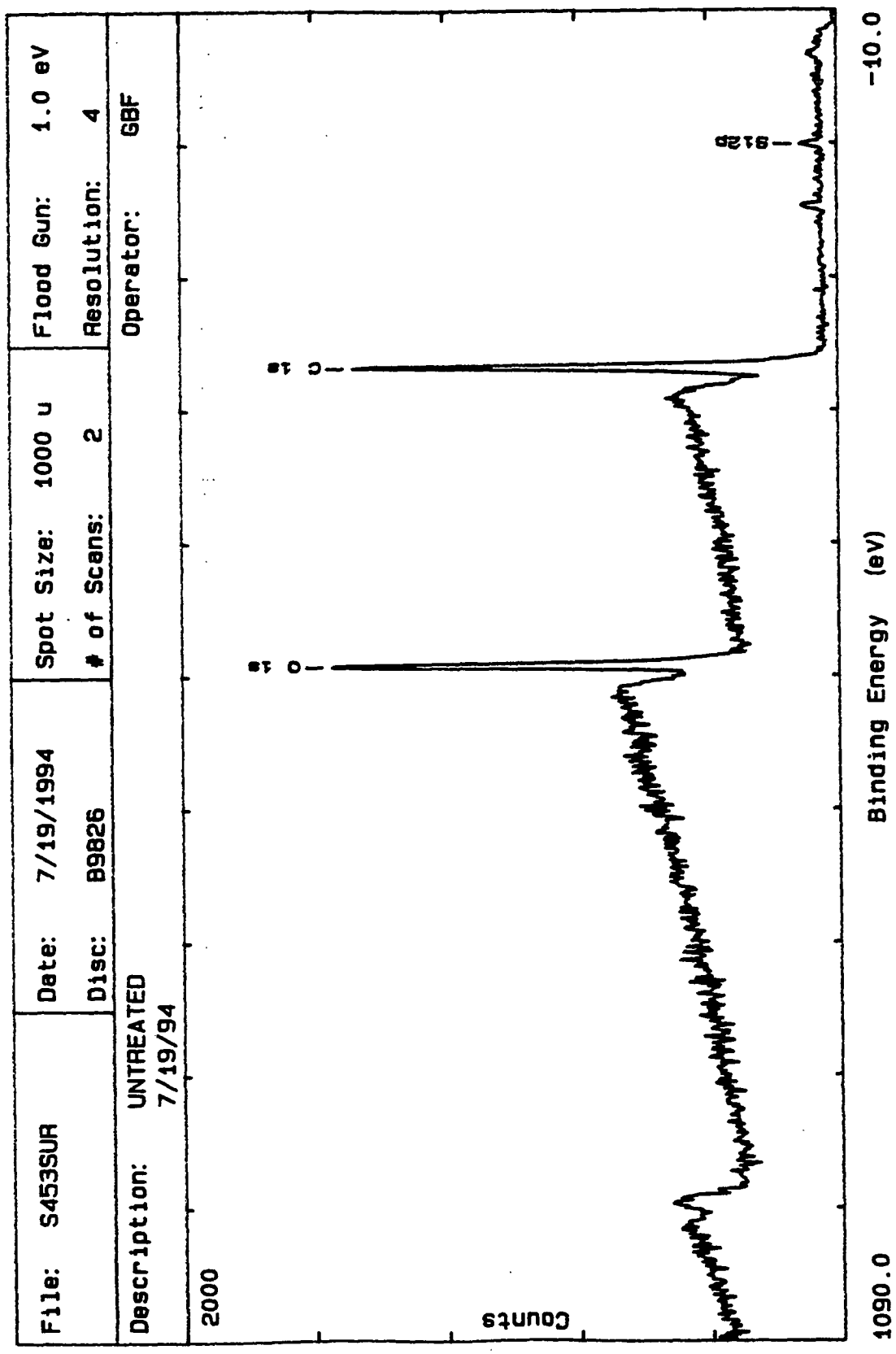

Figure X.3. ESCA survey spectra for PET-B, ICI Americas - Melinex®453

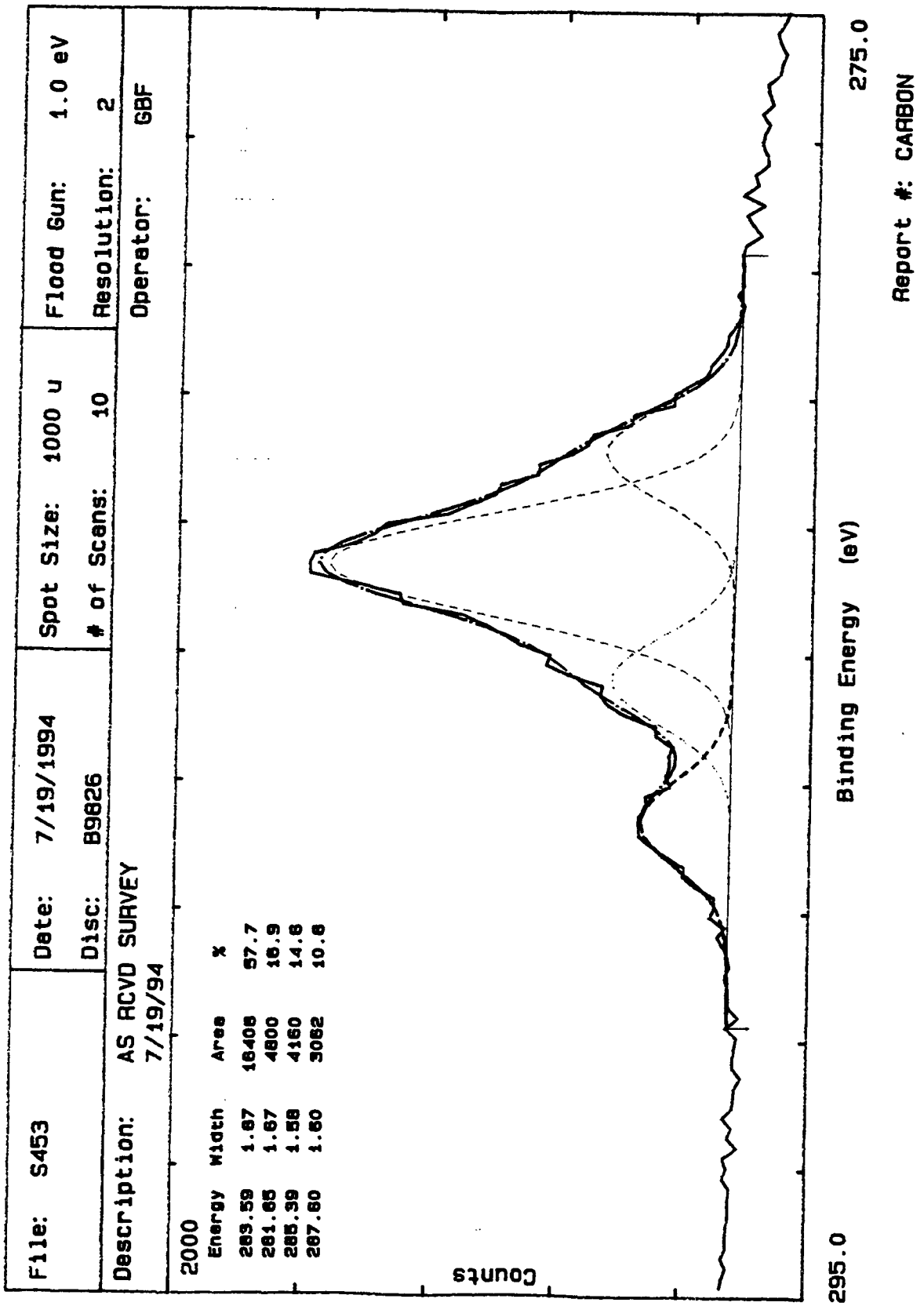

Figure X.4. ESCA high resolution carbon survey spectra for PET-B, ICI Americas - Melinex®453

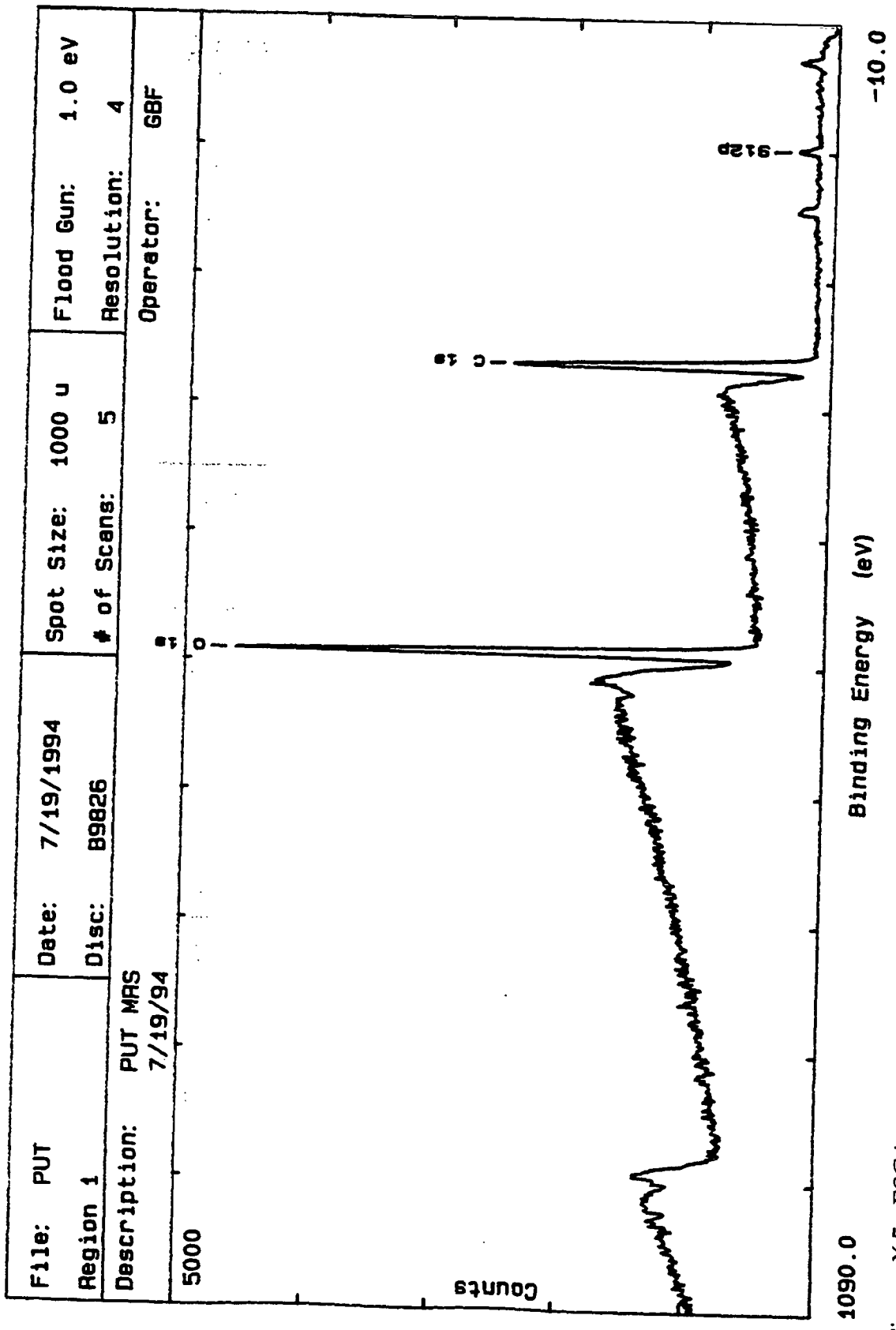

Figure X.5. ESCA survey spectra for CEL, Flexcel Incorporated - PUT002

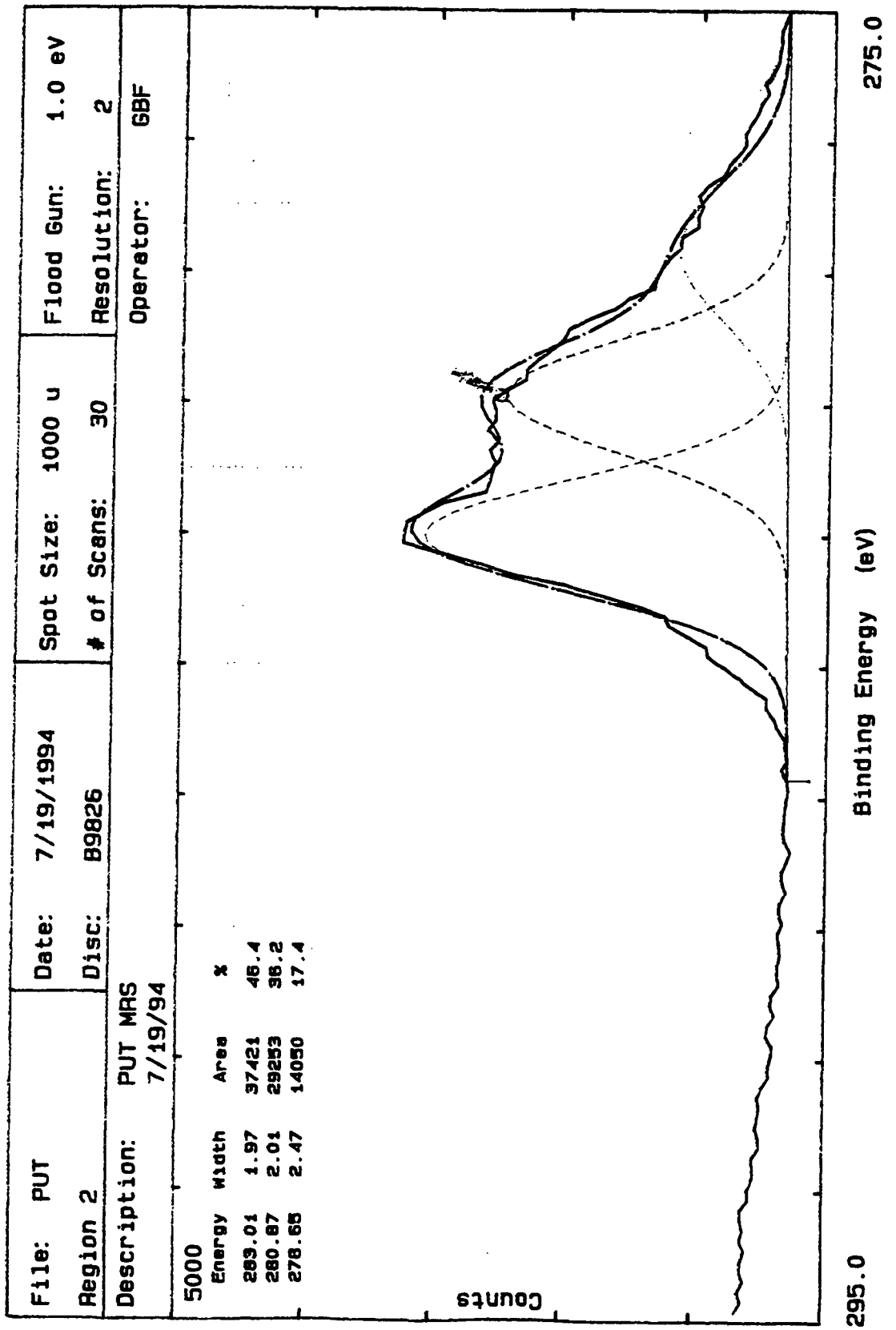

Figure X.6. ESCA high resolution carbon survey spectra for CEL, Flexcel Incorporated - PUT002

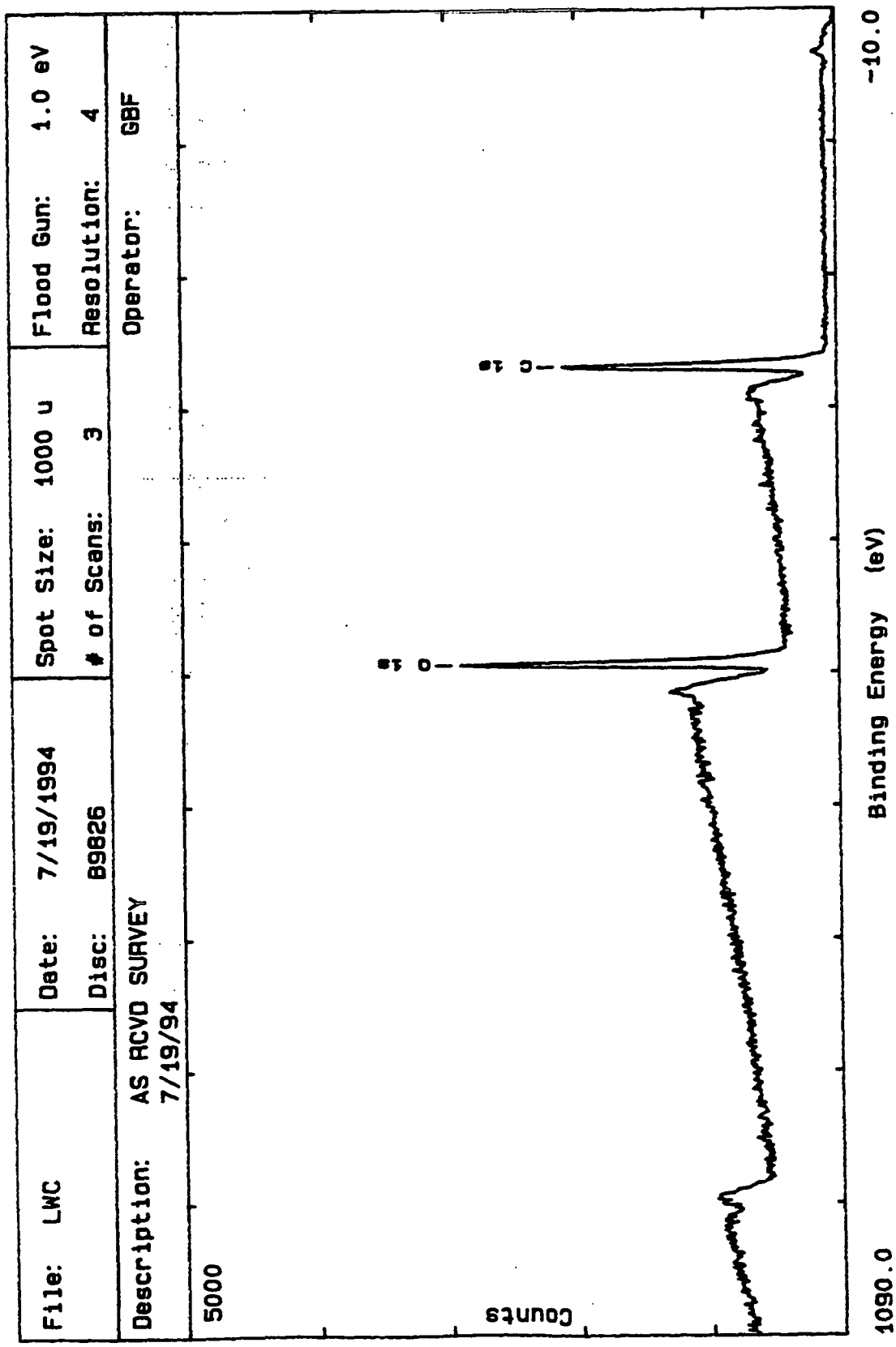

Figure X.7. ESCA survey spectra for LWC basestock, Champion International 24# Rotogravure base

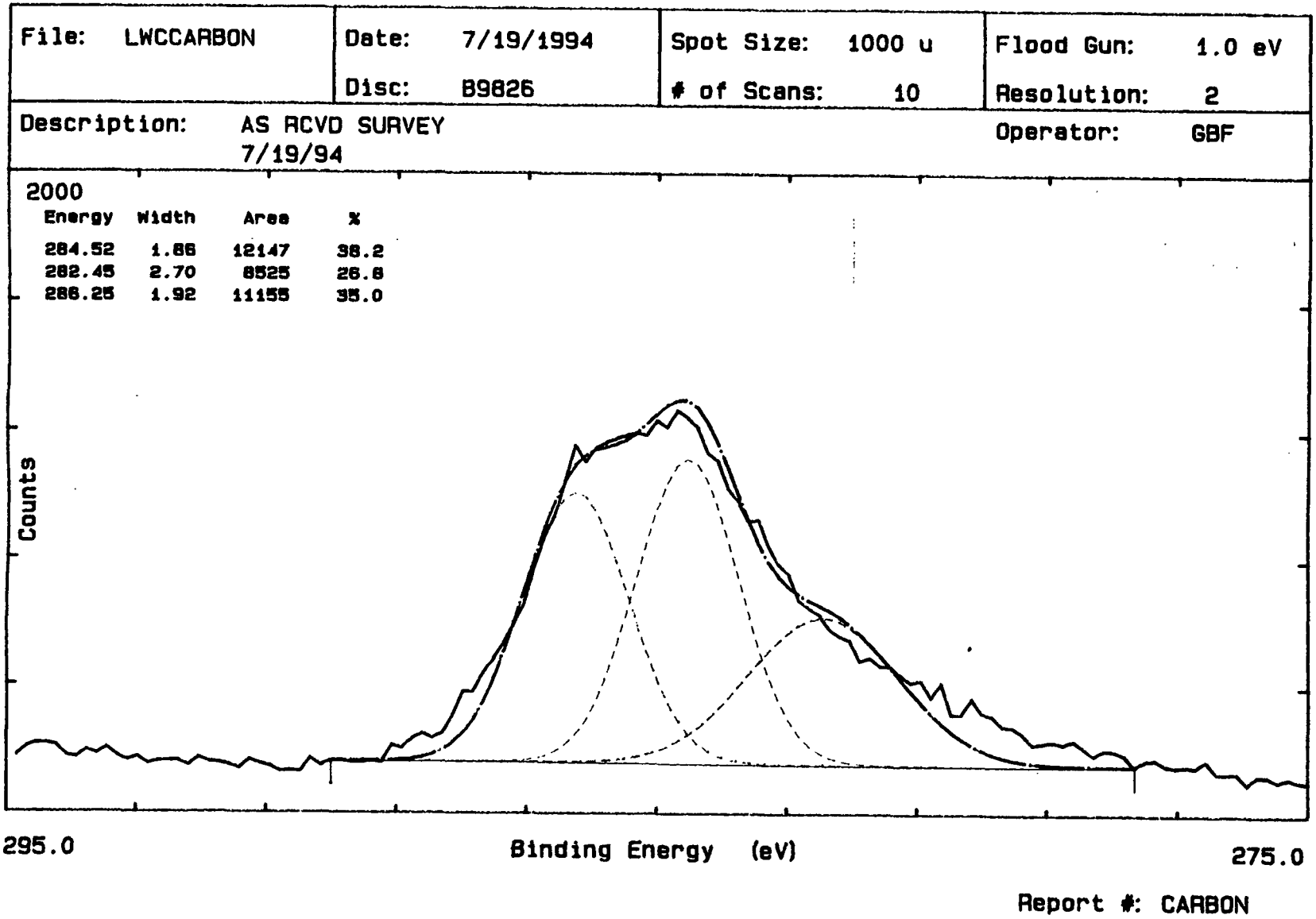

Figure X.8. ESCA high resolution carbon survey spectra for LWC basestock, Champion International 24# Rotogravure base

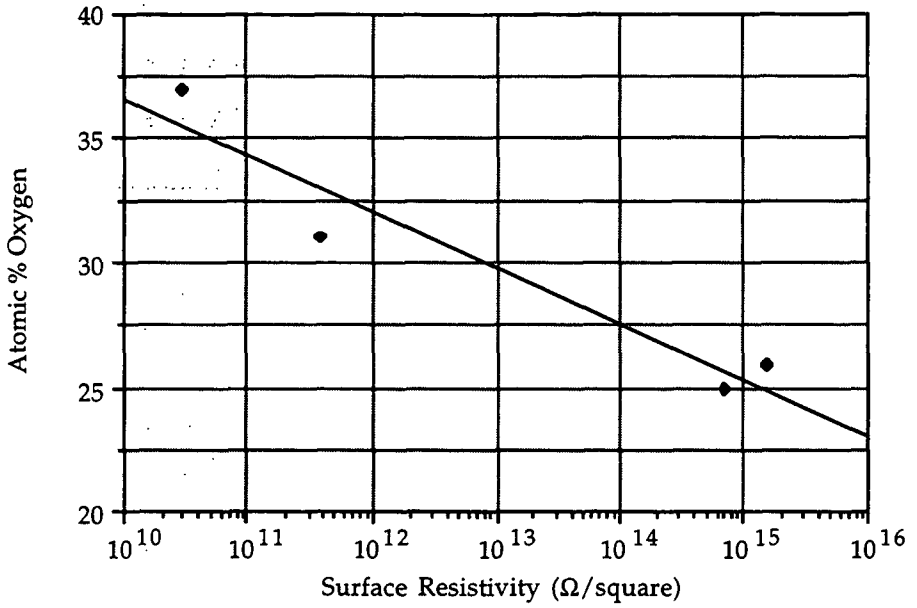

Figure X.9 Surface resistivity variation with mass % atomic oxygen.

APPENDIX XI

SCANNING ELECTRON MICROSCOPE PROCEDURE AND MICROGRAPHS

XI.1 Sample Preparation

Small (ca 5 x 5 mm) pieces of samples were painted down (around the edges) to 1/2" diameter aluminum stubs using carbon paint. These were air dusted and then sputter coated for 2 minutes with Au/Pd to obtain an electrically conductive surface. The coating thickness is about 100-300 Å and is not usually visible at magnifications below 60,000x. The sample stub are identified in Table XI.1 with the sample number shown in the upper left hand corner of the images.

Both sides of the coated PET-A were tested to determine side-to-side variations. This was necessary because of the uncertainty in roll loading at the unwind stand as discussed earlier in Section 4.2.7. The uncoated PET-B micrographs were qualitatively compared to the coated PET-A to determine the affect of the coating on the surface structure. The micrographs are contained in Figures XI.1 - XI.12.

Table XI.1 - SEM Sample Identification

Stub #	Type	Side	Surface Treatment
1	Coated PET-A	Inside	Coated
2	Coated PET-A	Outside	Coated
3	Uncoated PET-B	Inside	Uncoated
4	Cellulose acetate CEL	Inside	Uncoated

XI.2 Microscope Conditions

The JEOL JSM 6400 scanning electron microscope available at IPST was operated at 5 kV accelerating potential with the secondary electron (SE) detector. This low voltage was used to minimize beam damage and maximize surface imaging. Below 5 kV the resolution would drop, making features difficult to see.

A long working distance(WD) (39 mm) was used to get the low magnification (10-100x) images and a short working distance (9 mm) was used to optimize resolution. A small aperture (#4-50 μm) and low beam current condenser lens (CL) setting= 7 to 11 were used for optimum resolution. Sample tilt was 0°. The "spot size" also was varied as the magnification was changed and is given in Table XI.2 along with the numerical aperture. The "spot size" is loosely defined as the inverse of the coarse condenser lens setting and is unitless. Both Polaroid and digital images were taken.

Table XI.2 - Beam Conditions Used on JEOL JSM 6400

Magnification	1/"Spot Size"	WD(mm)	Ideal nanoamps
10x	7	39	6
100x	7	39	6
1000x	9	8	1
5000x	11	8	0.03
10000x	11	8	0.03

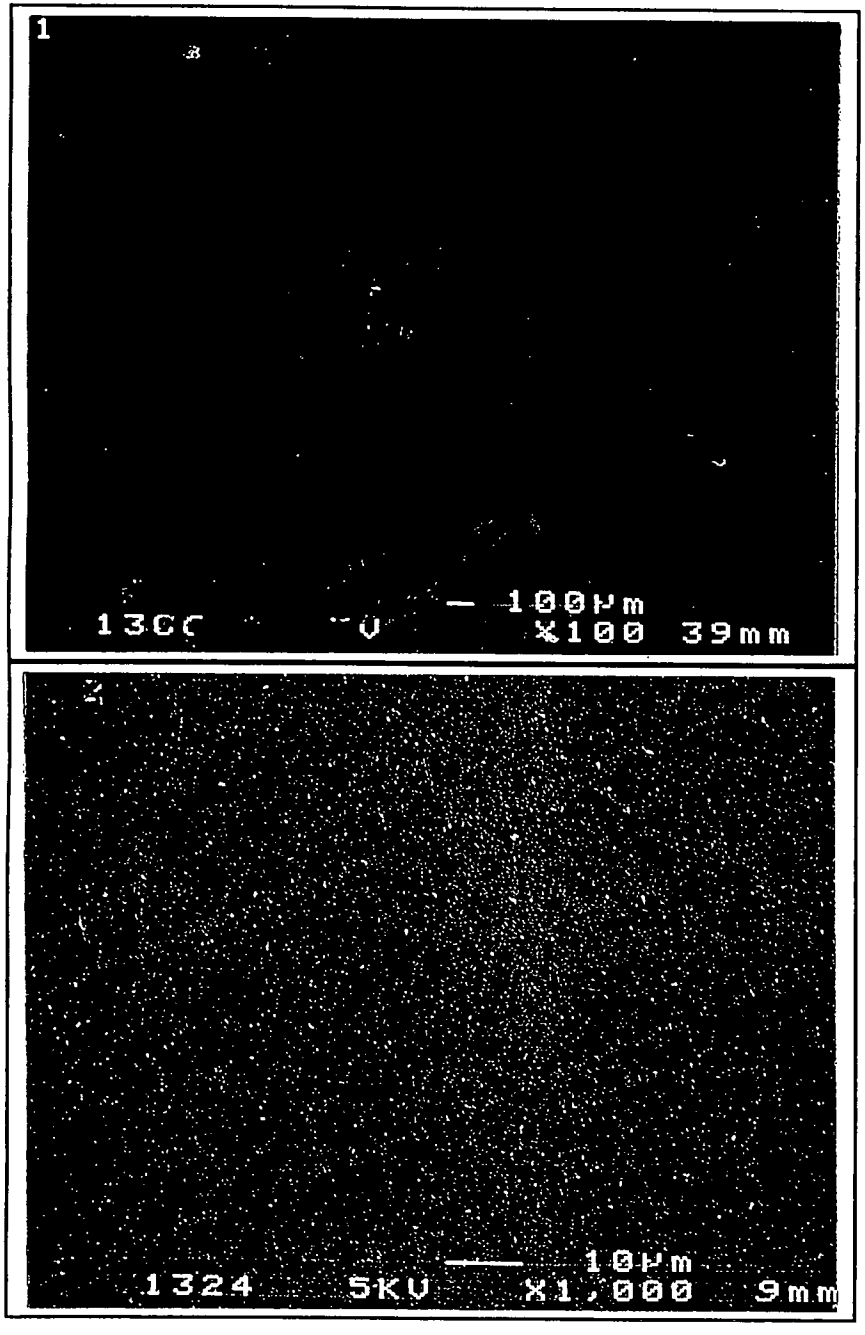

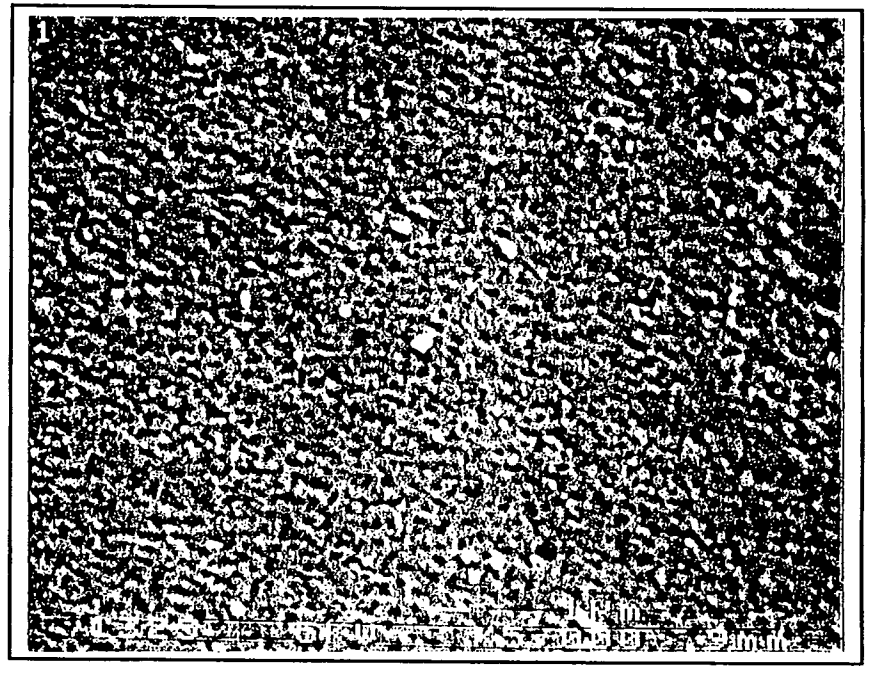

Figures XI.1, XI.2 and XI.3. SEM Images of *inside* surface of sample coated PET-A. (Upper left) Magnification 100X and 5kV electron beam. The markings on the lower middle portion are due to the film emulsion peeling away and not due to sample contamination. (Lower left) coated PET-A inside surface at magnification 1,000 X and 5kV electron beam. (Upper right) coated PET-A inside surface at magnification 5,000 X and 5 kV electron beam. Note the grainy appearance.

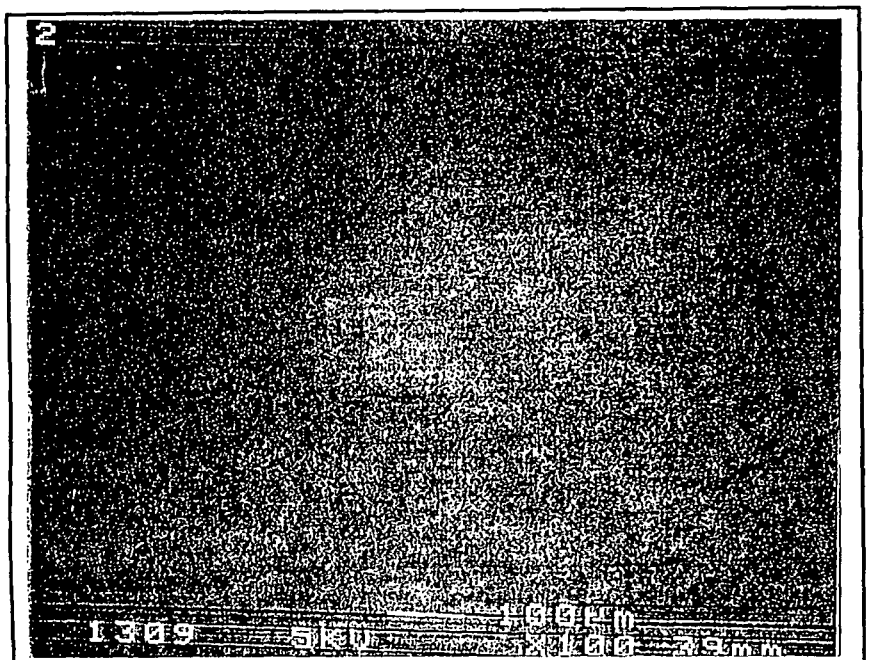

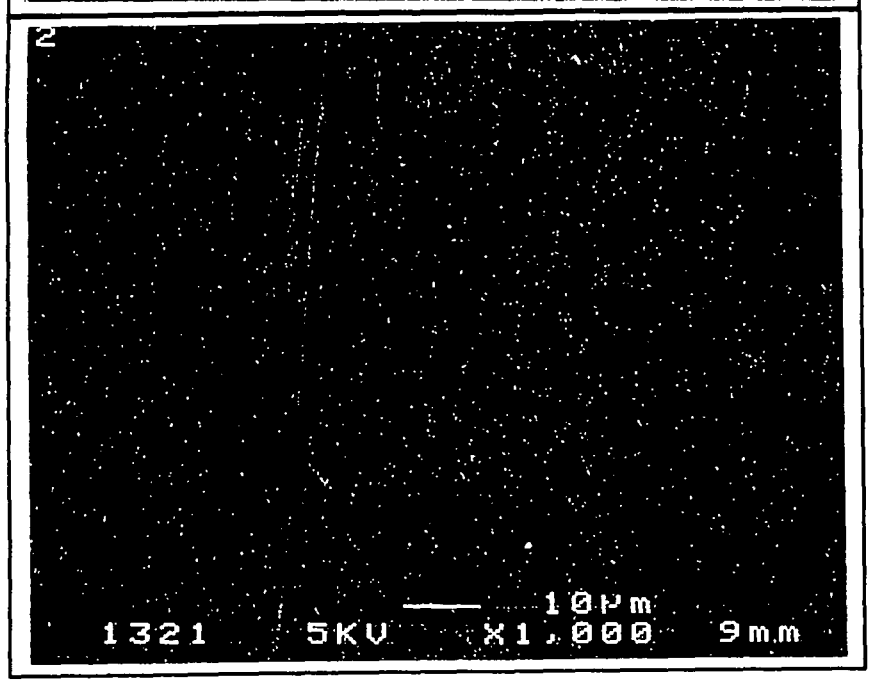

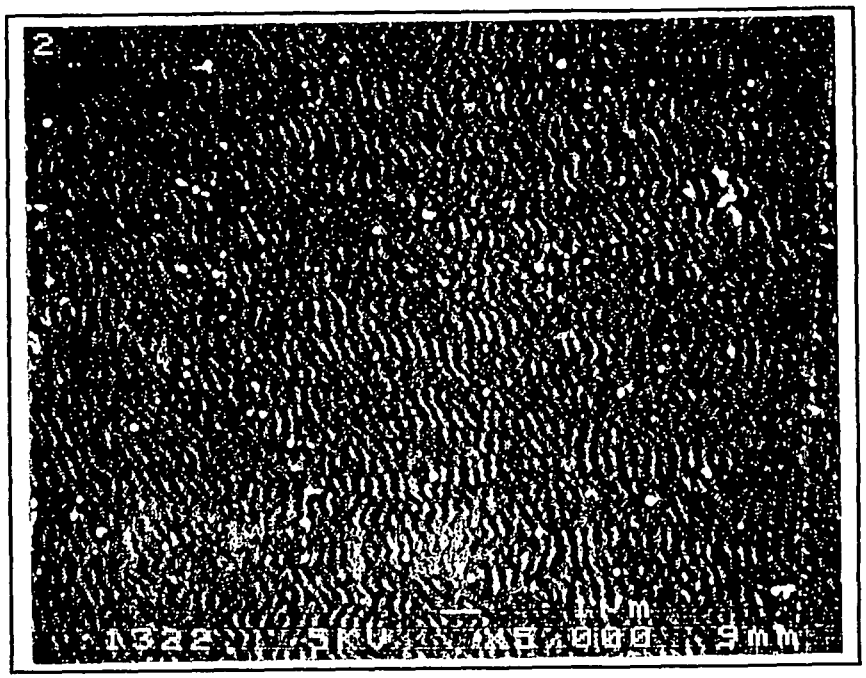

Figures XI.4, XI.5 and XI.6. SEM Images of *outside* surface of sample coated PET-A. (Upper left) Magnification 100X and 5kV electron beam. (Lower left) coated PET-A *outside* surface at magnification 1,000 X and 5kV electron beam. (Upper right) coated PET-A *inside* surface at magnification 5,000 X and 5 kV electron beam. Note the oriented striations that appear on the sample

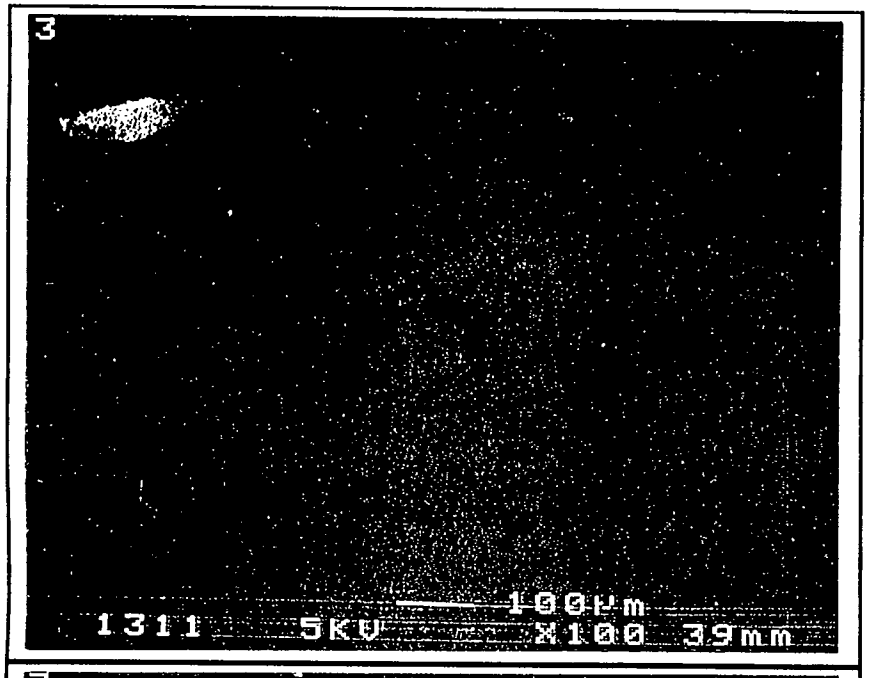

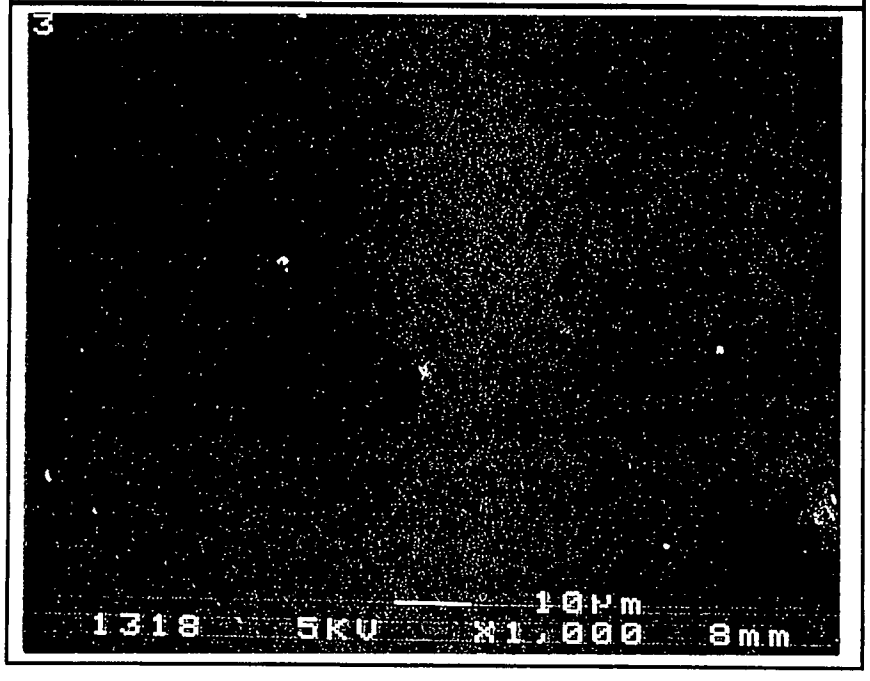

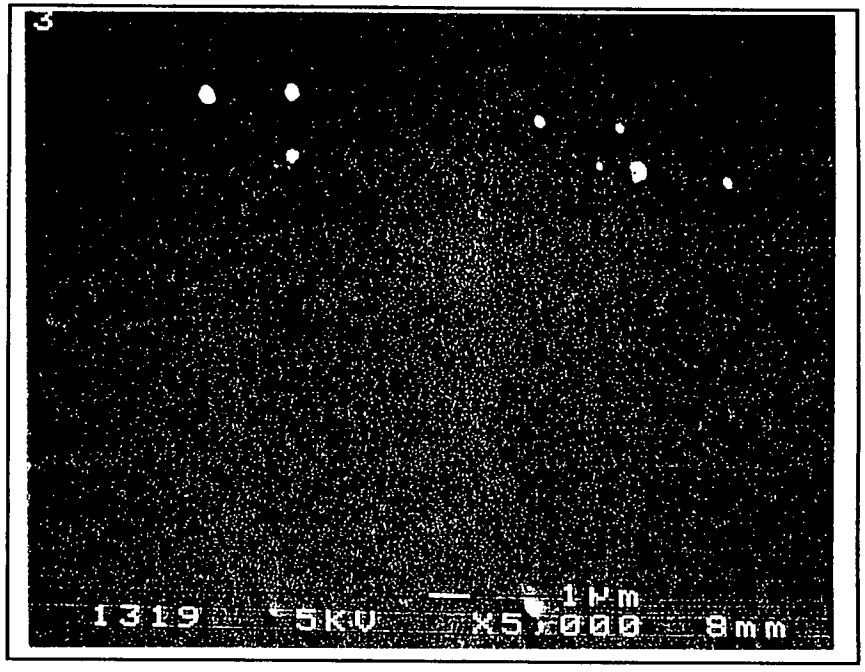

Figures XI.7, XI.8 and XI.9. SEM Images of *untreated inside* surface of sample uncoated PET-B. (Upper left) Magnification 100X and 5kV electron beam. (Lower left) uncoated PET-B surface at magnification 1,000 X and 5kV electron beam. (Upper right) uncoated PET-B surface at magnification 5,000 X and 5 kV electron beam.

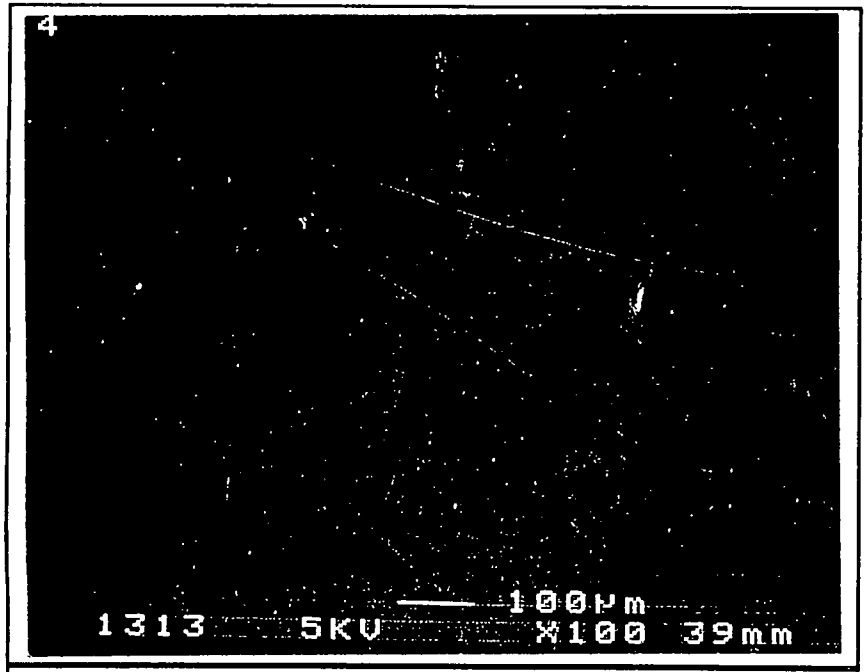

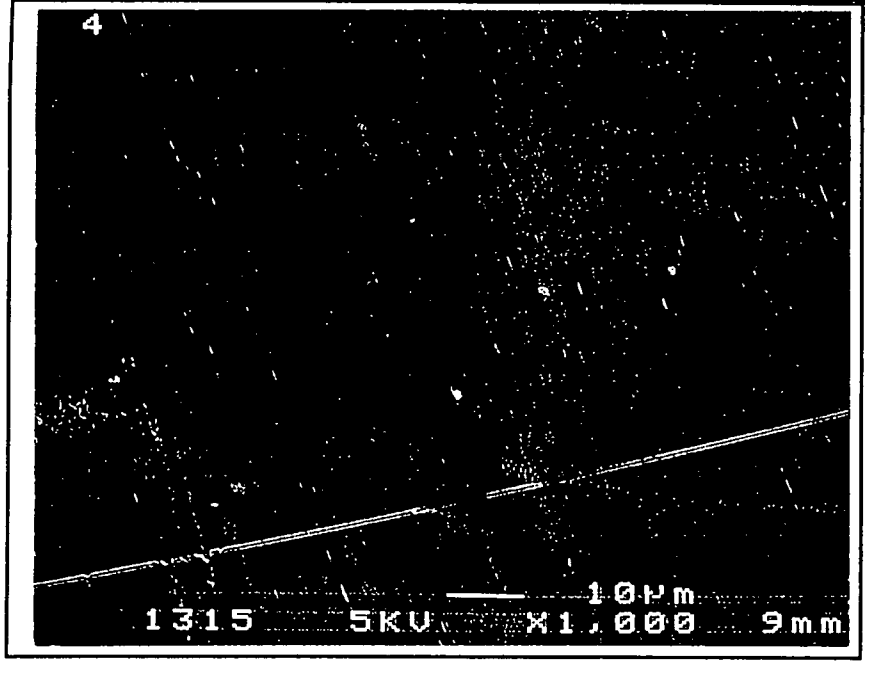

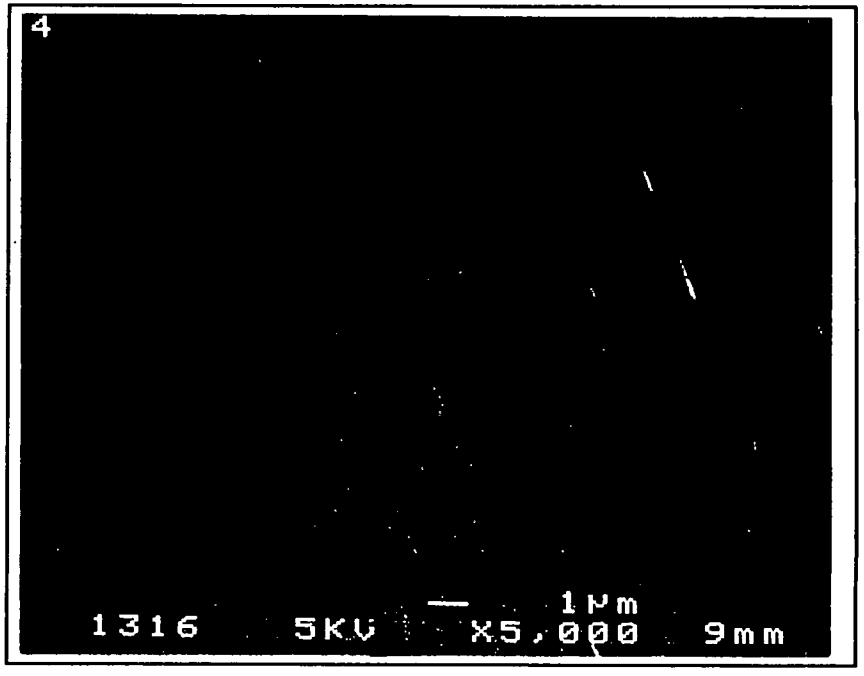

Figures XI.10, XI.11 and XI.12. SEM Images of surface of sample cellulose acetate. (Upper left) Magnification 100X and 5kV electron beam. (Lower right) cellulose acetate surface at magnification 1,000 X and 5kV electron beam. (Upper right) cellulose acetate surface at magnification 5,000 X and 5 kV electron beam.

APPENDIX XII

SURFACE ROUGNESS STATISTICS AND SYSTEMS

This Appendix discusses the details of the equipment and methods used to measure the substrate roughness. Section XII.1 discusses the surface statistics. In Section XII.2 the TALYSTEP system used at ECC International is discussed and the methodology for the measurements in Section XII.3. The Surfanalyzer system and methodology to obtain profiles in the MD direction are discussed in Sections XII.4 ad XII.5. Section XII.6 briefly covers the sample analyzed with the WYKO RST system.

XII.1 Surface Rougness Statistics

The International Organization for Standardization (ISO) has established guidelines for the terminology and equations of roughness parameters (ISO, 1982). These standardization procedures are essential for intercommunication of results and accurate machining of surfaces.

A surface can be assessed by more than fifty parameters (Lin and Hopfe, 1986), which may or may not be relevant for a system. Four of the commonly used parameters are defined as follows:

1) The arithmetic average roughness, R_a, is specified by calculating the arithmetical mean of the absolute values of the profile departures from the mean line within the sampling length, l, and given by Eq.[XII.1] or approximated by Eq.[XII.2] for n discrete profile deviations (ISO, 1982). R_a is the most commonly used parameter because it provides a simple value for accept-reject decisions.

$$R_a = \frac{1}{l}\int_0^l |z(x)|dx \qquad [XII.1]$$

$$R_a = \frac{1}{n}\sum_{i=1}^{n} |z_i| \qquad [XII.2]$$

2) The Root mean square (r.m.s.) deviation of the profile, R_q, is the value of the profile departures from the mean line within the sampling length, l (ISO, 1982). R_q is more sensitive to occasional highs and lows in the surface profile (ISO, 1982) and is given by Eq.[XII.3] and the discrete version for uneven sample lengths, l_i, given in Eq.[XII.4]. When the sample intervals are even Eq.[XII.4] reduces to Eq.[XII.5].

$$R_q = \sqrt{\frac{1}{l}\int_0^l z^2(x)dx} \qquad [XII.3]$$

$$R_q = \sqrt{\frac{1}{l}\sum_{0}^{n} z_i^2 l_i} \qquad [XII.4]$$

$$R_q = \sqrt{\frac{1}{n}\sum_{0}^{n} z_i^2} \qquad [XII.5]$$

Full information regarding any of the other parameters involving surface roughness is found in ISO 4287 (ISO, 1982).

XII.2 PAPERSCAPE Instrument

The PaperScape system used by ECC International, Inc. consists of a modified Rank-Taylor-Hobson Talystep Profilometer, also known as the TALYSTEP. The heart of the system is a diamond stylus with a 13-mm radius tip which follows the sample surface. An electronic transducer senses the stylus position in the z-direction and provides an electrical signal that can be amplified. Improvements to

the system include a) conversion of the analog stylus displacement signal to digital form, b) ability to do an x-y sample scan of up to 25.0 mm in each direction with stepper motors, and c) the automatic computation of surface statistics and profiles with the discrete data.

As mentioned earlier, magnification of the vertical stylus signal is possible. At a magnification of 4000, one digital unit represents a change in height of approximately 0.01 mm. This is based on an 8-bit A/D converter and thus an n-bit converter, n > 8, would provide higher resolution.

In order to quantify the principle waveforms found in the surface profile two techniques have been employed. These are the Fourier transform and the Walsh function. By computing the amplitudes of the waveforms, the macroroughness of the substrate can be determined in terms of a distribution of roughness wavelengths and amplitudes. This technique has found a powerful application in analyzing the effect of base sheet properties on the pigment coating surface structure, and thus in final coated sheet properties.

XII.3 Methodology with the TALYSTEP Instrument

All four samples were tested in multiple runs with different samples at 4000X magnification with 5 and 25 μm sampling intervals for 25 mm total length. The ECC sample code was used to discern among the different runs and is as follows. The first four characters, P057, indicate the project code. The next letter indicate the sample type with the codes A-D as follows:

A - Melinex™454; B - PUT 002; C - LWC Base; D - Melinex™453

The next two characters indicate the sample subset within a sample type and the number of times that it has been repeated. An example would be, P057BA1. This represents PUT 002, sample subset A repeated the first time. The entire set of profiles can be found in Progress Report#9. The data is summarized in the main body of this appendix.

Except for the LWC sample, all of the profiles showed deviations due to curvature of either the sample holder or of the substrate. In most instances the deviation appeared to be linear and therefore a linear curve was fit through the data to correct it to a planar surface. Any profile that appeared to contain a plateau or noise was considered erroneous based on previous profiles and operator experience. Interference was more of a problem because of the high amplification. The corrected z-height is based upon Eq. [XII.7], with m and b representing the slope and intercept respectively. x_i represents the position along the CD scan position and $\bar{z}$ the average z height along the entire scan length.

$$z_{i,corr.} = \bar{z} - (m \times x_i + b) + z_i \qquad [XII.7]$$

This fact is borne out that the slope for most of the samples varies from 4.5E-5 to 1.5E-4.

XII.4 Introduction to the Surfanalyzer™ System 4000

The System 4000 is manufacturered by Federal Products Corporation in Providence, RI. It is designed for either laboratory or shop use in the metalworking, computer, microcircuit, plastics, and film industries. The unit consists of four

components: a) controller, b) linear drive, c) probe, and d) printer/recorder. The controller supplies the values for the traverse speed, filter cutoff values, magnification, and parameter calculation, R_a, R_q, R_y, R_z. The linear drive can be adjusted from 0.02"/0.51 mm to 4"/101.6 mm traverse length and from 1"/2.5 mm per second to 0.01"/0.25 mm per second in the fast and slow traverse speeds, respectively. The probe has an 2.5 μm diamond stylus tip mounted in a breakaway holder. Recommended skid force is 0-40 gf/0.4 N.

XII.5 Methodology with SURFANALYZER

A Series 4000 unit available in West Nyack, NY, at Champion International was used to confirm if localized peaks displayed in CD direction scans continued through the substrate MD length. A traverse length of 97.4 mm for PET-A and 100.7 mm for the PET-B were chosen so that a representation of the entire CD profile could be viewed. A single scan of each CD profile was made at stylus speed of 2.5 mm/sec, high magnification, and 0.08-mm cutoff with the end of the trace running over the edge of the tape, thus serving as a reference marker to compare profiles taken at earlier positions.

The individual scans were digitized and overlayed using a graphics program to reconstruct the series. For Figure 4.14 of Chapter IV, PET-A peak #6 at 12.9 mm from the left edge is prevalent from the first scan at 0" to the last at 58". It varies in width from 7.5 to 9.5 mm at the base and is approximately 6-9 μm high. Since the tape thickness is only 1.5 mil (38.1 μm) this represents a significant departure in the thickness of the tape. Table XII.1 gives the peak positions in the CD direction from

the left edge and the number of defined peaks that pass through the traced lines. The number of times that a peak passes through the trace divided by the total number of scans is the frequency of occurrence. The criterion for determining if a peak passed through a trace line was made by visual inspection of the peak height and the CD position in relation to the previous and remaining MD, peaks taking into account the accuracy of the digitization and profilometer.

TABLE XII.1 - Frequency of Occurrence for Peaks on PET-A Scan#1 - Front (See Figure 4.14 for profiles)

Peak #	Dist. from right edge (mm)	# Occurrences	Frequency
1	80.9±0.2	7	50%
2	**73.5±0.2**	**13**	**92.9%**
3	58.2±0.2	6	42.8%
4	**47.2±0.2**	**12**	**85.7%**
5	27.3±0.2	6	42.8%
6	**12.9±0.2**	**14**	**100%**

TABLE XII.2 - Frequency of Occurrence for on Peaks PET-A - Scan#2 Front (See Figure XII.1 for profiles)

Peak #	Dist. from right edge±0.2 mm	# Occurrences	Frequency
1	91.7	4	30.8%
2	80.2	12	92.3%
3	68.5	13	100.0%
4	57.8	12	92.3%
5	48.9	8	61.5%
6	31.1	13	100.0%
7	23.5	12	92.3%

TABLE XII.3 - Frequency of Occurrence for Peaks on PET-A - Scan#2 Back (See Figure XII.2 for profiles)

Peak #	Dist. from right edge±0.2 mm	# Occurences	Frequency
1	70.3	11	84.6%
2	61.6	9	69.2%
3	44.0	9	69.2%
4	20.4	6	46.2%
5	14.1	12	92.3%

PET-B (Melinex™ 453) was scanned in the same manner as the previous sample except it was on the untreated side at 14 MD positions. Peak #3 of the PET-B scans is repeated multiple times and has an average base width of 5 mm and a height of 2-4 μm.

TABLE XII.4 - Frequency of Occurrence for Peaks on PET-B (See Figure XII.3)

Peak #	Dist. from right edge (mm)	# Occurences	Frequency
1	**95.6±0.2**	**14**	**100%**
2	**77.6±0.2**	**14**	**100%**
3	**51.2±0.2**	**14**	**100%**
4	33.5±0.2	2	14.3%
5	16.8±0.2	13	92.9%
6	8.6±0.2	1	7.1%

The first through third fundamental wavelengths from the TALYSTEP profiles are contained in Table XII.5. These analyses used the forward FFT function in PSIPLOT software. The Nyquist frequency determines the highest frequency component of a waveform that can be defined by sampling (Ramirez, 1975). The Nyquist frequency is determined by the sampling period and is given by $f_N = f_s/2 = T/2$. Since it takes at least two points per cycle to uniquely define a sinusoid of given amplitude and frequency, any components existing below or at the Nyquist frequency are correctly defined (Ramirez, 1975). The two Nyquist frequencies for the TALYSTEP data correspond to wavelengths of 10 μm and 50 μm and thus the data in Table XII.5 are valid because at 11,000 to 5,400 μm they are significantly above the Nyquist frequency.

XII.6 WYKO RST Measurements

The RST Plus Rough Surface /Step Test is manufactured by WYKO Corp., Tuscon, AZ. It is a noncontact optical profilometer capable of measuring step heights from 100 Å to 500 μm. The coated PET sample was submitted for a courtesy analysis and the results compared to the systems previously mentioned. With the sample tilt removed, R_a=1.09 μm and R_q = 1.44 μm which confirmed the earlier results.

Figure XII.1. Repeat overlapped scan profile of PET-A front side using the Surfanalyzer system. The maximum valley to peak distance is 10 µm. A total of 13 scans were collected starting at 0" out to 212" from the starting line.

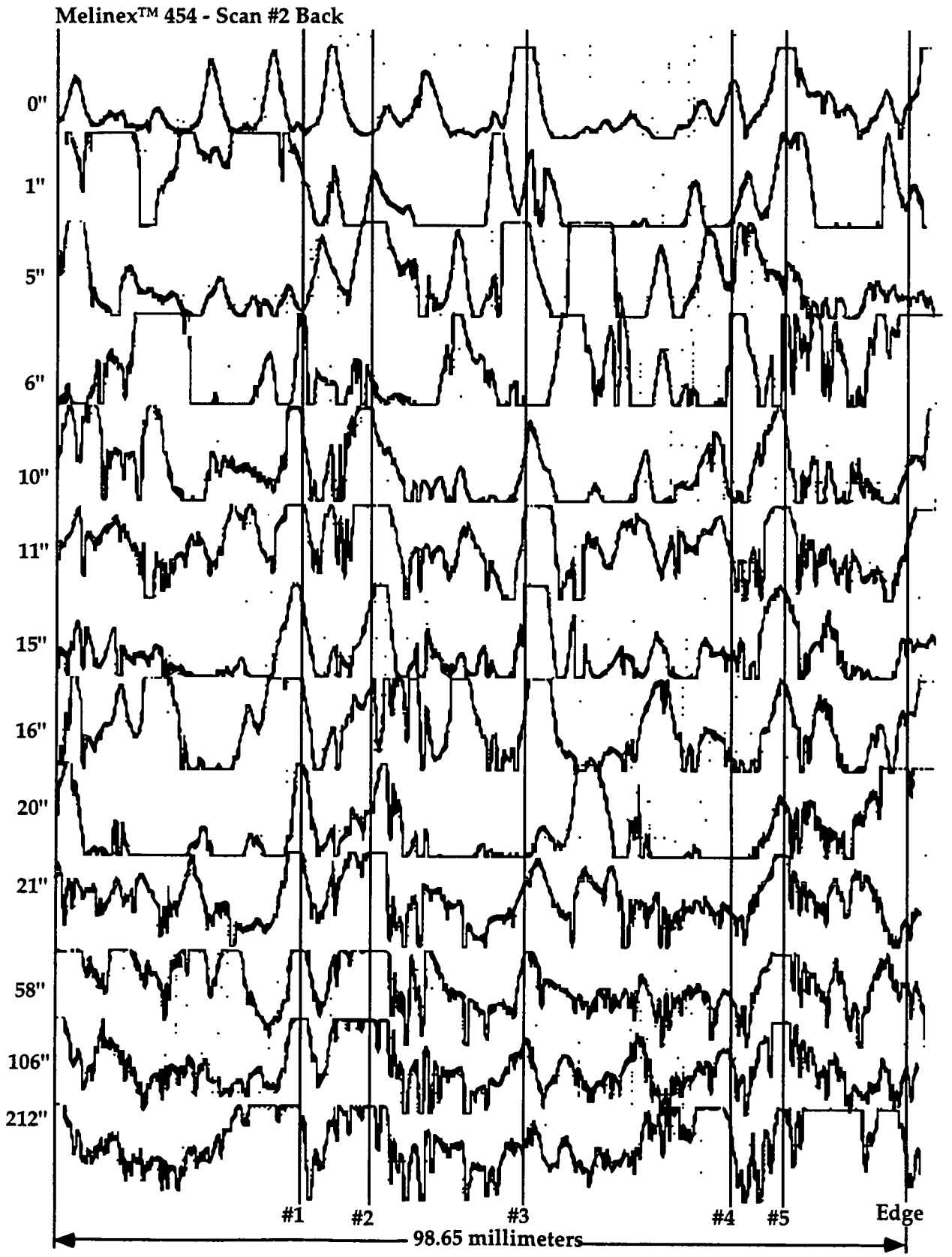

Figure XII.2. Repeat overlapped scan profile of PET-A back side using the Surfanalyzer system. The scans were taken at the same location as those from Figure XII.1.

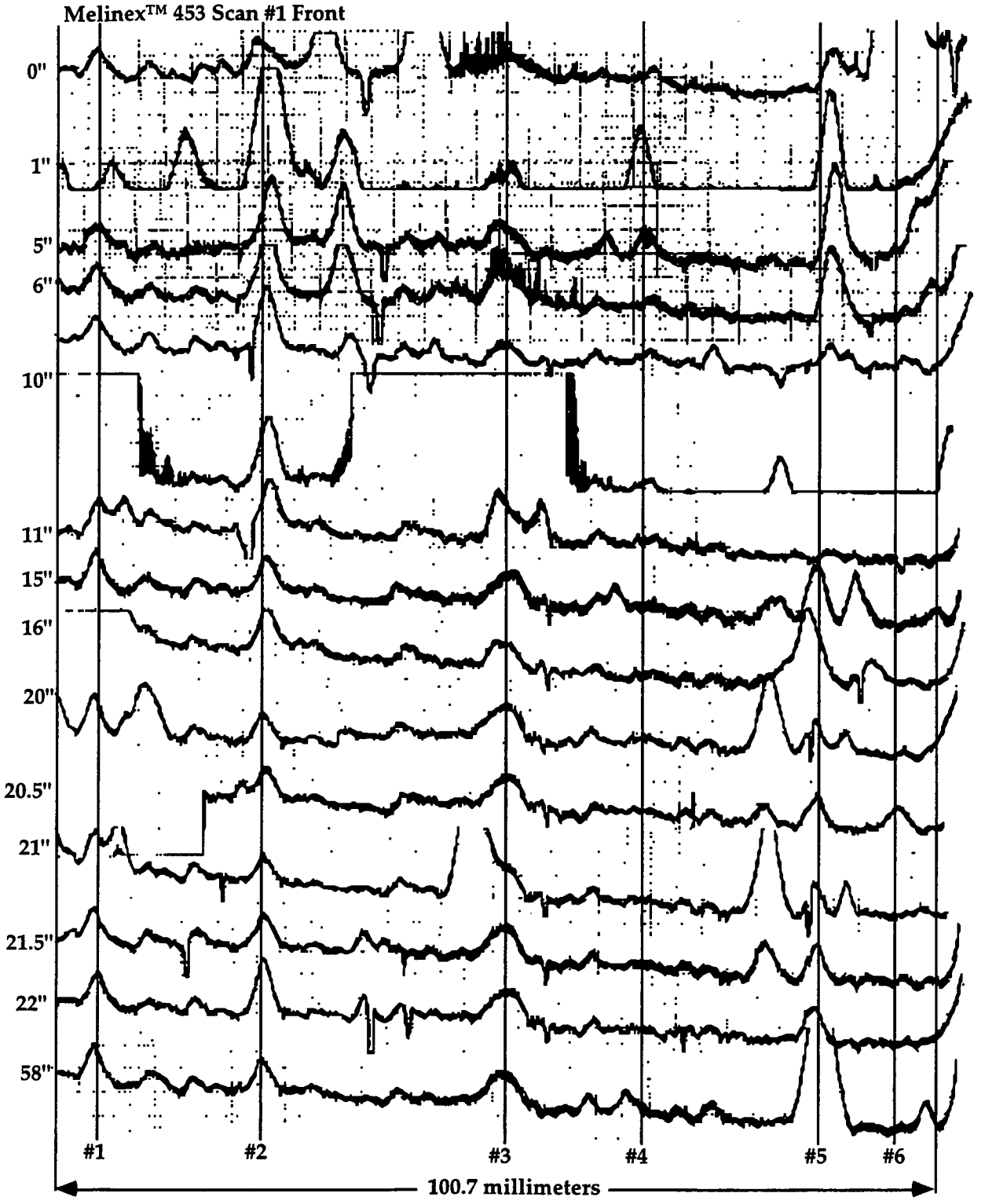

Figure XII.3. Overlapped scan profile of uncoated PET-B front side using the Surfanalyzer system.

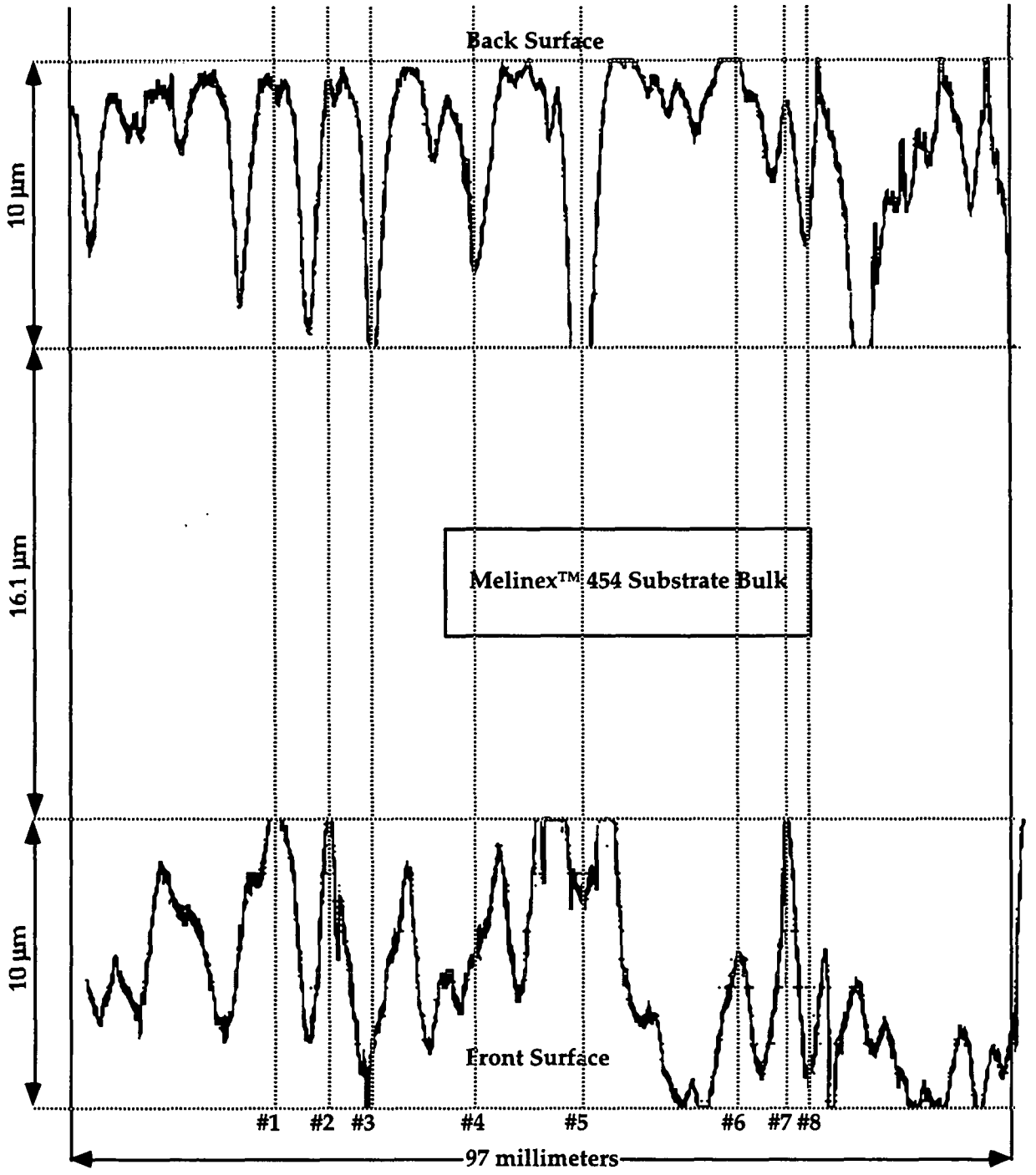

Figure XII.4. Comparison of front and back sides of PET-A scans #2 and #3 at 0" position with the bulk area of the material to scale in relation to the surface roughness. The scans are compared across the entire 97 mm width.

TABLE XII.5 - Fundamental FFT Wavelengths from TALYSTEP Profiles

PET-A - Melinex™ 454

Sample ID	Δx (μm)	#1 λ (μ)	#2 λ (μ)	#3 λ (μ)	Log(2) #1	Log(2) #2	Log(2) #3
AA10	25	12,804	3,663	2,132	13.64	11.84	11.06
AA11	25	5,128	2,841	1,828	12.32	11.47	10.84
AB2	25	8,547	5,128	3,663	13.06	12.32	11.84
AC4	25	5,128	3,663	2,841	12.32	11.84	11.47
AA9	5	13,653	8,192	4,096	13.74	13.00	12.00
AC2	5	8,192	4,096	2,731	13.00	12.00	11.42
Average (μm)		**8,909**	**4,597**	**2,882**	**13.02**	**12.08**	**11.44**
Stddev (μm)		**3,658**	**1,912**	**870**	**0.61**	**0.53**	**0.44**
Std Error %		41.06%	41.60%	30.18%	4.70%	4.38%	3.88%
					8,279	**4,327**	**2,772**
					1.53	1.44	1.36

CEL - PUT 002

Sample ID	Δx (μm)	#1 λ (μ)	#2 λ (μ)	#3 λ (μ)	Log(2) #1	Log(2) #2	Log(2) #3
BA2	25	5,128	1,828	2,840	12.32	10.84	11.47
BA1	5	13,653	5,120	8,192	13.74	12.32	13.00
BB1	5	13,653	6,827	3,413	13.74	12.74	11.74
Average (μm)		**10,812**	**4,592**	**4,815**	**13.27**	**11.97**	**12.07**
Stddev (μm)		**4,922**	**2,541**	**2,938**	**0.82**	**1.00**	**0.82**
Std Error %		45.52%	55.34%	61.03%	6.15%	8.35%	6.77%
					9,851	**3,998**	**4,298**
					1.76	2.00	1.76

LWC - LWC 24# Roto Basestock

Sample ID	Δx (μm)	#1 λ (μ)	#2 λ (μ)	#3 λ (μ)	Log(2) #1	Log(2) #2	Log(2) #3
CA2	25	12,800	1,600	6,400	13.64	10.64	12.64
CA3	25	1,829	3,657	5,120	10.84	11.84	12.32
CB2	25	3,657	2,844	776	11.84	11.47	9.60
CB3	25	8,533	5,120	2,844	13.06	12.32	11.47
CC2	25	5,120	1,506	1,969	12.32	10.56	10.94
CC3	25	1,280	1,969	3,657	10.32	10.94	11.84
CA1	5	5,120	2,926	3,413	12.32	11.51	11.74
CB1	5	2,409	4,551	8,192	11.23	12.15	13.00
CC1	5	8,192	5,120	2,048	11.23	12.15	11.00
Average (μm)		**5,438**	**3,255**	**3,824**	**11.87**	**11.51**	**11.62**
Stddev (μm)		**3,779**	**1,437**	**2,357**	**1.07**	**0.67**	**1.03**
Std Error %		69.49%	44.16%	61.63%	9.06%	5.81%	8.85%
					3,737	**2,917**	**3,142**
					2.11	1.59	2.04

PET-B - Melinex™ 453

Sample ID	Δx (μm)	#1 λ (μ)	#2 λ (μ)	#3 λ (μ)	Log(2) #1	Log(2) #2	Log(2) #3
DA2	25	4,267	12,800	3,200	12.06	13.64	11.64
DB2	25	8,533	5,120	2,560	13.06	12.32	11.32
DB3	25	8,533	5,120	2,560	13.06	12.32	11.32
DC2	25	6,400	3,200		12.64	11.64	
DC3	25	12,800	3,200	2,560	13.64	11.64	11.32
DA1	5	13,653	4,096		13.74	12.00	
DB2	5	20,480	10,240	3,724	14.32	13.32	11.86
DC1	5	13,653	8,192		13.74	13.00	
Average (μm)		**11,040**	**6,496**	**2,921**	**13.28**	**12.49**	**11.49**
Stddev (μm)		**5,153**	**3,544**	**528**	**0.72**	**0.76**	**0.25**
Std Error %		46.67%	54.55%	18.06%	5.42%	6.06%	2.16%
					9,964	**5,741**	**2,885**
					1.65	1.69	1.19

APPENDIX XIII

UNCERTAINTY ANALYSIS

This Appendix discusses the ASME error analysis applied throughout this work and how estimates of the bias and precision errors were propagated in calculations.

XIII.1 Using Linear Regression to Predict the Precision Index

The precision of a parameter is usually expressed in terms of imprecision and computed as the standard deviation of the test result (ASTM 1992). The precision index, S, i.e., population standard deviation σ, is determined by taking n repeated measurements of some parameter population, x_i (Abernathy et al. 1985).

$$\sigma = S = \sqrt{\frac{\sum_{i=1}^{n}(x_i - \bar{x})^2}{n-1}} \qquad \text{[XIII.1]}$$

When using regression to predict the value of a desired parameter as a function of the independent measured parameter, x_i, it is not possible to obtain the precision index for all values of the dependent parameter y_i. This presents a dilemma if the experimenter wishes to minimize the time spent determining S or if only a single measurement of x_i is available. The most common regression model uses least squares fitting and makes the assumption that the random error E_i, model error, must necessarily have a mean of zero (Walpole and Meyers 1989, 361). It is represented by,

$$y_i = A + Bx_i + E_i \qquad \text{[XIII.2]}$$

A further assumption is made that each random error has the same sample variance which is equivalent to S^2 (Walpole and Myers 1989, 366). The regression

sample variance, $S_{y,x}$, is a measure of the amount of error in the prediction of y, for an individual x. For example, if a regression of density vs. temperature, T, is calculated, $S_{y,x}$ represents the random component of density accuracy at any given temperature and can be substituted for the precision index, $\sigma = S$, at n-2 degrees of freedom, when properly corrected around $\bar{x}$. That is to say that the error of prediction is greater at values farther away from the mean measured parameter $\bar{x}$. Walpole and Myers (1989, 369) prove that $S_{y,x}$ is an unbiased estimate of S.

$$\sigma = S \approx S_{y,x}\sqrt{\frac{1}{n}+\frac{(x-\bar{x})^2}{S_{xx}}+1} \qquad \text{[XIII.3]}$$

where,

$$S_{xx} = \sum_{i=1}^{n}(x_i-\bar{x})^2 = \sum_{i=1}^{n}x_i^2 - n\bar{x}^2 \qquad \text{[XIII.4]}$$

It can be seen in Eq. [XIII.3] that as $n \rightarrow \infty$, i.e., we have a large sample size and close to $\bar{x}$, the regression sample variance is closely equivalent to the standard deviation. For n=5, the difference between assuming that $S = S_{y/x}$ and the exact expression in Eq. [XIII.3] is only 8% as shown in Table XIII.1.

Table XIII.1. Difference between large number of samples and exact for $\sigma = S = S_{y/x}$.

n	1	5	10	20	100
$\sqrt{\frac{1}{n}+1}$	1.41	1.08	1.048	1.025	1.004

For $n \leq 10$ the precision index, i.e., σ, should be corrected for the sample size, n. For the remainder of the calculations in this thesis, the error due to sample size will be calculated, while the contribution from $(x-\bar{x})^2$ will be neglected because all regressions are used primarily around $\bar{x}$.

XIII.2 Bias and Precision Errors and Propagating Errors

When combining errors, it is important to recognize that three arbitrary categories exist. These are calibration errors (e.g., regression), data acquisition errors, and data reduction errors, with each consisting of a bias, B, and precision, S, component (Abernathy et al. 1985). The root sum square (RSS) method is used to combine the precision and bias indices from the various, k, sources of error.

$$S = \sqrt{S_1^2 + S_2^2 + S_3^2 + \ldots S_k^2} \qquad [XIII.5]$$

$$B = \sqrt{B_1^2 + B_2^2 + B_3^2 + \ldots B_k^2} \qquad [XIII.6]$$

The precision error component can be thought of as the random error, while the bias error component is the systematic error which is considered to remain constant during a test. The bias error must be estimated, which can be difficult because the true value is not often known. Calibration can help in estimating the bias error as well as confirmation by independent methods. By taking a large number of samples the precision error can be statistically minimized (Rudemiller 1989; Abernathy et al. 1985).

Errors in measurements of various parameters, P, are propagated into the derived result, r, by some functional relationship, e.g., $Ca = \mu U/\gamma$, that describes the relationship between the result and its independent parameters. The relationship provides the sensitivity factors, θ_i, which indicate the error propagated into the result, r, because of some unit error in the parameter, P_k.

$$r = f(P_1, P_2 \ldots\ldots P_k) \qquad [XIII.7]$$

$$\theta_i = \frac{\partial r}{\partial P_i} \qquad \text{[XIII.8]}$$

According to ASME methodology, the bias and precision errors are kept separate until finally computing the uncertainty of a result. The precision and bias indices of the result are given by,

$$S_r = \sqrt{\sum_{i=1}^{k} \left(\theta_i S_{P_i}\right)^2} \qquad \text{[XIII.10]}$$

$$B_r = \sqrt{\sum_{i=1}^{k} \left(\theta_i B_{P_i}\right)^2} \qquad \text{[XIII.9]}$$

Finally, the uncertainty of a result is given by either the additive method (ADD) or the root sum square method (RSS) which provide confidence levels of 99% and 95%, respectively.

$$U_{r_{ADD}} = B_r + tS_r \qquad \text{[XIII.11]}$$

$$U_{r_{RSS}} = \sqrt{B_r^2 + \left(tS_r\right)^2} \qquad \text{[XIII.12]}$$

Table XIII.3 lists the functional relationships and sensitivity factors used to determine the error in the derived parameters from the raw experimental data. The precision indices for the independent parameters, μ, μ_g, ρ, γ, are discussed in the Appendix XVII. The precision indices are taken equal to σ at n-2 degrees of freedom for each of the regressions as discussed previously in Appendix Section XII.1. The bias error precision indices are contained in Table XIII.2. The bias errors were calibrated using viscosity standards, manufacturers specifications on surface tension, and the bias of the lab balance for density. For the low viscosity fluids, the bias in viscosity can be significant because a 20 cp. fluid with $\pm$ 0.5 cp. bias is $\pm$2.5% bias

percentage error, although the precision index is smaller. The SHIMPO tachometer used to calibrate the drives has an accuracy of 99.9% so the possible bias error was estimated to be ±0.1% of the substrate velocity. The type-T thermocouple has error limits of ±0.5°C or ±0.4%, whichever is greater. Since this unit was calibrated using an ice bath, and the regression equation for mV signal vs. T was linearized[1] over the temperature range (10-30°C), the bias error was assumed to be negligible (Eq.[XIII.13] and OMEGA[2] 1995, Z-123). This assumption is also valid because the same thermocouple was used for measuring the physical properties and temperature measurement during the experiments.[3]

$T(°C) = 24{,}839.56 \times mV + 0.355°C \qquad R^2 = 0.999, \sigma = \pm 0.03°C, \text{d.f.} = 19 \qquad [XIII.13]$

Table XIII.2 Bias errors for experimental independent parameters.

μ	ρ	γ	U	T
± 0.5 cp.	± 0.0001 g/cm^3	± 0.1 dynes/cm	± 0.001U	± 0.5°C

Moffat (1985) discusses a method of computerizing the uncertainty analysis by sequentially perturbing the data-reduction program. This makes use of a small interval to input the error into the equation for a given calculated parameter and then calculating the derivative numerically over a small interval. This avoids having to determine the partial derivatives and would have been applicable to our system for calculating the interface height, h_i, in Chapters IV and VI.

---

[1] A fifth-order polynomial is usually fitted over the entire -200 to 350°C range, but the curve may be better expressed over a small temperature range using a linear fit.

[2] NIST Thermocouple reference table for Type T thermocouple. The NIST will be revising the tables in 1995 or 1996.

[3] See Progress Report #6, p. 21, for calibration data.

Table XIII.3 - The functional relationships and sensitivity factors used in the uncertainty analysis for the experimental parameters.

Derived Parameter	Independent Parameters		Equations
Liquid Reynolds Number, Re	Liquid density and viscosity	Functional relationship	$Re = \frac{\rho U d}{\mu}$
	Length scale	Sensitivity factors	$\frac{\partial Re}{\partial \rho} = \frac{U d}{\mu}$
	Substrate velocity		$\frac{\partial Re}{\partial U} = \frac{\rho d}{\mu}$
			$\frac{\partial Re}{\partial \rho} = \frac{U d}{\mu}$
			$\frac{\partial Re}{\partial \mu} = \frac{-\rho U d}{\mu^2}$
Capillary Number, Ca	Liquid viscosity and surface tension	Functional relationship	$Ca = \frac{U \mu}{\gamma}$
	Length scale	Sensitivity factors	$\frac{\partial Ca}{\partial U} = \frac{\mu}{\gamma}$
	Substrate velocity		$\frac{\partial Ca}{\partial \mu} = \frac{U}{\gamma}$
			$\frac{\partial Ca}{\partial \gamma} = \frac{-\mu U}{\gamma^2}$

Table XIII.3 (Continued)

Capillary Length, L_c	Liquid density and surface tension	Functional relationship	$L_c = \sqrt{\frac{\gamma}{\rho g}}$
		Sensitivity factors	$\frac{\partial L_c}{\partial \gamma} = \sqrt{\frac{1}{4\gamma\rho g}}$
			$\frac{\partial L_c}{\partial \rho} = -\sqrt{\frac{\gamma}{4\rho^3 g}}$
Physical property number or Capillarity buoyancy number, N_{pp}	Liquid viscosity, density and surface tension	Functional Relationship	$N_{pp} = \frac{g\mu^4}{\rho\gamma^3}$
		Sensitivity factors	$\frac{\partial N_{pp}}{\partial \mu} = \frac{4g\mu^3}{\rho\gamma^3}$
			$\frac{\partial N_{pp}}{\partial \rho} = \frac{-g\mu^4}{\rho^2\gamma^3}$
			$\frac{\partial N_{pp}}{\partial \gamma} = \frac{-3g\mu^4}{\rho\gamma^4}$
Time scale, t_{pp}	Liquid density and surface tension	Functional relationship	$t_{pp} = \frac{\rho L_c^2}{\mu} = \frac{\gamma}{\mu g}$
	Capillary length	Sensitivity factors	$\frac{\partial t_{pp}}{\partial \rho} = \frac{L_c^2}{\mu}$

Table XIII.3 (Continued)

		Sensitivity factors (continued)	$\frac{\partial t_{pp}}{\partial \mu} = \frac{-\rho L_c^2}{\mu^2}$
			$\frac{\partial t_{pp}}{\partial L_c} = \frac{2\rho L_c}{\mu}$
Liquid Weber Number, We	Liquid density and surface tension	Functional relationship	$We = \frac{\rho U^2 d}{\gamma}$
	Substrate velocity	Sensitivity factors	$\frac{\partial We}{\partial \rho} = \frac{U^2 d}{\gamma}$
	Length scale		$\frac{\partial We}{\partial U} = \frac{2\rho U d}{\gamma}$
			$\frac{\partial We}{\partial d} = \frac{\rho U^2}{\gamma}$
			$\frac{\partial We}{\partial \gamma} = \frac{-\rho U^2 d}{\gamma^2}$
Interface Height, h_i	Thickness t_i and t_2	Functional relationships	$h_i = \frac{-b + \sqrt{b^2 - 4c}}{2}$
	Refractive indices η_1, η_2, η_4		$b = \left(\frac{t_1\eta_2 + t_2\eta_1}{\eta_1\eta_2} \right) - h_{i-1}$
	Deflection of current ruling line, δx_i		$c = -\left[h_{i-1} \left(\frac{t_1\eta_2 + t_2\eta_1}{\eta_1\eta_2} \right) + \frac{\delta y_i \eta_4 (y_i - y_{i-1})}{(\eta_4 - 1)} \right]$

Table XIII.3 (Continued)

	Spacing between rulings, $(y_i\text{-}y_{i-1})$	Sensitivity factors (continued)	$\frac{\partial h_i}{\partial b} = \frac{b - \sqrt{b^2 - 4c}}{2\sqrt{b^2 - 4c}}$
	Height at previous ruling location, h_{i-1}		$\frac{\partial h_i}{\partial c} = \frac{-1}{\sqrt{b^2 - 4c}}$
			$\frac{\partial c}{\partial \eta_1} = \frac{h_{i-1} t_1}{\eta_1^2}, \frac{\partial c}{\partial \eta_2} = \frac{h_{i-1} t_2}{\eta_2^2}, \frac{\partial c}{\partial t_1} = \frac{-h_{i-1}}{\eta_1}$
			$\frac{\partial c}{\partial \eta_4} = \frac{-\delta y_i (y_i - y_{i-1})}{(\eta_4 - 1)^2}, \frac{\partial c}{\partial t_2} = \frac{-h_{i-1}}{\eta_2}$
			$\frac{\partial c}{\partial h_{i-1}} = -\left(\frac{t_1 \eta_2 + t_2 \eta_1}{\eta_1 \eta_2}\right), \frac{\partial c}{\partial \delta y_i} = \frac{\eta_4 (y_i - y_{i-1})}{(\eta_4 - 1)}$
			$\frac{\partial c}{\partial (y_i - y_{i-1})} = \frac{\delta y_i \eta_4}{(\eta_4 - 1)}$
			$\frac{\partial b}{\partial t_1} = \frac{\partial b}{\partial t_2} = \frac{1}{\eta_1 \eta_2}, \frac{\partial b}{\partial \eta_1} = \frac{-t_1}{\eta_1^2}$
			$\frac{\partial b}{\partial \eta_2} = \frac{-t_2}{\eta_2^2}, \frac{\partial b}{\partial h_{i-1}} = -1$

APPENDIX XIV

CALCULATION OF Φ AND R_{eq} FOR DEFLECTOMETRY

XIV.1 Calculation of Φ

The angular digitization correction factor, Φ, is used to align the coordinate system (x,y,z) of the acquired digital or film-based images with the image analysis system coordinate reference frame (X,Y,Z). First, let us examine a simple system with a single ruling line out of alignment with respect to the X,Y,Z reference frame. When both frames are aligned, i.e., the optical grating rulings in either the x or y direction are parallel to their counterpart in the X,Y,Z system then Φ = 0°. The

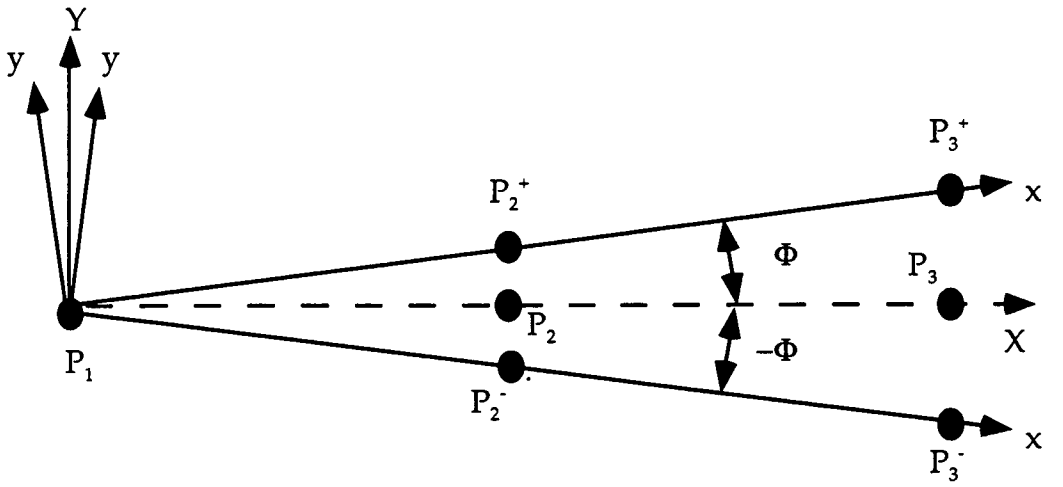

Figure XIV.1. The misalignment of a ruling line with respect to the image analysis axis.

correction factor otherwise can be calculated using Eq. [XIV.1], where x_2^+ and x_2^- are either the x+ or - position of point P_2^+ measured with the respect to the image analysis coordinate system.

$$\Phi = tan^{-1}\left(\frac{y_3^+ - y_1}{x_3^+ - x_1}\right) = -tan^{-1}\left(\frac{y_3^- - y_1}{x_3^- - x_1}\right) \qquad [XIV.1]$$

To correct a value that is below (-Φ) the following formula can be used:

$$y_3 = P_3 = (x_2 - x_3)tan\Phi + y_3^- \qquad [XIV.2]$$

To correct a value that is above (Φ) the following formula can be used:

$$y_3 = P_3 = (x_2 - x_3)tan\Phi + y_3^+ \qquad [XIV.3]$$

The value for the fringe position measured with the image analysis system must be corrected for the misalignment of the ruling. This misalignment may be systematic in the setup or be incurred during the digitization of the film. The above mentioned analysis has not shown how the ruling is "deflected" by the optical curvature of the interface but the same equations ([XIV.1-3]) can be applied if the curvature is uniform over the entire image. The data in Appendix VII range from Φ = -0.127° to 0.07°.

XIV.2 Calculation of R_{eq}

In Section 6.5 of Chapter VI two ronchi rulings were used to verify the correction angle between the substrate and optical axis, G, and also to calculate the shape of the triangular air film through geometric reconstruction. In Figure XIV.2, a segment of circle of radius R_{eq} is used to represent the gas liquid interface for a given position of y along the axisymetric centerline profile. R_{eq} is calculated based on the height h(x=0,y), and the width, W_1, and is given in Eq. [XIV.4].

$$R_{eq} = \frac{4h(y)^2 + W_1^2}{8h(y)} \qquad [XIV.4]$$

The results using Eq. [XIV.4] are compared in Fig. XIV.3 to the reconstructed profile in the Section 6.5 (Figs. 6.15 and 6.16) at 400 μm from the tail.

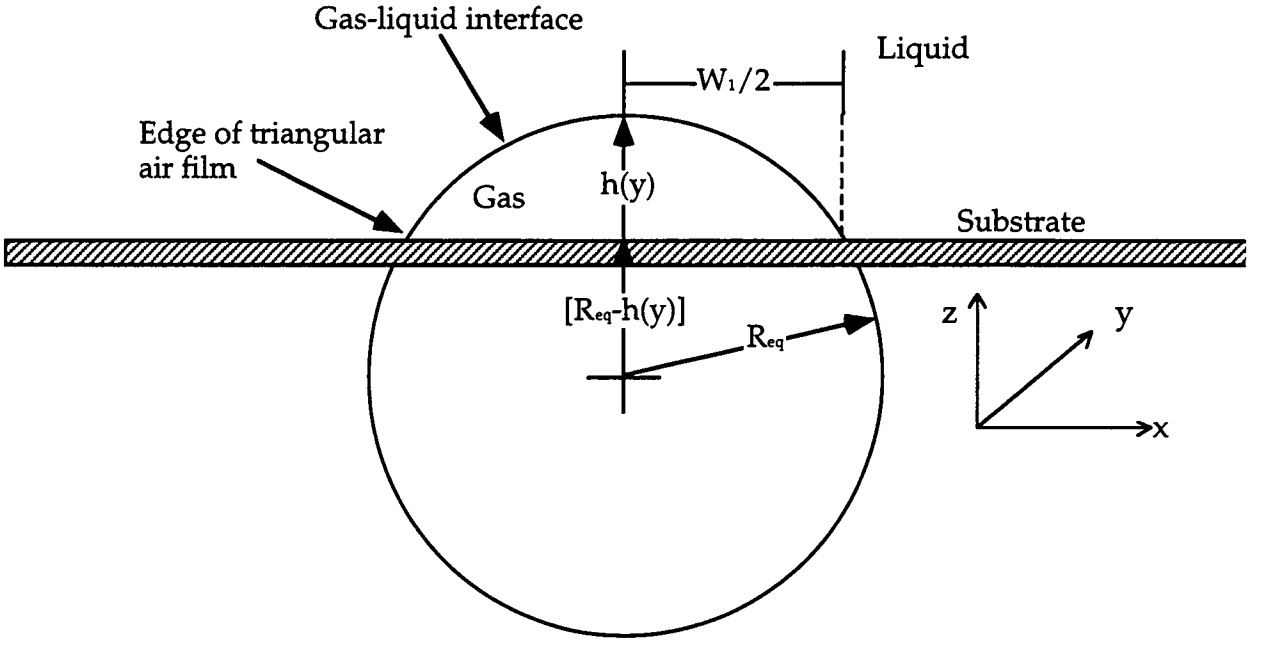

Figure XIV.2. Cross section for calculation of radius of curvature in the x-direction for an triangular air film.

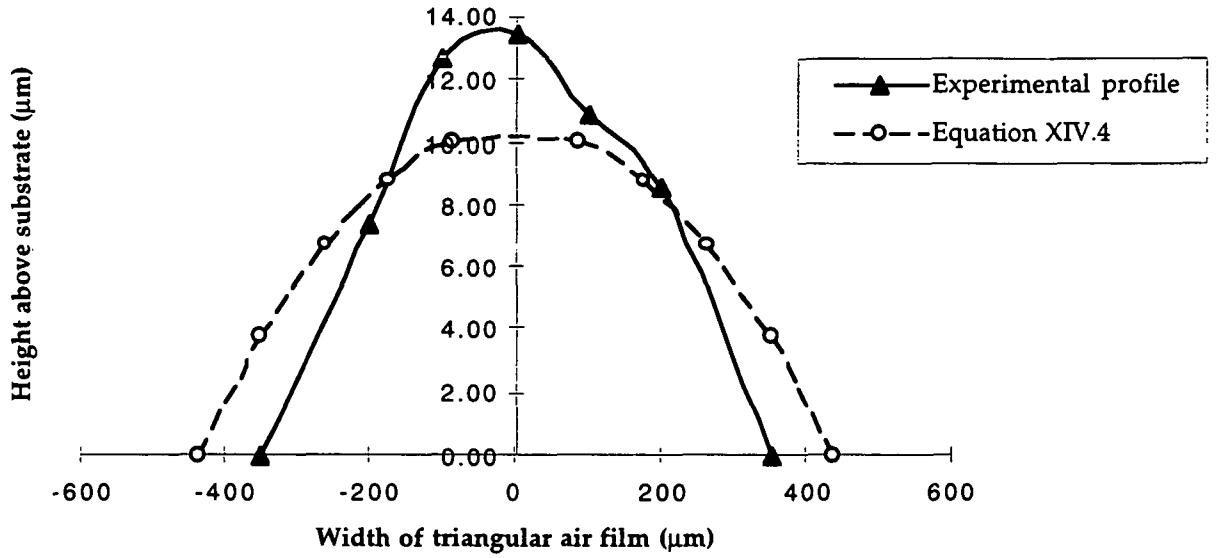

Figure XIV.3 Comparison of the experimental versus reconstructed profile for the cross section air of the triangular air film contained in the Chapter VI (Figs. 6.15 and 6.16). The equivalent radius of curvature was R_{eq} = 9,078 μm and the width was 873 μm.

APPENDIX XV

COPY OF PAPER FROM Aidun, Veverka and Scriven (1993)

This paper is provided for convenience after if was initially presented at the 1993 Tappi Coating Conference. The poor reproduction of the photo series at the end of paper can be overcome by viewing the photos in Veverka and Aidun (1991).

THE MECHANISM FOR EXCESSIVE AIR ENTRAINMENT IN COATING SYSTEMS

C.K. Aidun
Associate Professor
Institute of Paper Science and Technology
Atlanta, GA 30318

P.J. Veverka
Graduate Student
Institute of Paper Science and Technology
Atlanta, GA 30318

L.E. Scriven
Regents' Professor
University of Minnesota
Minneapolis, MN 55455

ABSTRACT

One of the objectives of our study is to determine the sequence of events leading to air entrainment. It is well known that, prior to air entrainment, the dynamic contact line destabilizes and forms sawtooth structures at a critical speed. Subsequently, two fundamentally distinct mechanisms can be foreseen to result in air entrainment. Further increase in speed could either force a stream of air through the tip of the V-shaped structures into the fluid, forming air bubbles in a periodic manner much like the air bubbles in a fish tank, or, as proposed by Scriven (1982 AIChE National Meeting), the air entrainment mechanism could involve the collapse of the thin air pockets and formation of bubbles.

Visualization experiments with a relatively dry and smooth surface plunging into a pool of liquid provide further insight into the mechanism. We have shown that with relatively smooth surfaces, the air pockets do indeed collapse and form air bubbles in a highly dynamic manner. As the air pockets, or V-shaped structures, form and elongate, the liquid surface destabilizes forming waves at the sides, and subsequently, nucleation sites form and the fluid contacts the solid surface. The surface tension forces rapidly expand the wetting region until a patch of air in the pocket becomes isolated and enters the liquid. Once surrounded by liquid, the isolated air patch rapidly forms a bubble. The sequence of events leading to air entrainment and the physics of the process are presented with the aid of long-wave stability analysis.

INTRODUCTION

Application of a thin liquid film on a flat substrate involves displacement of air by liquid. With flexible substrates, such as paper, photographic films, or magnetic tapes, the coating is continuously applied to a moving substrate. The speed of the substrate and, therefore, the rate of coating is limited by the maximum critical speed of displacing the air. Beyond this wetting speed, air cannot be totally displaced, and some patches of air remain on the surface or entrain into the liquid.

With the increasing demand for higher production rates, air entrainment has emerged as one of the leading problems in the coating industry. By air entrainment we mean a physically isolated patch of air or bubble that enters into the liquid phase. The critical speed for onset of air entrainment has been measured by many investigators [1-6]. Some of these measurements, however, are subjective and show inconsistent behavior. For example, some studies [1,2] indicate that the substrate entry angle significantly affects the critical air entrainment speed, while other studies [3,4] show no relation between the two. The effect of surface roughness on the critical speed for air entrainment has also remained unclear; some studies [5] show a strong interdependence, while others [6] indicate otherwise. It is probably the different experimental setups and substrate materials that are responsible for some of the inconsistencies.

In this study, we focus on the physical mechanism of air entrainment. In particular, we investigate the sequence of events which lead to formation of air bubbles and their entrainment into the liquid. We recognize at least two regimes of air entrainment [7]: (1) a microscopic regime, proposed by Miyamoto and Scriven [8] and further investigated by Miyamoto [9] and (2) a second regime at macroscopic scale where air bubbles in the order of few hundred microns and larger form at the wetting line and penetrate into the liquid.

In the microscopic regime, it is hypothesized that a thin air layer, less than a micron, forms at the dynamic contact line. Miyamoto and Scriven [8] analyzed the two-dimensional idealization of this flow and concluded that Kelvin-Helmholtz-type instabilities are likely to occur for thicker gas films, while a "disjoining collapse" instability of the interface will dominate for thinner air layers. Miyamoto [9] presents some experimental evidence of massive shear instability of the air film and formation of "craters."

This study focuses on the macroscopic regime of air entrainment where the entrained bubbles are too large to dissolve in the liquid and, therefore, remain in the system. We are primarily interested in the mechanism of the dynamic contact line instability and air entrainment with nonporous smooth surfaces although the general conclusions may apply to paper and photographic films, as well.

To study the kinetics of wetting, Deryagin and Levi [10] used a simple slot-like coating apparatus to reproduce the process of coating an emulsion on a flexible substrate. They used a wetting hopper with a square cross-section with sides equal to 2.4 cm. Using visualization techniques, they observed the deformation of the wetting line as they increased the substrate speed. At low base velocity, the contact angle is nearly zero, and "perfect wetting" is observed. As the coating speed increases, the meniscus deforms, and the contact angle increases to 180° as shown in Figure 1. They report that at this critical speed, a shift in the contact line is observed by the appearance of a triangle where contact between the liquid and the substrate is broken. At higher speeds, the triangular area grows to a point where the brake extends over the entire length of the contact as illustrated in Figure 1b.

The pioneering work of Deryagin and Levi [10] reveals an important event and limitation in the wetting of solids by liquid. A contact line, originally straight, breaks into a sawtooth pattern at a critical speed where the contact angle reaches 180°. This flow behavior at the wetting line seems to be universal in the sense that it occurs regardless of the substrate material and liquid properties. In the ideal situation where the contact line is infinitely long, this behavior can be viewed as transition from a two-dimensional flow to a three-dimensional state.

Blake and Ruschak [4] attribute this behavior to a maximum wetting speed above which the contact line has to incline with the flow direction in order to experience a wetting speed below the maximum value. A rigorous analysis of the contact line instability and formation of triangular air pockets remains to be undertaken.

There is no doubt, however, that a prerequisite for air entrainment in the wetting process is formation of these structures. The events that follow this transition and lead to air entrainment are addressed in this study.

EXPERIMENTAL SETUP

The studies of wetting a solid surface by a liquid fall into two general categories depending on the magnitude of the capillary number. At low capillary numbers where air entrainment is not an issue, the experimental setups usually consist of spreading a liquid drop over a surface or liquid movement under capillary forces. Air entrainment becomes important at higher capillary numbers where the meniscus deforms and destabilizes as described in the previous section. At this regime, the solid surface must move relative to the liquid in order to reach the air entrainment speed limit.

The experimental setup in this study consists of a rotating circular transparent roll halfway immersed in a pool of liquid. By rotating the roll, a dynamic contact line forms at the surface of the roll as it plunges into the liquid. A plastic blade is used to clean the surface of the roll as it emerges from the other side of the liquid surface. This is to keep the roll as dry as possible and to reduce the effects of liquid residuals left on the surface.

High-speed cinematography with 16 mm silver halide film is used to visualize the details of the dynamic contact line instability and air entrainment. In the first part of the experiments, the critical speed for the contact line instability, U_1, the air entrainment speed, U_2, and the other quantitative characteristics of the events are measured as a function of the fluid viscosity. The qualitative behavior of the air entrainment events is recorded with two different setups as described below.

In the first setup, we visualize the behavior of the contact line through the liquid side with the arrangement shown in Figure 2. This view has the advantage of generating a high degree of contrast at the solid/air and the liquid/solid interfaces if the light and the viewing angles are adjusted to form total internal reflection [11].

In our studies, we have used a high-speed 16 mm camera designed for the acquisition of photographic data pertaining to high-speed or short-lived events. It uses the rotary prism and continuous film flow principles of operation and is capable of filming up to 11,000 frames per second (fps) with a full-frame optical head. The high-speed camera is limited by its geometric aperture of f/3.2. A built-in crystal generator known as the timing light generator (TLG) driven at selected frequencies of 100, 1000, and 5000 Hz marks the inboard film edge. The TLG signal has an accuracy of 0.01% and thus provides high precision in determining elapsed time between events. Standard video and high shutter speed video (both 30 fps) were used unsuccessfully because of insufficient framing speed, although their immediate review of experimental result is a definite advantage.

As mentioned earlier, proper magnification, illumination, and contrast are required to obtain good results. It was decided that the best setup would include using a mirror and a Kiron f/4.5 70-210 mm zoom lens which allowed for filming of up to approximately 6' away from the subject. Distance markers were made on the roll's surface to determine sawtooth dimensions and to calculate the accurate linear roll speed from the TLG marks on the film. Four 1000W tungsten-halogen lamps were positioned directly over the experimental apparatus behind a diffuser shade to eliminate glare. Figure 2 presents the details of the experimental setup used in the visualization. Sufficient light was available for filming at 240 fps and an aperture of f/4.0 when using 400 ASA, 16 mm film. Upon viewing developed films, it was felt that the 240 fps framing rate provided sufficient detail between events, although higher roll velocities would require faster framing rates and thus more light. The maximum linear roll speed in the experiments reported here is 26.7 m/min.

The light angles are adjusted such that total internal reflection occurred at the solid/air interface within the air pocket of the sawtooth configuration. Wherever air entrainment was occurring, a dark area appeared in the positive final print with the reversal process. The transfer to video was made on a Rank Cintel machine via digital tape to super VHS. The video is a negative of the positive 16 mm film. A significant advantage of this dubbing process is that a frame-by-frame time code can be electronically "etched" onto the video image allowing for accurate identification of a particular segment of the film. The video signal is sent to an image analyzer for measuring the dimensions in each frame.

The above experimental setup provides excellent contrast between the solid/air and the solid/liquid interfaces. We also used a slightly different setup to visualize the air/liquid interface. In this part of the experiment, low angle lighting is used in conjunction with the high-speed camera. We placed a mirror inside the roll to view the contact line region with more clarity.

Finally, we should note that the roll used in our experiments is made of Plexiglas (methyl methacrylate) and, therefore, is not precisely round. This is mainly due to the somewhat flexible nature of Plexiglas when placed under pressure or temperature gradient. However, the total duration of the events that result in air entrainment, as we will report below, takes place in less than about 0.1 seconds. Considering that the linear surface velocity of the roll is about 25 m/min. for a roll diameter of 10 inches, the complete events occur in the span of 5% of the roll perimeter. Therefore, we believe that the effects of slight variations in the surface curvature are minimal and do not influence the mechanism revealed from this study.

FLOW VISUALIZATION RESULTS

The 16 mm silver halide film were analyzed to capture the details of air entrainment at the dynamic contact line. With the first experimental setup, the images produced a sharp contrast between the wet and the dry region of the solid surface. The triangular air pockets are clearly visible at the contact line, as shown in the first frame of Figure 3. Considering this image to be at time zero, the next 11 frames demonstrate the sequence of events forming an air bubble entraining into the liquid phase. The markers on the horizontal lines on the roll are one centimeter apart. The reflection of the markers are also apparent in frames 43 to 58. The thinner cross hairs on the camera lens divide the images into six sections. The three vertical lines are 16.3 mm apart. In these images, the solid surface is moving upward at a linear speed of 15.5 m/min.

The solid surface inside the air pockets represented by the darker triangles is dry, and therefore, the wetting line has a sawtooth structure. We explain the events leading to air entrainment by focusing on the second triangle from the left side of frames 43 to 58 of Figure 3. In general, the liquid ruptures the air film at the sides

of the triangle creating a nucleation of wetting site which expands rapidly isolating an air patch at the tip as shown in frames 43 to 54. This volume of air detaches from the surface (frame 55) and forms an air bubble which penetrates into the liquid phase as demonstrated in frames 56 and 58. The total elapsed time from nucleation of wetting to formation of an air bubble is about 50 ms. By measuring the volume of the bubble and the surface area of the triangle, we estimate the thickness of the air film to be between 10 to 50 micrometers. This is in good agreement with the value proposed by Scriven [7].

Although the formation of air bubbles has been revealed by these images, the physical mechanism initiating air film rupture and the nucleation of wetting remain hidden with this particular flow visualization technique. In principle, there are two completely different mechanisms which can initiate a liquid bridge. A hydrodynamic mechanism involving wave formation on the liquid surface inside the air pocket is proposed by Scriven [7]. The wave amplitude could grow large enough to eventually touch the solid surface. The second mechanism could be due to particles in the fluid or air which penetrate into the air pocket and provide a bridge between the solid and the liquid. Obviously, in the presence of particles in the air, the second mechanism can initiate nucleation of wetting. The question, however, is whether the hydrodynamic mechanism is sufficient for initiating a wetting site? In other words, is the liquid surface inside the air pocket unstable?

With the second experimental setup, we show that the hydrodynamic instability and formation of waves at the liquid surface is indeed a link in the events leading to air entrainment. In this setup, we focus on the liquid interface inside the air pockets. The first picture presented in Figure 4 shows a wavy surface at the two sides of the triangle. The subsequent pictures show wetting sites initiating at the sides followed by the same sequence of events leading to formation and entrainment of air bubbles, as presented before. The waves appear to travel toward the base of the triangle opposite to the direction of the solid surface motion. These waves have a wavelength in the order of few millimeters, while their amplitude is at least an order of magnitude smaller. In the next section, we take advantage of this fact and analyze the interfacial instability in the 'long-wave' limit.

LONG-WAVE STABILITY ANALYSIS

In light of the experimental results, it is useful to investigate the stability characteristics of the liquid/air interface inside the air pockets. The flow visualization results suggest that air flows into the air pocket with the solid surface at the mid section of the triangle base, changes direction, and moves outward along the sides. This clearly results in a complex three-dimensional flow pattern. For a rigorous stability analysis, one must solve the three-dimensional base state and examine its stability to spatial as well as temporal disturbances. A full stability analysis, however, is beyond the scope of this paper and shall be addressed in the future. In this study, we note that the thickness of the air layer is orders of magnitude smaller than the other two dimensions. Taking advantage of this fact, we unfold the problem into its two-dimensional idealization presented in Figure 5 where a schematic of the velocity profiles at sections A-A and B-B of Figure 5a are plotted in Figures 5b and 5c, respectively.

The air layer being much thinner than the liquid layer, we assume that the liquid extends to infinity with a constant velocity rV_S, where V_S is the velocity of the solid boundary and r is an additional parameter in the problem. Assuming that the thickness of the air layer is the same order as the liquid boundary layer thickness at the interface, the difference between the interface velocity and the free stream liquid velocity will be proportional to μ_a/μ_ℓ, where μ_a and μ_ℓ are the air and liquid viscosity, respectively. Since this ratio is much smaller than one, we neglect the shear stress at the air/liquid interface and, therefore, consider the liquid phase as an inviscid free stream with a constant velocity profile.

This problem is quite similar to the stability of the air layer studied by Lezzi and Prosperetti (1991) where they consider an air layer entrained by a liquid jet impinging into a stationary pool of liquid. The main differences between the two systems are the presence of a moving solid boundary in our system and our generalization of the pressure gradient term.

Using the lubrication approximations, the momentum equation for the air layer governing the base steady state flow reduces to

$$-\beta + \mu_a \frac{d^2 v^*}{dx^2} - \rho_a g = 0 \qquad (1)$$

where, $\beta \equiv \frac{dP}{dy}$, is the pressure gradient. The air viscosity, μ_a, density, ρ_a, and acceleration of gravity, g, are constants and $v^*(x)$ is the velocity profile in the air layer. The boundary conditions are $v^*(-d) = -V_s^*$, and $v^*(d) = -rV_s^*$ where the solid velocity, V_s^*, is a constant. By subtracting the liquid velocity from the dependent variable,

$$V(x) = v^*(x) - v^*(d), \qquad (2)$$

the boundary conditions reduce to $V(-d)=-V_S$ and $V(d)=0$. The problem is made nondimensional using the scales, d for length, $V_S=(1-r)V_s^*$ for velocity, $\frac{\rho_a d^2}{\mu_a}$ for time, and $\frac{\mu_a V_s}{d}$ for pressure. The nondimensional base state solution, V(x), is given by

$$V(x) = -\alpha (x^2 - 1) + \frac{1}{2}(x-1) \qquad (3)$$

where, $\alpha \equiv -\frac{(\beta + \rho_a g)d^2}{2\mu_a V_s}$.

Following standard linear stability analysis, we perturb the system by imposing infinitesimal disturbances $\underset{\sim}{v}_\ell(x,y,t)$ on the liquid velocity, $\underset{\sim}{v}(x,y,t)$ on air velocity, $p(x,y,t)$ on air pressure, $p_\ell(x,y,t)$ on liquid pressure, and $\eta(y,t)$ on the interface. The resulting linearized disturbance equations in the liquid phase are given by

$$\nabla \cdot \underset{\sim}{v}_\ell = 0 \qquad (4)$$

$$\frac{\partial \underset{\sim}{v}_\ell}{\partial t} + \varepsilon \nabla p_\ell = 0 \qquad (5)$$

where the liquid viscosity has been neglected and $\varepsilon \equiv \frac{\rho_a}{\rho_\ell}$ is the air to liquid density ratio. The equations for the air layer are

$$\nabla \cdot \underset{\sim}{v} = 0 \tag{6}$$

$$\frac{\partial u}{\partial t} + RV\frac{\partial u}{\partial y} = -\frac{\partial p}{\partial y} + \nabla^2 u \tag{7}$$

$$\frac{\partial v}{\partial t} + R(V\frac{\partial v}{\partial y} + u\frac{dV}{dx}) = -\frac{\partial p}{\partial y} + \nabla^2 v \tag{8}$$

where (u,v) and (u_ℓ, v_ℓ) are the x and y components of the disturbance air velocity, $\underset{\sim}{v}$, and liquid velocity, $\underset{\sim}{v}_\ell$. The Reynolds number is defined as $R \equiv \frac{\rho_a V_s d}{\mu_a}$.

The perturbed interface is given by

$$F(x,y,t) \equiv x - [1 + \eta(y,t)] = 0 \tag{9}$$

The velocity boundary conditions at the air-liquid interface and the solid surface are

$$u_\ell(1,y,t) = u(1,y,t) \tag{10a}$$

$$u(-1,y,t) = 0 \tag{10b}$$

$$v_\ell(1,y,t) = v(1,y,t) + V'(1)\,\eta(y,t) \tag{10c}$$

$$v(-1,y,t) = 0 \tag{10d}$$

where $V' \equiv \frac{dV}{dx}$ appears in (10c) due to the Taylor expansion of the velocity at the interface.

The balance in normal stress is given by

$$p_\ell(1,y,t) - p(1,y,t) = -2\left[\frac{\partial u}{\partial x}(1,y,t) - V'(1)\frac{\partial \eta}{\partial y}\right] + Ca^{-1}\frac{\partial^2 \eta}{\partial y^2} \tag{11}$$

where the capillary number, Ca, is defined by $\frac{\mu_a V_s}{\sigma}$ and σ is the surface tension. The tangential stress at the interface cannot be imposed because the liquid viscosity is neglected. The kinematics boundary condition, $\frac{DF}{Dt} = 0$, can be written as

$$\frac{\partial \eta}{\partial t} = R\ u(1,y,t) \tag{12}$$

The disturbance functions are expanded in normal modes by

$$\begin{bmatrix} \underset{\sim}{v}(x,y,t) \\ p(x,y,t) \\ \underset{\sim}{v}_\ell(x,y,t) \\ p_\ell(x,y,t) \\ \eta(y,t) \end{bmatrix} = \begin{bmatrix} \hat{\underset{\sim}{v}}(x) \\ \hat{p}(x) \\ \hat{\underset{\sim}{v}}_\ell(x) \\ \hat{p}_\ell(x) \\ \hat{\eta} \end{bmatrix} e^{\alpha + iky} \tag{13}$$

where by assuming that the wave number k is real, we focus our analysis to temporal instability. With this expansion, liquid phase Equations (4) and (5) can be solved to get

$$\hat{u}_\ell = A_\ell e^{-kx} \tag{14a}$$

$$\hat{v}_\ell = -iA_\ell e^{-kx} \tag{14b}$$

$$\hat{p}_\ell = \frac{s}{\varepsilon k} A_\ell e^{-kx} \tag{14c}$$

We expand the other unknown variables in terms of wave number, k, using the same asymptotic expansion as Lezzi and Prosperetti (1991), given by

$$s = k\,(s_0 + ks_1 + \ldots) \tag{15a}$$

$$\hat{u}(x,k) = k[u_o(x) + ku_1(x) + \ldots] \tag{15b}$$

$$\hat{v}(x,k) = v_o(x) + kv_1(x) + \ldots \tag{15c}$$

$$\hat{\eta}(k) = a_o + ka_1 + \ldots \tag{15d}$$

$$\hat{p}(x,k) = k[p_o(x) + kp_1(x) + \ldots] \tag{15e}$$

Substituting expansion (15) into Equations (6) to (8) and retaining the zeroth order terms in k, we get

$$u_o'(x) + iv_o(x) = 0 \tag{16}$$

$$u_o'(x) - p_o' = 0 \tag{17}$$

$$v_o' = 0 \tag{18}$$

The zeroth order boundary conditions corresponding to boundary conditions (10) to (12), respectively, are given by

$$ku_o(1) = \hat{u}_\ell(1) \tag{19a}$$

$$u_o(-1) = 0 \tag{19b}$$

$$v_o(1) = -V'(1)a_o \tag{19c}$$

$$v_o(-1) = 0 \tag{19d}$$

$$P_o(1) = \frac{s_o}{\varepsilon}u_o(1) + 2[u_o'(1) - iV'(1)a_o] \tag{20}$$

$$R\ u_o(1) = s_o a_o \tag{21}$$

The zeroth order solution to Equations (16) to (18) with boundary conditions (19) are given by

$$u_o(x) = \frac{i}{4}V'(1)a_o(x+1)^2 \tag{22}$$

$$v_o(x) = -\frac{1}{2}V'(1)a_o(x+1) \tag{23}$$

$$P_o(x) = \frac{i}{2}V'(1)a_o(x+1) + c \tag{24}$$

where c is a constant of integration. From (20) and (21), we get the zeroth order growth rate, given by

$$s_o = iRV'(1) \tag{25}$$

and

$$c = \left(\frac{s_o}{\varepsilon} - 1\right)u_o(1) \tag{26}$$

The zeroth order solution is purely imaginary and does not provide any information regarding stability. Therefore, we use solutions (22) to (26) along with the original expansion (15) to solve for the first order term.

The first order equations are

$$u_1' + iv_1 = 0 \tag{27}$$

$$u_1'' - p_1' = s_o u_o + iRvu_o \tag{28}$$

$$v_1'' = s_o v_o + iRVv_o + Rv'u_o \tag{29}$$

These equations are solved with the first order boundary conditions, given by

$$u_1(1) = 0 \tag{30a}$$

$$u_1(-1) = 0 \tag{30b}$$

$$v_1(1) = -iu_o(1) - V'(1)a_1 \tag{30c}$$

$$v_1(-1) = 0 \tag{30d}$$

$$p_1(1) = \frac{s_o}{\varepsilon}u_1(1) + \frac{s_1}{\varepsilon}u_o(1) + 2u_1'(1) - i2V'(1)a_1 + Ca^{-1}a_o \tag{31}$$

$$Ru_1(1) = s_o a_1 + s_1 a_o \tag{32}$$

as an eigenvalue problem for the eigenvalue s_1

$$s_1 = -iRV'(1) + RV'(1)\left[-\frac{1}{15}R + \left(0.4 - \frac{2}{3}R\right)\alpha\right] \tag{33}$$

With this first order correction, the temporal growth rate, after some algebraic simplifications, is found to be

$$s = ik(1-k)RV'(1) + \frac{R^2}{30}(16\alpha^2 - 1)k^2 + O(k^3) \tag{34}$$

which is similar to Lezzi and Prosperetti's (1991) $s^{(0)}$ mode[1]. From the base state solution (3), one can show that if $V'(1) < 0$, then $\alpha > \frac{1}{4}$ and the interface becomes unstable according to (34). This result is consistent with the experimental observations. In the middle region of the triangular air pockets where the air and the liquid phases flow in the same direction (Fig. 5b), $V'(1)$ is positive and (34) indicates that the flow is stable in agreement with the experimental observations which show a flat stable interface in that region, as shown in Fig. (4e). At the sides of the air pockets where the air stream is being forced to flow counter to the liquid (Fig. 5c), $V'(1)$ is negative and the above analysis predicts instability and wave growth, as observed experimentally.

The phase speed, ϕ, given by

$$\phi \equiv -\frac{\mathrm{Im}(s)}{k} \sim (k-1)RV'(1) + 0(k^3) \tag{35}$$

indicates that the direction of wave propagation depends only on the sign of velocity gradient at the air-liquid interface. Since $V'(1)$ at the side region of the triangular air pocket is negative, (35) indicates that the waves propagate in the positive y direction. This result is also consistent with the flow visualization experiments which show the waves propagate opposite to the direction of the solid and the air-liquid interfacial velocity.

SUMMARY AND CONCLUSIONS

Our flow visualization studies reveal a sequence of events which lead to the formation and entrainment of air bubbles into the liquid phase. This mode which results in formation of visible air bubbles is referred to as 'excessive' air entrainment. Depending on the flow field in the liquid, the air bubbles can remain adjacent to the solid surface, as shown in the curtain coating experiments [12], or get entrained into the liquid stream, as demonstrated in the present experiments. The mechanism of air bubble formation and its entrainment into the liquid phase has been investigated in this study.

In summary, the steady two-dimensional flow at the dynamic contact line becomes unstable as the speed of the solid surface increases beyond a critical limit, U_1. This instability gives rise to a steady three-dimensional flow that consists of a thin triangular air layer forming at the wetting line. The mechanism for this instability is not well understood and remains to be explored. Our experiments show that at a second critical speed, U_2, air bubbles form and penetrate into the liquid phase. The critical speeds U_1 and U_2 decrease by increasing the liquid viscosity as shown in Figure 6 [11].

Also, the shape of the triangular air pockets change with variations in the capillary number, Ca, base on the liquid viscosity and the roll linear velocity. The change in base angle and variations in height and base length are measured [11] and presented in Figures 7 and 8, respectively. These plots show that the base angle and the height length increase with the capillary number where the base length remains virtually constant. Therefore, as expected, the triangular air layers elongate as the capillary number increases. Our experiments and analysis show that the interface inside the air layer destabilizes promoting traveling waves. We hypothesize that as the air layer elongated, the waves can grow larger in amplitude while being convected until above a critical amplitude, the waves grow large enough where the crest contacts the solid boundary initiating the formation of air bubbles, as described above.

[1] There is a sign error in Equation (4) of Lezzi and Prosperetti (1991) where the second term in the right hand side should be

$$+(16\alpha^2 - 1)\left[\frac{Re}{30} + \ldots\right]Re\,k^2.$$

The long-wave stability analysis of the last section indicates that the unstable mode is proportional to k^2. This mode of instability is similar to the $s^{(o)}$ mode of Lezzi and Prosperetti (1991) and the long wave mode for flow down an inclined plane studied by Benjamin (1957). It is interesting to note that the long-wave approximation for this problem does not admit the Kelvin-Helmholtz modes although the stability depends primarily on the slope of the velocity at the interface. The results from the stability analysis of the idealized problem are in qualitative agreement with the experimental observations.

REFERENCES

1. B.S. Kennedy and R. Burley, "Dynamic Fluid Interface Displacement and Prediction of Air Entrainment," *J. Colloid Interface Sci.*, **62(1)**, 48, 1977.
2. R. Burley and B.S. Kennedy, "An Experimental Study of Air Entrainment at a Solid/Liquid/Gas Interface," *Chem. Eng. Sci.*, **31**, 901, 1976.
3. B. Bolton and S. Middleman, "Air Entrainment in a Roll Coating System," *Chem. Eng. Sci.*, **35**, 597, 1976.
4. T.D. Blake and K.J. Ruchak, "A Maximum Speed of Wetting," *Nature*, **282**, 489, 1979.
5. R. Burley and R.P.S. Jolly, "Entrainment of Air into Liquids by a High Speed Continuous Solid Surface," *Chem. Eng. Sci.*, **39**, 1357, 1984.
6. T.M. Sullivan and S. Middleman, "Roll Coating in the Presence of a Fixed Constraining Boundary," *Chem. Eng. Commun.*, **3**, 469, 1979.
7. L.E. Scriven, "How Does Air Entrain at Wetting Lines," presented at the International Symposium on Thin Film Coating, AIChE Spring National Meeting, Orlando, FL. (1982).
8. K. Miyamoto and L.E. Scriven, "Breakdown of Air Film Entrained by Liquid Coated on Web," Paper 106F, AIChE Annual Meeting, Los Angeles, CA. (1982).
9. K. Miyamoto, "On the Mechanism of Air Entrainment," *Industrial Coating Research*, 1, 71, 1991.
10. B.M. Deryagin and S.M. Levi, Film Coating Theory, Focal Press, London, 1959.
11. P.J. Veverka, "Air Entrainment in Low Speed Roll Coating," M.S. Thesis, Institute of Paper Science and Technology, 1991.
12. S.F. Kistler, "The Fluid mechanics of Curtain Coating and related Viscous Free Surface Flows with Contact Lines," Ph.D. Thesis, University of Minnesota, Minneapolis, 1984.
13. A.M. Lezzi and A. Prosperetti, "The Stability of an Air Film in a Liquid Flow," *J. Fluid Mech.*, **226**, 319, 1991.
14. T.B. Benjamin, "Wave Formation in Laminar Flow Down an Inclined Plane," *J. Fluid Mech.*, **2**, 554, 1957.

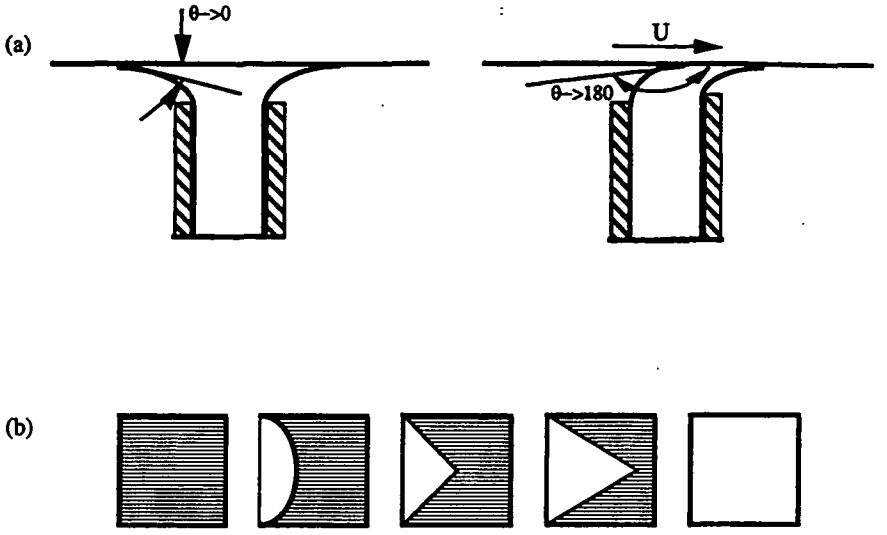

Figure 1. Schematic of the boundary displacement during wetting (from Deryagin and Levi [10]).

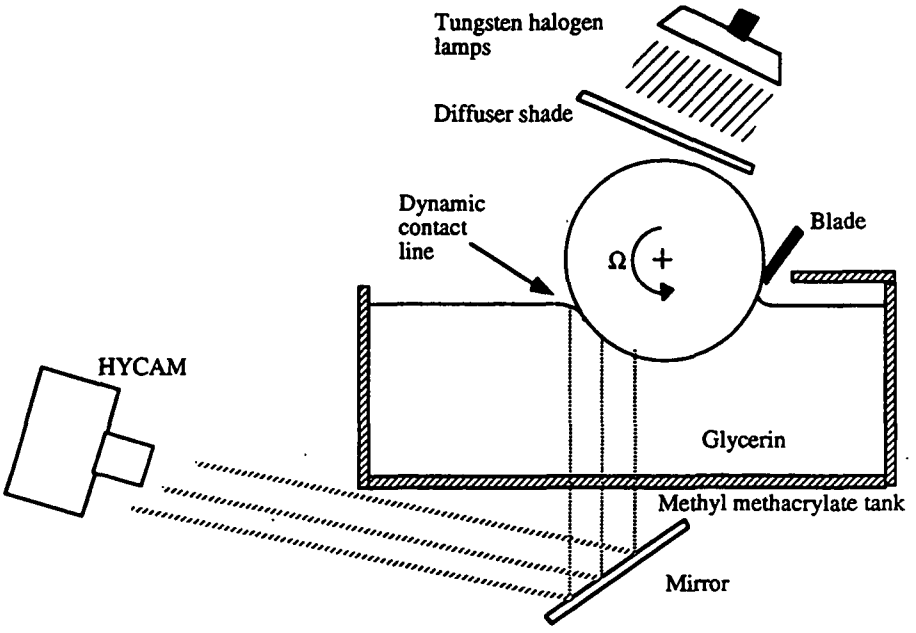

Figure 2. Schematic presentation of the experimental setup.

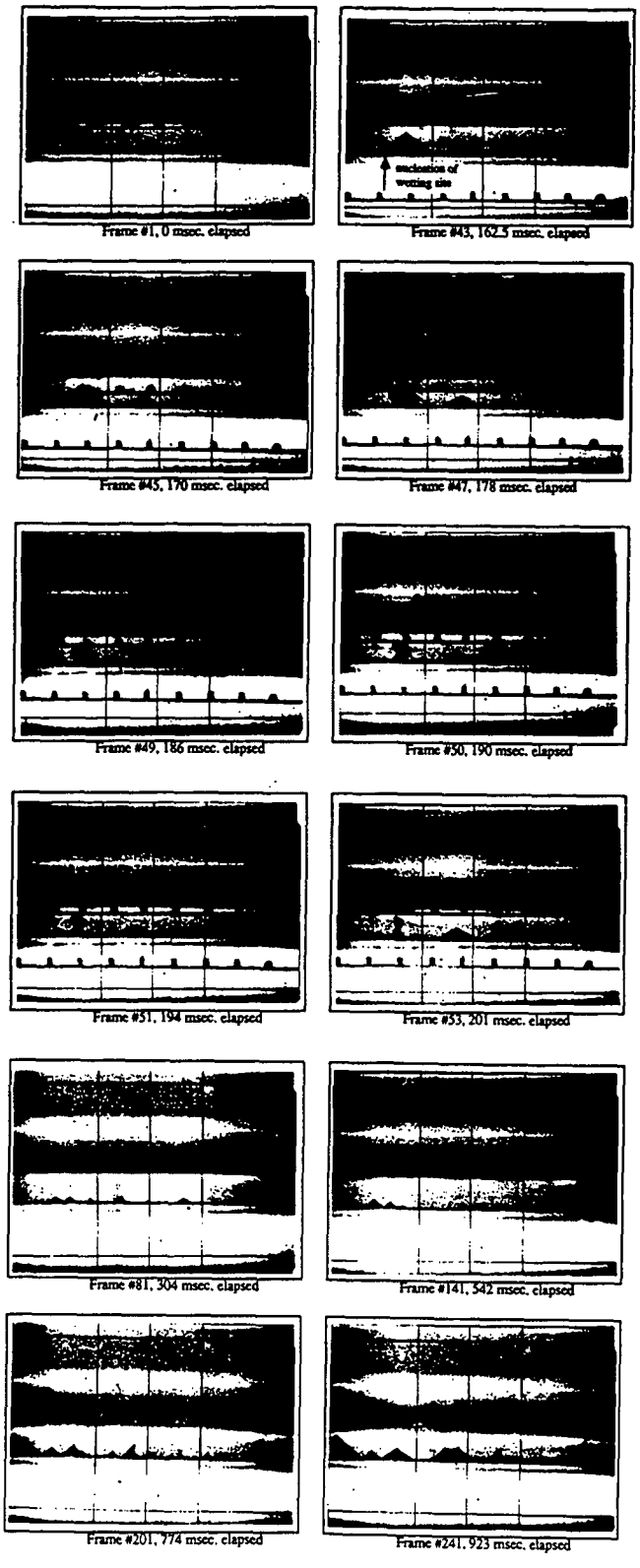

Figure 3. Frames 1 to 241 of the 16mm film showing the dynamics of air entrainment.

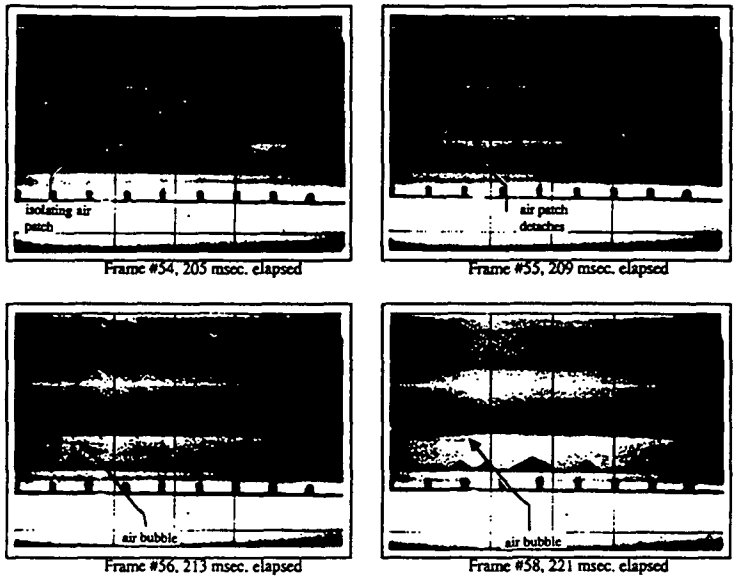

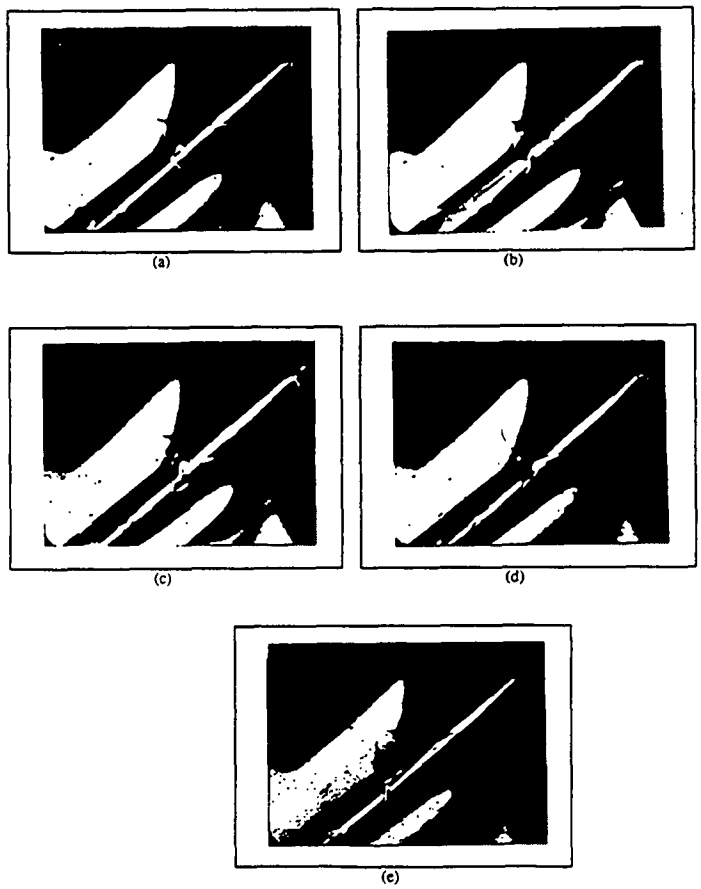

Figure 4. Sequence of events reproduced from the 16 mm film of the wavy interface inside the triangular air pockets at: (a) t = 0 msec., (b) t = 25 msec., (c) 59 msec., (d) 93 msec., and (e) 506 msec.

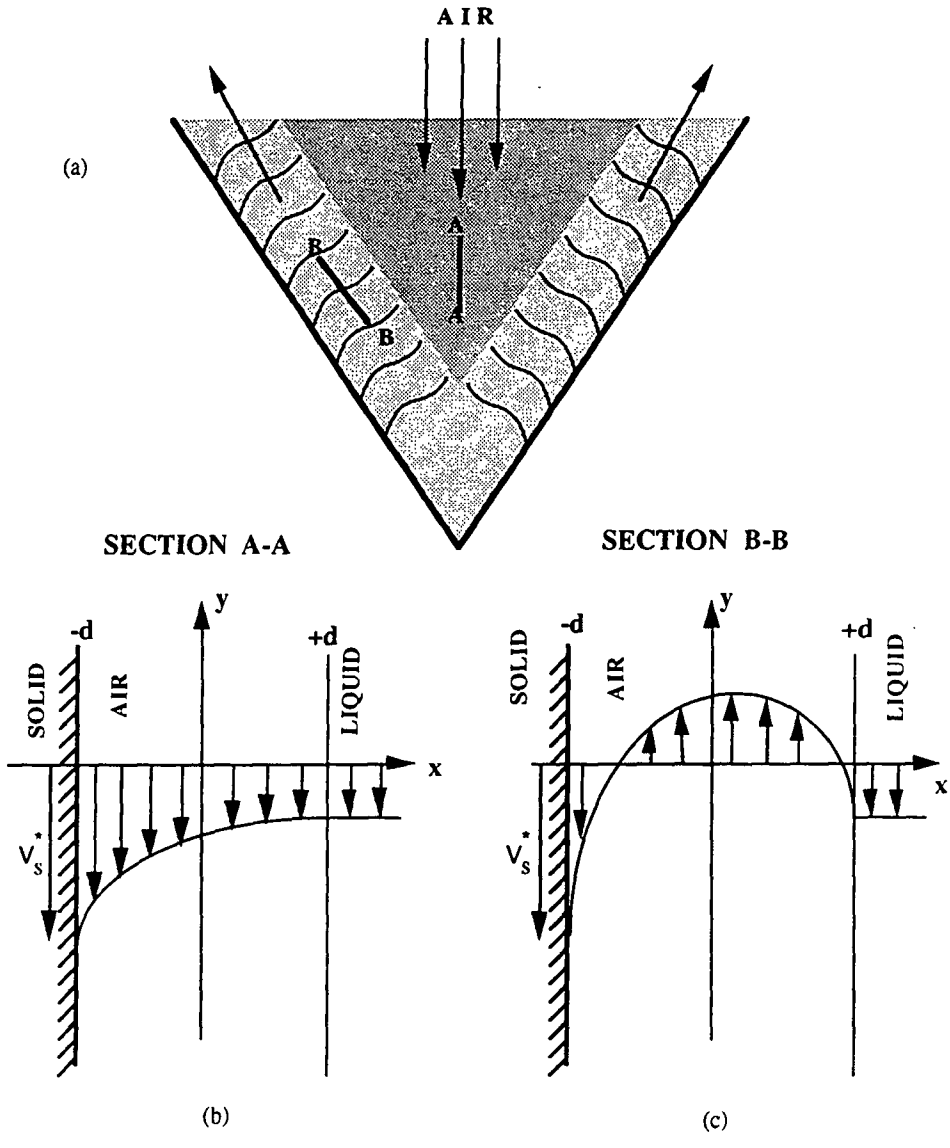

Figure 5. Schematics of the (a) triangular air layer, and the idealized air stream velocity profile in the (b) cross-section A-A and (c) cross-section B-B.

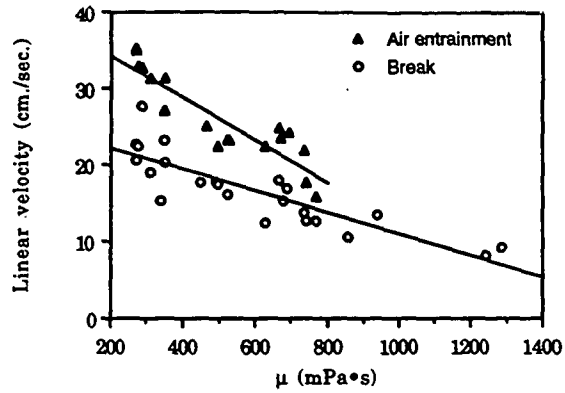

Figure 6. The critical speed, U_1 for dynamic contact line instability (break), and U_2 for air entrainment.

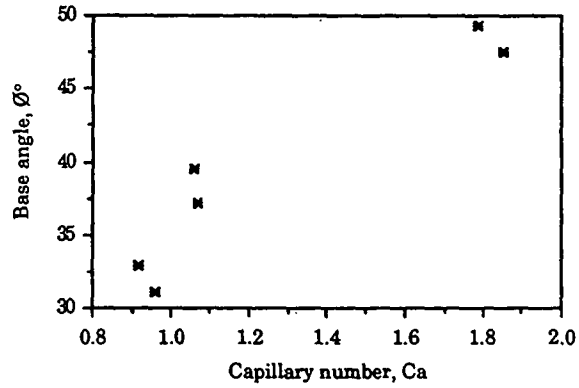

Figure 7. Variations in base angle with the Capillary number.

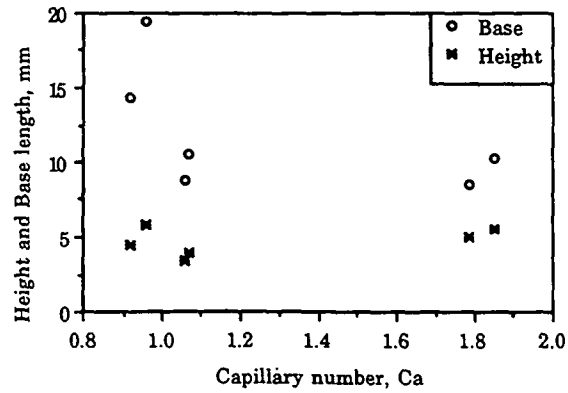

Figure 8. Variations of the height and base length with the capillary number.

APPENDIX XVI

ADDITIONAL EXPERIMENTAL DETAILS

This Appendix is broken into nine subsections

XVI.1 Unwind Rewind System

The unwind/rewind system provides motive power, guidance, tension control, and postapplication doctoring of the substrate. A 50:1 speed reducer was used to maintain the 3/4-HP DC motor at 25-100% of its rated 1725-rpm capacity. By varying the belt and gear dimensions as listed in Table XVI.1, a wide range of speeds

Table XVI.1. Theoretical speed range vs. available gear types.

	Low Range	Medium Range	High Range
Maximum speed (cm/min)	963.5	2141.2	6117.7
Type/reducer gear diam. (in)	A/2.807	A/2.807	C/8.020
Type/winder gear diam. (in)	C/8.020	B/3.609	B/3.609

Type A - Wood's P28-8M-30-QT; Type B - Wood's P36-8M-30-SH; Type C - Wood's P86-8M-30-SK

can be studied. Other gear diameters allow capability up to 30,500 cm/min (1000 ft/min). The RELIANCE 3/4-HP DC motor is controlled by a digital FENNER M-Trim 2 unit with analog output operating in closed-loop mode. The control signal comes from a 120-tooth gear ring proximity feedback sensor mounted on the motor

output shaft. The calibration data with the SHIMPO DT-105 hand-held digital tachometer for the different speed ranges are given in Table XVI.2.

Table 6. Calibration data using SHIMPO tachometer.

Speed Range	Slope, (cm/min)/ Volt	Intercept, cm/min	d.f.[a]	Actual range, cm/min	± σ, cm/min	R^2
Low	96.4	-9.6	5	0-966	0.4	0.9999
Medium	214.0	-16.1	6	0-2169	4.7	0.9999
High	612.7	-43.84	5	0-6155	17.0	0.9999

a - degrees of freedom

The cantilevered unwind reel is attached to the controlled magnetic particle brake. The measurement signal is provided by monitoring the in-line tension of the web around a 110° wrap with two MAGPOWR® RMTS1-15 rotating modular tensor sensors which is sent to the MAGPOWR® DIGITRAC™ controller. The DIGITRAC™ controller has either PI (proportional integral) or PID (proportional integral derivative) control algorithms programmed with a interactive automatic tuning algorithm. The PI algorithm gave the best performance for the experimental paper film coater using a proportional gain of zero and an integral time constant of 2.34 seconds. In total there are five rolls prior to the coating head including the live shaft tension sensors. The bearings on the rolls above and below the window "shoe" are ABEC-5/ISO GRADE-5 with a maximum inner ring radial runout of ± 0.00015 in. (3.8 μm).

The top precision roll is specified at total indicator runout (TIR) of ± 0.0002 in. (5.1 μm). The free span between the lower precision roll (TIR = ±0.002 in.) and a PFTE (Teflon™) platform is meant to reduce stretch of the tape by running the web

under the platform, thus enhancing high- and low-speed stability. It also acts as a platform for the Oriel 1000 W light source.

The remaining coating layer on the substrate is doctored by a second backing roll pressure-loaded blade system. It is necessary to remove all residual fluid from the tape to prevent slippage and telescoping of the reels. Although the coated side of the substrate is never in contact with the rubber drive rollers, leakage of fluid from the edges of the tape causes a decrease in the coefficient of friction as a lubricating film is developed. A FIFE SYMAT 25 web guidance system with an X-10 IR amplifier, in the S-wrap configuration, keeps the substrate in the same path.

In order to facilitate ease of operation in changing and loading the substrate, BOSCH safety chucks and TIDLAND air shafts were used with standard 4 in.-diameter cores. The safety chucks were mounted on linear bearings that allowed for vertical translation of the rewound reel as the diameter increases. Additionally, a pair of BIMBA trunnion-mounted air cylinders connected to the safety chucks facilitates lifting the loaded air shaft.

XVI.2 Coating Delivery and Application

The Newtonian coating fluid is transported to the coating head via 1/4"-Tygon™ tubing and a series of valves from a progressive cavity pump capable of 150 psi(g). The pump is driven by a GROVE 20:1 gear reducer connected to a RELIANCE 1750-rpm, 3/4-HP variable speed drive. This is also done to maintain the motor in the 25-100% operating range. An AW Company ZHM-01L positive displacement gear flow transmitter is used to measure the flow rate to the cavity. The 4-L pump

supply and the coating fluid recovery flasks are located on the optical bench. The 0-10 volt PI control signal for the supply pump comes from a PHILTEC 0-1 volt fiber optic displacement sensor located on the coating cavity. This non-contact method of sensing the liquid height allowed for precision level control as the flow rate varies proportionally to the line speed.

The PI algorithm is implemented using LABVIEW data acquisition and control software. The best tuning parameters are found to be a proportional gain of 175.0, and an integral time constant of 0.7 seconds and a setpoint of 0.25 V. Since the sensor is sensitive to IR light, any nonfiltered IR emissions, e.g. tungsten halogen light, will result in an aberrant measurement signal and loss of liquid height control. Under normal operating conditions, about 2-40 ml/min of liquid is delivered to the cavity to maintain the height within ±20 μm. Peak flows of 70-120 ml/min are maintained during startup as the cavity is filled. Leakage from the edges of the cavity prevents accurate determination of the coating thickness.

The coating shoe, borrowed from the term "press shoe" in wet paper pressing, provides a surface on which to load the cavity and for the substrate to slide over. The window at the shoe center can be manually positioned to maintain a continuous planar surface over which the tape slides and the shoe is grounded by a wire to the optical bench surface.

The angular deflection correction angle, G, was not explicitly measured for every experiment, a correlation based on the fluid viscosity was calculated to estimate G, i.e., blade loading to meter same t_c. The correction, G, increased with μ

as expected by classic slider bearing theory although the data did not permit exact quantification of the blade force (Denn, 1980, p.274).

XVI.3 Process Control and Data Acquisition Systems

A total of seven analog input signals and one analog output signal were acquired using a 12-bit A/D board (National Instruments MC-MIO-16L-9) on the IBM PS/2 77 DX2 computer. The board was operated using eight differential channels connected to a general purpose termination breadboard (National Instruments SC-2070). The type-T thermocouple signal was amplified by 100X, prior to the breadboard, using an OMEGA Omni-Amp III. Table XVI.3 summarizes the data acquisition system signals. A block diagram of the signal I/O paths and control systems is contained in Appendix IV.

Table XVI.3. Input/output signals to MC-MIO-16L data acquisition board.

INPUT SIGNAL	CHANNEL #	RANGE	GROUP #
Fiber optic displacement	0	0 - 1 V	0
3M Electrostatic voltmeter	1	± 2 V	0
Type T thermocouple	2	0 - 1 V	0
Digitrac load	3	0 - 5 V	1
Substrate velocity	4	0 - 10 V	1
ZHM flowmeter	5	0 - 1 V	1
Monroe voltmeter	6	± 3 V	2
OUTPUT SIGNAL			
Pump controller	0	0 - 10 V	

XVI.4 Computer Control Software

The main functions of the computer control software are data logging, control of liquid height in the coating cavity, and a graphical interface. The software chosen

was LabVIEW® 2.5.2 for Windows manufactured by National Instruments Corporation. LabVIEW uses a graphical programming language to create programs in block diagram form, as distinct from text-based languages used to create lines of code. LabVIEW programs are called *virtual instruments* (VIs) because their appearance and operation imitate actual instruments. The VI interactive user interface is called the *front panel* which receives instructions from the block diagram. Since VIs are hierarchical and modular, they can be used as top-level programs or as subprograms within other programs or subprograms.

A total of five VIs were designed for specific use with the experimental paper/film coater. Generic input/output and data logging VIs are not discussed as further details are found in the user manuals for LabVIEW. The front panel and block diagrams as well as descriptions of the VIs are contained in Appendix V. The five VI's are explained in Appendix V are:

- DATAACQ.VI
- DATAUNIT.VI
- PID.VI
- CAPILARY.VI
- REYNOLDS.VI

XVI.5 Imaging Components

The heart of the imaging system is a Wild-Heerbrugg M8 stereo zoom microscope. In the flow visualization of slide coating flows, Sweitzer (1988) used a Greenough-type SZM which has some advantages and disadvantages over the

common main objective type. More details about the magnification, resolving power, and aperture of the SZM are contained in an article by Schulueter and Gumpertz (1976). The M8 allows for continuous zoom magnifications from 6 to 50X, zoom ratio 8:1 with a 1X main objective. The field of view is defined as the area visible through the microscope when it is in focus, while the depth of field is the distance between the furthest and nearest subject that is in focus. As the magnification is increased, the field of view and depth of field decrease. The converse holds true for a decrease in magnification.

XVI.6 Types of Flow Visualization Experiments

Two types of flow visualization experiments were conducted: (1) **RAM**p type, and (2) **CA**pillary number type. Additional details regarding procedure are discussed later in the experimental section with applicability to the imaging system discussed here.

In a RAMp type of experiment, the substrate is uniformly accelerated at a slow rate from an initial speed to some final speed. The RAMp experiment is meant to capture U_v and U_{ae} over a long period, and thus, the CCD camera was used with a S-VHS recording deck and HORITA time code generator (TCG). The TCG creates an overlay on the video image displaying elapsed hours, minutes, seconds, and frame. Standard video operates at 30 Hz with each field scanning at 60 Hz. With a CCD operating in field mode, each field can uniquely be displayed using the proper playback equipment and an 'event' easily located using the time code overlay.

Rear lighting with an Oriel 1000 W tungsten halogen lamp for the RAMp experiments proved best when an opal glass diffuser lens was placed over the lamp aperture. The lamp is equipped with an IR absorbing mirror dramatically reducing radiate heating of the test section. During CApillary-type experiments, the lamp was tilted approximately 10° off the SZM primary objective axis and the opal glass diffuser removed. The photography lightmeter reading using a Goss Lumina Pro was greater than an EV value of 19 which is necessary with 200 ASA film at 500 fps and 1/9700th of a second exposure time.

In the CApillary-type experiment, both microscope ports were used with focusing conducted on the CCD monitor screen and switching back to the other port when running the LOCAM. To facilitate positioning of the SZM/LOCAM/CCD array uniformly and without changing alignment of the optical axis perpendicular to the shoe window, a traversing alignment system was designed. The LOCAM and SZM were both mounted on a dual offset shaft that maintained correct adapter to phototube distances while permitting angular adjustment. The LOCAM was supported by a lab scissor jack, while the CCD remained unsupported.

XVI.7 Image Analysis Software

OPTIMAS™ 4.1 for Windows was chosen for use with a Data Translation DT 2953 for the IBM PS/2. This 8-bit monochrome board with 2-bit overlay permits 256 grey-scale luminance values to be measured. This is important for discriminating between fringes and useless information in an individual frame.

OPTIMAS™ is a menu-driven package with advanced macro capability for collection of distance and luminance-based point, line, and area measurements. Measurements can be logged to file during a session or recorded manually.

The skeletonization algorithm allows for accurate identification of the start of a ruling line by using the line marker flag routine and the Ln_MarkerName_Points_X function. The line flag marker subroutine is a an automatic method for detecting changes in grey-scale values and extracting the coordinates to a file. A number of different settings[1] were tested for determining the grey-scale change criterion with the best detection level. It was found that using a large number[2] of sample intervals, 4096, for detecting the valleys, i.e., the fringe center, and marking where the gradient begins, gave the best results as seen by Table XVI.4 The previously mentioned capabilities permit many images to be measured

Table XVI.4 - Verification of Detection of Fringe Displacement with Distance Between Fringes = 80 μm

Data file = LNPNTS6.XLS
4096 Intervals, Weighted Average, Valleys, Gradient on, Weight Function = 5 Samples

Set#	dy_i Average (μm)	dy_i Std. Dev.(μm)	dy_i Bias Error(μm)	Standard Error	Count	t-dist (99%)	dy_i Total Error(μm) @99% CI
1	78.65	2.34	1.35	2.98%	18	2.567	7.36
2	79.03	1.82	0.97	2.31%	22	2.518	5.56
3	79.12	2.69	0.88	3.40%	20	2.539	7.71
5	78.79	2.51	1.21	3.18%	19	2.552	7.61
6	79.42	1.89	0.58	2.38%	9	2.896	6.04
7	78.77	2.54	1.23	3.23%	19	2.552	7.73
	Average	**2.30**	**1.04**				**7.00**

[1] See laboratory notebook page 144 for the different settings tested.
[2] With a large number of sample intervals the computer CPU can be slowed considerably without adequate RAM. The PS/2 33/66 DX2 had 32 Megs of RAM installed.

fairly rapidly (2-4/hour) with good accuracy in determining δy_i or δx_i. The accuracy is limited by the number of pixels that the frame grabber can handle and the resolution of the original image. For example, an image with a large number of fringes, c.a. 30, but low video resolution, c.a. 640 x 480 square pixel resolution (vertical x horizontal line), will have poor accuracy because of the low number of video lines that divide between each fringe (480 lines vertical/30 fringes = 16 lines/fringe). If the fringes are spaced at intervals of 100 μm, this results in the best detection level of 100 μm/16 lines = 6.25 μm/line. Therefore, it can be easily seen why the contrary situation with high resolution video and small number of fringes is desirable.

XVI.8 Operating Procedures for Coater

The experimental paper film coater at IPST is a versatile piece of equipment for studying a wide range of coating flows but requires care in operation. The system was debugged during the first six months of operation. Some of the major obstacles included:

- Inadequate doctoring by the second blade with low viscosity silicone oils (DC200-100 cSt and lower) and glycerol leading to slippage at the surface rewind. This was alleviated by using an extra operator to manually wipe the tape surface with towels prior to the winder nip.
- Mechanical interaction between the web tension control and the air table leading to vertical oscillations in the air table position. This was eliminated by proper tuning of the control parameters.

- High electrostatic voltage on the substrate prior to the DCL with the solution previously discussed in Section 4.1.2.

XVI.8.1 Experimental Procedures Checklist

In order to achieve continuity between experiments, a checklist was used. The checklist for startup and data acquisition are contained in Tables XVI.5 and XVI.6. Extra care was taken to ensure that all components were cleaned prior to operation. The shutdown procedure is contained in Table XVI.7 with emphasis on ensuring that the data file was recorded properly. If possible, the room temperature at the end of the experiment was documented with sometimes as much as 4°F change in room temperature observed over a two-hour period. This change does not significantly affect the liquid properties although the gas properties should be corrected.

Table XVI.5. Operational checklist for preparation and startup of experiment.

Phase I - Preparation	Experiment date					
1. Optical system components, either moiré of stereo zoom microscope components focused on region of interest?						
2. Initial temperature of coating fluid, room and room RH% recorded?						
3. Coating fluid degassed?						
4. Primary supply vessel filled to 4000 ml.?						
5. Moyno pump primed?						
6. Three-way valves through filters open?						
7. Valves to gear pump and coater head open?						
8. Coater head and shoe windows clean?						
9. Substrate loaded into unwind air shaft at 100 psi?						
10. Substrate threaded through path correctly?						
11. Substrate centered in web guide sensor viewing area?						
12. One complete wrap of substrate on rewind core and taped in place?						
12. Rewind core at 100 psi and lowered onto drive rolls?						
13. Substrate between edges of optical glass window?						
14. Optimal gap = 2.0 mm between roll#4 and window head shoe?						
15. Optimal gap = 5.0 mm between roll#5 and window head shoe?						
16. CSP-01 in AUTO mode, DIGITRAC to RUN mode and speed set to 100 cm./min.?						
17. CSP-01 in MANUAL mode and DIGITRAC to HOLD mode?						
18. Substrate path at equilibrium position after 2 min test?						
19. Coater head x, y, z positioned and blade gap to x.xx mm?						
20. Battery power for thermocouple and electrostatic voltmeter OK?						

Table XVI.6. Operational checklist for data collection during experiment.

PHASE II - Data Collection	Experiment date					
1. Fiber optic displacement sensor power on?						
2. Thermocouple amplifier power on?						
3. 3M Electrostatic sensor on?						
4. Computer on?						
5. Second blade air pressure on?						
6. Masterflex pump on at 70% power?						
7. Air knife and ionizing bar on?						
8. START/STOP switch on pump motor to START position?						
9. Smith Meter Flowmate power on and batch meter reset?						
10. LABVIEW for Windows opened and DATAACQ.VI opened?						
11. Data file name entered? (File code)						
12. Start pump control through LABVIEW?						
13. Acquire data when at steady state and visualization technique is ready?						
14. If using VCR, is voice data and time code on?						

Table XVI.7. Shutdown checklist after experiment completion.

PHASE III - Shutdown Procedure	Experiment date					
1. Power to drive unit off?						
2. STOP acquisition button on DATAACQ.VI depressed?						
3. FIFE guide to MANUAL and DIGITRAC to hold?						
4. Fiber optic sensor power off?						
5. Ionizing air knife power and air supply off?						
6. Electrostatic voltmeter off?						
7. OMNI-AMP IIIB thermocouple amplifier power off?						
8. START/STOP switch on pump motor to STOP position?						
9. Laser power off after 10 min cool down?						
10. LABVIEW for Windows closed?						
11. Data file names checked and reentered?						

Section XVI.9 Fluid Delivery System Changeover

When changing the fluid delivery system between miscible silicone oils of different viscosity or immicible glycerol and silicone oil, special care was taken to ensure that the delivery lines were clean. This cleanliness was important because the physical properties of the test fluids were predicted using a linear regression

based on the temperature range desired. First, the progressing cavity pump was fully disassembled and the stator and rotor cleaned with an appropriate solvent. Hexane and acetone were used on metal parts and hexane alone on rubber or acrylic parts. The 3/8" OD Tygon™ tubing, all fittings, and the ZHM 01 gear flowmeter were cleaned by blowing high-pressure compressed air until no further liquid could be removed. The coating delivery and recovery flasks were cleaned twice. First, with an appropriate solvent and second at high temperature using an industrial dishwasher. Any residual water and soap was purged prior to refilling with the next fluid.

After each RAMp- or CApillary-type experiment, it was also necessary to clean the surface winder rolls, precision rolls, window shoe, and the coater head. The surface winder is covered with Stow Woodwind's PRESTO CONDUCTIVE rubber formulation. The covering is resistant to short exposure to the acetone which was used as the primary cleaning solvent. The acetone was followed with an abrasive chlorine-based cleaner such, as Ajax™, and then fresh water. The mild abrasive action helped to promote a higher coefficient of friction even as the winder surface became covered with a thin layer of the coating fluid. The precision rolls and window shoe were both cleaned with acetone and hexane in that order, while the coater head was only cleaned with the nonpolar hexane because acetone is a strong solvent incompatible with methylmethacrylate (Plexiglass™).

APPENDIX XVII

DENSITY, VISCOSITY AND SURFACE TENSION OF TEST LIQUIDS

This appendix contains a brief discussion about the test fluids in Appendix section XVII.1 and then presents the relevant physical properties measured, namely density, viscosity and interfacial surface tension in Appendix section XVII.2.

XVII.1 Background on the Fluids

Silicone oil is a clear water-white colloid polymer and is available in kinematic viscosities from 0.65 to 100,000 cs with the trade name DC200® Linear polydimethylsiloxane polymers have the typical chemical composition $(CH_3)_3SiO[SiO(CH_3)_2]_nSi(CH_3)_3$ (Dow Corning 1991). Since the properties of a polymer such as silicone oil depend on molecular weight distribution and average molecular weight, blending of fluids with widely different viscosities can result in non-Newtonian behavior compared to fluids with normal molecular weight distributions (Kroschwitz 1990). Thus, pure silicone oils were used in all experiments. The approximate molecular weight representative samples of some of the silicone oils are given in Table XVII.1.

Table XVII.1. Molecular weight of silicone oil polymers (Sigma 1994).

Kinematic Viscosity (25°C) (cs)	Approx. Mol. Wt.
5	770
20	2,000
50	3,780
100	5,970
200	9,430
500	17,250
1,000	28,000
12,500	67,700

Glycerin or 1,2,3-propanetriol ($CH_2OHCHOHCH_2OH$) is a clear water-white viscous, hygroscopic fluid with a sweet taste. Its viscosity at room temperature (20°C) varies dramatically with water content dropping from 1487.0 cp. at 100% concentration to 27.6 cp. at 72% (Weast 1988-89)

XVII.2 Physical Properties of Test Fluids and Gases

Each of the fluids was tested in the 18-30°C temperature range, and the property (density, surface tension, viscosity) calibrated using linear regression and shown in Tables XVII.2 - XVII.4. For brevity the trade name DC200® is used in the tables to indicate silicone oil. The surface tension of most liquids decreases with temperature in a nearly linear fashion (Shaw 1980, 65). This is also true of density and viscosity when the linearization interval is small and no phase changes occur. The regression sample variance, $S_{y,x}$, can be substituted for the statistical standard deviation, $\pm \sigma$, without any correction if the temperature is close to the average value used for calculating the regression. Waldpole and Myers (1989, Chapter 9.5) provide methods for determining $\pm \sigma$ when calculating a parameter far from the average value and is also discussed in Appendix XIII. The viscosity of air at 50% RH was based on the data of Mason and Monchick (1964) at 1.5% mole percent water from psychrometric charts (Perry and Green 1980, Fig. 20-11).

The viscosity was tested primarily using a Rheometrics fluids spectrometer RFS II and also with a Haake RV2. The symbol, *, in the fluid column of Table XVII.4, indicates that the Haake viscometer was used. Density and surface tension

were tested over the same temperature range using a Hubbard-Carmick specific gravity bottle and a Cahn DCA 312 dynamic contact angle analyzer, respectively. Some of the fluids were tested in replicate, e.g., silicone oil 20 cs density, to verify methodology and accuracy.

Table XVII.2. Regression analysis for density (g/cm^3) of test fluids.

Fluid	Slope x 10^4, $(g/cm^3)/°C$	Intercept, g/cm^3	d.f.[a]	Range, °C	$\pm \sigma$, g/cm^3	R^2
DC200-10 cSt	-8.902	0.9553	3	18.0-27.9	0.0002	0.9982
DC200-20 cSt #1	-7.844	0.9706	10	20.5-27.3	0.0003	0.9790
DC200-20 cSt #2	-7.829	0.9710	3	17.0-28.1	0.0003	0.9950
DC200-100 cSt	-7.534	0.9837	7	16.8-29.1	0.0007	0.9586
DC200-200 cSt	-7.546	0.9845	5	18.2-28.1	0.0004	0.9654
DC200-350 cSt	-8.237	0.9891	7	18.3-31.4	0.0002	0.9968
DC200-545 cSt	-8.431	0.9919	2	21.8-27.5	0.0002	0.9942
DC200-1000 cSt #1	-8.453	0.9912	5	18.1-29.2	0.0003	0.9947
DC200-1000 cSt#2	-9.941	0.9972	4	23.1-28.1	0.0003	0.9861
99.7% Glycerol	-5.510	1.2720	3	22.0-30.7	0.0002	0.9851
99.7 % Glycerol #2	-6.162	1.2738	4	19.0-28.7	0.0003	0.9986
200 cp. Glycerol	-2.301	1.2371	2	19.4-28.6	0.0004	0.8962
100 cp. Glycerol	-6.680	1.2490	2	23.1-27.7	0.0001	0.9931
60 cp. Glycerol	-6.790	1.2282	2	19.2-29.2	0.0002	0.9970

a - degrees of freedom

Table XVII.3. Regression analysis for surface tension (dynes/cm) of test fluids.

Fluid	Slope x 10^2, (dynes/cm.)/°C	Intercept, dynes/cm.	d.f.[a]	Range, °C	± σ, dyne s/cm.	R^2
DC200-10 cSt	-6.528	21.42	8	16.6-27.3	0.19	0.7209
DC200-20 cSt	-3.986	21.11	8	19.2-29.5	0.08	0.8053
DC200-100 cSt	-14.214	24.43	12	18.8-24.7	0.18	0.7366
DC200-200 cSt	-11.677	23.83	8	17.3-28.0	0.17	0.8354
DC200-350 cSt	-12.125	24.65	4	21.4-22.7	0.12	0.9346
DC200-550 cSt	-8.816	24.91	7	17.1-27.4	0.22	0.7284
DC200-1000 cSt	-6.466	23.91	5	21.6-29.5	0.04	0.9821
99.7% Glycerol	-5.630	50.81	4	24.1-36.0	0.13	0.8819
99.7% Glycerol#2	-27.228	50.09	6	20.4-29.5	0.71	0.7062
200 cp. Glycerine	-27.507	54.95	4	16.8-29.2	0.71	0.8239
100 cp. Glycerine	-16.401	54.23	4	22.7-31.1	0.04	0.9966
60 cp. Glycerine	-67.011	61.55	6	17.5-28.6	0.93	0.8915

a - degrees of freedom

Table XVII.4. Regression analysis for viscosity (cp.) of test fluids

Fluid	Slope, cp./°C	Intercept, cp.	d.f.[a]	Range, °C	± σ, cp.	R^2
DC200-10 cSt *	-0.183	16.72	18	17.4-28.0	0.28	0.8690
DC200-20 cSt	-0.428	30.57	10	17.8-26.3	0.26	0.9611
DC200-100 cSt#1	-2.080	154.79	10	19.7-29.5	0.27	0.9586
DC200-100 cSt#2	-2.057	151.87	18	19.1-29.6	0.77	0.9677
DC200-200 cSt	-4.102	299.54	23	18.1-33.2	1.44	0.9951
DC200-350 cSt	-7.230	515.53	13	18.1-27.1	1.35	0.9963
DC200-545 cSt	-10.217	747.48	22	18.4-29.6	1.83	0.9976
DC200-1000 cSt #1	-20.181	1498.25	23	18.2-29.5	2.31	0.9992
DC200-1000 cSt#2	-18.414	1322.15	11	20.1-27.4	3.65	0.9944
DC200-1000 cSt #3	-21.779	1470.05	18	17.6-26.8	5.18	0.9941
99.7% Glycerol	-85.303	2878.97	22	20.6-29.4	64.76	0.9605
99.7% Glycerol#2 *	-41.635	1511.33	26	19.1-28.8	29.44	0.9538
200 cp. Glycerol *	-12.918	489.00	18	19.7-27.3	5.31	0.9763
100 cp. Glycerol	-7.720	299.63	13	19.4-27.5	2.42	0.9845
60 cp. Glycerol *	-4.121	168.11	14	19.4-29.2	2.53	0.9749
50% RH Air	4.819×10^{-4}	1.715×10^{-2}	2	0.0-30.0	7.89×10^{-6}	0.9999

a - degrees of freedom

* - indicates that the Haake viscometer was used for measurement.

APPENDIX XVIII

CALCULATIONS FOR SECTION 5.9

This Appendix contains the input code for the numerical integration with Mathematica[1], the output results, and sample calculations. The output results in Table XVIII.1 are contained in rows for x*, y* and $(\pi/4)\tau^*_{xx}$.

XVIII.1 Sample Calculations

Perry's (1967) air entrainment velocity was calculated using Eq. [2.2] for the conditions

μ = 10.6 p, γ = 22.5 dynes/cm, ρ = 0.9762 g/cm^3, and $\lambda_\mu = 0.26 \times 10^{-4}$

$$U_{ae} = 0.048\mu^{-0.74}$$

$$U_{ae} = 0.048(10.6\ p)^{-0.74} = 4.6\ cm/sec$$

The Deryagin length is calculated as

$$L_d = (\mu U_{ae}/\rho g)^{0.5}$$

$$0.225\ cm = [(10.6p)(4.6\ cm/sec)/(\ 0.9762\ g/cm^3)(\ 980.7\ cm/s^2)]^{0.5}$$

The coordinates x* and y* where the interface starts deforming and the DCL ends for Perry's (1967) cavity, d_c = 5.08 cm, are approximated by

$$(x^*, y^*=0) = [1-(0.3cm/d_c), 0] = (0.94, 0)$$

and

$$(0, y^*) = [0, (L_d/d_c)] = [0, (0.225\ cm/d_c)] = (0, 0.044)$$

---

[1] Wolfram Research Inc., Champaign, IL. , MacIntoshV.2.03

The intersection[2] with the line of maximum normal stress is at (x*, y*) = (0.985, 0.016) and the value of $(\pi/4)\tau^*_{xx}$ is -33.11 (see Table XVIII.1). This can be calculated as a dimensional stress from Eq. [5.20] as

$$\tau_{xx} = 2\mu\frac{\partial u^*}{\partial x^*} = \mu\frac{U}{d_c}\tau^*_{xx} = \left(\frac{4\times 10.6p}{\pi}\right)\left(\frac{4.6cm/s}{5.08cm}\right)(-33.11) = -404.6\ g/cm\ s^2$$

In our system, d_c = 3.51 cm, when U=4.6 cm/sec the intersection of the approximated interface profile with the line of maximum stress is at (x*, y*) = (0.98, 0.02). Finding the value of $(\pi/4)\tau^*_{xx}$ = -24.89 at these coordinates in Table XVIII.1 the dimensional stress can be calculated as

$$\tau_{xx} = 2\mu\frac{\partial u^*}{\partial x^*} = \mu\frac{U}{d_c}\tau^*_{xx} = \left(\frac{4\times 10.6p}{\pi}\right)\left(\frac{4.6cm/s}{3.51cm}\right)(-24.89) = -440.2\ g/cm\ s^2$$

The calculations used to approximate the differences in the normal stresses should interpreted with caution because we have had to approximate the interface profile. With actual experimental data for the interface profile, i.e. viewed from the side, these calculations could be used to obtain better estimates as the cavity aspect ratio varies.

---

[2] Plunging tape intersection of interface curve with line of maximum normal stress is given by (x*, y*) = (0.985, 0.016) and side driven cavity intersection (x*, y*) = (0.9725, 0.028)

In[3]:=
```
Clear[x]
```
In[4]:=
```
Clear[y]
```
In[5]:=
```
A=(1-x)*Sinh[p]*Sinh[p*x]
```
Out[5]=
```
(1 - x) Sinh[p] Sinh[p x]
```
In[6]:=
```
Z=Sinh[p]^2-p^2
```
Out[6]=

$$-p^2 + \text{Sinh}[p]^2$$

In[7]:=
```
B=p*x*Sinh[p-p*x]
```
Out[7]=
```
p x Sinh[p - p x]
```
In[8]:=
```
W=A/Z-B/Z
```
Out[8]=

$$\frac{(1 - x)\ \text{Sinh}[p]\ \text{Sinh}[p\ x]}{-p^2 + \text{Sinh}[p]^2} - \frac{p\ x\ \text{Sinh}[p - p\ x]}{-p^2 + \text{Sinh}[p]^2}$$

In[9]:=
```
T=D[W,x]
```
Out[9]=

$$\frac{p^2\ x\ \text{Cosh}[p - p\ x]}{-p^2 + \text{Sinh}[p]^2} + \frac{p\ (1 - x)\ \text{Cosh}[p\ x]\ \text{Sinh}[p]}{-p^2 + \text{Sinh}[p]^2} - \frac{\text{Sinh}[p]\ \text{Sinh}[p\ x]}{-p^2 + \text{Sinh}[p]^2} - \frac{p\ \text{Sinh}[p - p\ x]}{-p^2 + \text{Sinh}[p]^2}$$

In[10]:=
```
Clear[x]
```
In[11]:=
```
x=0.9775
```
Out[11]=
```
0.9775
```
In[14]:=
```
y=0.0225
```
Out[14]=
```
0.0225
```
```
Do[Print[NIntegrate[T*Cos[p*y],{p,10^-9,5000},
MinRecursion->3,MaxRecursion->10]]]
```
```
-22.0953
```

Table XVIII.1 Numerically Integrated Liquid Normal Stress for Section 5.9

x*	y*	(π/4)τ*xx
0.9	0	0.512
0.9	0.005	0.462
0.9	0.01	0.316
0.9	0.015	0.081
0.9	0.02	-0.228
0.9	0.025	-0.596
0.9	0.03	-1.004
0.9	0.035	-1.433
0.9	0.04	-1.867
0.9	0.045	-2.290
0.9	0.05	-2.690
0.9	0.055	-3.056
0.9	0.06	-3.383
0.9	0.065	-3.666
0.9	0.07	-3.905
0.9	0.075	-4.099
0.9	0.08	-4.251
0.9	0.085	-4.362
0.9	0.09	-4.438
0.9	0.095	-4.480
0.9	0.1	-4.494
0.91	0	0.467
0.91	0.005	0.398
0.91	0.01	0.199
0.91	0.015	-0.118
0.91	0.02	-0.530
0.91	0.025	-1.012
0.91	0.03	-1.534
0.91	0.035	-2.070
0.91	0.04	-2.595
0.91	0.045	-3.090
0.91	0.05	-3.540
0.91	0.055	-3.934
0.91	0.06	-4.269
0.91	0.065	-4.542
0.91	0.07	-4.755
0.91	0.075	-4.911
0.91	0.08	-5.016
0.91	0.085	-5.075
0.91	0.09	-5.093
0.91	0.095	-5.078
0.91	0.1	-5.033
0.92	0	0.420
0.92	0.01	0.041
0.92	0.02	-0.964
0.92	0.03	-2.283
0.92	0.04	-3.581
0.92	0.05	-4.631
0.92	0.06	-5.342
0.92	0.07	-5.722
0.92	0.08	-5.833
0.92	0.09	-5.748
0.92	0.1	-5.534
0.93	0	0.372
0.93	0.01	-0.188
0.93	0.02	-1.622
0.93	0.03	-3.374
0.93	0.04	-4.930
0.93	0.05	-6.020
0.93	0.06	-6.605
0.93	0.07	-6.773
0.93	0.08	-6.648
0.93	0.09	-6.341
0.93	0.1	-5.938
0.94	0	0.323
0.94	0.01	-0.554
0.94	0.02	-2.677
0.94	0.03	-5.011
0.94	0.04	-6.778
0.94	0.05	-7.740
0.94	0.06	-8.012
0.94	0.07	-7.817
0.94	0.08	-7.359
0.94	0.09	-6.781
0.94	0.1	-6.169
0.95	0	0.273
0.95	0.01	-1.207
0.95	0.02	-4.484
0.95	0.03	-7.513
0.95	0.04	-9.246
0.95	0.05	-9.728
0.95	0.06	-9.403
0.95	0.07	-8.677
0.95	0.08	-7.809
0.95	0.09	-6.939
0.95	0.1	-6.131
0.96	0	0.221
0.96	0.01	-2.547
0.96	0.02	-7.779
0.96	0.03	-11.299
0.96	0.04	-12.280
0.96	0.05	-11.678
0.96	0.06	-10.431
0.96	0.07	-9.059
0.96	0.08	-7.781
0.96	0.09	-6.668
0.96	0.1	-5.727
0.97	0	0.168
0.97	0.01	-5.832
0.97	0.02	-14.034
0.97	0.03	-16.499
0.97	0.04	-15.193
0.97	0.05	-12.809
0.97	0.06	-10.500
0.97	0.07	-8.573
0.97	0.08	-7.039
0.97	0.09	-5.834
0.97	0.1	-4.488
0.98	0	0.113
0.98	0.01	-15.887
0.98	0.02	-24.887
0.98	0.03	-21.189
0.98	0.04	-15.887
0.98	0.05	-11.778
0.98	0.06	-8.887
0.98	0.07	-6.865
0.98	0.08	-5.424
0.98	0.09	-4.372
0.98	0.1	-3.586
0.99	0	0.057
0.99	0.01	-49.943
0.99	0.02	-31.943
0.99	0.03	-17.943
0.99	0.04	-11.016
0.99	0.05	-7.339
0.99	0.06	-5.202
0.99	0.07	-3.863
0.99	0.08	-2.973
0.99	0.09	-2.353
0.99	0.1	-1.904
0.999	0	-0.454
0.999	0.002	-319.875
0.999	0.004	-110.634
0.999	0.006	-52.598
0.999	0.008	-30.340
0.999	0.01	-19.624
0.999	0.012	-13.675
0.999	0.014	-10.066
0.999	0.016	-7.739
0.999	0.018	-6.147
0.999	0.02	-4.988
0.999	0.022	-4.109
0.999	0.024	-3.439
0.999	0.026	-2.933
0.999	0.028	-2.544
0.999	0.03	-2.225
0.997	0	0.017
0.997	0.002	-141.994
0.997	0.004	-153.583
0.997	0.006	-106.649
0.997	0.008	-72.041
0.997	0.01	-50.484
0.997	0.012	-36.892
0.997	0.014	-27.966
0.997	0.016	-21.855
0.997	0.018	-17.514
0.997	0.02	-14.330
0.997	0.022	-11.931
0.997	0.024	-10.081
0.997	0.026	-8.627
0.997	0.028	-7.463
0.997	0.03	-6.518
0.995	0	0.029
0.995	0.002	-47.534
0.995	0.004	-95.153
0.995	0.006	-96.719
0.995	0.008	-80.769
0.995	0.01	-63.971
0.995	0.012	-50.390
0.995	0.014	-40.101
0.995	0.016	-32.392
0.995	0.018	-26.572
0.995	0.02	-22.117
0.995	0.022	-18.653
0.995	0.024	-15.918
0.995	0.026	-13.728
0.995	0.028	-11.950
0.995	0.03	-10.490
0.993	0	0.040
0.993	0.002	-19.896
0.993	0.004	-52.978
0.993	0.006	-69.718
0.993	0.008	-70.130
0.993	0.01	-63.020
0.993	0.012	-54.082
0.993	0.014	-45.674
0.993	0.016	-38.487
0.993	0.018	-32.563
0.993	0.02	-27.737
0.993	0.022	-23.811
0.993	0.024	-20.604
0.993	0.026	-17.965
0.993	0.028	-15.778
0.993	0.03	-13.950
0.991	0	0.052
0.991	0.002	-9.914
0.991	0.004	-30.557
0.991	0.006	-47.286
0.991	0.008	-54.740
0.991	0.01	-54.892
0.991	0.012	-51.148
0.991	0.014	-45.928
0.991	0.016	-40.523
0.991	0.018	-35.504
0.991	0.02	-31.069
0.991	0.022	-27.240
0.991	0.024	-23.968
0.991	0.026	-21.182
0.991	0.028	-18.809
0.991	0.03	-16.782
0.989	0	0.063
0.989	0.002	-5.569
0.989	0.004	-18.691
0.989	0.006	-32.068
0.989	0.008	-41.077
0.989	0.01	-44.981
0.989	0.012	-45.049
0.989	0.014	-42.847
0.989	0.016	-39.563
0.989	0.018	-35.933
0.989	0.02	-32.357
0.989	0.022	-29.028
0.989	0.024	-26.021
0.989	0.026	-23.350
0.989	0.028	-20.996
0.989	0.03	-18.931
0.987	0	0.074
0.987	0.002	-3.401
0.987	0.004	-12.081
0.987	0.006	-22.198
0.987	0.008	-30.577
0.987	0.01	-35.857
0.987	0.012	-38.142
0.987	0.014	-38.177
0.987	0.016	-36.776
0.987	0.018	-34.586
0.987	0.02	-32.048
0.987	0.022	-29.437
0.987	0.024	-26.908
0.987	0.026	-24.541
0.987	0.028	-22.370
0.987	0.03	-20.403
0.985	0	0.085
0.985	0.002	-2.203
0.985	0.004	-8.179
0.985	0.006	-15.769
0.985	0.008	-22.903
0.985	0.01	-28.317
0.985	0.012	-31.642
0.985	0.014	-33.090
0.985	0.016	-33.110
0.985	0.018	-32.164
0.985	0.02	-30.635
0.985	0.022	-28.800
0.985	0.024	-26.847
0.985	0.026	-24.896
0.985	0.028	-23.017
0.985	0.03	-21.248
0.983	0	0.097
0.983	0.002	-1.488
0.983	0.004	-5.751
0.983	0.006	-11.492
0.983	0.008	-17.366
0.983	0.01	-22.372
0.983	0.012	-26.017
0.983	0.014	-28.234
0.983	0.016	-29.207
0.983	0.018	-29.219
0.983	0.02	-28.552
0.983	0.022	-27.444
0.983	0.024	-26.077
0.983	0.026	-24.585
0.983	0.028	-23.056
0.983	0.03	-21.549
0.981	0	0.108
0.981	0.002	-1.033
0.981	0.004	-4.170
0.981	0.006	-8.572
0.981	0.008	-13.357
0.981	0.01	-17.773
0.981	0.012	-21.349
0.981	0.014	-23.899
0.981	0.016	-25.446
0.981	0.018	-26.131
0.981	0.02	-26.139
0.981	0.022	-25.651
0.981	0.024	-24.823
0.981	0.026	-23.780
0.981	0.028	-22.617
0.981	0.03	-21.400
0.9725	0	0.154197
0.9725	0.001	0.0582826
0.9725	0.002	-0.226439
0.9725	0.003	-0.69108
0.9725	0.004	-1.3214
0.9725	0.005	-2.09861
0.9725	0.006	-3.00038
0.9725	0.007	-4.00202
0.9725	0.008	-5.0776
0.9725	0.009	-6.20114
0.9725	0.01	-7.34755
0.9725	0.011	-8.49354
0.9725	0.012	-9.61818
0.9725	0.013	-10.7034
0.9725	0.014	-11.7341
0.9725	0.015	-12.6983
0.9725	0.016	-13.5871
0.9725	0.017	-14.3944
0.9725	0.018	-15.1166
0.9725	0.019	-15.7522
0.9725	0.02	-16.3017
0.9725	0.021	-16.7671
0.9725	0.022	-17.1516
0.9725	0.023	-17.4593
0.9725	0.024	-17.6949
0.9725	0.025	-17.8636
0.9725	0.026	-17.9707
0.9725	0.027	-18.0216
0.9725	0.028	-18.0219
0.9725	0.029	-17.9766
0.9725	0.03	-17.8908
0.9725	0.031	-17.7693
0.9725	0.032	-17.6165
0.9725	0.033	-17.4366
0.9725	0.034	-17.2333
0.9725	0.035	-17.0101
0.9725	0.036	-16.7702
0.9725	0.037	-16.5165
0.9725	0.038	-16.2514
0.9725	0.039	-15.9774
0.9725	0.04	-15.6965